NATIONAL AERONAUTICS AND SPACE ADMINISTRATION

Space Programs Summary 37-63, Vol. III

Supporting Research and Advanced Development

For the Period April 1 to May 31, 1970

JET PROPULSION LABORATORY
CALIFORNIA INSTITUTE OF TECHNOLOGY
PASADENA, CALIFORNIA

June 30, 1970

NATIONAL AERONAUTICS AND SPACE ADMINISTRATION

Space Programs Summary 37-63, Vol. III

Supporting Research and Advanced Development

For the Period April 1 to May 31, 1970

JET PROPULSION LABORATORY

CALIFORNIA INSTITUTE OF TECHNOLOGY

PASADENA, CALIFORNIA

June 30, 1970

SPACE PROGRAMS SUMMARY 37-63, VOL. III

Preface

The Space Programs Summary is a multivolume, bimonthly publication that presents a review of technical information resulting from current engineering and scientific work performed, or managed, by the Jet Propulsion Laboratory for the National Aeronautics and Space Administration. The Space Programs Summary is currently composed of four volumes.

Vol. I.   *Flight Projects* (Unclassified)

Vol. II.   *The Deep Space Network* (Unclassified)

Vol. III.   *Supporting Research and Advanced Development* (Unclassified)

Vol. IV.   *Flight Projects and Supporting Research and Advanced Development* (Confidential)

Contents

SPACE SCIENCES DIVISION

TELECOMMUNICATIONS DIVISION

Contents (contd)

Contents (contd)

Contents (contd)

ASTRIONICS DIVISION

Contents (contd)

I. Space Instruments

SPACE SCIENCES DIVISION

A. Results of the Near Infrared Multidetector Grating Spectrometer Study, L. W. Carls and P. W. Schaper

1. Introduction

In November 1969, the Near Infrared Multidetector Grating Spectrometer (NFIR)[1] was selected for the tentative payload of the *Nimbus F* spacecraft. During the first half of Calendar Year 1970, a study was funded to define the data management for the experiment and a conceptual engineering design of the instrument. The study will be concluded in May 1970 with a Conceptual Design Review and a presentation to representatives of the Goddard Space Flight Center (GSFC). The final selection of science experiments for the *Nimbus F* payload is expected by October 1970.

2. Conceptual Design of the Instrument

a. Functional requirements. A preliminary functional requirements document[2] was written which fully describes all functional aspects and interfaces of the NFIR instrument. The requirements outlined in this document were derived from the performance obtained with the balloon flight model (Ref. 1). They were extended to include the addition of a telescope required to narrow the field-of-view of the instrument, a scanning mirror to extend the geographical coverage to include points not directly below the satellite track, and a series of cloud cover and water vapor detectors.

b. Optical design. The analysis of the optical design of the instrument head was performed by Beckman Instruments, Inc. (Ref. 2). The layout of the optical elements is shown in Fig. 1. Reference 2 is a computerized

---

[1]*Near Infrared Multidetector Grating Spectrometer,* a proposal for the *Nimbus F* mission, Jet Propulsion Laboratory, Pasadena, Calif., 1968.

[2]*Functional Requirements Document,* under preparation (JPL internal document).
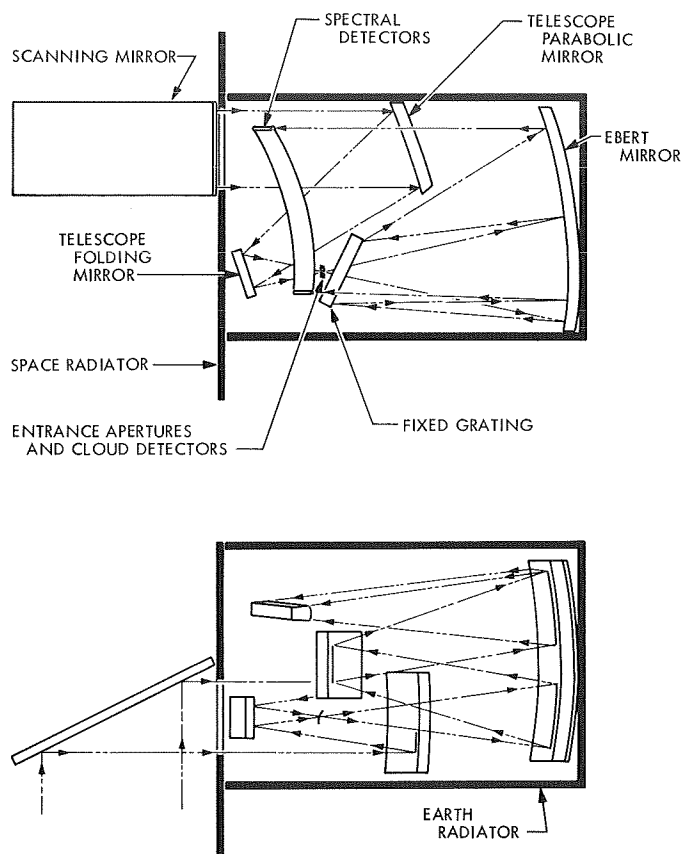
Fig. 1. NFIR head optics

ray-trace analysis of the monochromator design of the balloon flight instrument, optimized for minimum optical aberrations, and extended to include coverage of the 6-μ water band for the water vapor profile determination. A brief analysis of a 10-in. focal length parabolic telescope system is also included in the ray-trace analysis.

c. Thermal design. A thermal analysis showed that a flat plate radiator using second surface mirrors, with high reflectivity to absorptivity ratios, can be used to maintain the detector heat sink near 210°K. The radiator surface of 130 square inches was assumed to be oriented perpendicular to the spacecraft Y–Y axis viewing space. Radiator temperature fluctuations were kept within 2°K during one orbit. The proposed conceptual design also utilized a second radiator which looks toward earth and cools the instrument head to 255°K. This second radiator forms the underside of the instrument and is painted white.

d. Mechanical design. The mechanical design study resulted in the selection of moving mechanisms and prime

movers for these mechanisms. It was determined that three prime movers were required: the scanning mirror operator, the space viewing aperture operator, and the calibration wheel operator. The latter also controls the aperture selector for the dual entrance apertures.

The second phase of the mechanical design study resulted in the determination of the mechanical instrument/spacecraft interfaces. Figure 2 is an artist's conception of the NFIR instrument.

e. Electrical design. As part of this phase of the study, the integration (dwelling) times of all detectors were determined from signal-to-noise calculations. A detector design study was funded which resulted in a conceptual design of all detectors in the spectrometer head (Ref. 3).

The preamplifier, amplifier, demodulator integrator, and multiplexing circuitry was designed in block diagram form. A conceptual design for the data system was studied to arrive at a feasible scheme to feed the instrument output into the *Nimbus* Versatile Information Processor. Part types and counts were made to establish an approximate size for the electronics. It is estimated that two standard modules will be required.

3. Data Management

This portion of the study was broken into two phases. The first phase considers the reduction of data from the instrument (science and engineering data) to radiance versus wavelength listings. The second phase concerned itself with the methods to be employed for the conversion of spectral radiance information to temperature and water vapor profiles.

Two flow diagrams (Figs. 3 and 4) were generated, one for each phase. The engineering data reduction (first phase) shows little change in concept from that employed during the balloon experiment. New programming will be required to satisfy the added complexities of the flight instrument and the use of new computers.

The second diagram is based primarily on the programs developed for the inversion techniques by Chahine (Ref. 4). The complexity of this analysis is due to the requirement of obtaining meaningful soundings under varying conditions of cloud cover. It was shown that in most cases, meaningful profiles can be obtained, and in all other cases, data can be "flagged" for the experi-

menters and subsequently analyzed under non-real-time conditions.

4. Concluding Remarks

A study has been completed for the NFIR experiment, which can be used as a base line for a hard design of the instrument and for the detailed programming required to analyze all flight data as it is received. Detailed results of the study will be reported to the cognizant management center (GSFC) and NASA in late May 1970, and submitted in report form by the end of the fiscal year.

References

1. Schaper, P. W., and Shaw, J. H., "Performance of a Spectrometer Measuring Atmospheric Radiances Near 4.3 Microns," *Appl. Opt.*, Vol. 9, No. 4, pp. 924–928, Apr. 1970.

2. *Study of a Design Modification to the Infrared Multidetector Spectrometer for the Nimbus F Experiment*, Final Report. Beckman Instruments, Inc., Fullerton, Calif., Feb. 27, 1970.

3. *Study of Arrays of Detectors for the Nimbus F Near Infrared Multidetector Grating Spectrometer*, Final Report. Opt. Electronics, Inc., San Rafael, Calif., May 1970.

4. Chahine, M. T., "Determination of the Temperature Profile in an Atmosphere from its Outgoing Radiance," *J. Opt. Soc. Am.*, Vol. 58, 1968.
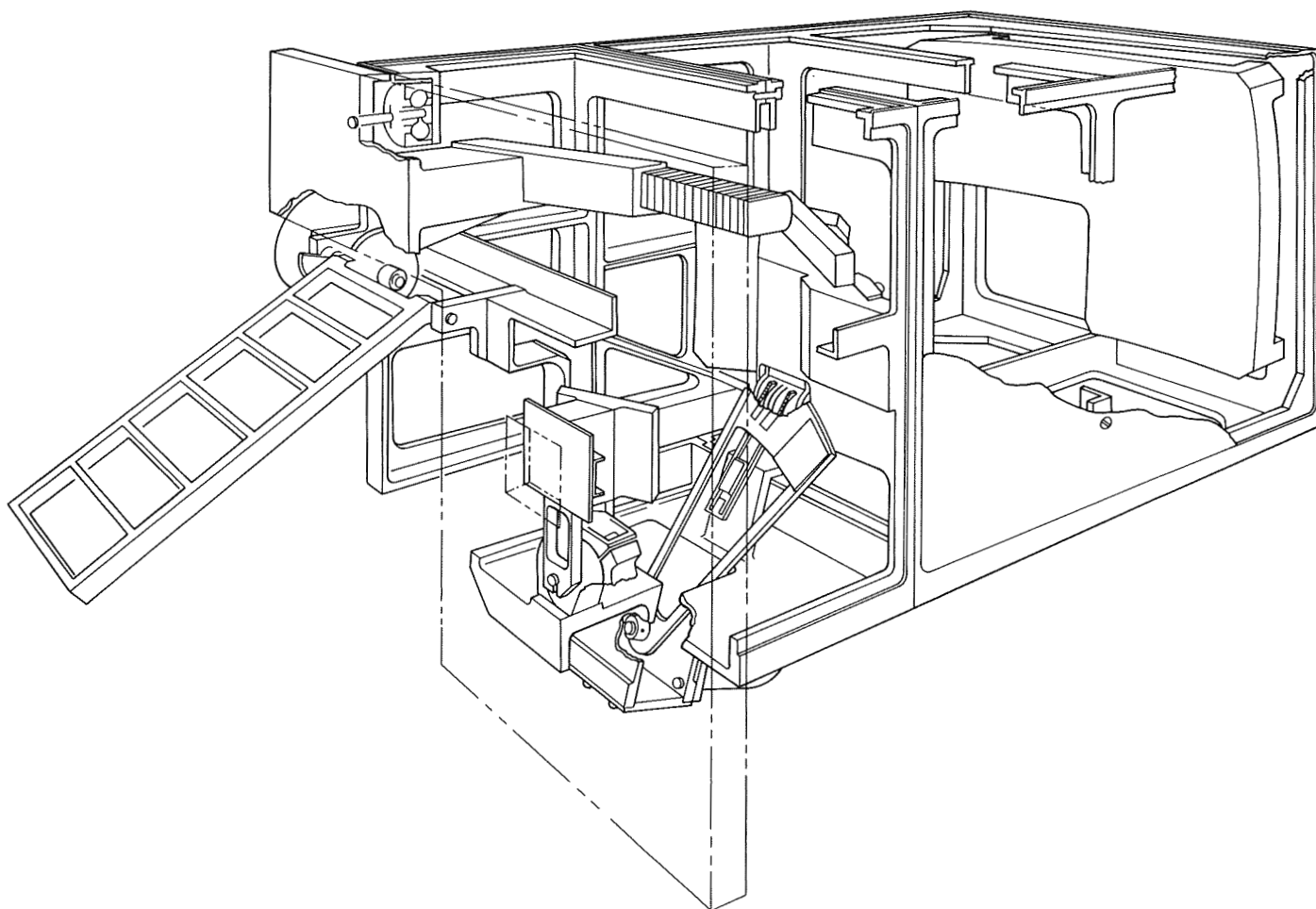
Fig. 2. NFIR instrument
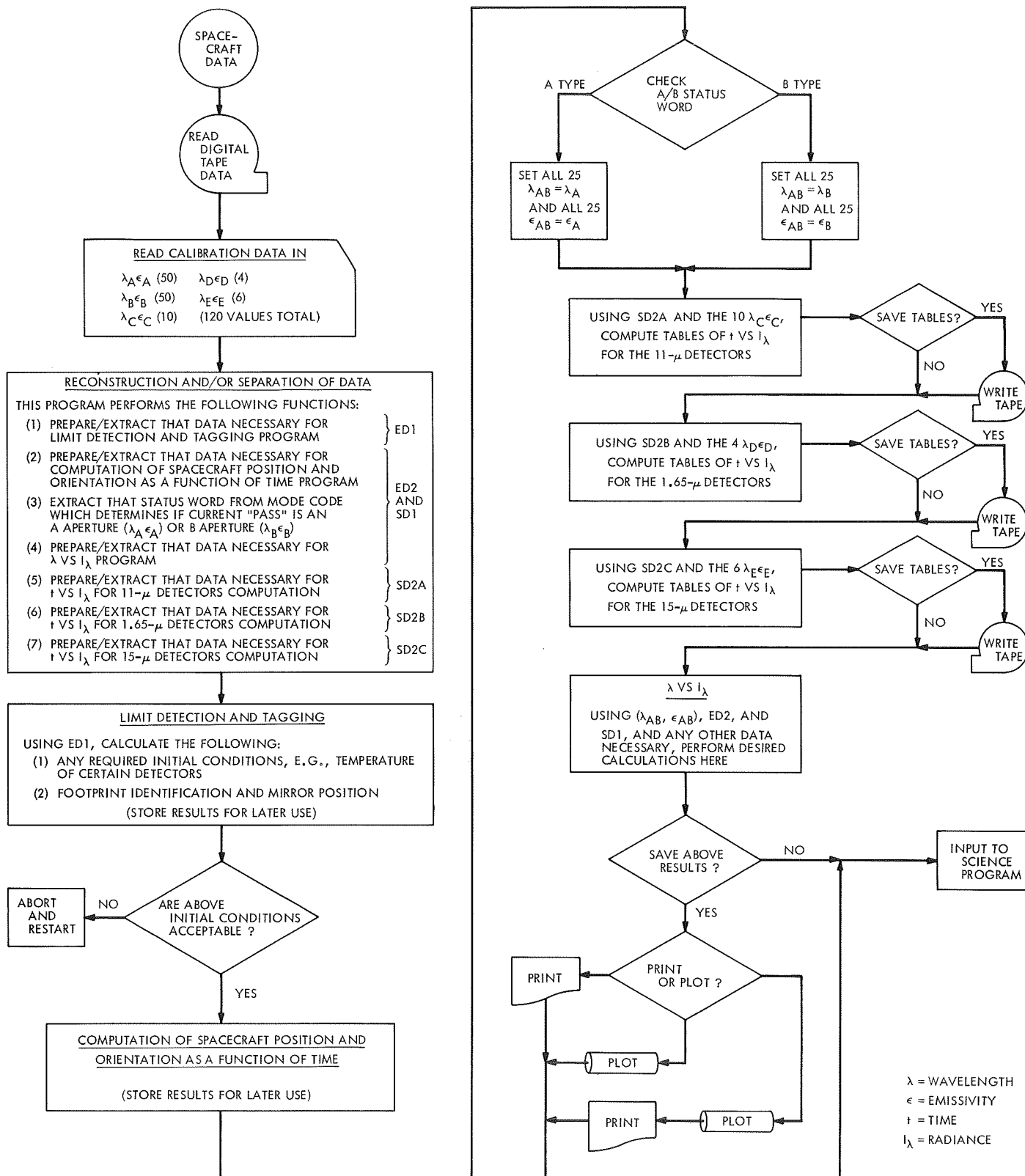
Fig. 3. Flow plan for engineering data reduction

Fig. 4. Flow plan for science data reduction

Legend:

T = TEMPERATURE
P = PRESSURE
N = FRACTIONAL CLOUD
I_λ = RADIANCE
I^* = EMISSION COMPONENT

II. Lunar and Planetary Sciences

SPACE SCIENCES DIVISION

A. A New Method for Determining SiO₂ Abundance in Silicate Glass From Powder Film Transmission Measurements in the Infrared, *J. E. Conel*

The significance of the so-called principal Christiansen frequency in crystalline silicates for compositional analysis, and the relationship between this frequency and important features of the emission spectra of powders, are pointed out in Ref. 1. The Christiansen frequency of a substance is conveniently determined from transmission measurements on thin ($\sim$30 μm) films of powder with particle sizes on the order of 10 μm or greater in diameter. This frequency is defined by the position of maximum transmission and represents the frequency of minimum scattering for the (average) complex refractive indices of the materials involved.

Transmission measurements on silicate glasses prepared from naturally occurring igneous rocks and the plagioclase mineral series have revealed a striking relationship between Christiansen frequency and SiO₂ abundance. The data illustrates a simple, rapid method for semiquantitative determination of silica abundances in synthetic rock

and mineral glasses and the crystalline material from which they were prepared. The glass preparation techniques used are described in detail in Ref. 2; the method of powder film preparation and analysis are described in Ref. 1. Glass compositions in all cases were independently determined by wet chemistry. The average infrared analysis time, including preparation of the glass, involved less than ½ h/sample.

The Christiansen frequency data for rock and plagioclase feldspar glasses are shown in Figs. 1 and 2, respectively. Ten rock glasses were selected from a suite of more than 100 available samples covering the entire range (and beyond) of SiO₂ abundance occurring in natural igneous rocks. The Christiansen frequency in rock glass is seen to follow closely the logarithmic abundance of SiO₂ by weight. A linear least-squares fit of the Fig. 1 data gives

$$\log(\text{wt\% SiO}_2) = -1.045 + 2.2 \times 10^{-3} \nu$$

where ν is in cm^{-1}; the standard deviation in $\log(\text{SiO}_2$ abundance) is 9.4×10^{-3}. A similar nearly linear relationship is found for the plagioclase feldspar glasses (Fig. 2).
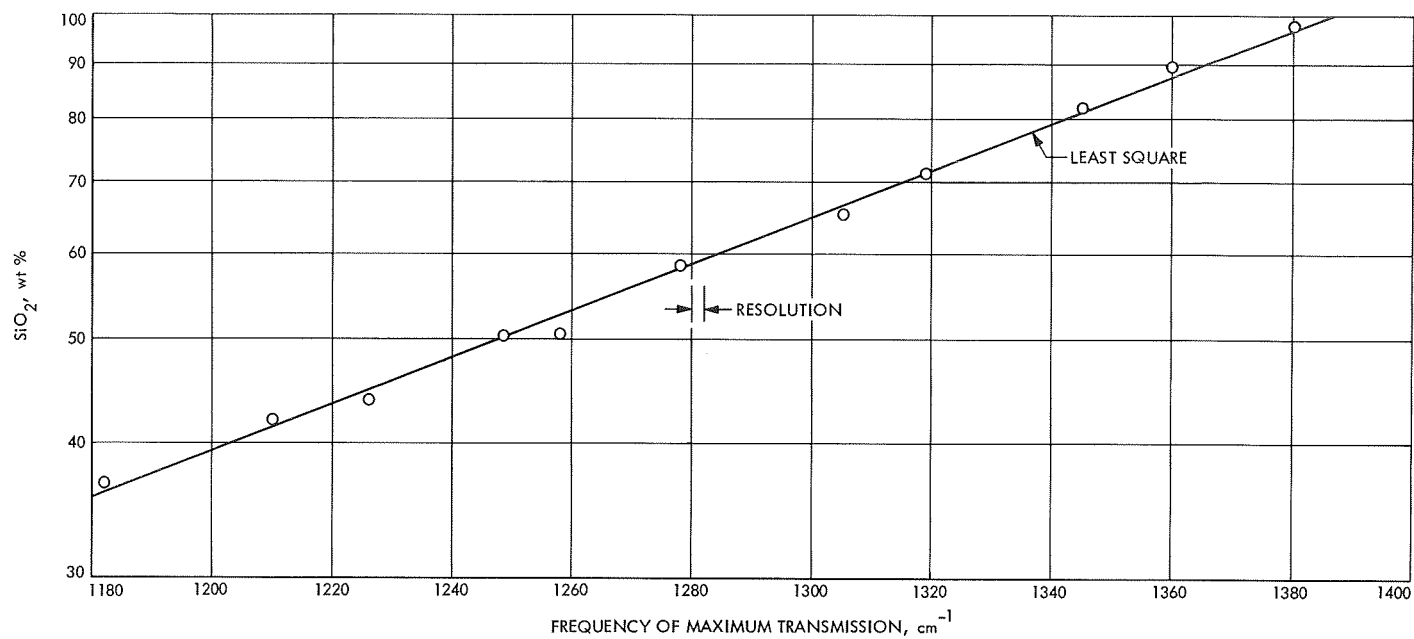
Fig. 1. Relationship between Christiansen frequency and SiO_2 abundance for synthetic rock glasses
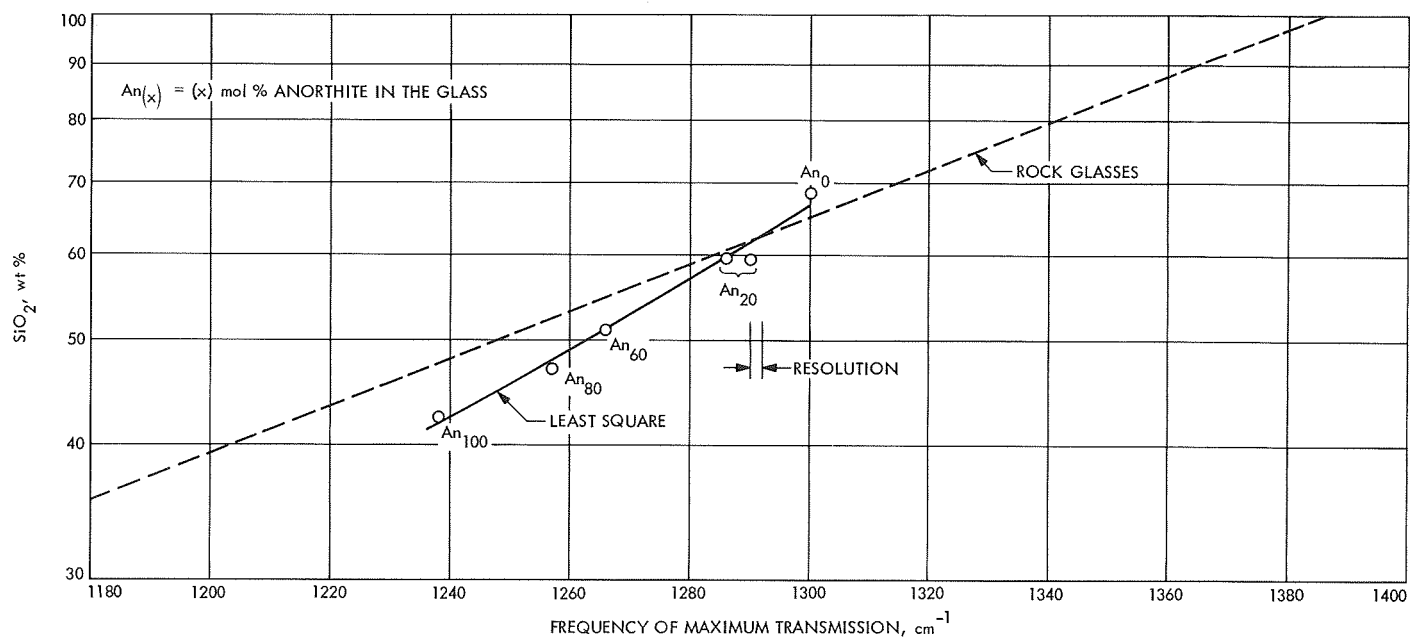
Fig. 2. Christiansen frequency of plagioclase feldspar glasses

The data points in this instance have been identified both by silica abundance and mol% An(Anorthite = $CaAl_2 Si_2 O_8$) in the glass. Data points for 20% An represent the type of spread encountered with individual treatment of supposed compositionally identical but different feldspars. Using least-squares techniques, these data are fit by a polynomial of second degree

$$\log(\text{wt}\%\, SiO_2) = 4.98 - 8.39 \times 10^{-3} \nu + 4.59 \times 10^{-6} \nu^2$$

with a standard deviation of 8.4×10^{-3}. A refinement of this curve will be made using mixtures of standard synthetic feldspars.

From the graphs, we can estimate the errors expected in SiO_2 abundance determination imposed by the spectral resolution used ($\simeq 2$ cm^{-1} throughout the interval). For rock glass, for example, the errors vary from 0.5% at 1180 cm^{-1} to 1% at 1380 cm^{-1}. Errors in glass abundance arising from statistical uncertainties in the data are $\pm 1\%$ (standard deviation of 10^{-2}) for SiO_2 abundance of 50%. Thus, with the present data and measurement techniques, abundance estimates are possible to within 1.5–2%.

Figures 1 and 2 show that ordinary rock and plagioclase glasses are distinguished on the bases of Christiansen frequency measurements except in cases where plagioclase glass contains less than 20% An; the small differences in curve slope and position arise from the substitution of Al for Si in the plagioclase glasses since the differences increase as the Al/Si ratio in plagioclase increases. A similar but more profound distinction was noted in X-ray analysis of these materials (D. Nash, SPS 37-20, Vol. IV, pp. 192–196). Apparently Al-substitution has less effect on lattice parameters governing infrared refractive indices in silicate glasses than on parameters governing X-ray diffraction properties.

In the preparation of glass powders for analysis by the present method, it is important to obtain particle size distributions with fragments predominantly greater than 10 μm in diameter. The reason for this is given in Ref. 1, where it is shown that the frequency of the transmission maximum obtained with quartz powder films as a function of particle size follows closely the minimum value of the coefficient of extinction Q_{ext} computed from Mie theory. As particle size decreases, the minimum in Q_{ext} shifts to shorter wavelengths; it asymptotically approaches a fixed value (determined by averaging both complex indices of refraction) as particle size increases. For quartz, the fixed value is determined as that wavelength where the real parts of the complex ordinary and extraordinary indices are, on the average, equal to unity. Transmission spectra of films of very small particles (~ 1 μm) do not determine the true Christiansen frequency. In practice, consistent results were obtained from the ≤ 37-μm particle size fraction obtained from ceramic or agate mortar grinding of glass samples.

Analysis of these results in terms of classical dispersion theory has not been made. We might expect, however, that the relationship displayed indicates systematic variations in glass structure with composition, and that a complete study could lead to new insights into structure and bonding in silicate glasses.

References

1. Conel, J. E., "Infra-red Emissivities of Silicate: Experimental Results and a Cloudy Atmosphere Model of Spectral Emission From Condensed Particulate Mediums," *J. Geophys. Res.*, Vol. 74, No. 6, pp. 1614–1634, 1969.

2. Nash, D. B., "New Technique for Quantitative SiO_2 Determinations of Silicate Materials by X-ray Diffraction Analysis of Glass," *Advance. X-Ray Anal.*, Vol. 7, pp. 209–235, 1964.

III. Bioscience

SPACE SCIENCES DIVISION

A. Pyrolysis of Natural Products: Identification of Products From Nucleotide Pyrolysis by High Resolution Mass Spectrometry, *H. G. Boettger and A. M. Kelly*

During the past years a long series of pyrolysis experiments on biologically important compounds has been conducted at JPL in preparation for life detection experiments on the planets (Refs. 1, 2, and 3).

The present study was designed to investigate possible alternative methods to the gas chromatograph/mass spectrometry (GC/MS) approach for the analysis of pyrolysis products from nucleic acid materials. The main reason for this investigation is to determine whether the lack of characteristic fragments in pyrolysis–GC/MS experiments is due to lack of characteristic products being formed under pyrolysis conditions or to their inability to pass through the gas chromatographic column.

The experimental setup includes a modified MS-902 and the computerized data system described previously

(Refs. 4, 5, and 6). The modifications on the MS-9 include a high capacity pumping system (700 liters/s at the diffusion pump), a direct coupled capillary or Scot-type GC column for the GC/MS part of the experiments, and a new heated probe for the MS-9 direct insertion lock. The oven for the gas chromatic column is fitted with a pyrolyzer and hypodermic injection port (Ref. 3). The oven can be operated isothermally and/or programmed from below ambient to 400°C. However, due to limitations on the columns which are suitable for the overall experiment, maximum operating temperatures did not exceed 220°C.

Figure 1 shows the modified probe for the MS-9 insertion lock. It is fashioned after the one described by Teeter, et al.[1] and is interchangeable with the standard probe. However, it can be heated to approximately 850°C and cooled to the temperature of liquid nitrogen. A thermocouple is located near the tip of the probe to monitor and/or control the temperature.

---

[1]Private communication.
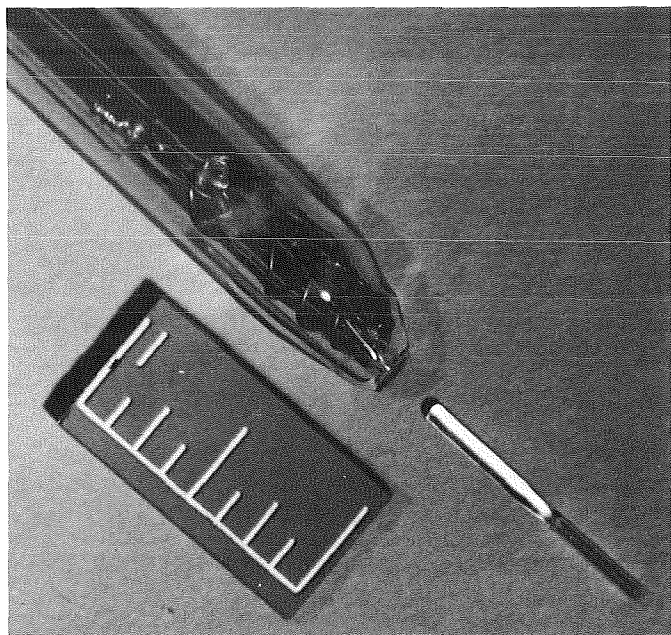
Fig. 1. Modified probe for MS-9 insertion lock

Table 1. Analysis of pyrolysis data

1. Record and digitize all spectra

2. Manually inspect pyrogram and spectra

3. Select those spectra which appear to be due to single components and submit them to a search of the library

4. Attempt identification of spectra due to multiple components by a combination of computer and manual methods

5. Peaks or components of a peak still unidentified are submitted to high-resolution mass analysis

6. Verify assignments by checking against GC retention data (in case of GC/MS)

During vacuum probe pyrolysis approximately 1 mg is loaded into the probe cavity and pumped down. Spectra are recorded at approximately 30-s intervals as the probe is heated at a programmed rate continuously or step-wise from ambient to 750°C. The beam monitor output is recorded during the entire run and marked automatically whenever a spectrum is taken. During all experiments spectra are recorded at a resolving power which is never less than that required for mass measurement. A dynamic resolving power of at least 1/5000 is preferred; however, useful data can be obtained at a lower resolving power.

The analysis of the data is carried out by our previously described data system in combination with frequent monitoring by the investigator. The reason for monitoring these data more frequently, in contrast to the usual high-resolution processing, is to eliminate redundant data and easily identified spectra at an early stage of the processing, and thus reduce the amount of data to be fully processed. Should questions arise at a later date, processing of part or all of these spectra can be resumed as required. The presently used system represents a simulation of man–machine interfacing on the remote console of a time-shared system such as the Univac 1108.

Table 1 summarizes the data flow. The recorded spectra are digitized and converted to mass versus intensity data.

The data are then inspected for obvious single-component spectra and separated from suspected multi-component spectra. From the former the spectra of readily identified substances are eliminated, while the remaining single-component spectra are submitted to a library search. The results of this search provide identification of the majority of this group. The remainder is submitted for elemental composition calculation and a final identification is attempted by conventional high-resolution techniques.

Meanwhile, the obvious mixture spectra are inspected for recognizable components. If these are detected, intensity-adjusted reference spectra are subtracted and the residuals are submitted for library search. Spectra which still can not be identified are also processed further by the high-resolution mode in order to get a handle on the mixture.

Finally, assignments are checked against standard spectra and, in the case of GC/MS, against retention data.

Typical results are shown in Tables 2 and 3. The nucleic acid bases, e.g., adenine, thymine, etc., are released intact at 175°C and dominate the part of the spectrum above mass 50. As the temperature of pyrolysis continues to rise, only low-mass fragments, such as HCN, CO_2, etc., are found in high intensity.

The data show that pyrolysis does indeed yield extremely characteristic fragments, at least under the conditions described above. The bases can be identified qualitatively and, hopefully, quantitatively with some

Table 2. Low molecular weight products of vacuum pyrolysis of DNA

Product	105°C	175°C	225°C	330°C	400°C	450°C	500°C	600°C	600°C
HCN	800	18000	19000	56000	98000	51000	132000	115000	14000
CO	20000	>125000	16000	60000	60000	<10000	55000	>125000	>125000
CO_2	13000	>210000	66000	144000	115000	36000	115000	190000	10000
CHO	800	43000	9000	12000	15000	5000	4000	7000	0
C_2H_5O	3000	12000	13000	15000	15000	11000	8000	7500	0
C_3H_3O	0	0	37000	10000	6000	4000	4000	4000	0
C_5H_5O	0	0	240000	—	26000	7000	4500	4000	15000
C_3H_3	1800	117000	18000	27000	15000	4000	5000	5500	0
C_3H_6	400	44000	1800	5500	5000	900	2000	1800	0
C_4H_7	2000	40000	2000	4700	5000	2400	3600	3600	0
CHNO	900	18000	1700	20000	11000	4700	7300	10000	0
$C_4H_4N_4$	0	17000	—	1100	900	0	0	0	0

Table 3. Higher molecular weight products of vacuum pyrolysis of DNA

Product	105°C	175°C	300°C	450°C	600°C
Cytosine	0	6500	450	0	0
Methylcytosine	0	600	0	0	0
Thymine	0	102000	10000	12000	12000
Adenine	0	80000	2400	1500	2100
Guanine	0	0	1600	0	0
Adenosine	0	800	0	0	0
Adenosyl	0	1700	0	0	0
Deox aden, $-2H_2O$	0	55000	3900	3400	2900
HCN	800	18000	56000	98000	132000

refinements of the technique, by a direct inlet furnace/ mass spectrometer experiment even though they are not sufficiently volatile to pass through a gas chromatograph.

The major products of nucleic acid pyrolysis using the vacuum probe technique are summarized in Table 4. In contrast, Table 5 shows the products found by GC/MS

Table 4. Major products of nucleic acid vacuum pyrolysis

Nucleic material	Product
DNA	Cytosine, methyl-cytosine, thymine, adenine, guanine, adenosine, deoxyadenosine
RNA	Same as DNA
Polyadenylic acid	Adenine, adenosisine
Polycytidylic acid	Cytosine
Flavin-adenine dinucleotide	Adenine, flavin
Polyadenylic-cytidylic acid	Adenine, cytosine
Polyuridylic acid	Uracil
Adenylic acid	Adenine
Cytidylic acid	Cytosine
Thymidine-5-triphosphate	Thymine
Uridine triphosphate	Uracil
Guanosine triphosphate	Guanine

Table 5. Products of DNA found by GC/MS pyrolysis at 500°C

HCN, CO_2, H_2O	Butanenitrile
Acetonitrile	Pyridine
Acrylonitrile	Methyl-pyridine
Methacrylonitrile	Methyl-pyrazine

pyrolysis at 500°C. These products are mostly of a minor nature, if one excludes HCN, CO_2, and H_2O. In addition, they are not characteristic of nucleic acid-type materials.

References

1. Bentley, K. E., et al., *AAS Sci. Technol.*, Vol. 93, p. 2, 1964.

2. Whitten, D. G., Bentley, K. E., and Kuwada, D., *J. Org. Chem.*, Vol. 31, p. 322, 1966.

3. Simmonds, P. G., Shulman, G. P., and Stembridge, C. H., *J. Chromatographic Sci.*, Vol. 7, p. 36, 1969.

4. Boettger, H. G., 15th Annual Conference on Mass Spectrometry and Allied Topics, May 14–19, 1967, Denver, Colo., N31, p. 90, 1967.

5. Boettger, H. G., American Chemical Society Western Regional Meeting, Anaheim, Calif., Oct. 30–Nov. 1, 1967, Abstract 233, 1967.

6. Boettger, H. G., 17th Annual Conference on Mass Spectrometry and Allied Topics, May 19–22, 1969, Dallas, Tex., 1969.

IV. Physics

SPACE SCIENCES DIVISION

A. General Relativistic Axially Symmetric Rotating Perfect Fluids, *B. K. Harrison*

There has been considerable recent interest in the self-gravitation of rotating dense bodies (Refs. 1 and 2). This has been due both to the discovery of pulsars and to the basic theoretical question of the possible effect of rotation on gravitational collapse. To facilitate the mathematical treatment of this problem, the author has examined the general relativistic equations for such a rotating system (specialized to perfect fluids with axial symmetry) and found that (a) the relativistic partial differential equations can be cast into an elegant form that uses vector differential operators in a two-dimensional curvilinear space, and (b) a variety of coordinate systems can then be chosen, each of which simplifies the equation in some way. In particular, one choice of coordinates reduces the number of dependent variables (metric tensor coefficients) to three, a simplification not previously exploited.[1]

---

[1]Private communication to the author from H. D. Wahlquist.

A more extensive and mathematically detailed description of this research will appear in the open literature.[2]

References

1. Wahlquist, H. D., *Phys. Rev.*, Vol. 172, p. 1291, 1968.

2. Hartle, J. B., and Thorne, K. S., *Astrophys. J.*, Vol. 153, p. 807, 1968.

B. Rates and Mechanism of Alkyne Ozonation, *W. B. DeMore*

1. Introduction

Ozonation of unsaturated hydrocarbons has occupied the attention of chemists for more than a century (Ref. 1). The alkene reaction with O_3 is now fairly well understood in terms of the Criegee mechanism (Ref. 2), within

---

[2]Harrison, B. K., *Phys. Rev.*, 1970 (in press).

the limitation that this mechanism essentially provides only a plausible route to product formation and says little about kinetic or thermochemical factors. Ozonation reactions traditionally have been studied in solution. Thus, the results apply only to that limiting case, which in effect is the high-pressure region of the reaction. Under the latter circumstances, excitation among the products, arising from reaction exothermicity, is rapidly quenched by the solvent. Also, there is some evidence that cage effects alter the reaction course in solution. The liquid phase work thus does not provide an adequate basis for understanding the role of hydrocarbon ozonation under gas phase conditions, such as in air pollution. For that purpose, one needs to know the identity, energy content, lifetime, and reaction paths of all intermediates and products of the reaction.

Even less is known about the ozonation of acetylenic hydrocarbons (Refs. 2 and 3), despite the fact that this is an important class of reactions that bears significant similarities and differences from the alkene ozonations. In regard to the air pollution problem, acetylene is an especially interesting case in connection with understanding the role of different hydrocarbon classes. Semiempirical classifications place acetylenes near zero in regard to photochemical smog activity (Ref. 4), a fact that is frequently attributed to the relatively slow rate of O_3 reaction with acetylenes. This is not entirely satisfactory, however, because O_3 is not present in the early stages of daily smog development. Thus, the slowness of the O_3 reaction should be irrelevant during the important early phases when, for example, NO is converted to NO_2. On the other hand, oxidation of hydrocarbons by atomic oxygen is usually considered to be the most important process at the outset of smog development. In that connection, acetylene reacts only about five times slower than ethylene,

which is very high on the scale of photochemical smog reactivity. Therefore, a fundamental understanding of acetylene oxidation would shed considerable light on the true role of different hydrocarbon classes in smog formation. For that reason, we have undertaken a general study of the oxidation of acetylenic hydrocarbons by both ozone and atomic oxygen.

In an earlier publication (Ref. 5 and SPS 37-51, Vol. III, pp. 189–193), rate measurements were reported that indicated that the O_3—C_2H_2 reaction is fundamentally different from olefin ozonation in regard to the rate-determining step. The pre-exponential factor for the acetylene reaction was found to be 10^3 times higher than for the olefin reaction, and the relative inertness of C_2H_2 to attack by O_3 was shown to result from a remarkably high activation energy of 10.8 kcal/mole. It is important to verify and extend these findings because, if correct, the acetylene ozonation would constitute the first case in which a 1,3 cycloaddition reaction (Ref. 6) has been shown to occur in a nonconcerted fashion. The cycloaddition reaction, which is quite general, is believed to proceed by simultaneous formation of two new bonds to give a 5-membered ring intermediate:

$$\hspace{3cm} (1)$$
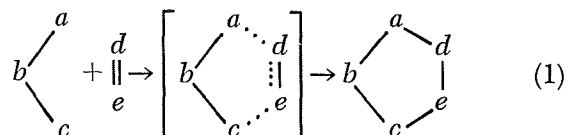
In Ref. 5 and SPS 37-51, Vol. III, it was shown that the pre-exponential factor of the O_3—C_2H_4 reaction was indeed consistent with a cyclic 5-membered ring transition state:

$$\hspace{3cm} (2)$$
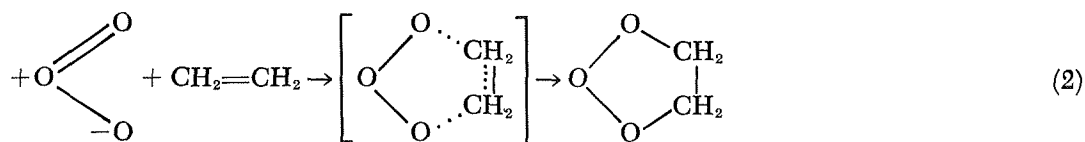
On the other hand, it was found that the pre-exponential factor of the C_2H_2 reaction was entirely too high to accommodate a cyclic intermediate, and an open-chain transition state was found to account more satisfactorily for the observed A-factor:

$$O_3 + C_2H_2 \rightarrow [H\dot{C}{=}CHO{-}O{-}\dot{O}] \rightarrow \text{products} \hspace{1cm} (3)$$
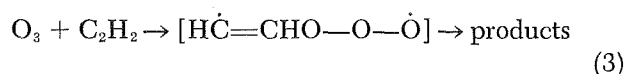
A more complete mechanism could not be deduced at that time, however, primarily because the equipment in use was not suitable for product analyses.

This article describes additional experiments on the ozonation of acetylene and several substituted acetylenes, using a long-path infrared spectrometer that yields an *in situ* product analysis in addition to rate measurements.

Coupled with thermochemical calculations by the method of group additivity (Ref. 7), the results provide considerable insight into the detailed mechanism of acetylene ozonation and tend to verify the earlier measurements and conclusions.

2. Experimental Methods

a. Apparatus. The long-path cell was a 40-meter White cell of Perkin-Elmer manufacture, attached to a Perkin-Elmer Model 421 infrared spectrometer. Two types of cell enclosure were used. One was a length of large-diameter pyrex tubing sealed at each end with O-ring flanges and the other was a similar length of aluminum tubing installed after the pyrex tube cracked. All metal surfaces inside the cell, with the exception of the gold mirrors, were heavily sprayed with a teflon coating ("GS-3," manufactured by Ram Chemicals, Gardena, California). This material is effective in reducing surface decomposition of ozone.

The cell was also fitted with an analyzing beam of 2537 Å light, with a path length of 51.5 cm, that permitted simultaneous monitoring of O_3 absorption in the strong Hartley band while observing the infrared spectrum. Thus, the ozone concentrations could be monitored either in the UV or IR using the 1053 cm^{-1} band. A linear relationship between the UV and IR optical densities was found, indicating satisfactory adherence of the IR absorption to Beer's law.

b. Chemicals. Acetylene (99.6% minimum purity), methylacetylene (96% minimum purity), and ethylacetylene (95% minimum purity) were purchased from Matheson. The acetylene was freed of acetone inhibitor by passage through a U-tube at −78°C. Dimethylacetylene was obtained from Farchan Research Laboratories. Gas chromatographic analysis (8-ft Porapak Q column) showed that all the substituted acetylenes contained a small acetylene impurity; this was insignificant in view of the similarity of reaction rates for the different acetylenes. The absence of olefin impurities was confirmed by the IR spectra. Ozone was prepared from a Tesla coil discharge in Matheson Ultra High Purity Grade O_2.

c. Procedure. The acetylene was first introduced into the evacuated cell at a pressure in the 0.5–3.0-torr range as measured with a Texas Instruments quartz spiral manometer. The cell was then pressurized to 500 torr with high-purity Ar, and then O_2 (usually 5 torr) was added. The total pressure was then increased to 700 torr

with additional Ar. An initial IR spectrum was taken in the range 2.5–15 μm. An appropriate quantity of O_3 (sufficient to give about 0.05 torr in the cell) was prepared in a 77°K U-tube just outside the cell and then carried into the cell by a flow of Ar through the U-tube. In some of the later experiments, the gas mixtures were stirred mechanically. Rates of O_3 disappearance were followed either by the UV or IR absorption. Rates of product formation could also be monitored in the IR.

Rate constants were calculated by plotting the O_3 optical density (OD) (either UV or IR) according to the equations

$$\frac{(OD)_t}{(OD)_o} = e^{-k't} \tag{4}$$

$$\ln(OD)_t = \ln(OD)_o - k't \tag{5}$$

Then

$$k(M^{-1}s^{-1}) = \frac{k'}{[alkyne]} \tag{6}$$

3. Results

a. Rate measurements. The ozone decay was accurately first-order in all experiments, as would be expected in view of the excess acetylene concentrations. However, there was evidence of complications arising from wall effects and also from secondary radical reactions that destroy ozone. The latter effect, which was not unexpected (see *Subsection 4*), was detected through an observed dependence of the reaction rate on the presence of O_2. Addition of 5 torr O_2 reduced the rate of O_3 decay by a factor of about 5 or 6 relative to the rate with no added O_2. Higher O_2 concentrations had no further effect. The existence of a wall reaction was indicated by an increase in the calculated rate constants at low alkyne concentrations (0.1–0.5 torr). For that reason, the measurements were made at higher concentrations, in the 2–3 torr range, at which point no further pressure dependence was noted. It is quite possible that the wall reactions actually involve the gold-surfaced mirrors, especially since the rates were insensitive to changing from the pyrex cell enclosure to the teflon-coated aluminum tube.

Results from a number of individual experiments are listed in Table 1. From those data, the rate constants

listed in Table 2 were selected as averages of the more reliable experiments (those at higher alkyne concentrations and with added O_2 to suppress radical decomposition of O_3).

It is significant that the rate constant for acetylene (Table 2) agrees very well with previous rate data based on our own measurements at low temperatures (-30 to $+10°C$) and those of Cadle and Schadt (Ref. 8) at 30°C. The three sets of data are summarized in an Arrhenius plot shown in Fig. 1.

Table 1. Rate data for alkyne ozonations at 21°C

P_{Alkyne}, torr	P_{O_3} (initial), torr	P_{O_2}, torr	O_3 monitored by	k, M^{-1} s^{-1}
HC≡CH				
0.35	0.017	0	IR	105.0
0.44	0.012	0	IR	96.0
0.45	0.024	1	IR	49.2
1.31	0.035	5	IR	17.5
2.02	0.033	5	IR	15.3
0.42	0.040	50	IR	19.7
1.77	0.034	5	UV	18.1
1.77	0.034	5	IR	19.4
1.70	0.042	5	UV	21.1
1.74	0.041	5	IR	17.1
1.76	0.027	5	IR	18.1
2.30	0.039	5	UV	19.7
2.30	0.039	5	IR	15.5
CH₃C≡CH				
0.42	0.049	5	IR	16.8
0.48	0.021	5	IR	17.5
1.10	0.020	5	IR	12.3
1.46	0.037	5	UV	18.5
1.52	0.041	5	IR	9.0
1.57	0.043	5	IR	8.7
2.00	0.016	5	IR	11.0
2.31	0.033	5	UV	16.4
CH₃C≡CCH₃				
1.85	0.030	5	UV	22.8
2.22	0.054	5	UV	27.2
2.48	0.031	5	UV	20.0
CH₃C₂C≡CH				
1.04	0.036	5	UV	32.3
1.82	0.032	5	UV	27.7
1.83	0.027	5	UV	20.3
2.34	0.036	5	UV	24.4
2.67	0.043	5	UV	17.7

Table 2. Rate constants for alkyne ozonations

Alkyne	k, M^{-1} s^{-1} (21 $\pm 1°C$)[a]
HC≡CH	18 ±3
CH₃C≡CH	13 ±7
CH₃C≡CCH₃	20 ±3
CH₃CH₂ C≡CH	24 ±8

[a]The error limits are based on scatter between different runs, and do not represent the absolute reliability of the rate constants (Subsection 4).
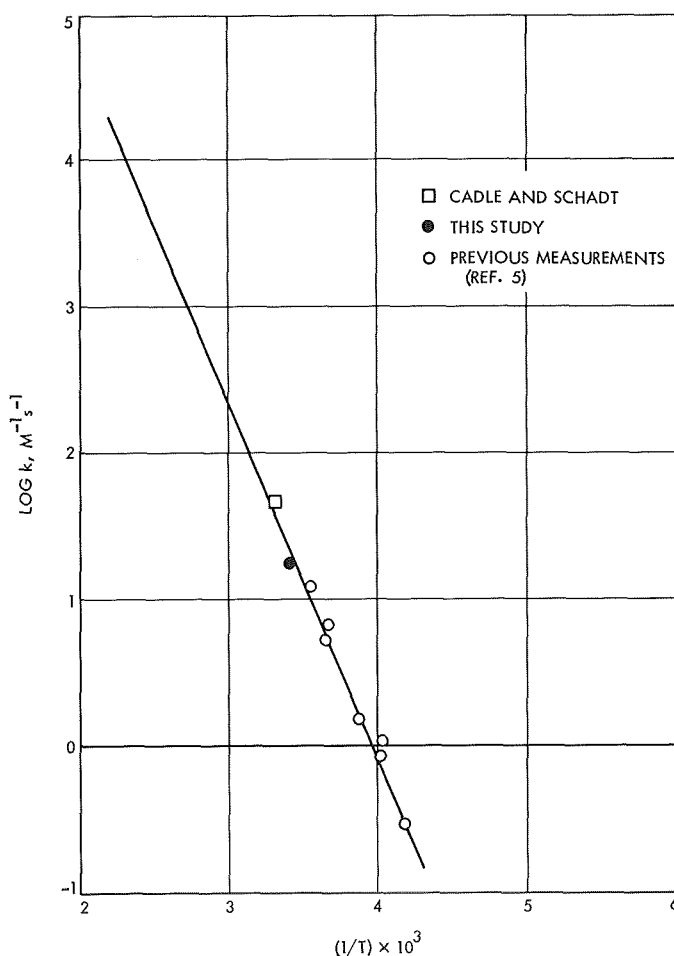
Fig. 1. **Summary of rate data for ozonation of acetylene**

b. Products. In the case of acetylene, the IR spectrum showed that HCOHCO (glyoxal), CO, CO_2, and HCOOH were products of the reaction. Glyoxal was identified by comparison with the IR spectrum of an authentic sample that was prepared by ethylene oxidation over SeO_2—P_2O_5. The amount of glyoxal formed corresponded to about one-quarter of the O_3 decomposed. However, the rate of glyoxal production was not proportional to the rate of O_3 decay. In most of the experiments, half of the glyoxal was formed in 1 min of reaction under conditions where the half-time of O_3 reaction was about 7 min. A surface reaction is suspected as the source of the glyoxal formation; in this connection, it has already been mentioned that the rate measurements showed evidence of a surface reaction. Further, many of the rate measurements showed an accelerated O_3 loss during the first 1 or 2 min of reaction. Experiments at different initial O_3 concentrations showed that the high initial rates of glyoxal formation were not the result of a high-order dependence on O_3 concentration.

The ratio of CO formed to O_3 reacted was 1.0 $\pm$0.2, and the rate of CO formation did not show anomalous behavior similar to that of glyoxal. The ratio $\Delta CO_2/$ $-\Delta O_3$ was about ¼, although this yield must not be taken too seriously in view of the occasional spurious formation of CO_2 when O_3 and any hydrocarbon are present in the cell. The formic acid yield was not suitable for measurement, largely because that product was observed to disappear rapidly (probably on the walls). The other alkyne products are listed in Table 3.

Table 3. Alkyne products

Alkyne	Products detected[a]
$CH_3C\equiv CH$	CO, CO_2, HCOOH, CH_2O, $CH_3COOH(?)$, CH_3COCHO
$CH_3C\equiv CCH_3$	$CO(?)$, CO_2, CH_2 CO, CH_3COOH, $CH_3COCOCH_3$
$CH_3CH_2 C\equiv CH$	$CO(?)$, CO_2, $CH_3 CH_2$ COCHO

[a]Not necessarily in order of relative amount.

Product analysis, particularly on a quantitative basis, was more difficult for the substituted alkynes because of interference in the IR spectrum by the parent alkyne. (Also, product analysis was more difficult partly due to the unstable nature of some of the products.) However, certain definite conclusions can be reached. First, it is clear that dimethylacetylene gives ketene and acetic acid as major products:

$$CH_3C\equiv CCH_3 + O_3 \rightarrow CH_3COOH + CH_2CO$$
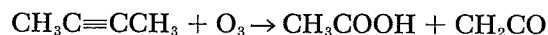
Biacetyl was also an important product, although as in the case of glyoxal it may not be formed in the homogenous gas phase reaction.

It is important to note that no CH_2CO was produced in the $CH_3C\equiv CH$ reaction.

4. Discussion

a. Rates. The data shown in Fig. 1 provide increasingly convincing evidence that the "high" A-factor for the O_3—C_2H_2 reaction is correct. There are three independent rate measurements in the upper temperature region (i.e., near room temperature), and the excellent agreement among them casts considerable doubt on the possibility of serious error. It is possible that all three rate measurements are slightly high owing to effects such as the observed surface reaction. However, the low temperature rates would probably also be slightly high, so that the general conclusions concerning the A-factor and activation energy would not be greatly altered.

The significance of the high A-factor is that the O_3—C_2H_2 reaction does not fit into the general mechanism involving concerted addition (Reaction 1), which has been put forward for 1,3 cycloaddition reactions (Ref. 6), despite the fact that the reaction almost certainly falls into that category.

The concept of concerted addition is mainly based on the assumption that two-step addition would produce charge separation and thus be energetically unfavorable:

$$O_3 + HC\equiv CH \rightarrow \left[\begin{array}{c} \ddot{O} \\ \ddot{O} \diagdown \diagup \ddot{O}^{\ominus} \\ \diagdown C = C^{\oplus} \diagup \\ H \diagup \qquad \diagdown H \end{array} \right] \qquad (7)$$

However, the charge separation need not develop fully (e.g., the biradical-type intermediate depicted in Reaction 3). Therefore, the principle of minimum charge separation may not be an infallible guide to reaction mechanism in every case. It may be noted that a two-step, biradical-type mechanism has been proposed by Firestone (Ref. 9) for 1,3 cycloaddition reactions. However, since at that time no evidence for high A-factors in these reactions had been put forward, it was necessary for Firestone to account for the low reaction probability by assuming a low transmission coefficient (in the terminology of transition-state theory) for which there is no precedent.

In connection with the question of concerted vs non-concerted addition, it is of interest to determine if any 1,3 cycloaddition reactions, other than the acetylene ozonation, show evidence of the high A-factors characteristic of open-chain intermediates. Unfortunately, few kinetic parameters have been measured for these reactions, and some of those that have been measured have not been quantitatively interpreted. For example, the ozonation of benzene in CCl_4 solvent gives an entropy of activation of -23 gibbs/mole (Ref. 10). This value of $\Delta S^{\ddagger}$ has been taken as evidence for concerted addition

(Ref. 6), but actually that entropy loss is more consistent with the following open-chain transition state[3]:

$$O_3 + C_6H_6 \rightarrow \left[\text{(structure)} \right] \quad (8)$$

The benzene ozonation, therefore, seems to show a behavior similar to that of acetylene in regard to the structure of the transition state in the rate-determining step.

A surprising result of the present work is that the substituted acetylenes react at the same rates, within experimental error, as does acetylene. This behavior contrasts sharply with that of the substituted alkenes. For example, the 2-butenes (cis and trans) react with O_3 about 10 times faster than ethylene (Ref. 11). Similarity of the rates at 21°C does not prove that the Arrhenius parameters for all the substituted acetylene ozonations are the same, although it seems unlikely that they are greatly different. Further work at other temperatures is planned to measure these quantities individually.

---

[3]The entropy of the open-chain structure was estimated by the method of group additivity (Ref. 7), using an approximate ring connection of 20 gibbs/mole. The result was 98 gibbs/mole, which gives $\Delta S^{\ddagger} = -23$ gibbs/mole.

b. Mechanism. The following steps are proposed for the overall gas phase O_3—C_2H_2 reaction:

$$O_3 + C_2H_2 \rightarrow [H\dot{C} = CH—O—O—O\cdot] \rightarrow \left[\text{(structure II)} \right] \quad (9)$$
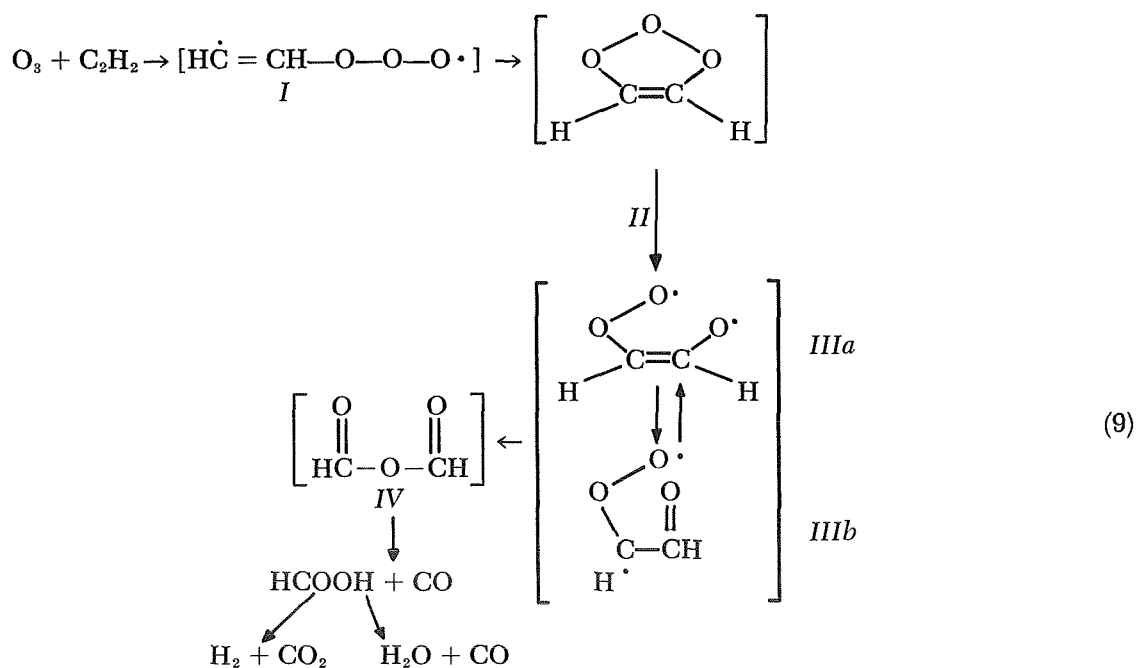
The intermediate *I* is included to account for the high *A*-factor, as already discussed. The 1, 2, 3 trioxolane, *II*, is the primary ozonide; approximate calculations indicate that it is formed with about 55 kcal/mole excess energy,[4] and that it should have a lifetime with respect to the ring-opening step of about 10^{-12}–10^{-13} s (Ref. 12).[5] It is somewhat uncertain, therefore, whether or not *II* can be isolated, even in the liquid phase at low temperatures.

The structures *IIIa* and *IIIb* are interesting in several connections, particularly because it is at that stage that the reaction differs most fundamentally from the alkene ozonation. The analogous intermediate in the latter case can undergo the following decomposition, which is approximately thermoneutral or slightly exothermic (Ref. 13):

$$O_3 + C_2H_4 \rightarrow O \overset{O \cdot}{\underset{CH_2\text{---}CH_2}{\diagdown}} \overset{\cdot}{O} \rightarrow \oplus \, O \overset{\ominus O}{\underset{CH_2}{\diagdown}} + CH_2O \tag{10}$$
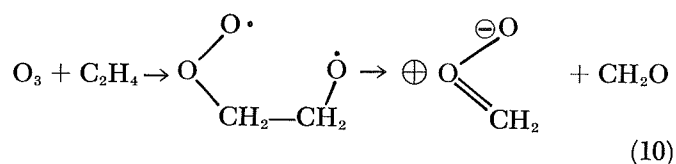
For *IIIb*, however, fission of the carbon–carbon bond at this point is energetically unfavorable owing to the high enthalpies of the products. For that reason, *IIIb* reacts in a different manner, probably giving the short-lived anhydride of formic acid, *IV*.

The principal evidence for postulation of *IV* as an intermediate comes from the experiments with dimethylacetylene. Although other mechanisms are possible, the formation of CH_3COOH and CH_2CO is best explained by the decomposition of acetic anhydride, which is known to give those products (Ref. 14):

$$\left[CH_3 C \overset{O \cdots H}{\underset{O\text{---}C \diagdown_O}{\diagdown}} CH_2 \right]^* \rightarrow CH_3 C \overset{OH}{\underset{O}{\diagdown}} + CH_2CO \tag{11}$$

The energy of the acetic anhydride is 207 kcal, assuming that all precursors (the homologs of *II* and *III*) are too short lived to suffer collisional deactivation. On that basis, and with the known rate parameters for the fission reaction, the lifetime of the excited acetic anhydride is estimated to be about $10^{-10.5}$ s.[6] This explains why acetic anhydride was not found as a product of the gas phase reaction (the rate of collisional quenching under the experimental conditions was about 10^9 s^{-1}). The observed fission of the acetic anhydride can be taken as evidence that no precursor has a lifetime greater than about 10^{-10} s.

The absence of ketene among the products of the $CH_3C \equiv CH$ reaction indicates that the mixed anhydride of formic and acetic anhydride decomposes by the more exothermic path,

$$[CH_3 \overset{O}{\overset{\|}{C}}\text{---}O\text{---}\overset{O}{\overset{\|}{C}}H]^* \rightarrow CH_3COOH + CO \tag{12}$$
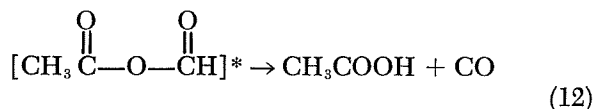
The intermediate formation of anhydrides seems first to have been proposed by Paillard and Wieland (Ref. 15) to explain product ratios in the ozonation of heptyne-1. That suggestion fell into disfavor, however, following the review of ozonation reactions by Long (Ref. 3), who considered that diketones were the actual reaction intermediates based on the fact that these compounds were isolated as products in certain alkyne ozonations. The idea of anhydrides as important intermediates has subsequently been revived by Criegee and Lederer (Re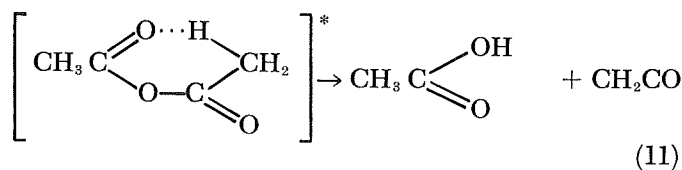f. 16) and, in Ref. 17, Dallwigk, Paillard, and Briner have actually demonstrated the formation of benzoic anhydride in the ozonation of diphenylacetylene. It would appear that the formation of diketones has more of the character of a side reaction, although it is possible that factors not presently recognized enter into the diketone formation.

The products of the alkyne ozonations are considerably energized by the reaction exothermicity, depending on the fraction of energy which appears as relative translational energy.

---

[4]The heat of formation of *II* is estimated to be 33 kcal/mole using group additivity (Ref. 7).

[5]The rate of ring opening was calculated from the equation $k = A(1 - E_a/E^*)^{s-1}$ (Ref. 12). The pre-exponential factor A was taken as 10^{14} s^{-1}; the excitation energy was taken as 16 kcal/mole (Ref. 13). For $s = 10$ active degrees of freedom, the result is $k = 10^{12.7}$ s^{-1}.

---

[6]Calculated in the same manner as in Footnote 5 with $A = 10^{12}$ s^{-1}, $E^* = 207$ kcal/mole, $E_a = 35$ kcal/mole, and $s = 20$ active degrees of freedom.

$$O_3 + C_2H_2 \rightarrow HCOOH + CO \qquad \Delta H = -205.2 \text{ kcal/mole} \tag{13}$$

$$O_3 + CH_3C\equiv CH \rightarrow CH_3COOH + CO \qquad \Delta H = -208.6 \text{ kcal/mole} \tag{14}$$

$$O_3 + CH_3C\equiv CCH_3 \rightarrow CH_3COOH + CH_2CO \qquad \Delta H = -187.9 \text{ kcal/mole} \tag{15}$$
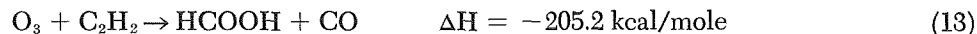
These products may therefore undergo additional fission reactions, including decarboxylation or dehydration of the acids (Ref. 18).

It is probable that radical production, as evidenced by the scavenging effect of added O_2, resulted from radical fission of the intermediate anhydrides. The 207-kcal energy of the acetic anhydride intermediate is sufficient to break any bond in the molecule.

The intermediates *IIIa* and *IIIb* bear a significant isoelectronic relationship to the proposed intermediates in the thermal isomerizations of vinylcyclopropane (Ref. 19) and cyclopropanecarboxaldehyde (Ref. 20),

vinylcyclopropane   cyclopentene   (16)

cyclopropanecarboxaldehyde   2,3 dihydrofuran   (17)
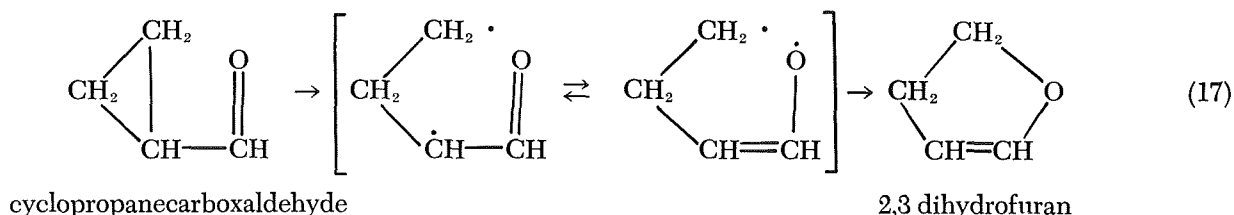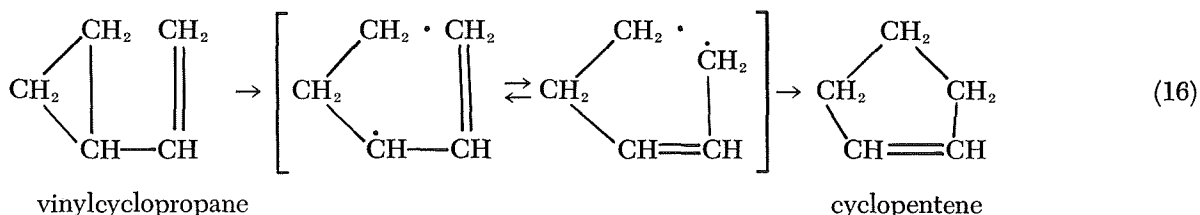
The dominant processes here are formation of cyclopentene and 2,3 dihydrofuran because of the thermodynamic stability of those products relative to the 1,2,3 trioxolane structure, *II*. For the vinylcyclopropane isomerization, the structure analogous to the acid anhydride would be 1,4 pentadiene. It is interesting to note that that product is formed as the major by-product, although only in about 1.6% yield. Such products are usually considered to result from H-migration, and it is not clear to what extent, if any, the skeletal rearrangements contribute. The major by-product in the cyclopropanecarboxaldehyde isomerization is $CH_3CH\!=\!CH\!-\!CHO$, which requires at least one H-migration.

c. Relation to alkene ozonation. As already discussed, olefin ozonation involves a zwitterionic intermediate of the following structure (see Reaction 10):
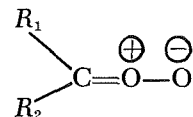
In solution (and frequently at low temperatures), the zwitterion is vibrationally thermalized and tends to react preferentially with the carbonyl compound that was simultaneously produced, or else to react with itself by dimerization or polymerization (Ref. 2). In the gas phase, however, rearrangement of the zwitterion will be favored because of the excess energy available to the zwitterion and also the absence of a cage effect, which tends to hold the zwitterion and carbonyl in close proximity. In this connection, it has been verified experimentally that

HCOOH is a product of the gas phase ozonation of ethylene, the rearrangement in this case being

$$[CH_2\overset{\oplus}{=}\overset{\ominus}{O}-O]* \rightarrow H\overset{O}{\overset{\|}{C}}-OH \qquad (18)$$
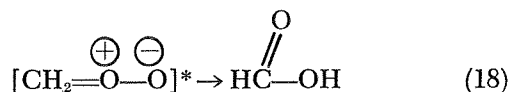
Processes of this type are probably more important under conditions such as in air pollution, but more information is needed on the rate and energy dependence of the rearrangement.

The other major products of the gas phase ethylene reaction were the carbonyl compound CH_2O and CO, the latter arising no doubt by dehydration of the formic acid, which may be produced with considerable excess energy.

An important relationship between the alkene and alkyne ozonations is that the alkyne ozonation essentially gives a zwitterionic structure directly, as can be seen by rewriting the electronic structure of $IIIb$:

$$(19)$$
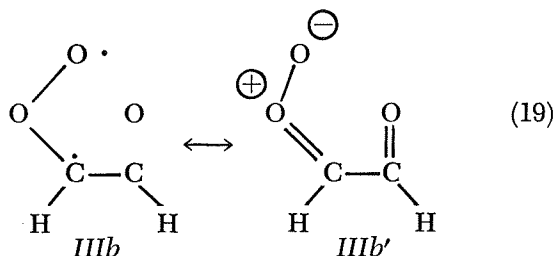
$$IIIb \qquad\qquad IIIb'$$

In this case R_1 and R_2 can be identified as H and CHO, respectively. Rearrangement of $IIIb'$ in a manner analogous to that of Reaction (18) then gives the anhydride.

5. Summary and Conclusions

The high A-factor of acetylene ozonation makes it doubtful that all 1,3 cycloaddition reactions occur by a concerted mechanism, as previously has been argued (Ref. 6). Further work on this and related systems is needed to clarify the situation, and to discover those factors that determine the initial mode of attack.

The mechanism of alkyne ozonation has been shown to be the formation of an energized acid anhydride as the primary product:

$$R_1 C{\equiv}CR_2 + O_3 \rightarrow [R_1 \overset{O}{\overset{\|}{C}}-O-\overset{O}{\overset{\|}{C}}R_2]* \qquad (20)$$
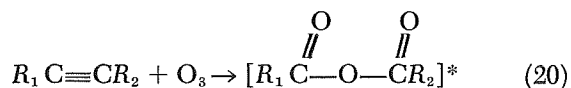
Unimolecular fission processes of the excited anhydride then give rise to the actual observed product distribution.

The alkyne ozonation is related to alkene ozonation in that the anhydride precursor is a zwitterionic intermediate similar to the type of zwitterions produced, along with carbonyl compounds, in the alkene ozonation. The present approach, emphasizing the role of related intermediates, thus offers a tractable mechanism for incorporation of all the ozonation reactions into models of photochemical air pollution.

An important remaining problem, particularly in regard to air pollution, is to determine the rates, mechanisms, and energy dependence of the zwitterion reactions.

References

1. Murray, R. W., *Account. Chem. Res.,* Vol. 1, p. 313, 1968.

2. Bailey, P. S., *Chem. Rev.,* Vol. 58, p. 925, 1958.

3. Long, L., Jr., *Chem. Rev.,* Vol. 27, p. 437, 1940.

4. Hurn, R. W., in *Air Pollution,* Second Edition, p. 55. Edited by A. C. Stern. The Academic Press, New York, 1968.

5. DeMore, W. B., *Int. J. Chem. Kin.,* Vol. 1, p. 209, 1969.

6. Huisgen, R., *Angew. Chem.* (International Edition), Vol. 2, pp. 565–598; 633–645, 1963.

7. Benson, S. W., et al., *Chem. Rev.,* Vol. 68, p. 279, 1968.

8. Cadle, R. D., and Schadt, C., *J. Chem. Phys.,* Vol. 21, p. 163, 1953.

9. Firestone, R. A., *J. Org. Chem.,* Vol. 33, p. 2285, 1968.

10. Nakagawa, T. W., Andrews, L. J., and Keefer, R. M., *J. Am. Chem. Soc.,* Vol. 82, p. 269, 1960.

11. Wei, Y. K., and Cvetanovic, R. J., *Can. J. Chem.,* Vol. 41, p. 913, 1963.

12. Benson, S. W., *The Foundations of Chemical Kinetics,* p. 231. McGraw-Hill Book Co., Inc., New York, 1960.

13. Benson, S. W., *Thermochemical Kinetics,* p. 173. John Wiley & Sons, Inc., New York, 1968.

14. Szwarc, M., and Murawski, J., *Trans. Faraday Soc.,* Vol. 47, p. 269, 1951.

15. Paillard, H., and Wieland, C., *Helv. Chim. Acta,* Vol. 21, p. 1356, 1938.

16. Criegee, R., and Lederer, M., *Ann. Chem.,* Vol. 583, p. 29, 1953.

17. Dallwigk, E., Paillard, H., and Briner, E., *Helv. Chim. Acta,* Vol. 35, p. 1377, 1952.

18. Maccoll, A., and Thomas, P. J., *Progr. React. Kin.,* Vol. 4, p. 119, 1967.

19. Wellington, C. A., *J. Phys. Chem.,* Vol. 66, p. 1671, 1962.

20. Wilson, C. L., *J. Am. Chem. Soc.,* Vol. 69, p. 3002, 1947.

V. Communications Systems Research

TELECOMMUNICATIONS DIVISION

A. Combinatorial Communication: Hide and Seek, Data Storage, and Entropy, R. McEliece and E. Posner

1. Introduction

In this article, we shall study the relationship between games of search and the optimum storage of information. In *Subsection 2*, we shall treat the case of finite sets, and in *Subsection 3*, a generalization to compact metric spaces.

Let X be a set, and let $S = \{S_1, S_2, \cdots, S_m\}$ be a finite collection of subsets of X, with $\cup S_j = X$. Regard the $x \in X$ as "data points," and the S_j as "subsets of allowed uncertainty," such that when a data point is selected, one is not interested in exactly which x it is, but rather in knowing an S_j (there may be more than one) in which it lies.

Under these assumptions, $\lceil \log_2 m' \rceil$ bits are needed to specify the S_j which contains an unknown data point, where m' is the fewest number of the S_j's which are needed to cover X.

However, if N data points are stored before it is attempted to specify the sequence of N S_j's, an average savings may be possible. Let X^N be the cartesian Nth power of X, and let S^N be the class of subsets of X^N of the form $S_{i_1} \times \cdots \times S_{i_N}$. Here, $\lceil \log_2 M \rceil$ bits are needed to specify the sequence of S_j's corresponding to an unknown sequence of N data points, where M is the fewest number of sets from S^N needed to cover X^N. Thus, $1/N \lceil \log_2 M \rceil$ can be interpreted as the number of bits per sample necessary to specify an S_j when a block code of (constant) length N is used.

Thus, we are led to the following definitions, which generalize those in Footnote 1 (brief version in SPS 37-62, Vol. III, pp. 64–75). The (one shot) S-*entropy* $H_S(X)$ is defined as

$$H_S(X) = \min_{\mathcal{T} \leq S} \log |\mathcal{T}|$$

where the minimization is taken over those subsets of S which cover X. (We disregard the rounding-off of the logarithm, and the base of the logarithm.) The limit

$$I_S(X) = \lim_{N \to \infty} \frac{1}{N} H_{S^N}(X^N)$$

---

[1]Posner, E. C., and E. R. Rodemich, "Epsilon Entropy and Data Compression," *Ann. Math. Statist.* (to be published).

the absolute S-entropy of X, is the minimum number of bits per sample needed when arbitrarily long block codes are used.

Now let us provide X with a probability measure P, and suppose the S_j are P-measurable. Define the (one-shot) S; P *entropy* of X, $H_S{}_{;P}(X)$ as the minimum Shannon entropy $H(\mathcal{U})$ of any partition $\mathcal{U}$ of X by subsets of the S_j; i.e., of any S-partition:

$$H(\mathcal{U}) = \sum P(T_k) \log \left(\frac{1}{P(T_k)} \right)$$

where $X = T_1 + T_2 + \cdots$ is the partition $\mathcal{U}$. Thus, $H_S{}_{;P}(X)$ is the minimum expected number of bits necessary to specify the source X when it is sampled according to the probability distribution P, where, again, the sets in S are the sets of allowed uncertainty, and round-off is ignored. The *absolute* $S;P$ *entropy* $I_S{}_{;P}(X)$ is defined as

$$I_S{}_{;P}(X) = \lim_{N \to \infty} \frac{1}{N} H_{S^N; P^N}(X^N)$$

where P^N is the product measure on X^N. Then $I_S{}_{;P}(X)$ is the minimum number of bits per sample necessary to describe X to within the uncertainty S when arbitrarily many samples can be stored and optimum variable-length coding is used.

We now change the subject and define a finite zero-sum two person $G(X;S)$, called "hide and seek, X; S." Player A "hides" in X by choosing a point $x \in X$; player B "seeks" player A by selecting one of the sets S_j. Player A must pay B one dollar if $x \in S_j$; otherwise, the payoff is zero. Now if X is *finite*, $G(X;S)$ has a value $v(S;X)$ which can be described as follows: If Y is any set, $\mathcal{A}(Y)$ is the class of all probability distributions on the finite set Y. The fundamental theorem of game theory (Ref. 1) implies

$$v(S;X) = \max_{Q \in \mathcal{A}(S)} \min_{x \in X} Q(\text{Star}(x)) = \min_{P \in \mathcal{A}(X)} \max_{S \in S} P(S)$$

where Star $(x) = \{S \in S \mid x \in S\}$.

This means that B can win at least $v(S;X)$, on the average, no matter what strategy A uses, provided he selects his sets S according to the probability distribution Q which achieves v. Conversely, A can assure himself of losing no more than $v(S;X)$, on the average, by selecting his point x according to a distribution P which achieves v. The distributions Q and P are called *optimal (mixed) strategies*.

In *Subsection 2*, we shall show the surprising result

$$I_S(X) = \log \frac{1}{v(x;S)} = \max_{P \in \mathcal{A}(X)} I_S{}_{;P}(X)$$

which is the purpose of this article. This determines $I_S(X)$ constructively, and shows that, in the worst case when "nature" has chosen that P which maximizes $I_S{}_{;P}(X)$ for P in $\mathcal{A}(X)$, no bits can be saved in storing outcomes of X by taking into account the distribution P of outcomes and using optimum variable-length coding with minimum expected word length.

2. The Main Theorem for Finite Sets

Theorem 1. *If X is finite,*

$$I_S(X) = \log \frac{1}{v(X;S)} = \max_{P \in \mathcal{A}(X)} I_S{}_{;P}(X)$$

Any P which achieves this last maximum is an optimum mixed strategy for the hider in $G(X;S)$, and conversely. In addition, any optimum mixed strategy Q for the seeker in $G(X;S)$ can be used to select a "random code" which comes arbitrarily close to achieving $I_S(X)$ for large enough N.

Remark. Let us note that it is possible that

$$H_S(X) > \max_{P \in \mathcal{A}(X)} H_S{}_{;P}(X)$$

For example, if X is the set of vertices of a pentagon, and if S consists of the pairs of adjacent vertices of X, it is obvious that

$$H_S(X) = \log 3$$

but it is not hard to show that

$$\max_P H_S{}_{;P}(X) = \log 5 - \frac{4}{5} \log 2$$

which is achieved when the probability of each vertex is 1/5.

Proof. Clearly, $I_S(X) \geq I_S{}_{;P}(X)$ for any P, since the (Shannon) entropy of M probabilities is always less than or equal to $\log M$. Also, since

$$\sum q_i \log \frac{1}{q_i} \geq \log \frac{1}{\max_i q_i}$$

it follows that

$$I_{S;P}(X) \geq \log \frac{1}{\max_{S \in S} P(S)}$$

and so

$$I_S(X) \geq \log \frac{1}{\min_P \max_S P(S)} = \log \frac{1}{v(X;S)}$$

To get the other inequality, we shall show that

$$I_S(X) \leq \log \frac{1}{\min_x Q(\text{Star}(x))} = \log \frac{1}{q}$$

say, for any Q in $\mathcal{A}(S)$.

For a fixed N and M, choose M sets $\mathbf{S}_1, \cdots, \mathbf{S}_M$ from S^N, according to the distribution Q^N. For a fixed $\mathbf{x} \in X^N$, we have

$$Q^N(\text{Star}(\mathbf{x})) \geq q^N$$

so that

$$Q^N\left(\mathbf{x} \in \bigcup_{i=1}^M \mathbf{S}_i\right) \leq (1 - q^N)^M$$

Thus, since there are n^N possible $\mathbf{x}$'s,

$$Q^N\left\{\text{for some } \mathbf{x}, \mathbf{x} \in \bigcup_{i=1}^M \mathbf{S}_i\right\} \leq n^N(1-q^N)^M$$

Hence, if $n^N(1 - q^N)^M < 1$, there will be at least one choice of the $\mathbf{S}_i$ for which $X = \cup \, \mathbf{S}_i$. But if

$$M > \frac{-N \log n}{\log(1 - q^N)}$$

this will be the case. Thus,

$$I_S(X) \leq \frac{1}{N} \log\left(\frac{-N \log n}{\log(1-q^N)} + 1\right)$$

Letting $N \to \infty$, we obtain

$$I_S(X) \leq \log \frac{1}{q}$$

as promised.

If we minimize this bound over Q, we obtain

$$I_S(X) \leq \log \frac{1}{\max_Q \min_x Q(\text{Star}(x))} = \log \frac{1}{v(X;S)}$$

so that equality follows.

To complete the proof, it remains to show

$$I_S(X) = \max_P I_{S;P}(X)$$

However, this follows immediately from the inequalities

$$I_S(X) \geq I_{S;P}(X) \geq \log \frac{1}{\max_S P(S)}$$

when P is chosen to minimize

$$\max_S P(S)$$

Application. Theorem 1 allows us to calculate the *absolute entropy* of a finite undirected graph, relative either to the class of *cliques*, or to the class of *talons*. Cliques are sets of diameter 1, talons are spheres of radius 1, under the metric in which the distance between two vertices is the length of the shortest path connecting them, or one more than the number of vertices if there is not a path connecting them.

For example, consider the graph below:
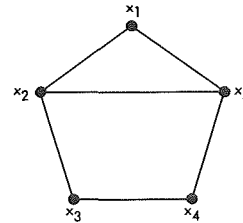
The maximal cliques are

$$\{x_1, x_2, x_5\}, \{x_2, x_3\}, \{x_3, x_4\}, \{x_4, x_5\}$$

If S is the set of maximal cliques, $I_S(X) = \log 2$, since the probability assignment $p_2 = p_3 = p_4 = p_5 = 1/4$, $p_1 = 0$ makes min $P(S) = \max P(S) = 1/4$ for $S \in \mathcal{S}$. The *talons* are

$$\{x_1, x_2, x_5\}, \{x_2, x_1, x_5, x_3\}, \{x_3, x_2, x_4\}, \{x_4, x_3, x_5\}, \{x_5, x_1, x_4, x_2\}$$

Here, $I_S(X) = \log 3/2$, because of the following pair of probability assignments:
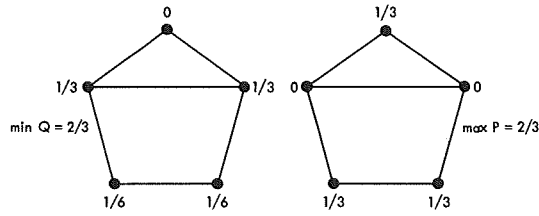
We close this subsection with a corollary to Theorem 1 for which we know of no other proof.

Corollary. Let X, $\mathcal{S}$; Y, $\mathcal{T}$ be as in Theorem 1, and let $\mathcal{S} \times \mathcal{T}$ denote the collection of subsets of $X \times Y$ of the form $S \times T$, $S \in \mathcal{S}$, $T \in \mathcal{T}$. Then,

$$I_{\mathcal{S} \times \mathcal{T}}(X \times Y) = I_\mathcal{S}(X) + I_\mathcal{T}(Y)$$

Proof. By Theorem 1, we need only prove

$$v(X \times Y; \mathcal{S} \times \mathcal{T}) = v(X; \mathcal{S})\, v(Y; \mathcal{T})$$

To prove this, use for the seeker the strategy $Q_X \times Q_Y$, where $Q_X \times Q_Y$ denotes product measure, an element of $\mathcal{A}(\mathcal{S} \times \mathcal{T})$, and Q_X is his optimal strategy in X; $\mathcal{S}$, whereas Q_Y is his optimal strategy for Y; $\mathcal{T}$. This proves that

$$v(X \times Y; \mathcal{S} \times \mathcal{T}) \geq v(X; \mathcal{S})\, v(Y; \mathcal{T})$$

Conversely, use for the hider $P_X \times P_Y$ an element of $\mathcal{A}(X \times Y)$, where P_X is optimal for X; $\mathcal{S}$ and P_Y for Y; $\mathcal{T}$ This shows

$$v(X \times Y; \mathcal{S} \times \mathcal{T}) \leq v(X; \mathcal{S})\, v(Y; \mathcal{T})$$

and this proves the corollary.

3. Compact Metric Spaces

In this subsection, we shall briefly consider the problem of calculating $I_S(X)$, where X is an arbitrary compact metric space, and $\mathcal{S}$ is the class of closed subsets of X of radius $\epsilon/2$ or diameter ϵ. Our results are incomplete, in that we shall prove the analogy of Theorem 1 only for all but a countable number of ϵ.

Thus, let $R(\epsilon)$ be the class of closed subsets of X which can be enclosed in spheres of radius $\epsilon/2$, and $D(\epsilon)$ be those closed sets of diameter $\leq \epsilon$. As in the finite case, we can define the game "hide and seek $(X; \mathcal{S})$," where $\mathcal{S} = R(\epsilon)$ or $D(\epsilon)$. However, to define the set $\mathcal{A}(\mathcal{S})$ of probability distributions on the set $\mathcal{S}$, it is convenient to make $\mathcal{S}$ itself into a compact metric space by means of the *Hausdorff metric* (Ref. 2). Thus, if F, $G \in \mathcal{S}$ define

$$d_H(F,G) = \max \left(\max_{x \in F} \min_{y \in G} d(x,y), \max_{y \in G} \min_{x \in F} d(x,y) \right)$$

It can be shown (Ref. 2) that under this metric $\mathcal{S}$ does indeed become a compact metric space. And it can also be shown (Ref. 3) that the game $G(X; \mathcal{S})$ does have a value $v(X; \mathcal{S})$, which is given by

$$v(X; \mathcal{S}) = \min_{\mu \in \mathcal{A}(X)} \max_{F \in \mathcal{S}} \mu(F) = \max_{\bar{\mu} \in \mathcal{A}(\mathcal{S})} \inf_{x \in X} \bar{\mu}(\text{Star}(x))$$

If $\mathcal{S} = R(\epsilon)$ or $D(\epsilon)$, we abbreviate $v(X; \mathcal{S})$ as $v(\epsilon)$, call

$$\lim_{\eta \downarrow 0} v(\epsilon - \eta) = v(\epsilon-)$$

and write $I_S(X)$ as I_ϵ.

Remark. One may wish to define the situation for $R(\epsilon)$ by measures on X, where the payoff to the seeker is 1 if and only if the distance between the hider's chosen point and that of the seeker is at most $\epsilon/2$. However, that the two approaches are equivalent follows from the selection theorem given in Ref. 4.

Theorem 2. *For all $\epsilon > 0$,*

$$\log \frac{1}{v(\epsilon)} \leq I_\epsilon \leq \log \frac{1}{v(\epsilon-)}$$

Consequently, with at most countable many exceptions

$$I_\epsilon = \log \frac{1}{v(\epsilon)}$$

In any case, for every ϵ we have

$$\log \frac{1}{v(\epsilon)} = \sup_{P \in \mathcal{A}(X)} I_{S;P}(X)$$

and $v(\epsilon)$ is continuous from above in ϵ.

Proof. We treat only the case $S = R(\epsilon)$, the case $S = D(\epsilon)$ being entirely analogous.

First of all, we note that the inequality

$$\log \frac{1}{v(\epsilon)} \leq I_\epsilon \tag{1}$$

remains true in the infinite case; the proof is the same as in Theorem 1.

The given ϵ is fixed. Next, fix η with $\epsilon - \eta > 0$. Let J be a partition of X into a finite number of subsets, each of which can be enclosed in a sphere of radius $\eta/2$. Let $\mathcal{S}(J)$ be the collection of subsets X which are unions of J-sets and are also in $R(\epsilon) = \mathcal{S}$. Then $\mathcal{S}(J)$ can be regarded as a collection of subsets of the finite set J. Denote the absolute entropy of this finite space by $I_{\mathcal{S}(J)}$, and the value of the corresponding game by $v(J)$. Then

$$I_\epsilon \leq I_{\mathcal{S}(J)} \tag{2}$$

since the sets in $\mathcal{S}(J)$ are also in $\mathcal{S}$.

Next, we claim

$$v(J) \geq v(\epsilon - \eta) \tag{3}$$

To see this, let P be a probability distribution on J which achieves

$$v(J) = \min_P \max_{S \in \mathcal{S}(J)} P(S)$$

We extend P to a probability on X by choosing a point in each set j of the partition J which is the center of a sphere of radius $\eta/2$ containing S, and assigning this point the probability $P(j)$; the desired measure is the atomic one concentrated at these points. If Y is any set in $R(\epsilon - \eta)$, then the union of those J-sets containing the points of positive probability in Y will be a set in $\mathcal{S}(J)$. Consequently,

$$\max_{S \in \mathcal{S}(J)} P(S) \geq \max_{Y \in R(\epsilon - \eta)} P(Y)$$

and so

$$v(J) = \min_{P \in \mathcal{A}(J)} \max_{S \in \mathcal{S}(J)} P(S)$$
$$\geq \inf_{P \in \mathcal{A}(X)} \sup_{Y \in R(\epsilon - \eta)} P(Y)$$
$$= v(\epsilon - \eta)$$

since the right-hand "inf" is over a larger set of probabilities. Combining Expressions (1), (2), and (3), we find

$$\log \frac{1}{v(\epsilon)} \leq I_\epsilon \leq I_{\mathcal{S}(J)} = \log \frac{1}{v(J)} = \log \frac{1}{v(\epsilon - \eta)}$$

Let $\eta \downarrow 0$ to obtain the inequality

$$I_\epsilon \leq \log \frac{1}{v(\epsilon -)}$$

To prove the last sentence of Theorem 2, note that as in the proof of Theorem 1

$$I_{S;P}(X) \geq \log \frac{1}{\sup_s P(S)}$$

for every $P \in \mathcal{A}(X)$, so that

$$\sup_P I_{S;P}(X) \geq \log \frac{1}{v(\epsilon)} = \sup_P \log \frac{1}{\sup P(S)} \tag{4}$$

Let us abbreviate Expression (4) as $r(\epsilon) \geq s(\epsilon)$; both r and s are decreasing functions of ϵ. We shall prove $r(\epsilon) = s(\epsilon)$ by showing that $r(\epsilon)$ is continuous from above in ϵ. Then if δ_n is any sequence of positive reals which decreases to zero such that for all n,

$$r(\epsilon + \delta_n) = s(\epsilon + \delta_n)$$

then as $n \to \infty$ we see that

$$r(\epsilon) = s(\epsilon +) \leq s(\epsilon)$$

which implies $r(\epsilon) = s(\epsilon)$.

Thus, it remains to show that

$$r(\epsilon) = \sup_P I_{\mathcal{S}(\epsilon);P}(X)$$

is continuous from above in ϵ. First of all, it is shown in Footnote 1 (paragraph 8, Corollary 1) that for fixed P,

$I_{S;P}$ is continuous from above in ϵ. Now for a fixed $\eta > 0$ pick P such that

$$I_{\epsilon;P} > \sup I_{\epsilon;P} - \frac{\eta}{2} \qquad (5)$$

where $I_{\epsilon;P} = I_{S(\epsilon);P}$. Next, pick δ such that for $\delta' \leq \delta$

$$I_{\epsilon+\delta';P} > I_{\epsilon;P} - \frac{\eta}{2} \qquad (6)$$

using the continuity of $I_{\epsilon;P}$ from above. Combining Expressions (5) and (6), we have

$$I_{\epsilon+\delta';P} > \sup_{P} I_{\epsilon;P} - \eta$$

for all $\delta' \leq \delta$. A fortiori, for S' sufficiently small depending on η we have

$$\sup I_{\epsilon+\delta';P} > \sup_{P} I_{\epsilon;P} - \eta$$

which proves the continuity of

$$\sup_{P} I_{\epsilon;P}$$

from above. This completes the proof.

4. Concluding Remarks

We conjecture that

$$I_{\epsilon} = \log \frac{1}{v(\epsilon)}$$

and point out that there is no hope of proving this in general by showing that $v(\epsilon)$ is continuous from below, since $v(\epsilon)$ frequently fails to be continuous from below. However, $v(\epsilon)$ is continuous in ϵ for many interesting choices of X: if X is a compact homogeneous space under an invariant metric and the invariant probability, the invariant probability of a sphere of radius $\epsilon/2$ is continuous in ϵ, and that probability measure is easily seen to be an optimum strategy. Here $v(\epsilon) = P_r$ (sphere radius $\epsilon/2$). Thus, n-spheres in Euclidean space, Lie groups, etc., are all included here.

Using the Hausdorff metric on $S(\epsilon)$ (Ref. 2) and the Prokhorov metric on $\mathcal{A}(X)$ (Ref. 5), it is possible to show that

$$\log \frac{1}{v(\epsilon)} = I_{S;P}(X)$$

for some P.

References

1. Weyl, H., "Elementary Proof of a Minimax Theorem due to von Neumann," *Chapter 2 in Contributions to the Theory of Games, Vol. 1: Annals of Mathematics Studies, No. 24*. Princeton University Press, Princeton, N. J., 1950.

2. Hausdorff, F., *Set Theory*, Vol. 28, Chelsea, New York, 1957 (reprinted).

3. Parthasarathy, T., "Minimax Theorems in Separable—Compact Metric Spaces," *J. Indian Stat. Assoc.*, Vol. 5, pp. 182–191, 1967.

4. Parthasarathy, K. R., *Probability Measures on Metric Spaces*. Academic Press, New York, 1967.

5. Prokhorov, Yu. V., "Convergence of Random Processes and Limit Theorems in Probability Theory," *Theory of Probability and its Applications*, Vol. 1, pp. 157–214, 1956 (translated).

B. Coding and Synchronization Research: Performance of a First-Order Digital Phase-Locked Loop, J. Holmes

1. Introduction

Recently, an all-digital, single-channel command system was proposed to meet the requirements of high reliability over extended periods of time for the Thermoelectric Outer Planet Spacecraft program. This command system uses a digital phase-locked loop (DPLL) to update the timing of the local oscillator (sampler). This provides coherent detection of the command bits which are biphase-modulated onto the squarewave subcarrier. The updating is accomplished by modifying the duration between samples by a fixed increment at regular intervals, the sign of the increment being opposite to the sign of the timing error. The timing error for this system is the time between the negative-going transition of the squarewave subcarrier and the time the DPLL thinks the transition occurred.

The purpose of this article is to develop a mathematical model of the DPLL and to analyze its performance. Three aspects of its performance are considered; (1) the

stationary bit error rate, (2) the stationary timing error variance, and (3) the mean time to first slip.

2. Description of the Digital Phase-Locked Loop

Functionally, the phase update system is diagrammed in Fig. 1. The input waveform $y(t)$ consists of a square-wave subcarrier (SC) plus white gaussian noise with one-sided spectral density N_0 watts/Hertz. An ideal low-pass presampling filter of one-sided bandwidth W Hertz conditions the input waveform so that it can be sampled by the analog-to-digital converter at a rate of $2W$ samples/s. If we let f_{SC} denote the subcarrier frequency, then there will be $2W/f_{SC}$ samples per subcarrier cycle. The transition sampler in Fig. 1 denotes the operation of outputing the sample where the DPLL thinks the negative-going transition occurs. The next block in the loop outputs the sign of this transition sample. Updating is accomplished by incrementing the clock at regular update times in the appropriate way; that is, if the sample lags the transition, an increment of timing is added at the next update time, and conversely. The clock with no input provides samples spaced every $f_{SC}/2W$ of a cycle apart. In the analysis to follow, it is assumed that there is no drift between the received subcarrier and the local clock. Also, it is assumed that the presample filter does not distort the subcarrier waveform. *Subsections 2 and 3* assume that the subcarrier is unmodulated; the modulated case is discussed in *Subsection 5*.

3. Random Walk Model

The method of analysis used is to model the timing error sequence as a random walk with the actual error between the sampling point and the negative-going transition being the "state" of the loop at that time. Since the error correction is a fixed amount Δ, we have a random walk with a countable number of states. We may associate these error states with points along the real line. Figure 2 illustrates the squarewave SC, along with the sample points for the case $2W/f_{SC} = 16$ and an error in centering of δ. Figure 3 illustrates the error state diagram for an offset of μ where, for example, the error at state -1 is $(\frac{1}{2} - \mu)\Delta$ deg, if Δ is specified in degrees.

The phase update is derived from the sum of M samples, one per SC cycle, at what the locally generated sampling circuit thinks is the negative-going transition of the squarewave subcarrier. The sum of M samples provides an estimate of which way the timing phase of the sampler timing should be "bumped" or incremented.
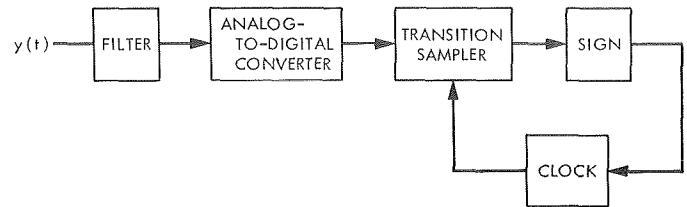
Fig. 1. Block diagram of phase update loop
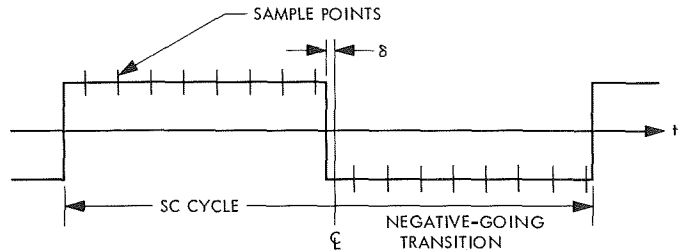
Fig. 2. Sample points of subcarrier waveform with offset δ
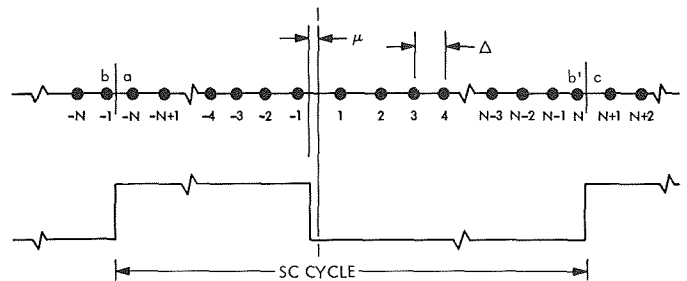
Fig. 3. Error state diagram and its relationship to received squarewave

In the case of no noise, it is clear that the timing error will oscillate back and forth in the two states nearest to the negative-going transition.

White noise, passed through an ideal low-pass filter of bandwidth W and then sampled at a rate $2W$ samples/s, produces independent samples. These samples have a variance of N_0W, where the spectral density N_0 and the bandwidth W are both one-sided parameters. The square-wave subcarrier is assumed to have amplitude A so that each sample has a signal-to-noise ratio given by

$$\text{SNR}_{\text{sample}} = \frac{A^2}{N_0 W} \tag{1}$$

and, therefore, the sum of M independent samples has a SNR given by

$$\text{SNR}_M = \frac{MA^2}{N_0 W} \qquad (2)$$

If the subcarrier is modulated by bits of period T_b (T_b is some multiple of the subcarrier period), then the bit detection SNR, assuming a perfectly synchronized digital integrate-and-dump circuit, is given by

$$\text{SNR}_b = \frac{2A^2 T_b}{N_0} \qquad (3)$$

The probability of the timing being bumped in the correct direction is p where

$$p = \text{erf}\left[\left(\frac{MA^2}{N_0 W}\right)^{1/2}\right] \qquad (4)$$

and it is $1 - p = q$ in the incorrect direction. We now have the parameters necessary to complete our random walk model. Referring to Fig. 3, we see that since there are a countable (but infinite) number of states, in the limit as the time increases without bound the stationary probabilities would all tend to zero and the phase error variance would be unbounded. To overcome this difficulty, we shall compute the stationary (steady-state) phase error variance modulo-one full cycle just as has been done for the continuous phase-locked loop. If Δ is measured in fractions of a cycle and if $\Delta = (2N)^{-1}$, then there will be $2N$ error states in a given SC cycle.

a. Zero timing offset. For the case when the timing offset parameter μ is zero, we can take into account the fact that errors are reduced modulo 2π by regarding the two outermost error nodes as "reflecting" states. Figure 4

illustrates a state transition diagram with one reflecting state and two regular states. The diagram is to be interpreted as follows: in either of the regular states the probability of moving to the left is q and to the right is p. In the reflecting state, q is the probability of remaining in the reflecting state and p is the probability of moving to the right one state. We can, therefore, visualize a reflecting boundary one half a sample space to the left of the reflecting state number 1. We see from Fig. 3 that moving from state a to state b mod 2π is the same in absolute error as being sent to b'. However, if μ, the offset, is zero, then the transition from state a to b is equivalent to being returned to a; hence, a reflecting barrier can be imagined to be located at the midpoint between a and b. We use this model and consider the effect of $\mu \neq 0$ later. Now, the state transition diagram can be reduced to one half the number of states from $2N$ to N, by noting that as far as the mean squared error is concerned the pairs of states -1 and 1 and -2 and 2, etc., contribute the same squared error. Hence, we may reduce our diagram to that illustrated in Fig. 5.

It can be shown that for this problem the stationary probabilities (Ref. 1) exist and are unique. Let us define P_k by

$$P_k = \text{Prob (error is in state } k\text{)}, \qquad 1 \leq k \leq N$$

then, since the steady-state probabilities exist, we have for $k \neq 1, N$

$$P_k = q\, P_{k-1} + p\, P_{k+1} \qquad (5)$$

That is, the probability of being in state k is the probability of being in state $k - 1$ times the probability of going from state $k - 1$ to state k plus the probability of being in state $k + 1$ times the probability of going from

Fig. 4. A reflecting state (1) and two regular states (2,3)
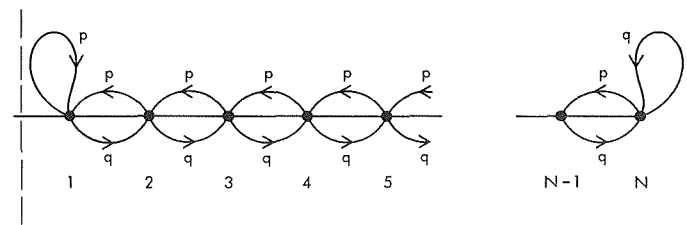
Fig. 5. Reduced state transition diagram for symmetrical case ($\mu = 0$) showing transition probabilities with reflecting states at each end

state $k + 1$ to state k. A general solution to Eq. (6) is of the form (Ref. 2)

$$P_k = A + B \left(\frac{q}{p} \right)^k \tag{6}$$

Our boundary conditions are given by

$$P_1 = p P_2 + p P_1$$
$$P_N = P_{N-1}q + P_N q \tag{7}$$

Using the boundary conditions, we see that P_k must be of the form

$$P_k = \left(\frac{q}{p} \right)^k B \tag{8}$$

where B is determined from

$$\sum_1^N P_k = 1 \tag{9}$$

(We assume that all the mass lies in the positive states.) Evaluating, we have that the stationary probabilities satisfy

$$P_k = \frac{1 - \dfrac{q}{p}}{1 - \left(\dfrac{q}{p} \right)^N} \left(\frac{q}{p} \right)^{k-1} \tag{10}$$

Let us now turn to the steady-state error performance. Since we have just obtained the steady-state error prob-abilities, it follows that the mean squared timing error (expressed in the units of Δ^2) is given by

$$\sigma_{TE}^2 = \sum_1^N \left(k - \frac{1}{2} \right)^2 \Delta^2 P_k \tag{11}$$

and the timing correction is made every T seconds. Expanding Eq. (11) and using Eq. (10), we have that

$$\sigma_{TE}^2 = \Delta^2 \frac{q}{p} \frac{1 - \dfrac{q}{p}}{1 - \left(\dfrac{q}{p} \right)^N} \sum_1^N k(k-1) \left(\frac{q}{p} \right)^{k-2} + \frac{\Delta^2}{4} \tag{12}$$

Now to evaluate the sum in Eq. (12), note that (letting $\alpha = q/p$) if

$$g(\alpha) = \sum_1^N \alpha^k \tag{13}$$

then

$$g''(\alpha) = \sum_1^N k(k-1)\alpha^{k-2} \tag{14}$$

and $g(\alpha)$ is easily evaluated since it is the sum of a geometric series. Differentiating $g(\alpha)$ twice, inserting the result in Eq. (12), and letting $\alpha = q/p$ produces the following expression for the stationary timing error variance with no timing offset ($\mu = 0$):

$$\sigma_{TE}^2 = \frac{\Delta^2}{4} + \frac{1}{1 - \left(\dfrac{q}{p} \right)^N} \Delta^2 \left\{ -N(N+1) \left(\frac{q}{p} \right)^N + 2 \left[\frac{\dfrac{q}{p} - (N+1) \left(\dfrac{q}{p} \right)^{N+1}}{\left(1 - \dfrac{q}{p} \right)} \right] + 2 \left[\frac{\left(\dfrac{q}{p} \right)^2 - \left(\dfrac{q}{p} \right)^{N+2}}{\left(1 - \dfrac{q}{p} \right)^2} \right] \right\} \tag{15}$$

Equation (15) is plotted as a function of the threshold bit SNR in Fig. 6 for the case $\mu = 0, \frac{1}{2}$ and when μ is averaged (see Subsection 4) for the case $M = 15$. This corresponds to an update every 15 subcarrier cycles.

b. Non-zero timing offset. Referring to Fig. 3, we see that, when $\mu \neq 0$, we can no longer fold over the negative states onto the positive ones since they are not at the same distance from the transition or center. Furthermore, the mod 2π solution appears to be only strictly valid when $\mu = 0$ since, as can be seen in Fig. 3, the error at state b reduced mod 2π corresponds to the error at b' and is, therefore, not reflected back to state a. However, at state c the absolute error mod 2π is the same as that at state a. Consequently, since the probabilities of states a and b are equal, the errors in reflection cancel out and

we still have an exact result for $\mu \neq 0$ when we reflect state b to a and state c to b'. So, for an offset of $\mu\,(\mu < \frac{1}{2})$, the variance is given by

$$\sigma_{TE}^2 = \frac{\Delta^2}{2}\sum_1^N (k - \tfrac{1}{2} - \mu)^2 \, P_k + \frac{\Delta^2}{2}\sum_1^N (k - \tfrac{1}{2} + \mu)^2 \, P_k \tag{16}$$

where P_k is the same value as found for the zero offset case. Rearranging Eq. (16), we obtain

$$\sigma_{TE}^2 = \frac{1}{1 - \left(\frac{q}{p}\right)^N}\,\Delta^2\left\{-N(N+1)\left(\frac{q}{p}\right)^N + 2\left[\frac{\frac{q}{p} - (N+1)\left(\frac{q}{p}\right)^{N+1}}{1 - \frac{q}{p}}\right] + 2\left[\frac{\left(\frac{q}{p}\right)^2 - \left(\frac{q}{p}\right)^{N+2}}{\left(1 - \frac{q}{p}\right)^2}\right]\right\} + \frac{\Delta^2}{4}(1 + 4\mu^2) \tag{17}$$

where $\mu \in (-\frac{1}{2}, \frac{1}{2})$. Clearly, σ_{TE}^2 is minimum when $\mu = 0$. We now can average σ_{TE}^2, assuming that μ is uniformly distributed in the region $(-\frac{1}{2}, \frac{1}{2})$ to account for random offset errors. Thus, Eq. (16) becomes

$$\sigma_{TE}^2 = \frac{1}{1 - \left(\frac{q}{p}\right)^N}\,\Delta^2\left\{-N(N+1)\left(\frac{q}{p}\right)^N + 2\left[\frac{\frac{q}{p} - (N+1)\left(\frac{q}{p}\right)^{N+1}}{1 - \frac{q}{p}}\right] + 2\left[\frac{\left(\frac{q}{p}\right)^2 - \left(\frac{q}{p}\right)^{N+2}}{\left(1 - \frac{q}{p}\right)^2}\right]\right\} + \frac{\Delta^2}{3} \tag{18}$$

This random variable characterization of μ would also account for a slow drift between the transmitter oscillator and the receiver clock. Figure 6 illustrates all three cases: $\sigma_{\max}\,(\mu = \frac{1}{2})$, σ_{av}, and $\sigma_{\min}\,(\mu = 0)$.
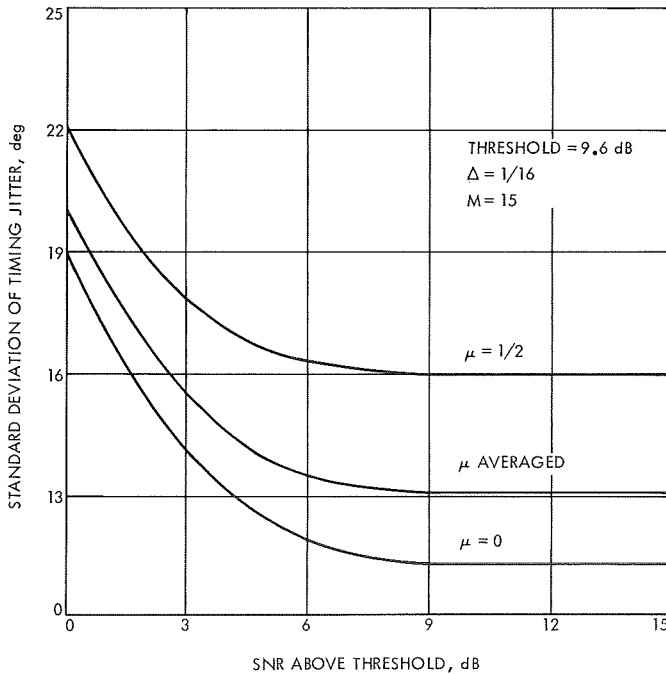
Fig. 6. Standard deviation of phase error
vs SNR above threshold

4. Mean First Slip Time

The time to slip π rad is important in the unmodulated case. The reason for this is that once π rad are slipped, with high probability synchronization would tend to be in error by one SC cycle.

First, we solve the general first-passage time problem again, using the random walk model. Because of the symmetry involved and the fact that each step is independent of the previous one, we may place a reflecting boundary at the origin, as before. State N shall be modeled by an absorbing state, which is characterized by the fact that once the system is in this state it remains there forever, that is, the probability of leaving is zero. Consequently, whenever the timing error is equivalent to being in state N, the process is stopped. Figure 7 illustrates the state transition diagram used to model the first-passage time problem. State 1 is reflecting and state N is absorbing. Rather than derive the individual probabilities p_n, which are the probabilities of the error corresponding to reaching state N in time n, and then
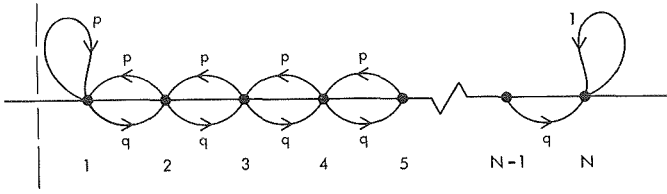
**Fig. 7. Reduced state transition diagram
for first passage-time model**

forming the average

$$\overline{T} = \sum_1^\infty n\, p_n \qquad (19)$$

we shall use a method indicated in Ref. 2.

Let T_k^N be the mean duration of the time it takes to reach state N, starting at state k. If the first move is to the right, the procedure continues as if the initial position had been $k+1$. The conditional expectation of the duration, assuming the move was to the right, is therefore $T_{k+1}^N + 1$. On the other hand, if a move is made to the left, the conditional expectation is $T_{k-1}^N + 1$. Therefore, the mean time T_k^N must satisfy

$$T_k^N = q\, T_{k+1}^N + p\, T_{k-1}^N + 1, \qquad k \neq 1, N \qquad (20)$$

with the boundary conditions

$$T_N^N = 0$$
$$T_1^N = q\, T_2^N + p\, T_1^N + 1 \qquad (21)$$

By direct substitution, it can be shown (Ref. 2) that

$$T_k^N = \frac{k}{p-q} + A + B \left(\frac{p}{q}\right)^k, \qquad p > q \qquad (22)$$

is a solution, hence, the unique one. Upon evaluating the boundary conditions, we obtain

$$T_k^N = \frac{k-N}{p-q} + \frac{\dfrac{1}{q} + \dfrac{1}{p-q}}{\left(\dfrac{p}{q}\right) - 1} \left\{ \left(\frac{p}{q}\right)^{N-1} - \left(\frac{p}{q}\right)^{k-1} \right\}$$

$$(23)$$

Since we are interested in times starting at $k = 1$, we have

$$T_N = \frac{1-N}{p-q} + \frac{\dfrac{1}{q} + \dfrac{1}{p-q}}{\dfrac{p}{q} - 1} \left(\frac{p}{q}\right)^{N-1}, \qquad (p > q) \qquad (24)$$

where T_N denotes the average number of steps to reach state N, starting at state 1. Here, $N = \frac{1}{2}\Delta$.

For example, at threshold (9.6 dB), using a step size of $\Delta = \frac{1}{16}$, the mean time to loss of sync becomes

$$T_8 = 7 \times 10^4 \text{ updates} \qquad (25)$$

However, a step size of $\Delta = \frac{1}{256}$ at threshold produces the extremely large mean time to loss of sync of

$$T_{128} = 4.2 \times 10^{28} \text{ updates} \qquad (26)$$

It is, therefore, clear that small values of Δ are very desirable to maximize the mean time to slip. As can be seen from Eq. (24), the mean slip time is exponential in N or equivalently in $\frac{1}{2}\Delta$.

5. Bit Error Performance

All the results obtained up to now are for the unmodulated case. We now obtain the bit error performance when the squarewave is modulated by a length 15 PN code with each PN symbol being one subcarrier cycle in duration. If the DPLL is going to function properly, it must impose only a negligible increase in error probability. It can be shown, that, if the nominal bit error rate is 1×10^{-5} and the SNR is at threshold ($E_b/N_0 = 9.6$ dB), the effect of incorrectly detecting bits is negligible, and, consequently, the results of the previous subsections still apply even with modulation present. But we must now consider the effect of timing error on the bit error probability.

The probability of error PE can be expanded to

$$PE = \sum_{\substack{k=-N \\ k \neq 0}}^{N} PE_k\, P_k \qquad (27)$$

in which PE_k is the bit error probability, given that the timing error is in state k and P_k is the probability of the timing error being in state k. With the assumption

that the presampling filter bandwidth is wide compared to the subcarrier frequency, it will be assumed that there is essentially no distortion in the squarewave subcarrier. Hence, the correlation function of the sampled square-wave will be of the form of a symmetrical staircase with the width of the "steps" being the spacing between samples. As long as the loop is in an error state such that the correlation function is on the top step, there will be no increase in error probability. Once the loop enters an error state other than those contained in the top step, the bit energy is decreased and the probability of error for that state is increased.

To maintain phase or timing coherence, the receiver must take into account the bit modulation. Since the presence of a negative bit will change the sign of the timing error correction, the timing can be updated only after the bit is detected. If a bit is incorrectly detected (an event of low probability), then the timing update would, with high probability, be in the wrong direction. The degradation in E_b/N_0 due to this timing error was determined by using Eq. (27), based on a nominal bit error rate of 1×10^{-5}, and is plotted in Fig. 8 for the case that 22 samples ($M = 22$) are used to obtain the timing update. The degradation is plotted as a function of the update size expressed in fractions of a cycle. Since the presampler filter was not considered in the above analysis, the results shown in Fig. 8 are lower bounds to the performance of the actual system.

The case when the squarewave subcarrier is distorted by the presampler filter is currently under study.
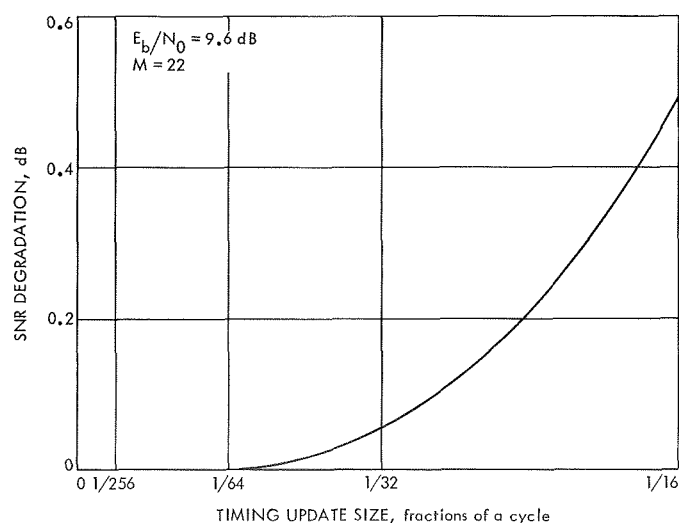
Fig. 8. SNR degradation vs timing update size

References

1. Fisz, M., *Probability Theory and Mathematical Statistics*, 3rd Edition, Chapter 7. John Wiley & Sons, Inc., New York, 1963.

2. Feller, W., *An Introduction to Probability Theory and Its Applications*, Chapter 14, Vol. I. John Wiley & Sons, Inc., New York, 1957.

C. Coding and Synchronization Research: Efficient Multichannel Space Telemetry,
S. Butman and U. Timor

1. Introduction

Let $a_1(t), \cdots, a_n(t)$ be n binary data streams, to be transmitted over one RF channel, by using n squarewave subcarriers $sq(\omega_i t)$, $i = 1, \cdots, n$. In the present deep space telemetry system (used for $n = 2$), we phase-modulate the carrier with $a_i(t) \, sq(\omega_i t)$, and transmit the signal

$$y(t) = 2^{1/2} \sin \left[\omega_0 t + \sum_{i=1}^{n} \theta_i \, a_i(t) \, sq(\omega_i t) \right] \qquad (1)$$

where the modulation angles θ_i are chosen according to the data power (or equivalently data rate) allocated to each data channel.

It is well known that for all $n > 1$ there is a power loss due to intermodulation. This loss increases with n, and even for $n = 2$ it is greater than the power in the weaker channel, a fact which discourages the use of such systems for $n > 2$.

Recently, we have suggested (SPS 37-62, Vol. III, pp. 57–60) a new efficient modulation system (Interplex) for $n = 2$, where the subcarriers are modulated by $a_1(t)$ and $a_1(t)a_2(t)$, respectively. In this case,

$$P_{\text{LOSS}} = \alpha \, P_{\text{RF}} \qquad (2)$$

where $\alpha = P_2/P_1$ is the ratio of power in the data channels. For small α (one channel has a high rate, and the other low rate) P_{LOSS} is negligible, and in no case does it exceed the RF power.

Using the new modulation scheme, we will investigate the multichannel telemetry system ($n \geq 2$) and show that:

(1) If one channel has high rate, and the remaining $(n-1)$ channels have low rates, we can design a system for higher n, keeping the power loss negligible.

(2) If all data channels have equal rates, the loss increases rapidly with n, which makes such systems impractical for $n > 3$.

We will first analyze in detail the case $n = 3$, and then consider the general case.

2. Analysis of Three-Channel Telemetry System

Let $a_1(t)$, $a_2(t)$, $a_3(t)$, where $a_i(t)$ is $+1$ or -1 for each t, be the data streams to be transmitted over one RF channel, let the required RF power for extracting the RF phase reference be P_{RF}, and the ratio of the powers for the data channels be

$$\alpha_i = \frac{P_i}{P_1} \leq 1, \qquad i = 2,3$$

We assume that P_{RF} is smaller than the higher rate data channel, i.e., $P_{RF} < P_1$.

The transmitted signal is

$$y(t) = 2^{1/2} \sin \left[\omega_0 t + \sum_{i=1}^{3} \theta_i x_i(t) \, sq(\omega_i t) \right] \qquad (3)$$

where we want to choose the θ_i and $x_i(t)$ such that the loss will be minimized.

Multiplying the received signals by $2^{1/2} \cos \omega_0 t$ and $2^{1/2} \sin \omega_0 t$ (assuming coherent detections), and performing subcarrier demodulation with the appropriate combinations of $sq(\omega_i t)$, we can separate the demodulated signals and the associated received power as follows:

Signal	Received Power
$x_1(t)$	$\widetilde{P}_1 = (\sin \theta_1 \cos \theta_2 \cdot \cos \theta_3)^2$
$x_2(t)$	$\widetilde{P}_2 = (\cos \theta_1 \sin \theta_2 \cdot \cos \theta_3)^2$
$x_3(t)$	$\widetilde{P}_3 = (\cos \theta_1 \cos \theta_2 \cdot \sin \theta_3)^2$
$x_1(t) x_2(t)$	$\widetilde{P}_{12} = (\sin \theta_1 \cdot \sin \theta_2 \cdot \cos \theta_3)^2$
$x_1(t) x_3(t)$	$\widetilde{P}_{13} = (\sin \theta_1 \cdot \cos \theta_2 \cdot \sin \theta_3)^2$
$x_2(t) x_3(t)$	$\widetilde{P}_{23} = (\cos \theta_1 \sin \theta_2 \cdot \sin \theta_3)^2$
$x_1(t) x_2(t) x_3(t)$	$\widetilde{P}_{123} = (\sin \theta_1 \sin \theta_2 \cdot \sin \theta_3)^2$
dc	$\widetilde{P}_{dc} = (\cos \theta_1 \cdot \cos \theta_2 \cdot \cos \theta_3)^2$

$$(4)$$

where $\widetilde{P}_{dc} = P_{RF}$ is the power available for the RF phase tracking.

Without loss of generality, we can assume that $\theta_1 \geq \max (\theta_2, \theta_3)$. It follows that $\theta_1 \geq 45$ deg, since otherwise P_{RF} will be greater than all other $\widetilde{P}$, which violates our assumption. Thus, we get

$$\frac{\widetilde{P}_1}{P_{RF}} = \frac{\widetilde{P}_{12}}{\widetilde{P}_2} = \frac{\widetilde{P}_{13}}{\widetilde{P}_3} = \frac{\widetilde{P}_{123}}{\widetilde{P}_{23}} = \tan \theta_1 > 1 \qquad (5)$$

a. Ideal case: $P_{RF} = 0$. By choosing $\theta_1 = 90$ deg, only 4 of the $\widetilde{P}$ quantities $(\widetilde{P}_1, \widetilde{P}_{12}, \widetilde{P}_{13}, \widetilde{P}_{123})$ are non-zero, and it is obvious that we should keep the largest three for the data channels. Hence, we assign

$$
\begin{aligned}
x_1(t) &= a_1(t) \\
x_2(t) &= a_1(t) \, a_2(t) \longrightarrow x_1(t) \, x_2(t) = a_2(t) \\
x_3(t) &= a_1(t) \, a_3(t) \longrightarrow x_1(t) \, x_3(t) = a_3(t)
\end{aligned}
\qquad (6)
$$

which yield

$$
\begin{aligned}
P_1 &= \widetilde{P}_1 = (\cos \theta_2 \cdot \cos \theta_3)^2 \\
P_2 &= \widetilde{P}_{12} = (\sin \theta_2 \cdot \cos \theta_3)^2 \\
P_3 &= \widetilde{P}_{13} = (\cos \theta_2 \cdot \sin \theta_3)^2
\end{aligned}
\qquad (7)
$$

The modulation angles θ_2 and θ_3 are given by

$$
\begin{aligned}
\tan^2 \theta_2 &= \frac{P_2}{P_1} = \alpha_2 \\
\tan^2 \theta_3 &= \frac{P_3}{P_1} = \alpha_3
\end{aligned}
\qquad (8)
$$

b. RF power is required to track the phase $(P_{RF} \neq 0)$. In this case, we no longer have $\theta_1 = 90$ deg, but $\theta_1 < 90$ deg. By the same choice of $x_1(t)$, $x_2(t)$, and $x_3(t)$, the power of the RF and the data channels will be

$$
\begin{aligned}
P_1 &= (\sin \theta_1 \cdot \cos \theta_2 \cdot \cos \theta_3)^2 \\
P_2 &= (\sin \theta_1 \cdot \sin \theta_2 \cdot \cos \theta_3)^2 \\
P_3 &= (\sin \theta_1 \cdot \cos \theta_2 \cdot \sin \theta_3)^2 \\
P_{RF} &= (\cos \theta_1 \cdot \cos \theta_2 \cdot \cos \theta_3)^2
\end{aligned}
\qquad (9)
$$

The modulation angles θ_2 and θ_3 are given by Eq. (8) as before, and θ_1 is given (Eq. 9) by

$$\cos^2 \theta_1 = P_{RF} (1 + \alpha_2) (1 + \alpha_3) \qquad (10)$$

If we defined the utilized power

$$P_u = P_1 + P_2 + P_3 + P_{RF}$$

then the lost power due to intermodulation is

$$P_{LOSS} = 1 - P_u = \frac{\alpha_2 \alpha_3}{(1+\alpha_2)(1+\alpha_3)} + (\alpha_2 + \alpha_3)P_{RF} \qquad (11)$$

We will next consider 3 cases of practical interest:

(1) Most of the power is allocated to the first channel (high rate), while the other two channels have low rates. Thus, we have $\alpha_2 \ll 1$ and $\alpha_3 \ll 1$. Hence,

$$P_{LOSS} \approx \alpha_2 \alpha_3 + (\alpha_2 + \alpha_3) P_{RF} \qquad (12)$$

is very small. Results for $\alpha_2 = \alpha_3 = \alpha$ are given in Fig. 9 for $P_{RF} = 0$ and $P_{RF} = 0.1$

(2) Two data channels have equal power ($\alpha_2 = 1$) and the third has a small power ($\alpha_3 \ll 1$). In this case,

$$P_{LOSS} \approx \frac{1}{2} \alpha_3 + (1 + \alpha_3)P_{RF} > P_{RF} \qquad (13)$$

Results for $P_{RF} = 0$ and $P_{RF} = 0.1$ are given in Fig. 9.

(3) All data channels have equal power, i.e., $\alpha_2 = \alpha_3 = 1$. In this case,

$$P_{LOSS} = 0.25 + 2 P_{RF}$$

If, for example, $P_{RF} = 0.1$, then 45% of the power is lost.
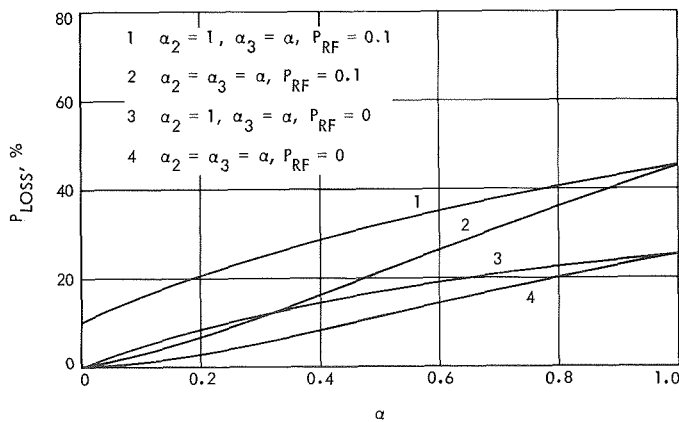
Fig. 9. Lost power for 3-channel telemetry
($\alpha_2 = P_2/P_1$, $\alpha_3 = P_2/P_1$)

3. n-channel Telemetry System

The above analysis (*Subsection* 2) can be generalized to the n-channel telemetry system.

Let $a_i(t)$, $i = 1, \cdots, n$ be the n binary data stream, and let the RF power P_{RF} and the power ratios

$$\alpha_i = \frac{P_i}{P_1} \leq 1, \qquad i = 2, \cdots, n \qquad (14)$$

be given.

The transmitted waveform is

$$2^{1/2} \sin \left(\omega_0 t + \sum_{i=1}^{n} \theta_i x_i(t) \, sq(\omega_i t) \right) \qquad (15)$$

where we want to determine $x_i(t)$ and θ_i to minimize the power lost due to intermodulation.

Using coherent detection, we could separate $2^n - 1$ possible combinations of the data streams, and we want to choose $x_i(t)$ such that the $a_i(t)$, $i = 1, \cdots, n$, will correspond to the n outputs with the higher power.

Each possible output of the form

$$S(t) = x_{i_1}(t) \, x_{i_2}(t) \cdots x_{i_k}(t)$$

will have the power

$$\widetilde{P}_{s_i} = \prod_{j=1}^{k} (\sin \theta_{i_j})^2 \prod_{\substack{m=1 \\ m \neq i_1, \cdots, i_k}}^{n} (\cos \theta_n)^2 \qquad (16)$$

while the RF power is

$$P_{RF} = \prod_{m=1}^{n} (\cos \theta_m)^2 \qquad (17)$$

Following the same arguments as before, we can choose the following system:

$$\left. \begin{array}{l} P_1 = \widetilde{P}_1 \\ P_i = \widetilde{P}_{1i}, \qquad i = 2, \cdots, n \end{array} \right\} \qquad (18)$$

that is,

$$x_1(t) = a_1(t)$$
$$x_i(t) = a_1(t)\,a_i(t), \qquad i = 2, \cdots, n \qquad (19)$$

Hence, $\theta_i,\ i = 1, \cdots, n$ can be determined from the following equations:

$$\tan^2 \theta_i = \alpha_i, \qquad i = 2, \cdots, n$$
$$\cos^2 \theta_1 = \frac{P_{\mathrm{RF}}}{\displaystyle\prod_{i=2}^{n} (\cos \theta_i)^2} = P_{\mathrm{RF}} \prod_{i=2}^{n} (1+\alpha_i) \qquad (20)$$

Thus,

$$P_1 = \frac{1}{\displaystyle\prod_{i=2}^{n} (1+\alpha_i)} - P_{\mathrm{RF}}$$
$$P_i = \alpha_i P_1, \qquad i = 2, \cdots, n \qquad (21)$$

and the lost power due to intermodulate is

$$P_{\mathrm{LOSS}} = 1 - \frac{1 + \displaystyle\sum_{i=2}^{n} \alpha_i}{\displaystyle\prod_{i=2}^{n}(1 + \alpha_i)} + P_{RF} \sum_{i=2}^{n} \alpha_i \qquad (22)$$

If

$$\alpha_i \ll 1, \qquad i = 2, \cdots, n$$

then

$$P_{\mathrm{LOSS}} \approx \frac{\displaystyle\sum_{i=2}^{n} \sum_{j=i+1}^{n} \alpha_i \alpha_j}{\displaystyle\prod_{i=2}^{n} (1 + \alpha_i)} + P_{RF} \sum_{i=2}^{n} \alpha_i \qquad (23)$$

For example, let

$$\alpha_i = \alpha \leq \frac{P_{\mathrm{RF}}}{n - 1}, \qquad i = 2, \cdots, n$$

Then

$$P_{\mathrm{LOSS}} \leq \frac{(n - 1)(n - 2)\,\alpha^2}{2} + P_{\mathrm{RF}}(n - 1)\,\alpha \qquad (24)$$

If $P_{\mathrm{RF}} = 10\%$, then $P_{\mathrm{LOSS}} < 1.5\%$. The results for $n = 4$, $\alpha_i = \alpha,\ i = 2,3,4$, and $P_{\mathrm{RF}} = 0$ or 0.1 are given in Fig. 10.

In the case of equal-energy channel, i.e., $\alpha_i = 1,\ i = 2, \cdots, n$,

$$P_{\mathrm{LOSS}} = \frac{2^{n-1} - n}{2^{n-1}} + (n - 1)\,P_{\mathrm{RF}} > \frac{1}{2} + (n - 1)\,P_{\mathrm{RF}},$$
$$n \geq 4 \qquad (25)$$

Thus, high loss prohibits the use of this method for equal rate multichannel telemetry. However, for one high rate channel and several low rate channels, the loss can be made negligible, and thus the new modulation scheme is very efficient and practical.

4. Conclusion

The improved performance of the Interplex modulation system for 2-channel telemetry can be extended to multichannel telemetry. The efficiency is particularly high in the case of one high rate data channel, and several low rate channels. We can, thus, build a unified 4-channel telemetry system for a space mission, where we will have a high rate (science) channel, and low rate (engineering, ranging, and verification of commands) channels. In this case, for example, we can have $P_{\mathrm{RF}} = 10\%$ and a power ratio of 1:25 (or smaller) in the low and high rate channels, while losing less than 1% of the total power.
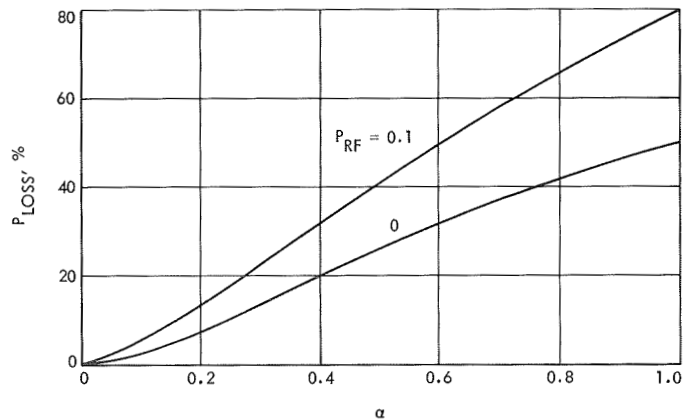

Fig. 10. Lost power for 4-channel telemetry
($\alpha_i = P_i/P_1 = \alpha,\ i = 2, 3, 4$)

D. Coding and Synchronization Research: Decision Rules for a Two-Channel Deep-Space Telemetry System, S. Butman, J. E. Savage,[2] and U. Timor

1. Introduction

Consider a two-channel, phase-modulated coherent telemetry system. The data streams $a(t)$ and $b(t)$ are binary waveforms of amplitude ± 1. The transmitted signal is

$$x(t) = 2^{1/2} \sin \left[\omega_0 t + \theta_1 a(t) \, \mathrm{sq}(\omega_1 t) + \theta_2 b(t) \, \mathrm{sq}(\omega_2 t) \right]$$

(1)

where $\mathrm{sq}(\omega_1 t)$ and $\mathrm{sq}(\omega_2 t)$ are squarewaves with frequencies chosen so that they are orthogonal and the θ_i's are the modulation angles. The received waveform is corrupted by an added noise, which we assume to be white gaussian with one-sided spectral density N_0.

Coherent carrier demodulation with $2^{1/2} \sin \omega_0 t$ and $2^{1/2} \cos \omega_0 t$, and coherent subcarrier demodulation, produce the following signals (SPS 37-62, Vol. III, pp. 57–60):

$$\left. \begin{aligned} r_1(t) &= \lambda_1 a(t) + n_1(t), & \lambda_1 &= \sin \theta_1 \cdot \cos \theta_2 \\ r_2(t) &= \lambda_2 b(t) + n_2(t), & \lambda_2 &= \cos \theta_1 \cdot \sin \theta_2 \\ r_3(t) &= -\lambda_3 a(t) b(t) + n_3(t), & \lambda_3 &= \sin \theta_1 \cdot \sin \theta_2 \end{aligned} \right\}$$

(2)

where $P_i \triangleq \lambda_i^2$ is the normalized signal power in $r_i(t)$, and $n_1(t), n_2(t), n_3(t)$ are statistically independent white gaussian noise processes with spectral density N_0.

Let the rates of $a(t)$ and $b(t)$ be $R_a = 1/T_a$ and $R_b = 1/T_b$, respectively, assume that $R_a > R_b$, and assume that

$$\frac{R_a}{R_b} = \frac{T_b}{T_a} = K$$

(3)

an integer. We can consider $a(t)$ as a binary sequence $\{a_i\}$ associated with rate R_a, and $b(t)$ as a binary sequence $\{b_j\}$ with rate R_b. Equivalently, by repeating every b_j K times, we can write $b(t)$ as a sequence $\{b_i\}$ with rate R_a. If we denote a sequence $\{y_i\}$ of rate R_a by y, we can

write the signals (Eq. 2) as:

$$\left. \begin{aligned} \mathbf{r}_1 &= \lambda_1 \mathbf{a} + \mathbf{n}_1 \\ \mathbf{r}_2 &= \lambda_2 \mathbf{b} + \mathbf{n}_2 \\ \mathbf{r}_3 &= -\lambda_3 \mathbf{c} + \mathbf{n}_3 \end{aligned} \right\}$$

(4)

where $\mathbf{c}$ is the sequence $\{a_i b_i\}$, and the components of $\mathbf{n}_1, \mathbf{n}_2$, and $\mathbf{n}_3$ are all statistically independent gaussian varieties with zero mean and variance

$$\sigma^2 = \frac{N_0}{2} T_a$$

(5)

From the $\mathbf{r}_i$'s, the receiver estimates the data sequences $\{a_i\}$ and $\{b_i\}$. In the next subsections, we will consider different decision rules and evaluate their performance.

2. Decision Rules

Assume that the components of **a** and **b** are statistically independent and equally likely to be ± 1. Then the maximum *a posteriori* (or optimum) rule and the maximum likelihood rule are equivalent. Let $p(\mathbf{r}_1, \mathbf{r}_2, \mathbf{r}_3 \mid \mathbf{a}, \mathbf{b})$ be the likelihood function. Then, we choose **a**, **b** to maximize this function, and denote the maximizing values $\hat{\mathbf{a}}$ and $\hat{\mathbf{b}}$.

This maximization can be done over successive groups of K components of **a** and **b**, because the components of **b** are equal over such groups and the groups are statistically independent. Considering one group at a time, the log likelihood function is proportional to

$$Q = \lambda_1 \sum_{i=1}^{K} a_i r_{1i} + \lambda_2 b \sum_{i=1}^{K} r_{2i} - \lambda_3 b \sum_{i=1}^{K} a_i r_{3i}$$

(6)

and the optimum rule chooses $\hat{a}_i$, $i = 1, \cdots, K$, and $\hat{b}$ to maximize Q.

Rule 1: the optimum rule (Fig. 11). Let

$$D \triangleq \sum_{i=1}^{K} r_{2i}$$

and compute

$$\left. \begin{aligned} Q_+ &= \lambda_2 D + \sum_{i=1}^{K} | \lambda_1 r_{1i} - \lambda_3 r_{3i} | \\ Q_- &= -\lambda_2 D + \sum_{i=1}^{K} | \lambda_1 r_{1i} + \lambda_3 r_{3i} | \end{aligned} \right\}$$

(7)
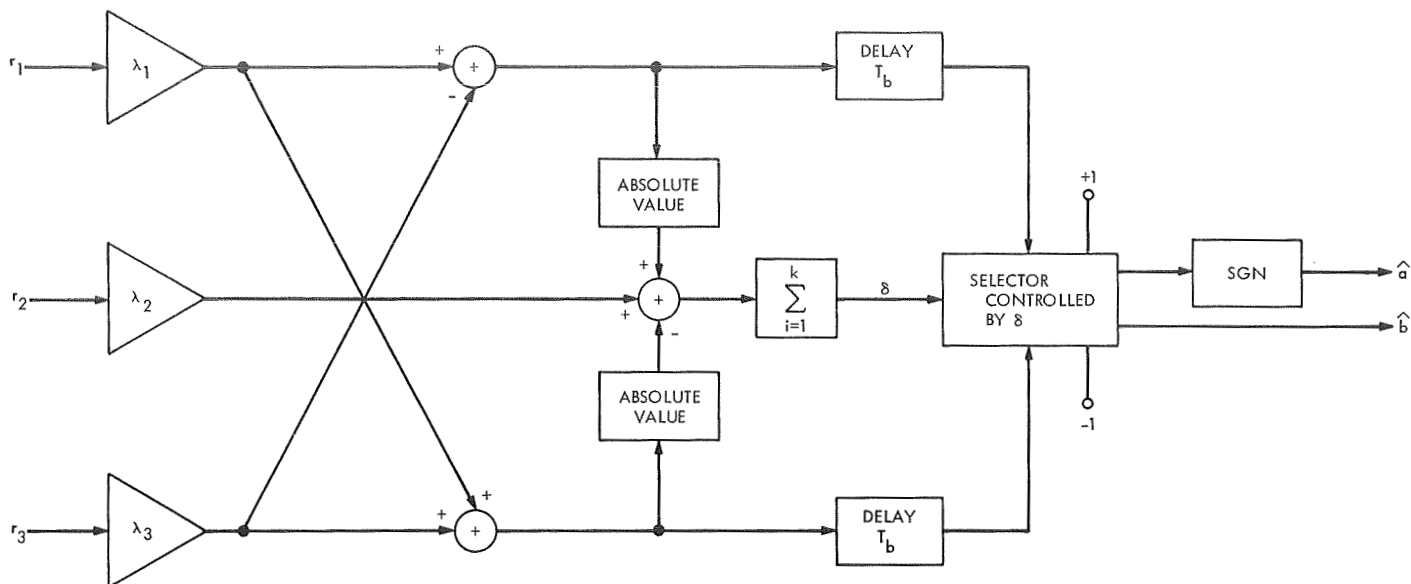
Fig. 11. Schematic diagram of decision rule 1

Then,

$$
\begin{aligned}
\hat{b} &= 1 \text{ and } \hat{a}_i = \text{sgn}(\lambda_1 r_{1i} - \lambda_3 r_{3i}), && \text{if } Q_+ \geq Q_- \\
\hat{b} &= -1 \text{ and } \hat{a}_i = \text{sgn}(\lambda_1 r_{1i} + \lambda_3 r_{3i}), && \text{if } Q_+ < Q_-
\end{aligned} \Bigg\}
$$

$$(8)$$

where sgn means "sign of."

In Rule 1, the a_i's and b are estimated simultaneously. By estimating b first and using this value to estimate the a_i's, or vice versa, we can have the following non-optimum rules (Fig. 12):

Rule 2.

$$
\begin{aligned}
\hat{b} &= \text{sgn } D \\
\hat{a}_i &= \text{sgn } (\lambda_1 r_{1i} - \lambda_3 \hat{b} r_{3i})
\end{aligned} \Bigg\}
$$

$$(9)$$

Rule 3.

$$
\begin{aligned}
\hat{a}_i &= \text{sgn}(r_{1i}) \\
\hat{b} &= \text{sgn} \left(\lambda_2 D - \lambda_3 \sum_{i=1}^{K} \hat{a}_i r_{3i} \right)
\end{aligned} \Bigg\}
$$

$$(10)$$

Finally, if we estimate $\hat{a}_i$ and $\hat{b}$ independently, we get
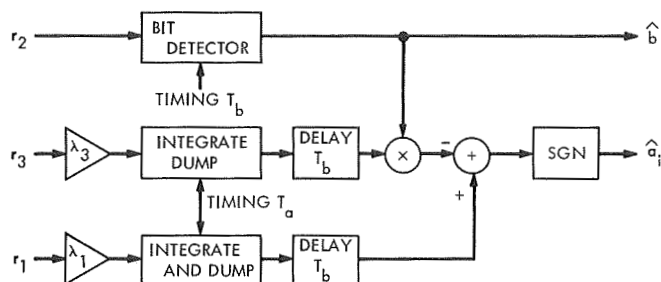
Fig. 12. Schematic diagrams of decision rules 2,3,4

Rule 4.
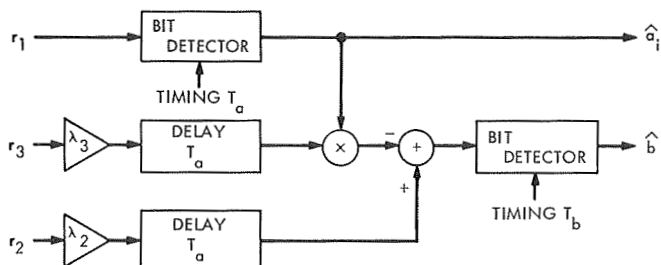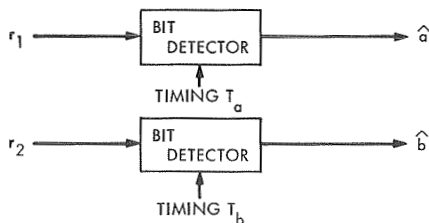
$$\left.\begin{aligned}\hat{a}_i &= \text{sgn}(r_{1i}) \\ \hat{b} &= \text{sgn}(D)\end{aligned}\right\} \qquad (11)$$

The various rules differ in the way we use the information in the intermodulation signal

$$r_3(t) = -\lambda_3 a(t) b(t)$$

In Rule 1, r_3 is used to estimate both $a(t)$ and $b(t)$, while in the other cases r_3 is used to estimate $a(t)$ only (Rule 2), $b(t)$ only (Rule 3), or is completely ignored (Rule 4).

If the power P_3 of $r_3(t)$ is small (i.e., $\lambda_1 \gg \lambda_3$ and $\lambda_2 \gg \lambda_3$), the various rules will perform satisfactorily since the equations are effectively decoupled. However, if $\lambda_1 \gg 0$ and $\lambda_3 \gg \lambda_2$, then a reliable decision on $\hat{a}_i$ can be made, and subsequently used to estimate $\hat{b}$ (Rule 3). These conditions prevailed on the *Mariner* Mars 1969 mission. However, the telemetry system used Rule 4, which is, as we shall see, decidedly inferior to Rule 3.

3. Performance of Rules 3 and 4

In both rules, the probability of error in estimating a_i is

$$p_a = \text{erfc}\left(\frac{2P_1}{N_0 T_a}\right)^{1/2} \qquad (12)$$

To estimate b, Rule 4 uses a similar procedure which yields an error probability

$$P_b = \text{erfc}\left[\left(\frac{2P_2}{N_0 T_b}\right)^{1/2} \cdot \frac{T_b}{T_a}\right] \qquad (13)$$

In Rule 3, $\hat{b} = \text{sgn}(r)$ and

$$\begin{aligned}r &= \sum_{i=1}^{K}(\lambda_2 r_{2i} - \lambda_3 \hat{a}_i r_{3i}) \\ &= b\left(\lambda_2^2 K + \lambda_3^2 \sum_{i=1}^{K} a_i \hat{a}_i\right) + \sum_{i=1}^{K}(\lambda_2 n_{2i} - \hat{a}_i \lambda_3 n_{3i}) \\ &= b[P_2 K + P_3(K - 2J)] + n\end{aligned}$$

where J is the number of errors which occur in estimating the a_i's, and n is a gaussian variate of zero mean and variance

$$\sigma_0^2 = (P_2 + P_3)\frac{N_0 T_b}{2}$$

Hence, the probability of error in estimating b by Rule 3 is

$$p_b^* = \sum_{J=0}^{K} p_b(J)\, P(J) \qquad (14)$$

where

$$p_b(J) = \text{erfc}\left\{\frac{(P_2 + P_3)K - 2P_3 J}{\left[(P_2 + P_3)\dfrac{N_0 T_b}{2}\right]^{1/2}}\right\} \qquad (15)$$

is the probability of error in estimating b when J errors had been made in estimating the K a_i's, and

$$P(J) = \binom{K}{J} p_a^J (1 - p_a)^{(K-J)} \qquad (16)$$

We will now derive lower and upper bounds to p_b^*, for the case where p_a is small. Consider the lower bound first. We note that $p_b(J)$ is a concave function for

$$J \le \frac{K}{2}\left(1 + \frac{P_2}{P_3}\right)$$

and we lower bound p_b^* by truncating the sum to $0 \le J \le K/2$ and then apply Jensen's inequality to give

$$p_b^* \ge \left[\sum_{J=0}^{K/2} P(J)\right] p_b\left[\frac{\displaystyle\sum_{J=0}^{K/2} J\,P(J)}{\displaystyle\sum_{J=0}^{K/2} P(J)}\right] \qquad (17)$$

If p_a is small, the truncated sums are approximately equal to their untruncated values, especially if K is large. Then,

$$p_b^* \gtrsim p_b(K p_a) = \text{erfc}\left\{\frac{[(P_2 + P_3 - 2P_3 p_a)K]^2}{(P_2 + P_3)\dfrac{N_0 T_b}{2}}\right\}^{1/2} \qquad (18)$$

and if $P_2/P_3 \ll 1$, as it is in the *Mariner* Mars 1969 system, then

$$p_b^* \gtrsim \text{erfc}\left[\left(\frac{2P_3}{N_0 T_b}\right)^{1/2}\frac{T_b}{T_a}(1 - 2p_a)\right] \qquad (19)$$

We next develop an upper bound to p_b^*. Observe that $p_b(J)$ is monotone, increasing in J, and has a value no

greater than 1. Then,

$$
\left.
\begin{aligned}
p_b^* &= \sum_{J=0}^{L-1} P(J)\, p_b(J) + \sum_{J=L}^{K} P(J)\, p_b(J) \\
&\leq \left[\sum_{J=0}^{L-1} P(J) \right] p_b(L) + \sum_{J=L}^{K} P(J) \\
&\leq p_b(L) + F(L)
\end{aligned}
\right\}
\tag{20}
$$

where

$$
F(L) = \sum_{J=L}^{K} P(J)
$$

A good choice for L is that for which

$$
p_b(L) = F(L) \tag{21}
$$

since $p_b(L)$ is increasing in L while $F(L)$ is decreasing in L for $L \geq Kp_a$. If K is large, $F(L)$ drops off very rapidly; however, $p_b(L)$ is changing slowly, especially if p_a is small. Therefore, for large K and small p_a, we will have $L \approx \alpha K p_a$, where for practical cases, α is of the order of 2 or 3. Thus,

$$
p_b^* \leq 2 p_b(\alpha K p_a) \approx 2 p_b(K p_a) \tag{22}
$$

which is approximately twice the lower bound.

5. Comparison Between p_b and p_b^*

We can now compare the existing rule with Rule 3, under the prevailing conditions of *Mariner* Mars 1969. Both rules estimate the variables a_j, which are data samples on the high rate link, with the same accuracy (or the same error probability p_a). Using the present decision rule on the low rate channel, the samples on the low rate link b_j are estimated with a probability of

error of

$$
P_b = \mathrm{erfc}\left[\left(\frac{2P_2}{N_0 T_b} \right)^{1/2} \cdot \frac{T_b}{T_a} \right]
$$

However, using the decision Rule 3, the error probability is

$$
p_b^* \approx \mathrm{erfc}\left[\left(\frac{2P_3}{N_0 T_b} \right)^{1/2} \cdot \frac{T_b}{T_a} (1 - 2p_a) \right]
$$

which is substantially smaller, since $P_3 \gg P_2$ and p_a is small. This reduction in p_b can be translated to a power reduction in the low rate channel and a power increase to the high rate channel for the same total transmitter power. The saving can be as much as 3 dB when the two channels have equal rates, as shown in SPS 37-62, Vol. III, for an essentially equivalent decision rule.

6. Conclusion

We have derived an optimum and a good suboptimum decision rule for a communication scheme now used in deep-space telemetry systems. By using the estimated high rate data a_j to estimate the low rate data, the suboptimum rule (Rule 3) yields a much lower error probability than the existing rule (Rule 4), since $P_3 \gg P_2$.

In the Interplex modulation scheme, introduced by Butman and Timor (SPS 37-62, Vol. III) an independent decision rule (like Rule 4) yields a low rate error probability of

$$
p_b = \mathrm{erfc}\left[\left(\frac{P_3}{N_0 T_b} \right) \cdot \frac{T_b}{T_a} \right] \approx p_b^*
$$

Thus, the advantage gained by Rule 3 is achieved there by a simple decision rule, without losing the independence in estimating a_j and b_j.

VI. Communications Elements Research

TELECOMMUNICATIONS DIVISION

A. Spacecraft Antenna Research: Preliminary RF Test of Conical Gregorian Antenna, A. C. Ludwig and J. Hardy

1. Introduction

A conical Gregorian reflector antenna is one of three new antenna concepts described in SPS 37-59, Vol. III, pp. 55–57. The initial concept was based on optical design principles which apply in the limit of zero wavelength. To verify that the concept does, in fact, work as an antenna when the wavelength is within one or two orders of magnitude of the size of the antenna, a small inexpensive prototype has been built and tested. The RF test of this model parallels a mechanical development effort on this antenna by the Engineering Mechanics Division at JPL, which included fabrication of the prototype and is described in *Chapter XI-A*.

2. Prototype Design

The geometry of the prototype model is shown in Fig. 1. When this geometry was selected there was some question about the effect of the subreflector blockage on the outgoing wave, and in this initial design the subreflector was made substantially smaller than the non-illuminated central region of the main reflector. This results in a large loss of aperture area and is possibly overconservative. This aspect of the design will be investigated in the future.

The feed selected for the antenna (Fig. 2) is a shortened version of a corrugated horn previously developed at JPL (SPS 37-58, Vol. III, pp. 61–64). Experimental amplitude and phase patterns of the feed are shown in Fig. 3. Assuming optical behavior of rays from the feed (Fig. 1), the resulting aperture illumination may be calculated, based on the conservation of power. The calculated illumination is compared to the aperture illumination which would result if the same feed were used with a conventional parabolic cassegrain antenna (Fig. 4). In Fig. 4, the aperture radius is plotted on an exponential scale such that scale segments of equal length represent equal segments of aperture area. The experimental feed pattern shown in Fig. 2 is nearly exponential, so the aperture illumination for the conventional antenna is nearly a straight line pattern. Using this calculated aperture illumination, the pattern and gain of the conical Gregorian antenna may be calculated using the standard aperture field integral.

3. Test Results

The prototype antenna was mounted back-to-back with a standard-gain horn (Fig. 5). Patterns were taken at X-band (8448 MHz) on the 1200-ft range on the JPL Mesa Antenna Range facility, and gain was measured by direct comparison with the standard-gain horn. In Fig. 6a the measured pattern is compared to the pattern computed by the aperture field method. The close agreement
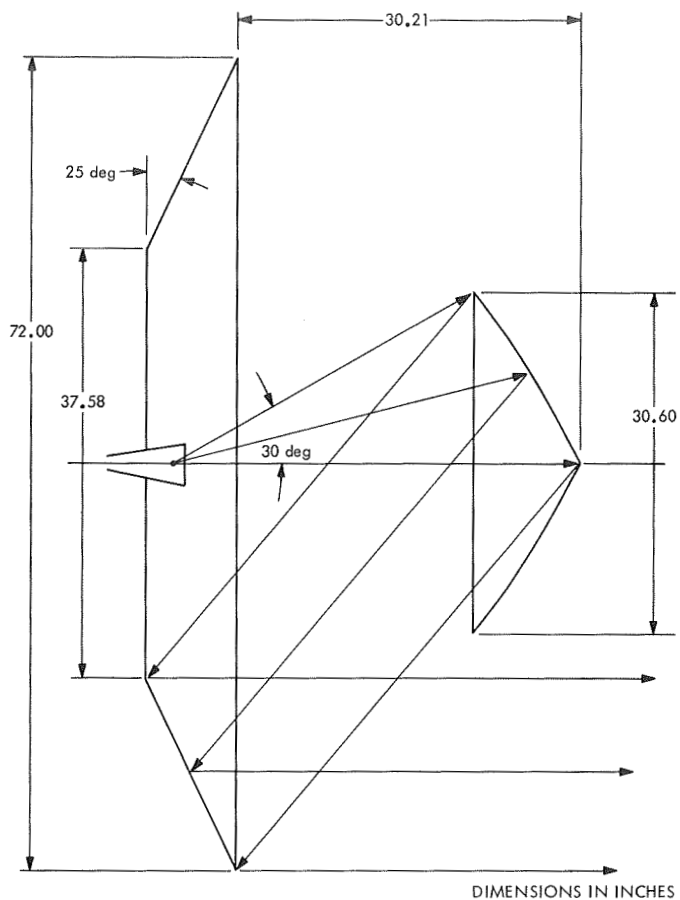
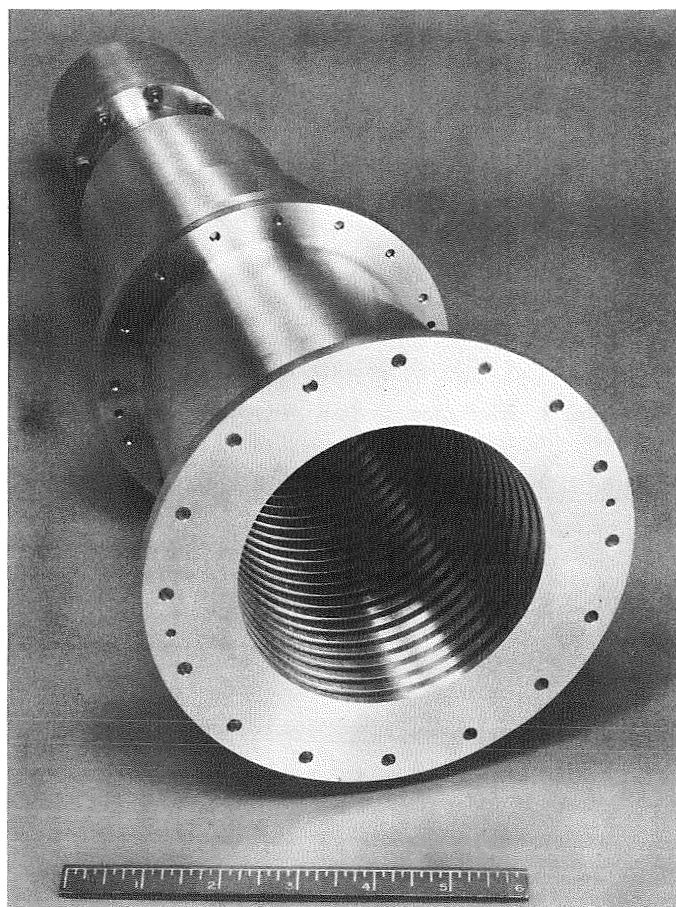**Fig. 1. Geometry of prototype conical Gregorian antenna**

DIMENSIONS IN INCHES

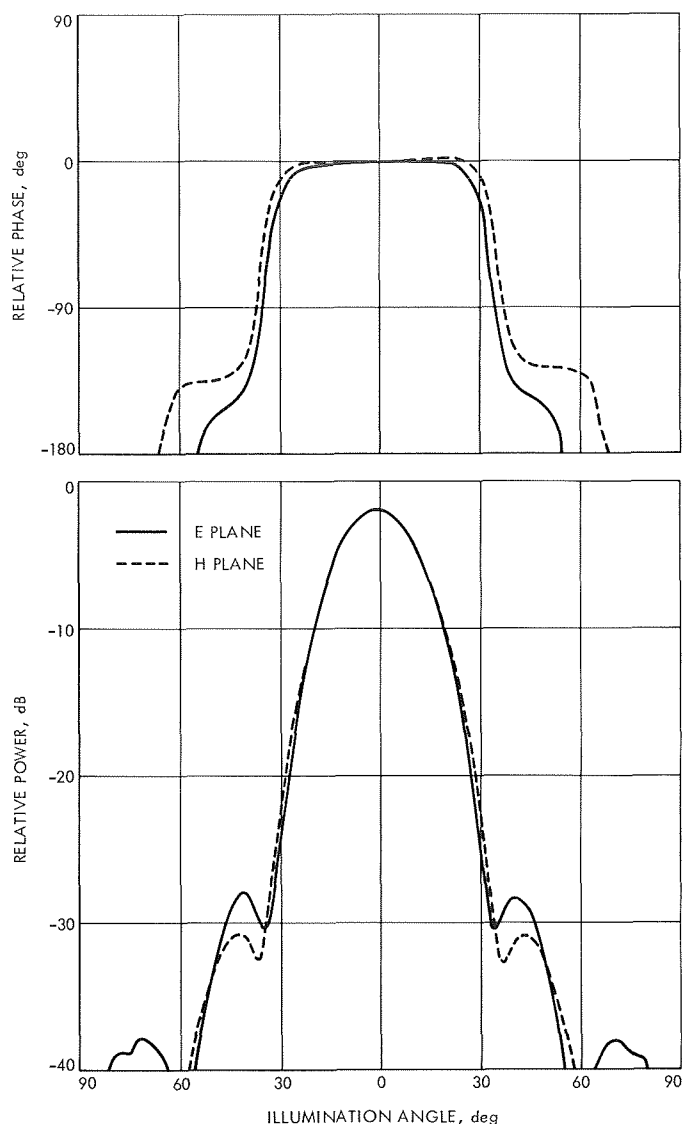**Fig. 2. Corrugated feed for prototype antenna RF tests**

Fig. 3. Radiation pattern of corrugated feed

strongly indicates that the optical principles used in the design and calculations are valid.

The measured gain at 8448 MHz was 40.8 ±0.75 dB. Compared to a uniformly illuminated full 6-ft-diam aperture, this corresponds to 46% efficiency. However, this value is not indicative of the performance potential of this antenna for the following reasons:

(1) The main reflector and subreflector surfaces were poor, due to the attempt to keep the model inexpensive, and result in surface losses of about 0.5 dB.

(2) The nonilluminated central area is large, as mentioned earlier.

With these effects included, the calculated gain is $41.06^{-0.60}_{+0.25}$ dB, which agrees well with the measured value. It is estimated that measured efficiencies of greater than 60% will be achieved with better designs.

The prototype was also tested, using an S-band monopulse feed developed for the Thermoelectric Outer Planet Spacecraft (TOPS) high-gain antenna (SPS 37-60, Vol. III, pp. 36–41). The resulting monopulse patterns are quite good, as shown in Fig. 6b. The S-band sum channel patterns are similar to the X-band pattern shown in Fig. 6a. This demonstrates that the conical concept does not impair monopulse performance, and also that the antenna behaves well at S-band, where the subreflector is only 5.5 wavelengths in diameter.

A very important feature of the conical design is that it is very insensitive to feed or subreflector defocusing. This is easily seen by referring to Fig. 1: if the feed and subreflector are moved as a unit, the reflected rays are translated but remain parallel to the desired ray paths. Therefore, *no* aperture phase error is introduced, and the only loss is due to the second-order effect of increased spillover. If the feed is moved relative to the subreflector, phase error is introduced, but the loss is small, due to the relatively small angle subtended by the feed pattern. During the RF tests of the antenna, the subreflector was defocused by 2 in. (1.44 wavelengths at the X-band test frequency), resulting in a gain degradation of only 0.8 dB. In a conventional parabolic antenna the gain loss would be about 9 dB for this amount of defocusing (SPS 37-62, Vol. III, pp. 87–90, so the conical antenna is dramatically better in this regard. The lack of aperture phase error was also substantiated experimentally by the fact that the pattern nulls remained deep in the presence of defocusing.

4. Conclusion

It has been demonstrated that the RF performance of the conical Gregorian antenna is consistent with the optical principles assumed in the design. The antenna also performs well in the monopulse mode of operation, and when the subreflector is less than 6 wavelengths in diameter.

Further work on the concept is clearly justified, and an attempt will be made to design a model with RF performance closer to the full potential of the design.
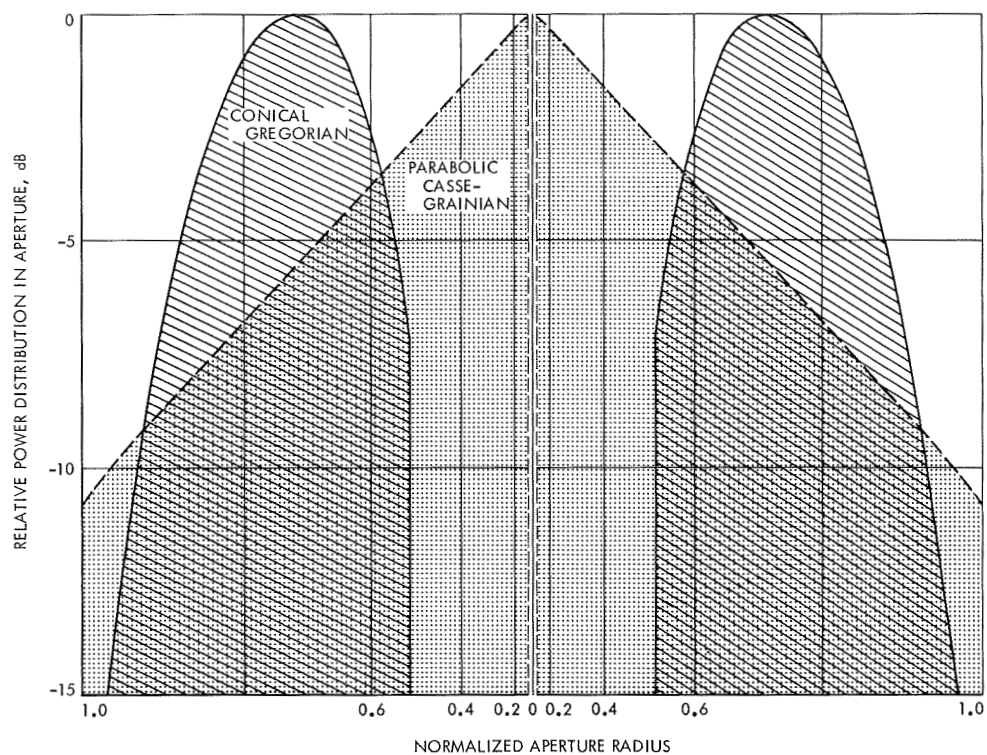
Fig. 4. Antenna aperture power distributions
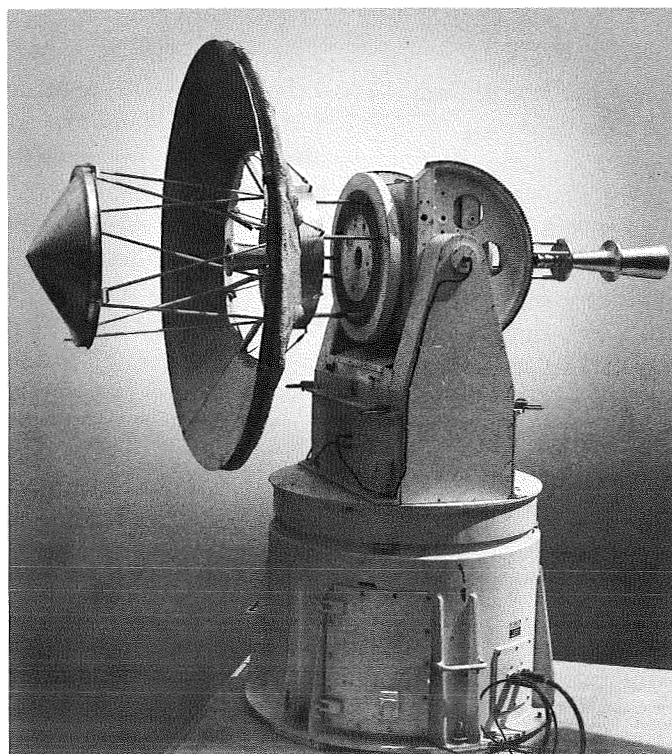
Fig. 5. Prototype antenna and gain-standard horn
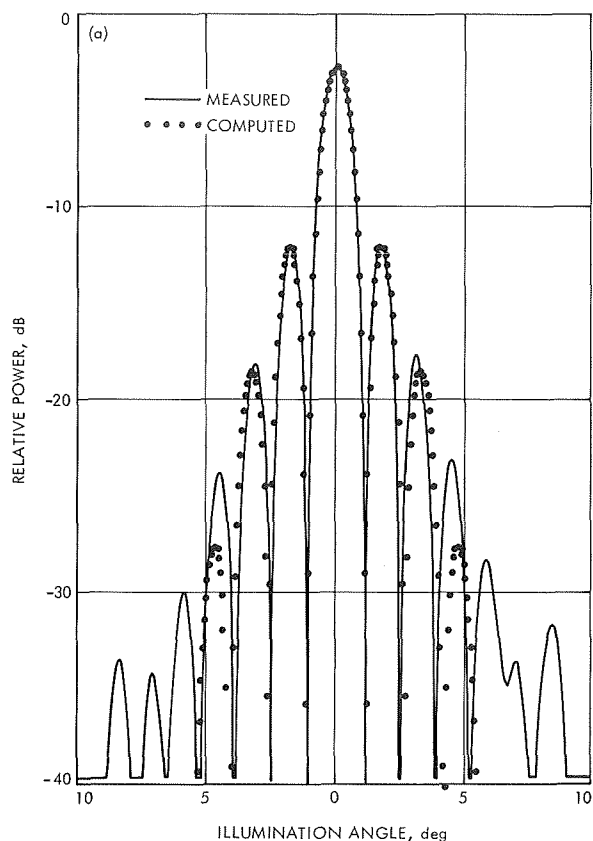
Fig. 6a. Conical Gregorian antenna radiation pattern
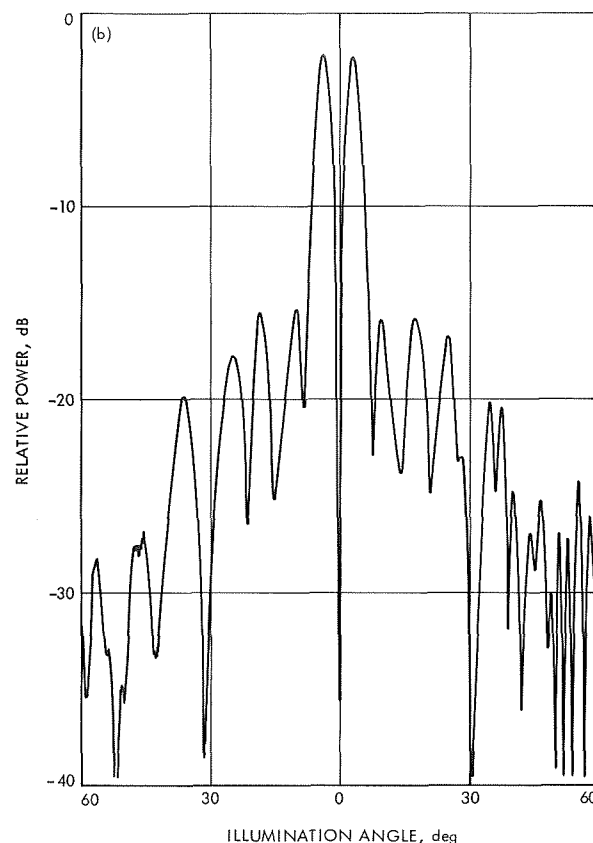
Fig. 6b. Conical Gregorian S-band monopulse pattern

B. Spacecraft Antenna Research: Further RF Test Results of Reflector Surface Materials for Spacecraft Antennas, K. Woo

1. Introduction

A waveguide measurement technique for determining the RF loss characteristics of reflector surface materials for spacecraft antennas was described in SPS 37-61, Vol. III, pp. 99–106. The measured RF reflectivity losses of several materials (gold-plated Chromel-R and copper-coated Dacron meshes, aluminum and stainless steel sheets) were reported. In this article, the RF loss characteristics of two additional surface materials—improved gold-plated Chromel-R mesh and Emfoil—determined by the same measurement technique are presented.

2. Results

The improved type gold-plated Chromel-R mesh was supplied by Prodesco, Inc. The mesh is composed of nichrome-type base material (74% Ni, 20% Cr, 3% Al, 3% Fe) plated with approximately 50 μin. of gold.

Table 1 shows the measured RF loss characteristics of a typical sample of the mesh (Fig. 7) at three different orientations and three different tensions. The data in the table indicate that this mesh exhibits less RF reflectivity loss than the similar mesh reported in the aforementioned reference. Equations (2) through (4) in the same referenced article can be used to calculate the portions of the incident power reflected by, absorbed by, and transmitted through the mesh. For example, for the case of 45-deg orientation and medium tension, the power incident on the mesh is 98.7% reflected, 0.9% absorbed by the mesh, and 0.4% transmitted through the mesh.

The Emfoil was supplied by Pallflex Corp. This material is composed of a copper foil (0.0005- to 0.0008-in. thick) applied to a glass epoxy laminate (0.007- to 0.009-in. thick). The measured RF reflectivity loss (power incident on the copper side) of Emfoil varies from test to test, ranging from 0.021 to 0.042 dB at 8448 MHz. This indicates that about 99.5 to 99.0% of the incident power will be reflected back at that frequency when this material is used as a reflector.

Table 1. Typical loss characteristics of Prodesco gold-plated Chromel-R mesh at 8448 MHz

Mesh orientation	Reflectivity loss, dB			Insertion loss, dB		
	No tension (loose)	Medium tension	Maximum tension	No tension (loose)	Medium tension	Maximum tension
0-deg direction parallel to E-field	0.051	0.047	0.051	27.8	26.0	24.2
45-deg direction parallel to E-field	0.074	0.056	0.054	24.5	24.5	23.3
90-deg direction parallel to E-field	0.053	0.041	0.039	27.4	27.8	25.8
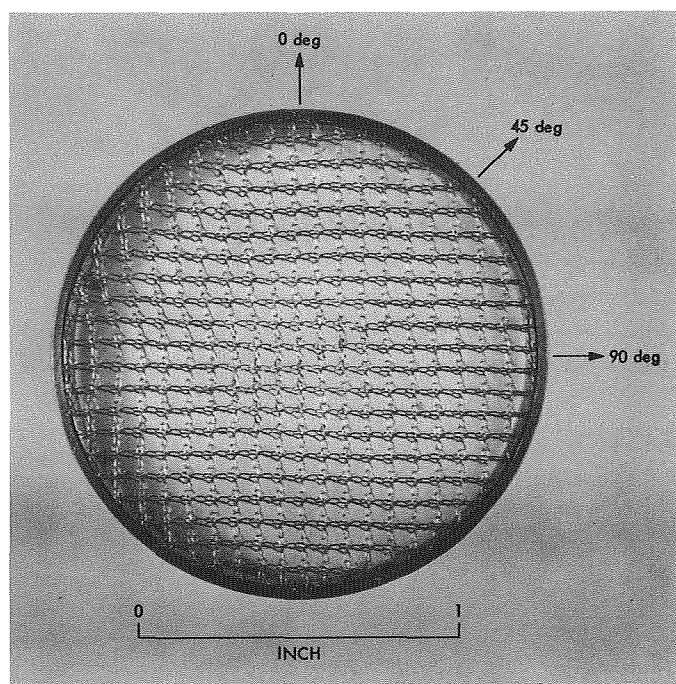
Fig. 7. Configuration of Prodesco gold-plated Chromel-R mesh

C. Spacecraft Antenna Research: Voltage Breakdown in Monopole Antennas at S-band, R. Woo

1. Introduction

Voltage breakdown in coaxial transmission lines has been thoroughly studied previously (Ref. 1). The antenna represents another component that is susceptible to voltage breakdown. In some cases, antenna breakdown occurs at fairly low levels of power. In this article, we report on investigations made with monopole antennas. Monopole antennas are of particular interest, since the results obtained may be applied to dipole antennas as well. The monopole antenna is also a common element used in feeding other antenna types.

The objective of this study was twofold. First, there was a need for breakdown data at S-band frequencies. Previous experiments were generally carried out at lower frequencies (Ref. 2). Second, it was desired to investigate the use of dielectrics to improve the power-handling capability of these monopole antennas.

2. Experimental Setup

Measurements were made at 2310 MHz at which level 700 W of CW power were available. The setup is shown in Fig. 8 and the schematic in Fig. 9. The monopole antenna was located over a 9-in.-diam ground plane in a 12-in.-diam pyrex bell jar. The feed of the monopole was designed so that it was breakdown-free. A dc biased pickup probe similar to the one used in previous experiments (Ref. 3) was used to detect breakdown. The vacuum system consisted of a roughing pump and a Vac-Ion pump. Pressures lower than 10^{-6} torr were readily achieved. Pressure was measured with an alphatron gauge. Radiation patterns were measured with a dipole antenna located on a revolving arm above the bell jar. To ensure the presence of electrons to start ionizing collisions, a 1-mCi Cobalt 60 source was located near the antenna.

3. Experimental Results

The monopole antennas used in these experiments were all $\lambda/4$ long and had flat tips. Radiation patterns were measured both with and without the bell jar. The patterns showed good agreement with each other in both cases. A typical radiation pattern is shown in Fig. 10.

The breakdown results for five monopole antennas whose diameters varied from 0.093 to 0.375 in. are shown in Fig. 11. It is evident that ionization breakdown
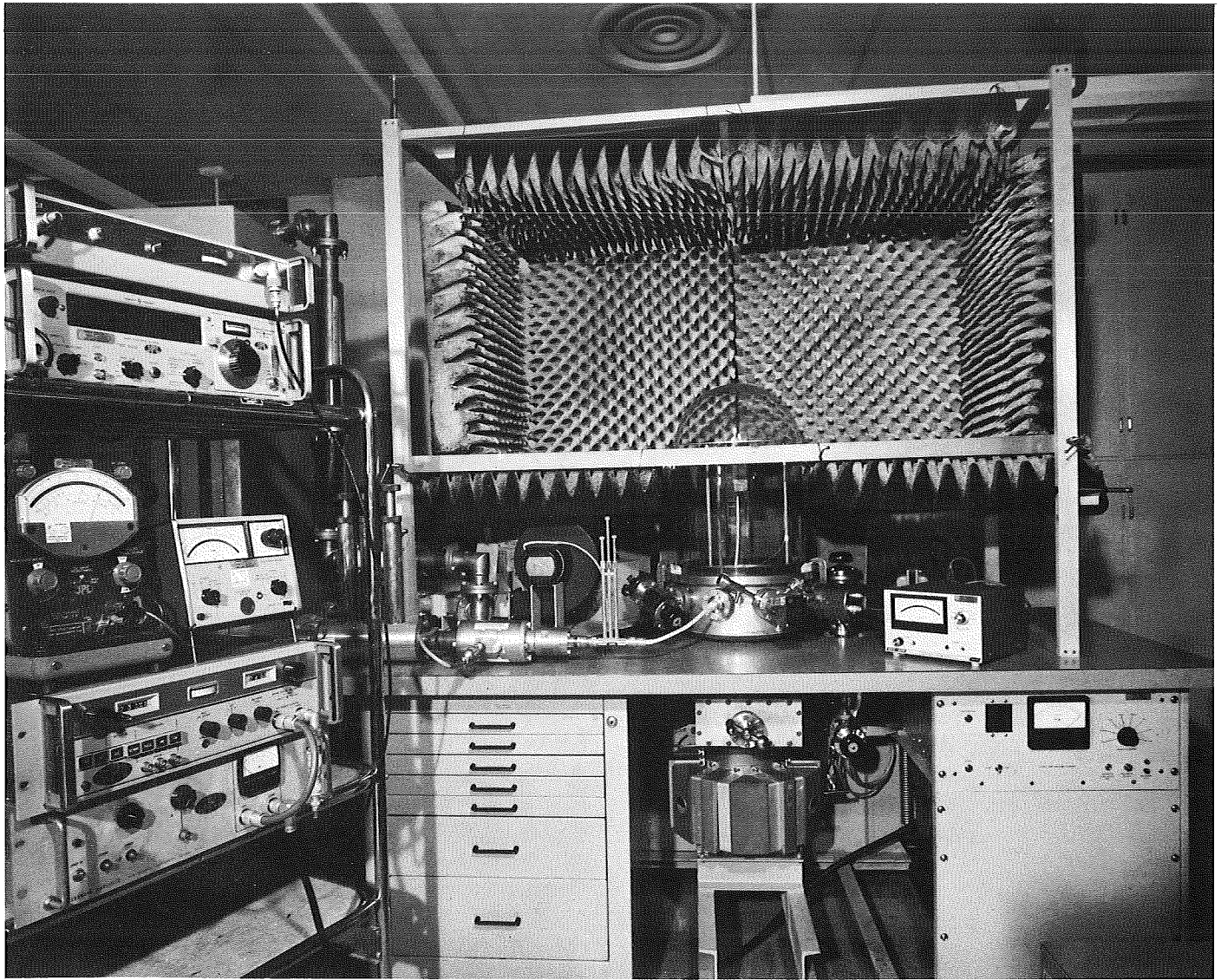
Fig 8. Test setup
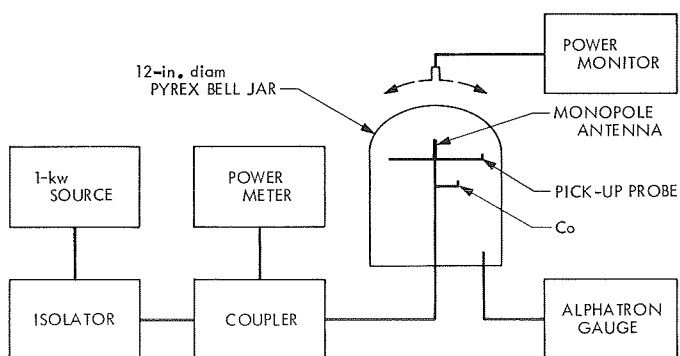
Fig. 9. Schematic of test setup
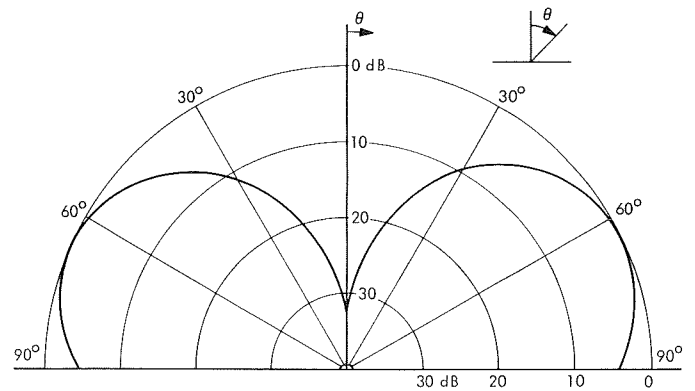
Fig. 10. Typical radiation pattern
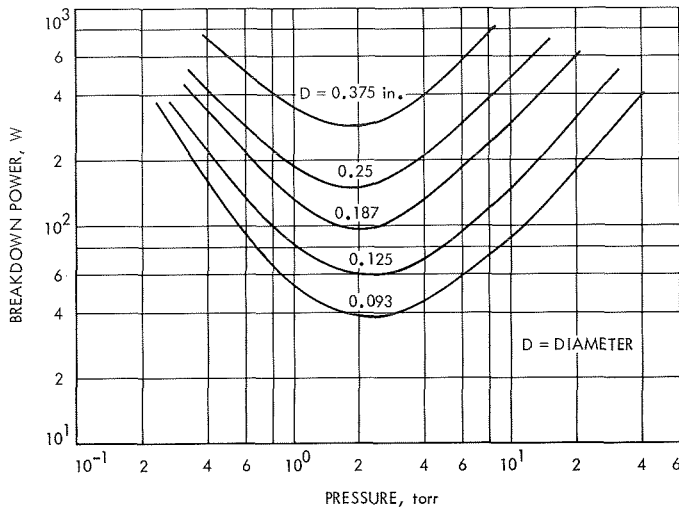
Fig. 11. Breakdown of monopoles with varying diameters

Fig. 12. Breakdown for monopoles in terms of similarity parameters

occurred. It is seen that an increase in monopole diameter results in a rapid rise of minimum breakdown power. According to Ref. 2, a λ/4-long 0.25-in. diam monopole handles 6 W at 240 MHz. In comparison, Fig. 11 shows that a λ/4-long 0.25-in.-diam monopole handles 150 W at 2310 MHz. Thus, it is seen that for a fixed-diameter monopole, breakdown power increases rapidly as frequency is increased. This behavior becomes more obvious when similarity parameters are introduced to represent the breakdown data. This has been done in Fig. 12 where the abscissa is p/f (p is pressure and f is frequency) and each breakdown curve corresponds to a product fd (D is the monopole diameter). In Ref. 2 a different set of similarity parameters was used. This particular set is not as useful as the one in Fig. 12. First, the effective electric field concept used introduces some error. Second, the minimum breakdown power levels are not explicitly shown. Third, the effects of changing frequency or monopole diameter on the breakdown power levels are not evident.

The minima of the curve in Fig. 12 are shown in Fig. 13 along with the data point from Ref. 2 where 'f was 240 MHz and D was 0.25 in. (6.35 cm). From Fig. 13 it is seen that significant power-handling improvement results when either frequency or monopole size is increased. The problem of voltage breakdown in monopole antennas, therefore, becomes less serious for higher frequencies.

By covering the monopole with a dielectric such as Teflon, the power-handling capability of the monopole may be improved. Teflon caps were used, and the cap

Fig. 13. Minima breakdown power as a function of fD

configuration is shown in Fig. 14. It was found that increasing the length L of the cap over 0.5 in. did not result in any power-handling improvement. The length of the cap was, therefore, fixed at 0.5 in. This behavior is not surprising, since the fields are highest at the tip of the monopole. These Teflon caps had very little effect on the impedance and radiation patterns of the monopole. Results for the 0.187-in.-diam monopole are shown in Fig. 15. The diameter of the cap was varied from 0.25 to 0.525 in. As can be seen, an improvement in
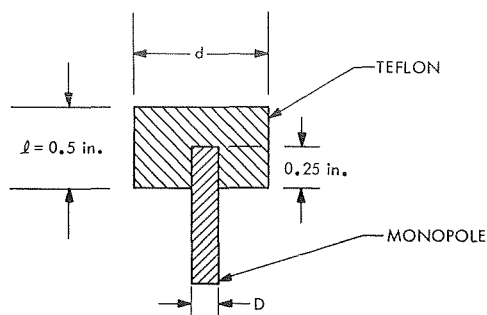
Fig. 14. Teflon cap configuration
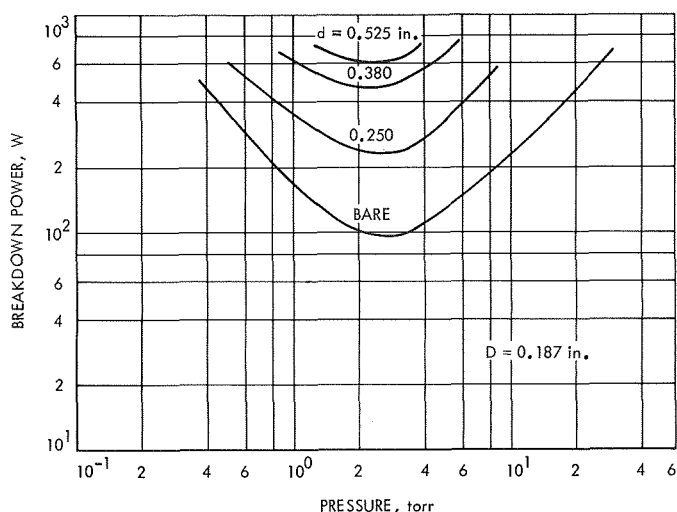
Fig. 15. Breakdown for a monopole antenna with varying sizes of Teflon cap

power handling of over six times that of a bare monopole was obtained. Similar significant improvement resulted for other monopoles, and the data is summarized in Table 2. It should be noted that the use of dielectrics

Table 2. Breakdown power for various cases of monopole and Teflon cap sizes

Teflon cap diameter d, in.	Monopole diameter D, in.				
	0.093	0.125	0.187	0.25	0.375
Bare ($d = D$)	39	60	98	150	290
0.25	220	230	230	a	a
0.380	300	360	460	a	a
0.525	300	360	600	a	a
[a]No breakdown up to 740 W.					

becomes more attractive as frequency is raised, since the volume, and consequently the weight, of the dielectric necessary is reduced.

4. Conclusion

Breakdown power levels for monopole antennas increase rapidly when either monopole diameter or frequency is increased. When voltage breakdown is a problem, dielectrics may be used to significantly improve the power-handling capability of monopole antennas.

References

1. Woo, R., "RF Voltage Breakdown in Coaxial Transmission Lines," *Proc. IEEE*, Vol. 57, No. 2, pp. 254–256, Feb. 1969.

2. Scharfman, W. E., and Morita, T., "Voltage Breakdown of Antennas at High Altitude," *Proc. IRE*, Vol. 48, No. 11, pp. 1881–1887, November 1960.

3. Woo, R., "Multipacting Discharges Between Coaxial Electrodes," *J. App. Phys.*, Vol. 39, No. 3, pp. 1528–1533, Feb. 1968.

VII. Spacecraft Telecommunications Systems

TELECOMMUNICATIONS DIVISION

A. Approximate Analysis of Command Lock Detector Performance, C. Carl

1. Introduction

To ensure that valid data is processed, flight command systems (such as for *Viking* and *Mariner*) typically gate the output data with a logic signal. This logic signal states, with high probability of accuracy, that the system is synchronized, i.e., in-lock and/or the proper signal is present. The purpose of this article is to find the statistics of the lock decision for the detector currently being used.

A block diagram of the lock detector under consideration is shown in Fig. 1. The command modulation (data and suppressed subcarrier) plus noise is bandpass limited, squarewave demodulated and matched filter detected (the subcarrier and bit timing are assumed to be known

exactly). To remove the data dependence, the absolute value of the integrator samples is taken; these values are then summed to form the random variable $e_0(t)$. When $e_0(t)$ exceeds the threshold d, "in-lock" is announced.

2. The Analytic Model

The exact performance of this detector is formidable, if not impossible, to describe rigorously. One difficulty is that the *squarewave* coherent demodulation of a non-filtered limiter output is not currently understood. Results are available for the case of *sine wave* demodulation of a filtered limiter output. The analytical model (Fig. 2) reflects this by the inclusion of the post-limiter bandpass filter and a sine-wave local subcarrier. For this case, J. C. Springett and M. K. Simon (*Section E*) have shown that the probability density of $z(t)$ is

$$p(z) = \frac{1}{\pi} \exp(-\rho) \left[\frac{1 + (\pi\rho)^{\frac{1}{2}} z \exp(\rho z^2) [1 + \mathrm{erf}\,(\rho^{\frac{1}{2}} z)]}{(1 - z^2)^{\frac{1}{2}}} \right], \qquad -1 < z < 1 \tag{1}$$

where

$$\text{erf}\,(x) = \frac{2}{\pi^{1/2}} \int_0^x \exp(-t^2)\,dt = -\,\text{erf}\,(-x)$$

$p = A^2/N_0 B$ is the input signal-to-noise ratio (SNR), N_0 is the single-sided noise spectral density, and B is the input bandpass filter noise bandwidth. The effect of data modulation $D(t)$ is to replace $p(z)$ by $p(Dz)$, which only folds the density about zero. The absolute value will remove this effect; hence, $D(t)$ is discarded. The low-pass filter indicated in the model is to remove the double frequency terms of the demodulation; it has no effect on the near-dc terms.

To model the integrator, we make use of a technique used by D. W. Boyd (SPS 37-41, Vol. IV, pp. 233–239). If we sample $z(t)$ at the Nyquist rate (note that the baseband data modulation bandwidth is $B/2$) we can approximate $z(t)$ by

$$z(t) \cong \sum_{i=-\infty}^{\infty} z\left(\frac{i}{B}\right) U\left(t - \frac{i}{B}\right)$$

where $U(t) = 1, 1/B \geq t \geq 0$, and zero elsewhere.

We have for the integral

$$\frac{1}{T_b} \int_0^{T_b} z(t)dt \cong \frac{1}{T_b} \int_0^{T_b} \sum_{i=0}^{BT_b-1} z\left(\frac{i}{B}\right) U\left(t - \frac{i}{B}\right)$$

$$\cong \frac{1}{T_b} \sum_{i=0}^{N-1} z\left(\frac{i}{B}\right) \int_{i/B}^{(i+1)/B} U\left(t - \frac{i}{B}\right)$$

$$\cong \frac{1}{T_b} \sum_{i=0}^{N-1} \frac{z\,(i/B)}{B}$$

or letting $z_i = z[(i-1)/B]$, the approximation becomes

$$\frac{1}{T_b} \int_0^{T_b} z(t)dt \cong \frac{1}{N} \sum_{i=1}^{N} z_i, \qquad N = BT_b \qquad (2)$$

We now complete the model by studying the two cases of interest.

3. Signal-Plus-Noise Case

With the integrator approximated by Eq. (2), the remaining operations are the absolute value and summing of n samples. If the lock channel SNR is high enough to
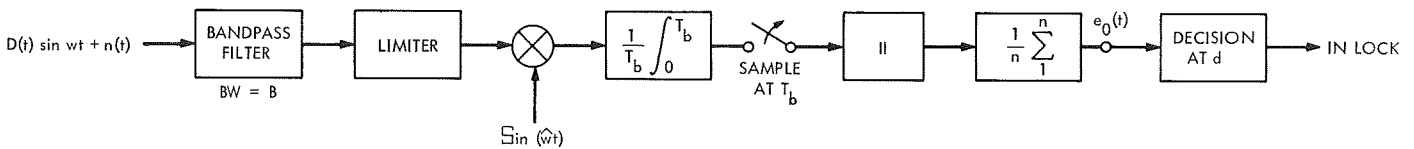
Fig. 1. Command lock detector
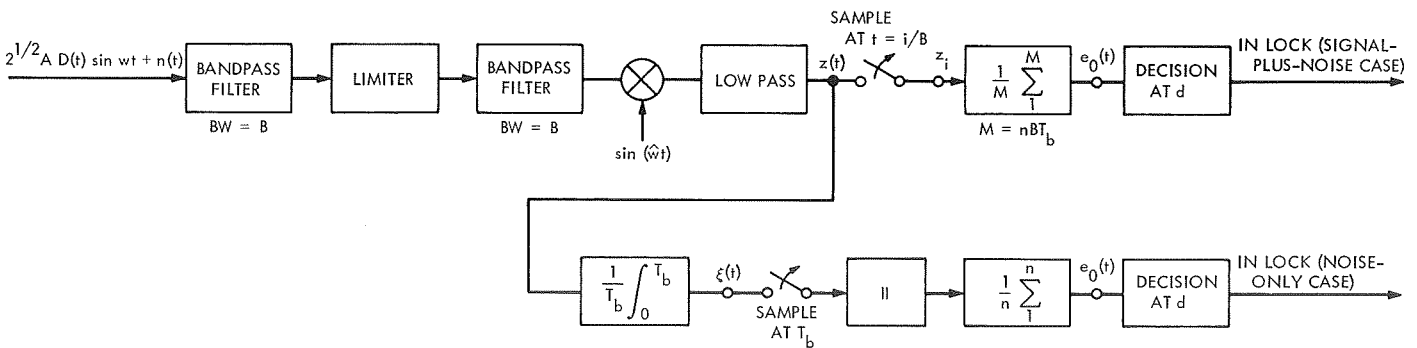
Fig. 2. Analytic model

provide an error probability less than 0.01, the absolute value may be ignored for computing the in-lock statistics (the "error rate" of this assumption is much less than the lock error rate). Hence $e_0(t)$ can be represented as (Fig. 2)

$$e_0(t) = \frac{1}{n} \sum_{i=1}^{n} \left| \frac{1}{T_b} \int_0^{T_b} z(t)dt \right| \approx \frac{1}{n} \sum_{j=1}^{n} \left(\frac{1}{N} \sum_{i=1}^{N} z_i \right) = \frac{1}{M} \sum_{i=1}^{M} z_i, \qquad M = nBT_b$$

$e_0(t)$ is always normalized to the interval $(-1, 1)$.

One would like to compute $P(e_0)$, the exact probability density of e_0, but this is a formidable task. Gallager (Ref. 1) has derived a useful asymptotic expression for the probability of error P (out-of-lock | signal)

$$P(\text{OL} \mid \text{S}) = \text{prob} \left\{ \frac{1}{M} \sum_{i=1}^{M} z_i \leq d \right\} = \left\{ \frac{1}{|\lambda_0| [2\pi N \mu''(\lambda_0)]^{1/2}} + 0 \left(\frac{1}{N^{1/2}} \right) \right\} \exp[N(\mu(\lambda_0) - \lambda_0 d)] \qquad (3)$$

where $\mu(\lambda)$ is the log of the moment-generating function of z

$$\mu(\lambda) = \ln[E\{e^{\lambda z}\}] = \ln \int_{-1}^{1} e^{\lambda z} p(z)dz$$

$0\,(\cdot)$ is a function approaching zero faster than $1/N^{1/2}$, and λ_0 is found from implicitly solving the equation

$$\mu'(\lambda_0) = d \qquad (4)$$

(d is the threshold). The exponential term in Eq. (3) will be recognized as the Chernoff bound. To find the moment-generating function of z, we first make the random variable transformation

$$z = -\cos \theta; \qquad \theta = \cos^{-1}(-z)$$

Thus

$$p(\theta) = p_z(-\cos \theta) \left| \frac{dz}{d\theta} \right|$$

$$= \frac{1}{\pi} \exp(-\rho) \{1 - (\pi \rho)^{1/2} \cos \theta \exp(\rho \cos^2 \theta)[1 - \text{erf}(\rho^{1/2} \cos \theta)]\} \qquad 0 < \theta < \pi$$

Now the moment-generating function is

$$M_z(\lambda) = E_z[\exp(\lambda z)] = E_\theta[\exp(-\lambda \cos \theta)] = \int_0^{\pi} \exp(-\lambda \cos \theta)\, p(\theta)d\theta$$

$$= \frac{1}{\pi} \exp(-\rho) \int_0^{\pi} \exp(-\lambda \cos \theta)d\theta - \left(\frac{\rho}{\pi} \right)^{1/2} \exp(-\rho) \int_0^{\pi} \exp(-\lambda \cos \theta) \cos \theta \exp(\rho \cos^2 \theta)d\theta$$

$$+ \left(\frac{\rho}{\pi} \right)^{1/2} \exp(-\rho) \int_0^{\pi} \exp(-\lambda \cos \theta) \cos \theta \exp(\rho \cos^2 \theta)\, \text{erf}(\rho^{1/2} \cos \theta)d\theta$$

$$= I_1 + I_2 + I_3$$

Evaluating the integrals, we have (using reference equations)

$$I_1 = \exp(-\rho)\, I_0(\lambda) \qquad\qquad \text{(Ref. 2, Eq. 9.6.16)}$$

$$I_2 = (\pi\rho)^{1/2} \sum_{n=0}^{\infty} \left[\frac{\rho^n}{2^{2n} n!} \sum_{m=0}^{n} \binom{2n+1}{n-m} I_{2m+1}(\lambda) \right] \qquad\qquad \text{(Ref. 2, Eq. 9.6.37; Ref. 3, Eq. 3.631-17)}$$

$$I_3 = \exp(-\rho)\, I_0(\lambda) \sum_{n=0}^{\infty} \frac{\rho^{n+1}}{(n+1)!} \qquad\qquad \text{(Ref. 2, Eq. 7.1.6; Ref. 3, Eqs. 3.621-3 and 3.631-17)}$$

$$+ \exp(-\rho) \sum_{n=0}^{\infty} 2(n+1)!\, \rho^{n+1} \left[\sum_{m=1}^{n+1} \frac{I_{2m}(\lambda)}{(n+1+m)!\,(n+1-m)!} \right]$$

where $I_n(x)$ is the modified Bessel function of order n. Collecting terms in $I_n(\lambda)$, and recognizing the series expansion of $\exp(\rho)$, we have, finally,

$$M_z(\lambda) = I_0(\lambda) + (\pi\rho)^{1/2} \exp(-\rho) \sum_{n=0}^{\infty} A_n(\rho) I_{2n+1}(\lambda) + \exp(-\rho) \sum_{n=1}^{\infty} B_n(\rho) I_{2n}(\lambda)$$

where

$$A_n(\rho) = \sum_{m=n}^{\infty} \frac{\rho^m}{2^{2m} m!} \binom{2m+1}{m-n}; \qquad B_n(\rho) = 2 \sum_{m=n}^{\infty} \frac{\rho^m\, m!}{(m+n)!\,(m-n)!}$$

are of hypergeometric form. As a check of $M_2(\lambda)$, one can verify the first two moments with Springett and Simon (*Section E*) (with limiter first zone power normalized to unity):

$$E(z) = \left.\frac{\partial M_z(\lambda)}{\partial \lambda}\right|_{\lambda=0} = \frac{(\pi\rho)^{1/2}}{2} \exp(-\rho)\, A_0(\rho) = \frac{(\pi\rho)^{1/2}}{2}\, {}_1F_1\left(\frac{1}{2}, 2, -\rho\right) = \left(\frac{\pi^2}{8}\right)^{1/2} \alpha$$

$$E(z^2) = \left.\frac{\partial^2 M_z(\lambda)}{\partial \lambda^2}\right|_{\lambda=0} = \frac{1}{2}\left[1 + \frac{\exp(-\rho) B_1(\rho)}{2}\right] = \frac{1}{2}\left[1 + \frac{\exp(-\rho)\rho\, {}_1F_1(2,3,\rho)}{2}\right] = 1 - \frac{1 - \exp(-\rho)}{2\rho}$$

where α is the limiter suppression factor and ${}_1F_1(a,b,x)$ is the confluent hypergeometric function. Returning now to the Gallager value (Eqs. 3 and 4), we need

$$\mu'(\lambda) = \frac{\partial}{\partial \lambda} \ln M_z(\lambda) = \frac{M_z'(\lambda)}{M_z(\lambda)}; \qquad \mu''(\lambda) = \frac{M_z''(\lambda)}{M_z(\lambda)} - [\mu'(\lambda)]^2$$

To solve for the optimum value of λ, λ_0, given d, one must solve (Eq. 4)

$$dM_z(\lambda) - M_z'(\lambda) = 0$$

or

$$d[I_0(\lambda) - I_0'(\lambda)] + d(\pi\rho)^{1/2} \exp(-\rho) \sum_{n=0}^{\infty} A_n(\rho) [I_{2n+1}(\lambda) - I_{2n+1}'(\lambda)] + d \exp(-\rho) \sum_{n=1}^{\infty} B_n(\rho) [I_{2n}(\lambda) - I_{2n}'(\lambda)] = 0$$

This equation was solved numerically on a computer using the standard Newton–Raphson method. λ_0 was then used in Eq. (3) to find $P(OL \mid S)$. The results for parameter values of practical interest are plotted in Fig. 3; some mean values for z vs SNR are also given in Fig. 3.
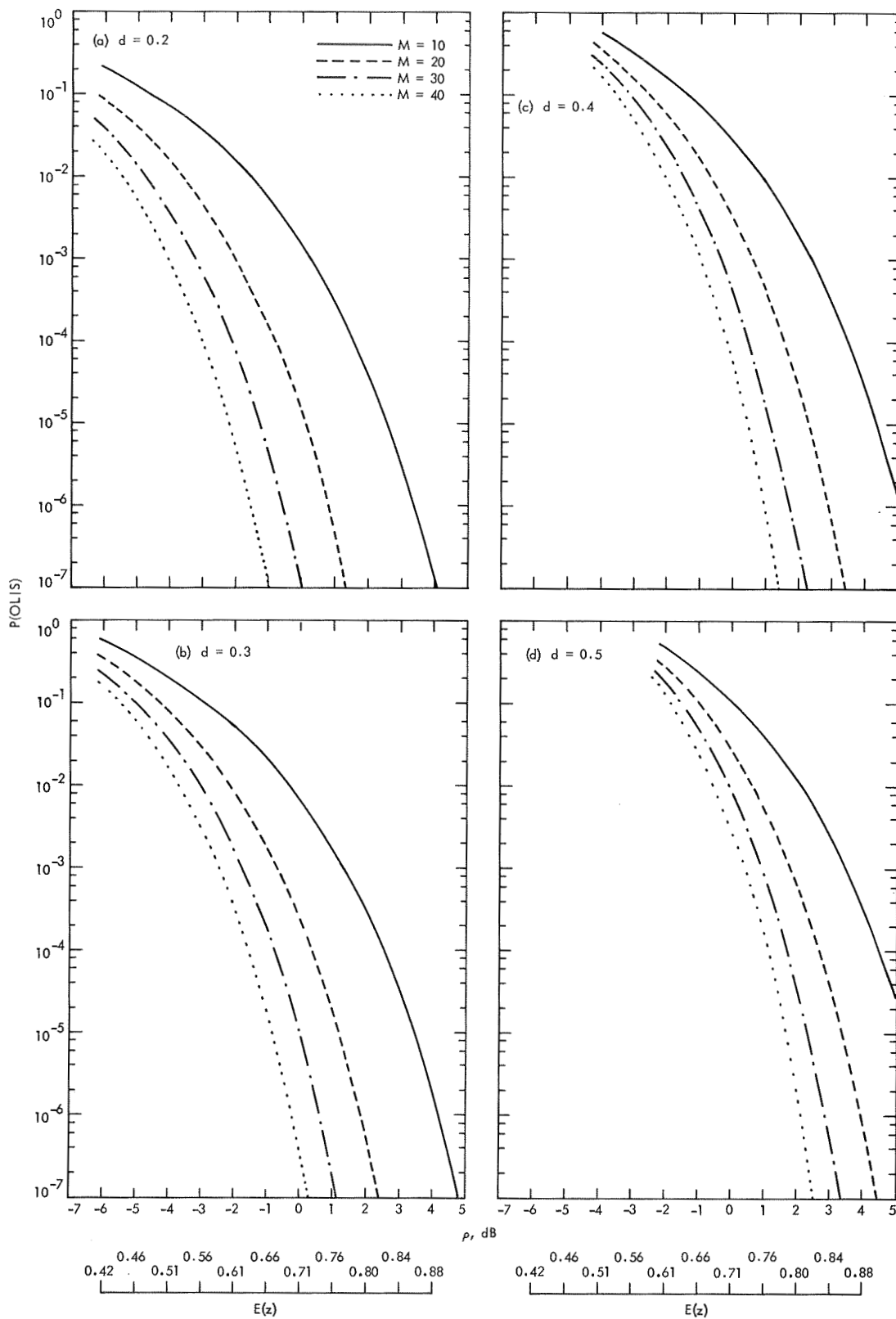
Fig. 3. P(OL | S) vs input SNR

One can observe that as d approaches $E(z)$, the performance degrades. The designer may use these curves by specifying ρ, BT_b, n, and d. If one wishes to describe performance vs lock ST_b/N_0, one can use

$$\left(\frac{ST_b}{N_0}\right)_{lock} = BT_b\, \rho$$

4. Noise-Only Case

For $\rho = 0$, the mean of z will be zero; hence, in this case, the absolute value cannot be neglected (Fig. 2). This would severely complicate the analysis were it not for the compensating observation that the integrator output $\xi(t)$ appears to quickly approach a gaussian variable with increasing BT_b. This has been observed experimentally; moreover, if one applies the Gallager value analysis at $\rho = 0$, $BT = 10$, and plots the results on normal probability paper, one gets the desired straight line. Hence, we will assume that $\xi(t)$ is a gaussian variable for $\rho = 0$. Completing the model for this case, we then are interested in the statistics of the sampled variable

$$e_0(t) = \frac{1}{n}\sum_{i=1}^{n} |\xi_i(t)|$$

with

$$P(|\xi_i|) = \frac{2}{(2\pi)^{\frac{1}{2}}\sigma}\exp\left(\frac{-\xi_i^2}{2\sigma^2}\right)$$

the folded normal density of ξ_i. The variance is found from Eqs. (34), (39), and (51) in *Section E* to be

$$\sigma^2 = n_0\left(\frac{1}{2T_b}\right) = \left(\sigma_z^2\,\frac{\pi\Gamma_0}{2B}\right)\left(\frac{1}{2T_b}\right) = \frac{\pi\Gamma_0}{8BT_b} = \frac{0.416}{BT_b}$$

where n_0 is the single-sided noise density at the coherent limiter output. For practical interest, we now assume that the input filter form factor $(1/\Gamma_0)$ rolls off at 6 dB/octave; hence, $(1/\Gamma_0) = 0.944$. The required error probability P (in-lock | noise) is

$$P(I\,L\mid N) = \text{prob}\,\{e_0 \geqslant d\}$$

Evaluating this for various values of n:

$$P(I\,L\mid N)_{n=1} = \text{erfc}\left(\frac{d}{2^{\frac{1}{2}}\sigma}\right)$$

$$P(I\,L\mid N)_{n=2} = 1 - \text{erf}^2\left(\frac{d}{\sigma}\right)$$

$$P(I\,L\mid N)_{n=3} = \int_d^\infty \int_0^{3x_1} \frac{12}{\pi(2^{\frac{1}{2}})\sigma^2}\,\text{erf}\left(\frac{x_2}{2\sigma}\right)\exp\left[-\frac{x_2^2}{4\sigma^2} - \frac{(3x_1 - x_2)^2}{2\sigma^2}\right]dx_2\,dx_1$$

$$P(I\,L\mid N)_{n=4} = \int_d^\infty \int_0^{4x_1} \int_0^{x_2} \frac{16}{\pi(\pi^{\frac{1}{2}})\sigma^3}\,\text{erf}\left(\frac{x_3}{2\sigma}\right)\exp\left(-\frac{x_3^2}{4\sigma^2} - \frac{(x_2 - x_3)^2}{2\sigma^2} - \frac{(4x_1 - x_2)^2}{2\sigma^2}\right)dx_3\,dx_2\,dx_1$$

These expressions were evaluated for various BT_b and n using the Univac 1108 multiple integral routine. The results are shown in Fig. 4.

5. Comparison with Experiment

A breadboard command detector was used to evaluate performance of the lock detector (Fig. 1). Results were also taken with a bandpass filter after the limiter, i.e., the hardware equivalent of the analysis $BT_b = 10$ for the

breadboard. Three sets of data were taken: $d = 0.32$, $n = 2$; $d = 0.389$, $n = 2$; and $d = 0.389$, $n = 4$. The experimental results with the bandpass filter, together with the analytic values, are shown in Fig. 5. The theory and experiment are in good agreement, especially in slope. The pessimistic offset of the P (OL | S) theory is, in part, due to the timing losses in the experiment (their effect on lock SNR and d). Accounting for these losses moves the theory 0.2–0.3 dB to the left, or almost in perfect agreement with the experimental results.
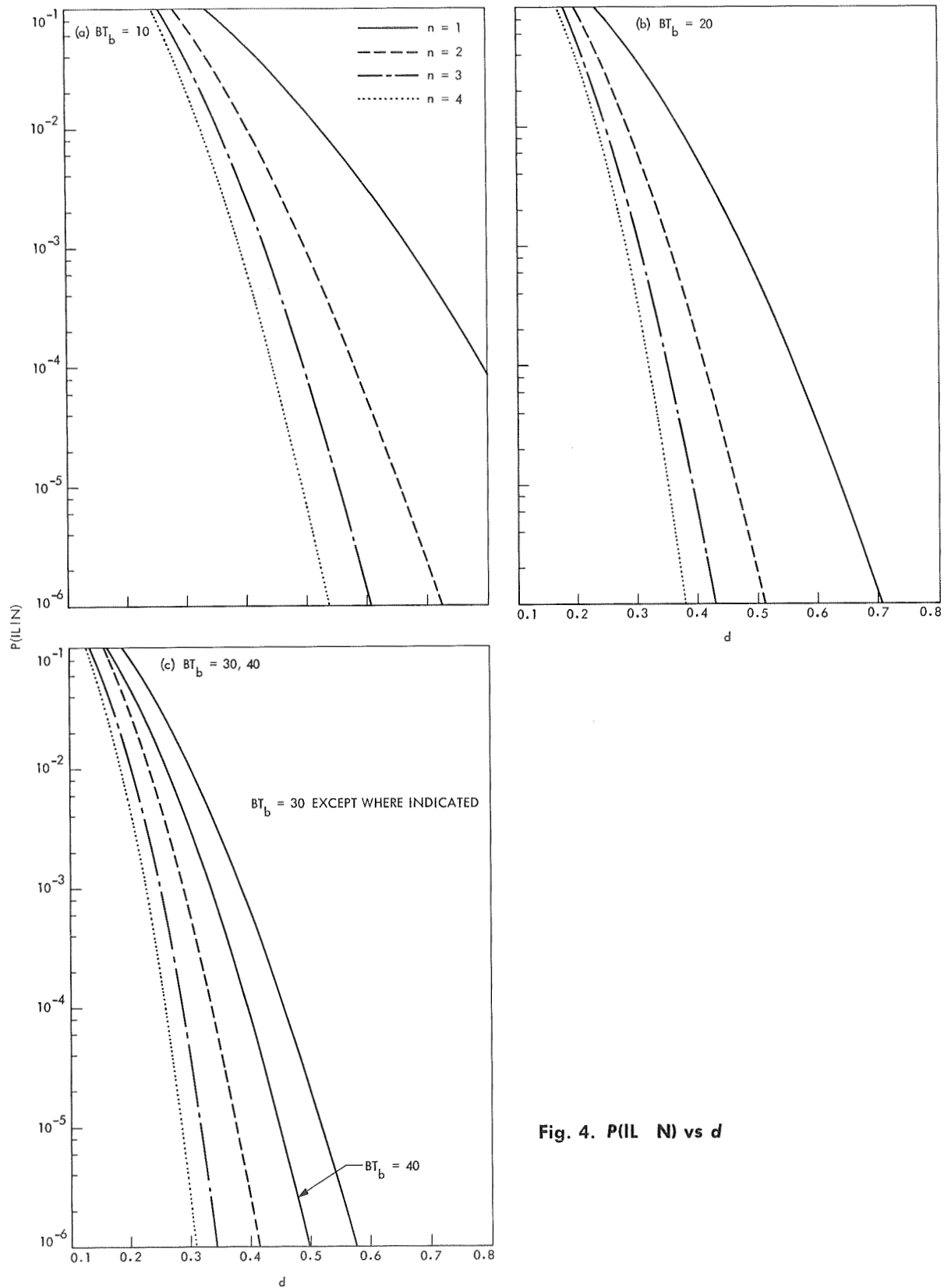
Fig. 4. P(IL ∩ N) vs d
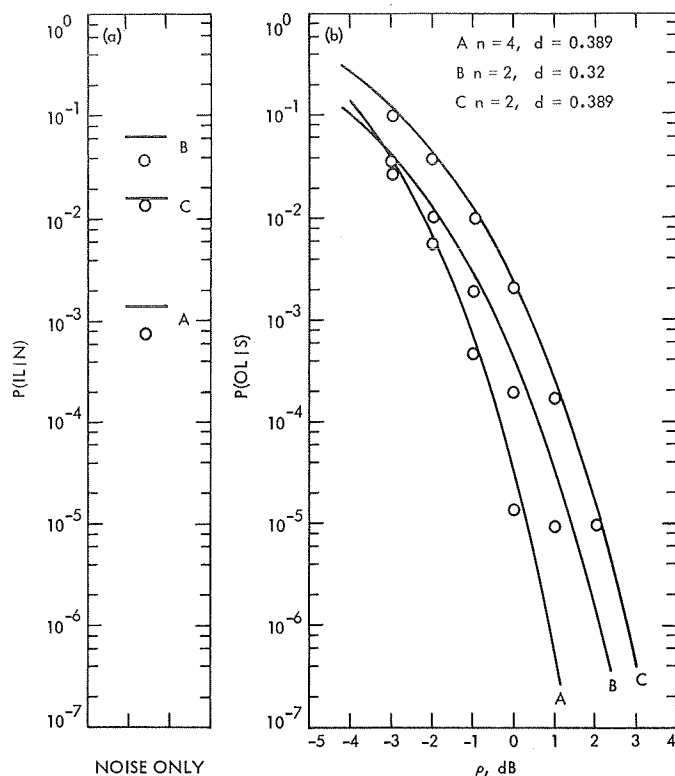
Fig. 5. Comparison of theory and experiment (BT_b = 10)

It has been experimentally observed that removing the bandpass filter after the limiter *improves* the performance by about 0.4 dB. As mentioned previously, this phenomenon is not fully understood and should be the subject of future work. Until this phenomenon is described analytically, the present analysis will serve as a useful bound on performance without the filter.

References

1. Gallager, R. G., *Information Theory and Reliable Communication*, p. 126 ff. John Wiley & Sons, Inc., New York, 1968.

2. *Handbook of Mathematical Functions*, National Bureau of Standards Applied Mathematics Series No. 55, 1964.

3. Gradshteyn, I. S., and Ryzhik, I. M., *Table of Integrals, Series, and Products*. The Academic Press, New York, 1965.

B. Cyclic Search Algorithms for Synchronizing Maximal Length Linear Shift Register Sequences, *R. L. Horttor*

1. Introduction

Communications between low-altitude satellites and a satellite at synchronous altitude can encounter a serious problem with multipath signals reflected from the earth's surface. Spread-spectrum techniques can be used to combat the problem, e.g., the carrier may be modulated by a linear shift register sequence that allows demodulation at the receiver to spread out the multipath and other interfering signal power. To accomplish this, synchronization of transmitter and receiver must be achieved. The purpose of this article is to compare two algorithms for synchronizing maximal length linear shift register sequences.

The first algorithm uses a Maximum Likelihood Estimate of the time phase. The locally generated code is correlated with the incoming signal for each possible time phase. The position yielding the highest correlation is the Maximum Likelihood Estimate of the time phase.

Although a true Maximum Likelihood Receiver tests all positions at once, hardware mechanization constraints necessitate a sequential procedure wherein the positions are tested serially. Hence, a more accurate term may be Serial Maximum Likelihood Receiver.

The serial procedure suggests that a favorable measurement might temporarily halt or terminate the search, and, at first glance, this amounts to a truncated Maximum Likelihood Test (which cannot be as good as a full test). However, the carrier tracking loop, which acts as a nearly independent decision device, first must lock in order for a favorable measurement to occur. The decision, then, is merely to remain at that point long enough to verify that the carrier loop will continue tracking. If so, the synchronization point has been found.

The second algorithm is a Sequential Probability Ratio Test that uses two thresholds separated by a no-decision region in which more data are taken until a decision can be made. In the present application, both thresholds would have the effect of delaying search in order for the loop to remain locked. Consequently, only the lower threshold is used, which suggests a "Quasi-Sequential Decision" procedure.

The principal analytical result of the work discussed in this article is a comparison of the Serial Maximum Likelihood and Quasi-Sequential algorithms.

2. Serial Maximum Likelihood Algorithm

A cursory discussion of the relevant estimation theory begins with a model for the received signal. Equation (1) depicts a pseudo-noise code amplitude modulated onto a

carrier at frequency ω_c. Thus,

$$r(t) = Ax(t - t_0) \cos(\omega_c t + \theta(t)) + n_1(t) \cos(\omega_c t + \theta(t))$$
$$+ n_2(t) \sin(\omega_c t + \theta(t)) \tag{1}$$

where t_0 is the code time phase, $\theta(t)$ is the carrier phase behavior, and $n_1(t)$, $n_2(t)$ are zero mean gaussian random processes.

An estimate of t_0 is derived from the decision variables $d(t_i,t_0)$. These are produced by correlating $r(t)$ with a locally generated version of the code and carrier function for each t_i. Hence,

$$d(t_i,t_0) = \frac{1}{T} \int_0^T dt \{Ax(t - t_0) \cos(\omega_c t + \theta(t))$$
$$+ n_1(t) \cos(\omega_c t + \theta(t)) + n_2(t) \sin(\omega_c t + \theta(t))\}$$
$$\times 2x(t - t_i) \cos(\omega_c t + \hat{\theta}(t)) \tag{2}$$

Equation (2) assumes the noise process is broadband compared to the signal $x(t)$. When this is not true, the locally generated version must be pre-distorted by a linear filter whose characteristics depend on the noise process autocorrelation function.

Some simplification in Eq. (2) may be achieved by expanding the cosine products and discarding terms in $2\omega_c t$. For the wide band noise case, multiplying the noise by $x(t - t_i)$ has no real effect and is ignored. This yields

$$d(t_i,t_0) = \frac{A}{T} \int_0^T dt \, x(t - t_0) x(t - t_i) \cos(\theta(t) - \hat{\theta}(t))$$
$$+ \frac{1}{T} \int_0^T dt \, [n_1(t) \cos(\theta(t) - \hat{\theta}(t))$$
$$- n_2(t) \sin(\theta(t) - \hat{\theta}(t))] \tag{3}$$

The codes correlate at the t_i corresponding to t_0, allowing carrier power to build, which in turn allows the carrier loop to lock. Phase error is near zero and the integration produces a non-zero-mean decision variable. For all other t_i, there is no code correlation, no carrier component, and no carrier lock. Hence, all other $d(t_i,t_0)$ have zero mean.

After the full code is searched, the largest value of $d(t_i,t_0)$ yields the Serial Maximum Likelihood Estimate of t_0. The probability of a correct decision is the probability that all other $d(t_i,t_0)$ are less than the correct one integrated over the possible values for the correct one. Hence,

P_c for orthogonal signal elements is

$$P_c = \int_{-\infty}^{\infty} \frac{dx}{(2\pi)^{1/2}} \exp\left\{ - \frac{[x - (\text{SNR})^{1/2}]^2}{2} \right\}$$
$$\times \left[\int_{-\infty}^{x} \frac{dy}{(2\pi)^{1/2}} \exp\left(- \frac{y^2}{2} \right) \right]^{N-1} \tag{4}$$

where SNR is the ratio of signal power to mean noise power and N is the code length in bits. Of course, the probability of error is

$$P_E = 1 - P_c \tag{5}$$

After the search is completed, the receiver returns to the best t_i, where the carrier loop presumably will re-acquire and continue tracking. If not, a mistake has been made and the procedure repeats. In the context of information transmission and detection, such a mistake is an irrecoverable error; by contrast, in synchronization problems, the only cost is additional search time. In that sense, then, the term "probability of error" has no meaning since it is merely the probability of missing on the first pass.

The search algorithm becomes a sequence of Bernoulli trials with probabilities P_E and P_c. Each trial requires N operations, so the generating function for the number of operations is

$$\left. \begin{aligned} J(s) &= \sum_{m=1}^{\infty} P_E^{m-1} P_c s^{mN} \\ J(s) &= \frac{P_c s^N}{1 - P_E s^N} \end{aligned} \right\} \tag{6}$$

Since $J(s) = $ unity when $s = 1$, the search must terminate sometime with probability 1. A state diagram is shown in Fig. 6.

$$J(s = 1) = \frac{P_c}{1 - P_E}$$
$$= \frac{P_c}{P_c} \tag{7}$$
$$= 1$$

The mean $\bar{j}_m$ of the number of operations is computed from the derivative of $J(s)$ evaluated at $s = 1$. Computing
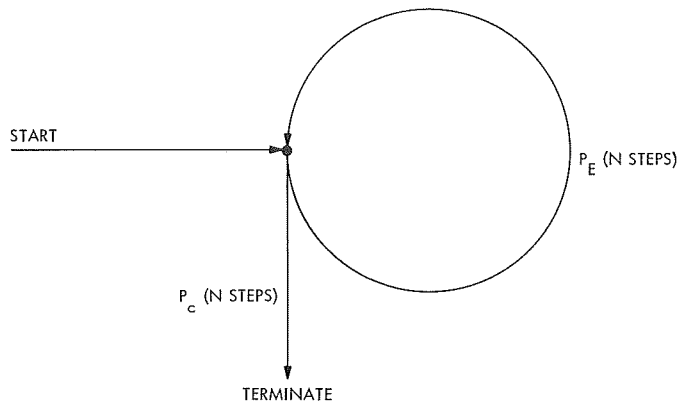
Fig. 6. Serial Maximum Likelihood search algorithm state diagram

the derivative yields

$$\bar{j}_m = \frac{d}{ds} J(s) \Big|_{s=1}$$

$$= \frac{P_c N s^{N-1}}{(1 - P_E S^N)^2} \Big|_{s=1} \tag{8}$$

$$= \frac{N}{P_c}$$

The variance of j_m is computed from the second derivative and combinations of the first derivative. In particular,

$$\text{var}[j_m] = J''(s = 1) + J'(s = 1) - J'^2(s = 1) \tag{9}$$

Computing the derivatives and substituting in gives

$$\text{var}[j_m] = \frac{N(N - 1)}{P_c} + \frac{2P_E N^2}{P_c^2} + \frac{N}{P_c} - \frac{N^2}{P_c^2}$$

$$= N^2 \frac{P_E}{P_c^2} \tag{10}$$

Equations (8) and (10) state that if P_E is zero (noise-free detection), the variance is zero and the mean is N. This is reasonable, because exactly N operations (one complete search) will be required.

3. Sequential Algorithm

There are two objections to the Serial Maximum Likelihood algorithm. First, there must be at least N operations

before search can be terminated. Since the correct synchronization point must be passed once in the search cycle, why should the search continue after a likely point has been located? A slight amount of additional time to check a promising point may eliminate many additional operations.

A more fundamental objection arises from the actual signal behavior before synchronization is obtained. Because of the relative motion of transmitter and receiver, the received signal and the locally generated version have different time bases. High correlation is a transistory condition. By the time a full search cycle is completed, the point where best correlation occurred has moved. That is, the estimate t_i of t_0 is no longer valid. Additional search must take place, though over a smaller uncertainty region. This problem can be avoided only by a search algorithm that can terminate when the synchronization point is encountered.

In a general detection problem, there are four possibilities resulting from the decision. These are as follows:

(1) The correct decision that signal is present can occur only if signal is present, P_{CP}.

(2) A false decision that signal is absent can occur only when signal is present, P_{FP}.

(3) A false decision that signal is present can occur only if signal is absent, P_{FA}.

(4) A correct decision that signal is absent can occur only if signal is absent, P_{CA}.

The probabilities P_{CA}, P_{FA}, P_{CP}, and P_{FP} are defined relative to a threshold. With a signal amplitude A and noise mean power σ_n^2, the threshold is located at $\gamma \cdot A$ (some fraction of the SNR).

Figure 7 shows the decision variable probability densities for the two cases of signal absent and present. When a measurement is made, the search either halts or continues depending on whether or not the threshold is exceeded. The shaded areas of the curves illustrate the kinds of errors involved.

In distinction from the usual decision problem, there is additional information that identifies which kind of mis-

Fig. 7. Detection probabilities

Fig. 8. Sequential search state diagram

take was made. A correct decision that signal is present is verified by the capability of the carrier loop to remain in lock. A false alarm halts the search for an additional measurement or until the carrier loop is obviously not in lock. Search then proceeds, with time as the only penalty. If the signal is missed, a full search cycle is guaranteed.

Acquisition time is the time required to make the first correct decision that signal is present. Since each decision is made by comparing a decision variable to a threshold, it may appear impossible to distinguish between a false alarm and a correct decision that signal is present (at the instant of measurement, the possibilities are indistinguishable). However, either possibility results in a halt sufficiently long for the loop to lock if the signal is present.

The above description suggests a state diagram (Fig. 8) consisting of a circle with N nodes, one of which corresponds to the signal location. Entry to the circle is equally probable at any node (observe that signal is present at the Nth node). However, since the entry point is uncertain, the location of N is, in effect, uncertain. The search may terminate only from the correct node.

Transitions between nodes (except for the Nth) are governed by the probabilities P_{CA}, P_{FA}. The process is a sequence of Bernoulli trials leading to a correct decision that signal is absent. The generating function $J_A(s)$ is, therefore, similar to that calculated in *Subsection 2*.

$$J_A(s) = \frac{P_{CA}s}{1 - P_{FA}s} \qquad (11)$$

The search begins at any node n and proceeds to node N. The resulting number of operations is dependent on a succession of $N - n$ Bernoulli sequences. Hence, that generating function $J_n(s)$ is

$$J_n(s) = J_A^{N-n}(s) \qquad (12)$$

The transition from node N to termination or continuation depends on the missed detection probability P_{FP}. One gets m operations at this point by passing it m times. With probability 1.0, there is one operation on each pass. Hence,

$$J_N(s) = s^m \qquad (13)$$

Halting at node N terminates search since the carrier loop will remain in lock until cycle slippage occurs. Proceeding from node N to node 1 is a missed detection and the search continues.

Continuation involves $(m - 1)$ additional trips around the cycle, with each trip requiring $(N - 1)$ node transitions. Consequently, $J_{con}(s)$ is

$$J_{con}(s) = [J_A(s)]^{(m-1)(N-1)} \qquad (14)$$

The complete generating function for the number of operations in a search that starts at node n and terminates after m cycles is the product of the previously defined components.

$$J_{nm}(s) = J_A^{N-n}(s) \cdot s^m \cdot [J_A(s)]^{(m-1)(N-1)} \qquad (15)$$

But n is a random variable uniformly distributed between 1 and N, and m trips around the cycle occurs after $(m-1)$ missed detections. Therefore, the generating function for the complete search is a sum of $J_{nm}(s)$ weighted by the joint probability density for (n,m).

$$P(n,m) = \begin{cases} \dfrac{1}{N} \, P_{FP}^{m-1} \, P_{CP} & 1 \leq n \leq N, 1 \leq m < \infty \\ 0 & \text{elsewhere} \end{cases} \qquad (16)$$

The total generating function $J(s)$ is

$$J(s) = \sum_{n=1}^{N} \sum_{m=1}^{\infty} J_{nm}(s) \, P(n,m) = \left[\frac{1}{N} \sum_{n=1}^{N} \left(\frac{sP_{CA}}{1 - sP_{FA}} \right)^{N-n} \right] \sum_{m=1}^{\infty} P_{FP}^{m-1} \, P_{CP} \, s^m \left(\frac{s\,P_{CA}}{1 - sP_{FA}} \right)^{(m-1)(N-1)} \qquad (17)$$

Redefining the summation variables gives

$$J(s) = \left[\frac{1}{N} \sum_{k=0}^{N-1} \left(\frac{sP_{CA}}{1 - sP_{FA}} \right)^k \right] \sum_{l=0}^{\infty} P_{CP} \, P_{FP}^l \, s^{1+l} \left(\frac{s\,P_{CA}}{1 - sP_{FA}} \right)^{l(N-1)} \qquad (18)$$

One may easily verify that $J(s = 1)$ is unity, indicating that the search does eventually terminate, as it should. Computation of the derivatives $J'(s)$ and $J''(s)$ is tedious, so only the results will be shown. The mean number of trials $\bar{j}_{acp}$ is

$$\bar{j}_{acq} = J'(s = 1) = \frac{N-1}{2} \frac{1}{P_{CA}} + \frac{1 + P_{FP}(N-1)/P_{CA}}{P_{CP}} \qquad (19)$$

The first term illustrates the mean starting node, while the second shows the cascade of Bernoulli trials resulting from a missed detection. Additionally, the number of cycles is a sequence of Bernoulli trials.

Derivation of the expression for variance is very much more tedious.

$$\text{var}\,[\bar{j}_{acq}] = \frac{1}{P_{CA}^2} \left[\frac{N^2 - 3N + 2}{3} + (N-1)P_{FA} \right] + \frac{N-1}{2P_{CA}} - \frac{(N-1)^2}{4P_{CA}^2} + [N + P_{FA}P_{CA}(N-1)]^2 \frac{P_{FP} + P_{FP}^2}{P_{CP}^2}$$

$$+ [N + P_{FA}P_{CA}(N-1)(2 - P_{FA}P_{CA})] \frac{P_{FP}}{P_{CP}} + \frac{1 + P_{FP}(N-1)/P_{CA}}{P_{CP}} - \left(\frac{1 + P_{FP}(N-1)/P_{CA}}{P_{CP}} \right)^2 \qquad (20)$$

It is difficult to visualize the physical significance of each term in Eq. (20), except for $\overline{j}_{\text{acq}}$ and $\overline{j}^2_{\text{acq}}$. The first term refers to the initial, partial cycle, while the second and third refer to successive searches caused by missed detection.

For noise free detection, Eqs. (19) and (20) reduce to

$$\overline{j}_{\text{acq}} = \frac{N-1}{2} \tag{21}$$

$$\text{var}\,[\overline{j}_{\text{acq}}] = \frac{N^2-1}{12} \tag{22}$$

These are, respectively, the mean and variance of an integer uniformly distributed between 1 and N. Since there will be no missed detection, the only uncertainty is starting point. Contrast these results with those of *Subsection 2* where exactly N steps were required.

4. Summary of Concepts and Assumptions

The assumption basic to the entire search and decision algorithm is the ability of the carrier tracking loop to lock early in the decision time interval. It cannot achieve lock anywhere but the synchronization point, and it will remain in lock only at the synchronization point.

The additional decision algorithm performs two functions: (1) it speeds the transitions between nodes where synchronization does not exist, and (2) it terminates the search at the node where synchronization does exist.

There are, therefore, two decision mechanisms operating in parallel to verify each other. The decisions are independent of each other. Independence is guaranteed because the noise processes are uncorrelated quadrature components of the input wide-band noise.

The philosophy of the synchronization algorithm may be compared to communication of data using noise-free feedback. Verification of false alarm or correct detection is performed by the phase-locked loop.

Calculations and plots of the search time performance will be subjects for future study.

C. Optimum Modulation Index for a Data-Aided, Phase-Coherent Communication System,

M. K. Simon

1. Introduction

In SPS 37-60, Vol. III, pp. 46–56, the concept of data-aided loops was introduced with regard to improving the carrier tracking function in a phase-coherent communication system. The analysis carried out and presented in that article was based on a single-channel system (Ref. 1) with a modulation index assumed to be already selected. Hence, the emphasis there was on the improvement in performance obtained for a given modulation index and not on the way in which this index should be chosen by the system design engineer.

In this article, results are presented for optimally choosing a modulation index where the criterion of optimization is minimum data detection error probability. The approach taken follows that of Ref. 1, which considers the same problem for a single-channel system employing a standard phase-locked loop as a carrier tracking device. It is shown in Ref. 1, and similarly in this article, that for a fixed total energy-to-noise ratio and loop bandwidth–symbol time product, a value of modulation factor does indeed exist that minimizes the data detector's error probability performance. Using this modulation index, one can determine the optimum power division between carrier and sideband channels as has previously been done. Finally, the minimum error probability performance of the data-aided system is compared with the ideal detection curve as a function of data signal-to-noise ratio (SNR) ST_b/N_0. The small deviation between the two results over a broad range of ST_b/N_0 is certainly worthy of note.

In what follows, it is assumed that the reader is thoroughly familiar with the material presented on data-aided carrier tracking loops in SPS 37-60, Vol. III. The notation used in that article will also be used here.

2. System Model

The received signal $y(t)$ in a single-channel, phase-coherent communication system can be expressed in the form (Ref. 1)

$$y(t) = (2P_c)^{1/2} \sin(\omega_0 t + \theta_0)$$
$$+ (2S)^{1/2} m(t) \cos(\omega_0 t + \theta_0) + n(t) \tag{1}$$

where $m(t)$ is the modulation and

$$P_C = m_1^2 P \left.\begin{array}{l}\\[1em]S = (1 - m_1^2) P\end{array}\right\} \qquad (2)$$

with m_1^2 denoting the signal modulation factor (i.e., $\cos^{-1} m_1$ is the modulation index) and P the total transmitted power. Also in the above, $n(t)$ is a white gaussian noise process of single sided spectral density N_0 in W/Hz, ω_0 is the carrier radian frequency, and θ_0 is the random phase to be tracked. When a second-order data-aided loop is used to track the RF carrier, then the probability density function of the phase error is approximately given by a Tikhonov distribution of the form

$$p(\phi) = N \exp\left[U_0\left(\phi\right)\right] \int_\phi^{\phi+2\pi} \exp\left[-U_0\left(x\right)\right] dx; \qquad |\phi| \leq \pi \qquad (3)$$

where N is the normalization constant and the potential function $U_0\left(\phi\right)$ is given by

$$U_0\left(\phi\right) = \frac{4\Omega_0}{N_0 K_u^2 \left[1 + M^2 \operatorname{erf}^2\left(R^{1/2}\right)\right]} \phi + \rho \left\{\left[1 + M^2 \operatorname{erf}^2(R^{1/2} \cos \phi)\right] \cos \phi + \frac{M^2}{(\pi R)^{1/2}} \operatorname{erf}\left(R^{1/2} \cos \phi\right) \exp\left(-R \cos^2 \phi\right)\right\} \qquad (4)$$

In Eq. (4), $\Omega_0 = \omega - \omega_0$ denotes the loop detuning, $R = ST_b/N_0$ is the data SNR and M^2 is defined by $M^2 = (1 - m_1^2)/m_1^2$. The quantity $\rho = 2P_C/(N_0 W_L)$ is the SNR in the loop bandwidth of a standard phase-locked loop and can be expressed as follows:

$$\rho = \frac{2R\delta}{M^2} = 2m_1^2 R_T \delta \qquad (5)$$

where δ is the reciprocal of the loop bandwidth–symbol time product; i.e., $\delta = 1/(W_L T_b)$ and $R_T = PT_b/N_0$ is the total energy-to-noise ratio at the transmitter.

Assuming a binary phase-shift keyed data format transmitted at rate such that the RF tracking phase error is essentially constant over a symbol time (e.g., $\delta \geq 5$), then the detector error probability P_E can be obtained from

$$P_E = \int_{-\pi}^{\pi} P_E\left(\phi\right) p\left(\phi\right) d\phi \qquad (6)$$

where

$$P_E\left(\phi\right) = \frac{1}{2} \operatorname{erfc}\left[R^{1/2} \cos \phi\right] \qquad (7)$$

As discussed in SPS 37-60, Vol. III, for values of $m^2 \leq 0.5$, the phase density $p(\phi)$ becomes trimodal thus introducing two additional unstable singularities into the system, while, at the same time, making the phase values $-\pi$, π act as stable nodes. In writing Eq. (6), we have assumed that no attempt has been made to resolve these phase ambiguities in $p(\phi)$. The necessary modification of this expression to resolve these ambiguities is discussed in SPS 37-60, Vol. III. Substituting Eqs. (3), (4), and (7) into Eq. (6) and assuming zero detuning, one can evaluate P_E as a function of m_1^2 for fixed R_T and δ. The results of such a computation are illustrated in Fig. 9. We note that for each value of R_T, an optimum modulation factor (in the sense of minimum P_E) exists and that this factor is a monotonically decreasing function of R_T. Figure 10 plots the minimum error probability (corresponding to the optimum modulation factor of above) as a function of data SNR in dB. For comparison purposes, the ideal performance curve described by $P_E = \frac{1}{2} \operatorname{erfc}\left(R^{1/2}\right)$ and the curve corresponding to optimum power division in a system employing a standard phase-locked loop are shown.

Reference

1. Lindsey, W. C., "Optimal Design of One-Way and Two-Way Coherent Communication Links," *IEEE Trans. Commun. Technol.*, Vol. Com-14, No. 4, pp. 418–431, Aug. 1966.
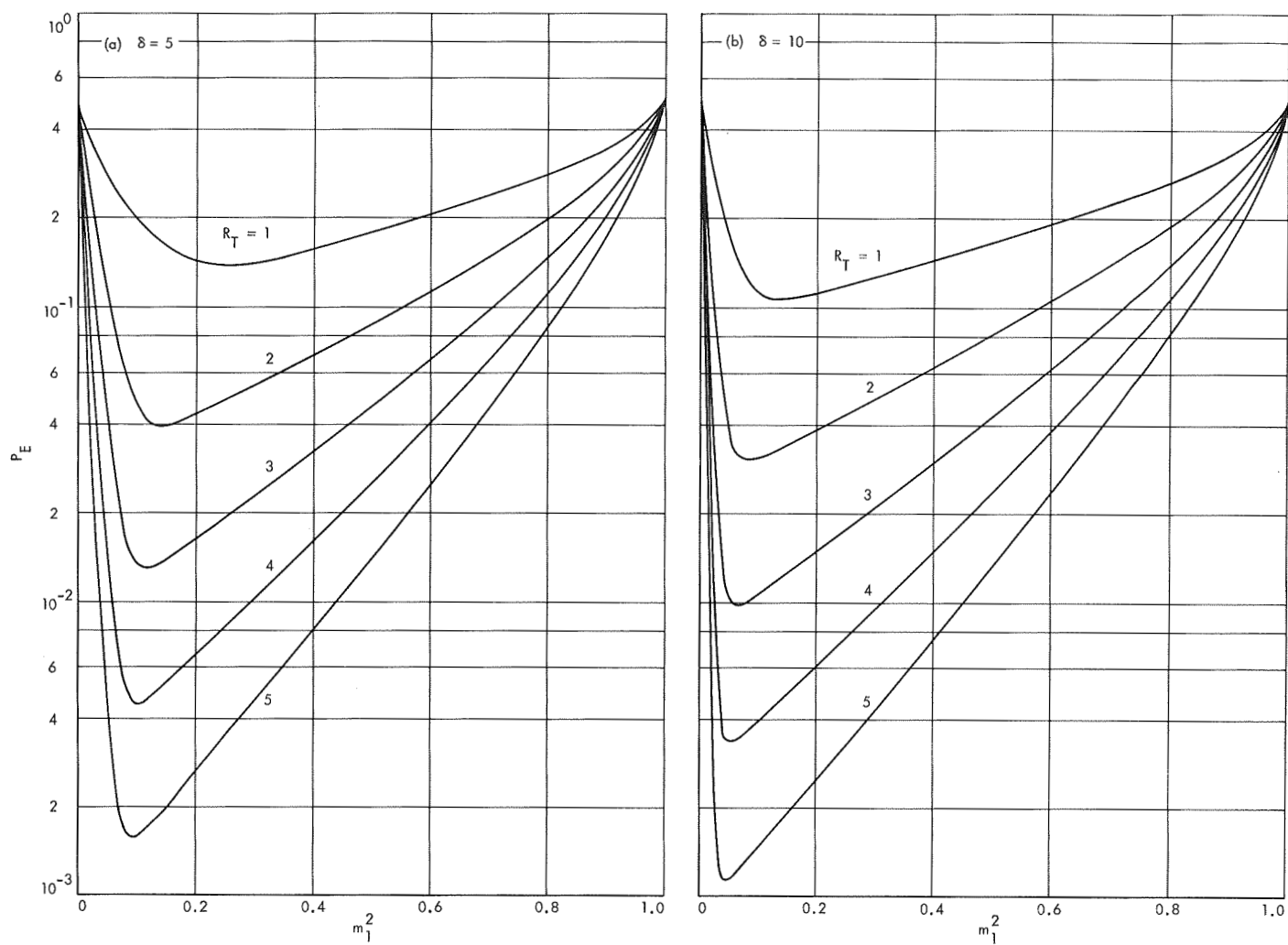
Fig. 9. Bit error probability vs signal modulation factor

The graph shows curves with annotations:

$P_E = 0.5 \left[1 - \mathrm{erf} \left(\frac{ST_b}{N_0} \right)^{1/2} \right]$

OPTIMUM POWER DIVISION $\delta = 5$ (DATA-AIDED LOOP)

OPTIMUM POWER DIVISION $\delta = 5$ (STANDARD PHASE-LOCKED LOOP)

Y-axis: P_E

X-axis: ST_b/N_0, dB
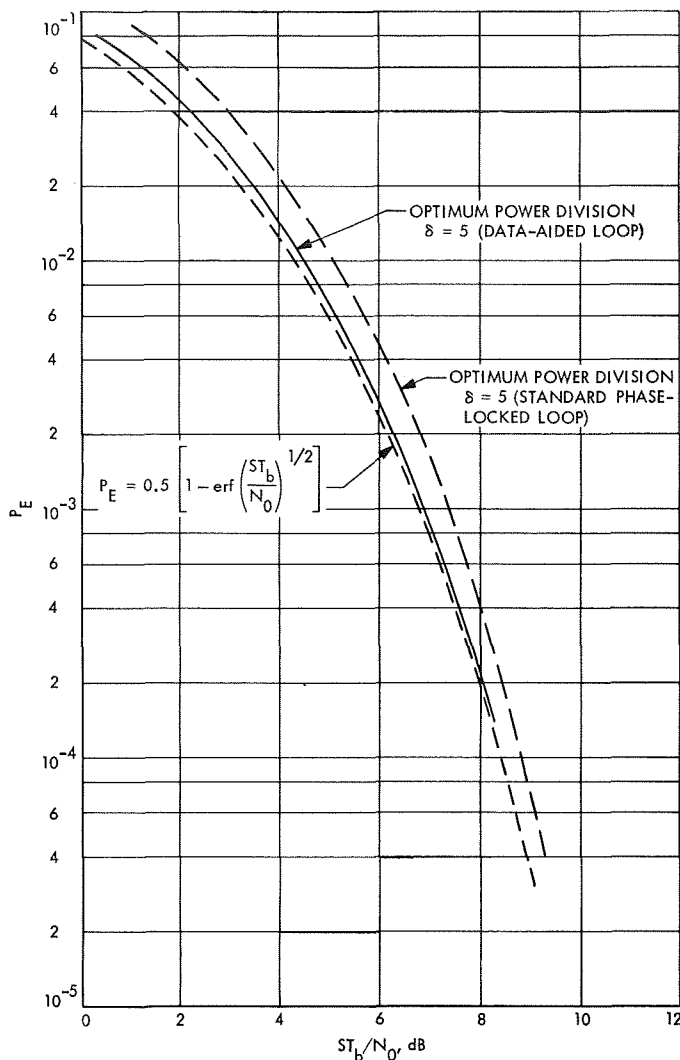
Fig. 10. Comparison of bit error probabilities vs ST_b/N_0

D. The Effect of Limiter Suppression on Command Detection Performance, *M. K. Simon*

1. Introduction

In the design of present-day vehicle transponders, the command modulation is recovered at a point in the RF tracking receiver that suffers a signal-to-noise ratio (SNR) loss due to the presence of the bandpass limiter (BPL). Conceptually, it is clear that the command information should be removed prior to transmission through the limiter, as is done for the ranging signal, thus improving the error probability performance of the data detector. Experimental verification of such a fact, when comparing RF losses between *Mariner* systems and a proposed digital command system, has been demonstrated in SPS 37-62,

Vol. III, pp. 93–99. Furthermore, the bandwidth of the narrow-band amplifier at the input to the BPL (typically less than 10 kHz) might be sufficiently narrow to filter out all or part of the command modulation, thus causing a further degradation in performance. This is so particularly if the command information is modulated on a subcarrier.

The purpose of this article is to investigate these various performance trade-offs using recent theoretical developments presented in Ref. 1 and *Section E* of this chapter. Specifically, the following three cases will be considered:

(1) The input filter to the BPL passes the total command modulation, which is subsequently transferred to the command detector from the phase detector in the phase-locked loop (PLL) portion of the carrier tracking receiver (present and past command transponders).

(2) The input filter to the BPL passes the total command modulation; however, the modulated carrier is also tapped off prior to entering this bandpass filter and is demodulated by the PLL reference in a separate phase detector to produce the command modulation.

(3) The input filter to the BPL completely filters out the command modulation, with the modulation being recovered as in case (2).

In cases (1) and (2), the BPL suppression factor, and hence the effective loop SNR, is a function of the *total* power-to-noise ratio in the input bandwidth. In case (3), the BPL loss is increased [relative to case (2)] since it is now only a function of the carrier component of the total power-to-noise ratio in the input bandwidth. Hence, with all other parameters unchanged, the effective loop SNR is reduced and the noisy reference loss increased. As we shall see, this effect produces a minor degradation in case (3) relative to case (2).

2. System Model

Consider the vehicle RF tracking receiver as illustrated in Fig. 11 (see SPS 37-57 Vol. I, pp. 17–22 for a more complete description). The signal at point ① can be
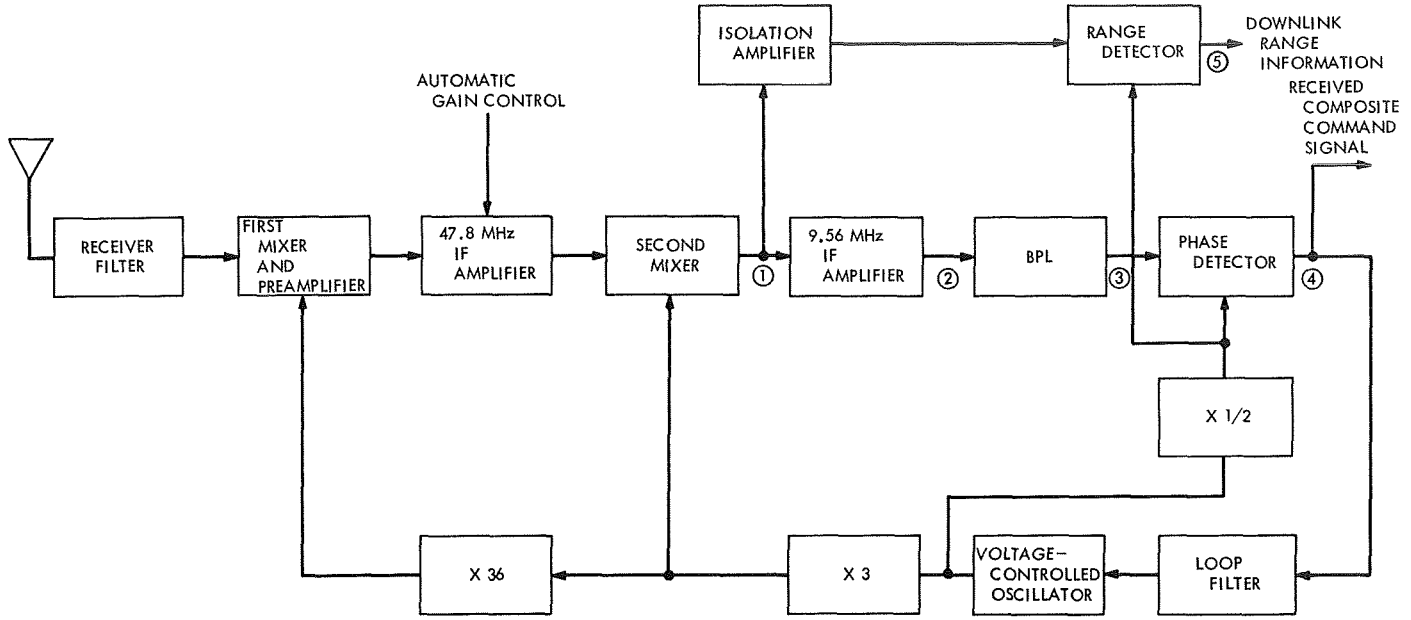
Fig. 11. Transponder receiver block diagram

characterized (with respect to the command modulation $m(t)$) by

$$y_{①}(t) = (2P)^{1/2} \sin(\omega_0 t + (\cos^{-1} m_1) m(t) + \theta_0)$$
$$+ 2^{1/2} [n_1(t) \cos(\omega_0 t + \theta_0) - n_2(t) \sin(\omega_0 t + \theta_0)]$$

(1)

In the above, m_1^2 is the command modulation factor, ω_0 is the IF carrier radian frequency, θ_0 the random phase to be tracked, and P is the total transmitted power. Also, $n_1(t)$ and $n_2(t)$ are zero mean "white" gaussian noise processes with single-sided spectral density N_0 in W/Hz. After passing through the BPL, the signal can be expressed in the form (Fig. 11, point ③),

$$y_{③}(t) = (2\widetilde{\alpha}_1^2 P_1)^{1/2} \sin[\omega_0 t + (\cos^{-1} m_1) m(t) + \theta_0] + 2^{1/2} [n_A(t) \cos(\omega_0 t + \theta_0) - n_B(t) \sin(\omega_0 t + \theta_0)]$$ (2)

where

$$n_A(t) = \frac{2(2)^{1/2}}{\pi} \left\{ -[(1 - m_1^2)\widetilde{\alpha}_1^2]^{1/2} + \frac{[(1 - m_1^2)P]^{1/2} m(t) + n_1(t)}{\{[((1 - m_1^2)P)^{1/2} m(t) + n_1(t)]^2 + [(m_1^2 P)^{1/2} - n_2(t)]^2\}^{1/2}} \right\}$$

$$n_B(t) = \frac{2(2)^{1/2}}{\pi} \left[(m_1^2 \widetilde{\alpha}_1^2) - \frac{(m_1^2 P)^{1/2} - n_2(t)}{\{[((1 - m_1^2)P)^{1/2} m(t) + n_1(t)]^2 + [(m_1^2 P)^{1/2} - n_2(t)]^2\}^{1/2}} \right]$$

(3)

and $\widetilde{\alpha}_1$ is the BPL suppression factor given by

$$\widetilde{\alpha}_1 = \left(\frac{\pi}{2}\right)^{1/2} \left(\frac{\rho_i}{2}\right)^{1/2} \exp\left(-\frac{\rho_i}{2}\right) \left[I_0\left(\frac{\rho_i}{2}\right) + I_1\left(\frac{\rho_i}{2}\right) \right]$$

(4)

Also, $P_1 = 8/\pi^2$ is the total power in the first spectral zone and the parameter ρ_i denotes the input SNR existing at point ②. More will be said about this quantity when each of the three cases posed in *Subsection 1* is treated.

If $m(t)$ is characterized by a digital data stream $d(t)$ and bi-phase modulated onto a square-wave subcarrier $s(t)$, then $y_{③}(t)$ can be rewritten as

$$y_{③}(t) = (2\widetilde{\alpha}_1^2 m_1^2 P)^{1/2} \sin(\omega_0 t + \theta_0)$$
$$+ [2\widetilde{\alpha}_1^2(1 - m_1^2)P]^{1/2} m(t) \cos(\omega_0 t + \theta)$$ (5)
$$+ 2^{1/2} [n_A(t) \cos(\omega_0 t + \theta_0) - n_B(t) \sin(\omega_0 t + \theta_0)]$$

with $m(t) = d(t) s(t)$.

Defining the PLL reference signal $r(t)$ by

$$r(t) = 2^{1/2} \cos(\omega_0 t + \hat{\theta}_0) \qquad (6)$$

where $\hat{\theta}_0$ is the PLL estimate of θ_0, then the phase detector output (neglecting second-order harmonics) is given by

$$\begin{aligned} y_{\textcircled{4}}(t) &= y_{\textcircled{3}}(t)r(t) \\ &= (\tilde{\alpha}_1^2\, m_1^2\, P_1)^{1/2} \sin\phi + n_A(t)\cos\phi - n_B(t)\sin\phi \end{aligned} \qquad (7)$$

with $\phi = \theta_0 - \hat{\theta}_0$ denoting the phase error process. As pointed out in *Section E*, n_A and n_B are, in general, not gaussian processes nor do they have equal mean-square values; however, they do always have zero mean. In order to properly apply the Fokker–Planck technique (which is necessary for finding the phase error density), certain reasonable assumptions must be made relative to the practical operating conditions of a PLL preceded by a BPL. If the loop bandwidth W_L is designed to be small relative to the equivalent noise bandwidth W_e at the phase detector output (Fig. 11, point $\textcircled{4}$), then the component noise processes n_A and n_B are approximately independent of the phase error process ϕ. Hence, from Eq. (7), the total noise power at the phase detector output is approximately

$$\sigma_e^2 = \sigma_{n_A}^2 \cos^2\phi + \sigma_{n_B}^2 \sin^2\phi \qquad (8)$$

where

$$\begin{aligned} \sigma_{n_A}^2 &= \frac{8}{\pi^2}\left\{(1 - m_1^2)\left[1 - \frac{1 - \exp(-\rho_i)}{2\rho_i} - \tilde{\alpha}_1^2\right] + m_1^2\left[\frac{1 - \exp(-\rho_i)}{2\rho_i}\right]\right\} \\ \sigma_{n_B}^2 &= \frac{8}{\pi^2}\left\{m_1^2\left[1 - \frac{1 - \exp(-\rho_i)}{2\rho_i} - \tilde{\alpha}_1^2\right] + (1 - m_1^2)\left[\frac{1 - \exp(-\rho_i)}{2\rho_i}\right]\right\} \end{aligned} \qquad (9)$$

If, in addition, the input SNR ρ_i is small (the usual case of interest for a PLL preceded by a BPL), then

$$\sigma_{n_B}^2 \approx \sigma_{n_A}^2 = \sigma_e^2 \qquad (10)$$

and it follows that the effective noise in the loop is approximately gaussian-distributed with one-sided flat spectrum $2\sigma_e^2/W_L$. Thus, the effective SNR in the loop bandwidth ρ_l is given by

$$\rho_l = \frac{2m_1^2 P}{N_0 W_L}\left(\frac{1}{\Gamma_p}\right) \qquad (11)$$

where Γ_p is defined in *Section E* by[1]

$$\begin{aligned} \Gamma_p &= \frac{\rho_i W_i}{\rho_e W_e} \\ &= \frac{1 - \exp(-\rho_i)}{\dfrac{\pi}{2}\left(\dfrac{\rho_i}{2}\right)\exp(-\rho_i)\left[I_0\left(\dfrac{\rho_i}{2}\right) + I_1\left(\dfrac{\rho_i}{2}\right)\right]^2\left\{1 + \left(\dfrac{4}{\Gamma_0 \pi} - 1\right)\exp\left[-\rho_i(1 - \pi/4)\right]\right\}} \end{aligned} \qquad (12)$$

and ρ_e, the effective SNR at the phase detector output, is defined by

$$\rho_e = \frac{\tilde{\alpha}_1^2 P_1}{\sigma_e^2} = \frac{2\tilde{\alpha}_1^2\, \dfrac{8}{\pi^2}}{N_{0e}W_e} \qquad (13)$$

---

[1] Γ_0 is the value of Γ_p at $\rho_i = 0$, which, for an ideal bandpass filter, is approximately equal to $1/0.862$.

3. Specification of Loop Parameters in Terms of System Design Point

It is quite common to characterize the up-link loop performance relative to a fixed design point, often called threshold. This point is normally chosen to correspond to a carrier SNR in the design point bandwidth $\Upsilon_0 = 2P_{c0}/(N_0 W_{L0})$ of 0 dB. Assuming then that $\Upsilon_0 = 1$, the effective SNR in the loop bandwidth can be expressed as

$$\rho_\ell = x \left(\frac{1}{\Gamma_p} \right) \left(\frac{1 + r_0}{1 + r_0/\mu} \right) \tag{14}$$

where

$$\left. \begin{aligned} x &= \frac{2m_1^2 P}{N_0 W_{L0}} \\[2mm] y &= \frac{W_{L0}}{W_i} \\[2mm] r_0 &= (\tilde{\alpha}_{10}^2 m_1^2 P_1)^{1/2} K \frac{\tau_2^2}{\tau_1} \\[2mm] \mu &= \frac{\tilde{\alpha}_{10}}{\tilde{\alpha}_1} \end{aligned} \right\} \tag{15}$$

with K denoting the PLL gain and τ_1, τ_2 the loop filter time constants. The symbol $\tilde{\alpha}_{10}$ represents the value of $\tilde{\alpha}_1$ at the design point.

The probability density function of the phase error $p(\phi)$ is derived via the Fokker–Planck apparatus in Ref. 1 with the result

$$p(\phi) = N \exp\left[U_0(\phi)\right] \int_\phi^{\phi+2\pi} \exp[-U_0(x)]dx \tag{16}$$

where N is a normalization constant and

$$U_0(\phi) = \beta\phi + \alpha \cos\phi \tag{17}$$

with

$$\left. \begin{aligned} \beta &= \left(\frac{r_0/\mu + 1}{r_0/\mu} \right) \frac{\rho_\ell}{2W_{L0}} \left(\frac{r_0 + 1}{r_0/\mu + 1} \right) \\[2mm] &\times \left[\Omega_0 - (m_1^2 P)^{1/2} K \left(1 - \frac{\tau_2}{\tau_1} \right) \overline{\sin\phi} \right] \\[2mm] \alpha &= \left(\frac{r_0/\mu + 1}{r_0/\mu} \right) \rho_\ell - \frac{(1 - \tau_2/\tau_1)}{(r_0/\mu)\, \sigma_{\sin\phi}^2} \end{aligned} \right\} \tag{18}$$

In computing the error probability performance of the command data detector, an important parameter to consider is loop bandwidth–symbol time product. Ordinarily, for command applications $\delta_0 = 1/(W_{L0}T)$ is sufficiently small (e.g., <0.5) such that the phase error can be assumed to vary rapidly over a symbol interval T. In cases (2) and (3), the noise affecting the data detection process is clearly gaussian since it has not been transmitted through the BPL. In case (1), the noise entering the matched filter detector (i.e., the phase detector output at point ④ in Fig. 11) is not gaussian, but, for small ρ_i, is approximately zero mean with a probability density function given in *Section E*. However, since the effective bandwidth of this noise is much wider than $1/T$, the integrate and dump action of the matched filter acts as a narrow-band filter and the output statistic is approximately gaussian. Hence, based on the above assumptions, the detector error probability P_E for all three cases is, to a good approximation, described by

$$P_E = \frac{1}{2}\, \text{erfc}\, (R_d^{1/2}\, \overline{\cos\phi}) \tag{19}$$

where

$$R_d = \frac{S_d T}{N_{0d}} \tag{20}$$

The parameters S_d and N_{0d} are the data signal and noise powers, respectively, which both depend upon which of the three cases is being considered.

a. Case (1). If the data signal applied to the matched filter detector is taken directly from the phase detector output (i.e., point ④ in Fig. 11), then

$$S_d = (1 - m_1^2)\tilde{\alpha}_1^2 P_1$$

$$N_{0d} = N_{0e} = \frac{2\sigma_e^2}{W_e} \tag{21}$$

An expression for N_{0e} in terms of the system design parameters can be obtained using the definition of Γ_p as in Eq. (12) with the result

$$N_{0e} = \frac{2m_1^2}{W_{L0}} \left(\frac{\tilde{\alpha}_1^2 P_1 \Gamma_p}{x} \right) \tag{22}$$

Combining Eqs. (21) and (22),

$$R_d = \left(\frac{1 - m_1^2}{m_1^2} \right) \frac{x}{2\Gamma_p \, \delta_0} \tag{23}$$

Also, in this case, the input SNR ρ_i, which affects the computation of $p(\phi)$, is given by

$$\rho_i = \frac{xy}{m_1^2} \qquad (24)$$

b. Case (2). When the data signal is obtained by demodulating the BPL input with the PLL reference signal (i.e., point ⑤ in Fig. 11), then

$$\left. \begin{aligned} S_d &= (1 - m_1^2)\, P \\ N_{od} &= N_0 \end{aligned} \right\} \qquad (25)$$

and, hence,

$$R_d = \left(\frac{1 - m_1^2}{m_1^2} \right) \frac{x}{2\,\delta_0} \qquad (26)$$

The parameter ρ_i is given by Eq. (24).

c. Case (3). For the case where the data signal is obtained as in case (2), but the input filter to the BPL completely filters out the modulation, then R_d is still given as in Eq. (26), but ρ_i now becomes

$$\rho_i = \left(\frac{1 - m_1^2}{m_1^2} \right) xy \qquad (27)$$

4. Numerical Results

A set of parameters typical of those to be used in the TOPS Program will now be chosen to serve as a numerical example. Letting $Y_0 = 1$, $r_0 = 2$, $W_{L0} = 18$ Hz, $W_i = 20$ kHz, $T = 0.25$, $\tau_2/\tau_1 = 0.002$, $m_1^2 = 0.7$ and $x = 9$ dB, we shall compare the error probability obtained from the three cases under consideration.

Case	ρ_i, dB	R_d, dB	P_E
(1)	4.914	8.196	1.6314×10^{-3}
(2)	4.914	8.842	7.6516×10^{-4}
(3)	4.912	8.842	7.6634×10^{-4}

In the above table, the difference between the error probabilities in cases (1) and (2) is strictly due to the effect of the BPL loss on R_d since the noisy reference loss (approximately 0.2 dB) is the same for both. This can be

seen from the fact that the effective SNR in the PLL ρ_l is the same in both cases. One concludes from this comparison that for the parameters fixed as chosen, one pays an error probability penalty of a factor of two or greater by extracting the data signal from the PLL phase detector output. The comparison between cases (2) and (3) shows a negligibly small difference in error probability due to the reduction in the effective loop SNR caused by filtering out the command modulation sideband power. Here, the penalty is strictly due to a change in the noisy reference loss, since R_d is the same for both cases, and is so small that it will be indistinguishable in practical receiver mechanizations. Further experimental verification of these results is planned.

Reference

1. Lindsey, W. C., "Nonlinear Analysis of Generalized Tracking Systems," *Proc. IEEE*, Vol. 57, No. 10, pp. 1705–1722, Oct. 1969.

E. An Analysis of the Phase Coherent–Incoherent Output of the Bandpass Limiter,

J. C. Springett and M. K. Simon

1. Introduction

The bandpass limiter has been the subject of much study in recent years. Most publications have been concerned with the various aspects of the first zone output, and the application of the limiter to systems wherein the question of coherency is not involved.

This article deals with the limiter followed by a coherent demodulator; the results are generally treated in terms of the phase-locked loop and coherent demodulation. The question of signal-to-noise spectral density at the output is also explored, since most often the limiter is followed by narrowband rather than zonal filters.

2. Preliminaries

Figure 12 is a block diagram of the bandpass limiter model under consideration. In this figure, $h_1(t)$ is a bandpass filter with center frequency ω_0, and equivalent noise
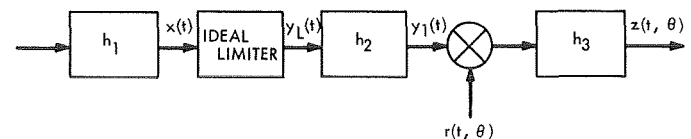

Fig. 12. Bandpass limiter model block diagram

bandwidth $B_i \ll \omega_0$, given by

$$B_i \triangleq \frac{1}{2\pi} \int_0^\infty \frac{|H(j\omega)|^2}{|H(j\omega_0)|^2} \, d\omega \qquad (1)$$

where H is the transfer function of the filter. (See Table 1 for definitions of symbols used in this article.) In the ensuing discussion, it makes no difference whether the

Table 1. Definition of symbols

$h(t)$	Weighting function of filter element
B_i	Noise bandwidth of limiter input filter
$H(j\omega)$	Filter transfer function
ω_0	Signal angular frequency
$s(t)$	Input signal
$n(t)$	Input noise
$x(t)$	Input signal-plus noise
$\phi, \phi(t)$	Random phase process
σ_n^2	Input noise variance
A	Input rms signal amplitude
$y_L(t)$	Total limiter output
$\gamma(t)$	Equivalent input signal-plus-noise phase
$y_1(t)$	Limiter first zone output
$\mu(\rho), \mu_z$	Mean of output signal
ρ	Input signal-to-noise ratio
$\alpha(\rho)$	Signal suppression factor
N_0	Input noise power spectral density
(S/N)	Signal-to-noise ratio
(S/N_0)	Signal-to-noise spectral-density ratio
$z(t)$	Ensemble following coherent demodulation
$r(t, \theta)$	Demodulation reference
θ	Angle between limiter signal and demodulation reference
σ_z^2	Output noise variance
Γ	Ratio of output to input signal-to-noise-spectral-density ratios
B_o	Output noise bandwidth
$r_n(\tau)$	Normalized input filter autocorrelation function
n_0	Output-noise power spectral density
$p(z)$	First-order probability density function

input filter is physically realizable as long as the foregoing conditions are met. The input signal is defined to be of the form

$$x(t) = s(t) + n(t) \qquad (2)$$

with

$$s(t) \triangleq 2^{\frac{1}{2}} A \cos (\omega_0 t + \phi) \qquad (3)$$

ϕ is a random phase uniformly distributed[2] on $-\pi, \pi$; and,

$$n(t) \triangleq 2^{\frac{1}{2}} [n_c(t) \cos (\omega_0 t + \phi) - n_s(t) \sin (\omega_0 t + \phi)] \qquad (4)$$

with

$$E[n_c(t) n_s(t)] = 0$$

$$E[n_c^2(t)] = E[n_s^2(t)] = \frac{\sigma_n^2}{2}$$

$$\sigma_n^2 = E[n^2(t)] = N_0 B_i$$

The one-sided noise-spectral-density at the input to the filter h_1 is N_0.

The ideal limiter function is defined such that

$$y_L(t) = \text{sgn} [x(t)] = \begin{bmatrix} +1 \ x(t) > 0 \\ -1 \ x(t) < 0 \end{bmatrix} \qquad (5)$$

and $E[y_L^2(t)] = 1$.

The input process $x(t)$ may be written in the equivalent form

$$x(t) = v(t) \cos [\omega_0 t + \phi + \gamma(t)] \qquad (6)$$

with

$$v(t) = 2^{\frac{1}{2}} \{[A + n_c(t)]^2 + n_s^2(t)\}^{\frac{1}{2}}$$

---

[2]The term ϕ may also be taken as $\phi(t)$, an information bearing signal; however, for convenience the stated assumption will be invoked without loss of generality.

and

$$\gamma(t) = \tan^{-1}\left\{\frac{n_s(t)}{[A + n_c(t)]}\right\}$$

Using the complex Fourier transform approach of relating the limiter output time function to that of the input, one obtains

$$y_L(t) = \frac{1}{2\pi}\int_C f(j\xi)\exp[j\xi x(t)]d\xi$$

$$= \frac{1}{j\pi}\int_C \frac{d\xi}{\xi}\exp\{j\xi v(t)\cos[\omega_0 t + \gamma(t) + \phi]\} \quad (7)$$

with $f(j\xi) = 2/j\xi$, the Fourier transform of dynamic path represented by the limiter. Expanding the exponential function in a series of Bessel cosine functions, the limiter output becomes

$$y_L(t) = \frac{1}{\pi}\sum_{m=0}^{\infty}\left\{\epsilon_m j^{m-1}\int_C \frac{J_m[\xi v(t)]}{\xi}d\xi\right\}\cos\{m[\omega_0 t + \gamma(t) + \phi]\}$$

$$= \frac{4}{\pi}\sum_{m=0}^{\infty}\left(\frac{1}{2m+1}\right)\cos\{(2m+1)[\omega_0 t + \gamma(t) + \phi]\}$$

$$= \frac{4}{\pi}\left\{\cos[\omega_0 t + \gamma(t) + \phi] + \frac{1}{3}\cos[3\omega_0 t + 3\gamma(t) + 3\phi] + \cdots\right\} \quad (8)$$

The output of the limiter may, therefore, be represented as a series of phase-modulated sinusoids beginning at frequency ω_0 and extending to all odd multiples of ω_0.

Each term in the series is referred to as the mth zonal term; thus, the $m = 1$ contribution is referred to as the first zone output, and we define

$$y_1(t) \triangleq \frac{4}{\pi}\cos[\omega_0 t + \gamma(t) + \phi] \quad (9)$$

Note, then, that the filter h_2 is a mathematical entity that selects only the first zone component. In reality, a physical bandpass filter can only approximate this condition since the spectrum of $\cos[\omega_0 t + \gamma(t) + \phi]$ extends on all ω; however, because of the assumed narrowband approximation ($B_1 \ll \omega_0$), the error is small. It can also be seen that $E[y_1^2(t)] = 8/\pi^2$ independent of $\gamma(t)$. Further, if $\gamma(t) = 0$ (no noise), then the output is a pure sine function whose amplitude is equal to that of the fundamental term of a unit-power squarewave of frequency ω_0.

3. Summary of Incoherent Results

The signal-to-noise ratio (S/N) of the first zone output $y_1(t)$ has been analyzed by many authors, the most notable being W. B. Davenport, Jr. (Ref. 1). The procedure

amounts to evaluating the amount of "carrier component" through formation of the second-moment function and averaging over the distributions on ϕ and $n(t)$. The well-known result permits the output $y_1(t)$ to be expressed in the form

$$y_1(t) = 2^{1/2}\mu(\rho)\cos(\omega_0 t + \phi) + n'(t) \quad (10)$$

where

$$\mu(\rho) = \frac{2(2^{1/2})}{\pi}\alpha(\rho) = \left(\frac{2\rho}{\pi}\right)^{1/2}\exp\left(-\frac{\rho}{2}\right)$$

$$\times\left[I_0\left(\frac{\rho}{2}\right) + I_1\left(\frac{\rho}{2}\right)\right] \quad (11)$$

I_0 and I_1 are modified Bessel functions of the first kind, and ρ is the limiter input S/N

$$(S/N)_i = \rho \triangleq \frac{A^2}{\sigma_n^2} = \frac{A^2}{N_0 B_i} \quad (12)$$

The function $\alpha(\rho)$ is commonly referred to as the signal component suppression factor and ranges in value between 1 and 0 as ρ ranges from ∞ to 0. The output signal power

is thus given by:

$$P_s = \mu^2(\rho) = \frac{8}{\pi^2}\,\alpha^2(\rho) \qquad (13)$$

Since $E[y_1^2(t)]$, the total signal-plus-noise output power, has already been shown to be invariant to ρ, then the output noise power is

$$P_n = \frac{8}{\pi^2} - \mu^2(\rho) = \frac{8}{\pi^2}\,[1 - \alpha^2(\rho)] \qquad (14)$$

The output, S/N, therefore, becomes

$$(S/N)_o^I = \frac{P_s}{P_n} = \frac{\alpha^2(\rho)}{1 - \alpha^2(\rho)} \qquad (15)$$

where the superscript I denotes incoherent. A more-or-less standard method of portraying this result is to plot the ratio of output-to-input S/N as a function of input S/N. Such plots appear in Fig. 13 where $10\log_{10}(\cdot)$ has been taken of the quantities so that the results are in dB. The well-known asymptotes that result as ρ tends to its limits are

$$\frac{(S/N)_o^I}{(S/N)_i} \to 2\ (+3\ \mathrm{dB})\ \text{as}\ \rho \to \infty \qquad (16)$$

$$\frac{(S/N)_o^I}{(S/N)_i} \to \frac{\pi}{4}\ (-1.05\ \mathrm{dB})\ \text{as}\ \rho \to 0 \qquad (17)$$
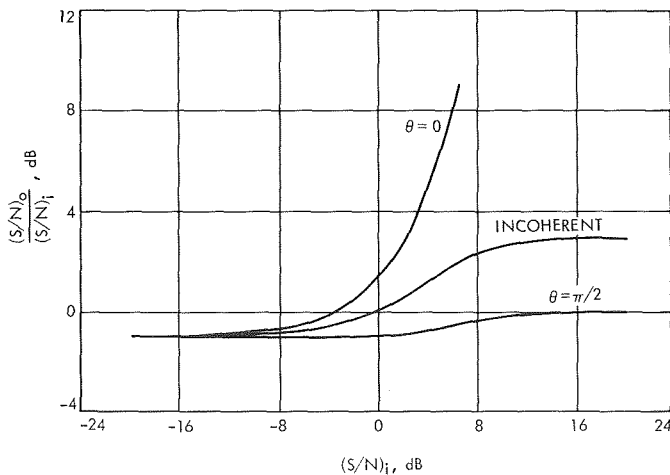

Fig. 13. Zonal SNRs

4. Signal-to-Noise Ratios Following Coherent Demodulation

Consider multiplying (demodulating) the limiter first zone output by a unit power-coherent reference,[3] i.e.,

$$y_1(t)\,r(t,\theta) = \frac{4}{\pi}\cos\left[\omega_0 t + \gamma(t) + \phi\right]$$
$$\times\ 2^{1/2}\cos\left(\omega_0 t + \theta + \phi\right) \qquad (18)$$

where θ is the demodulation reference angle with principal range $(-\pi/2, \pi/2)$. The angle θ, is not taken to be a random variable, but is dependent upon any specific application. For example, when $\theta = \pi/2$ (nominally), the output may become the embodiment of a phase-locked tracking loop; for $\theta = 0$, coherent am or phase-reversal demodulation can result.

The purpose of the filter h_3 is to remove the $2\omega_0$ term from the above product; i.e.,

$$z(t,\theta) \triangleq \frac{2(2^{1/2})}{\pi}\cos\left[\gamma(t) - \theta\right] \qquad (19)$$

Again, as was the case for h_2, the filter h_3 is a mathematical entity. Expanding the $\cos\left[\gamma(t) - \theta\right]$ term,

$$z(t,\theta) = \frac{2(2^{1/2})}{\pi}\cos\theta\cos\gamma(t) + \frac{2(2^{1/2})}{\pi}\sin\theta\sin\gamma(t) \qquad (20)$$

---

[3]Here, ϕ or $\phi(t)$ is taken as known *a priori* in the reference signal. In general applications, this may not be the case, and the reference signal might more properly be taken as

$$r(t,\theta) = 2^{1/2}\cos\left(\omega_0 t + \theta\right)$$

However, the signal $y_1(t)$ may also be written in the form

$$y_1(t) = \frac{\pi}{4}\cos\phi\cos\left[\omega_0 t + \gamma(t)\right] - \frac{4}{\pi}\sin\phi\sin\left[\omega_0 t + \gamma(t)\right]$$

and demodulating, we obtain

$$y_1(t)\,r(t,\theta) = \frac{4(2^{1/2})}{\pi}\cos\phi\cos\left[\omega_0 t + \gamma(t)\right]\cos\left(\omega_0 t + \theta\right)$$
$$+ \frac{4(2^{1/2})}{\pi}\sin\phi\sin\left[\omega_0 t + \gamma(t)\right]\cos\left(\omega_0 t + \theta\right)$$

Operating on these terms (conditioned on ϕ), the same mathematical forms are obtained as described in the subsequent text from the standpoint of mean, variance, etc., when the angle θ is appropriately chosen.

and substituting the $\gamma(t)$ previously defined, we obtain

$$z(\theta) = \frac{2(2^{\frac{1}{2}})}{\pi} \left\{ \frac{A + n_c}{[(A + n_c)^2 + n_s^2]^{\frac{1}{2}}} \cos \theta + \frac{n_s}{[(A + n_c)^2 + n_s^2]^{\frac{1}{2}}} \sin \theta \right\} \qquad (21)$$

(Henceforth, we also drop the functional notation with respect to t, remembering that we are dealing with a stochastic process). For the purpose of evaluating the S/N of z, we are interested in the first two moments of z; viz,

$$\mu_z \triangleq E[z(\theta)] = \frac{2(2^{\frac{1}{2}})}{\pi} \left\{ \cos \theta \, E \left[\frac{A + n_c}{((A + n_c)^2 + n_s^2)^{\frac{1}{2}}} \right] + \sin \theta \, E \left[\frac{n_s}{((A + n_c)^2 + n_s^2)^{\frac{1}{2}}} \right] \right\} \qquad (22)$$

$$\sigma_z^2 = E \left[z^2(\theta) \right] - \mu_z^2$$

$$= \frac{8}{\pi^2} \left\{ \cos^2 \theta \, E \left[\cos^2 \gamma \right] + \sin^2 \theta \, E \left[\sin^2 \gamma \right] + 2 \sin \theta \cos \theta \, E \left[\sin \gamma \cos \gamma \right] \right\} - \mu_z^2$$

$$= \frac{8}{\pi^2} \left[\cos^2 \theta - \cos 2\theta \, E \left(\sin^2 \gamma \right) \right] - \mu_z^2$$

$$= \frac{8}{\pi^2} \left\{ \cos^2 \theta - \cos 2\theta \, E \left[\frac{n_s^2}{(A + n_c)^2 + n_s^2} \right] \right\} - \mu_z^2 \qquad (23)$$

The evaluation of the expectations is reasonably straightforward given that n_c and n_s are independent and gaussian with variance $\sigma_n^2/2$. The results are

$$\mu_z = \left(\frac{2\rho}{\pi} \right)^{\frac{1}{2}} \exp \left(\frac{-\rho}{2} \right) \left[I_0 \left(\frac{\rho}{2} \right) + I_1 \left(\frac{\rho}{2} \right) \right] \cos \theta \qquad (24)$$

and

$$\sigma_z^2 = \frac{8}{\pi^2} \left[\cos^2 \theta - \left(\frac{1 - \exp(-\rho)}{2\rho} \right) \cos 2\theta \right] - \mu_z^2 \qquad (25)$$

We now examine the output S/N and the asymptotic behavior of μ_z and σ_z with ρ. Note, first, that μ_z is the same as that obtained for the incoherent case except for the $\cos \theta$ factor. For large ρ,

$$\mu_z \approx \frac{2^{\frac{1}{2}}}{\pi} \left(2 - \frac{1}{2\rho} - \frac{3}{16\rho^2} \right) \cos \theta \qquad \rho \gg 1 \qquad (26)$$

and for small ρ,

$$\mu_z \approx \left(\frac{2\rho}{\pi} \right)^{\frac{1}{2}} \cos \theta \qquad \rho \ll 1 \qquad (27)$$

In like manner, the asymptotic results for σ_z^2 become

$$\sigma_z^2 = \frac{4}{\pi^2 \rho} \left(\frac{1}{4\rho} \cos^2 \theta + \sin^2 \theta \right) \qquad \rho \gg 1 \qquad (28)$$

$$\sigma_z^2 = \frac{4}{\pi^2} \left[2 \cos^2 \theta - \exp(-\rho) \cos 2\theta \right] - \frac{2\rho}{\pi} \cos^2 \theta \qquad \rho \ll 1 \qquad (29)$$

Note that for $\rho \equiv 0$, $\sigma_z^2 = 4/\pi^2$, independent of θ. A general definition of the output S/N is now

$$(S/N)_o^\theta = \frac{\mu_z^2}{\sigma_z^2} \qquad (30)$$

As was done in the incoherent case, the ratio of output-to-input S/N is a quantity of interest. In this case, however, a bandwidth change of ½ accompanies the bandpass-to-lowpass transformation; in taking ratios, however, it is desirable to take this ratio into account. Thus, for the lowpass-to-bandpass ratios, we choose to take

$$\frac{(S/N)_o^\theta}{2(S/N)_i} = \frac{\mu_z^2}{2\rho \sigma_z^2} \qquad (31)$$

Two cases of θ are of predominant interest; $\theta = 0$ and $\theta = \pi/2$. First, we take the $\theta = 0$ case. The output-to-

input S/N ratio becomes

$$\frac{(S/N)_o^0}{2(S/N)_i} = \frac{1}{2} \frac{\exp(-\rho)\,[I_0(\rho/2) + I_1(\rho/2)]^2}{\frac{4}{\pi}\left\{1 - \left[\frac{1 - \exp(-\rho)}{2\rho}\right]\right\} - \rho\exp(-\rho)\,[I_0(\rho/2) + I_1(\rho/2)]^2} \tag{32}$$

This complex expression requires evaluation on a computer for any arbitrary ρ; however, as was done in the incoherent case, we again resort to the asymptotic results, which give

$$\frac{(S/N)_o^0}{2(S/N)_i} = 4\rho \qquad \rho \gg 1 \tag{33}$$

$$\frac{(S/N)_o^0}{2(S/N)_i} = \frac{\pi}{4 - 2\pi\rho} \qquad \rho \ll 1 \tag{34}$$

For large ρ, the ratio grows with ρ; for small ρ the result approaches $\pi/4$ as ρ approaches 0. A plot of the total function appears in Fig. 13, where it may be compared with the previously discussed incoherent result.

The second case, $\theta = \pi/2$, represents the phase detector for the phase-locked loop. Here, $\mu_z = 0$; however, if we adopt the phase-locked loop definition of the "signal" as being the slope of the function $z(\theta)$ at $\theta = \pi/2$, we have

$$\mu_{\pi/2} = E\left(\frac{dz(\theta)}{d\theta}\;\middle|\;\theta = \pi/2\right) = -\mu_0 \tag{35}$$

where $\mu_0 = \mu_z$ evaluated at $\theta = 0$ (i.e., the mean for the previously considered $\theta = 0$ case). Thus, the output-to-input S/N relationship becomes

$$\frac{(S/N)_o^{\pi/2}}{2(S/N)_i} = \frac{1}{2} \frac{\exp(-\rho)\,[I_0(\rho/2) + I_1(\rho/2)]^2}{\frac{2}{\pi}\left[\frac{1 - \exp(-\rho)}{\rho}\right]} \tag{36}$$

The asymptotic values for this case are

$$\frac{(S/N)_o^{\pi/2}}{2(S/N)_i} = 1 - \frac{1}{2\rho} \qquad \rho \gg 1 \tag{37}$$

$$\frac{(S/N)_o^{\pi/2}}{2(S/N)_i} = \frac{\pi}{4 - 4\rho} \qquad \rho \ll 1 \tag{38}$$

The complete result is plotted in Fig. 13. In this case, it can be seen that there is never a gain in S/N through the limiter, as was found for the incoherent and $\theta = 0$ cases at high S/N. This result agrees with work presented in SPS 37-54, Vol. III, pp. 201–204.

5. Signal-to-Noise Spectral Densities

In many applications of the limiter to communication receiver design, the output of the limiter is followed by a filter function whose bandwidth is much less than that of the zone. In such cases, it is desirable to know the noise-spectral-density of the output at ω_0 in the incoherent case and at zero frequency in the coherent cases.

It can be found, by studying the second-moment (autocorrelation) function of first zone output, that the output noise has maximum spectral density at $\omega = \omega_0$, and that it falls off in a shape and manner dependent on the characteristics of the limiter input filter. The value of the output noise-spectral-density at $\omega = \omega_0$ is also dependent upon the input filter.

In SPS 37-36, Vol. IV, pp. 241–244, a numerical evaluation of the output noise-spectral-density at $\omega = \omega_0$ was performed assuming that the input filter had an ideal rectangular frequency response characteristic. The result showed that the ratio of incoherent output-to-input signal-to-noise-spectral-density, as a function of ρ, approached 2.0 for large ρ, and 0.862 for small ρ. The complete result, as given in SPS 37-36, Vol. IV is reproduced in Fig. 14 and compared with the zonal S/N result. It should be noted that the calculated behavior of the signal-to-noise-spectral-density is only approximate since only a finite number (11 to be exact) of $S \times N$ and $N \times N$ terms making up the spectral density were evaluated. Compared to the ratio of zonal S/N, the spectral density case shows "less of a loss" for small ρ. From this fact, it can be inferred that the equivalent noise bandwidth of the first zone is greater than that of the input noise. In Ref. 2, R. C. Tausworthe derived a rational approximation to the spectral-density results and denoted
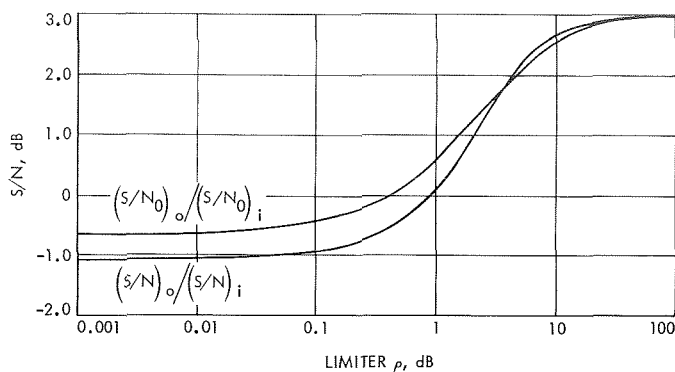
Fig. 14. Incoherent limiter first zone

the result by $1/\Gamma$; i.e.,

$$\frac{1}{\Gamma} \triangleq \frac{(S/N_0)_o^I}{(S/N_0)_i} = \frac{(S/N)_o^I}{(S/N)_i} \frac{B_o}{B_i} \tag{39}$$

where $(S/N_0)_o^I$ and $(S/N_0)_i$ are, respectively, the output and input signal-to-noise-spectral-density ratios, and B_o is the first zone noise-bandwidth.

The ensuing discussion develops a more generalized approximation for the ratio of B_o/B_i and applies it not only to the incoherent result, but also to the demodulated cases.

As noted, the output-noise spectral density is a function of the input filter characteristics and ρ. In the case of coherent demodulation, it is also a function of θ. To begin with, let us examine the case of $\rho = 0$, where the dependence on θ is also zero due to the fact that there is no input signal present. Thus, the limiter input consists of noise assumed to be Gaussian. A well-known result that relates the limiter output autocorrelation function to that of the input noise process is Prices' Theorem (Ref. 3). Let the normalized input noise autocorrelation function be given by

$$r_n(\tau) \cos \omega_0\tau, \qquad -\infty < \tau < \infty \tag{40}$$

where $r_n(\tau)$ is lowpass and has properties

$$r_n(0) = 1, \qquad |r_n(\tau)| < 1, \qquad \int_{-\infty}^{\infty} r_n(\tau)d\tau = \frac{1}{B_i}$$

Denoting the output autocorrelation function as $R_L(\tau)$, we have, by Prices' Theorem,

$$R_L(\tau) = \frac{2}{\pi} \sin^{-1} [r_n(\tau) \cos \omega_0\tau] \tag{41}$$

Expanding the arcsin in its power series, we obtain

$$R_L(\tau) = \frac{2}{\pi} \left[r_n(\tau) \cos \omega_0\tau + \frac{r_n^3(\tau)}{2\cdot3} \cos^3 \omega_0\tau + \frac{1\cdot3 r_n^5(\tau)}{2\cdot4\cdot5} \cos^5 \omega_0\tau + \cdots \right] \tag{42}$$

Next, expand the $\cos^n \omega_0\tau$ terms, keeping only those belonging to the first zone. With a little manipulation, it is found that the first zone autocorrelation function is

$$R_1(\tau) = \frac{2}{\pi} \left\{ r_n(\tau) + \sum_{k=1}^{\infty} \frac{[1\cdot3\cdot5\cdots(2k-1)]^2}{[2\cdot4\cdot6\cdots2k]^2(k+1)} \, r_n^{(2k+1)}(\tau) \right\} \cos \omega_0\tau \tag{43}$$

The output noise-spectral-density is, therefore, given by

$$\frac{2}{\pi} \left\{ \frac{1}{B_i} + \sum_{k=1}^{\infty} \frac{[1\cdot3\cdot5\cdots(2k-1)]^2}{[2\cdot4\cdot6\cdots2k]^2(k+1)} \int_{-\infty}^{\infty} r_n^{(2k+1)}(\tau)d\tau \right\} \triangleq n_0 \tag{44}$$

Since the output noise power is $8/\pi^2$ for the incoherent limiter, the output noise bandwidth B_o for $\rho = 0$ is, therefore,

$$B_o = \frac{8}{\pi^2 n_0} \qquad (45)$$

A further examination of the defining function for n_0 shows that bounds on this quantity can be obtained. Since

$$0 < \int_{-\infty}^{\infty} r_n^{(2k+1)}(\tau)d\tau < \frac{1}{B_i} \qquad (46)$$

we find that

$$n_0 > \frac{2}{\pi B_i} \qquad (47)$$

and

$$n_0 < \frac{2}{\pi B_i} \left\{ 1 + \sum_{k=1}^{\infty} \frac{[1 \cdot 3 \cdot 5 \cdots (2k-1)]^2}{[2 \cdot 4 \cdot 6 \cdots 2k]^2 (k+1)} \right\} = \frac{8}{\pi^2 B_i} \qquad (48)$$

Thus,

$$B_i < B_o < \frac{4}{\pi} B_i \qquad (49)$$

Denoting, then, the zero S/N ratio of output-to-input noise-spectral densities as $1/\Gamma_0$, we have

$$\frac{\pi}{4} < \frac{1}{\Gamma_0} < 1 \qquad (50)$$

These bounds are valid for both the incoherent and coherent cases. Therefore, Γ_0 is given exactly by

$$\Gamma_0 = 1 + B_i \sum_{k=1}^{\infty} \frac{[1 \cdot 3 \cdot 5 \cdots (2k-1)]^2}{[2 \cdot 4 \cdot 6 \cdots 2k]^2 (k+1)} \int_{-\infty}^{\infty} r_n^{(2k+1)}(\tau)\,d\tau \qquad (51)$$

Some typical values for $1/\Gamma_0$ are as follows:

Filter	$1/\Gamma_0$
Single pole RC	0.944
Gaussian	0.893
Ideal rectangular	≈ 0.862

We now look at the more general problem of finding a relationship between B_o and B_i for non-zero ρ and θ. First, since $B_o \geq B_i$, and $B_o \rightarrow B_i$ as $\rho \rightarrow \infty$, $1/\Gamma$ must always be greater[4] than the related output-to-input S/N ratio, as defined in *Subsection 4*, and merge into the S/N ratio as $\rho \rightarrow \infty$. Further, since the zonal results in Fig. 13 are all monotonic with ρ, the $1/\Gamma$ should also be monotonic with ρ. Finally, noting again the various zonal results, it is expected for any given ρ that the zonal noise-bandwidth would be maximum for $\theta = \pi/2$ and minimum for $\theta = 0$. Examination of the defining expression for the noise bandwidth, by differentiating with respect to θ, shows this to indeed be the case; i.e., the derivative is zero for $\theta = 0$ and $\theta = \pi/2$.

Taking all the forgoing into account, an exponential relationship of output-to-input bandwidth is postulated in the form

$$B_o(\rho, \theta) = B_i f(\Gamma_0) \exp[-g(\rho, \theta)] \qquad (52)$$

a number of specific $f(\Gamma_0)$ and $g(\rho, \theta)$ have been explored and the incoherent $1/\Gamma$ has been calculated for the purpose of comparison to the result in Fig. 14. Through this procedure, the following specific relationship was derived and found to compare within 0.1 dB for all ρ

$$B_o(\rho, \theta) = B_i \left\{ 1 + \left(\frac{4}{\pi \Gamma_0} - 1 \right) \exp\left[-\rho \left(1 - \frac{\theta}{2} \right) \right] \right\}$$

$$0 \leq \theta \leq \frac{\pi}{2} \qquad (53)$$

To obtain the $B_o(\rho)$ for the incoherent case, $B_o(\rho, \theta)$ is averaged over a uniform distribution on θ. The resulting $1/\Gamma$ curves for $1/\Gamma_0 = 0.862$ are shown in Fig. 15; also shown are lower and upper bounding curves obtained by letting $1/\Gamma_0 = \pi/4$ and $1/\Gamma_0 = 1$, respectively.

In summary, we have derived $\rho = 0$ asymptotic values for output-signal-to-noise-spectral-density, and rationally derived results for all $\rho > 0$, based upon an exact evaluation of $1/\Gamma_0$. The functional dependence on θ is conjectured, and, therefore, approximate to the exact (unknown) result.

---

[4]Note that the $1/\Gamma$ result from SPS 37-36, Vol. IV, shown in Fig. 14, crosses the zonal S/N curve for large ρ. This can be attributed to the numerical error associated with taking only 11 terms of the infinite series into the calculation.
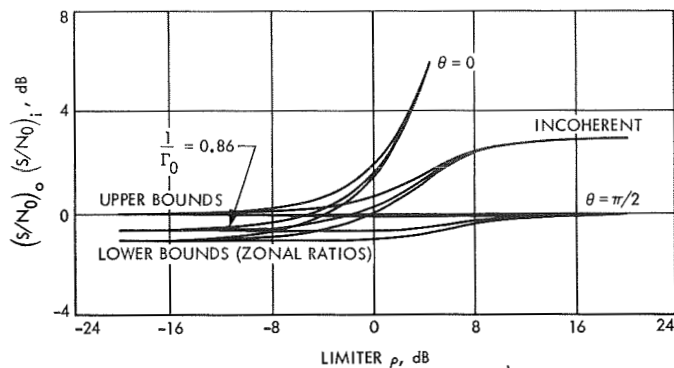
Fig. 15. Signal-to-noise spectral-density ratios

6. First-Order Probability Densities of the Lowpass Output

It is of interest to study the first-order probability density functions of the noise components $\cos \gamma(t)$ and $\sin \gamma(t)$ since the evaluation of the performance of a coherent demodulation preceded by a bandpass limiter depends heavily on the functional form of these distributions.

To begin, we consider the general problem of finding the density function of the random variable

$$z = \frac{y}{(x^2 + y^2)^{\frac{1}{2}}} \tag{54}$$

where x and y are independent Gaussian random variates with parameters $(\bar{x}, \sigma_x)$, $(\bar{y}, \sigma_y)$. Assuming $\sigma_x = \sigma_y = \sigma$,

Fig. 16. Probability density

and converting to polar coordinates via the transformation

$$x = r \cos \lambda \tag{55}$$

$$y = r \sin \lambda \tag{56}$$

the first-order density function for λ can be written as

$$p(\lambda) = \frac{1}{2\pi} \exp\left[-\frac{\bar{x}^2 + \bar{y}^2}{2\sigma^2}\right]\left[1 + \pi^{\frac{1}{2}}\left(\frac{\bar{x}\cos\lambda + \bar{y}\sin\lambda}{2^{\frac{1}{2}}\sigma}\right)\right]$$

$$\times \exp\left[\frac{(\bar{x}\cos\lambda + \bar{y}\sin\lambda)^2}{2\sigma^2}\right]\left[1 + \mathrm{erf}\left(\frac{\bar{x}\cos\lambda + \bar{y}\sin\lambda}{2^{\frac{1}{2}}\sigma}\right)\right] \qquad 0 \leq \lambda \leq 2\pi \tag{57}$$

where

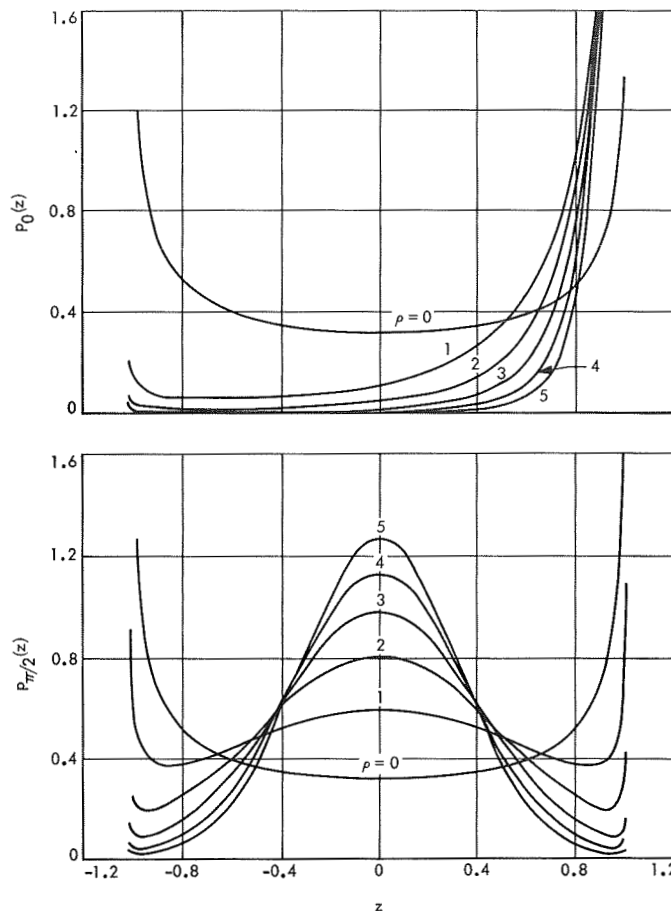$$\mathrm{erf}(x) = \frac{2}{\pi^{\frac{1}{2}}}\int_0^x \exp(-t^2)dt$$

Recognizing that $x/(x^2 + y^2)^{1/2} = \cos \lambda$ and $y/(x^2 + y^2)^{1/2} = \sin \lambda$, it is a relatively simple matter to get their distributions by a non linear transformation of coordinates. In particular, we are interested in the following two cases:

$$\text{Case I. } (\theta = 0) \begin{cases} y = A + n_c; & \overline{y} = A \qquad \sigma^2 = \dfrac{\sigma_n^2}{2} \\[2ex] x = n_s & ; \qquad \overline{x} = 0 \end{cases}$$

$$\text{Case II. } (\theta = \pi/2) \begin{cases} y = n_s & ; \qquad \overline{y} = 0 \qquad \sigma^2 = \dfrac{\sigma_n^2}{2} \\[2ex] x = A + n_c; & \overline{x} = A \end{cases}$$

Then, the probability density function of $\cos \gamma(t)$ is equal to the probability density function of z subject to the conditions of Case I; i.e.,

$$p_0(z) = \frac{1}{(1 - z^2)^{1/2}} \left[p(\sin^{-1} z) + p(\pi - \sin^{-1} z) \right]$$

$$= \frac{\dfrac{1}{\pi} \exp(-\rho) \{ 1 + (\pi\rho)^{1/2} z \exp(\rho z^2) [1 + \text{erf}(\rho^{1/2} z)] \}}{(1 - z^2)^{1/2}} \qquad -1 < z < 1 \qquad (58)$$

where

$$\rho = \frac{A^2}{2\sigma^2} = \frac{A^2}{\sigma_n^2}$$

To obtain the density function for $\sin \gamma(t)$, we again consider the density function for z (subject now, however, to the conditions of Case II). Then,

$$p_{\pi/2}(z) = \frac{\dfrac{1}{\pi} \exp(-\rho) \{ 1 + (\pi\rho)^{1/2} (1 - z^2)^{1/2} \exp[\rho(1 - z)^2] \text{erf} \{[\rho(1 - z)^2]^{1/2}\} \}}{(1 - z^2)^{1/2}} \qquad -1 < z < 1 \qquad (59)$$

These two density functions are illustrated in Fig. 16 for various values of ρ. As previously discussed, $p_0(z)$ has a mean given by $\alpha(\rho)$, whereas $p_{\pi/2}(z)$ is the zero mean for all ρ. Both distributions in the limit as $\rho \to 0$ behave like

$$p(z) = \frac{1}{\pi (1 - z^2)^{1/2}} \qquad (60)$$

However, for large ρ, $p_{\pi/2}(z)$ becomes Gaussian.

References

1. Davenport, W. B., Jr., "Signal-to-Noise Ratios in Band-Pass Limiters," *J. Appl. Phys.*, Vol. 24, No. 6, June 1953.

2. Tausworthe, R. C., *Theory and Practical Design of Phase-Locked Receivers*, Technical Report 32-819, Vol. I. Jet Propulsion Laboratory, Pasadena, Calif., Feb. 15, 1966.

3. Price, R., "A Useful Theorem for Nonlinear Devices Having Gaussian Inputs," *IRE Trans. PG IT*, IT-4, June 1958.

VIII. Spacecraft Power

GUIDANCE AND CONTROL DIVISION

A. Multi-Hundred-Watt Radioisotope Thermo-electric Generator Transient Performance,

W. D. Leonard[1] and O. S. Merrill

1. Introduction

One of the most critical problems associated with the integration of the multi-hundred-watt radioisotope thermoelectric generator (MHW-RTG) with the TOPS spacecraft is that of the RTG's operation in air during the launch phase. Because of the presence of oxidation-prone materials in the RTG, it must be designed in such a way as to permit operation in air without harmful effects.

Several methods of solving this problem in order to provide on-board electrical power during the launch phase have been proposed. Two of these methods have been investigated to determine the transient performance of the RTGs during this critical period. The first method employs a MHW-RTG with a water-cooled heat source, which does not deliver power at launch and hence must be supplemented with batteries to provide the necessary power until the RTGs are able to meet the power demands.

[1]Resalab Scientific Co., Menlo Park, Calif.

The second method employs MHW-RTGs which have been evacuated and back-filled with argon. (Xenon and krypton have been investigated subsequently, and both gases show a substantial improvement in power output over argon, as shown in Fig. 7). These units provide 50% of their design power at launch, and increase to full power in approximately 3 to 5 h. The first analysis discusses the water-cooled concept, assuming unobstructed radiation of waste heat to space. The second analysis discusses both the unsealed water-cooled concept and the sealed inert gas concept, taking into consideration the radiant interchange factors between the RTGs and their surroundings.

2. MHW-RTG With Water-Cooled Heat Source

The preliminary reference design of the MHW-RTG is shown in Fig. 1 with the principal components identified. It has the performance characteristics shown in Table 1. The water-cooled heat source concept of this design is shown in Fig. 2.

The thermal model used in this analysis consisted of eight nodes: the heat source, the ends of the RTG, the

RADIATOR

HEAT SOURCE

THERMOELEMENTS
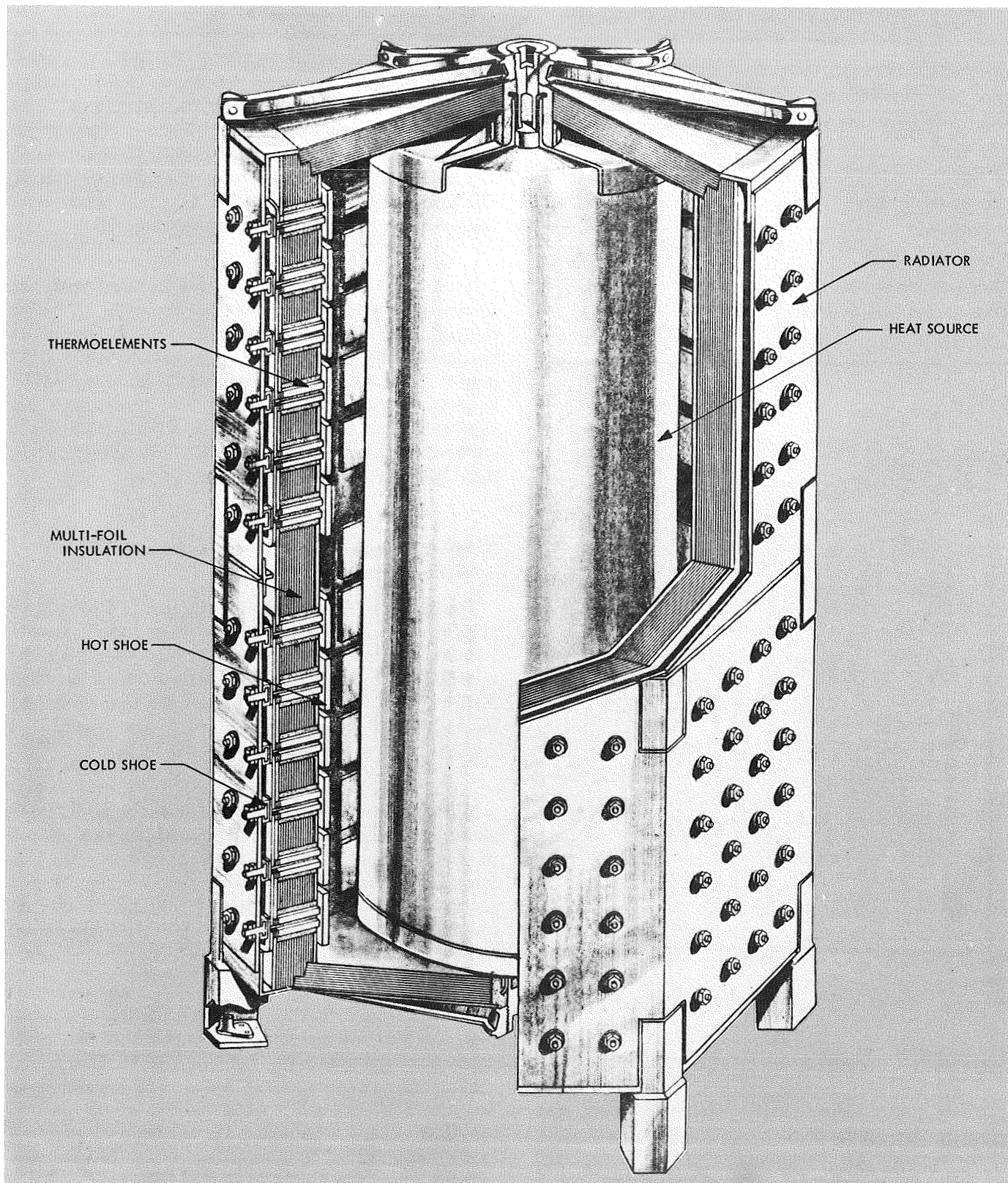
MULTI-FOIL
INSULATION

HOT SHOE

COLD SHOE

Fig. 1. Unsealed panel MHW-RTG design concept

Table 1. MHW-RTG preliminary reference design performance characteristics

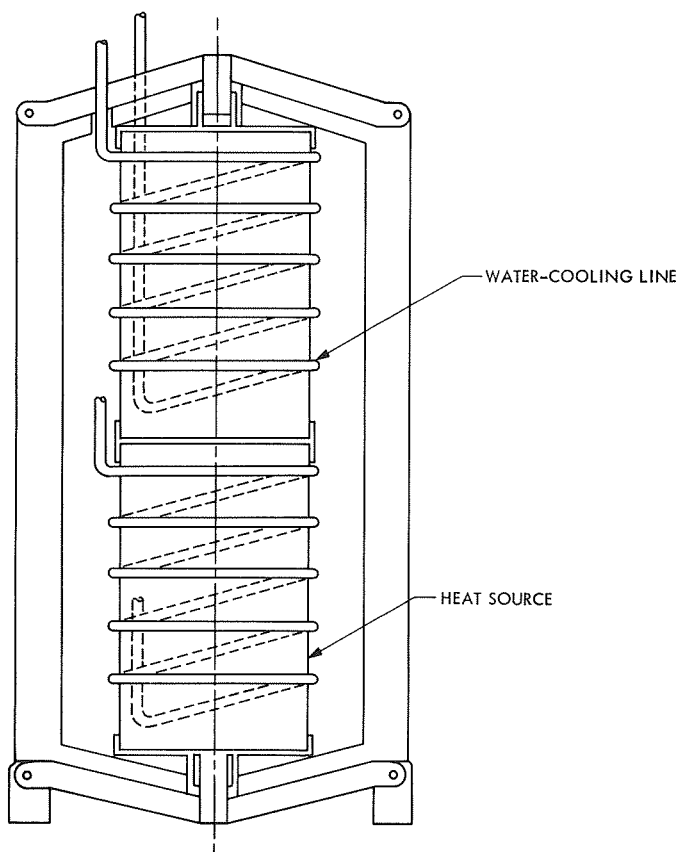| Measurement	Beginning of mission	End of mission
Power, W	148	114
Weight, lb	58.3	58.3
Specific power, W/lb	2.54	1.96
Voltage, Vdc	30	30
Fuel loading, W (th)	2000	1800
Hot-junction temperature, °F	2012	1885
Cold-junction temperature, °F	635	570
Efficiency, %	7.4	6.3

Fig. 2. MHW-RTG water-cooled heat source concept

hot /shoes, two regions in the thermoelements, two regions in the insulation between the thermoelements, and the radiator. The analysis assumes a fully deployed RTG with an unobstructed view of space, but with a 100°F sink temperature to account for incident solar radiation and reradiation from the spacecraft.

The results of the analysis are shown in Fig. 3. The heat source was assumed to be 300°F at launch, and the remainder of the RTG to be 100°F. The RTG was open-circuited until the generated voltage reached the design load voltage of 30 V. At that time, the circuit was closed and the RTG began to deliver power. This occurs about 45 min after launch. The RTG reaches 50% power 85 min after launch and 90% power 170 min after launch. The voltage curve shown is the available open-circuit voltage based upon the above assumptions.

If the RTG power profile is superimposed upon the mission load profile, the result is as shown in Fig. 4 for the period immediately after launch. If the area under the load profile is integrated from launch to the RTG power curve, the energy required to be supplied by batteries is about 260 W-h. The load profile does not show the 10- to 15-W power spikes. These spikes are of millisecond duration and represent little energy. Thus, their effect on battery sizing is negligible.

3. Effect of Radiant Interchange Factors on RTG Transient Performance

The effect on RTG transient performance of the launch position of the RTGs relative to the shroud and Burner II injection motor (Fig. 5) was determined for both the unsealed water-cooled RTG and the sealed inert-gas-filled RTG (Fig. 6). The view factors of the spacecraft and thermal shield are small compared to the shroud and Burner II and are therefore neglected.

The vacuum performance of the sealed multi-foil generator was assumed to be the same as that of the unsealed water-cooled generator in a vacuum. The performance of the sealed RTG was then determined as a function of the thermal conductivity of the gas used to back-fill the RTG. The results of this analysis are shown in Fig. 7.

It was assumed that a 2000-W heat source was used, that the load voltage was 30 V, and that the cold-junction temperature was held at 635°F. The actual cold-junction temperature at launch will depend upon how the RTG is cooled while on the launch pad. If forced-air cooling is provided, the temperature could be lower than 635°F. If natural convection is used, the cold-junction temperature could approach 1000°F, depending upon the emissivity of the various surfaces that the RTG "sees" in the launch configuration.
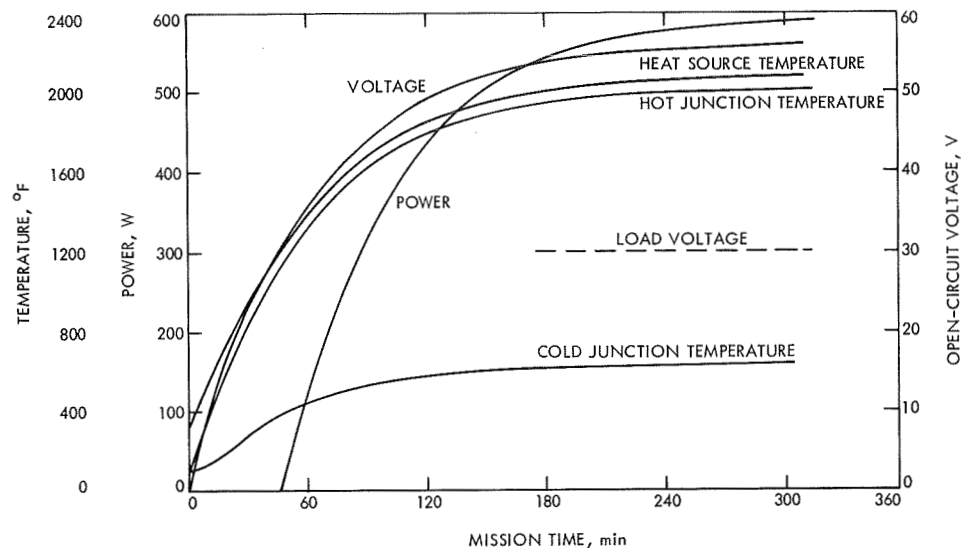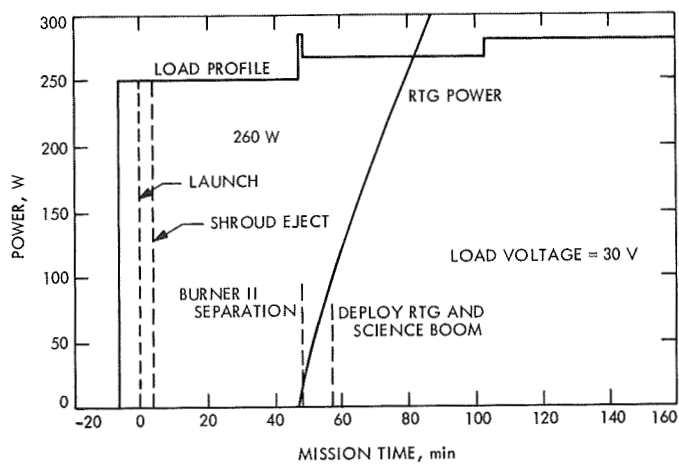
Fig. 3. MHW-RTG heatup transient

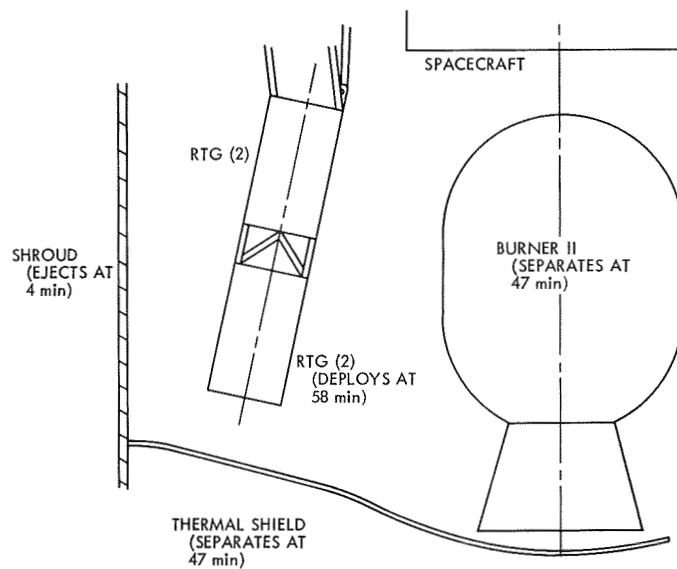**Fig. 4. Power transient of MHW-RTG with water-cooled heat source**
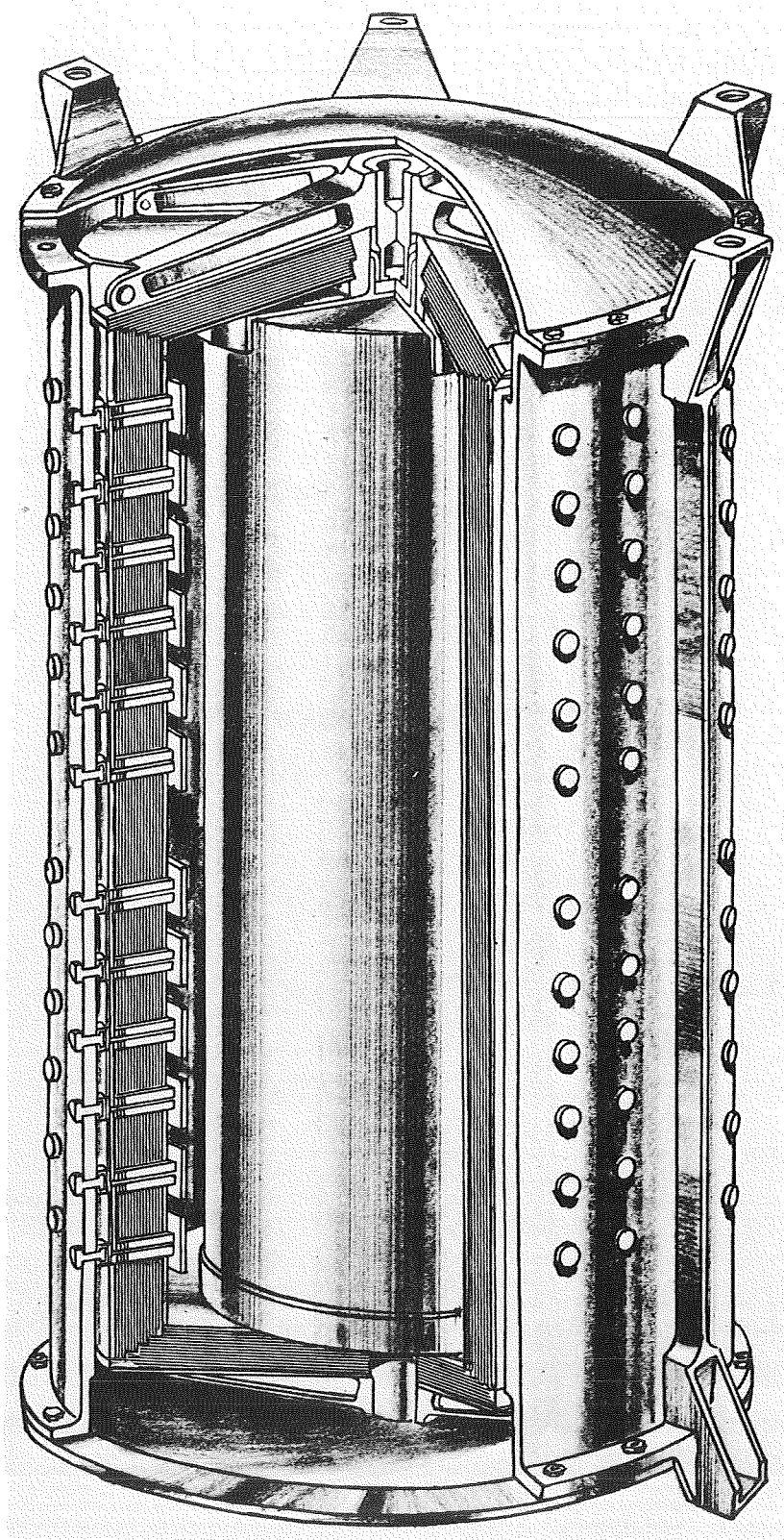

Fig. 5. RTGs in launch configuration

Fig. 6. Sealed-cylinder MHW-RTG design concept

Using argon at a pressure of 1 to 2 atm in the sealed RTG results in a hot-junction temperature of about 1700°F and a power output of about 50% of the vacuum value, i.e., 74-W for each of the four RTGs.

Figure 8 shows the effect of the shroud and burner II on the transient performance for both RTG concepts. The transient period is divided into three regions as shown in Table 2. During the first 4 min the shroud shields the RTG and results in a low view factor to space for the RTG radiator. At launch $(T) + 4$ min the shroud is ejected, and the view factor increases to nearly its final value. At $T + 47$ min separation from the Burner II occurs and from that point on, the view factor remains essentially constant.

Table 2. Transient sink conditions

Time, min	RTG view factor	Ambient conditions	
		Sealed	Unsealed
0–4	0.171	Argon	Air
4–47	0.626	Vacuum	Vacuum
47→	0.721	Vacuum	Vacuum

The view factors shown in Table 2 include the emissivities of the various surfaces involved as well as the geometry of the system. The determination of these view factors (or radiant interchange factors) is reported in *Section B*. The results of the unsealed RTG are virtually the same as in Fig. 3. This indicates that the external environment has little effect during the first 4 min on the water-cooled RTG.

However, for the sealed unit, the low view factor during the first 4 min results in the increasing of the cold-junction temperature from 635 to 705°F. After the shroud is ejected, the cold-junction temperature drops below its initial value and then begins climbing again until separation from Burner II occurs. The cold-junction temperature again drops slightly before leveling out at the 635°F design value. The hot-junction temperature climbs slowly from an initial value of 1693°F to the design value of 2012°F.

The power output for the two cases is shown in Fig. 9, superimposed onto the early mission load profile. Again

Fig. 7. Effect of gas conductivity on sealed MHW-RTG performance
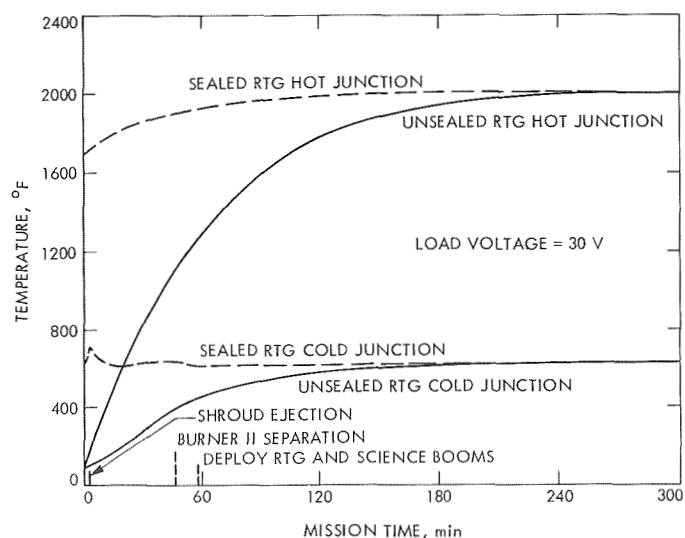
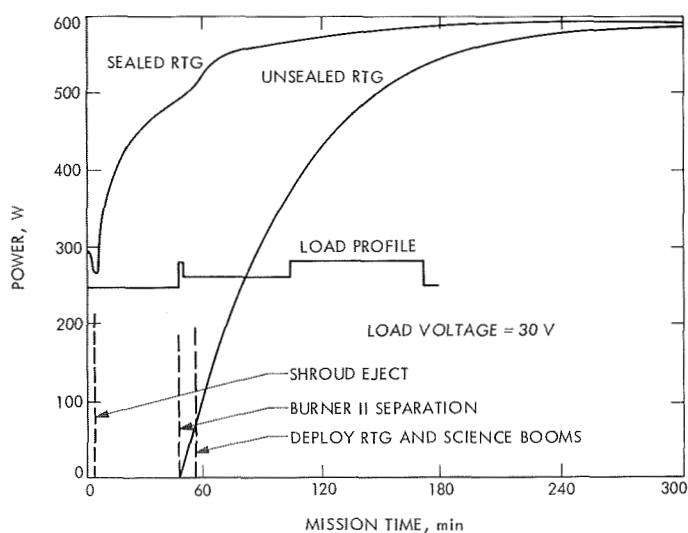Fig. 8. MHW-RTG temperature transient

Fig. 9. MHW-RTG power transient

the results of the unsealed RTG are identical to those presented previously. However, the sealed RTG exhibits the effects of the varying cold-junction temperature in a pronounced manner. The power drops from the initial value of 50% to about 45% and then climbs to 100% in 3 to 5 h. Both the effect of the shroud ejection and the Burner II separation are evident. For the sealed system it was assumed that the argon gas atmosphere was vented at the time of shroud ejection.

4. Conclusions

The sealed inert-gas-filled generator, even at its lowest point of power output, will provide the full power required, although the margin at this point is small. The unsealed water-cooled generator, however, does not provide the power required until approximately 80 min after launch. Furthermore, it must be supplemented by batteries capable of supplying 260 W-h of power until the RTGs can assume the full load. Both units attain 100% of design power within 5 h after launch.

B. Multi-Hundred Watt Radioisotope Thermoelectric Generator Radiant Interchange Factors, R. S. Caputo[2]

1. Introduction

As part of the task to determine the initial power transient of the radioisotope thermoelectric generator (RTG) after launch, the thermal environment of the RTG is evaluated. The analysis starts with the pad operation and continues through RTG deployment in orbit. The pad-cooling requirements are evaluated elsewhere.[3] This article concentrates on the radiant interchange factors between the RTG and the surrounding bodies during the sequence between pad operation and deployment. The overall radiant interchange factor $\mathcal{F}$ is found and transformed into a form for use as input into the transient RTG model.[4]

2. Discussion and Evaluation

The geometry–time sequence is shown in Fig. 10 where the bodies seen by the RTG are identified. At launch,

[2]Contract Employee, General Electric Missile and Space Div., King of Prussia, Pa.

[3]Caputo, R., *Pad-Cooling Requirements of the MHW-RTG for the TOPS Spacecraft*, April, 1970 (JPL internal document).

[4]Leonard, D., *MHW-RTG Transient Thermal Behavior*, March 16, 1970 (JPL internal document).
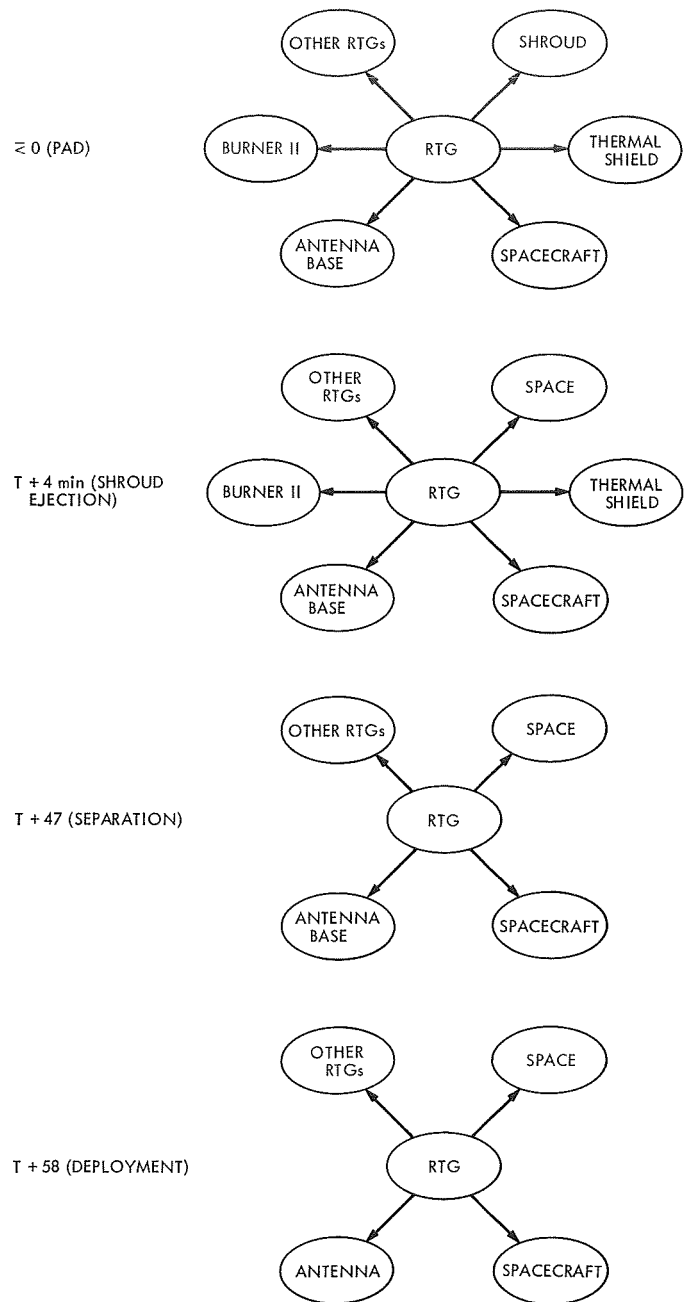
Fig. 10. Geometry–time sequence

forced-air circulation is discontinued and natural circulation begins. Even this mode of heat transfer will be negligible at approximately 4 min after launch, when the shroud is ejected.

During the first 4 min, most of the radiant interchange between the RTG and its surroundings will be to the shroud and thermal shield. The outside surface of

the shroud is heated to nearly $400°F$[5] during this time. The temperature of the inside face depends on the thermal impedance of the shroud wall. The inside wall temperature could vary from nearly $400°F$ to less than $100°F$.

a. Radiant interchange evaluation. At times greater than 4 min after launch, radiation is the only heat-transfer mechanism. To determine the thermal interaction of the RTG with its surroundings, the $\mathcal{F}$ of the RTG is evaluated. This factor is the radiant interchange factor from RTG to the bodies around it, which accounts for optical properties and relative positioning of the bodies.

The calculation of $\mathcal{F}$ can be handled in several ways. The most straight-forward is to separate the two aspects of $\mathcal{F}$ in the following manner:

$$\mathcal{F} = F_\epsilon F_{A_{ij}} \qquad (1)$$

where

F_ϵ emissive interchange factor (accounts for optical properties of bodies)

$F_{A_{ij}}$ geometric view factor from body i to j

A summary of the application of this approximate approach to some typical cases is shown in Table 3.

---

[5]Williams, A. N., Spacecraft Handling, March 3, 1969 (JPL internal report).

Table 3. $\mathcal{F}$ Components for typical applications

Application	$F_{A_{ij}}$	F_ϵ
Infinite parallel plates	1	$\dfrac{1}{\dfrac{1}{\epsilon_i} + \dfrac{1}{\epsilon_j} - 1}$
Close large plates	$0 < F_{A_{ij}} < 1$	$\dfrac{1}{\dfrac{1}{\epsilon_i} + \dfrac{1}{\epsilon_j} - 1}$
Small body i enclosed in large body j	1	ϵ_i
Small surface i far removed from large body j	$0 < F_{A_{ij}} < 1$	$\epsilon_i \epsilon_j$
Small body i enclosed in body j comparable size	1	$\dfrac{1}{\dfrac{1}{\epsilon_i} + \dfrac{1}{\epsilon_j} - 1}$

A more precise evaluation of $\mathcal{F}$ can be made by using Hottel's method (Ref. 1). Briefly reviewing this approach,

$$\mathcal{F}_{ij} = \frac{\alpha_j \epsilon_i A_j}{\rho_j A_i} \times \frac{{}_iD'_j}{D} \qquad (2)$$

where

α = absorptivity

ϵ = emissivity

ρ = reflectivity

A = surface area

i,j = surface identification

$$D = \begin{vmatrix} F_{11}A_1 - (A_1/\rho_1) & F_{21}A_2 \cdots & F_{n1}A_n \\ F_{12}A_1 & F_{22}A_2 - (A_2/\rho_2) & F_{n2}A_n \\ \cdot & \cdot & \cdot \\ \cdot & \cdot & \cdot \\ \cdot & \cdot & \cdot \\ F_{1n}A_1 & F_{2n}A_2 & F_{mn}A_n - \dfrac{A_n}{\rho_n} \end{vmatrix}$$

and, for example,

$${}_1D'_3 = \begin{vmatrix} F_{11}A_1 - (A_1/\rho_1) & F_{21}A_2 & F_{11}A_1 \\ F_{12}A_1 & F_{22}A_2 - (A_2/\rho_2) & F_{12}A_1 \\ F_{13}A_1 & F_{23}A_2 & F_{13}A_1 \end{vmatrix}$$

Hottel's method will more properly evaluate a radiation problem with reradiation about a cavity where several bodies interact. With either approach, the factor $\mathcal{F}_{ij}$ only identifies the relationship between the i and j body.

The net heat load which leaves body i is

$$(Q_i)_{net} = \sum_{j=1}^n \mathcal{F}_{ij} A_i \sigma (T_i^4 - T_j^4) \qquad (3)$$

If it is possible to define a constant sink temperature T_s, the total radiant interchange factor between body i and the sink s can be defined as

$$\mathcal{F}_{is} = \frac{\displaystyle\sum_{j=1}^n \mathcal{F}_{ij} \sigma (T_i^4 - T_j^4)}{\sigma (T_i^4 - T_s^4)} \qquad (4)$$

The net heat leaving body i is therefore

$$(Q_i)_{net} = \mathcal{F}_{is} A_i \sigma (T_i^4 - T_s^4) \tag{5}$$

b. Geometric view factor evaluation. For either the approximate or Hottel's method, the geometric view factor F_A must be evaluated. There are several ways to calculate F_A. Some of these are: a form factometer with a three-dimensional model, the CONFAC II computer code, view factor geometry tables and graphs, or a two-dimensional transparency view factor aid. The last method is used for the present purposes, but a form factometer could be used if greater precision is required.

The two-dimensional transparency calculates the geometric view factor from a differential area to a body in the x-y plane and considers it to be infinitely long in the z direction. By using it in two orthogonal planes, the results can be manipulated to give a good approximation of the three-dimensional view factor.

The four RTGs and six faces of each RTG are identified in Fig. 11. A basic symmetry exists so that only the view factors for RTG 1 and 3 will be calculated. The similar face on RTG 2 and 4 will have the same view. The RTG faces with the same view factors are listed in Table 4.

Table 4. RTG faces with equal view factors

(RTG, Face)	(RTG, Face)
(1,1)	(2,1)
(1,2)	(2,6)
(1,3)	(2,5)
(1,4)	(2,4)
(1,5)	(2,3)
(1,6)	(2,2)
(3,1)	(4,1)
(3,2)	(4,6)
(3,3)	(4,5)
(3,4)	(4,4)
(3,5)	(4,3)
(3,6)	(4,2)

RTG-to-RTG view factor. The F_A from one RTG to another is calculated based on design configuration 3[6] at

[6]Gram, M. B., *TOPS RTG Configuration*, Feb. 16, 1970 (JPL internal document).

(a) RTG NUMBER (b) FACE NUMBER
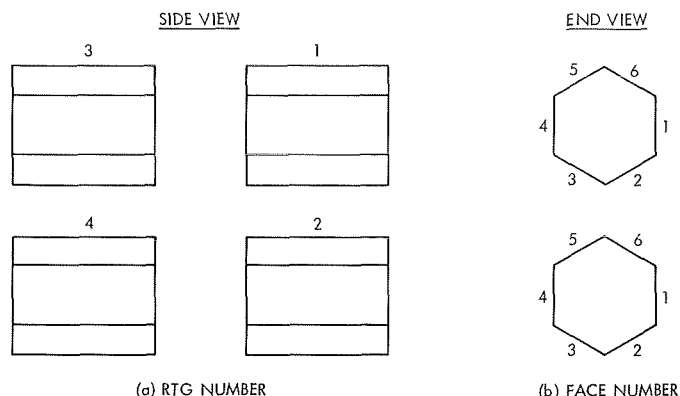
Fig. 11. Numbering systems for RTGs and RTG faces

a minimum separation of 16 in. The RTG view factors are shown in Table 5.

Due to symmetry the following view factors are equal for the RTG-to-RTG viewing:

$$(1,2) \rightarrow (2,6) = (1,3) \rightarrow (2,5)$$
$$(1,2) \rightarrow (2,5) = (1,3) \rightarrow (2,6)$$
$$(1,2) \rightarrow (4,6) = (1,3) \rightarrow (4,5)$$
$$(1,2) \rightarrow (4,6) = (3,2) \rightarrow (2,6)$$
$$(1,2) \rightarrow (4,6) = (3,3) \rightarrow (2,5)$$
$$(1,2) \rightarrow (4,5) = (1,3) \rightarrow (4,6)$$
$$(1,2) \rightarrow (4,5) = (3,2) \rightarrow (2,5)$$
$$(1,2) \rightarrow (4,5) = (3,3) \rightarrow (2,6)$$

The total view factor from face 2 or 3 of RTG 1 to the other RTGs is

$$F_{(1,2)} = F_{(1,3)} = \sum_i F_{(1,2)} \rightarrow i$$

Table 5. RTG-to-RTG view factors

View from (RTG, Face)	View from (RTG, Face)	F_A
(1,2)	(2,6)	0.050
(1,2)	(2,5)	0.039
(1,2)	(4,6)	0.015
(1,2)	(4,5)	0.012
(3,2)	(4,6)	0.038
(3,2)	(4,5)	0.034

where

$$i = (2,6), (2,5), (4,6) \text{ and } (4,5)$$

$$F_{(1,2)} = 0.116 = F_{(1,3)}$$

Also the view factor from face 2 or 3 of RTG 3 to the other RTGs is

$$F_{(3,2)} = F_{(3,3)} = \sum_i F_{(3,2)} \to i$$

where

$$i = (4,6), (4,5), (2,6) \text{ and } (2,5)$$

$$F_{(3,2)} = 0.099 = F_{(3,3)}$$

The other four sides of each RTG do not have a direct view to the other RTGs. Averaged over the entire RTG, the view factor from the inboard RTG to the other RTGs is about 0.04 and from the outboard RTG is about 0.035. The average F_A from RTG to RTG is considered to be 0.04.

RTG-to-shroud view factor. While in the stowed position and prior to shroud ejection, the RTG has a good view factor to the shroud. A summary of the F_A from each RTG face is shown in Table 6.

Table 6. RTG-to-shroud view factors

View from (RTG, Face)	F_A
(1,3), (2,5)	0.85
(1,4), (2,4)	0.98
(1,5), (2,3)	0.98
(1,6), (2,2)	0.52
(1,1), (2,1)	0.18
(1,2), (2,6)	0.21
(3,3), (4,5)	0.84
(3,4), (4,4)	0.97
(3,5), (4,3)	0.97
(3,6), (4,2)	0.49
(3,1), (4,1)	0.17
(3,2), (4,4)	0.16

The average view factor from the inboard RTG and outboard RTG to the shroud is 0.62 and 0.60, respectively.

The overall average F_A from the RTGs to the shroud is 0.61.

RTG-to-thermal-shield view factor. Prior to shroud ejection, the RTG can see the thermal shield at the Burner II to *Centaur* interface. Table 7 indicates the results for the view factors from the RTG to the thermal shield.

Table 7. RTG-to-thermal-shield view factors

View from (RTG, Face)	F_A
(1,1), (1,6), (1,2)	0.20
(1,3), (1,4), (1,5)	0.02
(3,1), (3,6), (3,2)	0.255
(3,3), (3,4), (3,5)	0.155

The average F_A from the inboard RTGs to the thermal shield is about 0.11, while the outboard RTGs have a 0.21 view factor to the shield. The overall F_A from the RTGs to thermal shield is considered to be 0.16.

RTG-to-Burner II view factor. Prior to separation, the RTGs are adjacent to the Burner II rocket. Table 8 contains the direct geometric view factors between the RTG faces and the Burner II surface.

Table 8. RTG-to-Burner II view factors

View from (RTG, Face)	F_A
(1,1)	0.56
(1,2)	0.39
(1,3)	0.026
(1,6)	0.11
(3,1)	0.37
(3,2)	0.28
(3,3)	0.018
(3,6)	0.08

The average view factor from the inboard RTG to Burner II is 0.18, while the outboard RTG has a 0.12 view factor. The overall F_A to Burner II is 0.15.

When the shroud and thermal shield are ejected, the outboard RTGs have a view to the Burner II nozzle. The

average F_A from these RTGs to the nozzle is 0.015, and from all four RTGs is considered to be 0.008.

RTG to spacecraft view factors. The base of the antenna is considered separately from the major equipment bays of the spacecraft. The direct view factors to the spacecraft in the stowed position are given in Table 9.

Table 9. RTG-to-spacecraft view factors

View from (RTG, Face)	F_A
(1,1), (1,2)	0.075
(1,3), (1,6)	0.008
(3,1), (3,2)	0.0225
(3,3), (3,6)	0.001

The average inboard F_A to the spacecraft is 0.027 and 0.008 for the outboard. The overall F_A to the spacecraft is considered to be 0.02.

In evaluating the RTG view factor to the antenna base in the stowed position (both RTG and antenna stowed), the average F_A for the inboard RTG is 0.022 and 0.019 for the outboard. The overall average is considered to be 0.02.

At RTG deployment at 58 min (antenna deployed shortly before this), the F_A to the spacecraft is reduced and an F_A exists to the antenna. The F_A to the spacecraft is shown in Table 10.

Table 10. RTG to spacecraft view factors after RTG deployment

View from (RTG, Face)	F_A
(1,1)	0.005
(1,4)	0.0025
(1,2), (1,3), (1,5), (1,6)	~0.0003
(3,1)	0.0031
(3,4)	0.0015
(3,2), (3,3), (3,5), (3,6)	~0.00015

The average view factor from the inboard RTGs is about 0.009, while it is 0.005 from the outboard RTGs. The overall average is considered to be 0.007.

RTG-to-space view factors. After shroud ejection at 4 min, the view factor from the RTGs to the shroud and thermal shield become view factors to space (average F_A to space is 0.76). The only exception is the small F_A to the nozzle of the Burner II rocket. After separation at 47 min, the view to the Burner II and nozzle become space views. At this point, the average F_A to space is 0.92. When the RTG is deployed at 58 min the view to space decreases to 0.89, which is only slightly below the value for the previous time period. This is evaluated by calculating the F_A to the other objects. The remainder, obtained by subtracting the view factor to all other bodies from unity, is considered to be the space view factor. For the deployed condition the average F_A to space for the inboard RTGs is 0.862, while it is 0.917 for the outboard RTGs.

RTG-to-antenna view factors (both deployed). The antenna is deployed 5 min before the RTG. The view factor between them is modest at this point and exists only for this short time period. The antenna deployment is therefore considered not to affect the view factors of the RTGs to its surroundings from 55 to 58 min after launch. At 58 min both the RTG and antenna are deployed. The view factors to the antenna envelope are shown in Table 11.

Table 11. RTG-to-antenna view factors (both deployed)

View from (RTG, Face)	View factor		
	Antenna envelope	30-deg cone angle	Antenna (net)
(1,4)	0.296	0.048	0.248
(1,3), (1,5)	0.148	0.012	0.136
(3,4)	0.14	0.014	0.126
(3,3), (3,5)	0.07	0.004	0.066

The antenna is a wire mesh with an estimated 15% blockage normal to the surface.[7] As the antenna is viewed at an angle to the normal, the blockage is increased in an unknown manner. For the purpose of a preliminary evaluation, it is assumed that the antenna is transparent within a cone angle of 30 deg to the surface normal, and completely opaque outside of this 30-deg angle. The estimated view factors to the 30-deg angle zone are given in Table 11. The net view factor to the antenna is the difference between these two F_A's and is also noted in

---

[7]Personal conversation with J. Starkey on March 30, 1970.

Table 11. The average inboard RTG view factor to the antenna is 0.087, while the outboard is 0.043. The overall average is 0.065.

These view factor estimates are summarized in Table 12 for the four identified time periods. This table contains the geometric relationships F_A between the RTGs and the surrounding bodies.

c. $\mathscr{F}$ calculation

$\mathscr{F}$ *for TOPS spacecraft.* In order to calculate the $\mathscr{F}$ for the RTG during these time periods, the emissive interchange factor F_ϵ must be evaluated. The surface properties of the various bodies should be known to determine F_ϵ. In order to properly evaluate the radiant heat transfer between the RTGs and the surrounding bodies, the temperature of these bodies should be known during the time period being evaluated. Neither the surface properties (Footnote 3) nor the temperatures of these bodies are known. To expedite the calculation, the following two

Table 12. View factors from RTG to surrounding bodies

Time, min	"Seen" body	View factor		
		Inboard RTG	Outboard RTG	Average
0→4	Shroud	0.62	0.60	0.61
	Thermal shield	0.11	0.21	0.16
	Burner II	0.18	0.12	0.15
	Other RTG	0.04	0.035	0.04
	Spacecraft	0.027	0.008	0.02
	Antenna base	0.022	0.019	0.02
4→47	Space	0.73	0.795	0.76
	Burner II	0.18	0.12	0.15
	Nozzle	—	0.015	0.008
	Other RTG	0.04	0.035	0.04
	Spacecraft	0.027	0.008	0.02
	Antenna base	0.022	0.019	0.02
47→58	Space	0.91	0.93	0.92
	Other RTG	0.04	0.035	0.04
	Spacecraft	0.027	0.008	0.02
	Antenna base	0.022	0.019	0.02
>58	Space	0.862	0.917	0.89
	Antenna	0.087	0.043	0.065
	Other RTG	0.04	0.035	0.04
	Spacecraft	0.009	0.005	0.007

assumptions are made for all the surrounding bodies that the RTG views:

(1) Surface emissivity ϵ_S equals 0.2.

(2) Surface temperature equals sink temperature.

Therefore, Eq. (4) becomes

$$\mathscr{F}_{is} = \sum_{j=1}^{n} \mathscr{F}_{ij} \qquad (6)$$

To evaluate $\mathscr{F}$, the approximate method is that expressed in Eq. (1). Reference is made to the examples in Table 3, and the F_ϵ used for this problem between the RTG and surrounding bodies is

$$\cfrac{1}{\cfrac{1}{\epsilon_{\text{RTG}}} + \cfrac{1}{\epsilon_S} - 1}$$

This approach is quite good for time greater than 4 min, where the significant view factor is to space. This is a poor approach for less than 4 min while the shroud is on and a significant amount of cavity reradiation exists. It is used for preliminary purposes and is considered acceptable due to the short duration of the condition.

The F_ϵ for the view to space is simply equal to ϵ_{RTG}. The results for the F_ϵ calculation is shown in Table 13.

Table 13. RTG emissive interchange factors

View	F_ϵ
Surrounding bodies	0.193
Space	0.85

Using this, as well as Eqs. (1) and (6) and the summary of the view factor results from Table 12, the average $\mathscr{F}$ from all four RTGs to sink is shown in Table 14. The inboard, outboard, and average $\mathscr{F}$ are noted. Since the basic geometric view factor data is given in Tables 4 through 11 for the various RTG panel faces, it is possible to calculate a $\mathscr{F}$ for each RTG panel during each time period.

Table 14. RTG $\mathscr{F}$ for TOPS spacecraft

Time, min	$\mathscr{F}$		
	Inboard	Outboard	Average
0→4	0.187	0.188	0.185
4→47	0.665	0.708	0.684
47→58	0.787	0.797	0.79
>58	0.751	0.790	0.77

$\mathscr{F}$ *adjustment for computer input.* The data in Table 14 is an estimate of the actual $\mathscr{F}$ that the RTG configuration 3 (Footnote 6) has to its surroundings. The reference design (Ref. 2) has a cold junction temperature of 635°F during space operation to a 100°F sink. The side panels of the RTG are assumed to see the sink with a view factor of unity. Therefore the $\mathscr{F}$ for the reference design is equal to the surface emissivity of 0.85.

The RTG used for the TOPS mission will most probably be adjusted in some way so that it achieves the same temperatures as the reference design. Since the $\mathscr{F}$ for the TOPS spacecraft is less than· the reference design $\mathscr{F}$ (0.77 compared to 0.85), the MHW-RTG used with TOPS will have to be de-tuned to some extent. This can be done by isotope fuel dilution or increased thermopile leg area. Fins could also be placed on the RTG to reduce temperatures.

Regardless of how the RTG used with TOPS is modified to meet reference design temperatures, the effect will be for the $\mathscr{F}$ to equal 0.85 to a 100°F sink so that the same equilibrium temperatures are achieved in vacuum. The data in Table 14 is adjusted to meet this condition. The results are shown in Table 15.

The RTG radiant interchange data is used for a computer evaluation of the RTG power transient after launch

Table 15. RTG $\mathscr{F}$ adjusted for reference design on TOPS spacecraft

Time, min	$\mathscr{F}$		
	Inboard	Outboard	Average
0→4	0.204	0.206	0.204
4→47	0.734	0.78	0.755
47→58	0.87	0.88	0.872
>58	0.83	0.872	0.85

(Footnote 4). For use with the computer code, a further adjustment must be made. The computer evaluation is based on the reference design in the following respects:

(1) 605°F fin-base temperature.

(2) 5.92-in. panel width.

(3) 8.26-in. panel length.

(4) 12 panels.

(5) 2000-W capsule fuel load.

(6) 100-W end losses.

(7) 148-W power production.

(8) 100°F sink temperature.

(9) 0.85 panel surface emissivity.

The $\mathscr{F}$ data must be modified so that the reference fin-base temperature will be achieved in equilibrium with a 100°F sink for the above conditions of size and heat load. The equation which governs the ability of the RTG to reject heat is

$$Q = f\mathscr{F}A\Delta\sigma T^4$$

where

Q = heat radiated by RTG panels, W

f = reference design correction factor

$\mathscr{F}$ = radiant interchange factor

A = panel radiating area, ft²

$\Delta\sigma T^4$ = difference in emissive power between fin-base and sink temperature, W/ft²

For the reference design

$$\Delta\sigma T^4 = 596.3 \text{ W/ft}^2$$

$$A = 4.07 \text{ ft}^2$$

$$Q = 1752 \text{ W}$$

$$\mathscr{F} = \epsilon = 0.85$$

Therefore

$$f = \frac{Q}{\mathscr{F}A\Delta\sigma T^4} = 0.85$$

The factor f accounts for panel fin efficiency as well as any discrepancies in proper definitions of the reference

design such as area or temperature. The $\mathcal{F}$ data of Table 15 must be multiplied by f for proper computer input. This is shown in Table 16.

Table 16. RTG $\mathcal{F}$ adjusted for computer input

Time, min	$\mathcal{F}$		
	Inboard	Outboard	Average
$0 \rightarrow 4$	0.173	0.175	0.173
$4 \rightarrow 47$	0.625	0.662	0.642
$47 \rightarrow 58$	0.739	0.748	0.740
>58	0.705	0.740	0.722

d. Effect of body emissivity on RTG $\mathcal{F}$. In determining the $\mathcal{F}$ for the RTG, the emissivity of the bodies seen by the RTG is assumed to be 0.2 (*Paragraph c*). The sensitivity of $\mathcal{F}$ to this variable is shown in Fig. 12 for three time periods. The average $\mathcal{F}$ is shown based on the TOPS spacecraft application results of Table 14. Except for the initial 4 min, the $\mathcal{F}$ is rather insensitive to the viewed surface emissivity.

3. Conclusions

The radiant interchange factors from the RTG to thermal sink temperature are shown in Table 16 for use as inputs to the transient computer code model. The results in the time periods of 47 to 58 min and for greater than 58 min are fairly similar and may be considered together to simplify the transient evaluation. The greater-than-58-min values should be used.

The calculation does not consider reradiation effects very well during the first 4 min. The calculated $\mathcal{F}$ during this time is lower than it should be, but is acceptable due to the short time duration. To further simplify the transient calculation, the first 4 min may be ignored and the 4- to 47-min values used over the entire 0- to 47-min time period.

The surface emissivity of the bodies surrounding the RTGs is assumed so that $\mathcal{F}$ may be calculated. With the exception of the time before shroud ejection, ϵ_S has only a small effect on the overall $\mathcal{F}$ of the RTG to the thermal sink.

The geometric view factors are shown for each panel of the RTGs to the various surrounding bodies during the four time periods identified. It is possible to use this sink information to evaluate temperature distortions in
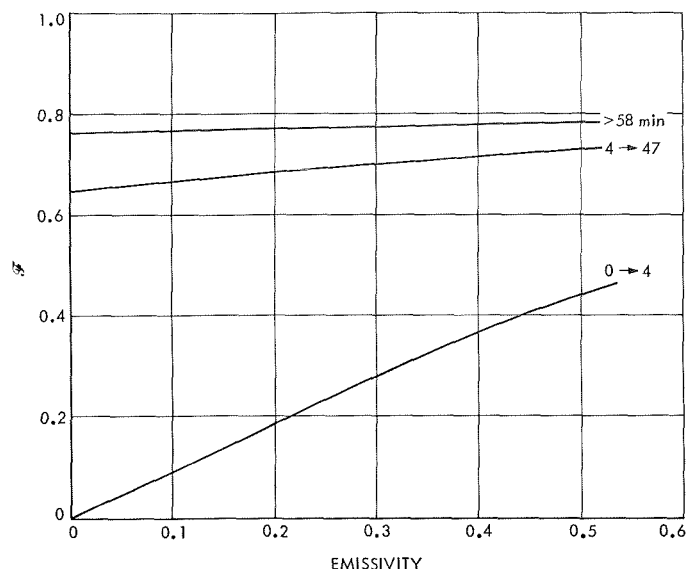

Fig. 12. RTG $\mathcal{F}$ versus emissivity of viewed bodies

the RTGs, as well as the local temperatures in bodies around the RTGs.

The blockage of the RTG's view to sink by the antenna and parallel RTGs causes higher temperatures in the RTGs than the reference design. An evaluation of the various methods of attaining design temperatures should be made, along with the effects of these methods on the RTG system performance.

References

1. Wiebelt, J. A., *Engineering Radiation Heat Transfer*, p. 115. Holt, Rinehart, and Winston, Inc., New York, 1966.

2. General Electric Corp., Space Division, King of Prussia, Pa., GESP-7034, *MHW-RTG Program Phase 1 Interim Report, Oct. 6, 1969 to Feb. 20, 1970*, March 1970.

C. Gamma Ray and Neutron Analysis for a 15-W(th) $Pu^{238}O_2$ Isotopic Heater, *M. A. Dore*

1. Introduction

An area of concern in utilizing radioisotope heat sources for thermal control on unmanned spacecraft is the extent of interference, if any, of gamma ray and neutron radiation from the heat source upon radiation-sensitive devices and materials aboard such a vehicle. Sensitive science instruments, especially radiation detectors, are of particular concern. Yet it is precisely these science instruments which will require accurate thermal

controlling. Also, a science package will most likely be located on a boom, well away from the main body of the spacecraft, making it difficult to utilize primary sources of heat. If the spacecraft derives its primary electrical power from radioisotope thermoelectric generators (RTGs), as will almost certainly be the case for outer planet missions, isotopic heaters will serve to further complicate the radiation distribution throughout the spacecraft.

A number of factors influence the effects this radiation will have upon spacecraft subsystems. Among these are the type of radiation (i.e., gamma or neutron), its spectral energy distribution, and either the dose rates or accumulated dose levels. Each of these is, in turn, dependent upon spacial position relative to the heater and/or RTGs, since the fluxes and spectra can vary tremendously with angle and distance.

The most significant complication is the considerable increase in flux and hardening of the gamma spectrum with elapsed time since fuel processing, if even trace quantities (just a few parts/10^6) of the fuel contaminant Pu^{236} are present, as is normally the case (SPS 37-59, Vol. III, pp. 112–115). Also, O^{18}, which has an abundance of 0.204% in natural oxygen, is responsible for well over two thirds of the neutrons emitted by oxide form fuel (e.g., PuO_2), due to $O^{18}(\alpha, n)^{21}Ne$ reactions. Much of the remaining neutron flux is due to (α, n) reactions with other light element impurities also present in only trace quantities. All of these impurities can, and do, vary significantly between differing batches of fuel.

Both this age dependence and the variations in impurity levels among fuel batches cause experimental determinations of radiation levels to have severely limited applicability. One alternative to experimental measurements is to utilize analytic methods, such as the code RAMPART used here. The Monte Carlo techniques employed by this code are among the most powerful, efficient, and accurate ways of mapping these radiation fields to the required detail (SPS 37-60, Vol. I, p. 34).

This final gamma ray and neutron radiation map may then be utilized to determine shielding requirements for specific detectors in given geometrical relationships to one (or more) such heaters and/or any RTGs which may be aboard. These results, together with further studies using highly purified biomedical grade fuel (0.3 parts/10^6 Pu^{236}), the solid cermet fuel form, and alternative heater designs may be of considerable significance

in determining whether use of such heaters will be acceptable aboard outer planet spacecraft.

2. Basic Assumptions

The basic design used for the heater is shown in Fig. 13 and is essentially identical to that specified for the *Apollo* lunar radioisotope heater (ALRH) as designed and fabricated by Mound Laboratories (Ref. 1). This design calls for a fuel loading of 15 W(th), utilizing $Pu^{238}O_2$ microspheres as the fuel form. An inner and outer fuel-liner of Ta–10 wt% W, surrounded by a Pt–10 wt% Rh oxidation barrier cladding comprise the primary fuel containment. This is then surrounded by a titanium fragmentation shield, a graphite heat shield, and a 304 stainless steel outer container. The entire assembly is mounted on a 6061 aluminum base plate. The only difference between the actual heater and that utilized for this computer analysis is the exclusion in the latter of the 12 rivets that fasten the assembly to the base plate. Since these rivets are themselves made of aluminum, their exclusion is of trivial consequence.

The gamma ray source spectra used were for nominal (81% Pu^{238} in Pu, 1.2 parts/10^6 Pu^{236}, natural abundance O^{18}) PuO_2 at five ages: 0, 1, 5, 10, and 18 yr after processing (SPS 37-56, Vol. III, pp. 128–133). This was done to allow comparison to the experimental results obtained by Mound for heaters with this nominal composition fuel. Applications of these or similar low wattage heaters to spacecraft, however, will probably require use of the already mentioned biomedical grade fuel, and studies involving specific mission designs should therefore consider each source component separately. Similarly, neutron sources consisted of (α, n) reactions with O^{18} and other light element impurities, and spontaneous fission neutrons. Induced fission neutrons were assumed to have the same spectral distribution as the spontaneous fission neutrons. This is a fairly accurate assumption for the type of spectra encountered from PuO_2 capsules, particularly since the induced fission is responsible for only a small fraction of the total emerging neutron flux.

Twelve detector points were used to make the maps, the first four of which are shown on Fig. 14. The other eight were arranged in four pairs, each pair consisting of a point 10 cm and a point 50 cm distant from the center or axis of the heater. These four pairs were located: (1) above the capsule on-axis, (2) on the radial midplane, (3) on a ray at 45 deg to the axis, and (4) on the base plane of the heater, all as indicated by the arrows included on Fig. 13. Since the heater has
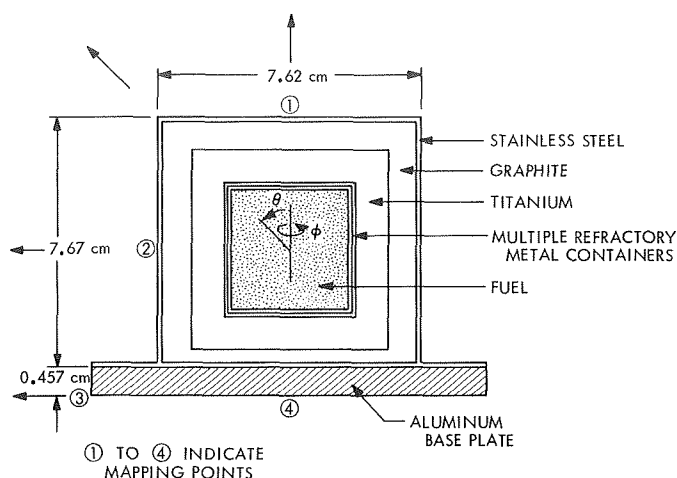
Fig. 13. 15 W(th) isotopic heater showing innermost mapping points

ϕ-symmetry, these points are sufficient to establish the radiation field for all space above the base plane. The radiation levels below the base plane will be highly dependent upon the thickness of the base plate and to whatever it may in turn be attached. Since these will vary with every design, and since Mound's results make no mention of this region, the single point on the bottom of the heater was considered sufficient for realizing the approximate magnitude of the shielding effects of the base plate for this preliminary study. The closed isodose curve shown in Fig. 14, which includes the lower hemisphere, is therefore an extrapolation based upon this one point and comparisons to the distribution above the heater; it is included only for completeness.

3. Results

A few typical results are included in the accompanying figures and tables. Figure 15 shows gamma dose rate as a function of fuel age and distance from the heater for points directly above the heater. Both dose rate and number flux are plotted for 0-yr-old neutron radiation in Fig. 16, again as a function of separation distance above the heater. An isodose plot for gamma radiation in the 5-yr-old case is included in Fig. 15. Table 17 is a tabulation of the corresponding isodose levels for neutrons from 0-yr-old fuel. In all cases, and for all detector points, complete 20-group spectra were generated as well.

For the given input assumptions, the code gives statistical errors to the gamma ray values of $\pm 10\%$, while the neutron values are within $\pm 5\%$. This is a little misleading, however, since the preferred-point technique used to produce these results (SPS 37-60, Vol. I) imparts
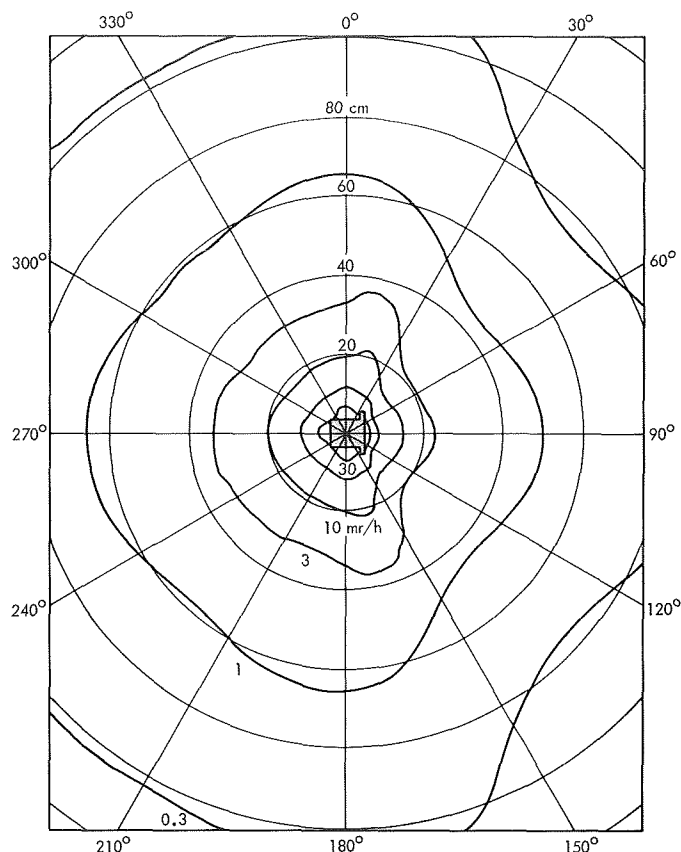

Fig. 14. Gamma ray isodose contours for 15 W(th) heater with 5-yr-old fuel

the same error to each point, i.e., all points are either high or low by the same percentage. Thus, even though the absolute values are only accurate to the above percentages, the shape of the curves is not distorted.

A comparison between these results and those published by Mound Laboratories is presented in Table 18. These are total dose rates, including both gamma rays

Table 17. Neutron isodose points for 15 W(th) Pu^{238}O$_2$ isotopic heater

Level of isodose contour, mrem/h	Distance from reference, cm			
	Upward along axis	45 deg	Radial midplane	Base plane
3.0	40.6	38.2	42.5	41.1
10.0	23.0	22.0	23.7	23.3
30.0	13.5	12.5	13.9	13.3
100.0	7.8	6.6	7.6	5.6
300.0	4.5	—	4.3	1.3

Fig. 15. Gamma ray dose rate for 15 W(th) heater

Fig. 16. Neutron dose rate and number flux for
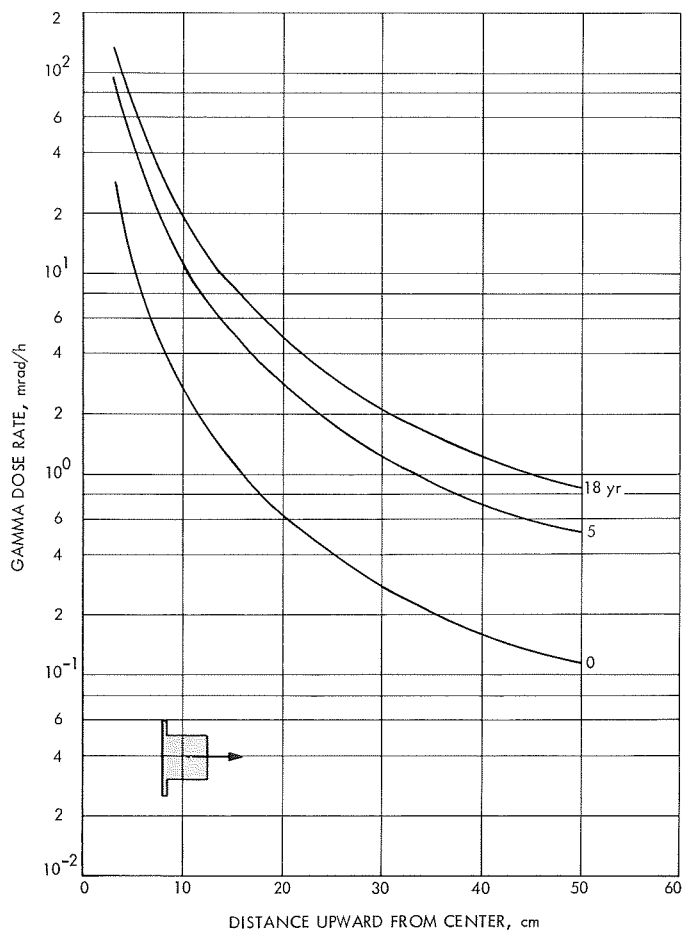15 W(th) heater

and neutrons. The values for neutron dose rates presented here include both the slight age dependence and an assumed 15% overall increase in neutron flux due to induced fission. The last three values given by Mound Laboratories were probably experimentally determined, the surface point having been extrapolated from these. These distant points seem to compare quite well with the results here if the fuel age used by Mound was 10 to 18 years, although this is unlikely. Fuel in the 2- to 5-yr-old range was most probably used to fill the actual
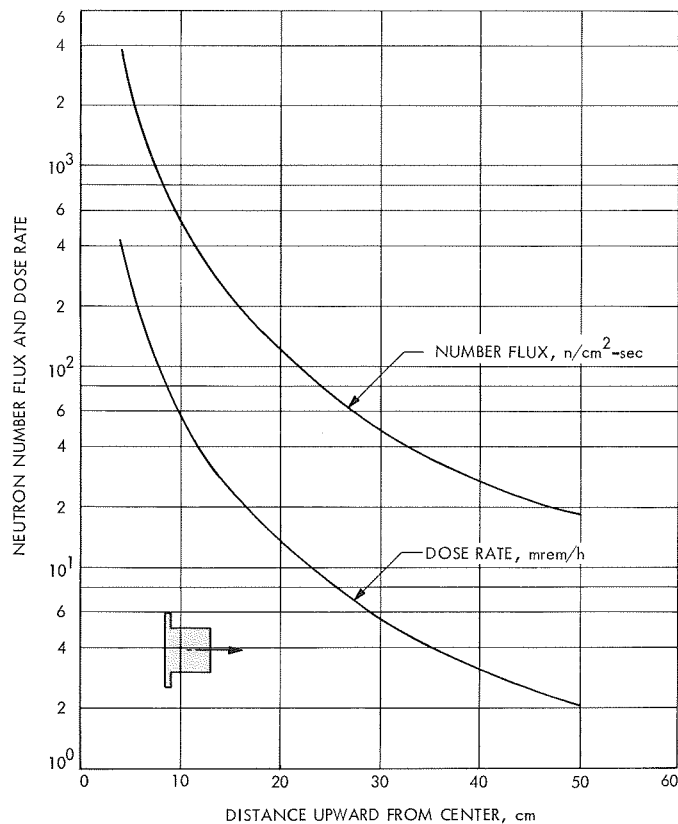
heaters. Note that if this were the case, the value for the surface point would be in close agreement for the two studies.

The probable situation, however, is that $1/r^2$ extrapolation to the center of the heater was used by Mound Laboratories, which would yield a value at the surface about 15% lower than actual, since the self-shielding of the fuel effectively shifts the center of the heater toward the detector point. This approach would bring this point, too, into agreement with the 10- to 18-yr levels predicted here. This, in turn, implies that the net source

Table 18. Comparison of results for 15 W(th) Pu^{238}O$_2$ isotopic heater

JPL	Dose rate, mrem/h			Mound Laboratory	
Location	0 yr	5 yr	18 yr	Location	Dose from total assembly, mrem/h
Surface (top)	452.2	517.5	557.3	Surface (max)	478 (extrapolated)
25 cm (Radial midplane)	9.43	10.95	12.43	25 cm	12
50 cm (Radial midplane)	2.36	2.74	3.11	50 cm	3
100 cm (Radial midplane, extrapolated)	0.589	0.684	0.777	100 cm	0.8

strengths (particularly for neutrons) used for the analytic work are 10 to 15% lower than what are actually required to duplicate the experimental results. There have also been other indications that this is the case (see *Section VIII-D* of this issue for gamma rays), and the problem is being considered intensely at present. It is this type of comparison between experimental and analytic results that allows the latter to operate as an effective and accurate tool in modeling the behavior of these radiation sources.

Reference

1. Kelly, D. P., and V. L. Avona, *Apollo Lunar Radioisotopic Heater Summary Report*, MLM-1637, Monsanto Research Corp., Mound Laboratory, April 30, 1969.
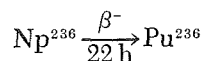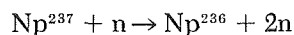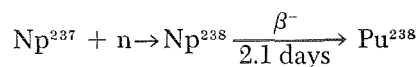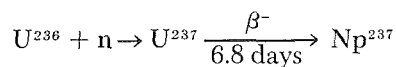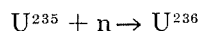
D. Absolute Gamma Ray Intensity Measurements of a SNAP-15A Heat Source, M. Reier

1. Introduction

A major activity in the development of nuclear power sources is the precise measurement of the neutron and gamma radiation emitted by radioisotope thermoelectric generators (RTGs). This information is necessary for a determination of the increased background in the line-of-sight of scientific detectors in the vicinity of an RTG. In addition to these transient effects, long-term exposure of instrumentation may result in damage and ultimate degradation of performance.

The neutrons come from the spontaneous fission of the Pu^{238} and the α-n reaction with light elements, and also O^{17} and O^{18} if the fuel is in the form of an oxide. The gamma rays come mainly from the decay of the Pu^{238} and the daughter products of Pu^{236}, an impurity of about 1 part/10^6 in the fuel.

Pu^{238} and Pu^{236} are made in reactors by the following reactions:

$$U^{235} + n \rightarrow U^{236}$$

$$U^{236} + n \rightarrow U^{237} \xrightarrow[6.8\,\text{days}]{\beta^-} Np^{237}$$

$$Np^{237} + n \rightarrow Np^{238} \xrightarrow[2.1\,\text{days}]{\beta^-} Pu^{238}$$

$$Np^{237} + n \rightarrow Np^{236} + 2n$$

$$Np^{236} \xrightarrow[22\,\text{h}]{\beta^-} Pu^{236}$$

Thermal and weapon production reactors make a lower ratio of Pu^{236}/Pu^{238} than fast reactors. Since the half-life of Pu^{236} is 2.85 yr and that of Pu^{238} is 87.4 yr, further reduction in the Pu^{236} content may be effected by waiting a few years for some of the Pu^{236} to decay to U^{232}. The uranium can then be chemically separated from the rest of the fuel.

The gamma radiation of a SNAP-15A source has been measured in detail as a part of a continuing effort to identify the spectra emitted by RTGs. In addition, the intensities of some of the gamma rays emitted by Pb^{212}, Bi^{212}, and Tl^{208} have been verified and new data on the intensities of Pu^{238} gamma rays has been obtained.

2. Heat Source

The SNAP-15A source is a right-circular cylinder having dimensions shown in Fig. 17. Haynes-25 is an alloy containing mainly cobalt, chromium, and tungsten. The total amount of Pu^{238} was 2.717 g. The fuel had been processed 5 yr prior to the measurement, at which time the Pu^{236} concentration was estimated by Mound Laboratory to be between 1 and 2 parts/10^6.
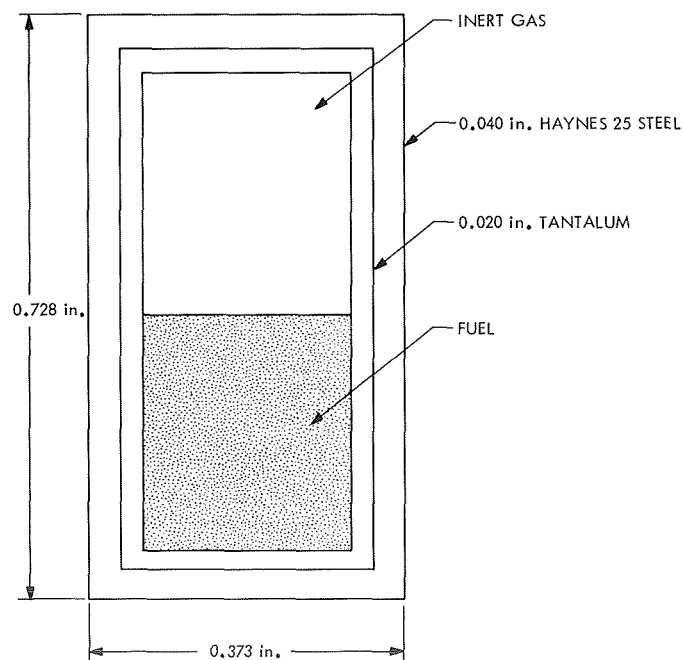

Fig. 17. SNAP-15A heat source

Although the power of a SNAP-15A source is about 1.5 W(th) compared with 1000 to 1500 W for a typical RTG, there are no major differences in the gamma-ray spectra emitted.

3. Experiment

All measurements were made using a Ge(Li) crystal having an active volume of 21.8 cm³ and a resolution of about 3 keV at 1.33 MeV.

The electronics consisted simply of a preamplifier, amplifier, biased amplifier, and 400-channel analyzer. The region from about 200 keV to 3 MeV was covered in seven runs. A typical spectrum is shown in Fig. 18. The photons viewed by the crystal were emitted in a radial direction from the source.

The data under the full-energy peaks were analyzed by the use of a code that fits photopeaks and a continuum to the function

$$\sum_n A_n \exp\left[-k_n(x - x_{0n})^2\right] + a_0 + a_1 x \qquad (1)$$

where x is the channel number.

Although the code can fit up to five photopeaks simultaneously, it was used in these measurements for a maximum of two in any analysis. In most cases, the peaks were sufficiently far apart so that individual ones were analyzed separately.

All intensities must ultimately be corrected for the detector efficiency. This was done by measuring the photo-
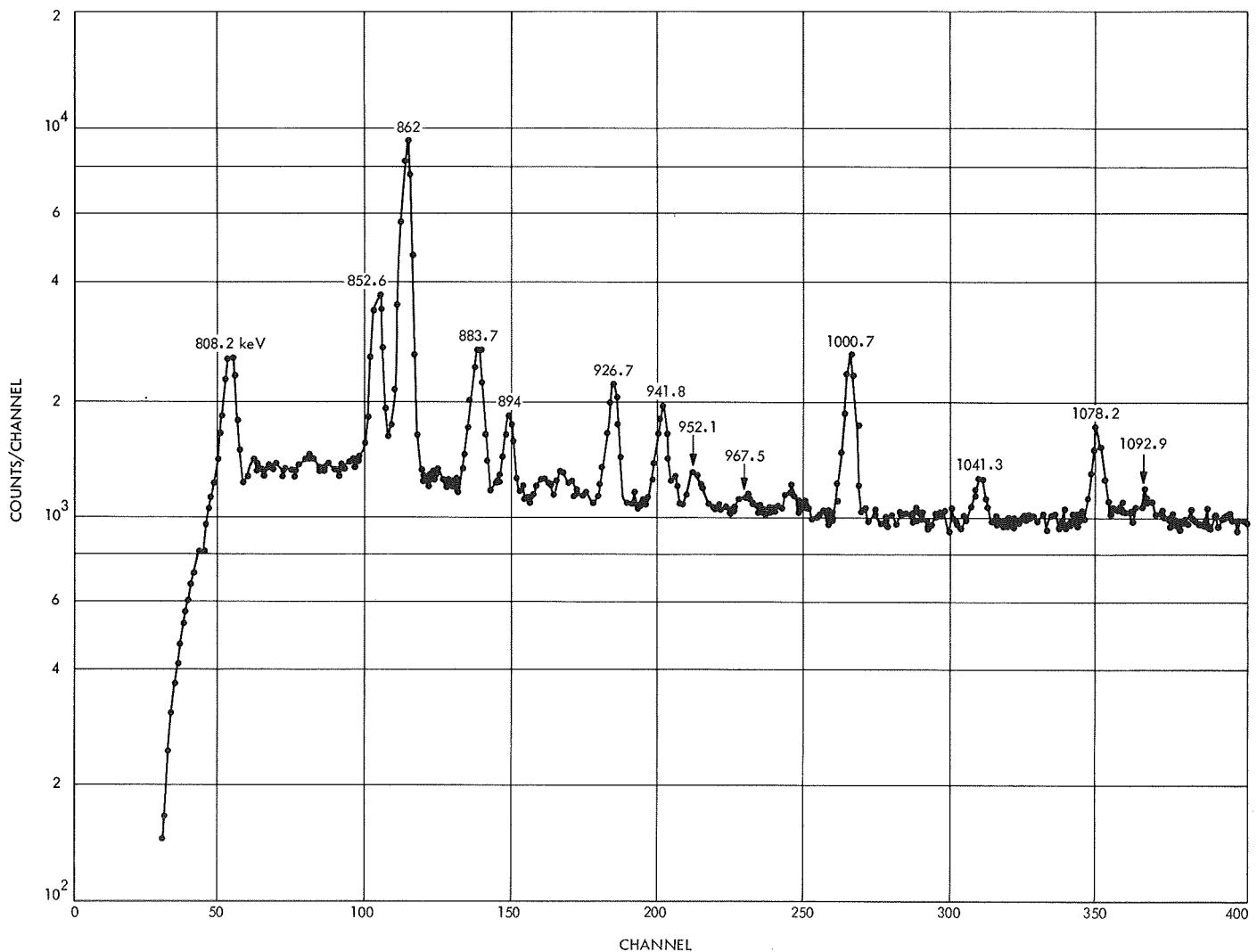

Fig. 18. Source spectrum from ~800 to 1115 keV

peak efficiency of the detector using seven calibrated point sources ranging in energy from 0.166 MeV to about 2.6 MeV. A log–log plot of the efficiency times the front area of the detector, ϵA, versus the energy E fell along a straight line.[8] A weighted least-square fit was made resulting in the equation $\epsilon A = 0.383\ E^{-1.33}$, where E is in MeV. From 1 to 4 MeV, the error in the fit is about 2%; at 250 keV it is about 4%.

All intensities reported were corrected for the self-shielding of the source and the attentuation by the tantalum and Haynes-25. The following equation was used:

$$\frac{I}{I_0} = \frac{1 - e^{-\mu_1 t_1}}{\mu_1 t_1} \cdot \exp - (\mu_2 t_2 + \mu_3 t_3) \qquad (2)$$

μ is the total attenuation coefficient for gamma rays at a particular energy. Subscripts 1, 2, and 3 refer to plutonium, tantalum, and Haynes-25, respectively. t is the effective thickness and is equal to $\pi/2\ R_1$ for the plutonium (R_1 is the radius of the fuel), $\pi/4 \cdot (R_2^2 - R_1^2)/R_2$ for the tantalum, and a similar expression for the Haynes-25. If $R_2 - R_1 \ll R_2$, the latter expression reduces to $\pi/2\ (R_2 - R_1)$, where $R_2 - R_1$ is the thickness of the tantalum. Equation (2) assumes that all photons which strike the crystal travel in a plane perpendicular to the source axis. Deviations from this would result in an undercorrection. It also assumes that a photon which scatters in the source and then is detected will become part of the continuum. This is valid because the resolution of the crystal is very small compared with the energy lost in any Compton collision.

4. Results

The source of most of the gamma rays observed fall into two general categories. These are Pu[238] and the daughter products of Pu[236]. The final data are shown in Tables 19 to 22. The errors result from the sum of the errors in the gaussian fit and the efficiency equation, and a 2% error based on an estimated 1% error in distance measurements. All data were corrected for detector efficiency and source absorption. The error in the attenuation correction has not been included. However, calculations have been made to estimate the effect of an uncertainty in the cross sections or the dimensions of the capsule on this correction. A 1% error in the absorption coefficient or radius of the fuel below about 200 keV

---

[8]The area is arbitrary, since it cancels out when ϵA is used in correcting the final data.

produces a corresponding error of about 1% in the attenuation. (A 1% error in the radius of the fuel would be a 0.005 in. error in the fuel diameter. This is considered unreasonably large.) At 1 MeV, the effect is reduced to about 0.25%. A 0.002-in. error in the thickness of the tantalum produces an error of 4% at 240 keV, 2.6% at 300 keV, and 0.5% at 1 MeV. The corresponding error in Haynes-25 is about one third that of tantalum at 240 and 300 keV and one half at 1 MeV. Even though the attenuation correction is about 25 at 240 keV, the error in this correction is not prohibitive. In addition, the results do not show a systematic trend when compared with other measurements as the energy is decreased. For these reasons, the data down to 240 keV was used despite the large attenuation corrections. The situation deteriorates rapidly below about 200 keV. Between 200 and 100 keV, the attenuation correction changes from 50 to 100. A 0.002-in. error in the tantalum thickness would produce an error of 35% in the correction at 100 keV. Although data exists for this region, the intensity values are not listed.

a. Pu[238]. Table 19 shows those lines resulting from Pu[238] decay. The mass of the Pu[238] when the measurement was made was 2.72 g. This information, in conjunction with the half-life, permits a calculation of the number of photons per disintegration. The data are compared with a recent measurement by Lederer et al. (Ref. 1) who used a 10-cm[3] Ge crystal having a resolution of about 2 keV. Although most of the intensity values agree within the listed errors, Lederer's values are systematically higher than those reported here.

b. Pu[236] daughter products. Although the initial concentration of Pu[236] in a Pu[238] heat source may be in the order of 1 part/10[6], the Pu[236] daughters become the major source of gamma activity in about 1 yr. Figure 19
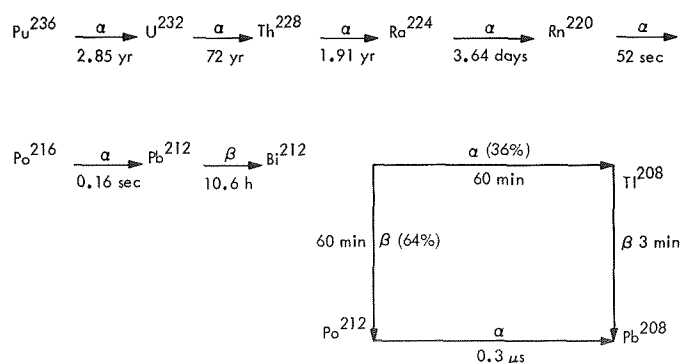

Fig. 19. Decay Chain of Pu[236]

Table 19. Pu²³⁸ absolute gamma-ray intensities

E, keV[a]	Intensity at crystal window, cm^{-2} sec^{-1}	Photons/disintegration $\times$ 10^8		Ratio $\left(\dfrac{Present}{Lederer}\right)$
		Present experiment	Lederer, et al. (Ref. 1)	
43.50 $\pm$0.04[b]			38000[b]	
UKα2			104 $\pm$15	
99.84 $\pm$0.04			9200 $\pm$600	
UK$'_{\beta 1}$			78 $\pm$20	
UK$'_{\beta 2}$			24 $\pm$16	
152.71 $\pm$0.05	18.9	seen	1270 $\pm$90	
200.9 $\pm$0.2			5 $\pm$1	
207.6	1.94	seen		
235.9 $\pm$0.3?			0.01 $\pm$0.005	
258.3 $\pm$0.2			0.011 $\pm$0.02	
299.2 $\pm$0.2			0.07 $\pm$0.02	
706.1 $\pm$0.3			0.14 $\pm$0.02	
708.42 $\pm$0.20			0.38 $\pm$0.04	
742.77 $\pm$0.10	4.18	6.35 $\pm$0.21	7.6 $\pm$0.7	0.84
766.39 $\pm$0.10[c]	18.1	26.7 $\pm$0.8	33 $\pm$3	0.82
786.30 $\pm$0.10[d]	3.43	4.98 $\pm$0.16	4.8 $\pm$0.4	1.05
805.8 $\pm$0.3			0.18 $\pm$0.02	
808.25 $\pm$0.15	0.70	0.999 $\pm$0.063	1.1 $\pm$0.1	0.92
851.70 $\pm$0.10	1.19	1.64 $\pm$0.06	1.9 $\pm$0.2	0.87
880.5 $\pm$0.3			0.23 $\pm$0.03	
883.23 $\pm$0.10	0.94	1.270 $\pm$0.048	1.1 $\pm$0.1	1.16
904.37 $\pm$0.15	0.054	0.072 $\pm$0.021	0.10 $\pm$0.02	0.73
926.72 $\pm$0.15	0.54	0.71 $\pm$0.04	0.83 $\pm$0.08	0.87
941.9 $\pm$0.2	0.44	0.58 $\pm$0.02	0.67 $\pm$0.07	0.88
946.0 $\pm$0.3	—	—	0.13 $\pm$0.02	—
1001.03 $\pm$0.15	0.86	1.08 $\pm$0.04	1.4 $\pm$0.2	0.78
1041.8 $\pm$0.3	0.16	0.20 $\pm$0.02	0.28 $\pm$0.02	0.71
1085.4 $\pm$0.3	—	—	0.11 $\pm$0.02	—
1462	1.31	1.46 $\pm$0.12	—	—

[a]Energy values taken from Ref. 1. The photon energies measured in this experiment agreed with the values in Ref. 1 to within 0.5 keV in most cases.

[b]The energy and intensity of this transition are taken from the literature.

[c]Tl²⁰⁸ has a line at 763.

[d]Bi²¹² has a line at 786.

Table 20. Tl²⁰⁸ absolute gamma intensityᵃ

Table 20. Tl^{208} absolute gamma intensity[a]

E, keV	Intensity, %			Intensity at crystal window, cm⁻² sec⁻¹
	Present experiment	Schupp (Ref. 3)	Dalmasso[b] (Ref. 4)	
277	9.1 ±1.3	8.6	8.4 ±1.5	0.41
486	—	0.1 ±0.1	—	—
510.8	35.9 ±1.9	25.3 ±1.2	26.4 ±3.0	6.43
584.5	87.6 ±4.3	85.1 ±4.0	86.4 ±5.6	18.5
763[c]	—	3.4 ±0.2	2.0 ±0.5	—
861.4	12.4 ±0.6	14.2 ±0.6	12.6 ±1.3	3.55
1093	0.46 ±0.11	0.7 ±0.1	0.7 ±0.5	0.147
2615	100	100	—	38.5

[a]2.615 MeV line assumed 100%.

[b]All intensities normalized to the intensity of the 584.5 line assumed to be 86.4 ±5.6%.

[c]Not resolved from 766 line in Pu^{238}.

Table 21. Bi^{212} absolute gamma intensity from β branch[a]

E, keV	Intensity, %			Intensity at crystal window, cm⁻² sec⁻¹
	Present experiment	Schupp (Ref. 3)	Dalmasso (Ref. 4)	
729.9	10.4 ±0.5	11.1 ±0.7	11.3 ±1.1	4.77
785[b]	—	1.7 ±0.3	1.5 ±0.3	3.43
893.9	0.58 ±0.03	0.66 ±0.07	0.62 ±0.17	0.30
952.1	0.25 ±0.03	0.16 ±0.04	0.51 ±0.28	0.14
1073.0	—	—	<0.1	—
1078.2	0.73 ±0.05	0.99 ±0.08	0.68 ±0.28	0.41
1512.8	0.61 ±0.12	0.49 ±0.05	—	0.39
1621	2.47 ±0.21	2.80 ±0.20	—	1.59
1800	—	0.17 ±0.03	—	—

[a]Relative to 2.614 MeV line of Tl^{208} assumed 100% of Tl^{208} decays and corrected for Bi^{212} α, β branching ratio.

[b]Pu^{238} also has a line at 786 keV.

Table 22. Pb^{212} absolute gamma intensity[a]

E, keV	Intensity, %			Intensity at crystal window, cm⁻² sec⁻¹
	Present experiment	Dalmasso (Ref. 4)	Emery (Ref. 5)	
116	Seen	0.54 ±0.18	—	0.40
176.7	—	<0.07	—	—
238.4	93 ±6	50.0 ±7.2	47 ±9	6.69
300.3	5.2 ±0.3	4.1 ±0.5	3.6 ±0.5	0.85
415.2				

[a]Relative to 2.614 MeV line of Tl^{208} assumed 100% of Tl^{208} decays and corrected for Bi^{212} α, β branching ratio.

for all gamma rays with an energy greater than 200 keV, the total activity of the Pu^{238} gamma rays is only about 4×10^4/sec.

c. Tl^{208}. If shielding is involved, this is the most important isotope because of the high-intensity 2.615 line. The data is shown in Table 20. The α, β branching ratio of Bi^{212} is known to about 0.3% (Ref. 2). It is also well established (Ref. 3) by γ–γ coincidence techniques that the 2.615 MeV transition from the first-excited state to the ground state occurs in 100% of the Tl^{208} decays. Agreement with previous measurements is excellent. Schupp used γ–γ and β–γ techniques employing scintillation counters. Dalmasso used a Ge crystal. Disagreement at 510.8 keV is not surprising, since this energy coincides with the annihilation gamma ray.

d. Bi^{212}. The data is shown in Table 21. The agreement is excellent in most cases. Also, as in Tl^{208}, there is no evidence of systematic deviation from other measurements.

e. Pb^{212}. The data for Pb^{212} is shown in Table 22. The two lines seen have an intensity considerably higher than that reported by Dalmasso (Ref. 4) and Emery (Ref. 5). The cause of this discrepancy has not yet been determined.

f. Pu^{236} impurity. If a measurement is made of the absolute intensity of a transition of one of the daughter products of Pu^{236}, the amount of Pu^{236} in the fuel at the time the fuel was processed can be calculated. The Po^{212}–Tl^{208} branching ratio is well known. In addition,

shows the decay chain of Pu^{236} leading to stable Pb^{208}. It can be seen that after a short while all the isotopes following Th^{228} are in equilibrium with the Th^{228}. Beginning with 1 μg of Pu^{236} in 1 g Pu^{238}, the Th^{228} activity after 5 yr will be about 3.2×10^5/sec compared with about 6×10^{10}/sec for the Pu^{238}. The latter figure, however, gives the alpha disintegration rate. If one considers the α/γ ratio

the probability that a Tl^{208} nucleus gives rise to a 2.615 MeV photon in 100% of the decays is well established. An absolute measurement of the 2.615 line gives unambiguous information on the original amount of Pu^{236} present in the fuel. A calculation was made using the data from this measurement. A value of 1.79 ± 0.07 parts/10^6 of Pu^{236} in the fuel at the time of processing was obtained. This compares with the value of 1 to 2 ppm assayed by Mound Laboratory. It is believed that by using this technique a precision of 10% is easily obtainable with a sample that is several months old and has a nominal concentration of 1 part/10^6 of Pu^{236}.

References

1. Lederer, C. M., Asaro, F., and Perlman, I., *Nuclear Chemistry Annual Report*, UCRL-18667, University of California Radiation Lab., Berkeley, Calif., 1968.

2. Giannini, M., Prosperi, D., and Sciuti, S., *Nuovo Cimento*, Vol. 21, p. 430, 1961.

3. Schupp, G., et al., *Phys. Rev.*, Vol. 120, p. 189, 1960.

4. Dalmasso, J., and Marsol, C., *Comptes Rendus*, Vol. 267B, p. 1366, 1968.

5. Emery, G. T., and Kane, W. R., *Phys. Rev.*, Vol. 118, p. 755, 1960.

IX. Guidance and Control Analysis

GUIDANCE AND CONTROL DIVISION

A. Television Image Processing for Navigation,
C. H. Acton, Jr.

An experiment in optical-approach navigation (Ref. 1 and SPS 37-51, Vol. III, pp. 50–52) was performed on the *Mariner* Mars 1969 mission. As part of the experiment, measurements from science and engineering instruments aboard the *Mariner* spacecraft were used to determine the spacecraft-centered direction to the center of Mars. This direction was used as an observable criterion in a navigation process to estimate the spacecraft trajectory relative to Mars during the approach to Mars. The experiment represented the first attempt to use data from an interplanetary spacecraft for the purpose of navigation, and was successful in producing good estimates of trajectories for both *Mariners VI* and *VII* spacecraft.

The experiment used pictures taken by the narrow-angle science TV cameras aboard the *Mariners VI* and *VII*. These narrow-angle cameras used a vidicon tube with an active target raster of 9.6 × 12.5 mm. The raster was electronically scanned in 704 lines and sampled at 945 picture elements, called *pixels*, per scan line. An optical focal length of 505 mm gave an angular field-of-

view of 1.1 × 1.4 deg and an angular resolution of ±3 arc-s per pixel. The video intensity of each pixel was digitized to 6 bits, and additional measurements were taken to allow the video intensity of each pixel to be reconstructed to 8 bits. This digital data was transmitted to earth where it was recorded on magnetic tapes.

A computer program was written to process the digital TV data (Ref. 2). The principal output was the location of the center of the Mars image. The program would search the digital data scan-line-by-scan-line. For each scan line, the video intensity of successive pixels would be determined by starting from a pixel location at the edge of the picture, viewing the dark space background off the image of Mars, and moving in the direction of the image of Mars. When, on the scan line, three successive pixels were encountered with video intensities greater than a reference video level (an input parameter), the number of the first of the three pixels was designated as the location of the lit limb of Mars. Spurious identifications of random data noise as the lit limb were avoided by waiting until three consecutive pixels whose video intensities were above the reference level were encountered.

To interpret the measured points on the image of Mars' limb, the figure of Mars was assumed to be ellipsoidal. The expected shape of the limb image was then elliptical. The measured locations of points on the lit limb were used in a weighted least squares process to estimate the location of the center of Mars in each TV picture. Image size, shape, and orientation in each TV picture also were estimated because of the significant uncertainties in these parameters. Size of the ellipse was defined by the semi-major axis of the image, while the shape of the ellipse was controlled by the offset of the focus from the center. The orientation of the image was defined as the angle between the direction of the semi-major axis of the ellipse and the direction of a scan line. A priori values of the estimated parameters of the ellipse were obtained from nominal values of Mars figure and spin axis direction, spacecraft-to-Mars range, and trajectory and TV parameters. A priori values for the estimated center location were obtained from visual inspection of 8 × 10-in. photographs that had been reconstructed from the digital TV data. A priori uncertainties were obtained by mapping the uncertainties of Mars figure, spin axis, spacecraft-to-Mars range, trajectory and TV parameters, and visual estimate of the center location into the five parameters being estimated.

Figure 1 is a typical picture of Mars used by the experiment. The lit limb measurements obtained from the digital data (Fig. 2) were used to estimate values for the five parameters. The estimate of the image center location was transformed into the direction to the center of Mars for use in the navigation experiment.

The image processing program was not fully operational at the time of the *Mariner* Mars 1969 encounter.
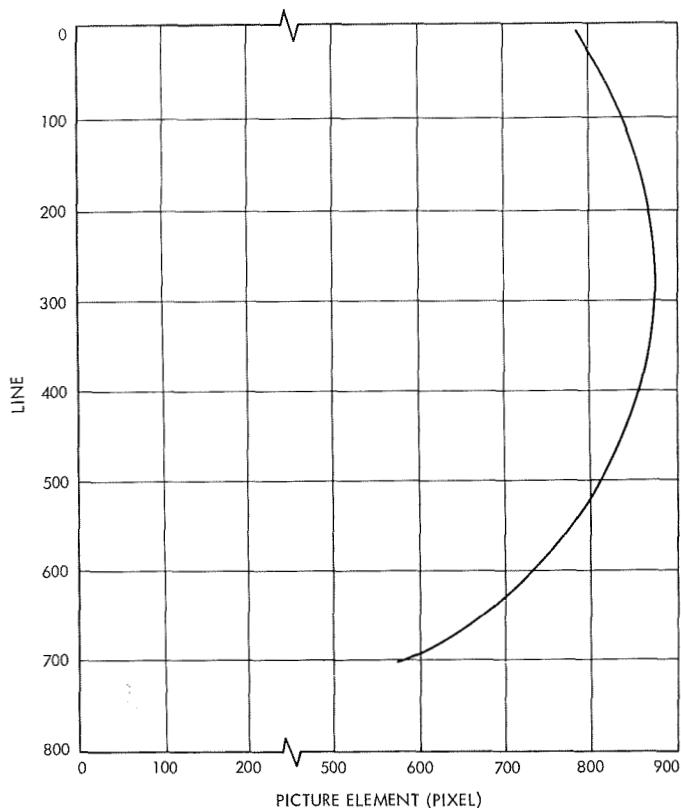

Fig. 1. Far encounter image of Mars

Fig. 2. Lit limb video data

However, center locations were estimated for selected pictures in near real time, demonstrating the feasibility of a real time processing capability. The estimates of size, shape, and spin axis orientation of Mars were not used during the near real time part of the experiment.

The program has now been completed and has been used to process all of the *Mariner* Mars 1969 far encounter pictures. Location estimates for the center of the Mars image obtained from this program are substantially better than those obtained by visual inspection. This increased accuracy is a result of the more accurate readout resolution obtained from a digital process as compared with visual inspection of 8 × 10-in. prints (1 pixel vs 10 pixels).

Modifications now in progress will result in a fully operational and highly flexible program for a navigation experiment on the *Mariner* Mars 1971 mission. The updated program will contain several significant new features:

(1) A more comprehensive limb search algorithm that will yield a more accurate set of data defining the lit line.

(2) Search algorithms to detect satellites and stars.

(3) Digital maps of selected areas from a given picture.

(4) Three-dimensional plots of digital intensity data as a function of line and pixel numbers for parts of the TV picture containing stars or satellites.

An example of the three-dimensional intensity plot feature is shown in Fig. 3 for video data obtained from a *Mariner* Mars 1971 breadboard narrow-angle TV camera picture of the star α Aurigae. The effective exposure was 0.5 s/pixel, and the intensity levels range from a minimum of 0 to a maximum of 56. The star image is spread out over several lines as a result of image motion during the exposure period.

References

1. Duxbury, T. C., and Breckenridge, W. G., "*Mariner* Mars 1969 Optical Approach Navigation," Paper 70-70, presented at the AIAA 8th Aerospace Sciences Meeting, New York, Jan. 19–21, 1970.

2. Duxbury, T. C., "Navigation Data from *Mariner* Mars 1969 TV Pictures," paper presented at the ION National Space meeting on Space Navigation—Theory and Practice in the Post-Apollo Era, NASA–Ames Research Center, Moffett Field, Calif., Feb. 17–19, 1970. Sponsored by the Institute of Navigation, Washington, D.C.
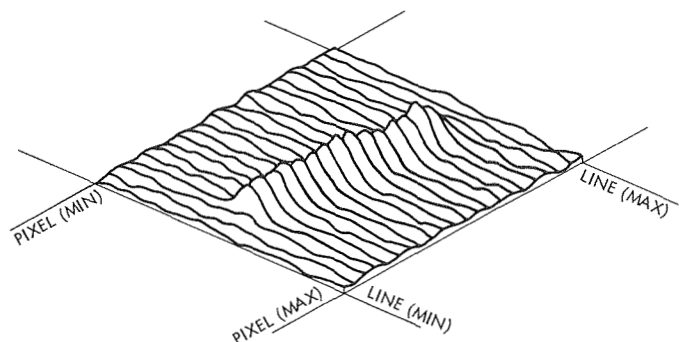
Fig. 3. Three-dimensional plot of star α Aurigae

X. Spacecraft Control

GUIDANCE AND CONTROL DIVISION

A. TOPS Attitude Control Reliability Study,
H. S. Lin

1. Introduction

There are two obvious methods of achieving a higher system reliability: (1) improve the reliability of the components, and (2) apply redundancy techniques. It can easily be shown for the second method that for perfect failure detection and sensing, maximum reliability improvement corresponds to redundancy of the lowest subsystem level. This summary presents the first part of a continuing study of the effects of imperfect sensing and switching to the system reliability for the TOPS Attitude Control System. General formulas of the reliability function are derived. The reliability of the system is expressed in terms of the failure rate of the operating unit, the failure rate of the standby unit, and the probabilities of proper operation of failure detectors and switching mechanism. For the constant failure rates, special cases are solved.

2. Operation of the System and Modes of Failure

A typical stand-by redundancy system usually consists of the following components: a sensing device, a switching mechanism, and m identical units. The block diagram of such a system for the case of $m = 2$ is shown in Fig. 1. Units A and B, in Fig. 1, are identical components and perform exactly the same function. If A fails, its failure detector will sense the failure and trigger the error flip-

flop; this, in turn, will disable unit A and enable unit B. Thus, B will take over the same function as A, and vice versa. The system may fail to operate in one of the following modes:

(1) Both units A and B fail.

(2) The switching mechanism fails and, in failing, stays permanently connected to A or B. The system ceases to function whenever A or B fails.

(3) One of the units has failed and a subsequent error in failure detection of the other unit will cause the system failure.
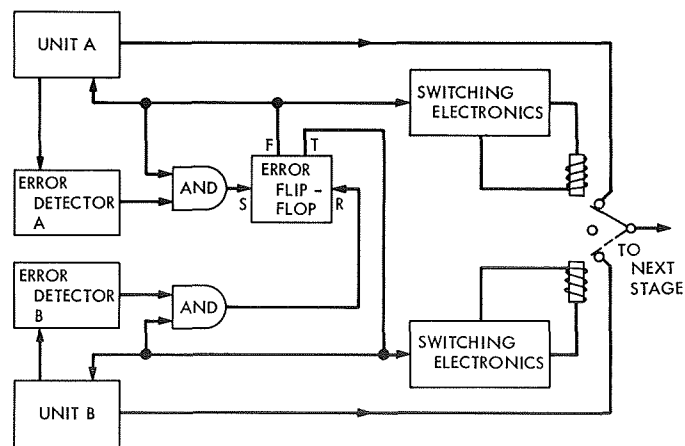
Fig. 1. Block diagram of a standby redundancy system

(4) One of the units has failed; a subsequent failure in the switching mechanism may cause a system failure if the switch is permanently connected to the non-operable unit.

(5) Random failures induced by transient during switching.

In the following section, a Markov process approach is used in obtaining a reliability function of the system.

3. Analytical Solution

The following states are defined:

State 1. The switching mechanism functions properly, both units are operable, and unit A is operating.

State 2. The switching mechanism functions properly, both units are operable, and B is operating.

State 3. The switching mechanism functions properly, unit B has failed, and unit A is operating.

State 4. Similar to state 3 except that unit A has failed and B is in operation.

State 5. The switching mechanism has failed, in failing it stays permanently connected to one of the units, and that unit, or both units, are operable.

State 6. Failure state for various failure modes described in *Subsection 2*.

The failure rates of the operating unit, the standby unit, the switching mechanism, and the detection device are assumed to be $\alpha(t)$, $\beta(t)$, $\gamma(t)$, and $\lambda(t)$, respectively. It should be noted that two different kinds of detection errors are possible: (1) error due to failure of the sensing device, and (2) error due to temporary failure in satisfying the predetermined detection criteria. The first kind of error is considered as unit failure and has been included in the determination of $\alpha(t)$. The second kind of error, which is transient in nature, has a failure rate defined by $\lambda(t)$. The conditional probabilities of the switch connected permanently to unit A or to unit B, given that a failure in the switching mechanism has occurred, are assumed to be P_A and P_B, respectively. In addition, the probability of a random failure of the system during the switching phase is assumed to be P_C. The state transition matrix of such a system is given by:

State transition matrix—1

State	1	2	3	4	5	6
1	$1 - (\alpha + \beta + \gamma + \lambda)\Delta t$	$(1 - P_C)\lambda\Delta t$	$\beta\Delta t$	$(1 - P_C)\alpha\Delta t$	$\gamma[1 - P_B P_C]\Delta t$	$P_C(\lambda + \alpha + P_B\gamma)\Delta t$
2	$(1 - P_C)\lambda\Delta t$	$1 - (\alpha + \beta + \gamma + \lambda)\Delta t$	$(1 - P_C)\alpha\Delta t$	$\beta\Delta t$	$\gamma[1 - P_A P_C]\Delta t$	$P_C(\lambda + \alpha + P_A\gamma)\Delta t$
3	0	0	$1 - (\alpha + \lambda + \gamma)\Delta t$	0	$\gamma P_A\Delta t$	$(\alpha + \lambda + \gamma P_B)\Delta t$
4	0	0	0	$1 - (\alpha + \lambda + \gamma)\Delta t$	$\gamma P_B\Delta t$	$(\alpha + \lambda + \gamma P_A)\Delta t$
5	0	0	0	0	$1 - (\alpha + \lambda)\Delta t$	$(\alpha + \lambda)\Delta t$
6	0	0	0	0	0	1

In case when $P_A = P_B = \frac{1}{2}$, the transition matrix can be reduced to four states. The new transition matrix is given to be:

State transition matrix—2

State	1	2	3	4
1	$1 - (\alpha + \beta + \gamma + P_C\lambda)\Delta t$	$[\beta + (1 - P_C)\alpha]\Delta t$	$\gamma\left(1 - \frac{1}{2}P_C\right)\Delta t$	$P_C\left(\lambda + \alpha + \frac{1}{2}\gamma\right)\Delta t$
2	0	$1 - (\alpha + \lambda + \gamma)\Delta t$	$\frac{\gamma}{2}\Delta t$	$\left(\alpha + \lambda + \frac{\gamma}{2}\right)\Delta t$
3	0	0	$1 - (\alpha + \lambda)\Delta t$	$(\alpha + \lambda)\Delta t$
4	0	0	0	1

where the new states are defined as follows:

State 1. The switching mechanism functions properly, both units are operable, and one is in operation.

State 2. The switching mechanism functions properly, one of the two units has failed, and the other is operating.

State 3. The switching mechanism has failed, in failing it stays permanently connected to one of the units, and that unit is, or both units are, operable.

State 4. Failure state of the system.

Let $P_i(t)$ be the state variable corresponding to the ith state; the difference and the differential equations of the state variables $P_1(t)$ through $P_4(t)$ can be given in the following form:

Difference Equations

$$P_1(t + \Delta t) = [1 - (\alpha + \beta + \gamma + P_C\lambda)\Delta t]P_1(t), \qquad P_1(0) = 1 \qquad (1)$$

$$P_2(t + \Delta t) = [\beta + (1 - P_C)\alpha]\Delta t P_1(t) + [1 - (\alpha + \lambda + \gamma)\Delta t]P_2(t), \qquad P_2(0) = 0 \qquad (2)$$

$$P_3(t + \Delta t) = \gamma\left(1 - \frac{1}{2}P_C\right)\Delta t P_1(t) + \gamma/2\,\Delta t P_2(t) + [1 - (\alpha + \lambda)\Delta t]P_3(t), \qquad P_3(0) = 0 \qquad (3)$$

$$P_4(t + \Delta t) = [P_C(\lambda + \alpha + \gamma/2)\Delta t]P_1(t) + (\alpha + \lambda + \gamma/2)\Delta t P_2(t) \qquad P_4(0) = 0 \qquad (4)$$
$$+ (\alpha + \lambda)\Delta t P_3(t) + P_4(t),$$

Differential Equations

$$\dot{P}_1 = -(\alpha + \beta + \gamma + P_C\lambda)P_1, \qquad P_1(0) = 1 \qquad (5)$$

$$\dot{P}_2 = [\beta + (1 - P_C)\alpha]P_1 - (\alpha + \lambda + \gamma)P_2, \qquad P_2(0) = 0 \qquad (6)$$

$$\dot{P}_3 = \gamma\left(1 - \frac{1}{2}P_C\right)P_1 + \gamma/2\,P_2 - (\alpha + \lambda)P_3, \qquad P_3(0) = 0 \qquad (7)$$

$$\dot{P}_4 = P_C(\lambda + \alpha + \gamma/2)P_1 + (\alpha + \lambda + \gamma/2)P_2 + (\alpha + \lambda)P_3, \qquad P_4(0) = 0 \qquad (8)$$

The general solution to the differential equations (Eqs. 5-8) are given by Eqs. (9)-(12).

General Solution

$$P_1(t) = \exp\left[-\int_0^t (\alpha + \beta + \gamma + P_C\lambda)dt_1\right] \qquad (9)$$

$$P_2(t) = \exp\left[-\int_0^t (\alpha + \lambda + \gamma)\,dt_1\right]\left[\int_0^t [\beta + (1 - P_C)\alpha]\exp\left[-\int_0^{t_1} [\beta - (1 - P_C)\lambda]dt_2\right]dt_1\right] \qquad (10)$$

$$P_3(t) = \exp\left[-\int_0^t (\alpha + \lambda)dt_1\right]\left[\int_0^t \left\{\gamma + \frac{1}{2}[\beta + (1 - P_C)\alpha - P_C\gamma]\right\}\exp\left\{-\int_0^{t_1} [\beta + \gamma - (1 - P_C)\lambda]dt_2\right\}dt_1\right]$$
$$- \frac{1}{2}\exp\left[-\int_0^t (\alpha + \lambda + \gamma)dt_1\right]\left[\int_0^t [\beta + (1 - P_C)\alpha]\exp\left\{-\int_0^{t_1} [\beta - (1 - P_C)\lambda]dt_2\right\}dt_1\right] \qquad (11)$$

$$P_4(t) = 1 - \exp\left\{-\int_0^t [\alpha + \beta + \gamma + P_c\lambda]dt_1\right\} - \frac{1}{2}\exp\left[-\int_0^t (\alpha + \lambda + \gamma)dt_1\right]\left[\int_0^t [\beta + (1-P_c)\alpha]\right.$$

$$\left.\exp\left\{-\int_0^{t_1}[\beta - (1-P_c)\lambda]dt_2\right\}dt_1\right] - \exp\left[-\int_0^t (\alpha + \lambda)dt_1\right]\left[\int_0^t \left\{\gamma + \frac{1}{2}[\beta + (1-P_c)\alpha - P_c\gamma]\right\}\right.$$

$$\left.\exp\left\{-\int_0^{t_1}[\beta + \gamma - (1-P_c)\lambda]dt_2\right\}dt_1\right]$$

$$(12)$$

The reliability of the system as a function of $\alpha(t)$, $\beta(t)$, $\gamma(t)$, $\lambda(t)$ and P_c is given to be

$$R = 1 - P_4$$

$$= \exp\left\{-\int_0^t [\alpha + \beta + \gamma + P_c\lambda]dt_1\right\} + \frac{1}{2}\exp\left[-\int_0^t (\alpha + \lambda + \gamma)dt_1\right]\left[\int_0^t [\beta + (1-P_c)\alpha]\right.$$

$$\left.\exp\left\{-\int_0^{t_1}[\beta - (1-P_c)\lambda]dt_2\right\}dt_1\right] + \exp\left[-\int_0^t (\alpha + \lambda)dt_1\right]\left[\int_0^t \left\{\gamma + \frac{1}{2}[\beta + (1-P_c)\alpha - P_c\gamma]\right\}\right.$$

$$\left.\exp\left\{-\int_0^{t_1}[\beta + \gamma - (1-P_c)\lambda]dt_2\right\}dt_1\right]$$

$$(13)$$

4. Special Cases

For the constant failure rates, i.e., $\alpha(t)$, $\beta(t)$, $\gamma(t)$, and $\lambda(t)$ equal to constants, the above equation can be simplified to

$$R(t) = \left[\frac{\gamma + \frac{1}{2}[\beta + (1-P_c)\alpha - P_c\gamma]}{\beta + \gamma - (1-P_c)\lambda}\right]\exp[-(\alpha + \lambda)t] + \frac{1}{2}\left[\frac{\beta + (1-P_c)\alpha}{\beta - (1-P_c)\lambda}\right]\exp[-(\alpha + \lambda + \gamma)t]$$

$$+ \left[1 - \frac{\beta + (1-P_c)\alpha}{2[\beta - (1-P_c)\lambda]} - \frac{\gamma + \frac{1}{2}[\beta + (1-P_c)\alpha - P_c\gamma]}{\beta + \gamma - (1-P_c)\lambda}\right]\exp[-(\alpha + \beta + \gamma + P_c\lambda)t] \quad (14)$$

which is a reliability function with decreasing failure rate. This reliability function can be used to determine the required optimal level of redundancy of a system to achieve the maximum overall system reliability. By letting $\gamma \to 0$, $\lambda \to 0$, $P_c \to 0$ and $\beta \to \alpha$, Eq. (14) reduces to

$$R(t) = 2\exp(-\alpha t) - \exp(-2\alpha t) \quad (15)$$

which is equivalent to the case of parallel redundancy. Again, instead of letting $\beta \to \alpha$, by making $\beta \to 0$, Eq. (14) reduces to

$$R(t) = \exp(-\alpha t)(1 + \alpha t) \quad (16)$$

which is the case of standard standby redundancy with perfect switching and sensing.

B. TOPS Attitude-Control Single-Axis Simulator Momentum-Wheel Tachometer Circuit,
L. S. Smith

1. Momentum Wheel

A simulation of a digital attitude-control system for an outer-planets spacecraft is being implemented on a single-axis gas-bearing table. Two thrusters and one momentum wheel are used to position the table. Vernier control will be accomplished with the momentum wheel while gross errors will be corrected by the thrusters. Additionally, the thrusters will be used to drive the wheel back to near-zero velocity when its torquing ability falls off due to speed saturation (1200 rpm). This drive action is called dumping.

To determine when the wheel is saturated, its speed must be measured. The Bendix Model X-1964136-1, 0.01 ft-lb momentum wheel provides a tachometer output

from a magnetic slug velocity detector. Basically, each revolution of the wheel produces eight sequential electrical pulses of speed-dependent amplitude having positive polarity for clockwise revolution and negative polarity for counterclockwise revolutions. Figure 2 shows the output amplitude vs speed.

Dumping is initiated at 1200 rpm and will be terminated as soon as a reversal of speed is detected. For example, should a clockwise speed buildup cause dumping, counterclockwise drive will be continuously applied to the momentum wheel until a counterclockwise revolution is detected. Note that the clockwise torque produced by the above dumping will be balanced by the action of a thruster.

2. Tachometer Implementation

Figure 3 presents a typical clockwise output signal from the velocity detector. Note that the general form of the output is the same throughout the rpm range. The positive peak excursion is approximately seven times the negative peak overshoot. To properly discriminate between the two excursions and, thus, determine wheel direction as well as speed, the absolute value of each excursion is compared to a voltage that is directly proportional to the wheel speed. This speed-dependent voltage will be approximately 30–60% the value of the expected excursion voltage (2–4 times greater than the expected opposite overshoot voltage). When the speed-dependent voltage is exceeded, one-eighth of a revolution in the respective direction will be indicated.

The tachometer block diagram is presented in **Fig. 4**. The velocity detector output is coupled directly into one

voltage comparator and via an inverter to another comparator. A counter-logic circuit performs a binary count of the comparator outputs for fixed intervals generated
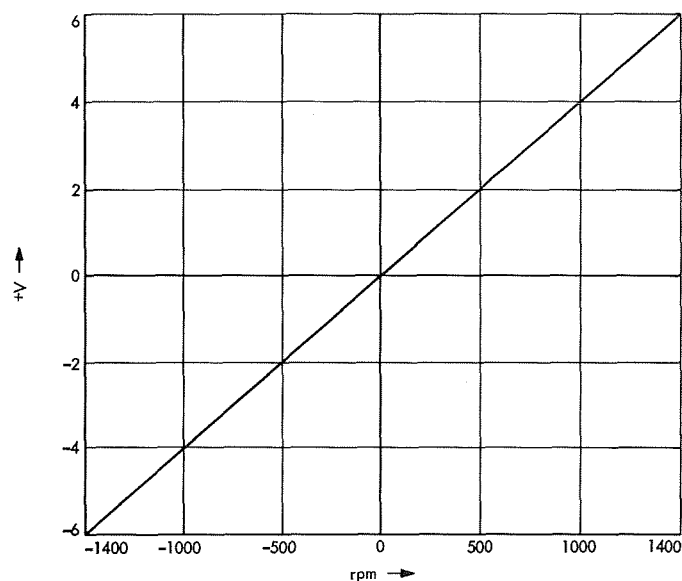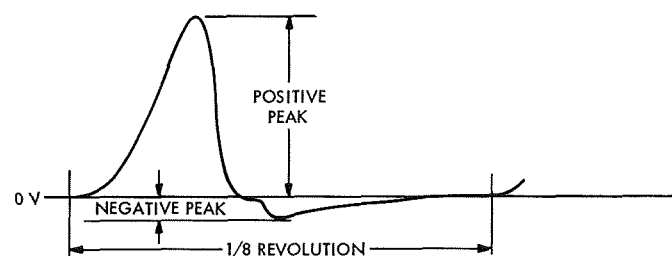

Fig. 2. Output amplitude vs speed

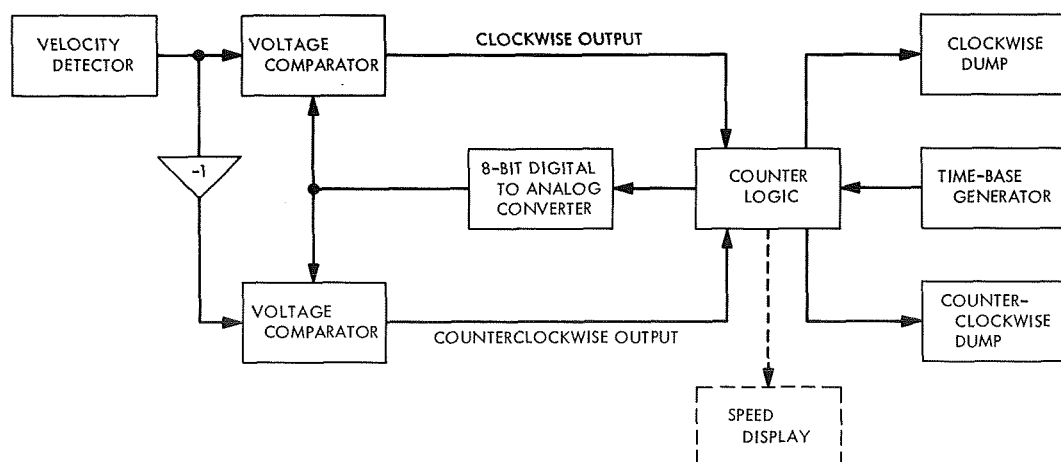**Fig. 3. Typical velocity-detector clockwise output signal**

Fig. 4. Tachometer block diagram

by a time-base generator. The number of pulses from one or the other of the comparators is directly proportional to the wheel speed. Subsequently, the count in the binary counter drives an eight-bit digital-to-analog converter to establish the speed-dependent voltage. The counter-logic circuit also monitors for dump speed and indicates dump direction. An optional wheel-speed and direction-display circuit can be easily incorporated in the present design for off-table visual monitoring.

C. Attitude Control of a TOPS-Based Outer Planet Orbiter Spacecraft, W. E. Dorroh, Jr.

1. Introduction

The TOPS-baseline attitude-control subsystem (SPS 37-58, Vol. III, pp. 117–121) requires few changes for use on the outer planet orbiter spacecraft of the 1980s. The major impact is in the autopilot system required to control the throttling valves of the liquid-fuel vernier engines; the TOPS autopilot is required to actuate the two mechanical gimbals of a single liquid-fuel engine.

Therefore, the discussion of the attitude control subsystem will be in terms of changes to TOPS, with brief descriptions of the TOPS where applicable.

2. Attitude Control Functions

The functions of the attitude control subsystem are basically those of TOPS, and are listed below:

(1) Reduce tip-off rates and acquire the Sun using the hot-gas thrusters.

(2) Roll the spacecraft about the sun line for science instrument calibration and mapping by using the reaction wheels. Acquire the star Canopus upon completion of the calibrations.

(3) After launch plus 250 days, accept sun sensor and Canopus tracker biases from central computer and sequencer to orient the roll axis, and thus the high gain antenna, toward the earth and the negative yaw axis toward the south ecliptic pole.

(4) Perform a roll–yaw turn sequence to orient the spacecraft for trajectory correction motor burns.

(5) Provide thrust vector control during motor burn.

(6) Unload reaction wheels when required, utilizing the hot gas thrusters.

(7) Provide the capability to utilize position error signals from the radio subsystem for earth pointing of the roll axis in lieu of the sun-sensor error signals.

3. Moments of Inertia

The addition of the large propulsion module to the basic TOPS spacecraft increases the moments of inertia from approximately 1500 to 1600 slug-ft^2 in yaw and roll and from approximately 300 to 500 slug-ft^2 in pitch. These changes are not enough to require changing the TOPS reaction wheels.

The attitude propulsion impulse requirements are shown in Table 1. Note that the effect of the larger inertias is offset by the shorter mission time and the fact that a gimballed vernier engine is used for roll control rather than the roll jets during motor burn.

Table 1. Attitude propulsion torque impulse requirements, lb-ft-s

Requirements	TOPS	Jupiter orbiter
Rate reduction	180	200
Solar disturbance torques	255	170
Third axis control	10	
Micrometeoroid and gravity gradient	150	100
Contingency	255	280
Total torque impulse	850	750

The monopropellant used in the vernier engines is compatible with the TOPS attitude propulsion thrusters. Since the torque requirements are the same as TOPS, a majority of the gas system hardware can be used without modification.

4. Gravity Gradient Torques

Gravity gradient torques acting upon an orbiting vehicle can, if they are of sufficient magnitude, cause the reaction wheels to be unloaded while in orbit. If possible, the wheels are sized such that the peak momentum can be stored without unloading.

A gravity gradient computer program (Ref. 1) was used to calculate the required momentum storage as a function of true anomaly; the results are shown in Fig. 5. Note that the peak storage requirement is 0.1 lb-ft-s, an order of magnitude less than the storage capability of the TOPS reaction wheels.

Using a simplified gravity gradient torque model, it can be shown that the maximum disturbance torque is given by:

$$T_m = \frac{2K_J I_{s/c}}{(N \cdot R_J)^3}$$

For the Jupiter orbiter, $K \approx 4.5 \times 10^{18}$ ft³/s², $R_J \approx 2.34 \times 10^8$ ft, $I \approx 1500$ slug-ft². Therefore,

$$T_m \approx \frac{1.05 \times 10^{-3}}{N^3} \text{ ft-lb}$$

For a periapsis of 2 Jupiter radii,

$$T_m \approx 0.13 \times 10^{-3} \text{ ft-lb}$$

which is two orders of magnitude less than the torque capability of the reaction wheels.

5. Sun and Earth Occultation

Figures 6–8 show the increasing occultation periods as a function of time in orbit. When only the sun or the earth is occulted, the other can be used as an attitude reference. Gyros must be used during periods of co-occultation, as shown in Fig. 8. Impending solar occultation, and the resulting switch to either radio or gyro reference, is logically determined from the sun sensor and sun gate signals as in TOPS.

6. Accelerometer

The accelerometer for the orbiter missions will be required to operate over a much wider dynamic range than for TOPS. The nominal requirements are shown in Table 2.

To achieve this wide dynamic range, the electronic capture loop used on TOPS must be redesigned; this will result in some cost in weight and power.

7. Canopus Tracker

The orbiter cruise attitude is rotated 90 deg about the roll axis from TOPS to allow full planetary coverage by
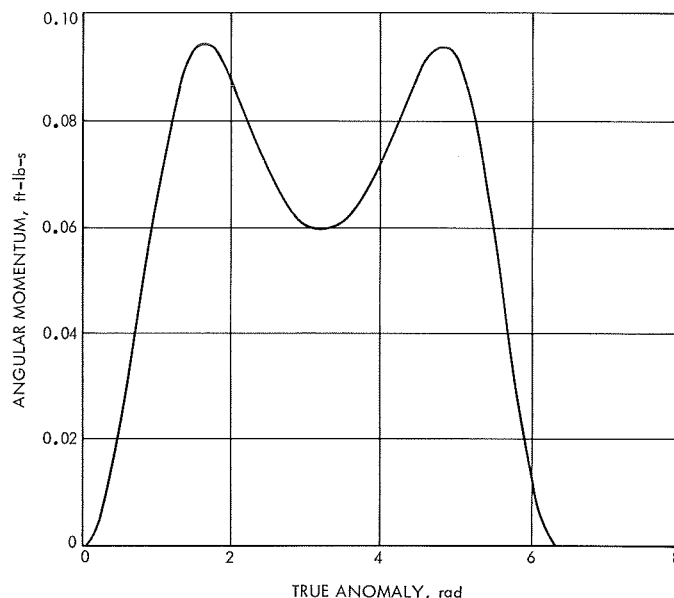

Fig. 5. Yaw angular momentum as a function of true anomaly

the science instruments throughout the orbit. This requires that the Canopus tracker be relocated on the science boom to achieve its required field of view. Preliminary analyses have shown no stability problems with this location (SPS 37-61, Vol. III, pp. 149–151).

8. Thrust-Vector Control

The autopilot for the orbiter will be significantly different from TOPS. The orbiter propulsion system consists of a high thrust (2300 ft-lb) single burn solid motor with three throttleable liquid verniers (10–50 ft-lb) mounted on a 2- to 3-ft radius around the solid.

The liquids provide the thrust for the interplanetary cruise maneuver, the orbit trim maneuvers, and approximately 5% of the orbit insertion impulse. The solid provides the main thrust for orbit insertion. In addition, the throttling capability of the liquids provides thrust vector translation to allow for center of mass uncertainties and migration.

Table 2. Accelerometer requirements

Maneuver	TOPS, g	Orbiter, g
Interplanetary cruise maneuvers	0.02	0.02–0.07
Orbit insertion maneuver		0.07–0.8
Orbit trim maneuvers		0.04–0.15
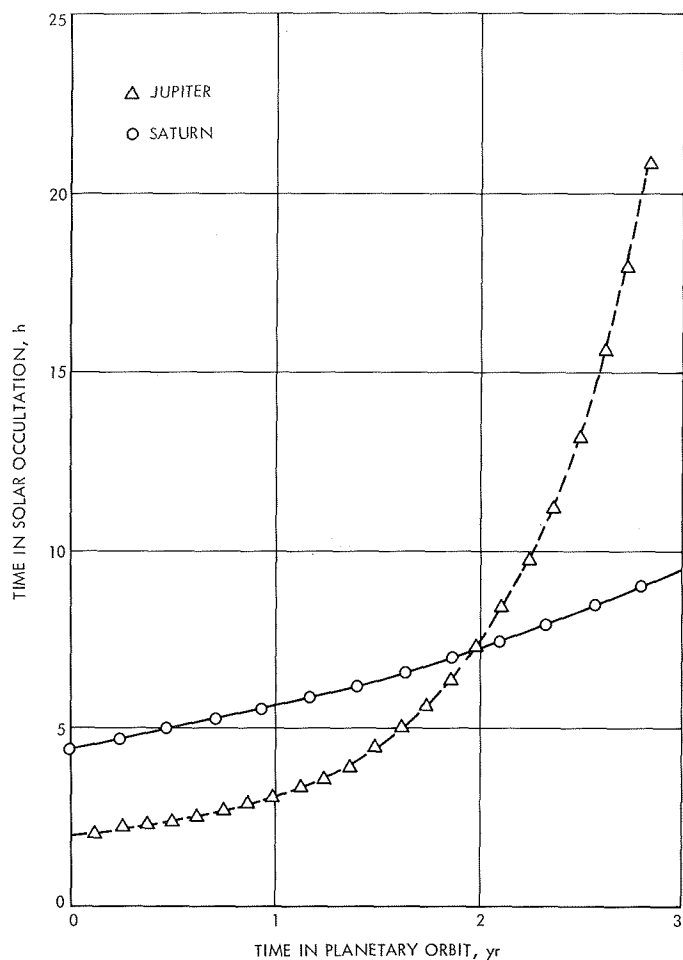
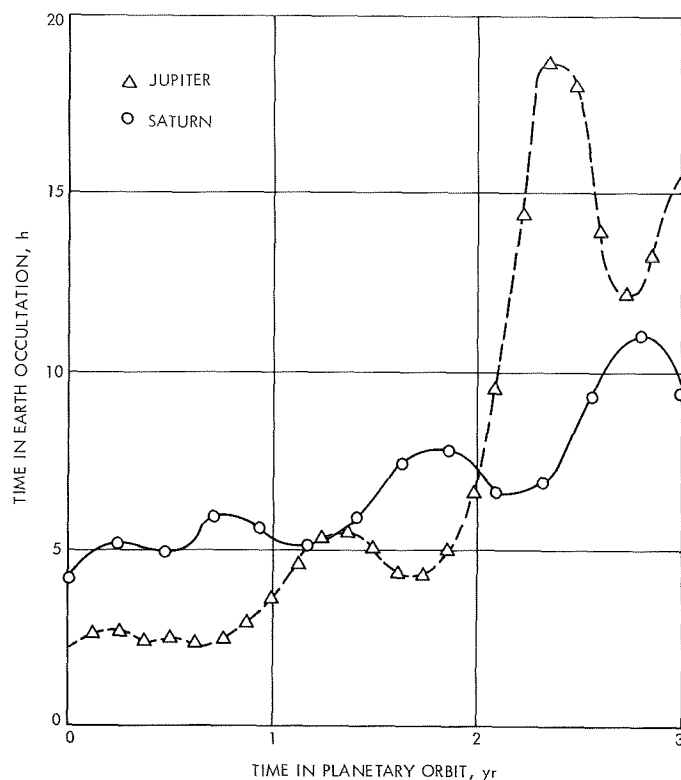Fig. 6. Solar occultation time vs time in orbit
resulting from planet oblateness

Fig. 7. Earth occultation time vs time in orbit
resulting from planet oblateness
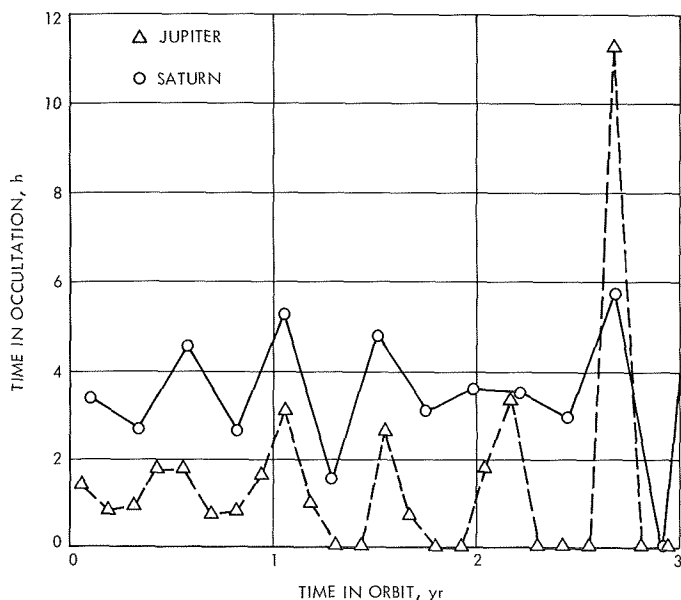
Fig. 8. Duration of co-occultation period

Since small misalignments in the outboard liquid-fuel verniers could produce roll torques which exceed the capability of the gas jets, one of the vernier engines is provided with a single-axis gimbal and actuator, similar to TOPS, for roll control.

A typical orbit-insertion thrust profile is shown in Fig. 9. Note that the verniers are brought on first to obtain control before the solid motor is ignited. The solid motor is ramped on to prevent excessive transient disturbances. The thrust is tailored to provide a constant acceleration throughout the burn, and the tail-off is ramped similarly to the turn-on. The verniers remain on after the solid motor has burned out to complete the required change in spacecraft velocity.

The autopilot is similar to that used on the *Surveyor* spacecraft. Angular rate and position errors are measured by the gyros and fed through lag compensators to raise

the dc loop gain. The pitch and yaw signals are mixed with a thrust level command and fed to the throttling valves of the three engines. The roll signal is fed directly into the gimbal actuator controller.
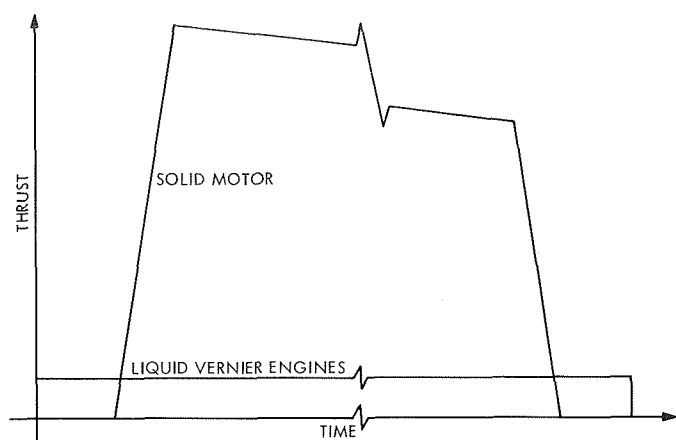
Fig. 9. Orbit insertion thrust profile

The valves are throttled around the nominal center position to maintain a constant thrust from the three engine combination.

Reference

1. Kerner, T., *Gravity-Gradient Effects on an Attitude-Controlled Satellite*, Technical Memorandum 33-409. Jet Propulsion Laboratory, Pasadena, Calif., Oct. 15, 1968.

D. Advanced Development Electrostatic Image Dissector, W. C. Goss

1. Introduction

Image dissectors, or scanning photomultipliers, are used as the direction sensing and star-brightness measuring element in the star tracker for attitude control of *Mariner*–class spacecraft. In essence, the image dissector is a photomultiplier with electron optics to re-form the image from the photocathode at a sampling aperture plate located at the entrance to the electron multiplier structure. A means of deflecting the electron image is provided either by transverse electrostatic or magnetic fields, in order to scan the electron image across the aperture for signal modulation purposes, and to provide field-of-view gimballing.

Either electrostatic or magnetic field effects may be used for focusing the electron image and for deflection. The magnetic technique has the advantages of providing a very uniform resolution over the field and of having magnetic coils external to the vacuum envelope. This leads to a relatively simple image-dissector tube structure.

The most significant disadvantages to the magnetic field approach lie in the very substantial weight and size of magnetic shielding required to prevent interference with spacecraft science experiments and the weight and power penalty associated with the magnetic coils.

The tracker used in all *Mariner* spacecraft to date, uses an electrostatically focused and deflected image dissector. Resolution has been adequate for all requirements and the power drain is low; i.e., typically 0.1 W to operate all functions of the image dissector. This approach has proven to be far simpler to utilize in an instrument.

Since 1934, image dissectors have been used for a variety of tasks and, in particular, were used in an early form of television (Ref. 1). Ruggedized units suitable for a space–borne application were not available until 1963, when development of the *Mariner* image dissector was successfully completed by CBS Laboratories of Stamford, Connecticut (under contract to JPL).

2. The Advanced Development Electrostatic Image Dissector

A second-generation image dissector is now under development at EMR-Photoelectric in Princeton, New Jersey (under contract to JPL). The new design is intended to provide improvements in production yield, performance stability, and environmental capability.

Figure 10 is a cut-away drawing of the new design. The electron–optical configuration has been left unchanged from the *Mariner* image dissector, otherwise the tube has been redesigned. The entire structure is a ceramic–metal stack which is jigged and radio-frequency brazed at assembly to maintain close dimensional control. Stainless steel A-286 is used throughout because of its exceptionally low magnetic retentivity. The fabrication yield ratio is expected to be greatly improved by this fabrication technique.

The photocathode used is the EMR Type U, a cesium-free, high-quantum efficiency photo-electron emitter that has been demonstrated to have excellent stability at high temperatures. This photocathode performs well at temperatures far in excess of the spacecraft type approval temperature limit of 167°F.

The electron multiplier is an incorporation of a standard EMR product line item. The dynodes are beryllium
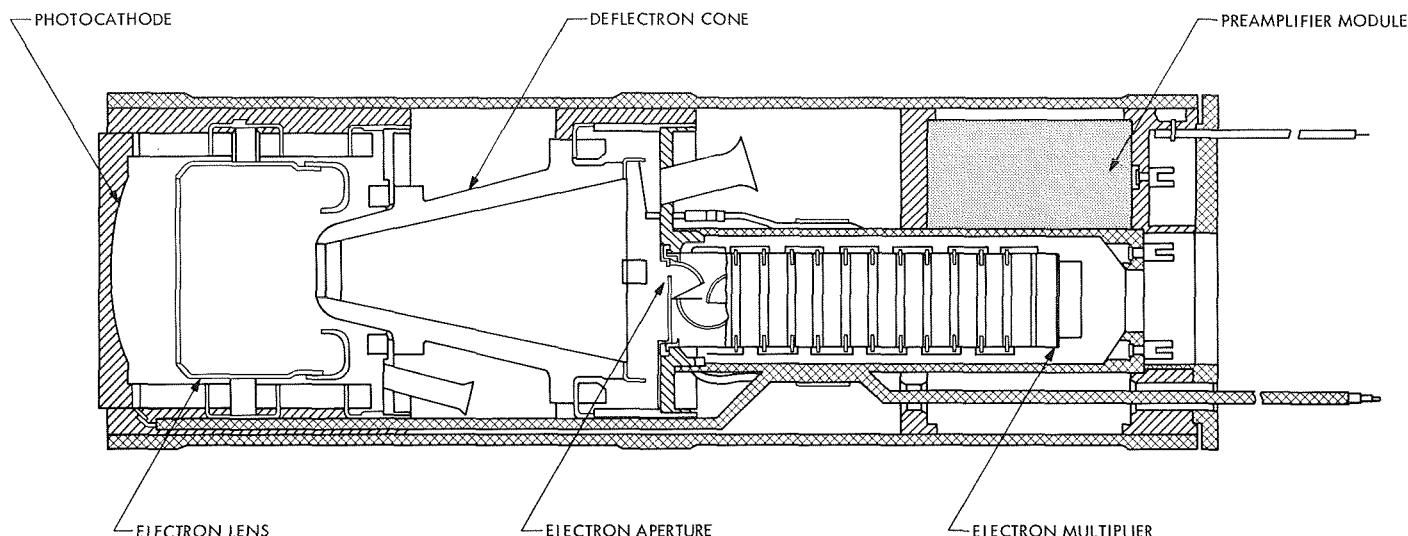
Fig. 10. Advanced development electrostatic image dissector

copper, the unit is an extremely low-leakage structure, and total dark current approaches the thermionic limit.

A consistent operational problem with electrostatic deflection techniques has been electrostatic charging of the insulator structures. Charge accumulation causes a redistribution of the electrostatic fields within the tube and, consequently, a shift in the null-pointing direction. A period of time ranging from minutes to hours is required for this condition to reach equilibrium, causing the expenditure of an undue amount of time on functional testing.

This new design incorporates a thin, slightly-conducting chromium oxide layer underlying the deflection pattern. The time constant for charge equilibrium to be established is expected to be approximately 1 ms.

The new design image dissector makes provision for a preamplifier module to be incorporated within the shield structure. The preamplifier is an FET type, common-mode rejection, and was designed at JPL under an effort parallel to the EMR contract. All high-voltage areas, including the preamplifier input terminals, are encapsulated to preclude the possibility of corona-type arc-over in a low gas-pressure environment.

The first units are scheduled to be delivered to JPL by midsummer 1970. A thorough evaluation and testing program is planned to be conducted at JPL during fiscal year 1971.

Reference

1. Farnsworth, P. T., *J. Franklin Inst.*, No. 218, p. 411, 1934.

E. The Nonlinear Equations of Motion for a Solar-Electric Powered Spacecraft, E. L. Marsh

1. Introduction

Recently, intense interest has focused on the idea of using solar-electric powered spacecraft for deep space missions. For the development of such spacecraft, new technology in several areas has been demanded. For example, new ideas in control system design, large flexible solar array design, and electric-propulsion engine design have been conceived and implemented. The work presented here is a first step in tying together some aspects of these three areas.

During the thrust phase of the mission, one means of providing three-axis attitude control is the combination of translation and gimballing of the solar-electric engines. This concept will be analyzed. Inclusion of the elastic effects of the flexible solar arrays was accomplished by utilization of Likins' hybrid coordinate procedures (Ref. 1).

Figure 11 shows the spacecraft to be analyzed. It is composed of a rigid central body B_1 to which are attached two flexible roll-out solar arrays A, and a solar-electric engine cluster E. Unit vectors b_1, b_2 and b_3 are fixed in B_1. Figure 12a shows E in more detail. The engine cluster consists of a large plate to which are fixed five
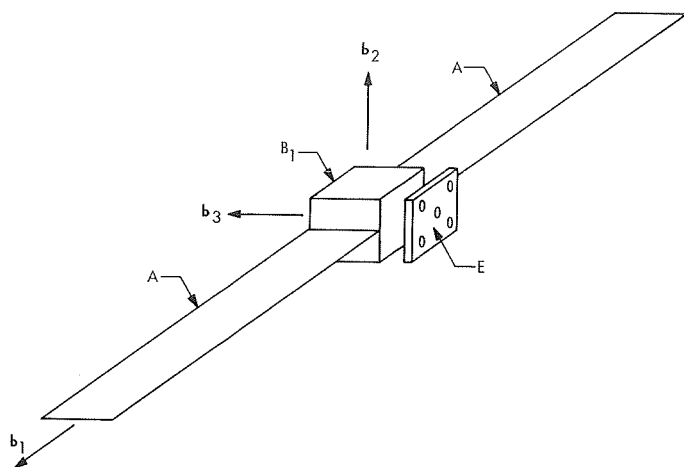
Fig. 11. Solar-electric spacecraft

(a)

(b)

Fig. 12. Engine cluster

denoted B_2; B_2 can translate parallel to the $\mathbf{b}_1$ and $\mathbf{b}_2$ directions. Figure 12b shows the cluster in an arbitrary configuration. Point 0 is the mass center of the entire spacecraft for the case of no engine translation or gimballing.

During the thrust phase, when E translates parallel to $\mathbf{b}_1$, a control moment parallel to $\mathbf{b}_2$ is exerted on the spacecraft. Translation parallel to $\mathbf{b}_1$ will produce a moment parallel to $\mathbf{b}_2$. Third-axis control is provided by gimballing engines B_3 and B_4. This generates a moment parallel to $\mathbf{b}_3$.

Figure 13 shows E in even greater detail. In addition to B_2, B_3, and B_4, bodies B_i, $i = 5$, $\cdots$, 13 are shown. These are associated with the mechanisms which translate E or rotate B_3 or B_4. A discussion of Fig. 14 will facilitate understanding Fig. 13.

Figure 14a shows the mechanism for translation parallel to $\mathbf{b}_1$. Both the stator and circular spline are fixed in B_{13}. Two tapes, wrapped about the drum, have one end attached to the drum and the other to B_1. The rotary motion of the rotor is transmitted through the conventional gear train and harmonic gear (consisting of the
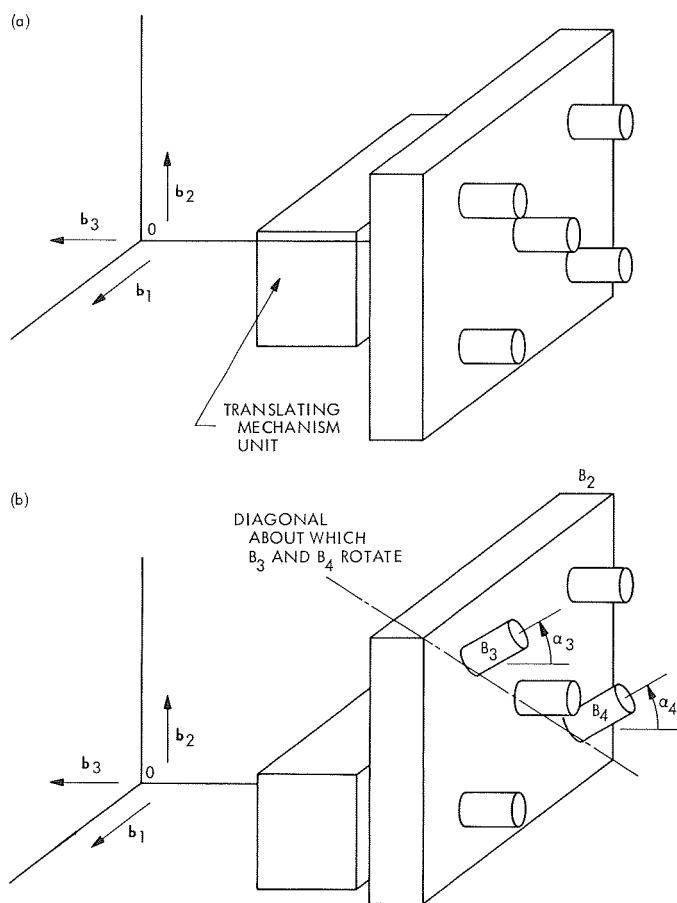

Fig. 13. Translator

electric propulsion engines, and a unit containing translating mechanisms. Two of the engines, B_3 and B_4, can rotate about the diagonal passing through the $\mathbf{b}_1$–$\mathbf{b}_2$ quadrant. The plate and the remaining three engines are

(a)

TAPE

DRUM

TAPE

ROTOR
STATOR
WAVE GENERATOR
FLEXSPLINE
CIRCULAR SPLINE
GEAR

(b)

GIMBALLED ENGINE
GEAR
BEARING
OUTPUT SHAFT
STATOR
ROTOR
GEAR
WORM GEAR
BLOCK

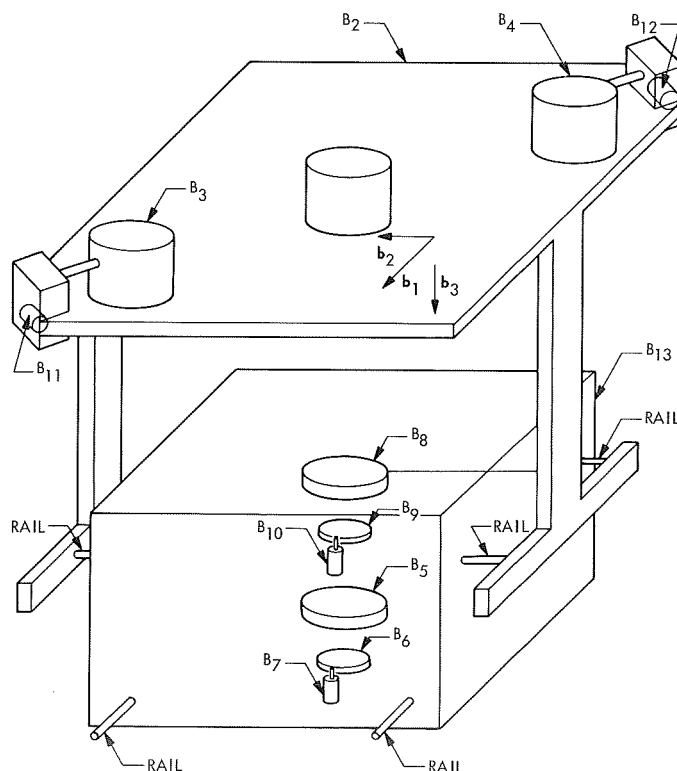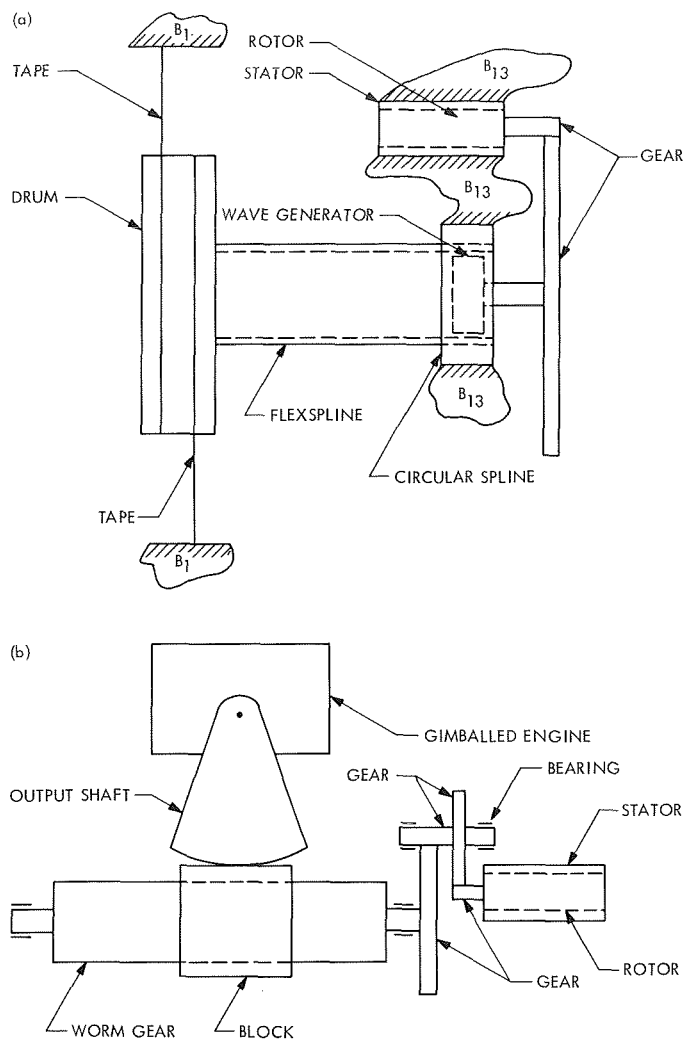**Fig. 14. Translating and gimballing mechanisms**

flexspline, circular spline, and wave generator) to the drum. This causes one tape to wind up while the other unwinds. Consequently, B_{13} translates and so does B_2, since it is constrained to do so by the rails parallel to b_2. A second assembly, similar to the one described, accounts for translation parallel to b_2, except that the tapes are attached to B_2 instead of B_1. In Fig. 13, the drum, large gear, and rotor for b_1 translation are denoted B_5, B_6, and B_7, respectively. For b_2 translation, they are denoted by B_8, B_9, and B_{10}. Notice that both translating assemblies are housed in B_{13}, which translates in the b_1 direction.

Associated with each gimballed engine are four spur gears, a worm gear, a block, a motor rotor, a stator, and an output shaft (Fig. 14b). Two tapes are attached to the output shaft and block. When the rotor is activated, rotational motion is transmitted through the conventional gear train to the worm gear, which converts the rotary motion to translational motion of the block; the latter acts on the output shaft through the tapes and causes the engine to rotate. Only the motor rotors B_{11} and B_{12} are shown in Fig. 14.

All of the items shown in Fig. 13 are assumed to participate substantially in the dynamics.

Differential equations of motion for the entire vehicle, the appendages A, and the rigid bodies B_2, $\cdots$, B_{13} will be stated.

2. Vehicle Equations

For the assembly of bodies shown in Figs. 11 and 13, the vehicle equation (Ref. 1) is:

$$\mathbf{T} = \mathbf{I} \cdot \dot{\boldsymbol{\omega}} + \boldsymbol{\omega} \times \mathbf{I} \cdot \boldsymbol{\omega} + \overset{\circ}{\mathbf{I}} \cdot \boldsymbol{\omega} + \mathcal{M}[\overset{\circ\circ}{\mathbf{c}} + 2\boldsymbol{\omega} \times \overset{\circ}{\mathbf{c}} + \boldsymbol{\omega} \times (\boldsymbol{\omega} \times \mathbf{c}) + \dot{\boldsymbol{\omega}} \times \mathbf{c}] \times \mathbf{c} + \frac{\mathcal{I}d}{dt} \int \mathbf{p} \times \overset{\circ}{\mathbf{p}} \, dm \qquad (1)$$

where

$\mathbf{T}$ = torque applied to vehicle

$\mathbf{I}$ = vehicle inertia dyadic

$\boldsymbol{\omega}$ = angular velocity of B_1 in inertial space

$\mathcal{M}$ = total vehicle mass

$\mathbf{c}$ = mass center shift vector

$\mathcal{I}$ = an inertial reference frame

$\mathbf{p}$ = position vector of a generic point of the vehicle with respect to 0

dm = differential element of mass

$(\cdot)$ = derivative of a vector or dyadic in $\mathcal{I}$, or the derivative of a scalar

$(\circ)$ = derivative of a vector or dyadic in $\mathbf{b}$, a reference frame in which the unit vectors $\mathbf{b}_1, \mathbf{b}_2, \mathbf{b}_3$ are fixed

In more detail, the matrix form of the vehicle equation is:

$$T = \left[I^* + \sum_{i=2}^{13} (-M_i \, \widetilde{p}^{i*} \widetilde{p}^{i*} + T^{iT}I^i T^i) \right] \dot{\omega} + \widetilde{\omega} \left[I^* + \sum_{i=2}^{13} (-M_i \, \widetilde{p}^{i*} \widetilde{p}^{i*} + T^{iT}I^i T^i) \right] \omega$$

$$+ \, [2M(\Sigma_{E0}R + r)^T q - Rq^T M \Sigma_{E0} - \Sigma_{E0}^T MqR^T - r^\dagger (Mq)^{\dagger T} - (Mq)^\dagger r^\dagger + \Sigma_{0E}^T (\widetilde{q}M - M\widetilde{q}) \Sigma_{0E}] \dot{\omega}$$

$$+ \left\{ - \sum_{i=2}^{13} M_i [\dot{\widetilde{p}}^{i*} \widetilde{p}^{i*} + (\dot{\widetilde{p}}^{i*} \widetilde{p}^{i*})^T] + \sum_{i=2}^{13} (\dot{T}^{iT}I^i T^i + T^{iT}I^i \dot{T}^i) \right\} \omega$$

$$+ \, \mathcal{M}(\ddot{c} + 2\widetilde{\omega}\dot{c} + \widetilde{\omega}\widetilde{\omega}c + \dot{\widetilde{\omega}}c)\widetilde{}c$$

$$+ \sum_{i=2}^{13} [M_i (\widetilde{p}^{i*} \ddot{\widetilde{p}}^{i*} + \widetilde{\omega}\widetilde{p}^{i*} \dot{p}^{i*}) + (\dot{T}^{iT}I^i T^i + T^{iT}I^i \dot{T}^i + \widetilde{\omega}T^{iT}I^i T^i)\omega^i + T^{iT}I^i T^i \dot{\omega}^i]$$

$$+ \, (\widetilde{\omega}R)\widetilde{}\Sigma_{E0}^T M\dot{q} + \widetilde{R}\Sigma_{E0}^T M\ddot{q} + \widetilde{R}\widetilde{\omega}\Sigma_{E0}^T M\dot{q} + \Sigma_{E0}^T \widetilde{r}M\ddot{q}$$

$$+ \, \Sigma_{0E}^T M\ddot{q} + \widetilde{\omega}\,\Sigma_{0E}^T M\dot{q} - \widetilde{\omega}\Sigma_{E0}^T \widetilde{r}M + \Sigma_{0E}^T M(\Sigma_{0E}\omega)\widetilde{}\dot{q}$$

$$- \, \Sigma_{E0}^T (\widetilde{r}\Sigma_{E0}\omega)\widetilde{}M\dot{q} + \Sigma_{0E}^T \dot{\widetilde{q}}M \Sigma_{0E}\omega + \widetilde{\omega}\Sigma_{0E}^T \widetilde{q}M \Sigma_{0E}\omega - \widetilde{\omega}\Sigma_{0E}^T M\widetilde{q}\Sigma_{0E}\omega$$

$$+ \, \widetilde{\omega}\{2[M(\Sigma_{E0}R + r)]^T q - Rq^T M \Sigma_{E0} - \Sigma_{E0}^T MqR^T - r^\dagger (Mq)^{\dagger T} - (Mq)^\dagger r^{\dagger T}\} \omega$$

$$+ \, \{2[M(\Sigma_{E0}R + r)]^T \dot{q} - R\dot{q}^T M \Sigma_{E0} - \Sigma_{E0}^T M\dot{q}R^T - r^\dagger (M\dot{q})^{\dagger T} - (M\dot{q})^\dagger r^{\dagger T}\} \omega \tag{2}$$

where

$T =$ applied torque matrix

$I^* =$ inertia matrix for B_1 and A in the undeformed state

$M_i =$ mass of B_i

$p^{i*} =$ position vector of P_i^*, the mass center of B_i, with respect to 0

$T^i =$ transformation matrix from principal axes of B_i to principal axes of B_1

$I^i =$ inertia matrix for B_i

$\omega =$ angular velocity of B_1 in $\mathcal{J}$

$M =$ mass matrix for A

$R =$ position vector of a point Q on the appendage B_1 interface with respect to 0

$r =$ position vector of the mass center of a sub-body of A with respect to Q

$q =$ deformation coordinate vector for A

$\Sigma_{E0} =$ the matrix $[E \, 0 \, E \, 0 \, \cdots \, E \, 0]^T$ of size $6n \times 3$ where E is the 3×3 identity matrix

$\Sigma_{0E} =$ the matrix $[0 \, E \, \cdots \, 0 \, E]^T$

$c =$ mass center shift vector

$\sim =$ when applied to a 3×1 vector, $v = [v_1 v_2 v_3]^T$, $\widetilde{v}$ means

$$\begin{bmatrix} 0 & -v_3 & v_2 \\ v_3 & 0 & -v_1 \\ -v_2 & v_1 & 0 \end{bmatrix}$$

when applied to a $2n \times 3$ matrix, $v = [v^1 0 v^2 0 \cdots v^n 0]^T$, where v^i is a 3×1 vector, $\widetilde{v}$ means

$$\widetilde{v} = \begin{bmatrix} \widetilde{v}^1 & & & & & & \\ & 0 & & & & & \\ & & \widetilde{v}^2 & & & & \\ & & & 0 & & & \\ & & & & \cdot & & \\ & & & & & \cdot & \\ & & & & & & \widetilde{v}^n \\ & & & & & & & 0 \end{bmatrix}$$

$(\ )^T =$ the transpose of a matrix

$(\ )^\dagger =$ if $v = (v^1 0 v^2 0 \cdots v^n 0)^T$, then $v^\dagger = (v^1 0 v^2 0 \cdots v^n 0)$

An expression for c is

$$c = - \frac{1}{\mathcal{M}} \left(\Sigma_{E0}^T Mq + \sum_{i=2}^{13} M_i \delta^i \right) \tag{3}$$

where δ^i is the displacement vector for B_i.

If engines B_2, B_3, and B_4 are thrusting at the constant level F, and there are no disturbance torques exerted on the vehicle other than from the thrust, then

$$T = \left\{ p^{2*0} + \frac{1}{\mathcal{M}} \left[(\mathcal{M} - m)r^1 + (\mathcal{M} - \bar{m})r^2 - \Sigma_{E0}^T Mq \right] \right\}^{\sim} \begin{bmatrix} 0 \\ 0 \\ F \end{bmatrix}$$

$$+ \left\{ p^{3*0} + \frac{1}{\mathcal{M}} \left[(\mathcal{M} - m)r^1 + (\mathcal{M} - \bar{m})r^2 - \Sigma_{E0}^T Mq \right] \right\}^{\sim} \frac{1}{2^{1/2}} \begin{bmatrix} Fs_3 \\ -Fs_3 \\ 2^{1/2} Fc_4 \end{bmatrix}$$

$$+ \left\{ p^{4*0} + \frac{1}{\mathcal{M}} \left[(\mathcal{M} - m)r^1 + (\mathcal{M} - \bar{m})r^2 - \Sigma_{E0}^T Mq \right] \right\}^{\sim} \frac{1}{2^{1/2}} \begin{bmatrix} Fs_4 \\ -Fs_4 \\ 2^{1/2} Fc_4 \end{bmatrix} \tag{4}$$

where

p^{i*0} = position vector of P_i^*, the mass center of B_i, with respect to 0 for the nominal state

$m = \sum_{i=2}^{13} Mi$

$\bar{m} = M_2 + M_3 + M_4 + M_{11} + M_{12}$

$r^1 = [-r\alpha_5 \ 0 \ 0]^T$

$r^2 = [0 - r\alpha_s \ 0]^T$

α_i = the angle through which B_i turns relative to B_1

$s_i = \sin \alpha_i$

$c_i = \cos \alpha_i$

3. Appendage Equations

The appendage equation is taken directly from Ref. 1, Eqs. (94) and (95).

$$M(E - \Sigma_{E0}\Sigma_{E0}^T M/\mathcal{M})\ddot{q} + \left\{ 2M \left[(\Sigma_{E0}\omega)^{\sim} - \Sigma_{E0}\tilde{\omega}\Sigma_{E0}^T \frac{M}{\mathcal{M}} \right] + M(\Sigma_{0E}\omega)^{\sim} + (\Sigma_{0E}\omega)^{\sim}M - [M\Sigma_{0E}\omega]^{\sim} + D' \right\} \dot{q}$$

$$+ \left\{ M(\Sigma_{0E}\dot{\omega})^{\sim} - (M\Sigma_{0E}\dot{\omega})^{\sim} - (\Sigma_{0E}\omega)^{\sim}(M\Sigma_{0E}\omega)^{\sim} + (\Sigma_{0E}\omega)^{\sim}M(\Sigma_{0E}\omega)^{\sim} + M \left[(\Sigma_{E0}\dot{\omega})^{\sim} - \Sigma_{E0}\tilde{\dot{\omega}}\Sigma_{E0}^T \frac{M}{\mathcal{M}} \right] \right.$$

$$\left. + M \left[(\Sigma_{E0}\omega)^{\sim}(\Sigma_{E0}\omega)^{\sim} - \Sigma_{E0}\tilde{\omega}\tilde{\omega}\Sigma_{E0}^T \frac{M}{\mathcal{M}} \right] + K \right\} q = - M\Sigma_{0E}\dot{\omega} - (\Sigma_{0E}\omega)^{\sim}M(\Sigma_{0E}\omega) - M\left\{ \Sigma_{E0} \left[\theta\ddot{x} - (\tilde{R} + \tilde{e})\dot{\omega} \right. \right.$$

$$\left. \left. + \ddot{e} - 2\dot{e}\omega + \tilde{\omega}\tilde{\omega}(R + e) \right] - \tilde{r}\Sigma_{E0}\dot{\omega} - (\Sigma_{E0}\omega)^{\sim}(\Sigma_{E0}\omega)^{\sim}r \right\} + \lambda \tag{5}$$

where the new symbols mean

D' = damping matrix

K = stiffness matrix

$\theta\ddot{x}$ = acceleration of 0 in $\mathcal{I}$ expressed in terms of $\{b\} = [b_1 b_2 b_3]^T$

λ = forces and torques, other than from structural interactions which are applied to the sub-bodies

4. Rigid Body B_i $(i = 2, \cdots, 13)$ Equations

The units $B_2, \cdots, B_{13}$ constitute the translator. Equations for the coordinates associated with its translation and the gimballing of B_3 and B_4 are required. It appears as if the use of Lagrange equations provides the most convenient means of determining these equations. The standard form for these equations is:

$$\frac{d}{dt}\left(\frac{\partial L}{\partial \dot{y}_i}\right) - \frac{\partial L}{\partial y_i} = Q_i \tag{6}$$

where L is the Lagrangian for the spacecraft, y_i is a generalized coordinate, and Q_i is the generalized force corresponding to y_i. The L is

$$L = K - P \tag{7}$$

where K and P are the kinetic and potential energies, respectively, of the spacecraft. Equations (2) and (3) govern the behavior of ω and q. In using Eq. (6), then, we will restrict our attention to coordinates other than ω and q.

The following assumptions are made for the translator assembly (Figs. 13 and 14):

(1) For the translator assemblies, friction is associated only with the motor rotor.

(2) For the translator assemblies, only the output shaft (flexspline) has non-infinite stiffness.

(3) For the translator assemblies, only the rotor, the large gear associated with the harmonic drive, and the output drum masses and inertias will be considered.

(4) For the gimballing assemblies, only the motor rotor and engine masses and inertias will be considered.

(5) Friction will be associated with the motor rotor only.

(6) Non-infinite stiffness is associated only with tapes which cause B_3 and B_4 to gimbal.

(7) All bearings except the gimballing bearings are smooth.

(8) All gear contacts are smooth.

(9) The mass centers of B_3 and B_4 lie on their gimbal axes.

(10) The rails are not smooth.

The nonlinear equations of motion for α_3, α_4, α_5, α_7, α_8, α_{10}, α_{11}, and α_{12} are

$$I_1^3\left[\ddot{\alpha}_3 + \frac{1}{2^{\frac{1}{2}}}(\dot{\omega}_1 + \dot{\omega}_2)\right] - (I_3^3 - I_1^3)\left[\frac{1}{2^{\frac{1}{2}}}c_3(\omega_1 - \omega_2) - s_3\omega_3\right]\left[\frac{1}{2^{\frac{1}{2}}}s_3(\omega_1 - \omega_2) + c_3\omega_3\right] - K\left(\frac{\alpha_{11}}{\nu_3} - \alpha_3\right) = -d_3\alpha_3$$

$$\tag{8}$$

$$I_1^3\left[\ddot{\alpha}_4 + \frac{1}{2^{\frac{1}{2}}}(\dot{\omega}_1 + \dot{\omega}_2)\right] - (I_3^3 - I_1^3)\left[\frac{1}{2^{\frac{1}{2}}}c_4(\omega_1 - \omega_2) - s_4\omega_3\right]\left[\frac{1}{2^{\frac{1}{2}}}s_4(\omega_1 - \omega_2) + c_4\omega_3\right] - K\left(\frac{\alpha_{12}}{\nu_3} - \alpha_4\right) = -d_4\alpha_4$$

$$\tag{9}$$

$$(mr^2 + I_3^5)\ddot{\alpha}_5 - mrE^{1T}\theta\ddot{x} - \mu r\dot{\omega}_2 + I_3^5\dot{\omega}_3 - \overline{m}r^2(\dot{\omega}_3\alpha_8 + \omega_3\dot{\alpha}_8) - (\omega_2^2 + \omega_3^2)(mr^2\alpha_5 - 2M_7p_1^{70}) + \overline{m}r^2\omega_1\omega_2\alpha_8 - \mu r\omega_3\omega_1$$

$$- \overline{m}r^2\omega_3\dot{\alpha}_8 - mr(E^{3T}\omega_2 - E^{2T}\omega_3)\theta\dot{x} - k\left(\frac{\alpha_7}{\nu_1\nu_2} - \alpha_5\right) + \frac{m^3}{\mathfrak{M}^2}r^2\ddot{\alpha}_5 + \frac{m^2\overline{m}}{2}r^2\ddot{\alpha}_8 + \frac{m^2}{\mathfrak{M}}rE^{1T}(\theta\dot{x} + \theta\ddot{x}) - mr\dot{c}_1^A$$

$$- 2\frac{m^2}{\mathfrak{M}}r^2\ddot{\alpha}_5 + \frac{mr\mu}{\mathfrak{M}}\dot{\omega}_2 + \frac{m}{\mathfrak{M}}r^2\overline{m}(\dot{\omega}_3\alpha_8 + \omega_3\dot{\alpha}_8) + \frac{m^2r}{\mathfrak{M}}\ddot{c}_1^A + mr\omega_3\dot{c}_2^A - mr\omega_2\dot{c}_3^A + \left(\frac{\overline{m}m}{\mathfrak{M}}\right)r^2\omega_3\dot{\alpha}_8 - mr(\dot{\omega}_2c_3^A + \omega_2\dot{c}_3^A)$$

$$- \dot{\omega}_3c_2^A - \omega_3\dot{c}_2^A) + \frac{m\overline{m}}{\mathfrak{M}}r^2(\dot{\alpha}_8\omega_3 + \alpha_8\dot{\omega}_3) + \frac{m^2r}{\mathfrak{M}}(\dot{\omega}_2c_3^A + \omega_2\dot{c}_3^A - \dot{\omega}_3c_2^A - \omega_3\dot{c}_2^A) + \frac{m^2r}{\mathfrak{M}}(-\omega_3E^{2T}\theta\dot{x} + \omega_2E^{3T}\theta\dot{x})$$

$$+ \frac{\overline{m}m}{\mathfrak{M}}r^2\dot{\alpha}_8\omega_3 + mr\omega_3(\omega_3c_1^A - \omega_1c_3^A) - mr\omega_2(\omega_1c_4^A - \omega_2c_1^A) + \frac{2m^2}{\mathfrak{M}}r^2\alpha_5\omega_3^2 + \frac{m\mu r}{\mathfrak{M}}\omega_1\omega_3 - \frac{m\overline{m}}{\mathfrak{M}}r^2\alpha_8\omega_1\omega_2 + \frac{2m^2}{\mathfrak{M}}r^2\alpha_5\omega_2^2$$

$$-\frac{m\overline{m}}{\mathfrak{M}}r^2\omega_2\omega_1 - \frac{m^2}{\mathfrak{M}}r\dot{c}_2^A\omega_3 + \frac{m^2}{\mathfrak{M}}r\dot{c}_3^A\omega_2 - \frac{m^2r}{\mathfrak{M}}(\omega_3c_1^A - \omega_1c_3^A)\omega_3 + \frac{m^2r}{\mathfrak{M}}(\omega_1c_2^A - \omega_2c_1^A)\omega_2 - \frac{2m^3}{\mathfrak{M}^2}r^2\alpha_5\omega_3$$

$$-\frac{2m^3}{\mathfrak{M}^2}r^2\alpha_5\omega_2^2 + 2\frac{m^2\overline{m}}{\mathfrak{M}}\alpha_8\omega_1\omega_2 = -\frac{rF}{2^{1/2}}(s_3 + s_4) - d_1r^2\dot{\alpha}_5 \tag{10}$$

$$\left(I_3^7 + \frac{I_3^6}{\nu_2^2}\right)\ddot{\alpha}_7 + \left(I_3^7 - \frac{I_3^6}{\nu_2}\right)\dot{\omega}_3 + k\left(\frac{\alpha_7}{\nu_1\nu_2} - \alpha_5\right) = -d\dot{\alpha}_7 + T_7 \tag{11}$$

$$(\overline{m}r^2 + I_3^8)\ddot{\alpha}_8 - \overline{m}rE^{2T}\theta\ddot{x} + \overline{\mu}r\dot{\omega}_1 + I_3^8\dot{\omega}_3 + \overline{m}r^2(\dot{\omega}_3\alpha_5 + \omega_3\dot{\alpha}_5) - (\omega_1^2 + \omega_3^2)\overline{m}r^2\alpha_8 + \overline{m}r^2\omega_1\omega_2\alpha_5 - \overline{\mu}r\omega_2\omega_3 - \overline{m}r(E^{1T}\omega_3$$

$$- E^{3T}\omega_1)\theta\dot{x} + \overline{m}r^2\omega_3\dot{\alpha}_5 - k\left(\frac{\alpha_{10}}{\nu_1\nu_2} - \alpha_8\right) + \frac{m\overline{m}^2}{\mathfrak{M}^2}r^2\ddot{\alpha}_8 + \frac{m^2\overline{m}}{\mathfrak{M}^2}r^2\ddot{\alpha}_5 + \frac{m\overline{m}}{\mathfrak{M}}rE^{2T}(\dot{\theta}\dot{x} + \theta\ddot{x}) - \overline{m}r\ddot{c}_2^A$$

$$- \frac{2\overline{m}^2}{\mathfrak{M}}r^2\ddot{\alpha}_8 - \frac{\overline{m}r\mu}{\mathfrak{M}}\dot{\omega}_1 - \frac{\overline{m}m}{\mathfrak{M}}r^2(\dot{\omega}_3\alpha_5 + \omega_3\dot{\alpha}_5) + \frac{m\overline{m}}{\mathfrak{M}}r\ddot{c}_2^A - \overline{m}r\omega_3\dot{c}_1^A + \overline{m}r\omega_1\dot{c}_3^A - \frac{\overline{m}m}{\mathfrak{M}}r^2\omega_3\dot{\alpha}_5$$

$$- \overline{m}r(\dot{\omega}_3c_1^A + \omega_3\dot{c}_1^A - \dot{\omega}_1c_3^A - \omega_1\dot{c}_3^A) - \frac{m\overline{m}}{\mathfrak{M}}r^2(\dot{\alpha}_5\omega_3 + \alpha_5\dot{\omega}_3) + \frac{m\overline{m}}{\mathfrak{M}}r(\dot{\omega}_3c_1^A + \omega_3\dot{c}_1^A - \dot{\omega}_1c_3^A - \omega_1\dot{c}_3^A)$$

$$+ \frac{m\overline{m}r}{\mathfrak{M}}(\omega_3E^{1T}\theta\dot{x} - \omega_1E^{3T}\theta\dot{x}) - \frac{m\overline{m}}{\mathfrak{M}}\dot{\alpha}_5\omega_3 - \overline{m}r\omega_3(\omega_2c_3^A - \omega_3c_3^A) + \overline{m}r\omega_1(\omega_1c_2^A - \omega_2c_1^A)$$

$$- \frac{m\overline{m}}{\mathfrak{M}}r^2\alpha_5\omega_1\omega_2 + \frac{\overline{m}\mu r}{\mathfrak{M}}\omega_2\omega_3 + \frac{2\overline{m}^2}{\mathfrak{M}}r^2\alpha_8\omega_3^2 + \frac{\overline{m}^2}{\mathfrak{M}}r^2\omega_1^2 + \frac{m\overline{m}}{\mathfrak{M}}r\dot{c}_1^A\omega_3 - \frac{m\overline{m}}{\mathfrak{M}}r\dot{c}_3^A\omega_1 + \frac{m\overline{m}r}{\mathfrak{M}}(\omega_2c_3^A - \omega_3c_2^A)$$

$$- \frac{m\overline{m}r}{\mathfrak{M}}(\omega_1c_2^A - \omega_2c_1^A)\omega_1 - \frac{2m\overline{m}r^2}{\mathfrak{M}}\alpha_8\omega_3^2 - \frac{2m\overline{m}^2}{\mathfrak{M}}\alpha_8\omega_1^2 = -\frac{rF}{2^{1/2}}(s_3 + s_4) - d_2r^2\dot{\alpha}_8 \tag{12}$$

$$\left(I_3^{10} + \frac{I_3^9}{\nu_2^2}\right)\ddot{\alpha}_{10} + \left(I_3^{10} - \frac{I_3^9}{\nu_2}\right)\dot{\omega}_3 + k\left(\frac{\alpha_{10}}{\nu_1\nu_2} - \alpha_8\right) = -d\dot{\alpha}_7 + T_{10} \tag{13}$$

$$I_2^{11}\left[\ddot{\alpha}_{11} + \frac{1}{2^{1/2}}(-\dot{\omega}_1 + \dot{\omega}_2)\right] + K\left(\frac{\alpha_{11}}{\nu_3} - \alpha_3\right) = -C\dot{\alpha}_{11} + T_{11} \tag{14}$$

$$I_2^{11}\left[\ddot{\alpha}_{12} + \frac{1}{2^{1/2}}(-\dot{\omega}_1 + \dot{\omega}_2)\right] + K\left(\frac{\alpha_{12}}{\nu_3} - \alpha_4\right) = -C\dot{\alpha}_{12} + T_{12} \tag{15}$$

where

$\omega_i = \mathbf{b}_i \cdot \boldsymbol{\omega}, i = 1,2,3$

$c_i = \cos\alpha_i$

$s_i = \sin\alpha_i$

K = spring constant associated with the gimballing mechanisms

ν_3 = gear ratio associated with the gimballing mechanisms

k = spring constant associated with the translating mechanisms

d = damping constant associated with the translating or gimballing mechanisms

$E^{1T}, E^{2T}, E^{3T} = [1\ 0\ 0],\ [0\ 1\ 0],\ [0\ 0\ 1]$

c_i^A = measure number of mass center shift due to flexibility

ν_1, ν_2 = gear ratios associated with the translating mechanisms

C = damping constant associated with the gimballing mechanisms

$\mu = \Sigma M_i p_3^{i*}$, where p_3^{i*} is the $\mathbf{b}_3$ component of p^{i*0}, the value of p^{i*} for the nominal state

$\overline{\mu} = M_2 p_3^{2*} + M_3 p_3^{3*} + M_4 p_3^{4*} + M_{11} p_3^{11*} + M_{12} p_3^{12*}$

T_i = torque applied to B_i

5. Solution of the Equations of Motion

It can be shown by substitution that

$$\left.\begin{array}{l} \omega = \alpha = \lambda = T_7 = T_{10} = T_{11} = T_{12} = 0 \\[4pt] x = x_o, \theta = \theta_o \\[4pt] q = q_o = -K^{-1}M\Sigma_{E0}\theta_o\ddot{x}_o \end{array}\right\} \quad (16)$$

and

$$x_o = \left[\begin{array}{ccc} 0 & 0 & \dfrac{3F}{\mathfrak{M}}t^2 \end{array}\right]^T$$

is a solution to Eqs. (2), (5), and (8)–(15). Determination of the linearized variational equations associated with this solution and introduction of the active control equations establishes the base for a stability analysis by means of root locus procedures or eigenvalue analyses.

Reference

1. Likins, P. W., *Dynamics and Control of Flexible Space Vehicles*, Technical Report 32-1329, Rev. 1. Jet Propulsion Laboratory, Pasadena, Calif., Jan. 15, 1970.

F. TOPS Inertial Reference Unit, *P. J. Hand*

The baseline design for the Thermoelectric Outer Planet Spacecraft (TOPS) attitude control system specifies an all-digital mechanization. As part of this system, a digital inertial reference unit (IRU) is being developed. The IRU design approach utilizes single-degree-of-freedom, floated, rate-integrating gyros optimized for digital operation which implies active temperature control. In order to conserve power required for gyro-temperature control, a low-thermal loss IRU is under development.

Testing has recently been performed to establish some baseline data for a preliminary version of the TOPS IRU. As a first effort, an existing item of hardware was used for the initial testing. The assembly was originally a prototype IRU design intended for an earlier spacecraft program. Inasmuch as the design concept for that IRU is applicable to the current investigation, it appeared that some valuable data could be obtained from further testing of this unit. The basic design utilizes a highly-polished, low-emissivity inner element containing the gyros and accelerometer, which is isolated from the outer case by plastic spacers. The outer case fits the normal JPL modular hardware packaging configuration. After the inner element was repolished, the unit was reassembled with simulated gyro heat sources. Figure 15 is a photograph of the disassembled IRU.

Testing proceeded in two parts. First, the input power required to hold the gyros at each of three possible operating temperatures, 115, 125, and 135°F, was evaluated as a function of external air temperature in a typical circulating-air temperature chamber (Fig. 16). The package was then placed in a typical equipment case and attached to a temperature-controlled plate in a vacuum chamber. The chamber was evacuated to about 2×10^{-6} torr and the temperature-controlled plate and equipment case were temperature stabilized. The power input to
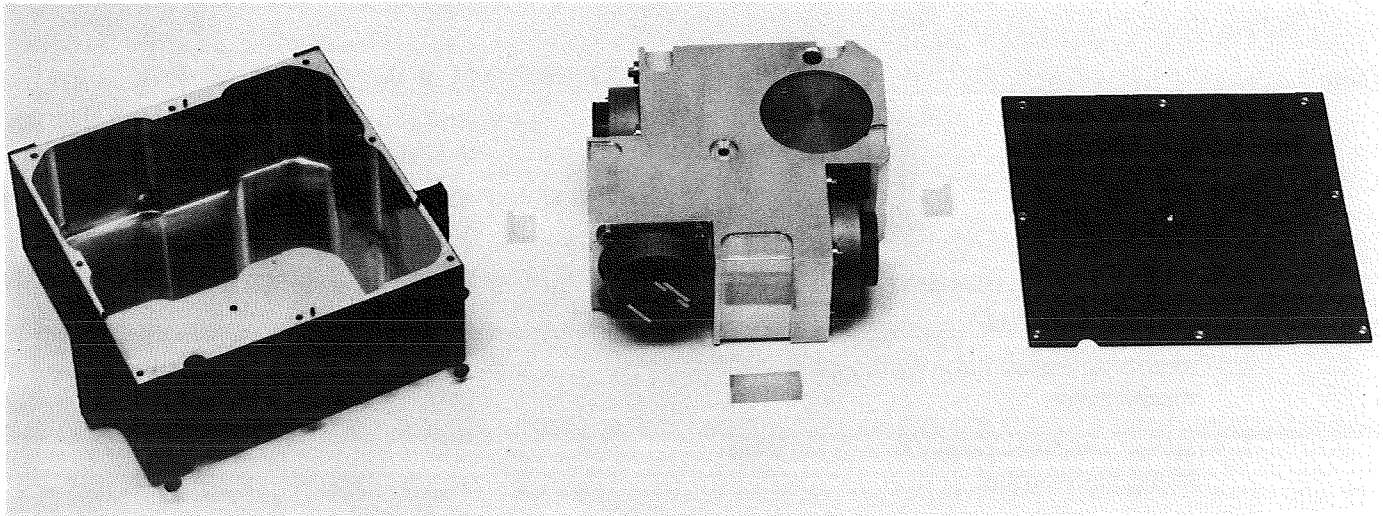

Fig. 15. Disassembled IRU

control the gyros at the same temperatures as before was again measured; the results are presented in Fig. 17.

The expected TOPS gyro-spin motor power input is 4.5 W/gyro. With this fixed minimum power input (13.5 W for three gyros), it can be seen from Figs. 16 and 17 that the existing design will overheat at all present design ambient temperatures when operated in a hard vacuum. This indicates that a new design must be directed toward

a controlled thermal loss package rather than a minimum loss design. This experimental IRU will be modified to provide a somewhat more lossy thermal design and will be subjected to the same tests again. From these iterations, it is anticipated that a starting point for the actual TOPS IRU thermal design can be reached.
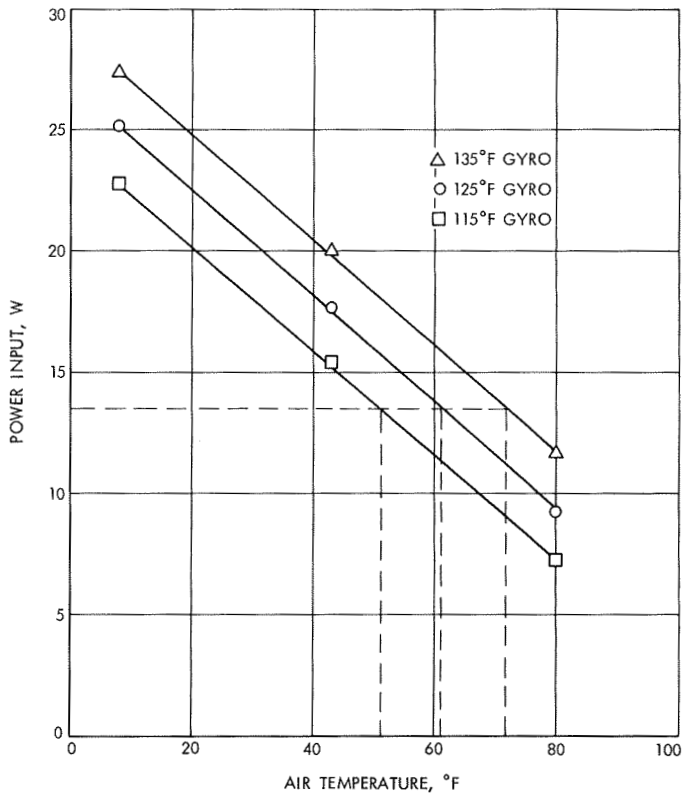
Fig. 16. Inertial reference unit operating in air
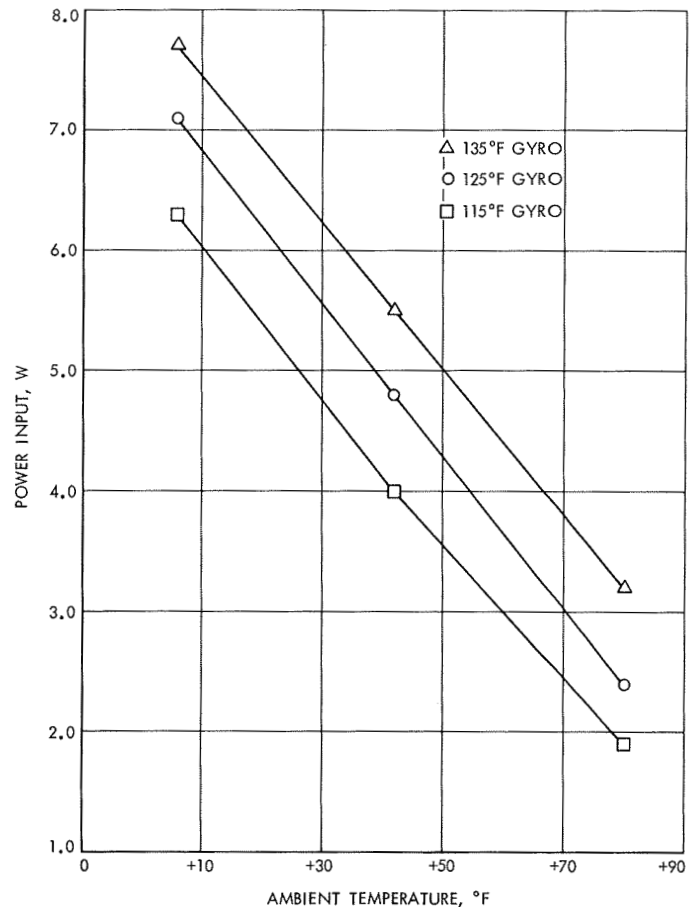
Fig. 17. Inertial reference unit operating in a vacuum

XI. Materials

ENGINEERING MECHANICS DIVISION

A. Development of a Conical–Gregorian High Gain Antenna, J. G. Fisher

1. Introduction

As discussed previously (SPS 37-62, Vol. III, pp. 176–179), doubly curved, rigid surfaces cannot be folded. For this reason, parabolic antennas larger than those that can be designed with petals must use some form of rib-and-mesh design. A number of types have been built, tested, and used, and their technology is fairly well developed. However, all designs with mesh suffer a common problem. Because of chording in both the radial and circumferential directions, the mesh cannot be made to assume a true parabolic shape. In the higher frequency antennas, the deviation from desired shape caused by mesh chording is a large part of the total permissible surface error. The "reverse pillowing" problem can be reduced by using more ribs, but it cannot be eliminated. However, if the main reflector is made conical, furling by simple folding of the surface becomes possible and, at least in theory, the pillowing error can be reduced to zero. The use of a conical main reflector is possible by use of a special

Gregorian subreflector, as previously described (SPS 37-59, Vol. III, pp. 55–57). A prototype model of the conical–Gregorian antenna is being tested (*Chapter VI-A.*) Development of a conical–Gregorian high gain antenna has been started. This article describes the fabrication effort.

2. Basic Configuration

The basic design is shown in Fig. 1. Reduced to elements, the antenna consists of a central hub that carries the feed at its center, and supports radial straight ribs at its periphery. Angled support struts hold the Gregorian subreflector in position. For the antenna to furl to a diameter roughly the size of the subreflector, the ribs must fold inward between the subdish supports. The geometry of the assembly points strongly toward eight ribs and eight, angled, subreflector supports. Figure 2 shows an early assembly. A screw mechanism is provided to permit adjustment and alignment of the subreflector with respect to the antenna axis and feed. Provision is also made to slide the feed axially in the center hub.
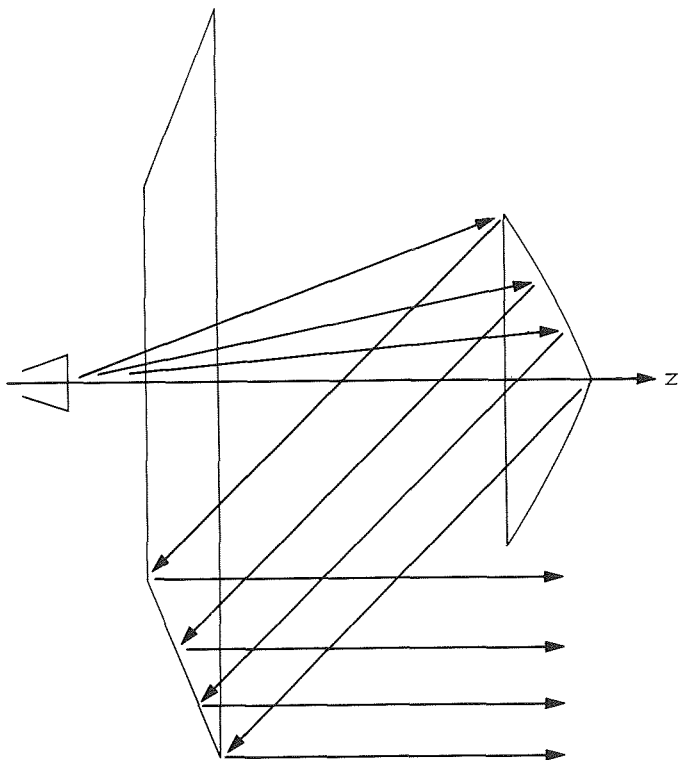
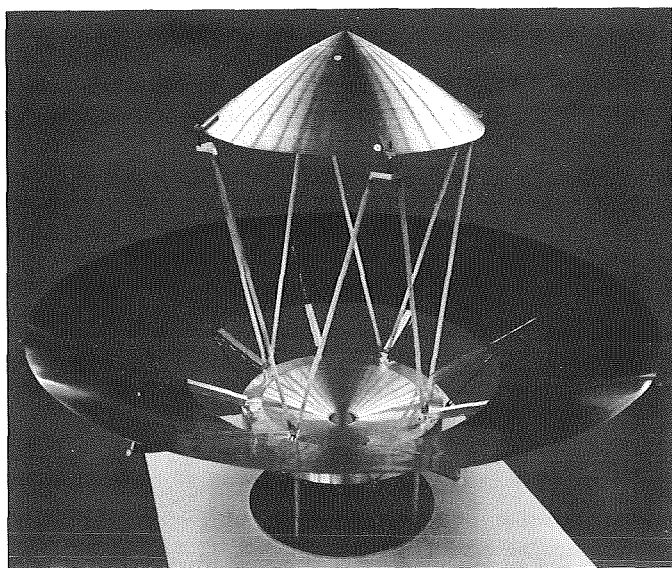**Fig. 1. Conical reflector with Gregorian type of parabolic subreflector**

In this early design, the ribs consisted of aluminum piano hinges, with two aluminum angles bonded to the hinge legs, and this subassembly bonded in turn to the reflector surface, which in the model shown was 0.005-in.-thick, hard-rolled, type 301 stainless steel. Figure 3 shows a cross section of the rib assembly. This design was intended to permit easy bending of the reflector surface during the furling operation without introducing a bend sharp enough to produce plastic deformation. Each of the eight gores was to form a simple "U" as the ribs rotated upward and in between the subdish supports. With deployment, the strain energy in the reflector surface would straighten out the gores, which would assume a true conical surface as the angles met each other and the hinge closed to the position shown in Fig. 3a.

3. Assembly Procedure

To assure that the deployed angle was correct, the rib–gore assembly was done on a precisely jiggered plaster mandrel. At the axis of this mold cone was a steel plug, machined to the feed diameter so that it would position the center hub precisely. The gores were positioned on the plaster surface and taped in position, and were located by scribed radial lines in the mandrel at the rib

Fig. 2. Early 6-ft conical–Gregorian antenna assembly

The supports for the subreflector are thin-wall fiberglass epoxy tubes, and the reflector is an aluminum spinning. The center hub was machined from a solid aluminum plate.

(a) DEPLOYED POSITION
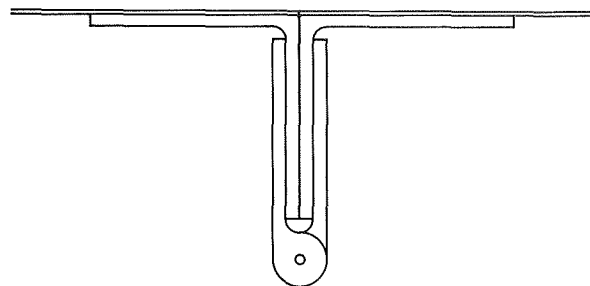
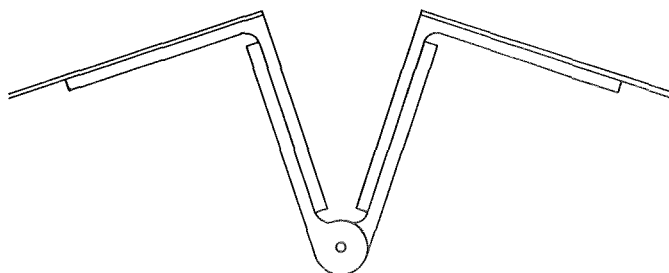(b) PARTLY FURLED POSITION SHOWING SAG FROM GRAVITY

Fig. 3. Early rib assembly

positions. The ribs were held down with lead shot bags during the bonding operation (Fig. 4). Heat lamps were positioned to warm the epoxy adhesive and hasten the cure.

This latter step proved to be a mistake. The aluminum rib assemblies, standing away from the mandrel surface, warmed rapidly, while the stainless steel surface material was kept cool by the massive plaster mandrel. The ribs expanded, and the epoxy adhesive set up. On cooling to room temperature, the stainless reflector surface was rather wrinkled at the rib bonds. Worse, as the main reflector assembly was lifted vertically from the mandrel, the stainless steel surface would not retain its conical shape in the 1-g field. Even in the face-up position the rib hinges sagged open (Fig. 3b) and the reflector surface deformed to accommodate the distortion. While the antenna probably would have been good in a zero-g field, there was no convenient way to run the RF tests in a 1-g field. Two models would be needed: one for RF evaluations, and another for furling tests.

4. RF Test Model

The first step toward rigidifying the reflector surface was to introduce braces from the hub to each rib, with turnbuckles for adjustment. These braces, which can be seen in Fig. 2, would serve also to hold the hinges closed and prevent sagging. However, even with the braces, the
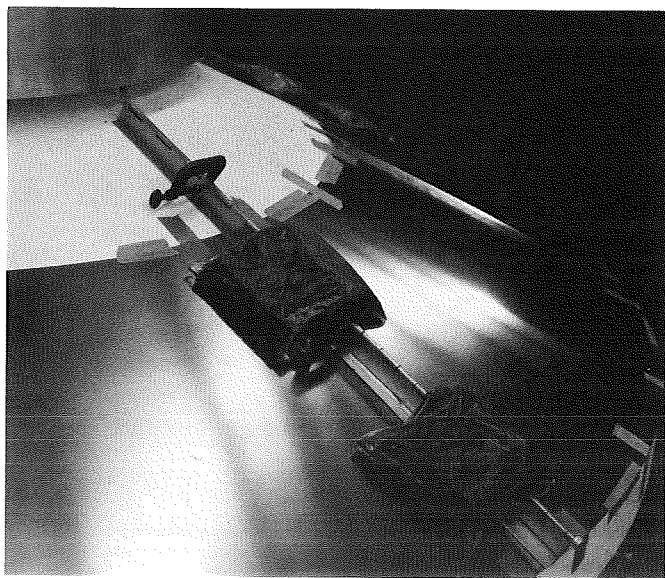
Fig. 4. Partly assembled antenna showing clamps and shot bags during bonding operation

stainless steel surface sagged appreciably when the antenna was rotated to a horizontal position, as would be needed for RF testing. Therefore, a second antenna was assembled and rigidified with a lightweight foam. The reflector surface for the second unit would be a composite glass cloth–epoxy material bearing a half-mil layer of copper. The total thickness of this new material was between 0.008 and 0.010 in. It also would sag with gravity, but it was to be reinforced with 4 lb/ft³ polyurethane foam sprayed on the back surface. Test samples sprayed on cardboard appeared satisfactory, but as a precaution against the deformation of shrinkage the spraying was done in several layers. The foam was free to expand, and it was believed that distortion should be minimal. Figure 5 shows the antenna on its mold after the spraying operation and before the masking and excess foam were removed. Figure 6 shows the completed assembly mounted for testing. As a stiffening agent, the foam was a complete success. As a distortion preventive, it was not. Considerable shrinkage occurred, pulling the glass–epoxy reflector surface away from the plaster mandrel, and producing an effect similar to reverse pillowing in mesh antennas. A straightedge laid on elements of the conical surface indicated a distortion of as much as 0.100 in. Nonetheless, an RF test was decided upon. The subreflector was mounted on the center hub, and aligned with a plumb bob, cross threads, and a steel scale. The assembly was turned over to the Telecommunications Division for testing. In these tests the antenna behaved in an entirely predictable manner, with a remarkably symmetrical pattern. It was quite insensitive to changes in subreflector-to-main-reflector distance, and showed considerable promise. Further development of furling capability was decided upon.

5. Furling Development

It had become apparent from the first experiments that the rib configuration with an offset hinge, while theoretically good in a zero-g field, was practically unworkable on earth. To avoid sagging, the hinge pins should be in radial line elements of the conical reflector surface. To test this idea with minimum expense, the original 0.005-in.-thick stainless steel gores and the original ribs with the angles removed were reassembled on the mandrel. Double-backed tape was used to cover the hinge pin and avoid filling with adhesive, which would rigidify the joint. This ploy was successful, but afterward the tape proved difficult to remove. After mounting the subreflector, an attempt was made to furl the antenna. Figure 7 shows the result. The surface furled as expected, and would open out without assistance except for the 1-g
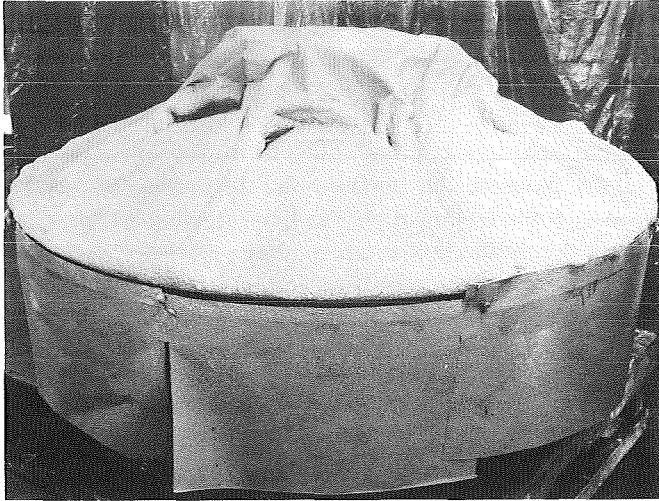
Fig. 5. Main reflector of antenna after rigidifying surface with sprayed foam. Excess foam and masking not yet removed
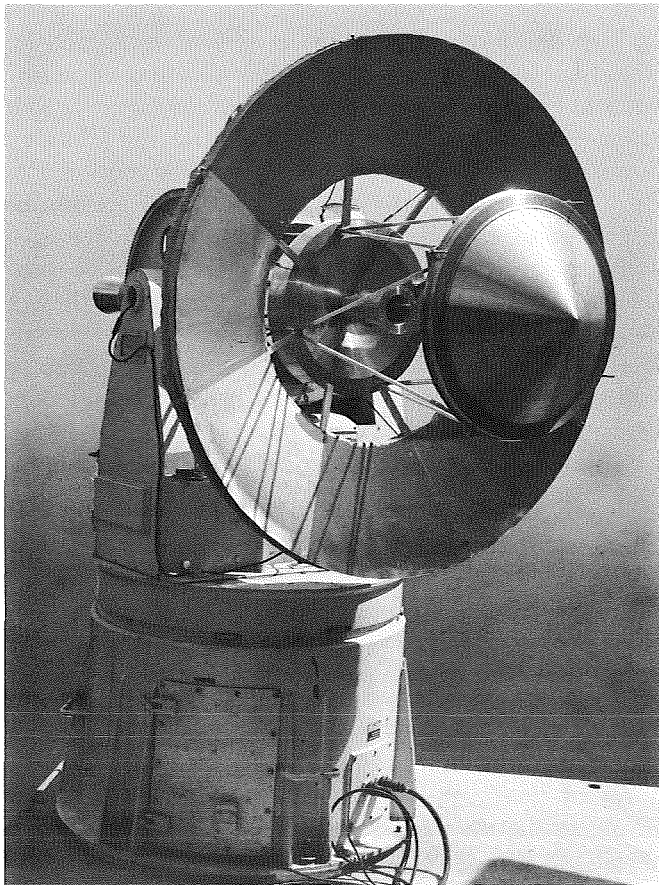

Fig. 6. Foam-rigidified antenna positioned on mount for RF testing
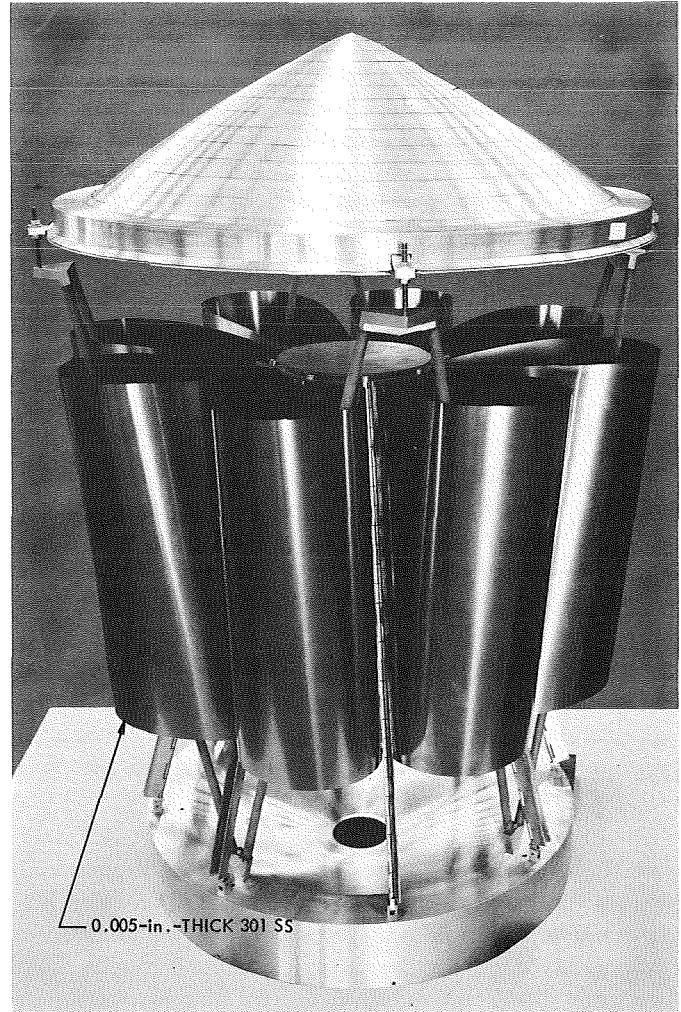

0.005-in.-THICK 301 SS

Fig. 7. Furled antenna

field. Because the surface still sagged when rotated from the antenna axis vertical position, some compromise with gravity was necessary. The furled shape indicated that a 0.020-in.-thick 2024-T3 aluminum, which has only about a third the density and modulus of elasticity as stainless steel, might work acceptably. On the one hand, increasing the thickness by a factor of four would greatly increase the stiffness, and rough experiments indicated that it might hold its shape. On the other hand, more strain energy would be stored in the furled condition, so that some means of controlling deployment rate might be needed. Careful inspection of the stainless steel surface in the deployed condition indicated that the ribs were sagging somewhat and the gores were flattening; instead of a true circular cone, there was a tendency toward an octagonal shape. This effect could be minimized by curving the gores to the conical shape before bonding them, to minimize bending loads across the hinges.

6. Future Development

The fabrication of a new set of gores with the 0.020-in.-thick 2024-T3 material has been started. The gores will be precurved. A positive actuating mechanism to control deployment and to position and lock the ribs when they are fully open may be necessary. Preliminary design of this mechanism has begun.

B. Spacecraft Adhesives for Long Life and Extreme Environments, *W. Roper*

1. Introduction

Future planetary exploration will require spacecraft with their scientific payloads to function in environmental extremes and for missions lasting far longer than those that have been attempted. The outer planet Grand Tour missions are typical of these future missions. In these flights, extreme cold ($-375°F$) for periods extending to 12 yr are expected. Although parts of the spacecraft will be thermally controlled for satisfactory operation of, for example, electronics, some external components (antenna, structure) will nevertheless be subjected to the full temperature extreme.

At the other end of the temperature scale, near-sun missions (Mercury, Venus, solar probes) will require the spacecraft to function in high temperature environments. Components such as sun sensors, thermal shields, and solar panels will be required to function for extended periods at temperatures above $400°F$. Also large and rapid thermal transients will probably be encountered, particularly during periods of sun occultation and spacecraft maneuvers.

These new environments will impose extremely high demands on the spacecraft materials, particularly on the adhesive materials that are widely used within the spacecraft in both structural and nonstructural applications. An extremely long life and a high reliability will be demanded of these materials in the new environmental extremes.

To select those adhesive systems that can meet the rigorous performance expected for future planetary missions, a two-phase approach was undertaken. In the first phase, a general review was made to establish the new polymer systems and, of these, which have potential as adhesive materials. The review included not only the published literature, but contact with many of the researchers in the field and the many commercial producers of adhesive materials. From this phase, adhesive materials which showed potential for spacecraft use were selected. In the second phase, the materials selected will be given limited laboratory testing to further characterize them as potential spacecraft adhesives. The test conditions will simulate those to be encountered in future planetary missions. Some testing of physical and mechanical properties will determine performance after prolonged exposure to elevated and cryogenic temperatures and performance under conditions of high thermal shock. The information and data obtained will greatly assist in the selection of materials for future spacecraft.

2. Phase I: Adhesive Materials Review

The initial survey phase of this work unit was started at the beginning of FY 1970 and candidate spacecraft adhesives have been selected. A thorough literature survey was made, and over 40 research and commercial organizations concerned with new materials and adhesives development were contacted. The results of Phase I work are summarized in the following discussion.

A high performance adhesive, as defined in this article, is one that exhibits long-term (1000 h or more) performance at temperatures above $450°F$ and, in the cryogenic region, $-320°F$ and lower. The ability of the adhesive to exhibit such a performance depends largely on the intrinsic properties of the basic polymer that constitutes most of the adhesive. Sometimes the minor constituents—stabilizers, plasticizers—may also be important in producing the high performance of a particular adhesive system. However, for achieving performance in the more severe space environments, the use of these minor additives becomes more and more restrictive and ultimately is completely precluded. The basic characteristics of the primary polymeric material is therefore of fundamental and major importance.

A review of some of the general features of the more recent polymer systems is of interest in determining future high performance spacecraft adhesives. Table 1 (Refs. 1–14) lists some of the newer polymeric materials that have been researched during the last decade. Some of these have achieved commercial availability while others have been dropped or are under current research. In recent years, the so-called ladder and semiladder polymers—the new generation of polymers—have been extensively investigated. These polymers possess inherently rigid chains and are formed by the linking of aromatic or heterocyclic rings. Although the polymers are essentially linear, some crosslinking does occur. These

materials are prime candidates for high temperature adhesive applications, as they possess high glass transition temperatures and exhibit no discrete melting point. Table 1 shows that glass transition temperatures ranging from 500 to 900°F are typical of these materials. The polymers show inherent potential for stability to thermal decomposition. The aromatic and heterocyclic rings contribute to high resonance bond energies and, consequently, high resistance to thermal degradation and decomposition. Table 1 shows some typical thermogravimetric analysis data on these polymers which indicate their high thermal stability.

Some efforts are being made to develop the inorganic or semiorganic polymers. Investigation of these materials has been promoted by the high thermal stability achieved in the past with the silicon polymers. Bond energy considerations indicate that greater thermal stability can be ultimately achieved with inorganic polymers (which involve ionic bonding) than with organic polymers (involving covalent bonding).

Table 1 shows two typical semiorganic polymers—the carboranylene-siloxanes and the diazadiphosphetidines.

The former is a boron-silicon linear polymer (Refs. 12, 13) that is commercially available as an elastomeric material (Dexsil), and the latter is a complex organophosphorous resin (Ref. 14) that is a developmental material.

In general, the newer semiorganic polymers cannot be considered for spacecraft adhesive use because of the need for further development. In the future, however, they may prove to be excellent candidates for spacecraft adhesives.

For performance as adhesives in cryogenic environments, the RTV silicones and the polyurethanes have been widely used materials. The methyl–phenyl RTV silicones have been evaluated at temperatures as low as $-423°F$ (Ref. 15); however, their normal long-term operating range has been limited to -160 to $+400°F$ where elastomeric properties are required. Adhesive lap shear strength is reported to be unchanged between room temperature and $-423°F$. At room temperature, test specimen failures are cohesive, whereas at $-423°F$ failures are adhesive. Embrittlement of the materials is therefore evidenced at the cryogenic temperatures. These

Table 1. Some recently researched polymeric materials. Typical thermal properties

Polymer systems	Structural class	Glass transition temperature (Tg), °F	Polymer softening/ Melting temperature (approx), °F	TGA data,[a] °F	Reference
(1) Aromatic polysulphone	Simple linear	$-150, 375$	660–750	930–1020	(2)
(2) Aromatic polyamide-imide (AI)	Semiladder	510	750	750[b]	(1)
(3) Polybenzimidazole (PBI)		$-94, 590, 806$	Decomposes	480	(1, 3)
(4) Polybenzothiozole (PBS)		550		1110	(4)
(5) Polybenzoxazole (PBO)		775–815		750–1110	(5)
(6) Aromatic polyimide (PI)		510–725		710–785	(1, 6)
(7) Polyquinoxaline (PQ)		720–735		930	(7)
(8) Polyphenylquinoxaline (PPQ)		755–810		1020	(7)
(9) Polyimidazoquinazoline (PIQ)		—	Decomposes	600[c]	(9)
(10) Polyiminobenzoxazole		—	347–436	750[b]	(8)
(11) Polyiminobenzothiazole	Semiladder	—	300–390	570[b]	(8)
(12) Polyimidazopyrrolone (PIP, Pyrrone)	Ladder	885	Decomposes	750–930	(1, 10)
(13) Polyimidazobenzophenanthroline (BBB & BBL)	Ladder	—	Decomposes	750–840	(11)
(14) Carboranylene-siloxane	Simple linear	-30	405	—	(12, 13)
(15) Diazadiphosphetidine	Ladder	—	Decomposes	660–885	(14)

[a]Typical thermogravimetric analysis (TGA) data for representative polymers. Temperatures shown indicate onset of polymer decomposition in air.
[b]TGA data taken in nitrogen.
[c]Temperature for an isothermal weight loss of 4% after 120 h in air.

materials can be considered only in nonstructural adhesive applications because of their limited adhesive shear strength of approximately 500 psi.

Many polyurethane-based adhesives are commercially available and have been widely used in cryogenic environments. Adhesive lap shear strengths in the structural adhesive range (approximately 5000 to 8000 psi) with accompanying high peel strengths have been reported at temperatures as low as $-423°F$ (Ref. 16). However, these materials are limited to a maximum elevated temperature use of approximately 250°F.

It has been found that many of the recent aromatic heterocyclic polymers that have been developed primarily for elevated temperature use also show good cryogenic performance in composites and adhesives. It is believed that a combination of linearity, high density, and high glass transition temperature (T_g), which are consequences of aromatic–heterocyclic structure, make possible a stress release mechanism in these materials at low temperatures (Ref. 17). Not all the polymers listed in Table 1 show potential as adhesive materials. Many can be considered only as laminating resins (for composites) since they are too rigid when cured to be useful as adhesives.

Table 2 (Refs. 18–20) lists the polymers that may be currently considered as potential spacecraft adhesive materials. All are of the aromatic–heterocyclic polymer class. Some are commercially available, and some are only developmental materials. Typical chemical structures of the materials are shown in Fig. 8. As discussed earlier, this class of polymer shows the best promise as high temperature materials. No new semiorganic polymer, which exceeds the performance of the current silicones, is available for consideration as an adhesive material.

Table 2. High performance adhesive materials

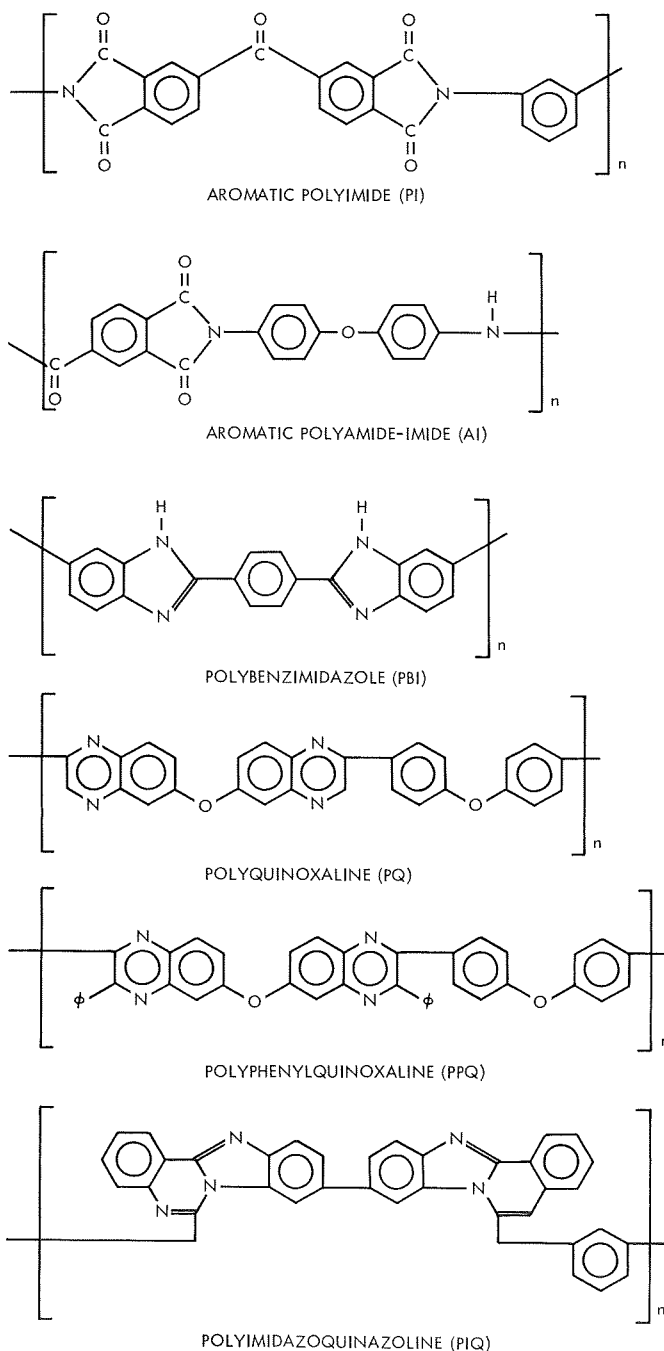| Polymer type	Trade name	Manufacturer/ Developer
Polyimide	FM-34	American Cyanimid (See Ref. 18)
	Metlbond 840	Whittaker-Costa Mesa (See Ref. 19)
	PI-5505	Du Pont[a]
Polyamide-imide	AI-1030	Amoco Chemicals
	AI-1137	(See Ref. 21)
Polybenzimidazole	Imidite 850	Whittaker-Costa Mesa (See Ref. 20)
Polyquinoxaline	PQ (Developmental)	Whittaker-San Diego
Polyphenylquinoxaline	PPQ (Developmental)	Whittaker-San Diego
Polyimidazoquinazoline	PIQ (Developmental)	Whittaker-San Diego
[a]E. I. du Pont de Nemours & Co., Fabric & Finishes Dept., Philadelphia.		

Fig. 8. Typical (idealized) structure of high performance adhesive materials

The polymer types that have already established commercial availability as adhesives are the polyimide (PI), the polyamide-imide (AI), and the polybenzimidazole (PBI). Figures 9 and 10 show typical adhesive lap shear data on these commercial materials and compare their long- and short-term elevated temperature performance. Figure 9 shows clearly the better short-term exposure
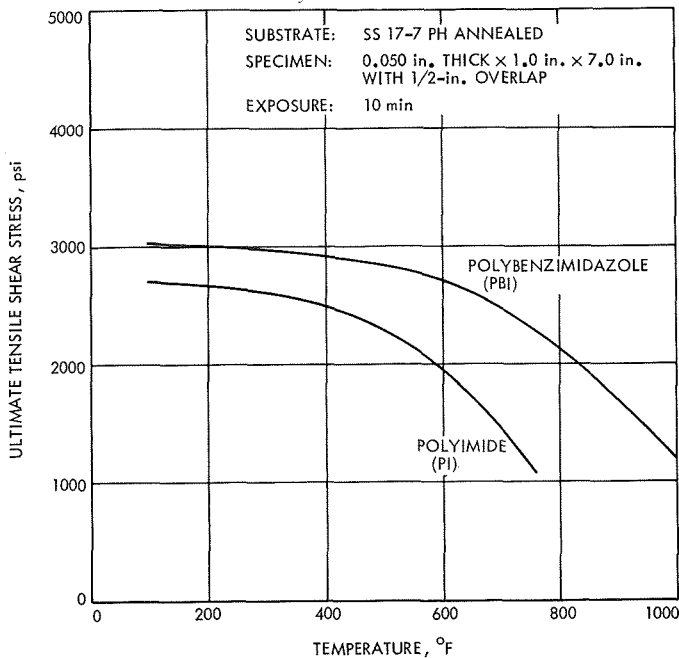
capability of PBI compared with PI. Figure 10 shows the superior aging performance of PI. The main feature of the AI adhesive is its higher initial strength (Fig. 10); however, the AI system is inferior to PI in aging at elevated temperature.

Figure 11 shows lap shear data on a typical PBI adhesive at cryogenic temperatures. In the cryogenic temperature region, as these data indicate, the lap shear strength of PBI tends to increase and finally level to a constant value; PBI apparently remains tough and retains its adhesive qualities. The PBI adhesive is reported to be an excellent cryogenic adhesive (Ref. 20). The commercial PI and PBI materials are commonly supplied as resin-impregnated glass-fabric tapes. At present, the AI material is sold as a liquid resin that must be further processed by the user into an adhesive material. Aluminum powder is generally compounded into the AI resin to improve its thermal performance. The aluminum-filled AI resin can then be processed into an adhesive "prepreg" which is used to form glass fabric reinforced bonds. On the other hand, the resin may be coated directly onto the bonding substrates and cured into unreinforced bonds. The thermal aging properties of all these commercial materials are improved by adding a small amount of antioxidant, such as arsenic pentoxide or arsenic thioarsenate, to the prepolymer.
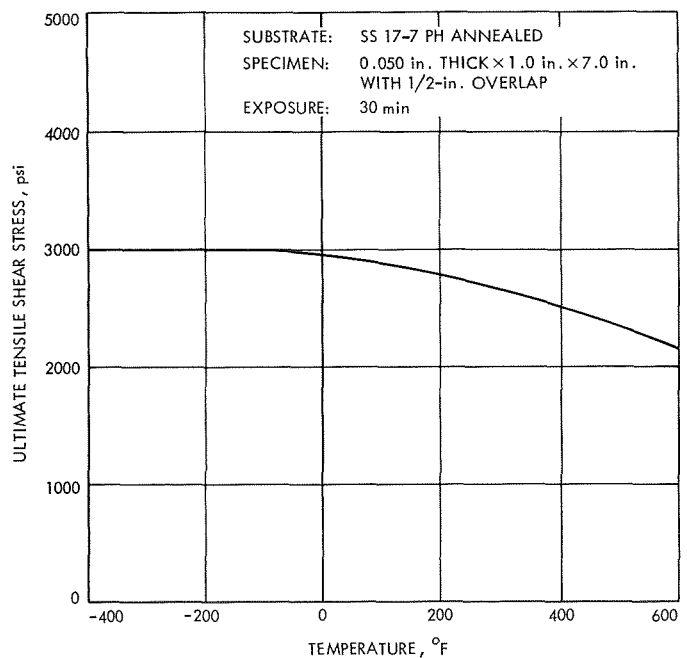

Fig. 9. Comparison of elevated temperature performance of typical polyimide and polybenzimidazole adhesives (Refs. 18, 19)
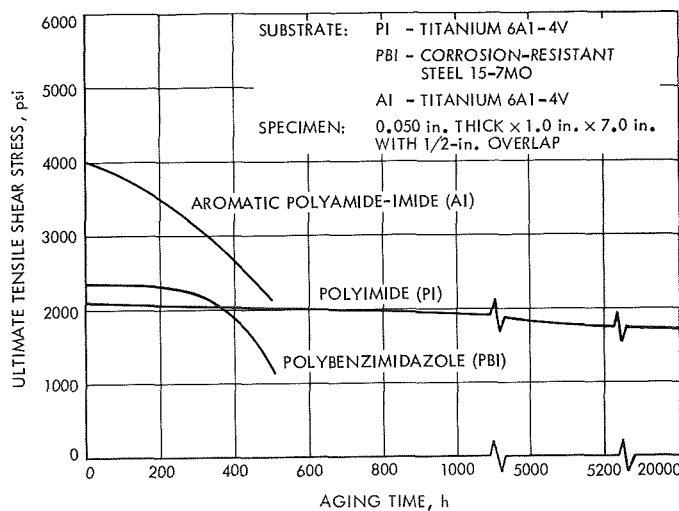
Fig. 10. Comparison of long term aging at 500°F of typical high performance adhesives (Refs. 18, 20, 21)

Fig. 11. Effect of low temperature on polybenzimidazole adhesive strength (Ref. 18)

One of the major problems with all these commercial materials is that their polymerization, or cure, is a condensation type of reaction that results in the evolution of volatile products (i.e., water, phenol). The volatile reaction, if not properly controlled, will result in bonds with high porosity. Perforated substrates are sometimes required to facilitate the removal of such volatile products. Research is at present being undertaken to reduce the amount of volatiles produced with the polyimide system. One improved PI imide system has already been commercially developed (Ref. 6) but is restricted for use in composites only. Development of this improved PI into an adhesive material is being pursued.[1]

Of the three commercial materials, PBI has the most rigorous and extensive curing system. Curing pressures between 15 and 200 psi are used, as well as step-by-step curing from 430 to 600°F. In some cases, a 750°F post-cure in a nitrogen atmosphere is required for optimum bond strength. These elevated curing temperatures therefore significantly limit the use of PBI in bonding applications. The PI curing system is less rigorous. Curing pressures of the order of 25 psi and curing temperatures of 350°F with 550°F post-cures are normal. The AI system requires a 550°F cure at 15 to 100 psi with a 600°F post-cure.

The chemical structures of the developmental materials, polyquinoxaline (PQ), polyphenylquinoxaline (PPQ), and polyimidazoquinazoline (PIQ), are shown in Fig. 8. These materials, also formed by condensation type polymerizations, also have volatile reaction products during cure.

Although PQ is still considered a developmental material, it can be commercially obtained as a resin solution. In order for this material to achieve commercial importance as an adhesive, its thermal performance will have to exceed that of the current PI materials. This would mean that its continuous-use temperature would have to exceed approximately 500°F. Data on long-term elevated temperature aging are not currently available but it is believed that PQ should exceed 600°F (Ref. 22). Although no data have been published on the subject, the cryogenic performance of PQ, as with most materials with high T_g values, should be quite good.

The other developmental materials, PIQ and PPQ, have the most promise for exceeding the limit of PQ. Reports state that PIQ performs at 1000°F for 10 min and that efforts are being made to extend that time to about 1 h (Ref. 22). It is reasonable to assume that the curing systems of these materials will also take place in high temperatures and under high pressures. At present, no cryogenic performance data on these materials as adhesives have been reported.

Only PPQ is available commercially, on a restricted basis. It is reported that PIQ, which is still under extensive development, will not be commercially available for some time if at all.[2]

3. Selection of Spacecraft Adhesives

As a result of this adhesives review, some selections of potential spacecraft adhesives can, therefore, be made. The adhesive materials that now appear to be the most immediately applicable to spacecraft use are the PI, the PBI, and the newly developed PQ and PPQ polymers. Further development of PIQ systems is required before their potential for spacecraft use can be adequately evaluated.

For structural adhesive applications requiring long-term service at 500°F, the polyimide adhesives are currently the best adhesive materials. For short-term service (10 min), the polybenzimidazoles can be considered for temperatures up to 1000°F. The polyimide adhesives can be used in metal-to-metal bonding of all common metals; however, aluminum substrates are not used with polybenzimidazole because of the high curing temperatures required. The PBI material is normally used with the common high temperature substrates such as titanium, stainless steel, and beryllium.

The amide-imide systems do not show any distinct advantage over the polyimides for high temperature performance. The systems are processed with apparently the same difficulty as the polyimides and their long-term performance at elevated temperature is significantly poorer than the polyimides. Nothing is known of the performance of this material at cryogenic temperatures.

To exceed the polyimide elevated temperature level, the polyquinoxaline systems (PQ, PPQ) can be considered; their long-term performance should be in the 500 to 600°F range. But these polymers still require some further development in the area of optimum adhesive formulation and processing. In metal-to-metal bonding,

---

[1]Personal communication with R. Sproule, TRW Systems Group, Redondo Beach, Calif.

[2]Personal communication with W. P. Fitzgerald, Whittaker Corp., Research & Development/San Diego Division.

they will also be restricted in use to the common high temperature substrates. The cryogenic performance must also be established.

At present, the polybenzimidazole adhesives appear to be the best cryogenic adhesive materials. As shown previously, these materials have been evaluated at temperatures as low as −423°F. The high curing temperatures of the PBI system should be considered in any potential spacecraft application.

4. Phase II: Adhesives Testing

In the second phase of this NASA work unit, some laboratory evaluation will be performed on the new adhesive materials selected to establish their applicability for spacecraft use. The evaluation will include thermal shock testing as well as long-term aging at both elevated and cryogenic temperatures. The materials to be included in this testing will be the current available polyimide, polybenzimidazole, polyquinoxaline, and polyphenylquinoxaline adhesives.

References

1. Lee, H., Stoffey, D., and Neville, K., *New Linear Polymers*, McGraw-Hill Book Company, N.Y., pp. 183–192, 267–304, 207–264, and 353–356, 1970.

2. Hale, W. F., et al., "Thermal Stability of Polyarylethers Prepared by Aromatic Nucleophilic Substitution," *Am. Chem. Soc. Polymer Preprint*, Vol. 7, pp. 503–512, 1966.

3. Gillham, J. K., "Thermomechanical Behaviour of a Polybenzimidazole System by Torsional Braid Analysis," *Am. Chem. Soc. Polymer Preprint*, Vol. 7, pp. 513–519, 1966.

4. Hergenrother, P. M., Wofgang, W., Levine, H. H., "Polybenzothiazoles I—Synthesis and Preliminary Stability Evaluation," *J. Polymer Sci.*, Part A, Vol. 3, pp. 1665–1674, 1965.

5. Levine, H., *Polybenzimidazoles and other Aromatic Heterocyclic Polymers for High Temp Resistant Structural Laminates and Adhesives*, AFML-TR-64-365, Part 1, Vol. 2. Air Force Materials Laboratory, Wright-Patterson AFB, Ohio, November 1964.

6. P13N Polyimide Laminating Varnish, Technical Bulletin PSD/PLV-60-101, TRW Systems Group, Redondo Beach, Calif., April 1969.

7. Hergenrother, P. M., Levine, H. H., "Phenyl Substituted Polyquinoxalines," *J. Polymer Sci.* A-1, Vol. 5, pp. 1453–1466, 1967.

8. Evers, R. C., *Preparation of Polyiminobenzoxazoles and Benzothiazoles*, AFML-TR-68-363. Air Force Materials Laboratory, Wright-Patterson AFB, Ohio, April 1969.

9. Sanders, B. Y., Fitzgerald, W. P., Levine, H. H., *High Temperature Resins for Structural Laminates and Adhesives*, AFML-TR-69-303. Air Force Materials Laboratory, Wright-Patterson AFB, Ohio, October 1969.

10. Jewell, R. A., "Thermal Degradation Studies of Several Pyrrone Films," *J. Appl. Polymer Sci.*, Vol. 12, pp. 1137–1145, 1968.

11. Deusem, R. L. Van, Goins, O. K., Sicree, A. J., "Thermally Stable Polymers from 1, 4, 5, 8-Naphthalenetetracarboxylic Acid and Aromatic Tetraamines," *J. Polymer Sci.*, Part A-1, Vol. 6, pp. 1777–1793, 1968.

12. Papetti, S., et al, "A New Series of Organoboranes. VII, The Preparation of Poly-m-carboranylene siloxanes," *J. Polymer Sci.*, Part A-1, Vol. 4, pp. 1623–1636, 1966.

13. Sperling, L. H., et al., "Elastomeric and Mechanical Properties of Poly-m-carboranylenesiloxanes," *J. Appl. Polymer Sci.*, Vol. 10, pp. 1725–1735, 1966.

14. Washburn, R. M., et al., "Phosphorus Containing Resins and Composites for Environmental Extremes," in *Proceedings of 15th National SAMPE Symposium, Los Angeles, Calif., April 1969*.

15. Robinson, D. E., Schreihans, RTV *Silicones as Sealants and Adhesives for Cryogenic Applications*, CDS-554 Engineering Development Laboratory. North American Aviation, Inc., Space and Information Div., Los Angeles, Calif., February 1964.

16. Technical Bulletin *3M Adhesive PA 3515 B/A*, 3M Company, Minicom Div., St. Paul, Minn.

17. Gosnell, R. B., Levine, H. H., "Some Effects of Structure on a Polymer's Performance as a Cryogenic Adhesive," proceedings of Polymers in Space Research, American Chemical Society, Symposium held at the Jet Propulsion Laboratory, Pasadena, Calif., July 1968.

18. Technical Bulletin, *FM-34 Adhesive Film*. American Cyanamid Co., Bloomingdale Dept., Havre de Grace, Md.

19. Technical Bulletin, *Metlbond 840 Adhesive*. Whittaker Corp., Narmco Materials Div., Costa Mesa, Calif.

20. Technical Bulletin, *Imidite 850 Adhesive*. Whittaker Corp., Narmco Materials Div., Costa Mesa, Calif.

21. Technical Bulletin HT-7c, *High Temperature Adhesives Based on Amoco Amide-Imide Polymers*. Amoco Chemicals Corp., Chicago, Ill.

22. "Polymer Chemists Seek Plastics that Beat Heat, *Product Engineering*, pp. 84–88, November 1969.

XII. Applied Mechanics

ENGINEERING MECHANICS DIVISION

A. Optimum Shell Design, A. E. Salama and R. G. Ross, Jr.

1. Introduction

When a shell is subjected to multiple loading conditions, which may or may not be related, the shell thickness must be determined so that all design requirements are satisfied, separately and collectively. For efficiency, the shell must also be constructed from the least amount of material.

If the cost of manufacturing the shell is disregarded, the optimum design would be that which yields a minimum weight satisfying the design requirements (or constraints). The constraints may be one or any combination of the following:

(1) Manufacturing limits on the shell thickness at any location in the shell may be specified.

(2) Eigenvalue type constraints, on either the jth buckling load or the mth natural frequency or both, may be imposed.

(3) Constraints on maximum allowable deflection may be required.

(4) Using a suitable yield criterion, the shell may be required to withstand the applied loads without initial yielding.

In the present study a unified approach to the design of shells of revolution subjected to general loading is considered, and two methods for obtaining the minimum weight of a shell under certain constraints are compared. The two minimization techniques employed here are a direct search method known in the literature as the Simplex method (Ref. 1), and a gradient method known as the variable metric method (Refs. 2 and 3). While the Simplex method requires only function evaluation during the search, the variable metric method requires both function and partial derivative evaluation. The objective function to be minimized is the shell total weight (or material volume) subjected to one or more of the previously mentioned constraints.

2. Formulation of the Design Problem

In order to make the minimization problem computationally feasible and valid for all rotationally symmetric shells under general loading, the shell is physically discretized into a number of finite elements, each of which is a conical frustum with curved meridian and with constant thickness T_i. The elements join together at nodal circles for which the shell generalized displacements are defined. Although the elements are defined with equal meridional arc length L, the thicknesses of the individual elements are distinct and serve as the design variables (Fig. 1).
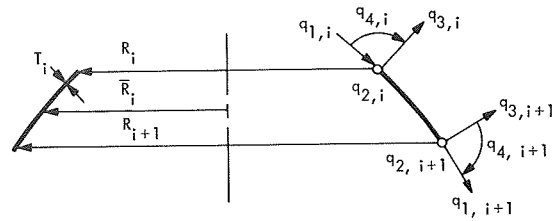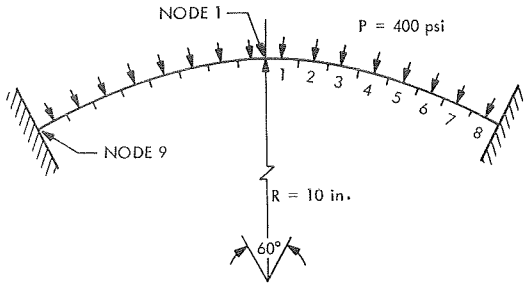
Fig. 1. Discretized shallow spherical shell and element definition

In accordance with the above simplification, the constraint evaluation is obtained by using the finite element technique to solve the pertinent governing equations. Thus, the first constraint considered earlier can be expressed mathematically by

$$\frac{T_i}{T_\ell} - 1 \geqq 0 \tag{1}$$

if the variable T_i is desired to be above or equal to a lower limit T_ℓ, and can be expressed by

$$\frac{T_u}{T_i} - 1 \geqq 0 \tag{2}$$

if T_i is desired to be below or equal to an upper limit T_u.

Let $[K]$, $[M]$, $[S]$ be the total structural stiffness matrix, total mass matrix, and total geometric stability matrix, respectively, for the discretized shell. Also let $\{Q\}$, $\{F\}$ be the vectors of generalized displacements and generalized forces at the nodes, respectively. The matrices are derived by the method described in Refs. 4 and 5, with both membrane and bending actions considered. The mathematical elements of each of these matrices and vectors, except the force vector $\{F\}$, are functions of the structural element thickness T_i. For example, the dependence of the mass matrix $[M]$ upon T_i is realized upon expressing the mass density of the shell per unit volume. On the other hand, the dependence

of the stiffness matrix $[K]$ and the stability matrix $[S]$ upon T_i is realized through the familiar expressions for the shell membrane and bending rigidities:

$$C_i = \frac{ET_i}{1 - \nu^2}$$

and

$$D_i = \frac{ET_i^3}{12(1 - \nu^2)}$$

where $E =$ modulus of elasticity and $\nu =$ Poisson's ratio. Thus, if p_j and ω_m, respectively, are the buckling pressure for the jth buckling mode and the natural frequency for the mth vibration mode, constraint evaluation of the second type is obtained from solution of

$$[K]\{Q\} + p_j[S]\{Q\} = 0 \tag{3}$$

for the buckling load, and from solution of

$$[K]\{Q\} - \omega_m^2[M]\{Q\} = 0 \tag{4}$$

for the natural frequency. These constraints may then be expressed in the dimensionless forms

$$\frac{p_j}{p^*} - 1 \geqq 0 \tag{5}$$

and

$$\frac{\omega_m}{\omega^*} - 1 \geqq 0 \tag{6}$$

in which p^* and ω^* are the specified buckling pressure and natural frequency.

Constraints of the third type may be imposed on the shell under general loading. If the loading is time-dependent, the shell response is obtained from

$$[M]\{\ddot{Q}\} + [K]\{Q\} = \{F(t)\} \tag{7}$$

By integrating Eq. (7) over the time domain in question, one can obtain the global maximum deflection occurring over the entire time domain.

If the constraint is imposed on the global maximum radial deflection $q_{3,i}$ of Fig. (1), occurring at node i, the

third constraint takes the dimensionless form:

$$\frac{q_3^*}{q_{3,i}} - 1 \geqq 0 \tag{8}$$

in which q_3^* is the maximum allowable radial deflection, and $q_{3,i}$ is obtained by solving Eq. (7).

For constraints of the fourth type, Von Mises' yield criterion may be employed. The mathematical expression for the constraint applied to the stresses at the middle of the ith element is then

$$[\sigma^{*2}/(\sigma_{\phi i}^2 - \sigma_{\phi i}\sigma_{\theta i} + \sigma_{\theta i}^2 + 3\tau_{\phi\theta i}^2)] - 1 \geqq 0 \tag{9}$$

in which ϕ is the meridional coordinate, θ is the loop coordinate, and σ^* is the yield stress. Again, the stresses are evaluated from the solution of Eq. (7), and the global maximum is computed for the entire quantity of the left side of Eq. (9).

It is important to note here that except for the first constraint, all the constraints mentioned are nonlinear implicit functions of the variables. Furthermore, since all of the constraint equations (except those of the second type) express the state of the constraint at a particular element of the shell, there will generally be as many constraint equations as there are discrete finite shell elements for each constraint. The general form of the constraint equations, Eqs. (1), (2), (5), (6), (8), and (9) for the nth constraint at the ith element is then

$$C_{ni} - 1 \geqq 0 \tag{10}$$

3. Conversion of the Constrained Design Problem to an Unconstrained Problem

Several techniques are available in the literature for constrained and unconstrained minimization. An excellent account of these techniques is given in Ref. 6.

One of the most used techniques for constrained minimization problems is the interior penalty function method (Ref. 7). In this method, the minimum of the objective function is realized as a sequence of unconstrained problems in which the unconstrained function to be minimized is the objective weight function augmented by a penalty function for the constraints. Each sequential unconstrained minimization requires several iterations, and an improved minimum is found for each.

Such a technique results in solving several unconstrained problems and is therefore relatively inefficient.

Another reason for its inefficiency is that the penalty function terms in the unconstrained function are always active, although the constraints may not be violated for a particular set of design variables. As a result, if a gradient method is used for minimization, all partial derivatives of the constraints with respect to the variables need to be evaluated for each iteration within each unconstrained minimization, regardless of whether any of the constraints are violated. This process can be a very expensive one, especially if the constraints are implicit functions of the variables, as is the case here.

To overcome these disadvantages, consider the following function:

$$\Phi = \sum_{n=1}^N \sum_{i=1}^P \lambda_{ni}(C_{ni} - 1)^2 + 2\pi\rho L \sum_{i=1}^P \overline{R}_i T_i \tag{11}$$

where

$$\lambda_{ni} = 0, \qquad C_{ni} < 1$$

and

$$\lambda_{ni} > 0, \qquad C_{ni} \geqq 1$$

In Eq. (11) Φ is the unconstrained function in which the last summation term explicitly expresses the total weight of the shell, with $\rho =$ the weight of the shell per unit volume, $L =$ meridional arc length of each shell element, $\overline{R}_i =$ the mean radius of element i, and $P =$ total number of shell elements. The first double summation term is a weighted sum of penalty functions, each of which corresponds to the nth violated constraint for element i of the shell. Of course, if a violated constraint is of the eigenvalue type, there will be only one penalty function for the entire shell for this particular constraint.

The set of multipliers λ_{ni}, although they may be taken equal, are generally assigned different positive values. The choice of their values is governed by the relative importance, in the designer's judgment, of the various constraints and how close he wishes the solution at the minimum to satisfy them. It is desirable, however, to assign large enough values for these multipliers so that, at least for the initial guess of the design variables, the two terms of Eq. (11) do not differ greatly. This precaution serves as a means of giving both the constraints and the weight functions equal opportunity to be optimized.

4. Minimization of the Unconstrained Function

Like all minimization techniques of an iterative nature, an initial set of starting values for the variables is required. In accordance with Eq. (11), the form in which the Φ-function was defined does not impose any restriction on the starting values for the design variables. They may be ones that satisfy or violate some or all of the constraints. This advantage saves the designer the additional work of having to solve for design variables that satisfy all constraints before he can initiate the minimization.

With an initial guess for the set of design variables T_i, and depending on which constraints are to be considered, the pertinent governing Eqs. (3), (4), and (7) need to be solved. The results obtained are then used to evaluate the unconstrained function Φ. A suitable minimization algorithm is then used to obtain an improved set of design variables that will yield a lower value for Φ. The just-calculated improved set of variables are next used to compute another improved set. The iterative process is repeated until the variation in each of the T_i is within a prescribed tolerance.

a. Example. Consider the spherical cap shown in Fig. 1 where the dimensions, loading, and other parameters are given. The natural frequency ω is obtained by solving Eq. (4).

Discretizing the shell into eight finite elements gives rise to eight element thicknesses T_i. The design variables were taken as $x_i \equiv (T_i)^{1/2}$, in order to allow the design variables to go negative. With four degrees of freedom at each nodal circle, the total mass and stiffness matrices are each 36×36. The boundary conditions $q_{1,1} = q_{2,1} = q_{1,9} = q_{2,9} = q_{3,9} = q_{4,9} = 0$, reduce these matrices to 30×30 for the vibration computations. For the equilibrium solution of the shell under a static symmetric loading, the stiffness matrix is further reduced to 23×23. Due to the lengthy form of the stiffness and mass matrices, they are not given herein.

The design requirements are $\omega^2 \geq \omega^{*2} = 2.23$ Hz, and $\sigma_i \leq \sigma^* = 15,000$ psi, for all $i = 1$ to 8. In this case, the Φ function requires, at the most, nine constraint evaluations per iteration, one for the eigenvalue and eight for the stresses. Fewer violated constraints require fewer constraint evaluations.

While eigenvalue-type constraints require solving the corresponding eigenvalue problem of Eq. (4), stress evaluations are obtained by solving Eq. (7) where

$\{\ddot{Q}\} = 0$. The solution of Eq. (7) is a vector $\{Q\}$ of generalized shell displacements which can be decomposed into its constituents of eight subvectors of six elemental generalized displacements $\{q_i\}$. The meridional and hoop stresses are evaluated at the middle of element i from

$$\sigma_{\phi i} = \frac{E}{1 - \nu^2} \left[\epsilon_{\phi i} + \nu\,\epsilon_{\theta i} - \left(\pm \frac{x_i^2}{2} \right) (k_{\phi i} + \nu\,k_{\theta i}) \right]$$

$$\sigma_{\theta i} = \frac{E}{1 - \nu^2} \left[\epsilon_{\theta i} + \nu\,\epsilon_{\phi i} - \left(\pm \frac{x_i^2}{2} \right) (k_{\theta i} + \nu\,k_{\phi i}) \right]$$

$$(12)$$

The strains $\epsilon_{\phi i}$, $\epsilon_{\theta i}$, and the curvatures $k_{\phi i}$, $k_{\theta i}$ of Eq. (12) are obtained in terms of $\{q_i\}$ in the usual manner of the finite element method (Ref. 8). The stresses of Eq. (12) are then used to compute the maximum combined stress σ_i^2 appearing in the denominator of Eq. (9).

While the constraints evaluation described above is required for both the Simplex and variable metric methods, the latter method requires additional partial derivatives information. Analytic derivatives were found necessary for reliable derivative information.

To evaluate the partial derivatives of the stress constraint at element i where the stresses are violated, Eq. (12) is rewritten in the more general matrix form:

$$\sigma_{\phi i} = \{S_{\phi i}(x_i)\}^T \cdot \{q_i(x_1, \cdots x_P)\}$$

$$\sigma_{\theta i} = \{S_{\phi i}(x_i)\}^T \cdot \{q_i(x_1, \cdots x_P)\} \qquad (13)$$

in which $\{S_{\phi i}\}$, $\{S_{\theta i}\}$, $\{q_i\}$ are 6×1 vectors. It is emphasized here that while $\{S_{\phi i}\}$ and $\{S_{\theta i}\}$ depend only on the local x_i, $\{q_i\}$ depends on all x_j, $j = 1, \cdots P$. For conciseness, the stresses of Eq. (13) will be rewritten as $\sigma_{\phi i} = S_{\phi i}^T q_i$ and $\sigma_{\theta i} = S_{\theta i}^T q_i$, so that the combined Von Mises stress σ_i^2 is given by

$$\sigma_i^2 = q_i^T S_{\phi i} (S_{\phi i} - 0.5\,S_{\theta i})^T q_i + q_i^T S_{\theta i} (S_{\theta i} - 0.5\,S_{\phi i})^T q_i$$

$$(14)$$

The partial derivatives of the stress constraints of the form of Eq. (9) are obtained in a straightforward manner once $(\sigma_i^2)_{,x_j}$ is evaluated for $j = 1, \cdots, i, \cdots, P$. This is done by differentiation of Eq. (14) which yields the vector of

partial derivatives:

$$(\sigma_i^2)_{,x_j} = q_i^{\mathrm{T}} S_{\phi i} \left[(S_{\phi i} - 0.5\,S_{\theta i})^{\mathrm{T}} q_{i,x_j} \right.$$

$$+ (S_{\phi i,x_i} - 0.5\,S_{\theta i,x_i})^{\mathrm{T}} q_i]$$

$$+ (q_i^{\mathrm{T}} S_{\phi i,x_i} + q_{i,x_j}^{\mathrm{T}} S_{\phi i})(S_{\phi i} - 0.5\,S_{\theta i})^{\mathrm{T}} q_i$$

$$+ q_i^{\mathrm{T}} S_{\theta i} [(S_{\theta i} - 0.5\,S_{\phi i})^{\mathrm{T}} q_{i,x_j}$$

$$+ (S_{\theta i,x_i} - 0.5\,S_{\phi i,x_i})^{\mathrm{T}} q_i)]$$

$$+ (q_i^{\mathrm{T}} S_{\theta i,x_i} + q_{i,x_j} S_{\theta i})(S_{\theta i} - 0.5\,S_{\phi i})^{\mathrm{T}} q_i$$

$$(15)$$

In Eq. (15) the commas followed by a variable means that the partial derivative is taken with respect to this variable.

The derivatives q_{i,x_j} are obtained by differentiating Eq. (7) with $\ddot{Q} = 0$, to give

$$\{Q_{,x_j}\} = -[K]^{-1}[K_{,x_j}]\{Q\} \qquad (16)$$

q_{i,x_j} are obtained by decomposing $\{Q_{,x_j}\}$ into its eight vectors of q_{i,x_j}.

For the natural frequency constraint, the derivatives

$$\left(\frac{\omega^2}{\omega^{*2}} \right)_{,x_j}$$

are needed. These are obtained by differentiating the Rayleigh quotient

$$\omega^2 = \frac{\{Q\}^{\mathrm{T}} [K] \{Q\}}{\{Q\}^{\mathrm{T}} [M] \{Q\}} \qquad (17)$$

to give

$$\left(\frac{\omega^2}{\omega^{*2}} \right)_{,x_j} = \frac{\{Q\}^{\mathrm{T}} [K_{,x_j}]\{Q\} - \omega^2(\{Q\}^{\mathrm{T}} [M_{,x_j}]\{Q\}])}{\omega^{*2}(\{Q\}^{\mathrm{T}} [M]\{Q\})} \qquad (18)$$

Calculations for the present example were carried by both the Simplex and variable metric methods, using the steps described above. Figure 2 shows a semilogarithmic representation of the time required on a Univac 1108 digital computer versus values obtained for the unconstrained function Φ. This figure shows a faster convergence for the Simplex method over the variable metric method.
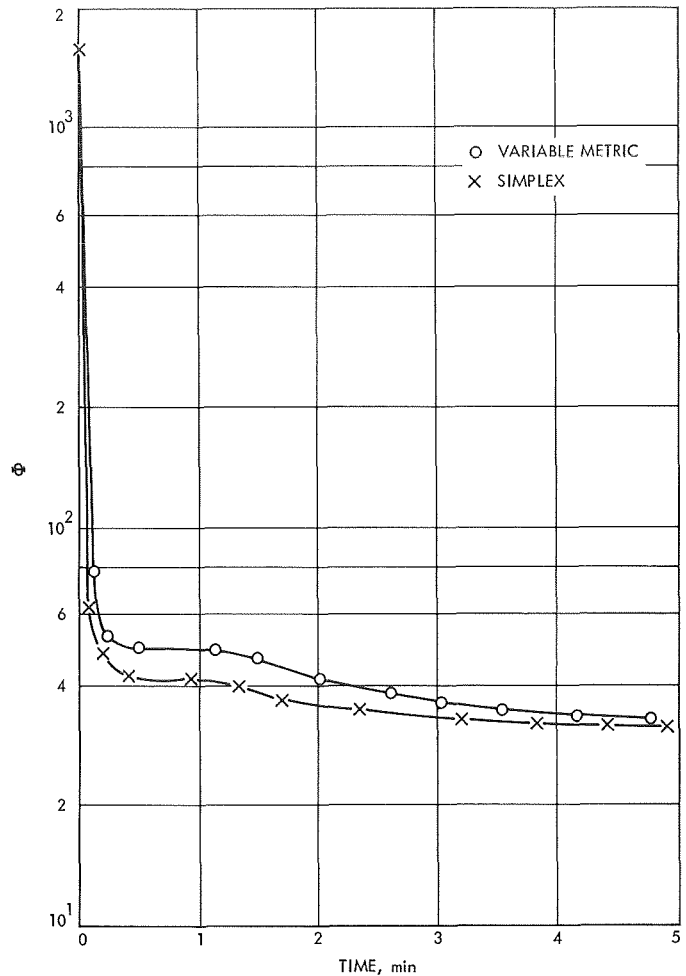
Fig. 2. Comparison of Simplex and the variable metric methods

Table 1 gives additional information for the starting initial stage and the final results obtained by both methods. The initial set of x_i satisfied all the σ_i's but produced a rather severe violation in the lowest eigenvalue ω^2. This caused the rather high function value $\Phi = 1652.21$. A number of iterations were carried out by both methods, and both were given a total machine time of about 4.8 min. During the 4.8 min, 88 function-with-derivative evaluations were performed by the variable metric method, while 152 function evaluations were needed by the Simplex method. Although during intermediate iterations, design variables x_i were generated that produced violations of some of the constraints; the final design variables obtained by both methods satisfied all of the constraints. However, as shown in Table 1, the Simplex method was superior to the variable metric method in this example, because it achieved a lower volume for the shell with more conservative margins for stresses and natural frequency.

Table 1. Minimization results for a spherical shell ($\lambda_i = \lambda = 10,000$; 2 circumferential harmonics for ω)

Element number		1	2	3	4	5	6	7	8
Initial	$x_i =$	0.6	0.6	0.6	0.6	0.6	0.6	0.6	0.6
	σ_i/σ^*	0.585	0.471	0.474	0.472	0.444	0.363	0.351	0.624
	$\dfrac{\omega^2}{\omega^{*2}} = 0.597$; $\phi = 1652.21$; total shell volume $= 30.31$								
Final by variable metric	x_i	0.939	1.451	0.712	0.508	0.408	0.287	0.455	0.845
	σ_i/σ^*	0.269	0.163	0.476	0.546	0.67	0.927	0.985	0.257
	$\dfrac{\omega^2}{\omega^{*2}} = 1.0014$; $\phi = 36.04$; total shell volume $= 36.04$								
Final by Simplex	x_i	0.575	1.13	0.667	0.553	0.431	0.408	0.769	0.640
	σ_i/σ^*	0.304	0.212	0.338	0.425	0.813	0.628	0.221	0.633
	$\dfrac{\omega^2}{\omega^{*2}} = 1.046$; $\phi = 34.06$; total shell volume $= 34.06$								

Total shell material volume for a uniform shell ($x_i^2 = T_i = 0.525$ in.) whose $\omega = \omega^*$ and $\sigma_i^2 < \sigma^{*2}$ at all locations is 44.0 in.³ Thus, the material saving is 23%.

5. Conclusions

The form of the unconstrained function suggested herein is simple and does not require the designer to have great insight when applying it to the general problem of optimum shell design. In addition, it is defined in such a manner as to minimize the required computational effort.

In comparing the Simplex with the variable metric technique, the Simplex method showed faster convergence and obtained lower values for the function. It is realized, however, that this may not always be the case, and that the superiority of one minimization algorithm over another depends (among other things) upon the form of the function to be minimized and whether or not it is continuous everywhere in values and derivatives. Above all, it depends upon the effort required to compute the partial derivatives. Because the constraints in the example presented are implicit functions of the variables, derivatives evaluation requires a major portion of the computation. In addition, although function values of Φ are continuous across the boundary representing the beginning of constraints violation, the partial derivatives are discontinuous. These two reasons do not affect the efficiency of the Simplex method as much as that of the variable metric method. Therefore, they account for the superiority of the Simplex method in obtaining the minimum of the suggested unconstrained function.

References

1. Nedler, J. A., and Mead, R., "A Simplex Method for Function Minimization," Comput. J., January 1965, pp. 308–313.

2. Davidon, W. C., Variable Metric Method for Minimization, A.E.C. Research and Development Report, ANL-5990, 1959.

3. Fletcher, R., and Powell, M. J. D., "A Rapidly Convergent Descent Method for Minimization," Comput. J., Vol. 6, 1963, pp. 163–168.

4. Percy, J. H., et al., "Application of Matrix Displacement Method to Linear Elastic Analysis of Shells of Revolution," AIAA J., Vol. 3, No. 11, 1965, pp. 2138–2145.

5. Stricklin, J. A., Navaratna, D. R., and Pian, T. H. H., "Improvements on the Analysis of Shells of Revolution by the Matrix Displacement Method," AIAA J., Vol. 4, No. 11, 1966, pp. 2069–2072.

6. An Introduction to Structural Optimization, Solid Mechanics Study No. 1, Edited by M. Z. Cohn, University of Waterloo, Waterloo, Ontario, Canada.

7. Fiacco, A. V., and McCormick, G. P., "The Sequential Unconstrained Minimization Technique for Nonlinear Programming, A Primal-Dual Method," Manage. Sci., Vol. 10, No. 2, January 1964, pp. 360–366.

8. Navaratna, D. R., "Computation of Stress Resultants in Finite Element Analysis," AIAA J., Vol. 4, No. 11, November, 1966, pp. 2058–2060.

XIII. Electronic Packaging and Cabling
ENGINEERING MECHANICS DIVISION

A. Large-Scale Hybrid Prototype—Method of Functionally Checking Hybrid Layouts Prior to Processing, E. R. Bunker, Jr.

A study of the thick film hybrid fabrication procedure showed that, like many other complex electronic fabrication procedures, many steps are required between initiation until final testing to determine if the original layout was adequate or not. A brief summary of the hybrid process is as follows: layout of the circuit in the hybrid configuration at some scale factor (usually ten times), photographic reproduction to the required size, fabrication of masks, screening, and firing conductor patterns, then insulation patterns, followed by more conductor patterns, then resistor patterns, trimming of resistors to required tolerances and values, installation of active and passive components, and finally testing. Not until the last step can a discrepancy or error in the layout, or cross coupling effects due to capacitance between conductors that cross over or run for a distance closely parallel, be determined. Several complete iterations of this process are usually necessary before a satisfactorily operating, complex hybrid module can be obtained. Figure 1 shows the various art work patterns necessary

before photographic reduction for the fabrication of a complex circuit; Fig. 1a shows the first conductor pattern to be screened and fired, followed by Fig. 1b, which is the insulating layer of glass with suitable windows for interconnection with the second conductor pattern (Fig. 1c). Figures 1d and 1e are screened resistor patterns. The two circles in each pattern are for alignment purposes.

An overall study of this process to see if any shortcuts could be taken in evaluating functionally the adequacy of the hybrid layout resulted in the large-scale hybrid prototype (LASHP) approach. A preliminary analysis showed that the functioning of a hybrid electronic circuit would be expected to be independent of the physical size of the circuit if the following three constraints were met: (1) skin effect is negligible, (2) lead inductance is negligible, and (3) the dimensions of the conductors are small compared with the wave length of the highest frequencies present.

As can be seen in Fig. 2, the LASHP approach is to take the completed art work at, say ten times the final size, and from it make a full size (10 times) conductor

(b) GLASS PATTERN
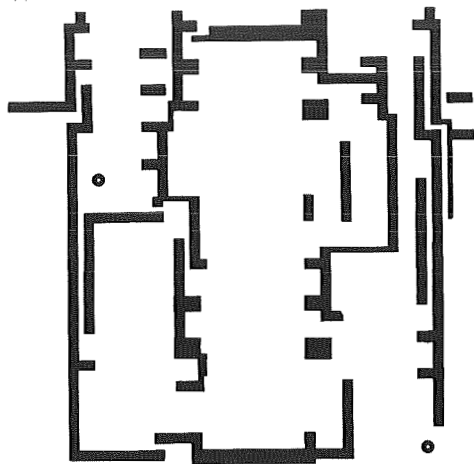
(a) FIRST CONDUCTOR PATTERN
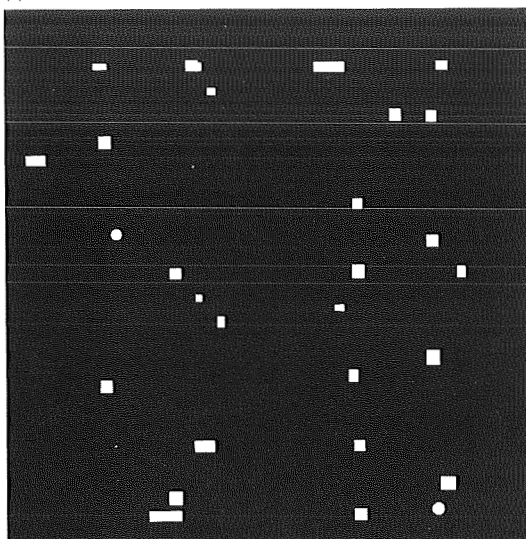
(c) SECOND CONDUCTOR PATTERN
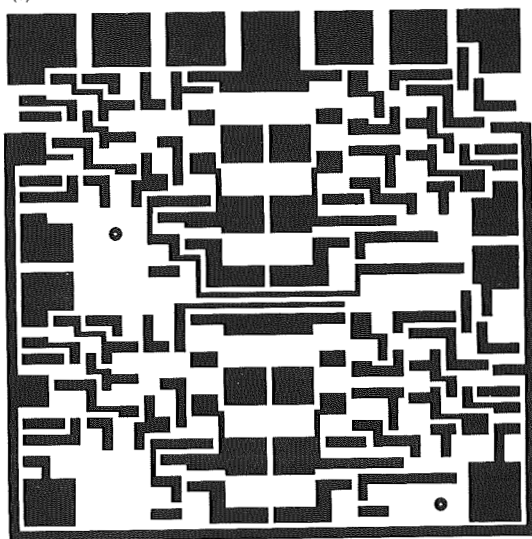
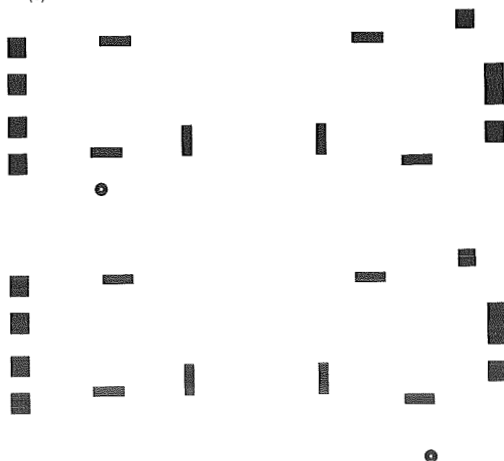(d) FIRST RESISTOR PATTERN
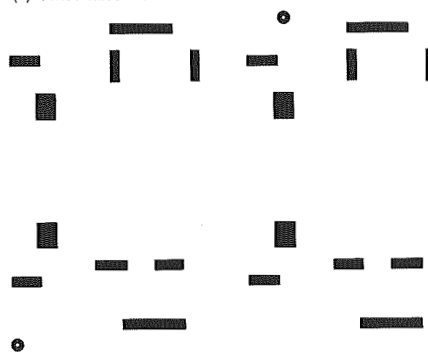
(e) SECOND RESISTOR PATTERN

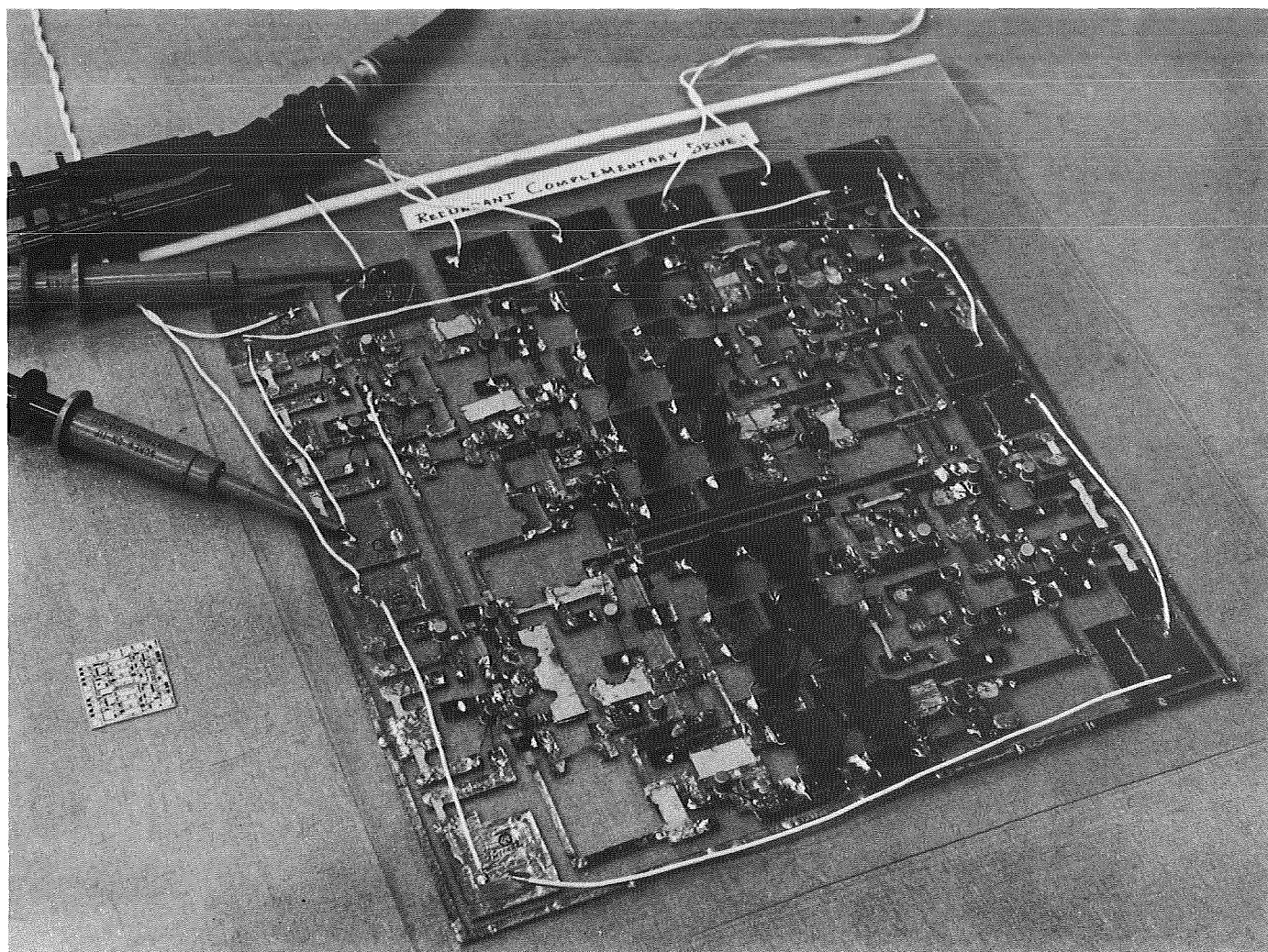Fig. 1. Art work patterns used in complex circuit fabrication

Fig. 2. LASHP undergoing electric test (hybrid model is to left of LASHP)

pattern using adhesive-backed copper tape on a pyrex glass sheet in accordance with the conductor pattern in Figure 1a, identical in size and configuration. With windows cut out for interconnection between the two layers of conductor, insulation for crossovers as in Fig. 1b is provided by tape whose thickness is equal to K^2 times the final hybrid substrate insulation thickness, where K is the reduction factor. Since in this example, K is equal to 10 times, this would be 100 times the screened glass thickness. Thus, the capacitive coupling between conductors due to one crossing the other can be reproduced exactly with insulating tape of the proper thickness. The second layer of conductors (Fig. 1c) is added with conducting tape as before. Screened-on resistors are simulated by resistance paper conductively bonded to the conductors. "Trimming" to the required values is achieved by a sharp knife cutting away excess material. Conventional components to be added to the

thick film substrate, such as resistors, capacitors, and transistors in TO-5 cans, rather than chip configurations, are then connected to the conductors by means of soldering. Connections to the outside world are made by soldering onto the connection pads along the edge, as shown in Fig. 2.

The circuit shown in Figs. 1 and 2 is that of the redundant complementary driver, which would be used to drive the binary tree for the STAR computer. The value of the LASHP configuration was shown in the complex circuit. After the art work was completed and checked very carefully, a complete LASHP was constructed using the copper conducting tape, insulating tape, and resistance paper for the screened-on resistors of Figs. 1d and 1e. Because of the difficulty of obtaining a low resistance connection between the paper resistor and the

copper conductors, some composition resistors were substituted. Conventional-sized components, such as transistors in TO-5 cans, ceramic capacitors, and some resistors, all representing the chip equivalents in the final hybrid configuration, were soldered in place.

The LASHP was connected into the STAR computer breadboard and tested. It was found immediately that there were several errors in it, including one buss interconnecting various transistors that was not terminated properly. Upon correction of this on the LASHP and concurrently on the art work, the functional large-scale module performed properly in the STAR computer breadboard. With the corrected artwork, the hybrid processing was initiated, resulting in the hybrid assembly shown to the left of the LASHP in Fig. 2. Initial tests showed that this hybrid performed quite satisfactorily in the STAR computer breadboard.

Evaluation of the LASHP concept was also done by fabrication of a simple circuit on which more data is available. This circuit was the hybrid layout of the utility test module, which was previously fabricated using discrete components in the Wirecon cordwood configuration SPS 37-40, Vol. IV, pp. 37–40. This is a six-transistor JK flip-flop configuration used as a common logic element. Before the LASHP approach had been conceived, a hybrid equivalent of the Wirecon utility module, employing leadless inverted devices (LIDs), was laid out and fabricated on a ceramic substrate. It was planned to compare the functioning of the hybrid equivalent with the extensive previous history of the Wirecon configuration. However, it was found that, for comparison purposes, transistors with characteristics identical to those used in the Wirecon were not available in the LID configuration. At this point, it was decided to make a LASHP configuration from the original art work, so that the functioning could be compared with both the hybrid and the Wirecon modules. Transistors in TO-5 cans with characteristics identical to the LID were used after correcting some eccentricities of the test equipment and replacing a transistor which had been damaged inadvertently in the Wirecon module. As time allows, three-way comparison of the functioning of the circuits will be made.

B. TOPS Electronic Packaging and Cabling,
R. H. Dawe

Electronic packaging and cabling involve the mechanics of translating electronic schematics and components into equipment capable of performing its electrical design function. It is the application of engineering methods and techniques to mechanical design, fabrication, interconnection, and integration to assure operation of electronic equipment in specified environments. This equipment performance must be predictable and not degraded by environmental stresses imposed by fabrication, inspection, test, repair, ground atmosphere, launch, and space.

Realistically, the final electronic package is a compromise of the ideal obtainable. This is caused by several conditions, primarily technology limitations and usually scheduling and funding. Conservative design dictates the necessity to go with "used" techniques rather than new or proposed techniques that have many "unknown" factors.

The thermoelectric outer planet spacecraft (TOPS) program provides a rare opportunity to not only look for but to try new system concepts of configurations for which there are no immediately established flight dates. For such a program, considerable thought is necessary to arrive at the best approach in which new techniques can be tried.

The first step in arriving at this approach is to review the past for insight and direction. There are several simple physical principles that have formed the basis of the JPL packaging system. These are:

(1) Hard mount technique that minimizes relative movement between components and joints at all levels of the system.

(2) Use of a short thermal conduction path from heat sources to a primary radiative thermal control surface.

(3) Packaging in functional units that use connectors for all levels of interconnect where testing or field assembly are required.

(4) Standard assembly and subassembly envelopes.

(5) Use of an integrated structural concept where each item added to the system contributes to the structural system integrity.

(6) Use of temporary fasten-on fixtures to prevent handling damage at all levels of fabrication and installation.

(7) Design so that all electrical parts and interconnections are inspectable at a level where they are no longer mechanically moved or stressed.

The application of these principles has been successful over many years and there are no good reasons to abandon them. However, the techniques of implementing these principles can be new. Anticipating component development and redundancy requirements, desirable TOPS electronic packaging and cabling objectives are:

(1) Develop a system of packaging and interconnections that provides increased part density, contributes to component long life, and maximizes environment immunity of the electronic equipment.

(2) Minimize flight weight by more extensive use of handling and assembly tooling.

(3) Provide capability for parallel electrical and mechanical operations in system assembly and test.

The principles and objectives are summarized in Table 1 for use as a guide for trade-offs during design.

Table 1. Trade-off considerations for reliability optimization

Minimize	Maximize
Volume	Design flexibility—late change accommodation
Weight	
Costs	Component and interconnect density
Temperature rise of electrical parts above ambient assembly	Rigidity
	Ease of Fabrication
Number and type of electrical joints	Repairability
	Operational reliability
Length and number of electrical interconnects	Subsystem functional integrity
Number and type of mechanical fasteners	Electrical interconnect Insulation integrity Signal/noise shielding-separation Contact integrity
Unknowns	
	System test capability
	Isothermal design
	Structural integrity
	Environmental protection Launch Space vacuum Micrometerorite Radiation

Flight electronic assemblies required to meet mission objectives consist of two general types. One type consists of those assemblies that require a location to fulfill a specific functional requirement, such as look angle or field of view. These are normally more mission-dependent and are defined later in a program. These assemblies usually fall in the "form follows function" category, and configuration cannot be generalized. The other type called (type 1) is not view-dependent and makes up the majority of system electronics assemblies. These type 1 assemblies are applicable to many types of missions and perform the basic spacecraft operational and communication chores.

Type 1 electronics assemblies can be grouped to optimize such system aspects as structural and thermal integrity, length and weight of electrical interconnects, operational flexibility, and reliability. The grouping of this equipment into a compartment allows standardization, which provides the opportunity of a more thorough analysis, test, and refinement of the mechanical subsystem. The early testing assures mechanical adequacy prior to the time when necessary changes can be catastrophic to costs and schedule during the building of the electronic assemblies. Reduced system weight, volume, design time, number and types of materials, and parts can result in reduced costs, shorter schedules, and improved reliability.
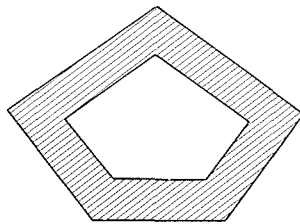
In the development of the packaging configuration for the electronic compartment for Type 1 assemblies, a study was made of different configurations, using the interconnect area as a defining method. Figure 3 portrays cross sections of various configurations. Based on the trade-offs given in Table 1, the capped double bar configuration would be a prime choice. The weakness of this arrangement was the need for access to four of the six sides for installation of assemblies. The problem of integrating the electronics compartment into the spacecraft is reduced by using the double bar configuration. The installation and removal of an assembly is required from only two sides, which allows considerably more freedom to the spacecraft configuration.

The approach taken in sizing the electronics compartment for TOPS was to obtain estimates from the subsystem cognizant engineers of the change in the functional complexity of their subsystem over that of *Mariner* Mars 1969. This figure, or range, times the *Mariner* Mars 1969 volume provided a first-order estimated range of the TOPS requirements. This figure was reviewed by considering the type of components that
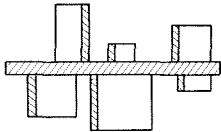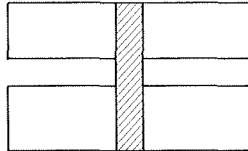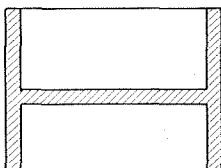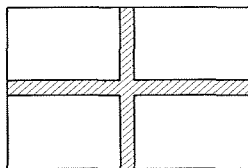
HAND CONNECTED
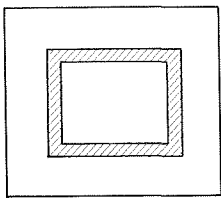
POLYGON   CAPPED POLYGON
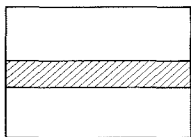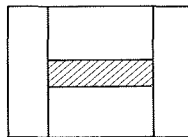
DOUBLE (SINGLE) TABLETOP   I

H   CRUCIFORM

PLUG-IN

SINGLE BAR (CAPSULE SYSTEM ADVANCED DEVELOPMENT)

DOUBLE BAR   CAPPED DOUBLE BAR

Fig. 3. Packaging configurations

would be available and the judgement factor applied to obtain a volume estimate for design (Table 2).

This figure was revised after additional system study. The increase in volume estimate of several of the subsystems resulted in some additional system redundancy requirements and the complexity of instituting the redundancy. Tables 2, 3, and 4 show the revised estimates for TOPS compared to *Mariner* Mars 1969.

Although the weight of electronic equipment is important, the emphasis and concern is on volume. Weight

is closely related to volume since packaging densities of flight equipment have had a rather narrow range, usually between 0.020 to 0.040 lb/in³. Generally speaking, if the volume is reduced in a well-packaged system, the weight is also reduced.

The proposed electronics compartment (Fig. 4) used plug-in assemblies. The compartment is $21.5 \times 18.6 \times 49.5$ in. The salient features of the electronics compartment are as follows:

(1) The system interconnect assembly contains all the wiring between subsystems and connectors for operational support equipment direct access and system wiring outside the compartment. Various combinations of routing and harness separations are available. The interconnect area utilizes 50-mil center connectors and provides considerable flexibility in the type of wiring. System connectors can be located on the four sides of the interconnect core. Operational support equipment ground test connectors are located on the $+X$ side only.

(2) The structure, by its box-type arrangement, is intended to carry most of the loads on the exterior structural elements of the compartment surfaces.

(3) The shear and thermal control surfaces are attached to the base of the electronic assemblies. These surfaces would have the active temperature control devices. The other sides of the compartment would have thermal insulation and meteroid protection, as required.

(4) Aluminum is the material contemplated for the structure and electronic chassis. However, the plan is to keep the shape simple to allow the widest choice of more exotic materials, if needed or practical.

Some of the electronic assembly location rationale for this configuration included the following:

(1) The radio subsystem was located to minimize the RF antenna plumbing.

(2) The radio and power as the two primary heat dissipators are located on opposite sides at extreme ends to equalize the thermal stress.

(3) An attempt was made to minimize wiring on units that have most communication, such as the central data handling subsystem.

Table 2. Electronics compartment subsystem comparisons

Subsystem	Mariner Mars 1969		TOPS	
	Volume, in.^{3}	Weight, lb	Volume, in.^{3}	Weight, lb
Radio frequency	1,340	56.0	1,980	86
Command	300	8.0	290	8
Power (no battery)	1,520	38.7	1,600	50
Central data handling				
Central computer and sequencer	600	24.0	1,600	40
Central processor unit	835	21.5	680	14
Data storage unit	1,110	37.2	1,980	76
Central clock	—	—	150	4
Attitude control	775	28.7	1,300	29
Pyro	280	8.6	216	8
Approach guidance	—	—	350	12
Data automation	580	13.8	—	—
Television	520	11.7	400	15
Science instrument electronics	—	—	600	20
	7,860	248.2	11,146	362
Structure	—	85.9	—	49
Cabling	10,130	41.9	4,500	14
Total	17,990	376.0	15,646	425

Table 3. Electronics compartment Mariner Mars 1969 and TOPS volume comparison

Spacecraft	Volume, in.^{3}				
	System cabling	Subsystem cabling	Packaging space		Total packaging and cabling
			Used	Available	
Mariner Mars 1969	4,190	5,940	7,860[a]	900	18,980
TOPS	4,500	—[b]	11,146	854	16,500

[a]No battery.
[b]Part of packaging volume.

Table 4. Electronics compartment Mariner Mars 1969 and TOPS weight comparison

Spacecraft	Weight, lb			
	Electronic assemblies	Structure	Cabling	Total
Mariner Mars 1969	248.2	85.9	41.9	376.0
TOPS	362	49	14	425

(4) The pyro is located for direct access to squib cables.

Figure 5 shows a comparison of the *Mariner* Mars 1969 configuration and the configuration chosen for TOPS drawn to the same scale.

A typical type 1 electronic assembly (Fig. 6) has the module interconnect with the same 50-mil connectors used for the system interconnect. The unit shown could package 10,000 fourteen-lead integrated circuits in a volume of 600 in.^{3} with a 408-pin-system interconnect capability.

RADIO FREQUENCY 2002

CPU 2045

ATTITUDE CONTROL 2007

AG 2014
CC 2019
TV 2048

2047

2044

SCIENCE 2041

2040

SYSTEM INTERCONNECT 2009

DSU 2016

CMD 2003

CC&S 2005

POWER 2004

PYRO 2008

AG   APPROACH GUIDANCE
CC   CENTRAL CLOCK
CC&S CENTRAL COMPUTER AND SEQUENCER
CMD   COMMAND
CPU   CENTRAL PROCESSOR UNIT
DSU   DATA STORAGE UNIT
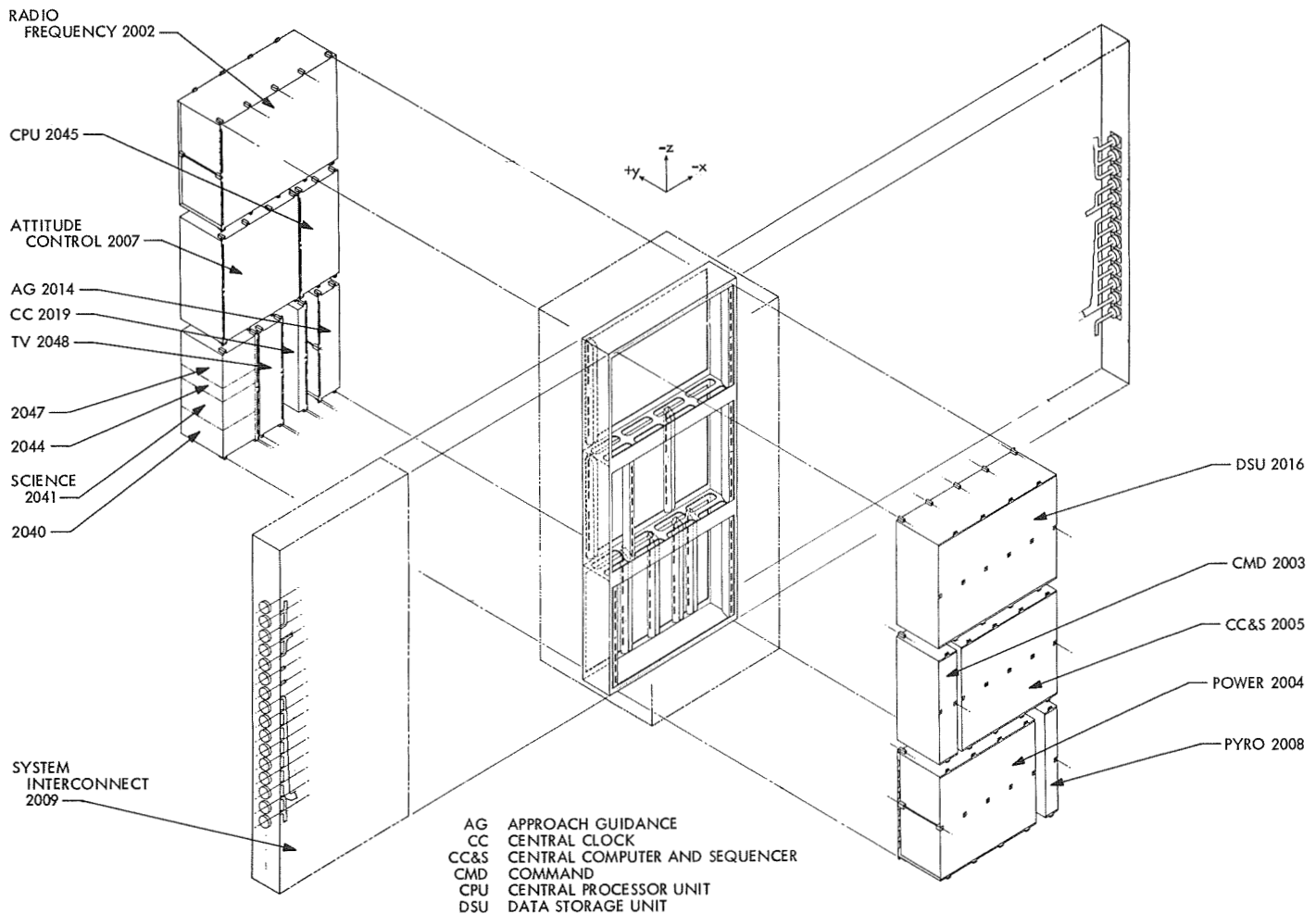
Fig. 4. TOPS electronics compartment concept

MARINER MARS 1969   TOPS

A   A   B   B

SECTION AA   SECTION BB

☒ ELECTRONIC PACKAGING
   (EACH CONFIGURATION HAS IDENTICAL VOLUMES)

▨ SYSTEM INTERCONNECT

▨ SUBSYSTEM INTERCONNECT

▤ ACCESS AREA TO CABLING WITH ENVELOPE
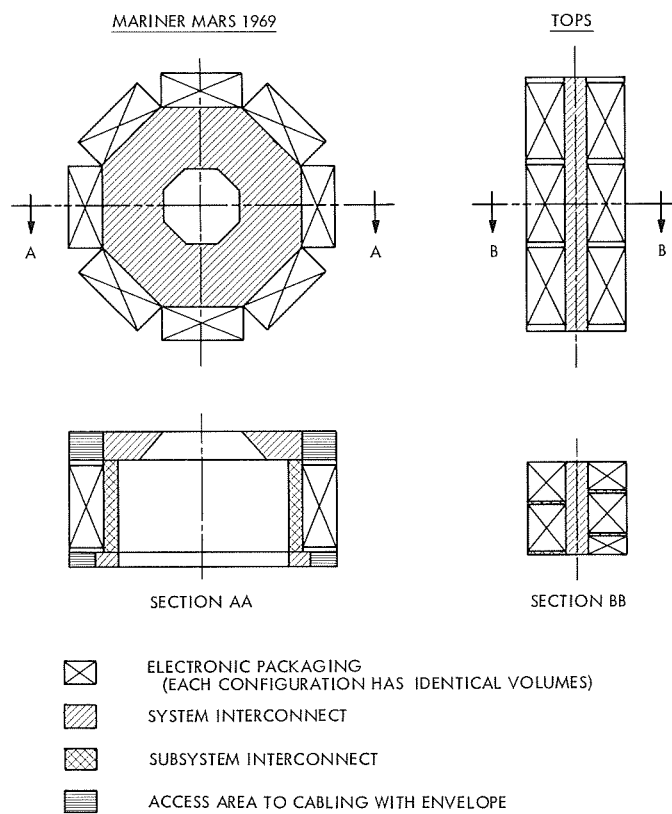
Fig. 5. *Mariner* Mars 1969 vs TOPS electronics
compartment configuration

BOTTOM VIEW

MODULE

ATTACHMENTS TO
THERMAL CONTROL
AND SHEAR PANEL

CAPTIVE FASTENERS
TO STRUCTURE

TOP VIEW

SYSTEM
INTERCONNECT

SUBSYSTEM
INTERCONNECT

CONNECTOR SUPPORT
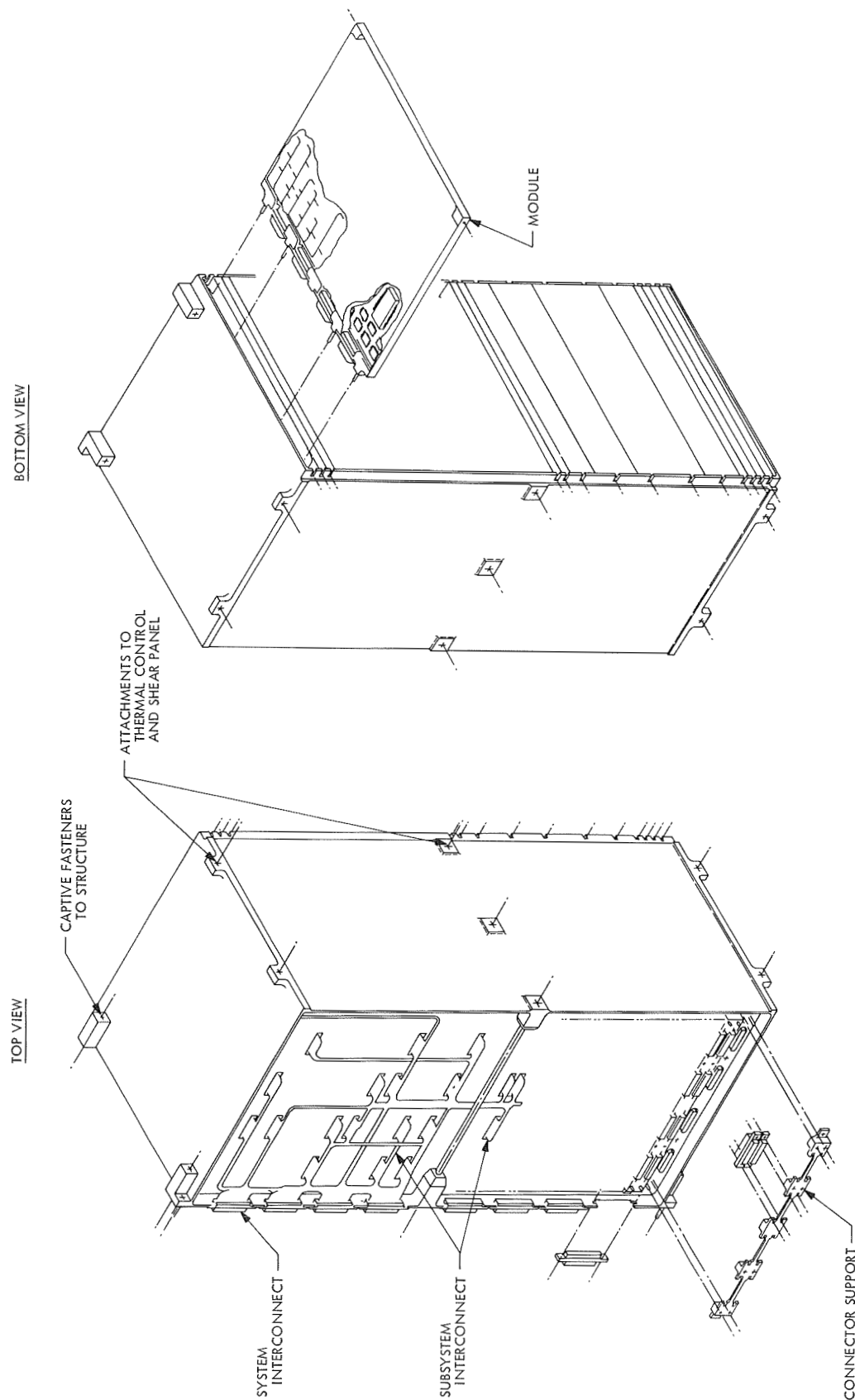
Fig. 6. Typical type 1 electronic assembly

XIV. Spacecraft Computer

ASTRIONICS DIVISION

A. STAR Computer Software, J. A. Rohr

1. Introduction

The JPL self-testing-and-repairing (STAR) computer is currently being developed by the Astrionics Division. The organization of this machine is described in Ref. 1. The use of the computer in unmanned interplanetary travel for guidance and control computation, as well as onboard processing of scientific data, is described in SPS 37-46, Vol. IV, pp. 57-62. An overview of the software system for the STAR computer is presented in SPS 37-50, Vol. III, pp. 75-77. The assembler and loader are described in SPS 37-52, Vol. III, pp. 27-30. The simulator and system executive program are described in SPS 37-55, Vol. III, pp. 90-92. The software system previously described is implemented on the IBM 7094. The second version of the software system is implemented on the Univac 1108. The additions and modifications made while developing the second version are described here.

2. STAR/SYS

The initial version of the STAR computer software system is called STAR/SYS. This version runs on the IBM 7094. STAR/SYS consists of four components: an

assembler (SCAP), loader (LOAD), simulator (STAR), and executive control program (SYSTEM). All components are stored on magnetic tape. A small binary deck is used to initially load SYSTEM. SYSTEM then controls the processing of a STAR/SYS run. The other three components are read from tape and executed as required by the control cards in the runstream.

3. STAR*SYSTEM

The second version of the STAR computer software system is called STAR*SYSTEM. This version runs on the Univac 1108. This version is a conversion and extension of the initial version. STAR*SYSTEM, like STAR/SYS, consists of four components: an assembler (SCAP), loader (LOAD), simulator (STAR), and executive control program (SYS). All components are collected into one segmented absolute module. The 1108 EXEC 8 operating system automatically loads the segments as needed.

SYS is the main segment of STAR*SYSTEM. It contains the subroutines used by all components (e.g., READ, PRINT, PUNCH) and subroutines which control the processing of a STAR*SYSTEM run.

SYS is a completely new program for STAR*SYSTEM rather than a conversion of SYSTEM from STAR/SYS. Because of the automatic loading of segments performed by EXEC 8 and since all the routines which communicate with the executive system are significantly different in the second version, it was more convenient to rewrite, rather than convert this control segment. An additional benefit was that the control card language was greatly simplified from that used in the initial version. In STAR*SYSTEM, only three control cards exist: 'JOB to mark the beginning of a job, 'SCAP to mark the beginning of an assembly, and 'DATA to mark the beginning of a data deck or execution of a program. Various options associated with various phases of a job may be specified as parameters on control cards.

SCAP, the assembler, is one segment which is used by SYS. When a 'SCAP control card is detected, SYS calls SCAP. If the SCAP segment is not in core, it is automatically loaded.

The primary extension to SCAP in the second version is the addition of a CALL pseudo-operation which is used for calling subroutines. This pseudo-operation accepts a name or expression for the subroutine being called, a parameter list, and an error or alternate return list. The code generated consists of a transfer to the subroutine, a transfer around the in-line parameter list, and the parameter list itself. The parameter list consists of up to three sections. The first section, always present, is a word specifying the number of parameters in the CALL. The second section gives the addresses of the parameters, if any. The third section is a series of transfer instructions for the error or alternate returns, if there are any.

MEMORY exists as a separate segment (under SYS) in STAR*SYSTEM. (In STAR/SYS it was included separately in LOAD and STAR). This segment contains the simulated memory used by both LOAD and STAR, as well as a memory dump subroutine. This segment resides in core with either LOAD or STAR.

LOAD, the loader, is another segment under SYS. When the loader is used, both the MEMORY and LOAD segments must be in core. Other than separating the memory into a separate segment, no modifications or extensions were made to LOAD in the second version.

STAR, the simulator, is the last segment under SYS. When STAR is used, the MEMORY segment must also be in core. By using the same memory segment for LOAD and STAR, the simulated memory does not have to be reloaded before beginning simulation after loading. Besides separating the memory into a separate segment, two extensions were made to the second version of STAR: trace control was added and the simulator dump instructions were implemented. Also, the simulator was updated to agree with the current hardware configuration of the STAR computer.

The trace function provided in STAR gives a dump of all simulated registers, when specified. Originally, a trace line was given after each simulated instruction. In many cases, a selective trace is desirable to reduce the amount of execution time and printout for a run. By adding trace control to STAR, the trace line can be produced only when desired. The control statements implemented allow specifying a trace of every instruction, every transfer instruction, every input–output instruction, any specified opcode or variant, any specified memory location or block of consecutive memory locations, or any combination of the above. In addition, the beginning of the trace may be delayed until any specified time. Finally, a full trace may also be specified in which the contents of the simulated busses at the end of the instruction are printed.

The simulator dump instructions allow register or memory dump to be activated by program commands. Four instructions are provided. Two provide register dumps which are identical to the trace and full trace printouts. The other two provide memory dumps. One dumps the entire simulated memory. The other dumps a portion of the memory specified by limits in the two index registers.

4. STAR*LIBRARY

A file called STAR*LIBRARY has been created on the 1108 to hold the source decks for STAR computer programs. With these decks available on-line, it is possible to use demand terminals to generate load modules with only a few input card images. Since binary cards can be read and punched only at the main site, it is usually easier to reassamble a deck (without printout) than to try and include relocatable binary decks.

The first group of programs in STAR*LIBRARY are the bootstrap and absolute loaders. Two sets of programs are provided. One bootstrap-loader, absolute-loader, core-initializer set does not use the logic processor. This set does not check the checksum of a card and uses an uncoded initial program address. The other loader set

does use the logic processor. The checksum of each card is checked. If an error occurs during reading, the program halts so the card can be reread.

Another group of programs in STAR*LIBRARY implements multiplication, division, and floating-point operations by using the logic processor's arithmetic capability. Integer and fractional multiplication and division are provided. Also, double-word products and dividends may be used. The nonzero magnitude of floating-point numbers is approximately 16^{-9} to 16^{+7}.

Another group of programs provides input–output for STAR computer programs. One subroutine reads cards from the card reader. This subroutine checks for proper reading. If the card is read incorrectly, the program halts so that the card can be reread. A program to be added to this group in the near future will facilitate typewriter input–output of all number types.

The final program in STAR*LIBRARY is the computer-accessed-telemetry system (CATS) program. This program was developed by R. Easton to simulate the CATS operation and the assumed interactions with the STAR computer while gathering, processing, and formatting data for telemetry and onboard monitoring programs. In addition, the CATS program is a prototype for a STAR computer program which would back up the CATS operation in case of a CATS hardware failure.

5. Conclusion

Software for the STAR computer is comprised of three types of programs. Programs of the first type are used to prepare programs to be run on the STAR computer. The initial version, STAR/SYS, and the second version, STAR*SYSTEM, of the programming subsystem for the STAR computer have been completed on the IBM 7094 and Univac 1108, respectively. Programs of the second type are execution aids for programs running on the STAR computer: these programs are the operating system for the machine. An initial version of the operating system is now being developed for the STAR computer. The third type of program is the user or applications program. These programs may be commonly used subroutines or special-purpose programs, such as would be used on an interplanetary mission. Several subroutines and one applications program have been written for the STAR computer. In the future, the operating system will be developed further and more subroutines and applications programs will be written.

Reference

1. Avizienis, A. A., Mathur, F. P., Rennels, D. A., and Rohr, J. A., "Automatic Maintenance of Aerospace Computers and Spacecraft Information and Control Systems," Paper 69-966, *Proceedings of the AIAA Aerospace Computer Systems Conference,* Los Angeles, California, September 8–10, 1969. (Also issued as JPL Technical Report 32-1449.)

XV. Spacecraft Measurements

ASTRIONICS DIVISION

A. Pattern Recognition: Invariant Stochastic Feature Extraction and Classification by the Sequential Probability Ratio Test—Theory and Experimental Results for the Two-Class Problem, J. P. Hong

1. Introduction

In SPS 37-58, Vol. III, pp. 80–84, random lines are used to obtain a feature extraction algorithm in which the extracted features are insensitive to rotation and translation of the pattern within the retina. It can be shown that the statistics of the total intersection length of the random line and the pattern is such an invariant feature (Ref. 1). The choice of random line intersection length as a feature extractor is an arbitrary one. It is hypothesized that the statistics of the number of intersections that a random line makes with a pattern is also such an invariant feature. Furthermore, it may be less sensitive to the font. It is demonstrated that the probability density function of the line intersection length could be used to decide from which letter the random features are taken. It is stated that classification of the block letters **L** and **H** with unfailing accuracy is possible with 2000 samples.

This article presents the mathematics necessary to predict the average number of observations that are needed to properly classify unknown letters. The theory presented herein also allows one to make a *trade-off between the number of required samples and the accuracy of the classification.*

2. Sequential Probability Ratio Test

Simple hypothesis testing is an important area of statistics that has applications in many fields (Ref. 2). In particular, many results are available for the simple two-hypothesis problem. In this subsection, a brief outline of the structure of the sequential probability ratio test (SPRT) is presented.

It is assumed that two probability density functions (PDFs), f and g, associated with hypotheses H_1 and H_2, respectively, are known to the experimenter. Suppose X samples are taken from a PDF. The question is, "Which population, f or g, did the X samples come from?" Tests can be performed on X and, hopefully, the results will indicate that X is taken from f or g; consequently, one hypothesis will be verified.

It is immediately obvious that the test on X is statistical in nature; hence, there is always the danger of verifying the incorrect hypothesis. For this discussion, e_{ij} is defined as the error of verifying hypothesis i when,

in fact, the samples are taken from the PDF associated with hypothesis j. In the two-hypothesis problem, $e21$ is often called the error of the second kind and $e12$ is called the error of the first kind. Certainly, it is desired to minimize eij.

The next question that arises is, "How many samples must be taken to assure a certain error rate and must they be taken all at once?" Wald (Ref. 3) answered these questions in 1947. A sequential test, which performs at a desired error rate, is possible; that is, the samples are taken one at a time until a satisfactory test is performed, then no further samples are taken. A more readable introduction to SPRT is given by Fu (Ref. 4).

The probability ratio (the likelihood ratio) $\lambda_n(i,j)$ for a sample $\mathbf{X} = (x_1 \cdots x_n)$ is

$$\lambda_n(i,j) = \frac{p_n(\mathbf{X} \mid H_i)}{p_n(\mathbf{X} \mid H_j)}$$

If the samples are independent, then

$$\lambda_n(i,j) = \prod_{k=1}^{n} \frac{p(x_k \mid H_i)}{p(x_k \mid H_j)} \qquad (1)$$

Two boundaries are established and the test has three results:

(1) Take $n + 1$ samples if $B < \lambda_n < A$.

(2) Accept hypothesis H_1 if $\lambda_n \geq A$.

(3) Accept hypothesis H_2 if $\lambda_n \leq B$.

A and B are defined as

$$\left. \begin{aligned} A &= \frac{1 - e21}{e12} \\[2ex] B &= \frac{e21}{1 - e12} \end{aligned} \right\} \qquad (2)$$

The SPRT procedure is easier to visualize if the logarithm of Eqs. (1) and (2) is taken:

$$\mathcal{A} = \ln A$$
$$\mathcal{B} = \ln B$$
$$L = \ln \lambda_n(i,j) = \sum_{k=1}^{n} \ln \frac{p(x_k \mid H_i)}{p(x_k \mid H_j)} = \sum_{k=1}^{n} z_k(i,j)$$

where (Ref. 5)

$$z_k(i,j) = \ln \frac{p(x_k \mid H_i)}{p(x_k \mid H_j)}$$

The random variable z_k is a well-known function of x_k. Hence, the simplest form of the SPRT can be used. First, the sum of z_k is observed; then, a decision is made based on this sum and $\mathcal{A}$ and $\mathcal{B}$. It is noted that L is a submartingale (Ref. 6) or a random walk (Ref. 7). Thus, questions concerning n, such as the expected number of samples to be taken, can be answered (Ref. 8):

$$\mathcal{E}(n \mid H_1) \geq \frac{(1 - e21)\,\mathcal{A} + e21\,\mathcal{B}}{\mathcal{E}(z \mid H_1)}$$

$$\mathcal{E}(n \mid H_2) \geq \frac{e12\,\mathcal{A} + (1 - e12)\,\mathcal{B}}{\mathcal{E}(z \mid H_2)} \quad \text{(Ref. 7)}$$

Unfortunately the probability that n is large is always finite. Hence, there is the unpleasant prospect of a test "never" ending.

This problem can be circumvented by arbitrarily stopping the sampling after a prescribed number of samples N. The test is then changed to a Bayes' test. Wilks (Ref. 7) shows that for large N, the error rates $e'12$ and $e'21$ are nearly $e12$ and $e21$, respectively. To show this all that is needed is to note for large N; L becomes a sum with many terms. The central limit theorem is then invoked.

This procedure is applied to the pattern recognition problem in the following subsections. The two hypotheses are: H_1, that **H** is the unknown letter; and H_2, that **U** is the unknown letter. The extracted features are extremely simple, and hence the cost of sample taking is not considered. However, to terminate every test, the test is truncated after 200 samples are taken.

3. Feature Extraction

The area of interest is called the retina. It is assumed that the pattern lies somewhere within the retina. Random lines are chosen so that they intersect the retina "uniformly." Figure 1 shows a retina with a few random lines intersecting it. If there is a pattern within the retina, the random lines may intersect them as shown in Figs. 2 and 3. The total length of the intersection with the pattern is found for one random line. This is the sampled feature of the pattern. The ith sample is labeled x_i (Fig. 4).
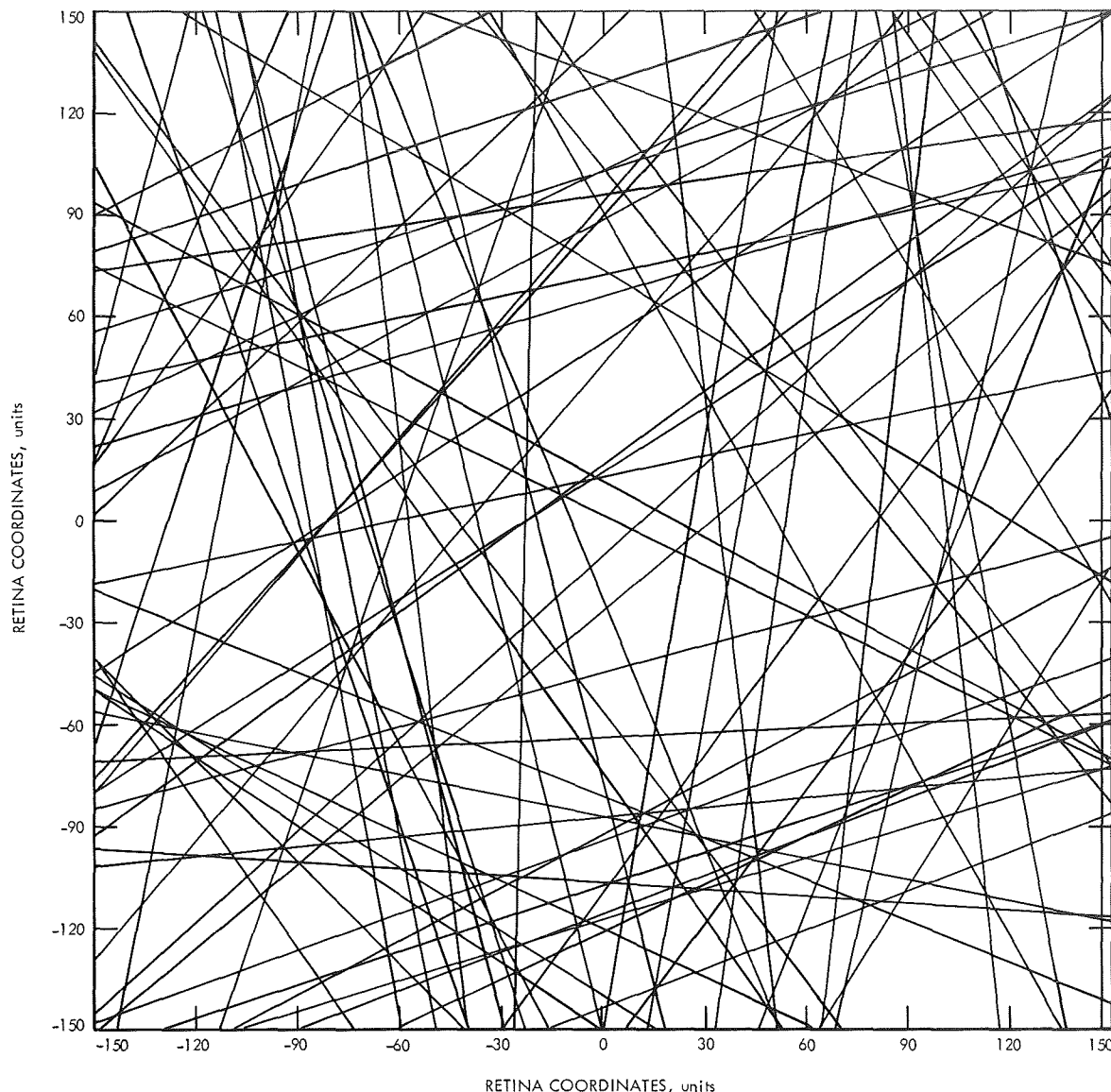
Fig. 1. Random lines in the retina

The features extracted in this manner are invariant to rotation, translation, or "mirror" imaging; i.e., the random variable x is invariant under these transformations (Refs. 1 and 6). Hence, these features have an advantage over those taken by a raster or a dot-matrix scan, which requires tight alignment (SPS 37-58, Vol. III).

For the experiment, the block letters **H** and **U** are used because of their similarity. Their areas are equal and they have identical convex hulls. Only a small horizontal strip, which is less than 12% of the total area, is different. Certainly, if an algorithm distinguishes similar letters, it will also work for dissimilar ones.

The probability density function (PDF) of the random line intersection length (PDF of x) must be obtained. Theoretically, it is possible to compute such a PDF for any pattern. However, it requires far less effort to experimentally estimate the PDF. This is done by repeatedly choosing a random line, then finding its intersection length to form a histogram of x. For the block letters **H** and **U**, the histogram does not change significantly after 5000 samples. Hence, 50,000 independent x's are taken to generate an approximate PDF for each of these letters. Figure 5 shows the PDF for **H** and **U**. Approximately 24% of the random lines have zero intersection with either letter. This is due to the fact that both letters
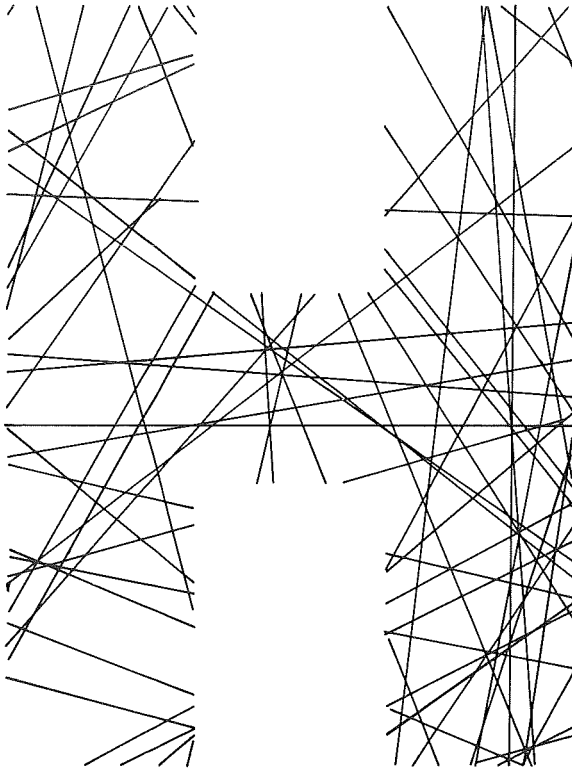
Fig. 2. Random lines intersecting **H**
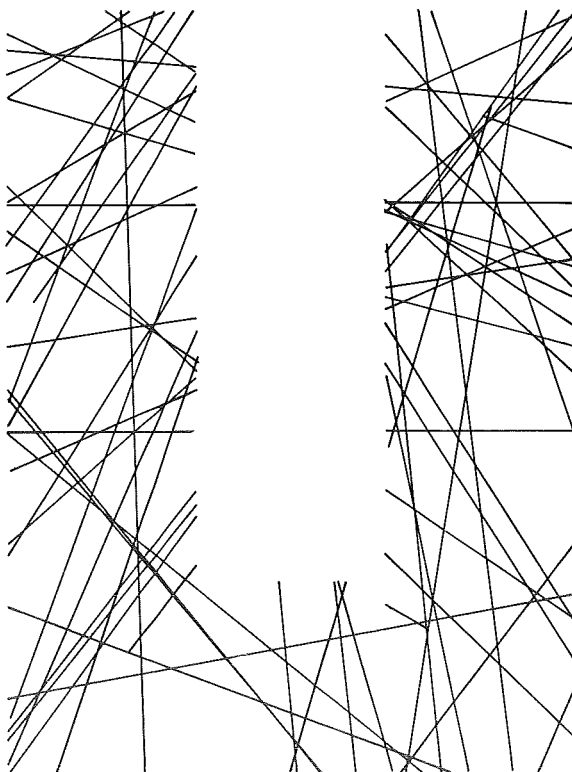
Fig. 3. Random lines intersecting **U**
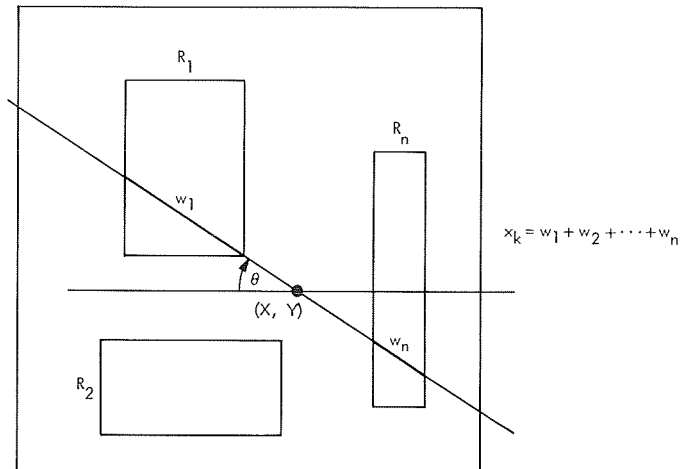
Fig. 4. Random lines intersecting rectangles

$$x_k = w_1 + w_2 + \cdots + w_n$$
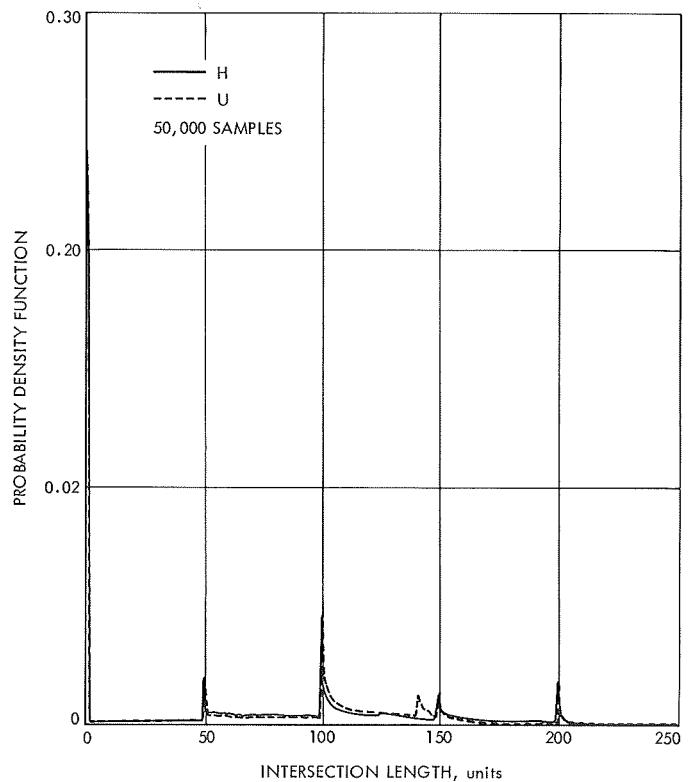
Fig. 5. PDF of random line intersection length

have identical convex hulls. The probability of zero intersection is a function of only the convex hull. (The convex hull of a figure may be formed by joining every pair of points within a pattern by a straight line.)

The PDF of x conditioned on the event that there is an intersection is displayed in Fig. 6. The sharp peaks in
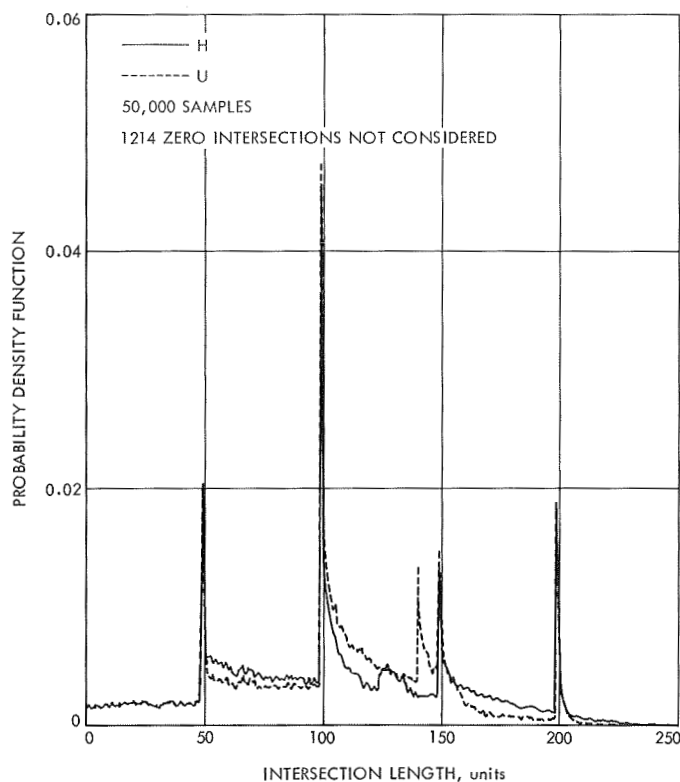
Fig. 6. PDF conditioned upon intersection
(f(0) not shown)

Fig. 7. Cumulative distribution function

Fig. 8. Expected number of samples for a
significance of e12 and e21

the PDF are due to the major dimensions of the letters. The peak at 50, for instance, corresponds to the height of the horizontal segment of the letters. The peak at 100 is due to the width of the two vertical legs. An examination of the two letters will show that a line can intersect **U** more frequently than **H** with a length of 140; the experimental PDF shows this fact. The PDF for both letters are not easily expressible in a compact form, and often it is difficult to distinguish them.

A clearer view of the PDF of x is possible by observing the integral of the PDF. Figure 7 is the cumulative distribution function. Both functions begin at 0 and become 1.0 as x becomes large. Seemingly, there is not much difference between the two functions. Yet, as it will be shown, the difference is sufficient to make classifications possible at predetermined error rates.

4. Classification

A natural question which arises is, "How many features are necessary before a classification can be made?" Application of the sequential probability ratio test results in the smallest average number of required samples for a decision at a given error rate. Figure 8 is a plot of the

expected number of samples needed for various error rates. An interesting point to observe is at the error of the first kind and the error of the second kind (definitions in *Subsection 2*) equal to 1%, where the expected number of required samples is only 70. (*It indicates that this method can perform the chore of character recognition at*

a higher performance level and for less computation than is now commercially possible.)

Figure 9 shows the $\mathcal{E}(n)$ in terms of the logarithm of the error rate. This plot shows that even at error rates of 1 in 10,000, the required number of samples is less than 200.

5. Experimental Results

The points Ⓐ and Ⓑ on Fig. 9 are due to experimental results. The block letter **H** is placed in the retina. Appropriate experimental PDFs are assumed known at the beginning of the test. Actually, only the *a priori* calculable table of the likelihood ratio (the z, as defined in *Subsection* 2) is needed.

Random lines are cast and the x_i features extracted. The values for $z(x_i)$ are found in a table and added to L (which is zero at the beginning of an experiment). If L is greater than $\mathcal{A}$, which is a function of the two kinds of error rates, a decision in favor of **H** is made. If L is less than $\mathcal{B}$, which is also a function of the two kinds of error rates, then a decision in favor of **U** is made. Otherwise, another random line is cast and x_i+1 is found. An arbitrary upper limit on the number of samples per experiment is set at 200. This ensures finiteness of the algorithm. If the maximum of 200 samples is reached, and the sequential probability ratio test is not terminated, then a Bayes' test is used instead (Ref. 9). That is, a check for the sign of L is made and if it is positive, the pattern is declared **H**. If not, the pattern is declared **U**.

In compact algorithmic notation, one SPRT experiment is as follows:

(1) $L \leftarrow 0; i \leftarrow 0.$

(2) Cast random line; $i \leftarrow i+1; n \leftarrow i.$

(3) Find x_i, $L \leftarrow L+z\,(x_i).$

(4) If $L > \mathcal{A}$, then **H**, $D = 1$; terminate.

(5) If $L < \mathcal{B}$, then **U**, $D = 0$; terminate.

(6) If $i = 200$, go to 7; otherwise, go to 2.

(7) If $L > 0$, then **H**, $D=1$; otherwise, **U**, $D=0$; terminate.
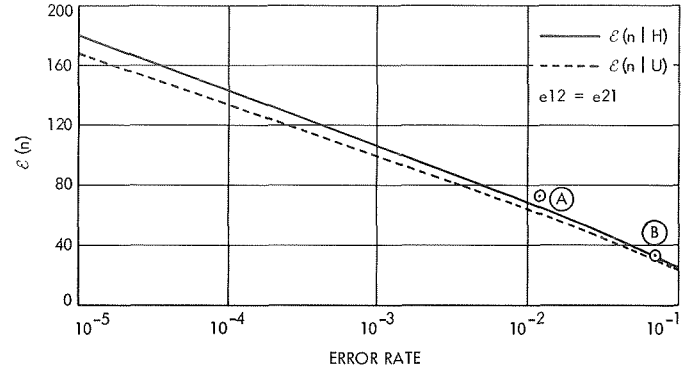
Fig. 9. Expected number of samples vs log of error rate

Hence, at the end of experiment j, the number of samples needed, n_j, is available, and

$$\bar{n} = \frac{1}{M} \sum_{j=1}^{M} n_j$$

gives the average number of samples required to make a decision. The letter D in the above algorithm stands for the decision; $D_j=1$ means **H** on the jth experiment. Thus,

$$\bar{D} = \frac{1}{M} \sum_{j=1}^{M} D_j$$

is equal to the ratio of the number of correct decisions to the total number of experiments and the error rate of the second kind is $e21 = (1 - \bar{D})$; M is the number of experiments performed.

Point Ⓐ on Fig. 9 is obtained by performing the above experiment 7600 times, having found $\mathcal{A}$ and $\mathcal{B}$ corresponding to $e21 = e12 = 0.01$. The result is $\bar{n} = 76$ and $e21 = 0.012$, which is close to the computed $\mathcal{E}(n)$ for $e12 = e21 = 0.01$. Running the experiment 850 times, with $\mathcal{A}$ and $\mathcal{B}$ corresponding to $e21 = e12 = 0.1$, gives point Ⓑ. Again, the result $\bar{n} = 34$ and $e21 = 0.07$ is close to the computed curve.

The sum of the likelihood function L is a random variable. In fact, it is a *random walk*. Figure 10 shows the random trajectories for L for four arbitrary choices of experiments; $\mathcal{A}$ and $\mathcal{B}$ for these experiments correspond to $e12 = e21 = 0.1$. Experiments 1 and 2 terminate before $\mathcal{E}(n)$ and experiments 3 and 4 take more samples than $\mathcal{E}(n)$. They all cross the $\mathcal{A}$ threshold; hence, correct decisions are made.

Figure 11a shows the intersection lengths which caused the random walk shown in Fig. 11c. Figure 11b shows what the intersections would be if the pattern were U. Again observe the correct decision which is made with only 11 random features.

6. Concluding Remarks

In order to complete the pattern recognition problem for the characters of the English language, the multiclass problem must be studied. Multiclass hypothesis testing is not satisfactorily solved in general and has not been applied adequately to statistical pattern recognition.

An investigation into the application of the sequential technique to the multiclass classification problem would yield a *random race*, rather than a *random walk*, in which each runner takes random steps toward his goal. The invariant feature extraction algorithm is well suited as the input for such a statistical classifier.

Further studies could yield the parameters needed in the design of a practical character recognition machine.

References

1. Ferguson, T. S., *Mathematical Statistics: A Decision Theoretic Approach*, Chapter 4. Academic Press, New York, 1967.

2. Guttman, I., and Wilks, S. S., *Introductory Engineering Statistics*, p. 155. John Wiley & Sons, Inc., New York, 1965.

3. Wald, A., *Sequential Analysis*. John Wiley & Sons, Inc., New York, 1947.

4. Fu, K. S., *Sequential Methods in Pattern Recognition and Machine Learning*, p. 171. Academic Press, New York, 1968.

5. Selin, I., *Detection Theory*, p. 92. Princeton University Press, Princeton, N. J., 1965.

6. Doob, J. L., *Stochastic Processes*, pp. 348 and 457. John Wiley & Sons, Inc., New York, 1953.

7. Wilks, S. S., *Mathematical Statistics*, p. 494. John Wiley & Sons, Inc., New York, 1962.

8. Feller, W., *An Introduction to Probability Theory and Its Applications*, Volume I. John Wiley & Sons, Inc., New York, 1968.

9. Weber, C. L., *Elements of Detection and Signal Design*, p. 23. McGraw-Hill Book Co., Inc., New York, 1968.
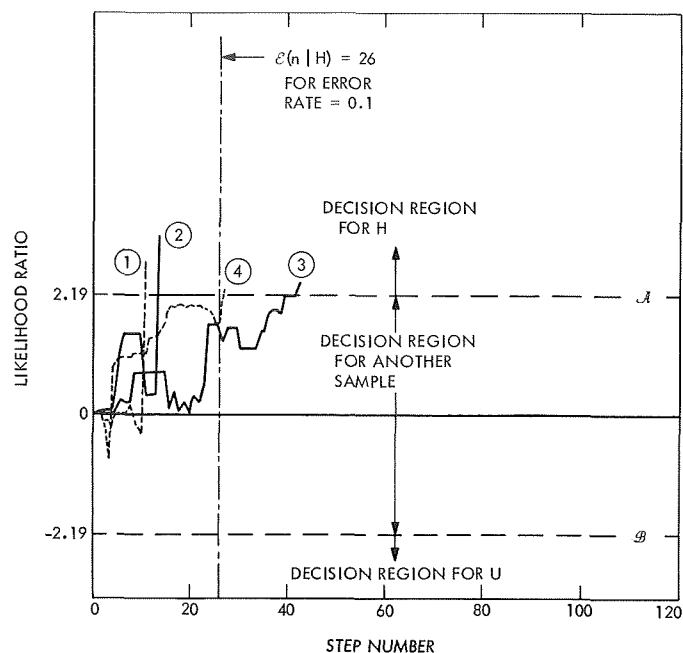
Fig. 10. Random walk of the likelihood ratio

(a) INTERSECTIONS WITH H   (b) INTERSECTIONS WITH U

(c) RANDOM WALK CROSSING DECISION BOUNDARY
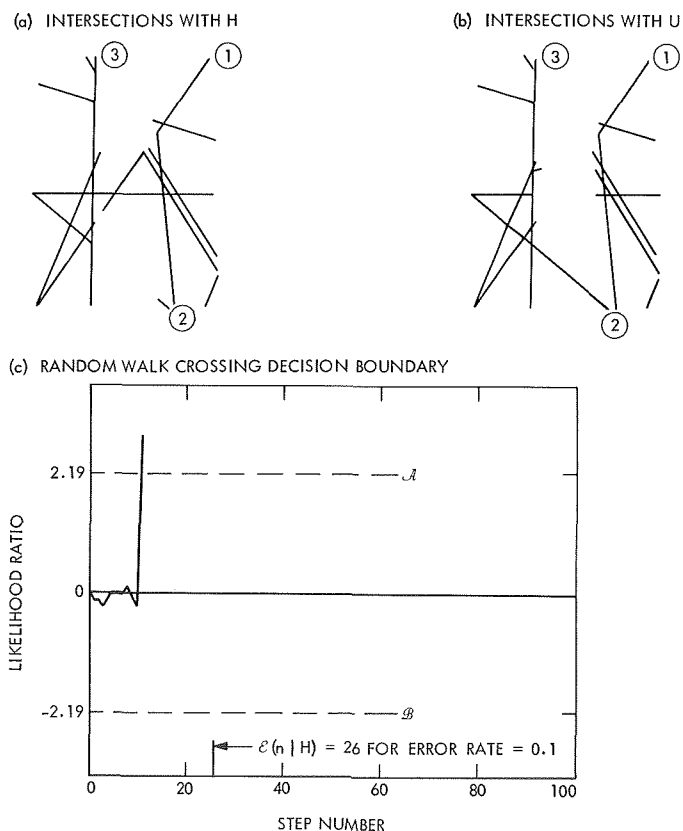
Fig. 11. Random lines used in an actual experiment

XVI. Spacecraft Data Systems

ASTRIONICS DIVISION

A. Evaluation of Recording Tapes for Use in Spacecraft Magnetic Tape Recorders,

J. K. Hoffman, S. H. Kalfayan,[1] and R. H. Silver[1]

Another step of a continuing effort to solve problems related to the reliability of magnetic tape in typical spacecraft tape recorder applications was completed by the Spacecraft Data Systems Section (see SPS 37-56, Vol. I, pp. 21–28). The work involved the investigation of tape

---

[1]Polymer Research Section, Propulsion Division.

to magnetic head frictional drag characteristics under certain environmental conditions. The immediate significance of this program is its applicability to the development of the *Mariner* Mars 1971 data storage subsystem.

The results of Phase I of the subject investigation are presented in *Chapter XIX-B* of this volume as part of the report by the Propulsion Division whose personnel and facilities are supporting this effort. Further evaluation of data and additional testing is currently in process.

XVII. Space Simulators and Facility Engineering
ENVIRONMENTAL SCIENCES DIVISION

A. Application of Imposed Magnetic Fields to Compact-Arc Lamps, *C. G. Miller and R. E. Bartera*

1. Introduction

The Jet Propulsion Laboratory SS15B solar simulator uses a cluster of 37 lamps at 20-kW input each (740 kW total). The light from all lamps is combined by means of an integrating lens system (Ref. 1) and a 23-ft single-piece collimator. This arrangement provides a 15-ft-diam beam of the same intensity as true sunlight at earth orbit outside the atmosphere (Fig. 1). The half angle subtended by the artificial sun is <1 deg, and the spectrum is essentially the xenon arc spectrum.

The system is designed to accept additional power by increasing the number of lamps in the cluster from 37 to 61 (20-kW each) for a total input of 1.22 MW. This extra power can be used to increase the beam diameter from 15 ft to 20 ft, but without improving the collimation angle, increasing the intensity, or improving the spectral characteristics. Unless the radiation field of the lamp is changed, improvements in any of the latter three characteristics can only be obtained at the expense of degrading other performance characteristics. A net improvement in performance can only come from an increased intrinsic brightness of the emitting area of each arc. In 1966, a program was begun at JPL to study the mechanism of the light-emitting processes for the xenon compact-arc lamps with the ultimate purpose of developing higher performance lamps suitable for advanced solar simulation work.

2. Arc Lamp Brightness

The optical system of the solar simulator projects an image of the brightest spot of the discharge field by a lens-and-mirror system into the work field. Figure 2 shows a representative distribution of brightness in the discharge area of a xenon compact-arc lamp. The peak brightness value comprises a cylinder approximately 2 mm in diam and 3 mm in length, located just off the tip of the cathode, and is the useful input area for the solar
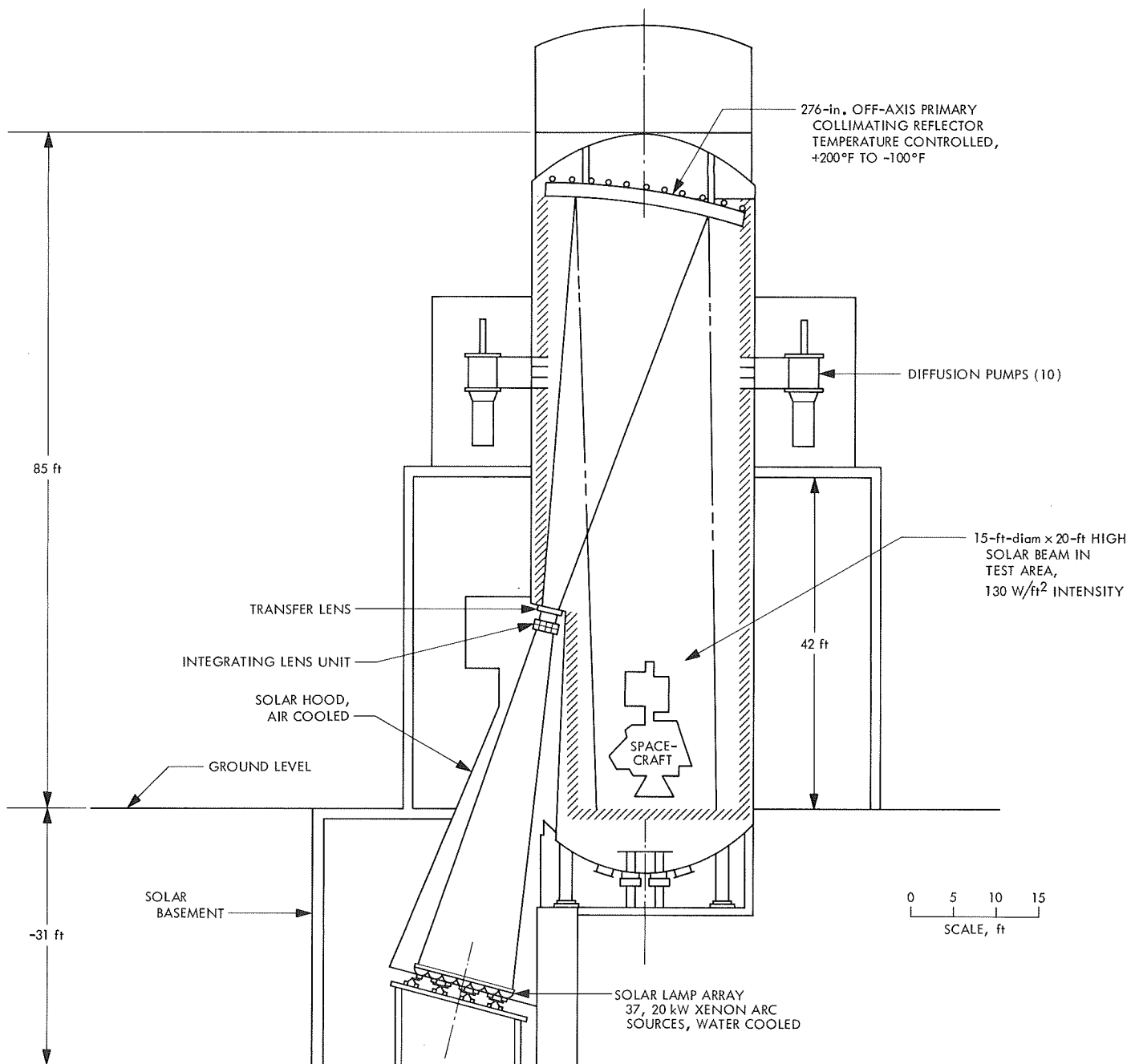
Fig. 1. JPL 25-ft space simulator

Labels on figure:

276-in. OFF-AXIS PRIMARY COLLIMATING REFLECTOR TEMPERATURE CONTROLLED, +200°F TO -100°F

DIFFUSION PUMPS (10)

15-ft-diam × 20-ft HIGH SOLAR BEAM IN TEST AREA, 130 W/ft^2 INTENSITY

85 ft

42 ft

TRANSFER LENS

INTEGRATING LENS UNIT

SOLAR HOOD, AIR COOLED

GROUND LEVEL

SPACE-CRAFT

SOLAR BASEMENT

-31 ft

0   5   10   15
SCALE, ft

SOLAR LAMP ARRAY 37, 20 kW XENON ARC SOURCES, WATER COOLED

Fig. 2. Representative brightness distribution

ANODE

50
100
500
1000
3000
5000
PEAK 10,000 cd/mm^2

CATHODE

10 mm

LAMP VOLTAGE 44 V
LAMP CURRENT 455 A

system optics. An increase in the brightness of this specified area of the arc source, even if obtained by redistribution of the light in the remainder of the field, would be advantageous. A change in the brightness of the specified area of the arc source can, in general, be obtained by a change in the operating parameters of the lamp; this leads to a redistribution of the energy in the arc area. Such a gain in the brightness of the imaged area does not necessarily mean increased efficiency, and does not necessarily imply increased overall luminosity. The characterization of gain can only be accomplished by measuring microbrightness distributions in the manner depicted in Fig. 2, rather than total luminous output of the discharge.

It has been convenient to study the effects of increased power in the lamp by considering, separately, a number of independent factors. The factors that are particularly pertinent are:

(1) Gas composition and density.

(2) Anode heat transfer.

(3) Specific emission of cathode and arc resistance.

(4) Spatial stability of the cathode spot and overall stable operation of the lamp.

(5) Gas pressure in relation to container strength.

Each of these factors is being examined separately and intensively. The order of presentation is roughly that in which they are amenable to improvements in upgrading the performance of the lamps.

3. Applicable Magnetic Means for Improvements in Operation

The factors (2), (3), and (4) listed in *Subsection 2* can be controlled by magnetic means. This article describes technology that has been developed to date concerning magnetic means to control these factors. Results of work on the control of factors (1) and (5), which are not amenable to magnetic control, will be discussed separately.

a. Increase in anode capacity. Anode heat loading has been the limiting factor in lamp operation. Some time ago, a lamp system was developed which used one cathode and a number of anodes (SPS 37-56, Vol. III, pp. 173–175). In this system, each anode sequentially served as the anode of the arc for a short time, the current being time-shared among all the anodes. Thus, each anode had a duty cycle of $1/N$ and the cluster carried N times the average permissible power loading of a single anode in normal service. The switching from anode to anode was an *electrostatic* switching arrangement, the anodes being connected to the outputs of a rectified polyphase a-c current and the discharge occurring between the one common cathode and whichever anode had momentarily the greatest positive potential with respect to the cathode. The brightness of the useful imaged area increases as more power is deposited in it. For the polyanode case discussed here, the power in the emitting arc spot was N times the power possible with a single anode; the radiated power was almost N times as much. While the operation was satisfactory, the mechanical complexity was considerable (Fig. 3).

Magnetic control made it possible to eliminate the complexity of the electrostatic switching method described. A single water-cooled anode, shown schematically in Fig. 4, had three electromagnets imbedded in the tip of the diverter; the three electromagnets were energized from a three-phase power source such that the magnetic field drove the arc foot around the contact area of the anode. The attachment point then became a circle coaxial with the center line and partway up the anode structure. Figure 5 shows the magnetic field and the anode. The method of rotating an arc in a circular path
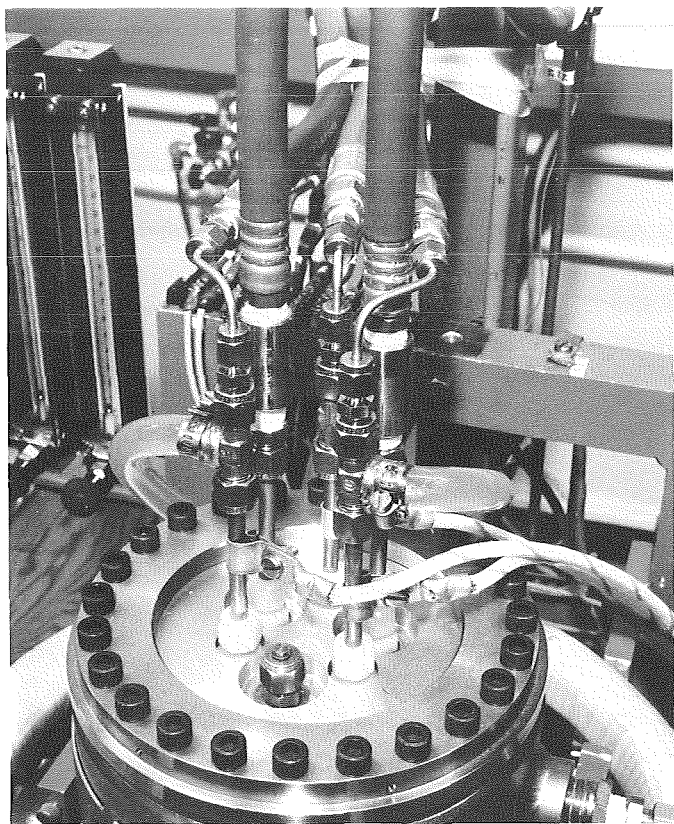
Fig. 3. Anode electrostatic switching arrangement

Fig. 4. Triple-magnet, water-cooled anode

by the interaction of a radial magnetic field and a longitudinal arc current, demonstrated earlier by E. Laue,[1] provided input powers of up to 50 or 100 kW in that work. The method described is satisfactory for future lamps if suitable anodes having built-in magnets could be incorporated into them.[2]

In order to apply the principle of increasing the power handling capability of a lamp by spreading the contact points of the anode foot on the anode over a large area to an existing lamp, external magnets were used on an intact lamp of the current production model with no internal modification.

The results are shown in Fig. 6, which is a multiple exposure photograph showing the anode contact at the extremities of its travel and the stability of the location of the cathode spot, in spite of the excursions of the anode foot.

---

[1]Laue, E., *Rotating Arc–Final Report*, 1959 (JPL internal document).

[2]A subsequent development, by R. E. Bartera, has been made in which a dc magnetic winding inserted in the anode can take the place of the more complex three polyphase ac windings described.

Thus, it appears that lamps already installed in solar simulator lamp banks can have their input power rating and the brightness of the cathode-emitting spot materially increased by the use of magnetic windings external to the individual lamp and its reflector system.

b. Improvement in cathode conditions. An increased current density from the cathode into the arc can provide a higher brightness in the emitting area just off the cathode. A water-cooled cathode was made up with a single magnet imbedded in it to give a longitudinal field (Fig. 7). The enhancement of the brightness of the emitting area of the arc, in this case, depends on two factors: (1) the dimunition of the size of the emitting area at the tip of the cathode, and (2) the effective increase of the arc column resistance. An increase in the
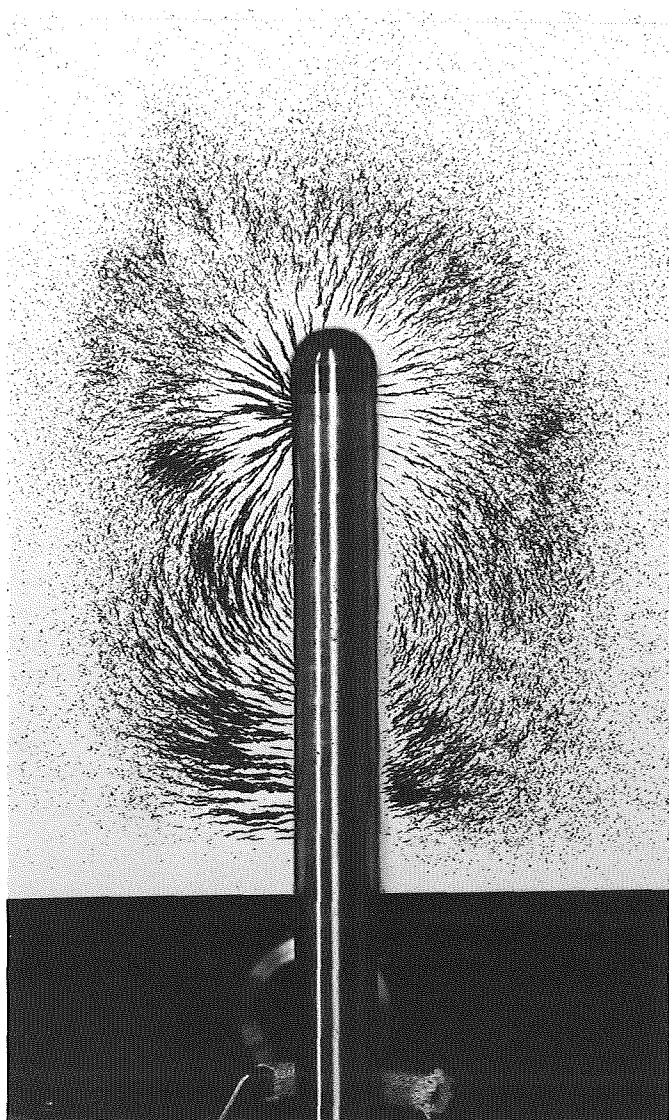
Fig. 5. Anode magnetic field

Fig. 6. Multiple exposure of anode contact

arc column resistance requires an increased applied voltage to maintain a given current in the arc; this constitutes an increased power input to the arc, resulting in higher brightnesses.

c. Spatial stabilization of cathode hot-spot and arc lamp stable operation. Another application of magnetic control to lamp operation is given in connection with the stability problem. An assembly of lamps is used in the solar simulator (Fig. 8). In operation, an interaction occurs among the lamps because of the stray magnetic fields developed by the individual lamp current feed lines, which are of different lengths and run adjacent to soft iron framework in various directions.

Such stray magnetic fields of one lamp and its supply leads on another lamp in a reflector in proximity to it, give rise to lamp instability, flickering, and blow-out. The time-averaged brightness of any one of the lamps is reduced, in this fashion, at the expense of performance of the whole solar simulator.

Such difficulties can be eliminated by magnetic means: e.g., by winding several turns of wire on the base of the reflector of each lamp, and allowing the current from the lamp to flow through the coil. Figure 8 shows the arrangement of reflectors and coils. For the locations of
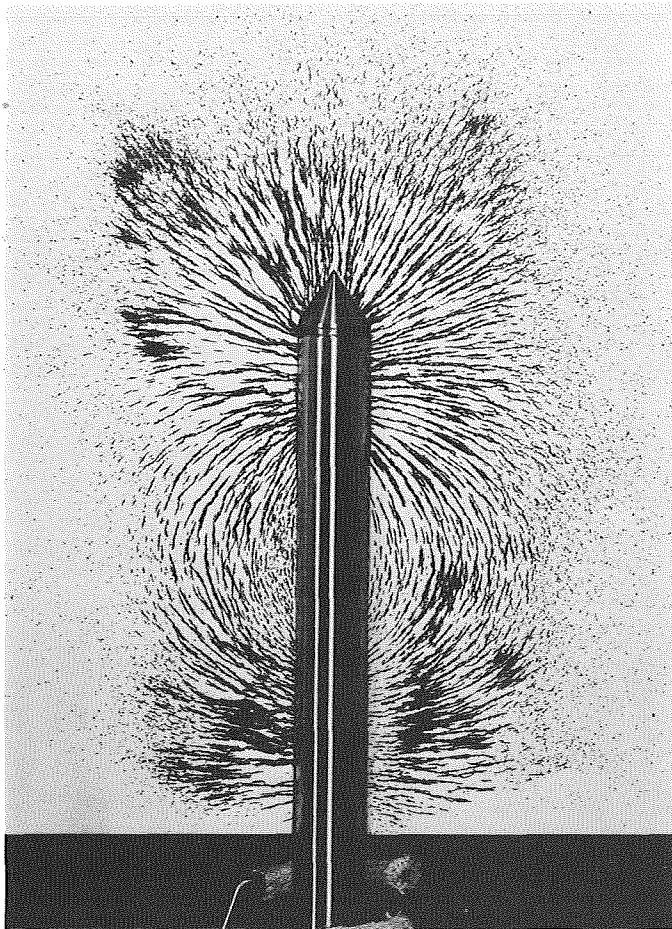
Fig. 7. Single-magnet water-cooled cathode
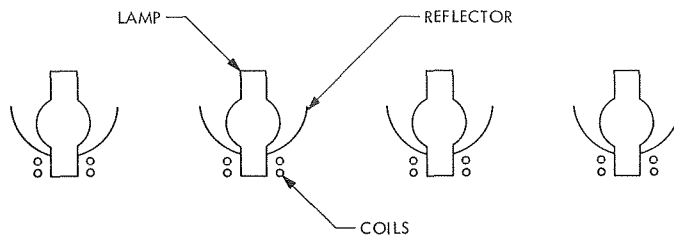
Fig. 8. Solar simulator lamp assembly

the coils and the reflector sizes used, the coils developed 2000 A-t and produced a magnetic field of approximately 100 G directed longitudinally along the cathode axis, which allows the arc to run stably and eliminates flickering and disturbances.

One benefit realizable from the use of such longitudinal magnetic fields is that somewhat greater brightness and luminous output can be obtained from the lamps, in addition to the stabilization of operation. For any given set of arc operating conditions and gas pressure, application of the longitudinal magnetic field requires an increased voltage to maintain current flow in the arc. This constitutes increased power input which produces greater brightness in the emitting area.

Reference

1. Bartera, R. E., Riise, H. N., and Miller, C. G., "Solar Simulators at the Jet Propulsion Laboratory (JPL)," *Appl. Optics,* Vol. 9, p. 1068, 1970.

XVIII. Solid Propellant Engineering

PROPULSION DIVISION

A. Initiation of Explosives by Laser Energy,
V. J. Menichelli and L. C. Yang

1. Introduction

The effects of laser and other intense light sources on the ignition of explosive materials have been extensively investigated (Refs. 1 and 2). Laser pulses in the free running mode (millisecond duration) can generally ignite pyrotechnic materials and primary high explosives. Some correlation with respect to sensitivity and the reflectance of the material has been made. Also, the sensitivity of some explosives can be increased considerably by introducing fine metallic particles such as gold, zirconium, etc. Some preliminary work on the initiation of explosives by laser energy is discussed in Ref. 3.

The advantages of a laser-initiated system over presently used electrical methods are increased safety and reliability. Electromagnetic radiation and spurious electrical signals pose serious safety problems for electro-explosive devices (EEDs). Inherent to all spacecraft and launch systems are long electrical cables and powerful electromagnetic transmitting devices. Electrically initiated explosive devices contain wire bridge circuits and electrical cables capable of picking up spurious signals by induction and/or electromagnetic radiation by coupling. There are numerous documented reports of inadvertent initiation of EEDs because of the aforementioned phenomena (Ref. 4). These problems have led to the introduction of 1-W, 1-A, no-fire initiators and exploding

bridgewire devices that have reduced susceptibility to inadvertent initiation. However, the complexity of these devices has resulted in costs much higher than conventional EEDs[1] to achieve the same degree of reliability.

Increased safety can be achieved because the laser provides a unique form of energy. In general, materials have not been observed to lase naturally, nor are they expected to lase except under very deliberate and positive means. Laser-initiated devices would not contain electrical circuits or be directly tied into electrical equipment and, therefore, would be immune to the electrical environments associated with space vehicles. The safeguards necessary to achieve electrical immunity in conventionally constructed EEDs would be eliminated, and reliability would be increased because of the simplicity of the device. The laser-initiated device would consist of a metal body to contain the explosive material and a window through which the laser energy would enter. Transfer of this energy from the laser source to individual explosive components is possible with the use of fiber optics.

2. Laser-Generated Shock Phenomenon

By inducing a high laser-generated shock into an explosive material it is possible to replace sensitive explosive materials with less sensitive secondary high explosives, thus improving safety. The basic features of

---

[1]Squibs, primers, detonators, etc., used in non-nuclear weapons.

the free running mode laser appear to remain when the light source is a Q-switched laser having a nominal duration ≤ 25 ns; however, this phenomenon is not well understood at present. Several reports on the interaction of a Q-switched laser with materials such as carbon and various metals have revealed this to be a shock phenomenon. The propagation velocity of the shock (plasma) measured in high vacuum (10^{-5} torr) or low-pressure air (2 torr) is of the order of 10^6 cm/s depending on the laser energy. The propagation of the plasma and its shock strength are normally measured by high-speed photography and/or an ionization probe.

An experiment was designed that would interact thin metal films with the Q-switched laser energy and observe the shock phenomenon. The size of doped particles in explosives is normally in the micron range. The depth of damage to a metal surface from a Q-switched laser is also in the micron range. Thus, it is more relevant to investigate thin films of material so that the damage and generated shock can be investigated as a function of the thickness of the film. It was required that the induced shock be applied directly to explosives; to accomplish this it was necessary to generate the shock by placing the thin metal film on a transparent surface with the medium facing the focused laser beam.

A Korad K-1Q laser system with a ruby rod capable of producing 0–4 J of pure Q-switched laser energy was used as the energy source. The event was recorded with a Beckman-Whitley Model 200 simultaneous framing and streak camera. This camera has a maximum writing speed of 6.9 mm/μs at a mirror rotation speed of 2500 rev/s. Operation at 1000 or 2000 rev/s was adequate for this experiment.

Some early experiments with thin-film metals were conducted in air. It was clear that the phenomenon could not be investigated successfully under these conditions, partly because of the ionization of air near the focal point of the target. It appeared that the plasma first grew longitudinally (parallel-axis), and then a luminous boundary expanded radially. This was especially true at higher energies. However, an experiment with thin-film carbon was successful (Fig. 1). Later, experiments were performed in a vacuum in a Pyrex desiccator that employed a Welch mechanical pump to produce a stable, 1-torr vacuum. This was not considered a good vacuum; however, the propagation of the luminous boundary was well observed. Under these vacuum conditions, ionization of the air is greatly reduced, and the framing utility of the camera yields no meaningful data because of the rapidity of the phenomenon. Therefore, only streak
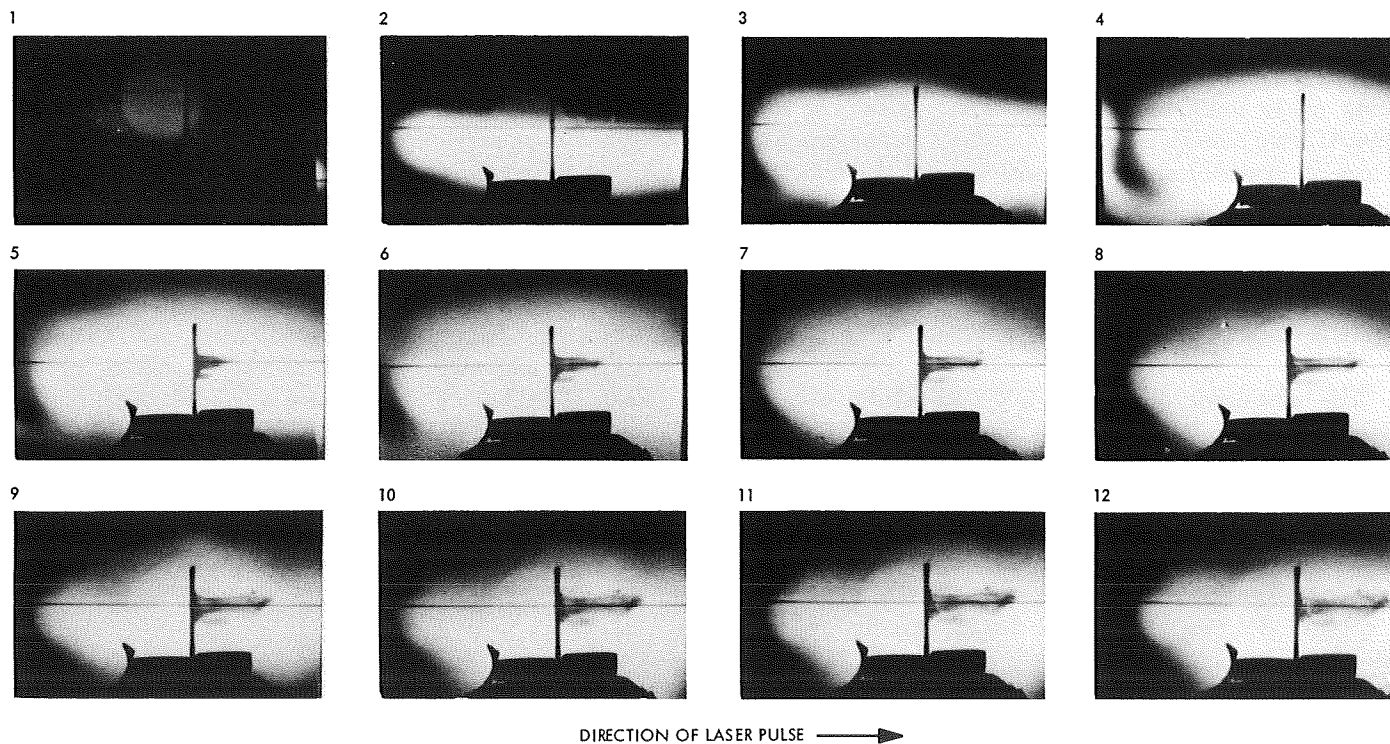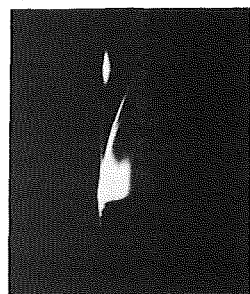

DIRECTION OF LASER PULSE ➡

Fig. 1. Sequence of Q-switched laser pulse impacting a thin film of carbon
placed on the far side of a glass plate

camera pictures were recorded. The results of various materials tested are shown in Fig. 2; not all of the materials were deposited on glass, but all were made with a laser power of 1.67 J. The thin samples without hard backing showed a concave phenomenon and in cases with a glass backing resulted in damage to the glass. The streak camera pictures indicate that the plasma moves before the termination of the laser pulse, which is in agreement with other investigators (Ref. 5).
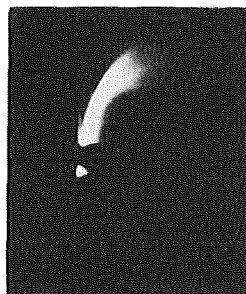
3. Conclusions

(1) The more absorptive samples (e.g., carbon) generate higher shocks than the more reflective samples (e.g., aluminum).

(2) Samples relatively poorer in heat diffusion (e.g., steel) generate higher shocks.

(3) The initial shock front seems independent of the film thickness but the propagation of the shock is dependent on thickness.

(4) The plasma expansion velocities are high ($\sim$cm/μs), beyond that needed for high-explosive detonation (5 cm/μs), even after extrapolation to atmospheric pressure.

References

1. Barbarisi, M. J., and Kessler, E. G., *Initiation of Secondary Explosives by Means of Laser Radiation*, TR 3861. Picatinny Arsenal, Dover, N.J., May 1969.

2. Moses, S. A., and Popick, H., *Final Report Laser Initiating Systems for Explosives (LISE)*, Report DAC-61770. McDonnell–Douglas Astronautics Co., Jan. 1969.

3. Menichelli, V. J., and Yang, L. C., *Laser Initiation of Explosives*, Technical Report 32-1474. Jet Propulsion Laboratory, Pasadena, Calif., Apr. 30, 1970.

4. Constant, P. C., Rhodes, B. L., and Chambers, G. E., *Investigations of Premature Explosions of Electroexplosive Devices and Systems by Electromagnetic Radiation Energy* (U), Midwest Research Institute, Apr. 1962 (Confidential).

5. Basor, N. G., et. al., *Sov. Phys.—JETP*, Vol. 24, No. 4, pp. 659–666, Apr. 1967.

Fig. 2. Propagation of a plasma luminous boundary generated by a Q-switched ruby laser observed with a streak camera at 1 torr

B. Theoretical Arguments Supporting the Instantaneous Burning Rate Measurements for Solid Propellants During Depressurization Made at JPL, R. L. Klaus

1. Introduction

In microwave measurements made at JPL recently, it was found that the instantaneous burning rates of solid propellants subjected to depressurization transients were initially higher than the corresponding (i.e., at the same pressure) steady-state burning rates. This behavior is qualitatively illustrated in Fig. 3 for a case in which extinction occurs and for one in which it does not.[2] In both cases, the instantaneous burning rate is higher than the steady rate at the corresponding pressure during the early part of the transient, but eventually drops below the steady-state value. When extinguishment of the propellant occurs, the burning rate continues to drop to zero; when it does not occur, it eventually recovers and becomes equal to the steady-state value $\bar{r}/r_0$. Because

[2]Curves based on data taken by Dr. David Norton, for a non-aluminized polyether urethane propellant.
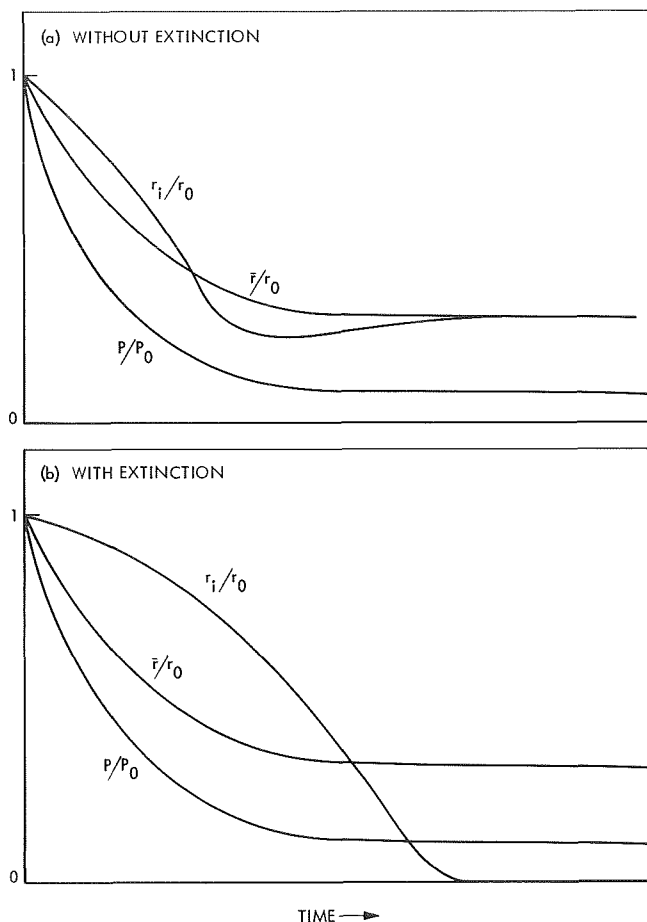
Fig. 3. Transient burning rates

these results are apparently in conflict with the predictions of existing theory, a possible theoretical justification for this phenomenon is offered here.

2. Assumptions

To simplify the discussion and to focus on the salient points, certain assumptions are made which, though probably not strictly true, are reasonable.

a. Assumption 1. The propellant is a homogeneous solid that is chemically inert except for a chemical decomposition taking place at its surface. Subsurface chemical reactions could be considered but would not alter the qualitative conclusions and are ignored for the present.

b. Assumption 2. The decomposition at the surface is chemical in nature and its rate is controlled by the kinetics of decomposition of the solid. This implies that the decomposition at the surface is only a monotonically increasing function of surface temperature, but not a

function of pressure or rate of heat transfer to the surface from the gas or from the surface into the solid. This assumption is valid for reactions of the type

$$A(\text{solid}) \rightarrow B(\text{gas})$$
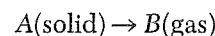
where B can be a mixture of gases, and where the above reaction is irreversible (or far removed from equilibrium). It is thought that in an actual propellant, the dominant controlling parameter for surface reaction is, in fact, the surface temperature, although pressure may exert some influence. Unless this influence is considerable, it will also not alter the qualitative conclusions to be drawn here.

c. Assumption 3. The gas phase is *quasi-steady*. By this it is meant that the temperature and concentration profiles that exist during the transient period are exactly the same as those that would exist at the steady state *for the same system pressure, surface temperature, and burning rate*. (For a burning rate that depends exclusively on surface temperature, mention of the burning rate in the definition of the quasi-steady gas phase is, of course, redundant.) It has been well established that the times for relaxation of the gas-phase temperature and concentration profiles are much smaller than those for the relaxation of the temperature profile in the solid. Thus, the quasi-steady gas is a reasonable assumption and serves to focus attention on the thermal lags in the solid, which are the source of the observed depressurization phenomenon. It is important to realize that the profiles are to be determined from the instantaneous pressure and surface temperature. Thus, as the pressure and surface temperature change during the course of the transient, the temperature profiles (and hence, the instantaneous rate of heat transfer from the gas to the solid) also change. However, the instantaneous values are assumed to be the same as if the steady state were to prevail in the gas phase at the instantaneous values of the surface temperature and pressure.

d. Assumption 4. The steady-state stagnation flame temperature[3] is independent of pressure. This would be true if the gas-phase heat capacity were independent of pressure, which would be true if the equilibrium gas-phase composition were independent of pressure. The latter is not precisely true, but in actual fact, flame temperatures are quite constant with pressure. Again, this

---

[3]All reference to temperature will be taken to be to stagnation temperatures. Since the flow rates of the gases away from the propellant surface are small, these stagnation temperatures should not differ materially from the static temperatures.

approximation does not affect the qualitative conclusions to be drawn here.

3. Arguments

a. Flame temperature dependence. From thermodynamic considerations alone, it may be shown that the equilibrium flame temperature of the propellant depends only on its thermodynamic properties and ambient temperature, and is always higher for a higher ambient temperature. This is illustrated in Fig. 4, which sketches the thermodynamic path for two combustion situations that differ in their ambient temperature. The total enthalpy change for the entire combustion process is, of course, zero. The process may be visualized to take place in two parts: a decomposition of the solid into gaseous products at ambient temperature, then a heating of the products to the flame temperature. From the first law of thermodynamics for flow systems,

$$\Delta H = 0 = L_i + \int_{T_{ai}}^{T_{fi}} C_{pg} dT \qquad (1)$$

where i may be either 1 or 2, L_i is the decomposition energy at T_i, C_{pg} is the gas-phase heat capacity and T_{ai} and T_{fi} are the ambient and flame temperatures corresponding to i. Two equations similar to Eq. (1) may be written that correspond to T_{a1} and T_{a2}. However, because the change in any thermodynamic state variables is independent of path, L_2 may be calculated in terms of L_1 and the heat capacities:

$$L_2 = - \int_{T_{a1}}^{T_{a2}} C_{ps} dT + \int_{T_{a1}}^{T_{a2}} C_{pg} dT + L_1 \qquad (2)$$

This may be used to eliminate L_2 in favor of L_1 and, in addition, when the two original equations are subtracted,
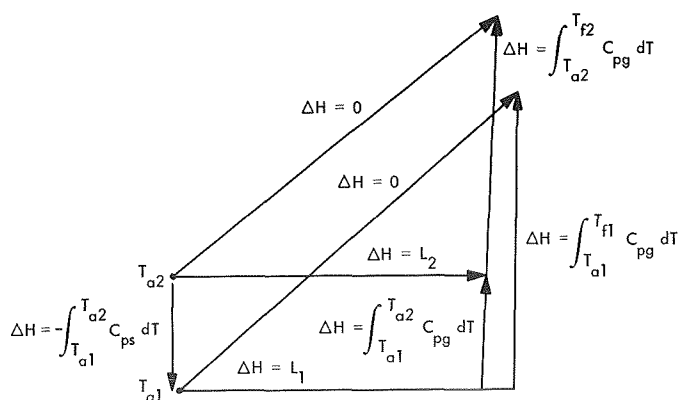

Fig. 4. Thermodynamic representation of combustion

$$\int_{T_{f1}}^{T_{f2}} C_{pg} dT = \int_{T_{a1}}^{T_{a2}} C_{ps} dT \qquad (3)$$

is eventually obtained. Because the heat capacities are always positive, it is clear that a higher flame temperature will be attained for a higher ambient temperature. This conclusion applies to the steady state only because the effect of energy accumulation or depletion in the system has not been included.

b. Pressure vs burning rate and extinguishment. It will now be shown that a finite step-function decrease in pressure (infinite dp/dt) will always extinguish a propellant and that its instantaneous burning rate in the initial part of the transient will be greater than the corresponding steady-state value will now be argued.

Consider two steady-state temperature profiles that exist at two pressures but at the same ambient temperature. The one at the higher pressure is represented by curves a and b, and the one at the lower pressure is represented by curves c and d of Fig. 5. At the higher pressure, the slopes of the curves at the surface are greater than for those at lower pressure. This corresponds to a greater heat transfer from the gas phase to the solid, which results in a higher surface temperature and, hence, a greater decomposition rate. Because the gas is quasi-steady, the decomposition rate is equal to the burning rate; however, because the ambient temperature is the same in both cases, the flame temperature is the same. These phenomena have all been well established.

Suppose that the pressure in the gas is suddenly lowered from the higher to the lower of the two pressures just mentioned. It is assumed that the gas phase immediately adjusts itself to this new pressure, but that the surface temperature responds more slowly. In fact, it is assumed that an instant after the step change in pressure, the surface temperature has not yet changed, although because of the decrease in pressure, the heat transfer from the gas to the solid has abruptly changed. Thus, the solid-phase temperature profile immediately after the change is still given by curve a, but the gas-phase temperature profile is now given by curve f. Two features of this curve are of particular importance: (1) its slope at the interface has decreased (because it is at lower pressure) and (2) the maximum temperature that is attained (which may be thought of as an unsteady-state flame temperature) has increased.

This somewhat surprising result can be justified in two ways. First, the sudden change in gas-phase pressure
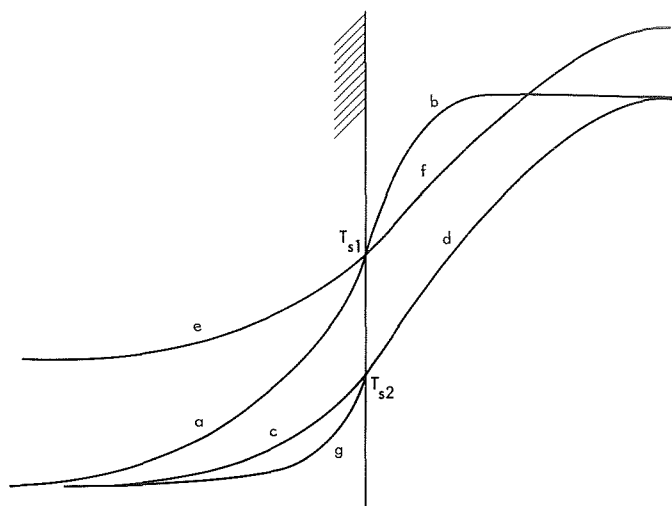
Fig. 5. Solid and gas phase temperature profiles

decreases the heat transfer to the solid. However, because the temperature of the gases emerging from the solid has not changed, the decrease in heat transfer leaves more energy available to raise the temperature of the gases. A second justification comes from an answer to the question: To what steady-state temperature profile in the *solid* does the gas-phase temperature profile given by curve f correspond? Since the surface energy effects at T_{s1} are unchanged, the steady-state solid temperature profile would look like curve e, with a smaller derivative at the surface than curve a, because the derivative of curve f is less than that of curve b. Because the steady-state solid temperature profiles are all exponential in shape, the ambient temperature for curve e clearly has to be higher than for curve a. However, from the thermodynamic arguments advanced previously, a higher ambient temperature gives rise, in the steady state, to a higher flame temperature, which is exactly what has been asserted.

The difficulty in accepting this assertion exists because it has been commonly thought that the flame temperature is a boundary condition that can arbitrarily be imposed on the gas-phase model. This very plausible assumption has been found to be untrue (Ref. 1). It was shown that a specification of temperature, pressure, and mass flux (which may not be independent of temperature) are the only boundary conditions necessary to completely determine the profiles in the gas phase, including the flame temperature.

The events throughout the extinction transient may now be followed as a result of curves a and f being established as those that exist in the solid and gas

immediately after the step-function change in pressure. Clearly, since the rate of heat transfer to the solid has decreased, the surface temperature (and, in fact, the entire temperature profile in the solid) begins to drop. However, it does not drop abruptly because of the thermal lag of the solid. In the initial part of the transient, the surface temperature is clearly higher than the steady-state surface temperature corresponding to the new pressure that would be given by T_{s2}. If the rate of decomposition is related only to the surface temperature, it follows that it will initially be greater than the corresponding steady-state value.

In the initial part of the transient, more heat is being transferred into the solid in the transient state than in the corresponding steady state. This can be seen from a comparison of the shapes of curves a and e of Fig. 5, which are the initial transient and steady-state curves, respectively. Moreover, as the surface temperature drops, the corresponding steady-state curve in the solid also drops but as long as the surface temperature is greater than T_{s2}, it has a corresponding ambient temperature that is always above T_{a1}. Thus, the transient surface derivative is always greater than the corresponding steady-state derivative.

Whether or not the propellant ultimately extinguishes depends on the surface temperature derivative in the solid as the surface temperature passes through T_{s2}. It will now be shown that the temperature profile at that instant is of the shape of curve g, with a derivative greater than that of the steady-state profile. This being the case, it is clear that the temperature of the surface will continue to drop until ambient conditions prevail and extinguishment has been accomplished.

The argument proceeds through a comparison between the total amount of energy in the solid as the temperature proceeds from T_{s1} to T_{s2} for the steady and unsteady profiles at corresponding surface temperatures. The total amount of energy in the solid at any instant will be equal to the integral of $C_{ps}dT$, integrated from the surface to a point at an infinite distance into the solid. Clearly, there is more energy in the solid for curve e (initial steady-state profile) than for curve a (initial unsteady-state profile). However, because the gas is quasi-steady, and because the energy of reactions at the surface depends only on the surface temperature, at any instant corresponding to any surface temperature between T_{s1} and T_{s2} exactly the same amount of energy is transferred into the solid during the depressurization transient. This is the same as if the solid proceeded through a series of states in which the profiles were those corresponding to steady

burning. Thus, the total energy in the solid when the surface temperature reaches T_{s2} is less in the transient case than for the series of steady states. Even though the end points of curve g in Fig. 5 coincide with those of curve a, the curve must lie below it, which implies that there is a higher derivative at the surface. This completes the argument that extinguishment always occurs for finite step changes in pressure.

4. Discussion

These arguments have pertained to a step-function decrease in pressure, but it is not difficult to see how they apply for more gradual decreases in pressure. Because of the rapid relaxation of the temperature profile in the gas phase, the heat transfer to the surface will always decrease much more rapidly than the surface temperature. If the burning rate is related to this temperature during the initial part of the transient, it will be greater than that corresponding to steady burning conditions at the same pressure. For a true step-function decrease in pressure it was predicted that the system would always extinguish. However, for a finite depressurization rate, whether or not extinguishment occurs depends on the various heat transfer rates. If the depressurization is sufficiently slow, a point may be reached where the sum of the heat transfer from the gas to the surface and surface energy effects is equal to or greater than the heat transferred into the solid. Under these conditions extinguishment may not occur. For example, in Fig. 3a, the minimum point on the curve for r_i/r_0 corresponds to an instant at which the energy transfer from the gas is equal to the energy transfer into the interior of the solid and, from that point on, the surface temperature and, hence, the burning rate begin to rise until a new steady state is reached.

Reference

1. Klaus, R. L., "Contribution to the Mathematical Theory of Solid Propellant Ignition and Extinction," 6th ICRPG Combustion Conference, CPIA Publication 192, Vol. I, Dec. 1969.

C. An Improved Newton–Raphson Algorithm for Finding the Roots of Equations for Solid Propellant Combustion Studies, R. L. Klaus and S. Wilson

1. Introduction

There are several problems of recent interest in rocket applications that require the determination of the roots of nonlinear equations. These include the solution of certain transcendental equations in heat transfer problems, and the theoretical determination of propellant combustion instability. The Newton–Raphson method is perhaps the most well-known and widely used iterative method for solving such nonlinear equations. If the equation to be solved may be expressed as $f(x) = 0$, the Newton–Raphson formula for the nth approximation for a root r_n based on a known previous approximation r_{n-1} is

$$r_n = r_{n-1} - \frac{f(r_{n-1})}{f'(r_{n-1})} \qquad (1)$$

where f' is the derivative of f. Given a first approximation, this formula may be used successively to find increasingly more accurate values of the root. There are several significant pitfalls with the use of this method:

(1) It may not converge at all even though a root does exist. Convergence is very strongly influenced by the shape of the function, which must be checked in each case (according to criteria discussed in textbooks on numerical analysis) to insure that convergence does indeed occur.

(2) The formula, as it stands, merely finds a root, but there is no restriction on which root is found. There are many important equations that have more than one root although one particular root is sought. Thus, it is desirable for any root-finding algorithm to converge to the particular root of interest.

(3) There is a problem of convergence criterion. It is not necessarily true that when two successive approximations agree to within a specified tolerance, that the root has been found to within that tolerance. Wherever there are large values of f', in fact, the new approximation can be extremely close to the old one even though it may be quite far removed from the actual root.

(4) Even if convergence is eventually obtained, the procedure may converge quite slowly, particularly if successive approximations are made in a region where the slope of the function is quite a bit larger than the slope in the neighborhood of the root. It is desirable for an algorithm to detect this condition and, if it occurs, to switch to another method.

In short, the Newton–Raphson method frequently results in a very rapid convergence to a root. However, under certain circumstances it can fail or be very inefficient. In any automated root-finding algorithm, these circumstances should be automatically detected. The algorithm presented here deals with all these problems.

A set of subroutines exists in the JPL computer program library to solve multi-variable sets of equations. For a single equation, however, they are somewhat cumbersome to use. The present algorithm is relatively simple and direct, and, for the purposes of finding roots to functions of one variable, has a relatively low overhead in terms of computer storage and time.

2. Description of the Algorithm

A FORTRAN subroutine has been developed that uses Eq. (1) to find the roots of functions. However, as the subroutine proceeds, certain tests are performed to insure that the method is converging and is efficient. In the event that the method is not convergent or is slow, the algorithm performs an interval halving before again proceeding with the Newton–Raphson method. Thus, the method will always converge and will proceed with at least half the speed of interval halving.

To control which root is found in a multi-root equation, an interval is specified on input. The value of the function must have opposite signs at the end points of the interval. If this is not true, the routine will detect an error condition, print out a diagnostic and return to the calling program. If the signs do differ, there is obviously at least one root in the interval and the routine will find it. If there is more than one root, the routine will proceed but there is no way of controlling which root will be found. Thus, it is the user's responsibility to choose the interval so that there is exactly one root in it.

The routine begins at the left-hand side of the interval and attempts the Newton–Raphson method to find a better approximation. If the next approximation falls outside the interval, a flag is set to indicate this, the calculation is disregarded, and a new calculation is attempted beginning at the other side of the interval. If any new approximation falls within the interval, a check is performed on the sign of the function evaluated at that point to determine whether or not the root has been passed. If it has, this becomes the new opposite limit and the next Newton–Raphson approximation begins there. If not, another test is performed to determine whether or not the routine is proceeding efficiently. The amount by which the most recent approximation differs from the previous one is added (or subtracted, depending on the direction of approach) to the latest approximation and the sign of the function again evaluated to determine whether or not the root was passed. If so, the routine concludes that the calculation is proceeding efficiently and it continues; if not, the routine sets the

flag to indicate this condition and tries the calculation from the other side.

If the flags on both sides of the interval have been set to indicate that the method has failed or is proceeding slowly, the routine tests the sign of the function evaluated at the mid-point of the interval. Based on this result, this point becomes the new left- or right-hand limit of the interval and a Newton–Raphson calculation is attempted from this point.

Every point tested that falls within the interval as it exists at that moment eventually may become either a new left- or right-hand interval limit, depending on the sign of the function evaluated at that point. Thus, the interval is shrinking as the function continues to be evaluated at various points. The test on the efficiency of the Newton–Raphson method fails whenever it is shown to be less efficient than interval halving, and the routine then switches to this method for one iteration.

Convergence is taken to have occurred when the interval has shrunk to below the specified tolerance. This is clearly an absolute indication that the root has been found to within the tolerance. A relative error convergence test is used. That is, convergence is indicated when either

$$r_l + \epsilon |r_l| \geq r_r \qquad (2)$$

or

$$r_r - \epsilon |r_r| \leq r_l \qquad (3)$$

where r_r and r_l are the right- and left-hand limits of the interval, respectively, and ϵ is the specified tolerance. These tests are performed unless zero is included in the interval, in which case it is conceivable that convergence might never take place if the root were sufficiently close to zero. Therefore, if zero is within the original interval, a lowest tolerance is set.

$$\epsilon^* = \epsilon(r_{r0} - r_{l0})$$

where r_{r0} and r_{l0} are the original limits. When the tests represented by Eqs. (2) and (3) are performed, the maximum of the two values ϵ^* and $\epsilon |r_l|$ is used in Eq. (2) and the maximum of ϵ^* and $\epsilon |r_r|$ in Eq. (3).

The algorithm has been written as a FORTRAN function subroutine called SØLV1. This subroutine re-

turns the root that was found. It has the following calling sequence:

FUNCTIØN, SØLV1 (FUNC, CØNST1, DFUNC, CØNST2, TØL, NITLIM, XLØ, XHI, NITAC, IER)

The subroutines FUNC and DFUNC are themselves functions with the calling sequence:

FUNCTIØN FUNC (X, CØNST1)

FUNCTIØN DFUNC (X, CØNST2)

which calculate $f(x)$ and $f'(x)$, respectively, where X is the argument and CØNST1 and CØNST2 are arrays that can store constants that are used in the two functions. These functions must, of course, be supplied by the user and represent the particular function whose roots are sought.

The parameter TØL is the specified tolerance on the root; NITLIM is a specified maximum number of iterations permitted; XLØ and XHI are the initial left- and right-hand limits of the interval, respectively (these are not changed during the course of the calculation). The output variable NITAC, which is the actual number of function evaluations performed by the routine and IER, is an output error detection flag with the following significance: 0 indicates that no errors were detected; 1 indicates that the maximum number of iterations allowed by NITLIM was equalled; -1 indicates that the sign of the function at each end of the interval was the same and no root was sought; -2 indicates that the interval was improperly specified.

3. Discussion

The routine was tested with several known functions to insure its proper operation, accuracy, and efficiency. Several polynomials of differing degree and shape but known roots were tested. Roots were correctly determined to six significant figures (in all cases) as requested in relatively few function evaluations. In the polynomials tested, the maximum number of function evaluations never exceeded 11, but this does not mean that there are not many situations in which a greater number of evaluations would be required.

Because it was of interest in connection with important heat transfer calculations, roots of the function

$$f(x) = x \tan x - C = 0$$

were sought for values of C ranging from 10^{-3} to 10. This equation has an infinite number of roots; thus it was necessary to carefully specify the desired interval. The first six roots were determined for all values of C tested and in every case they agreed exactly with the tabulated data in Ref. 1.

Finally, because it was of interest in the design of insulation for rocket chambers, the following transcendental equation was also tested:

$$f(x) = x \tan x - [C_2 - C_1 x^2] = 0$$

There are multiple roots here that necessitated careful selection of the intervals. Roots correct to 6 significant figures were always found within approximately 10 function evaluations.

It is felt that this algorithm is quite general, accurate, and efficient. For a continuous function (provided that a proper interval can be specified and that the function differs in sign at the end points of the interval), it will always return a root to within the specified tolerance regardless of the shape of the function within the interval.

Reference

1. Carslaw, H. S., and Jaeger, J. C., *Conduction of Heat in Solids,* Second Edition, p. 491. Oxford Press, London, 1959.

D. Basic Equations in the Mathematical Modeling of the Gas Phase of a Burning Solid Propellant, *R. L. Klaus*

1. Introduction

In any mathematical model of steady or unsteady combustion of a solid propellant, the goal of the gas-phase model is to provide a means of calculating the energy fed back to the decomposing solid from chemical reactions in the gas phase, and a means of calculating the temperature of the emerging gases after all chemical reactions have gone to completion. The model should be based on the fundamental conservation equations for a compressible fluid.

Because the chemistry and geometry (for an actual, composite propellant) are very complex, certain simplifications are usually made in the basic fluid mechanical equations to permit their analysis and solution. This results in tractable equations that contain certain "lumped parameters," which are probably best obtained

from comparison with experimental measurements. If these parameters can be obtained from steady-state measurements, much has been gained because measurement of these parameters under unsteady conditions (e.g., ignition, extinction, or oscillatory combustion) are much more difficult to make. In this way, data from steady-state measurements can be extended to unsteady-state conditions. The purpose of this treatment is to develop a set of equations that describes a simple gas-phase model for a burning propellant, to discuss their mathematical behavior and the choice of a proper set of boundary conditions, and to give supporting physical arguments and explanations.

In the model, the energy fed back from the flame to the solid will be taken to be due to heat conduction and will be calculated by

$$\dot{q}_s = -k_{gs} \frac{\partial T}{\partial x}\bigg|_s$$

where all symbols are defined in Table 1. This heat transfer rate is determined by consideration of the governing conservation equations, a scheme for chemical reaction, and the imposition of boundary conditions that both conform to physical reality and permit a solution of the differential equations. The importance of a proper set of boundary conditions has not received its deserved attention. One recent study (Ref. 1), for example, incorporates boundary conditions that will be shown to lead to an ill-posed problem.

The model considered here is one-dimensional, beginning at the gas–solid interface (taken as $x = 0$) and extending to a distance away from it sufficient for chemical reactions to have gone to completion. If no stimulus is being applied to the flame side of the gas phase, steady conditions (temperature, gas velocity, and species concentrations) are attained there. The case in which, because of the presence of an ignition stimulus, the temperature does not reach a steady value at the edge of the developing flame (i.e., at the point where the chemical reactions have gone to completion) will also be considered.

Changes in pressure through the gaseous zone will be ignored. This is a reasonable assumption because the zone is thin and because pressure disturbances are propagated much more rapidly than changes in the other profiles. This approximation introduces a considerable simplification of the mathematical model in that it permits

Table 1. Nomenclature

A, B, C	designations for reacting species
a_i	unsteady accumulation of species i per unit length
b, c	stoichiometric coefficients
C_i	molar concentration of species i
C_p	heat capacity at constant pressure
C_1, C_2	integration constants
D	pre-exponential factor
E	activation energy
g_0	gravitational constant
g_1, g_2	functions defined by Eqs. (9) and (10)
ΔH_r	molar heat of reaction of the gases
h	enthalpy
I_1, I_2	functions defined by Eqs. (30) and (31)
J_i	diffusive flux of species i
$K_1 - K_8$	non-dimensional constants
k	thermal conductivity
L	characteristic length
M_i	molecular weight of species i
$\mathcal{M}$	average molecular weight
m	mass flux
m_r	ratio of mass fluxes defined by Eq. (29)
P	pressure
q	energy flux
R	gas constant
r_i	rate of accumulation of species i by chemical reaction
S_i	stoichiometric coefficients
T	temperature
t	time
u	gas velocity
x	distance
y	change of variable
ρ	mass density
ω_i	mass fraction of species i

Subscripts

c	conduction
g	gas phase
i	species designation
j	reference
r	reaction
ref	reference
s	conditions that exist at the surface
0	conditions that exist at $x = 0$
∞	conditions that exist as $x \to \infty$

Superscripts

*	non-dimensionalized variable

the momentum equation to be dropped from consideration. However, it also introduces a certain ambiguity because (as will be seen) it leads to the prediction that the effect of mass and energy introduction on the propellant side of the gas phase is felt immediately on the flame side, which, mathematically, is an infinite distance away. This is contrary to one's physical intuition, which suggests that a finite time must elapse before such effects are felt.

The resolution of this ambiguity lies in the fact that the constant pressure assumption is equivalent to the assumption that pressure disturbances propagate with infinite velocity, carrying with them the effect of mass and energy addition to the flame side of the region in an infinitesimal amount of time. This should not be disturbing, however, because, when measured on the time scale on which the temperature and velocity profiles actually develop, the effect of mass and energy addition is felt essentially instantaneously on the flame side. It means, however, that care must be taken in the statement of the boundary conditions, lest what seems like a plausible set from physical considerations actually leads to an ill-posed problem because of the approximation regarding pressure.

2. Mathematical Development

With the omission of the momentum equation as indicated, the overall conservation equations and equation of states may be written as follows:

Overall continuity:

$$\frac{\partial \rho}{\partial t} + \frac{\partial}{\partial x}(\rho u) = 0$$

Species continuity:

$$\frac{\partial \rho_i}{\partial t} + \frac{\partial}{\partial x}(\rho_i u) + \frac{\partial}{\partial x}(J_i) = r_i$$

Energy:

$$\frac{\partial}{\partial t}(\rho h) + \frac{\partial}{\partial x}(\rho u h) + \frac{\partial \dot{q}_c}{\partial x} - \frac{\partial P}{\partial k} = 0$$

State:

$$\rho = \frac{P}{RT} \frac{\prod_i M_i}{\sum_i \omega_i \prod_{j \neq i} M_j}$$

The mass density of species i is defined by $\rho_i = \omega_i \rho$. Conservation of mass leads to the conclusion that

$$\rho = \sum_i \rho_i$$

$$\sum_i \omega_i = 1$$

The diffusive and heat conductive fluxes are, respectively, given by:

$$J_i = -\rho D_i \frac{\partial \omega_i}{\partial x}$$

$$\dot{q}_c = -k_g \frac{\partial T}{\partial x}$$

In general, the multicomponent diffusivities are complicated functions not only of temperature and pressure but also of local composition. However, the latter effect will be ignored.

A gas-phase reaction will be assumed of the form

$$A + bB \rightarrow cC$$
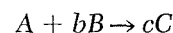
This reaction will be taken to be first order in both A and B. It will further be assumed that the reaction rate can be represented by an Arrhenius rate expression. Thus,

$$r_A = -C_A C_B \left[D \exp\left(\frac{-E}{RT}\right) \right]$$

where C_i is the molal density of i, given by:

$$C_i = \frac{\omega_i \rho}{M_i}$$

where D and E are constants. The stoichiometry of the reaction leads to relationships between the various rates of production of species:

$$r_b = b r_A$$
$$r_c = -c r_A$$
$$r_i = 0 \qquad (i \neq A, B, C)$$

Total enthalpy can be expressed in terms of enthalpies of individual species and, hence, in terms of heat capacities C_{pi} and temperature as follows:

$$h = \sum_i \omega_i h_i + \frac{u^2}{2g_0}$$

$$dh_i = C_{pi} dT$$

In the flame zone, the term $u^2/2g_0$ is so much smaller than the terms containing h_i that it is dropped from all future equations. It is also advantageous to define the total mass flux $\dot{m}$ and local average molecular weight $\mathcal{M}$ as follows:

$$\dot{m} = \rho u$$

$$\mathcal{M} = \frac{\prod\limits_{i} M_i}{\sum\limits_{i} \omega_i \prod\limits_{j \neq i} M_j}$$

With these definitions, the set of equations can eventually be reduced to

$$\dot{m} = \dot{m}(0,t) - \frac{P}{R} \int_0^x \frac{\partial}{\partial t} \left(\frac{\mathcal{M}}{T} \right) d\xi \tag{1}$$

$$\frac{P}{R} \frac{\partial}{\partial t} \left(\frac{\omega_i \mathcal{M}}{T} \right) + \frac{\partial}{\partial x} (\dot{m}\, \omega_i) - \frac{\partial}{\partial x} \left(\rho D_i \frac{\partial \omega_i}{\partial x} \right) = S_i \left(\frac{\omega_A \omega_B P^2 \mathcal{M}^2 D}{R^2 T^2 M_A M_B} \right) \exp \left(\frac{-E}{RT} \right) \tag{2}$$

$$\frac{P}{R} \left[\left(\sum_i \omega_i c_{pi} \right) \frac{\partial \mathcal{M}}{\partial t} + \sum_{i \neq j} (h_i - h_j) \frac{\partial}{\partial t} \left(\frac{\omega_i}{T} \right) \right] + \left(\sum_i \omega_i c_{pi} \right) \frac{\partial}{\partial x} (\dot{m}T) + \sum_{i \neq j} (h_i - h_j) \frac{\partial}{\partial x}\, \dot{m}\, \omega_i) - \frac{\partial}{\partial x} \left(k_g \frac{\partial T}{\partial x} \right) - \frac{\partial P}{\partial t} = 0 \tag{3}$$

where $S_A = -1$, $S_B = -b$, $S_C = C$, and $S_i = 0\ (i \neq A,B,C)$.

The overall continuity equation has been replaced by Eq. (1), which is explicit in $\dot{m}$. In Eqs. (2) and (3), the densities have been eliminated in most places in favor of $\dot{m}$. An equation of the form of Eq. (2) can be written for every species, but one of these will not be independent. In Eq. (3), the enthalpies have been cast into such a form that they are expressed relative to a reference species j.

Boundary conditions can be written both for T and each ω_i except one.

$$T(0,t) = T_0(t) \tag{4}$$

$$\dot{m}(0,t)\, \omega_i(0,t) - \left(\rho D_i \frac{\partial \omega_i}{\partial x} \right)_{0,t} = \dot{m}_{i0}(t) \tag{5}$$

where Eq. (4) expresses the fact that the temperature is given at the surface, and Eq. (5) is a mass balance of species i at the surface, assuming that $\dot{m}_{i0}$, the total mass flux of i at the surface, is also given. It may seem that because the equations are of second order, additional boundary conditions should be written, but as will be shown, if integrations are carried out to $x^* \to \infty$, additional boundary conditions would overdetermine the problem and render solution impossible.

Although the discussion could be pursued with these equations, for the sake of simplicity equations which are simplified still further will be considered. However, the same behavior would be found in the more general equations. Consider two species, one being the reactant and the other the product. Both species are assumed to be of equal molecular weight with equal heat capacities and thermal conductivities, which quantities are also taken to be constant. Further, it is assumed (in keeping with the results of the kinetic theory of gases) that (ρD_i) is constant. When all of these additional assumptions are inserted into the equations, and the equations are non-dimensionalized, the following equations are obtained:

$$\dot{m}^* = \dot{m}^*(0,t^*) + K_8 \int_0^{x^*} \frac{1}{T^{*2}} \frac{\partial T^*}{\partial t^*} d\xi \tag{6}$$

$$\frac{\partial^2 \omega_A}{\partial x^{*2}} - K_1 \frac{\partial}{\partial x^*} (\dot{m}^*\, \omega_A) = g_1^* \tag{7}$$

$$\frac{\partial^2 T^*}{\partial x^{*2}} - K_4 \frac{\partial}{\partial x^*} (\dot{m}^* T^*) - K_5 \frac{\partial}{\partial x^*} (\dot{m}^* \omega_A) = g_2^* \tag{8}$$

$$g_1^* = K_2 \frac{\omega_A^2}{T^{*2}} \exp \left(\frac{-K_3}{T^*} \right) + K_6 \frac{\partial}{\partial t^*} \left(\frac{\omega_A}{T^*} \right) \tag{9}$$

$$g_2^* = K_7 \frac{\partial}{\partial t^*} \left(\frac{\omega_A}{T^*} \right) - \frac{\partial P^*}{\partial t^*} \tag{10}$$

with boundary conditions,

$$T^* (0,t^*) = T_0^* (t^*) \tag{11}$$

$$\dot{m}^* (0,t^*)\, \omega_A (0,t^*) - \frac{1}{K_1} \frac{\partial \omega_A}{\partial x^*} (0,t^*) = \dot{m}^* (0,t^*) \tag{12}$$

and non-dimensionalized variables and constants,

$$x^* = \frac{x}{L} \qquad\qquad T^* = \frac{T}{T_{ref}} \qquad\qquad t^* = \frac{t}{t_{ref}}$$

$$\dot{m}^* = \frac{\dot{m}}{\dot{m}_{ref}} \qquad\qquad P^* = \frac{PL^2}{k_g T_{ref} t_{ref}} \qquad\qquad K_1 = \frac{L\,\dot{m}_{ref}}{\rho\, D_A}$$

$$K_2 = \frac{DP^2 L^2}{\rho\, D_A R^2 T_{ref}^2} \qquad K_3 = \frac{E}{R T_{ref}} \qquad K_4 = \frac{\dot{m}_{ref} C_\rho L}{k_g}$$

$$K_5 = \frac{\dot{m}_{ref} \Delta H_r L}{k_g T_{ref}} \qquad K_6 = \frac{PM \Delta H_r L^2}{\rho\, D_A R T_{ref} t_{ref}} \qquad K_7 = \frac{PM \Delta H_r L^2}{R T_{ref}^2 k_g t_{ref}}$$

$$K_8 = \frac{PML}{R T_{ref} \dot{m}_{ref} t_{ref}}$$

The convention on ΔH_r is that an exothermic reaction corresponds to a positive ΔH_r.

The first term in g_1^* is the non-dimensionalized rate of depletion of species A by chemical reaction per unit distance; the second is the non-dimensionalized unsteady rate of accumulation of species A per unit distance. For convenience this is expressed as:

$$g_1^* = -r_A^* + a_A^*$$

The function g_2^* is the non-dimensionalized unsteady rate of accumulation of energy per unit distance.

The non-dimensionalization results in the emergence of eight non-dimensional groups $K_1, K_2, \cdots, K_8$. The last three of these are discarded when a quasi-steady gas is considered because time dependence is dropped from the equations. The choice of reference temperature is arbitrary but it makes sense to choose $T_{ref} = T_0(0)$. Thus, for the unsteady case, $T_0^*(0)$ will equal 1 and for the quasi-steady case, the boundary condition expressed by Eq. (12) becomes:

$$T^*(0) = 1 \tag{13}$$

In similar fashion, $\dot{m}_{ref}$ may be chosen to be $\dot{m}_{ref}(0,t^*)$. For the quasi-steady case, $\dot{m}^*$ is constant and the boundary condition on ω_A becomes:

$$\omega_A(0) - \frac{1}{K_1} \frac{d\omega_A}{dx^*} (0) = 1 \tag{14}$$

Thus, the quasi-steady problem would still have five non-dimensional parameters. If integrations are carried out between 0 and ∞, one more parameter can be eliminated by fixing L. If, for example, elimination of K_1 were desired, L would be set equal to $K_1(\rho D_A)/\dot{m}_{ref}$. Looking at the parameters on another level, it is discovered that if constants that are specifications of the problem, or available for thermodynamics, are eliminated, four lumped parameters remain: the two kinetic constants, D and E; and two transport coefficients, k and (ρD_A). In a model of this level of approximation, it is probably appropriate to eliminate one of the two transport parameters, either from a generalized correlation between the two or by the commonly used assumption that the Lewis

number is equal to unity, which leads to $\rho D_A = k/C_p$. Thus, the model being used here may be thought of as essentially a three-parameter model. These parameters should be determined by matching the model to experimental results.

The equations are now in a form that makes it possible to examine their behavior. If Eq. (7) is formally integrated, one obtains:

$$\frac{\partial \omega_A}{\partial x^*} - K_1 \dot{m}^* \omega_A = \int_0^{x^*} g_1^* \, d\xi - K_1 \dot{m}^*(0,t^*) \tag{15}$$

where the boundary condition expressed by Eq. (11) has been used to evaluate the integration constant. A second integration yields

$$\omega_A = \exp\left(K_1 \int_0^{x^*} \dot{m}^* \, d\xi\right) \left\{ C_1 - \int_0^{x^*} \exp\left[-K_1 \int_0^{\zeta} \dot{m}^* \, d\xi\right] \left[K_1 \dot{m}^*(0,t^*) - \int_0^{\zeta} g_1^* \, d\xi\right] d\zeta \right\} \tag{16}$$

which gives rise to one additional integration constant. If Eq. (8) is formally integrated twice, two integration constants are again obtained, one of which may be evaluated through the boundary conditions expressed by Eq. (12). The two resulting equations of interest are:

$$\frac{\partial T^*}{\partial x^*} = K_4 \dot{m}^* T^* - K_5 \dot{m}^* \omega_A + \int_0^{x^*} g_2 \, d\xi + K_4 \dot{m}^*(0,t^*)(C_2 - T_0^*) \tag{17}$$

$$T^* = \exp\left(K_4 \int_0^{x^*} \dot{m}^* \, d\xi\right) \left[C_2 + \int_0^{x^*} \exp\left(-K_4 \int_0^{\zeta} \dot{m}^* \, d\xi\right) \left(K_5 \dot{m}^* \omega_A + \int_0^{\zeta} g_2^* \, d\xi\right) d\zeta \right] + \frac{\dot{m}^*(0,t^*)}{\dot{m}^*(x^*,t^*)} (T_0^* - C_2) \tag{18}$$

The evaluation of the two remaining integration constants in Eqs. (16) and (18) depends on whether or not an external stimulus is being applied to the flame side of the gas-phase model. Consider the case where this is not true: In this instance, the equations should be applied over the semi-infinite interval $0 \leq x^* \leq \infty$. If this is the case, C_1 and C_2 must be chosen so as to keep the solutions finite. The resulting equations are

$$T^* = \frac{\dot{m}^*(0,t^*)}{\dot{m}^*(x^*,t^*)} \left[T_0^* + \int_0^{\infty} \exp\left(-K_4 \int_0^{\zeta} \dot{m}^* \, d\xi\right) \left(K_5 \dot{m}^* \omega_A + \int_0^{\zeta} g_2^* \, d\xi\right) d\zeta \right] - \int_{x^*}^{\infty} \exp\left(-K_4 \int_{x^*}^{\zeta} \dot{m}^* \, d\xi\right)$$

$$\times \left(K_5 \dot{m}^* \omega_A + \int_0^{\zeta} g_2^* \, d\xi\right) d\zeta \tag{19}$$

$$\omega_A = \int_{x^*}^{\infty} \exp\left(-K_1 \int_{x^*}^{\zeta} \dot{m}^* \, d\xi\right) \left[K_1 \dot{m}^*(0,t^*) - \int_0^{\zeta} g_1^* \, d\xi\right] d\zeta \tag{20}$$

Equations (19) and (20) indicate that, for the case of no externally applied stimulus, the two boundary conditions expressed by Eqs. (11) and (12) are sufficient to completely determine the problem. In fact, additional boundary conditions might lead to an ill-posed problem. Clearly, from Eq. (20) $\omega_A \to 0$ as $x^* \to \infty$ as expected. The non-dimensionalized temperature $T^*(\infty,t^*)$ is given by

$$T^*(\infty,t^*) = \frac{\dot{m}^*(0,t^*)}{\dot{m}^*(x^*,t^*)} \left[T_0^* + \int_0^{\infty} \exp\left(-K_4 \int_0^{\zeta} \dot{m}^* d\xi\right) \left(K_5 \dot{m}^* \omega_A + \int_0^{\zeta} g_2^* \, d\xi\right) d\zeta \right] \tag{21}$$

and, thus, cannot be arbitrarily specified as a boundary condition. For future reference, a formula for the temperature derivative can also be derived:

$$\frac{\partial T^*}{\partial x^*} = K_4 \left[\dot{m}^* T^* - \dot{m}^*(\infty,t^*) T^*(\infty,t^*)\right] + K_5 \dot{m}^* \omega_A + \int_0^{x^*} g_2^* \, d\xi \tag{22}$$

From a mathematical standpoint, the sufficiency of two boundary conditions is due to the singular point in the two differential equations at $x^* \to \infty$. This singularity can be exposed by making the change of variables $(y = 1/x^*)$ and examining the behavior at $y = 0$. The two equations transform to:

$$\frac{\partial^2 \omega_A}{\partial y^2} + \frac{2}{y}\frac{\partial \omega_A}{\partial y} + \frac{K_1}{y^2}\frac{\partial}{\partial y}[\dot{m}^*\omega_A] = \frac{g_1^*}{y^4}$$

$$\frac{\partial^2 T^*}{\partial y^{*2}} + \frac{2}{y}\frac{\partial T^*}{\partial y} + \frac{K_4}{y^2}\frac{\partial}{\partial y}[\dot{m}^*T^*] + \frac{K_5}{y^2}\frac{\partial}{\partial y}[\dot{m}^*\omega_A] = \frac{g_2^*}{y^4}$$

The point $y = 0$ is clearly a singular point of the equations and results in the fact that no additional boundary conditions may be applied at that point. It should be emphasized that this change of variables merely exposes the singularity; it is actually there, although hidden, in the original equations. Moreover, it is not true, as has been suggested recently (Ref. 2), that the problems associated with integrating equations that contain singular points are avoided if they are at infinity rather than at some finite value. If a singular point is in the domain of integration, even if it is at one of its limiting values such as infinity, it influences the behavior of the equations over the entire interval and must be carefully considered.

Having discussed the behavior from the mathematical standpoint, it is also possible to rationalize it from physical considerations. First, it is helpful to note the behavior of mass fraction, temperature, and their derivatives as $x^* \to \infty$. It has already been established that $\omega_A(\infty,t^*) = 0$. Thus,

$$-\int_0^\infty r_A(\xi)\,d\xi = K_1\dot{m}^*(0,t^*) \qquad (23)$$

because if the mass fraction of species A at the flame is zero, the integral of the local rate of reaction must be equal to the total amount of species A introduced into the system at $x^* = 0$, which, in non-dimensionalized form is equal to $K_1\dot{m}^*(0,t^*)$. Also, if the integrated rate of depletion by reaction is exactly equal to the rate of input, then the integrated rate of unsteady accumulation must be zero. Thus,

$$\int_0^\infty a_A^*(\xi)\,d\xi = 0 \qquad (24)$$

from which it also follows that

$$\int_0^\infty g_1^*\,d\xi = K_1\dot{m}^*(0,t^*) \qquad (25)$$

If this information is inserted into Eq. (15) evaluated at $x^* \to \infty$, one obtains:

$$\frac{\partial \omega_A}{\partial x^*}(\infty,t^*) = 0$$

Also, Eq. (22) can be applied at infinity, bearing in mind that because g_2^* differs from a_A^* only by a constant, and since the latter vanishes when integrated as in Eq. (24), the former also vanishes when integrated over that interval. Thus,

$$\frac{\partial T^*}{\partial x^*}(\infty,t^*) = 0$$

so that both the temperature and mass fraction derivatives vanish as $x^* \to \infty$.

Returning to the physical rationale for the behavior at $x^* \to \infty$, it is clear that ω_A vanishes because, for finite reaction kinetics, all of species A eventually disappears due to chemical reaction. The situation with the temperature is as follows: Since all of species A reacts, there is a certain fixed energy effect associated with this chemical decomposition. The net energy carried into the system at $x^* = 0$ is due both to the bulk motion of the gas phase at its temperature, T_0^*, and the conductive heat transfer, which is proportional to the temperature derivative at $x^* = 0$, which, in turn, is fixed by the details of the gas-phase model. However, the sum of the energy entering the gas phase at $x^* = 0$ and the energy effect due to chemical reactions must equal the energy leaving the system at $x^* \to \infty$. It has already been shown that the temperature derivative vanishes there, so that the energy leaving the system must be accounted for by a rise in temperature of the exiting gases above that of those entering. This temperature rise must be of such a magnitude as to exactly account for the energy leaving the system. Thus, if the other energies are fixed by the parameters of the gas phase, the temperature of the

exiting gases must also be fixed and, therefore, cannot be arbitrarily specified as an additional boundary condition.

Returning to Eqs. (16) and (18) and the case for which an external ignition stimulus is being applied to the gas phase at the plane of the developing flame, this ignition stimulus is in the form of a finite heat transfer rate and, hence, temperature gradient at the flame. However, it has already been shown that the temperature derivative vanishes as $x^* \to \infty$. Thus, it is necessary to consider integrations over a finite interval that, with no loss of generality, may be taken to be $0 \le x^* \le 1$. This choice makes the parameter L in the non-dimensionalization equal to the thickness of the flame zone.

Because the singular point at $x^* \to \infty$ is now not a factor, it is possible to specify two additional boundary conditions at $x^* = 1$. Although several choices are possible, the following was chosen:

$$\omega_A(1,t^*) = 0$$

$$T^*(1,t^*) = T_1^*(t^*)$$

These conditions indicate that it has been specified that the reactions have gone to completion at $x^* = 1$ (in fact, this may be taken to be the definition of the edge of the flame) and that a certain predetermined temperature is attained. If these conditions are inserted into Eqs. (16) and (18) to evaluate the integration constants, the following are obtained:

$$\omega_A = \int_{x^*}^1 \exp\left(-K_1 \int_{x^*}^\zeta \dot{m}^* \, d\xi\right)\left[K_1 \dot{m}^*(0,t^*) - \int_0^\zeta g_1^* \, d\xi\right] d\zeta \tag{26}$$

$$T^* = \frac{T_1^*\left[\dot{m}_r(x^*) - I_1(x^*)\right] + T_0^*\left[I_1(x^*)\dot{m}_r(1) - I_1(1)\dot{m}_r(x^*)\right]}{\dot{m}_r(1) - I_1(1)} + \frac{I_2(1)\left[I_1(x^*) - \dot{m}_r(x^*)\right]}{\dot{m}_r(1) - I_1(1)} + I_2(x^*) \tag{27}$$

$$\frac{\partial T^*}{\partial x^*} = \dot{m}^*\left[K_4 T^* + K_5 \omega_A\right] + \int_0^{x^*} g_2 \, d\xi + \frac{K_4 \dot{m}^*(0,t^*)\left[I_2(1) + I_1(1)T_0^* - T_1^*\right]}{\dot{m}_r(1) - I_1(1)} \tag{28}$$

where

$$\dot{m}_r(x^*) = \frac{\dot{m}^*(0,t^*)}{\dot{m}^*(x^*,t^*)} \tag{29}$$

$$I_1(x^*) = \exp\left(K_4 \int_0^{x^*} \dot{m}^* \, d\xi\right) \tag{30}$$

$$I_2(x^*) = \int_0^{x^*} \exp\left(K_4 \int_\zeta^{x^*} \dot{m}^* \, d\xi\right)\left(K_5 \dot{m}^* \omega_A + \int_0^\zeta g_2^* \, d\xi\right) d\zeta \tag{31}$$

By reasoning similar to that used for integration over the semi-infinite interval, it can again be shown that the derivative of ω_A vanishes at $x^* = 1$. However, the derivative of temperature does not, in general, vanish at this point. In fact, this becomes the means by which the external ignition stimulus can be brought to bear on the developing flame. A finite temperature derivative at this point implies the existence of heat transfer from the bulk gases into the gas-phase portion of the combustion process, even though the chemical reactions of the flame have gone to completion.

Thus, the important differences between the two cases may be stated as follows: In one case the integrations are carried out to $x^* \to \infty$, and the singular point in the equations at this point prevents any additional boundary conditions to be specified there. It develops that the mass fraction of A and its first derivative vanish there, as does the derivative of the temperature. The temperature itself is determined by an overall energy balance on the gas phase, and may not be specified as a boundary condition. In the second case, the integrations are carried out over a finite interval. This permits the application of two addi-

tional boundary conditions, which may conveniently be chosen to depict complete depletion of A and the attainment of a specified temperature at the edge of the flame. In this case, although the derivative of ω_A again goes to zero at the edge of the flame, the derivative of the temperature does not vanish on either side of the finite flame zone. Thus, once the temperatures at each side of the gas phase are specified, the temperature derivatives are determined and must be calculated from the gas-phase model. The details of how the finite-interval model interfaces with various ignition stimuli are beyond the scope of this discussion.

Although the behavior of interest has been demonstrated for the unsteady equations, in actual practice one usually uses the quasi-steady equations because the response time of the gas phase is so much less than that of the solid.

The working quasi-steady equations are shown in Eqs. (32–41). In the case of a semi-infinite flame zone, a change of variables was made so that numerical integrations may be carried out over a finite interval. This procedure also exposes the singular point at $x^* \to \infty$. Also, Eq. (35) has been written in integrated form because it is explicit, whereas Eq. (32) is retained as a differential equation because the integrated form is implicit in ω_A. The quasi-steady equations shown are the working equations that must be solved numerically in order to solve the gas-phase model.

Semi-infinite flame:

$$\frac{d^2\omega_A}{d\lambda^2} - \left[\frac{K_1}{(1-\lambda)^2} + \frac{2}{1-\lambda} \right] \frac{d\omega_A}{d\lambda} = \frac{K_2\omega_A^2}{(1-\lambda)^4 T^{*2}} \exp\left(\frac{-K_3}{T^*} \right) \tag{32}$$

$$\omega_A(0) - \frac{1}{K_1} \frac{d\omega_A}{d\lambda}(0) = 1 \tag{33}$$

$$T_\infty^* = 1 + K_5 \int_0^1 \frac{\omega_A(\xi)}{(1-\xi)^2} \exp\left[-K_4\left(\frac{\xi}{1-\xi} - \frac{\lambda}{1-\lambda} \right) \right] d\xi \tag{34}$$

$$T^* = T_\infty^* - K_5 \int_\lambda^1 \frac{\omega_A(\xi)}{(1-\xi)^2} \exp\left[-K_4\left(\frac{\xi}{1-\xi} - \frac{\lambda}{1-\lambda} \right) \right] d\xi \tag{35}$$

$$\frac{dT^*}{d\lambda} = \frac{K_5}{(1-\lambda)^2} \left\{ \omega_A(\lambda) - \int_\lambda^1 \frac{\omega_A(\xi)}{(1-\xi)^2} \exp\left[-K_4\left(\frac{\xi}{1-\xi} - \frac{\lambda}{1-\lambda} \right) \right] d\xi \right\} \tag{36}$$

$$x^* = \frac{\lambda}{1-\lambda} \tag{37}$$

Finite flame:

$$\frac{d^2\omega_A}{dx^{*2}} - K_1 \frac{d\omega_A}{dx^*} = \frac{K_2\omega_A^2}{T^{*2}} \exp\left(\frac{-K_3}{T^*} \right) \tag{38}$$

$$\omega_A(0) - \frac{1}{K_1} \frac{d\omega_A}{dx^*}(0) = 1 \tag{39}$$

$$T^* = \frac{T_i^*[1 - \exp(K_4 x^*)] + T_0^*[\exp(K_4 x^*) - \exp(K_4)]}{[1 - \exp(K_4)]}$$

$$+ K_5 \left\{ \int_0^{x^*} \omega_A(\zeta) \exp[K_4(x^* - \zeta)] d\zeta - \left[\frac{1 - \exp(K_4 x^*)}{1 - \exp(K_4)} \right] \int_0^1 \omega_A(\zeta) \exp[K_4(1 - \zeta)] d\zeta \right\} \tag{40}$$

$$\frac{dT^*}{dx^*} = K_5\omega_A + \left[\frac{K_4 \exp(K_4 x^*)}{1 - \exp(K_4)}\right]\left\{T_0^* - T_1^* + K_5\int_0^1 \omega_A(\zeta)\exp[K_4(1-\zeta)]\,d\zeta\right\} \tag{41}$$

Definition of constants:

$$K_1 = \frac{L\dot{m}}{\rho D_A} \qquad\qquad K_2 = \frac{D\rho^2 L^2}{\rho D_A R^2 T_0^2} \qquad\qquad K_3 = \frac{E}{RT_0}$$

$$K_4 = \frac{C_p L\dot{m}}{k_g} \qquad\qquad K_5 = \frac{\dot{m}\Delta H_r L}{k_g T_0}$$

References

1. Gopalakrishnan, A., *Theoretical Studies on Solid Propellant Ignition*, Report 2005-FR, Contract NAS 7-571. Consolidated Engineering Technology Corp., Mountain View, Calif., Oct. 1968.

2. Merkle, C. L., Turk, S. L., and Summerfield, M., *Extinguishment of Solid Propellants by Rapid Depressurization*, Aerospace and Mechanical Sciences Report 880, p. 47. Princeton University, Princeton, N.J., Jul. 1969.

E. Low-Modulus Propellant for Case-Bonded, End-Burning Motors, H. E. Marsh, Jr., and D. Udlock

1. Introduction

A new capability has been added to the technology of solid propellant rocket motors. High-performance motors with thrust levels greatly reduced over previously attainable levels can now be provided for missions requiring low-acceleration propulsion, such as the insertion into orbit of spacecraft with lightly structured appendages already deployed. This new capability was demonstrated in the form of a fully case-bonded, end-burning motor configuration (SPS 37-55, Vol. III, p. 185 and Ref. 1). Two 12-in.-diam, flight-weight motor chambers were loaded, temperature cycled, and fired successfully. The propellant employed was JPL 540J (Ref. 2), which was used in the *Syncom* and *Advanced Technology Satellite* programs (Refs. 3 and 4).

Lower thrust levels are possible with the end-burning motor configuration because greatly reduced ratios of burning surface to propellant mass are attainable than are possible with conventional, internal-burning, solid propellant motors. Case bonding is essential for high performance because of the large savings in inert-component mass provided by its use. The great obstacle to the fabrication of case-bonded, end-burning motors has been the large triaxial strains imposed on such propellant grains by normal cyclings of pressure and temperature, and the lack of propellants with mechanical properties capable of withstanding such strains (see *Section XVIII-F*).

The preliminary demonstration of this new motor technology was possible because of the inherent high strain capacity of JPL 540J propellant. However, it was found in further testing that another quality of JPL 540J propellant mechanical properties (viz., the modulus) is marginal, on the high side, for this application. A new method of formulating led to a new family of propellants, based on JPL 540J, affording controllable mechanical properties in the low modulus realm.

2. Utilization of JPL 540J in Case-Bonded, End-Burning Motors

The first two case-bonded, end-burning motors of this program were successful. Subsequent tests with flight-weight chambers yielded mixed results. A summary of all of these tests, along with pertinent mechanical property values, is given in Table 2.

Four observations are drawn from the data in Table 2. First, with the possible exception of batch EB-1, the strain capacity of the JPL 540J propellant appears to be sufficiently high for this application. Second, each property exhibits a wide range of values. This is typical quality control experience with JPL 540J; however, it has been a manageable difficulty with previous applications. Part of the generally experienced JPL 540J property variation has been correlated with batch-mixer size. Third, a property qualitatively characterized as the *modulus* is too high. This statement is made this way because the precisely critical property is not known and therefore not measured. Propellant batch EB-9 represents a combination of the two problems: high modulus and troublesome quality control. The tensile strength

of 185 psi is unusually high for JPL 540J, but its departure from nominal is even greater than it appears. This is because the formulation is a modification (oxidizer particle size and distribution) that usually yields lower values. The formulation modification referred to is the use of a trimodal blend of oxidizer particle sizes instead of the usual bimodal blend. The overall average particle size of the trimodal blend is larger than that of the bimodal blend to reduce the burning rate almost 10%. Fourth, the propellant-to-insulation-to-chamber wall bonding system is generally good. Thus, the goals selected for propellant development became the lowering of modulus and the improvement of reproducibility.

3. Reduction of Propellant Modulus

Quantitatively, the mechanical property goals for an improved end-burning propellant were decided to be within the ranges tabulated below.

Property	Value
Tensile strength S_m (at maximum load)	40–100 psi
Secant modulus S_m strain at maximum load)	25–65 psi
Elongation	Must be above 100% (150% is optimum)[4]

It was expected that propellants with such properties would be suitable for use in the fully case-bonded, end-burning motor configuration, with regard to the two types of failure mentioned: propellant strain failure and chamber failure (including bond failure as well as buckling). The soft extremes of the above ranges were set as "first guesses" at the limits of two other problems: propellant machinability and slump (the term used to describe the detrimental deformation of a propellant under its own weight).

a. Network theory and propellant formulation.

Formulation studies and quality control of the fuel-binder component of the JPL 500 series of polyether-urethane/ammonium perchlorate/aluminum propellants have used polymer network theory as a tool for many years (CBS

[4]These tensile properties are measured on an Instron tester at 72°F and a 2-in./min extension rate. Standard ICRPG tensile specimens are used. The measured gage length of 2 in. is replaced by a value of 2.7 in. to correct for deformation in the end sections.

63 Part II, p. 54 and Ref. 5). More fundamental studies of network polymer formation phenomena have been made recently (SPS 37-42, Vol. IV, p. 106; SPS 37-48, Vol. III, p. 95; SPS 37-49, Vol. III, p. 177; SPS 37-60, Vol. III, p. 200 and Ref. 6). General principles learned in the course of this work were applied to the problems of lowering the modulus and improving reproducibility.

There are three basic characteristics of network polymers that determine, along with two other factors, the mechanical properties of the material. These characteristics are the degrees of: (1) chain extension, (2) chain branching, and (3) chain termination. The two other factors that will not be discussed here are: (1) the degrees of freedom (or flexibility) of the basic polymer chain, and (2) the concentration and type of non-network material. The three network characteristics can be related quantitatively to the propellant ingredients recipe (with certain simplifying assumptions, the chief one being that the reaction of alcohol with isocyanate to form urethane is the only chemical reaction that occurs). A qualitative view of the relationship among the three network characteristics and propellant properties is also employed. It is important to keep in mind that all practical man-made polymers are mixtures of various sizes and complexities of molecules because of the randomness of the chemical reactions making them.

Two mutually reactive difunctional compounds can unite to form extended chain polymer molecules (Fig. 6a). The average chain length depends on the stoichiometric ratio and the completeness of reaction. In the polyether-urethane propellant binder system, the two difunctional components are 2,4-tolylene diisocyanate and hydroxyl-terminated polypropylene oxide (also known as polypropylene glycol). The latter material is not a pure compound in the usual sense, but a prepolymer, already a chain molecular substance, with an average molecular weight of about 2000 separating the two hydroxyl groups.

If a trifunctional compound is introduced into the above mixture before reaction, chain branching also occurs along with chain extension. In the JPL polyether-urethane binders, trimethylol propane is used. Other triols can be used with equal success. Under ideal conditions of stoichiometric balance, equal reactivity, and complete reaction, all of the branches become cross linking sites (Fig. 6b). All of the chains are tied together and form one large network molecule. It can be visualized that if the concentration of cross links is high, the polymer will be rigid. Conversely, a combination of low

Table 2. Summary of tests performed on JPL 540J propellant in flight-weight, case-bonded, end-burning motors

| Propellant batch | Mechanical properties | | | Motor | | Results |
	Maximum stress, psi	Strain at maximum stress, %	Secant modulus, psi	Number	Weight, lb	
JS-43	104	160	65	P67, P83	60	No failure from pressure cycling and temperature cycling (-65 to 165°F)
JS-49	75	139	54	P78	60	Successfully fired
EB-1	145	82	177	P45	60	Aft end pull-away. Repaired[a] and successfully fired
EB-8	126	129	98		800	Successfully fired
EB-9	185	145	126	P50, 78(2), 99	60	Chamber walls buckled[b]

[a]See *Section XVIII-F.*
[b]See *Figs.* 9 and 10.

cross link concentration with flexible chains will lead to a highly extensible rubber.

Certain conditions can interfere with both chain extension and cross linking production by chain branches. The most obvious of these conditions are lack of complete reaction and imbalance between reactive groups (excess hydroxyl, for instance). The essential characteristic imparted to a polymer by these conditions is chain termination. Chain termination can, of course, be effected directly by the addition of a monofunctional ingredient. A large amount of chain termination interferes completely with network polymer formation (Fig. 6c). In the case where a small amount of chain termination exists, a network polymer is still produced, but there is a proportion of non-cross-linking branches. Additionally, some fraction of the starting material will not be part of the network, but will be in solution as a sol fraction, which functions as a plasticizer.

In any of the three systems in Fig. 6, long chains will always be present. A typical chain between two branch points may have as many as 100 difunctional units in series. Theoretically, these chains can contain millions of units.

b. Low-modulus formulations. The main formulating objective to produce a low modulus in the propellant is to increase chain extension at the expense of cross linking. The direct (but impractical) approach is to reduce the concentration of the trifunctional component. The wide control range of mechanical properties of JPL 540J propellant (see Table 2) is directly related to the low triol concentration in that formulation. Earlier formulation studies indicated that quality control deteriorates further at still lower levels. Theoretical studies of basic network polymer parametric equations (SPS 37-48, Vol. III, p. 95 and Ref. 6) substantiated the direct effect of triol concentration on strength-indicating parameters. Sensitivity was found to be inversely proportional to triol concentration, while much less affected by the other formulating parameters.

All of the other ways to enhance chain extension at the expense of cross linking are indirect, because they depend upon chain termination. Chain terminating approaches have the disadvantage of producing sol fractions. Nevertheless, an investigation was undertaken to determine if some benefit was to be found.

Reduction of the extent of reaction to create chain termination is not practical because of control difficulties and was excluded. A screening study of three sets of exploratory formulations designed to introduce chain termination was made. Two off-stoichiometric sets, one excess hydroxyl and one excess isocyanate, both with estimated compensating elevations in triol level, failed to yield attractive results. However, on the basis of these limited data, it cannot be concluded that these are fruitless approaches.

(a) POLYMER SYSTEM 1. CONSISTS OF DIFUNCTIONAL COMPONENTS
THAT REACT TO BUILD CHAINS

REACT TO YIELD EXTENDED CHAIN POLYMERS
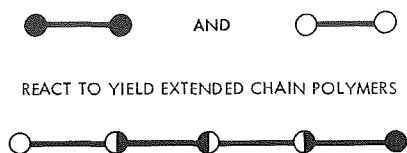
(b) POLYMER SYSTEM 2. CONSISTS OF POLYMER SYSTEM 1 AND SOME
TRIFUNCTIONAL COMPONENTS
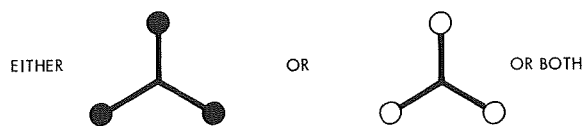
REACT WITH SYSTEM 1 TO YIELD CROSS-LINKED NETWORKS
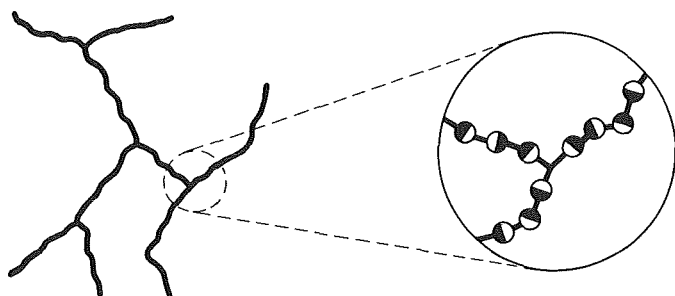
(c) POLYMER SYSTEM 3. CONSISTS OF POLYMER SYSTEM 2
(DIFUNCTIONAL AND TRIFUNCTIONAL COMPONENTS)
AND MONOFUNCTIONAL COMPONENTS
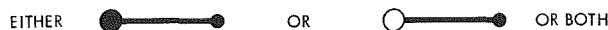
REACT TO TERMINATE OR FRUSTRATE PROPAGATION OF CHAINS
(DEPENDING ON THE QUANTITY OF MONOFUNCTIONAL COMPONENTS
INTRODUCED)
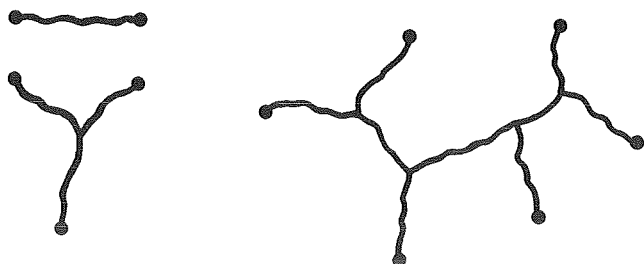
Fig. 6. Interaction of monofunctional, difunctional,
and trifunctional compounds

Fortunately, the third exploratory set quickly demonstrated a capability to produce the desired mechanical properties. Chain termination was produced in this set by the use of the monofunctional alcohol 1-decanol. This alcohol was chosen because of its availability, and its use is continuing. A summary of the investigations of this technique is given in Fig. 7. The diagonal lines represent constant values of the excess of trifunctional hydroxyl over monofunctional hydroxyl. The two numbers associated with each point are the tensile strength (at maximum load) and percent elongation (at maximum load) values obtained with the formulation. With the exception of one data point, a strong correlation of both elongation and tensile strength with the formulating parameters is evident. This correlation has made it easy to formulate propellants with predetermined properties. The formulation shown in Fig. 7 (tensile strength of 74 psi and elongation of 154%) was adopted for motor testing.

4. Low-Modulus Propellant in Case-Bonded, End-Burning Motors

The reduction in modulus was achieved primarily at the expense of tensile strength. However, the tensile strength remains high enough to resist slumping. Tests presently in progress indicate that no appreciable stress relaxation takes place at room temperature. A flight-weight motor chamber (28 in. diam) was loaded as a case-bonded, end-burning motor with about 800 lb of a propellant formulation with a tensile strength lower than the chosen one. The measured properties of this particular propellant batch were: tensile strength, 30 psi; elongation, 178%; and secant modulus, 17 psi. This motor has been stored, nozzle down, for 30 days. Periodic measurements of the vertical position of selected points on the propellant surface were made. Displacements are small but measureable, and it is concluded that no significant deformation has occurred. Future tests of this motor will include elevated temperatures and changed attitudes with respect to the vertical. A test with the motor lying on its side would probably be a more severe test. As was expected, no evidences of propellant failure in elongation or failures due to high modulus have been observed.

Some measure of the reproducibility of the new propellant formulation has been obtained in the course of preparing batches for motor testing. Tensile test data of three batches are shown in Table 3. Some variation is observed. To a degree, mix size appears to be a factor. There are too few data for definite conclusions to be made; however, the reproducibility is far superior to
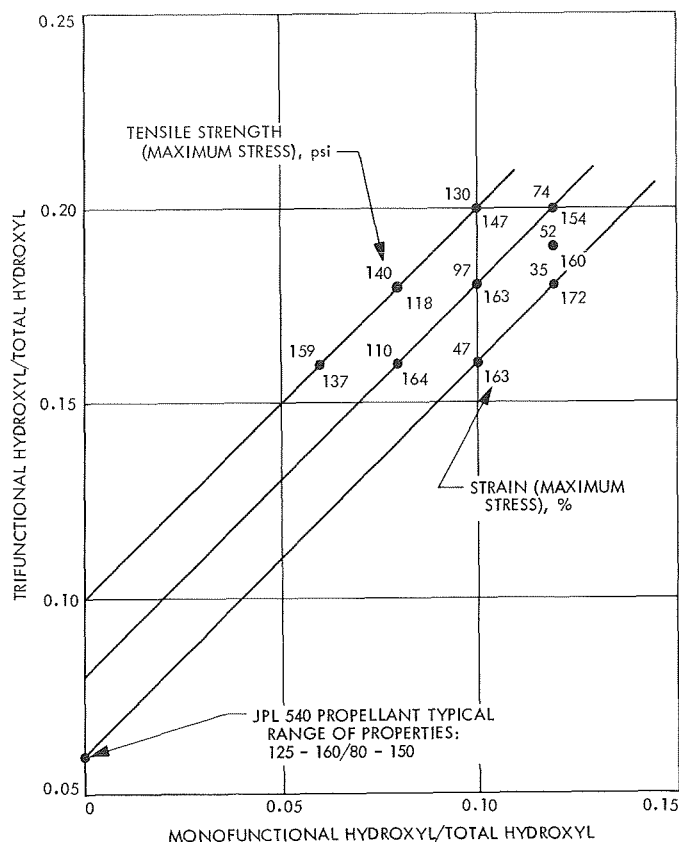
Fig. 7. Physical properties of propellants containing 1-decanol

what would have been expected if these ranges of properties had been sought by the direct method of lowering triol concentration. There is the possibility that a change in the process (adding 1-decanol later in the mix cycle instead of during an early high-temperature period) will effect better control by reducing the tendency for evaporative loss of that volatile material.

5. Concluding Remarks

A new solid propellant family, based on JPL 540J, has been developed that offers controllable mechanical properties of very high elongation and very low modulus. This development was achieved by employing a new binder formulating technique based on polymer network theory.

The essential feature of the new binder formulating technique is the introduction of controlled amounts of chain termination by the use of monofunctional binder ingredients. Preliminary tests indicate that selected members of the new propellant family can perform well in a new case-bonded, end-burning motor configuration that requires these special properties.

Table 3. Batch to batch reproducibility

Batch size	Mixer size	Physical properties		
		Maximum stress, psi	Strain at maximum stress, %	Secant modulus, psi
800 g	1 pt	74	154	48
250 lb	25 gal	57	156	37
1200 lb	150 gal	64	172	37

References

1. Shafer, J. I., *Long-Burning Time Motors for High-Incremental-Velocity Maneuvers at Low Acceleration*, CPIA Publication 188, Vol. 1, Apr., 1969 (Confidential).

2. Anderson, F. A., *Properties and Performance of JPL 540 Propellant*, Technical Memorandum 33-131. Jet Propulsion Laboratory, Pasadena, Calif., Apr. 30, 1963 (Confidential).

3. Anderson, R. G., Gin, W., and Kohorst, D. P., "The *Syncom I* JPL Apogee Rocket Motor," Technical Memorandum 33-143. Jet Propulsion Laboratory, Pasadena, Calif., Sept. 16, 1963 (Confidential).

4. Anderson, R. G., *The Applications Technology Satellite Apogee Rocket Motor: A Summary Report*, Technical Memorandum 33-338. Jet Propulsion Laboratory, Pasadena, Calif., Oct. 31, 1969.

5. Marsh, H. E., Jr., "Formulations and Quality Control in Polyurethane Propellants," *Ind. Eng. Chem.*, Vol. 52, p. 768, Sept., 1960.

6. Marsh, H. E., Jr., and Hutchison, J. J., *Functionality Determination Through Flory Network Theory*, Publication 187, p. 55. Chemical Propulsion Information Agency, Applied Physics Laboratory, Johns Hopkins University, Baltimore, Md., Mar. 1969 (Confidential).

F. Solid Propellant Spacecraft Motors, *J. I. Shafer*

1. Introduction

The basis for the development effort on long-burning, high-performance motors is summarized in SPS 37-55, Vol. III, p. 185. The case-bonded, end-burning motor, a concept to aid achievement of a long-burning, high-performance motor, appeared very promising when 60-lb flight-weight motors were successfully pressure tested in simulated static firings over the temperature range −65 to +165°F. It is believed that case-bonded (in contrast to mechanically stress-relieved), end-burning charges will: (1) increase motor mass fraction by reducing insulation weight and increasing propellant weight, and (2) provide better support against charge creep in storage, against

ground handling forces, as well as vibration and inertial acceleration forces during vehicle launch.

This article describes the work accomplished to extend that effort; more specifically it discusses:

(1) Tests that demonstrate the feasibility of firing case-bonded, end-burning, flight-weight motors without mechanical stress relief in the 60- and 800-lb motor classes.

(2) Work to increase the motor burning time further by the use of lower burning rate propellants.

(3) Efforts to assess the need for zone curing the propellant at high pressure.

(4) Evaluation of propellant mechanical properties when used for a case-bonded, end-burning design.

(5) Determination of the propellant vacuum specific impulse or characteristic velocity at the unusually low chamber pressures desired for low-thrust, long-burning-time applications.

2. Feasibility of the Case-Bonded, End-Burning Design

Because of difficulties in detecting motor flaws with X-rays, it was necessary to actually static fire flight-weight, case-bonded, end-burning motors to confirm motor integrity and demonstrate feasibility of the concept. Two static firings with 60-lb, subscale motors and one static firing with the large 780-lb motor were made. Table 4 summarizes some motor characteristics and Table 5 summarizes the static firing results. In Table 5, the results for the original 60-lb *Syncom* and 760-lb *ATS* motors are referenced for comparison. Figure 8 shows a cross section of the 780-lb motor.

All end-burning motors utilized propellant JPL 540J and were zone cured at 140°F under 175-psi pressure (SPS 37-55, Vol. III). This propellant type was adopted because of its low modulus and unusually high elongation; characteristics that permit large chamber strains without inducing high stresses within the propellant charge or at the propellant–insulation interface.

Motor P78 was intended to demonstrate feasibility of the case-bonded design concept. Motor P45 was a precursor for the large 780-lb motor demonstration; P45 was cast deliberately with a lower propellant elongation, closer to that expected in the large motor, and designed to produce a lower operating chamber pressure. Motor P45 exhibited bond weakness and partial separation in
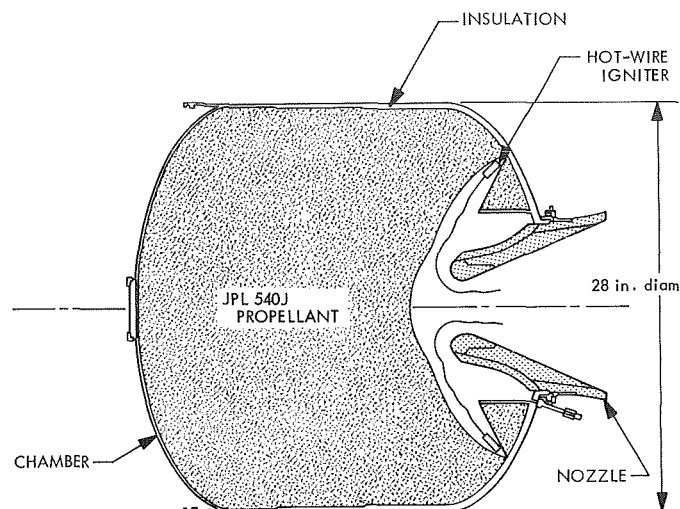
Fig. 8. Cross section of 780-lb motor

the nozzle dome while the charge was being trimmed to contour. This problem may have been caused by an error during the curing cycle (three days of zone cooling of the aft end of the motor instead of one) rather than a basic inadequacy of the propellant's mechanical properties. The void in the separated region was filled with epoxy resin, the resin was cured, and the motor was static fired. As desired, action times for the three motors were 2–2½ times as long as those of the reference radial-burning motors. Despite the longer burning times, increases in nozzle throat areas were inconsequential.

The propellant characteristic velocity c^* for motors P78 and T10 seemed unaltered from those of their reference motors even though their pressures were unusally low. However, the characteristic velocity dropped about 1.8% in motor P45, presumably because of the combination of very low pressure and small motor size.

The fact that the characteristic velocity (and presumably specific impulse) appears to have changed only slightly (if any) is particularly gratifying and warrants further investigation for future spacecraft motor applications that require high performance through high mass fraction. Other solid propellant investigators have assumed that specific impulse values would decrease as pressures were decreased below 400–500 psi for aluminized propellants. However, it seems plausible that the lower mass flow rate of these long-burning motors maintains relatively complete combustion of the aluminum because of the longer residence time of the combustion products in the motor.

Table 4. Characteristics of cast-in, fully case-bonded, end-burning motors

Item	Motor		
	60 lb (P78)	60 lb (P45)	780 lb (T10)
Propellant (JPL 540J)			
Cure temperature, °F	140	140	140
Cure type	Zone	Zone	Zone
Cure pressure, psi	175	175	175
Maximum tensile strength, psi	75	147	126
Elongation at maximum stress, %	139	85	129
Propellant weight, lb	56.82	56.58	778
Chamber			
Type	410 chrome steel	410 chrome steel	6Al 4V titanium
Proof pressure, psi	290	290	225
Length, in.	12.8	12.8	28.8
Diameter, in.	12.06	12.06	28.1
Weight, lb	3.84	3.92	24.4
Insulation (NBR Gen-Gard V-52)			
Thickness, in.	0.40–0.20	0.40–0.20	0.40–0.10
Weight, lb	7.23	7.03	37.4
Nozzle (submerged; carbon and silica cloths)			
Expansion ratio	15.5	14.1	11.0
Throat diameter, in.	1.303	1.484	3.546
Weight, lb	4.73	5.08	23.0

Table 5. Static firing results of cast-in, case-bonded, end-burning motors

Item	Motor				
	60-lb Syncom[a] (reference)	60 lb (P78)	60 lb (P45)	760-lb ATS[a] (reference)	780 lb (EB-1) (end burner)
Motor temperature, °F	60	60	60	60	60
Type of test	Horizontal	Horizontal	Horizontal	Horizontal spin	Vertical
Action time, s	19.55	39.4	48.2	42.5	110.0
Mean effective pressure, psia	197	178	101	205	110
Maximum pressure, psia	258	197	118	260	136
Propellant characteristic velocity c^*, ft/s[b]	4918	4915	4827	4969	4958
Average mass flow $\dot{m}$, lb/s	3.1	1.44	1.2	18.1	7.1
Change in throat area, %	0.5–1.5	1.5	2.0	1.5	0.3
Inert weight exhausted, lb	0.5	0.72	0.79	9.0	12.5
Weight of Al_2O_3 slag, lb	Trace	0.043	0.29	Trace	Trace

[a]From motor qualification data.
[b]Based on loaded propellant weight and average throat area.

The weight of aluminum oxide slag or residue, which was inconsequential in the original or reference motor, was small but definitely noticeable in the first firing (P78). However, the slag formed a pronounced puddle in the bottom of the motor after the second firing (P45). Chemical analysis revealed that over 60% of the slag was unburned aluminum.

Because the longer burning time of the large motor (T10) might permit the slag to pyrolize the chamber insulation locally and burn a hole in the chamber at or near the end of burning, it was decided that T10 would be fired vertically, nozzle end up, so that the combustion gases would entrain any condensing slag. If the slag problem persisted in subsequent 60-lb motor firings, it was believed that the problem might be resolved by converting from the submerged nozzle to an external nozzle design at a slight penalty in the motor length.

With the successful firing of these three motors, it is believed that the concept of case-bonded, end-burning motors, without mechanical stress relief, in the 60- and 800-lb classes has been demonstrated as technically feasible. It is now desirable to examine the practicality of the concept and the limits of its applicability.

3. Practicality of the Case-Bonded, End-Burning Design

Because potential spacecraft applications such as planetary orbit-insertion motors require low acceleration and therefore long burning times (SPS 37-55, Vol. III), propellant JPL 540J had been adopted temporarily as a well established propellant with the necessary mechanical properties. However, it will be supplanted with a propellant having higher performance and the inherently lower burning rate required as soon as practicable.

Saturethane propellant, a urethane-cured, saturated-hydrocarbon and ammonium-perchlorate system under development for heat sterilizable motor applications, had the very low burning rate required: 0.094 versus 0.14 in./s at 100 psia. Efforts shifted to the Saturethane system despite several inherent drawbacks for case-bonded, end-burning applications:

(1) Its higher cure temperature (190°F versus 140°F) would induce more severe tension stresses in the charge as it cooled from the cure temperature.

(2) Its mechanical properties were less suitable.

(3) Cost of the Saturethane prepolymer and variability in its lot-to-lot mechanical properties were undesirably high.

Development problems tend to fall into two categories (motor processing and motor testing).

a. Motor processing. Table 6 summarizes the characteristics for five motors cast from two batches of Saturethane propellant. The propellant in the first batch for motors P84 and P96 had been deliberately tailored to have a very high modulus (relatively) in an attempt to learn whether zone curing at high pressure was better than the standard JPL bulk cure at 50 psi. An earlier effort to make this differentiation with a low modulus propellant (SPS 37-55, Vol. III) had resulted in both motors passing even the severest tests. The new, high-modulus propellant, along with the pronounced propellant contraction from the abnormally high cure temperature (190°F), would aggravate the tension stresses on cooling from cure and insure failure, hopefully, of one of the motors. Indeed, stresses were sufficiently severe that both charges separated in the nozzle dome at the propellant–insulation interface by about $\frac{3}{16}$ in.

In the second batch of three motors (P102, P103, and P85), the propellant modulus was decreased as much as binder tailoring in the Saturethane formulation would permit with the new lot of prepolymer. The cure pressure was raised to 275 psi in an effort to successfully process motors with Saturethane propellant. Although the propellant–insulation separation was markedly reduced, it was not eliminated. Subsequent tests of the elevated temperature bond strength of Saturethane propellant to Gen-Gard 4010 insulation revealed that its bond was much poorer than for propellant JPL 540J to either Gen-Gard 4010 or V-52 insulation (Table 7). On cooling from the 190°F cure, tension and/or shear stresses at the Saturethane propellant–4010 insulation interface had developed at a high enough temperature that the poor bond strength was exceeded. The JPL 540J/Gen-Gard V-52 combination successfully withstood cool-down from a 140°F cure in motors P78, P45, and T10.

Recent propellant development work to reduce burning rate has shown that trimodal blends of coarse oxidizer decrease the burning rate of the polyurethane propellant JPL 540J to a rate not much greater than that for Saturethane. Because of this, and unfavorable ballistic results from Saturethane propellant (discussed later), work was discontinued on the latter in favor of JPL 540 coarse (Table 8).

Motors from batch EB-9 (JPL 540 coarse), which was cured at 140°F, suffered severe buckling of the thin-walled (0.12 in.) cylindrical section (Fig. 9a) when the

Table 6. Characteristics of case-bonded, end-burning motors using Saturethane propellant

Item	High-pressure zone cure evaluation		Saturethane propellant evaluation		
Batch	JS 51	JS 51	JS 50	JS 50	JS 50
Motor	P84	P96	P102	P103	P85
Propellant					
Type[a]	VHM	VHM	HM	HM	HM
Designation	xs-6	xs-6	xs-54	xs-54	xs-54
Flame temperature, °F	4688	4688	4688	4688	4688
Cure temperature, °F	190	190	190	190	190
Cure type	Bulk	Zone	Zone	Zone	Zone
Cure pressure, psi	50	175	275	275	275
Maximum tensile strength, psi	315	315	197	197	197
Elongation at maximum stress, %	33	33	48	48	48
Secant modulus, psi	945	945	411	411	411
Propellant weight, lb	—	—	52.7	52.1	51.8
Chamber (410 chrome steel)					
Proof pressure, psi	290	290	290	290	290
Length, in.	12.8	12.8	12.8	12.8	12.8
Diameter, in.	12.06	12.06	12.06	12.06	12.06
Weight, lb	3.87	3.84	3.92	3.86	3.90
Insulation (Gen-Gard 4010)[b]					
Thickness	0.26–0.10	0.26–0.10	0.26–0.10	0.26–0.10	0.26–0.10
Weight, lb	4.27	4.10	4.06	3.95	4.07
Nozzle (carbon cloth–phenolic)					
Type	—	—	Submerged	Submerged	External
Expansion ratio	—	—	21	50.2	50.0
Throat diameter, in.	Unfired	Unfired	1.123	1.127	1.124
Weight, lb	—	—	4.58	6.93	8.04[c]
Result (on cooling from cure)	Severe propellant–insulation separation in nozzle dome		Some propellant–insulation separation. Propellant in most of nozzle dome removed and motors fired		

[a]VHM = very high modulus; HM = high modulus.
[b]Ethylene propylene terpolymer rubber base with silica and/or asbestos filler supplied by General Tire and Rubber Co.
[c]Includes weight of adapter for external nozzle.

(a) SEVERE BUCKLING
(STANDARD CURE)

(b) SLIGHT BUCKLING
(175-psi CURE)

Fig. 9. Buckling of cylindrical section of chamber

Table 7. Propellant–insulation bond strength

Propellant–insulation	Peel strength, in.-lb		
	72°F	110°F	140°F
Saturethane–Gen-Gard 4010	31	9	Negligible
JPL 540J–Gen-Gard 4010	40	—	14
JPL 540J–Gen-Gard V-52	23	—	10

so no attempt was made to static fire. Chamber buckling and insulation separation were eliminated in batch JS 52 by decreasing the propellant modulus and increasing the cure pressure to 275 psi.

A gross analysis of the volume changes that occur in the motor during concurrent depressurization and cool-down from cure has been made as an aid in determining the pressure to be used during cure. This analysis also helps explain case buckling or propellant separation at a cure pressure of 175 psi and successful cool-down from 275 psi.

At the completion of cure, the charge will have been formed somewhat oversize in the expanded (i.e., pressurized) motor case and with large compression forces on the propellant. For a 60-lb motor, cool-down and depressurization occur simultaneously in three steps: one third of the reductions each day for three days. When cooling, the propellant and case contract; when depressurized, the case contracts and the propellant expands slightly (Table 9).

Thus, adjustment of the cure pressure in the 60-lb chrome steel case to 275 psi (cure temperature of 140°F) produced negligible volume change when cooled to ambient (60°F). In a gross sense, the procedure minimizes the relative motions of propellant and insulation while maintaining compression loads throughout cool-down to avoid buckling of the thin wall and rupture of the interface bond. Adoption of a pressure of about 195 psi would provide corresponding conditions for a titanium case that has a lower modulus of elasticity.

The following preliminary propellant mechanical properties[5] have been adopted for tailoring propellants for

standard cure was used. Buckling was only slight for motors with charges zone cured at 175 psi (Fig. 9b). Inspection with X-rays revealed minor separation between the propellant and insulation in the buckled region

---

[5]As measured on an Instrom tensile tester at 72°F and 2-in./min strain rate using an effective gage length of 2.7 in.

Table 8. Characteristics of case-bonded, end-burning motors using polyurethane propellant

Item	JPL 540 cure and vacuum specific impulse evaluation			Low modulus propellant cure check and vacuum specific impulse determination	
Batch	EB-9	EB-9	EB-9	JS 52	JS 52
Motor	P78(2)	P99	P50	P33	P97
Propellant (JPL 540 coarse)					
Type[a]	RM	RM	RM	LM	LM
Designation	xs-65	xs-65	xs-65	JS 52	JS 52
Flame temperature, °F	5260	5260	5260	5260	5260
Cure temperature, °F	140	140	140	140	140
Cure type	Zone	Zone	Bulk	Zone	Zone
Cure pressure, psi	175	175	50	275	275
Maximum tensile strength, psi	185	185	185	98	98
Elongation at maximum stress, %	140	140	140	94	94
Secant modulus, psi	132	132	132	104	104
Propellant weight, lb	—	58.73	—	57.10	56.75
Chamber (410 chrome steel)					
Proof pressure, psi	290	290	290	290	290
Length, in.	12.8	12.8	12.8	12.8	12.8
Diameter, in.	12.06	12.06	12.06	12.06	12.06
Weight, lb	4.43	4.27	4.10	3.63	4.28
Insulation (Gen-Gard 4010[b])					
Thickness	0.26–0.10	0.26–0.10	0.26–0.10	0.4–0.2	0.4–0.2
Weight, lb	4.07	4.03	4.04	5.87	6.20
Nozzle (carbon cloth–phenolic)					
Type	No firing	No firing	No firing	Submerged	Submerged
Result (on cooling from cure)	Chamber buckled slightly	Chamber buckled slightly	Chamber buckled severely	No buckling	No buckling

[a]RM = reference modulus; LM = low modulus.
[b]Ethylene propylene terpolymer rubber base with silica and/or asbestos filler supplied by General Tire and Rubber Co.

case-bonded, end-burning motors having a case length-to-diameter ratio of about one:

Property	Value
Maximum uniaxial tensile strength, psi	40–100
Elongation at maximum tensile strength, %	>100
Secant modulus, psi	25–65

The higher modulus values are limited by case buckling and perhaps by propellant pullaway; the lowest value is limited by an inability to machine propellant contours because of its softness and by creep properties in large spacecraft motors. Creep tests are currently underway in an 800-lb motor to confirm the acceptability of the lower modulus value (see *Section XVIII-E*).

It is recognized that initial values for mechanical properties are more important than maximum properties; however, for process control purposes, the latter are more easily defined. Of two propellants with equal maximum values, the one with the lower initial modulus is favored.

Table 9. Volume changes

Item	410 chrome steel 60-lb chamber, in.^{3}	Titanium 6 Al 4V 780-lb chamber, in.^{3}
Total chamber volume	1151	14,620
Depressurization from 275 psi	−12.5	—
from 175 psi	—	−140
Propellant expansion with depressurization from 275 psi	+0.63	—
from 175 psi	—	+5.1
Propellant thermal shrinkage (cooling from 140°F to 60°F)	−13.8	−178
Case thermal shrinkage (cooling from 140°F to 60°F)	−1.52	−17.2
Amount case volume change exceeded propellant volume change	+0.95 (i.e., some net compression)	−15.7 (i.e., some net tension)

Table 10. Static firing results of case-bonded, end-burning motors

Item	Motor			
	60-lb Syncom[a] (reference)	P102	P103	P85
Motor temperature (°F)	60	60	60	60
Propellant	JPL 540	Saturethane	Saturethane	Saturethane
Type of test	Horizontal	Vertical (nozzle down)	Vertical (nozzle down)	Vertical (nozzle down)
Action time, s	19.55	65.8	63.4	64.4
Mean effective pressure, psia	197	129.8	130.9	149
Maximum pressure, psia	258	150.6	152.6	173
Maximum thrust, lb	—	—	236.2	242
Propellant characteristic velocity c*, ft/s[b]	4918	4865	4765	4760
Average mass flow $\dot{m}$, lb/s	3.1	0.843	0.844	0.825
Change in throat area, %	0.5 to 1.5	−1.77	−4.2	16.8
Inert weight exhausted, lb	0.5	0.2	0.2	0.12
Weight of Al_2O_3 slag, lb	Trace	1.49	1.41	0.53
Vacuum specific impulse ($\epsilon = 50$), lb-s/lb	286	Atmospheric firing	257	261

[a]From motor qualification data; internal burning design.
[b]Based on loaded propellant weight and average throat area.

b. Static firing tests. Although the Saturethane propellant charges in motors P102, P103, and P85 had separated somewhat from the insulation in the aft dome on cool-down, all three could be static fired by removing the separated portion (Table 10). Data for the radial burning 60-lb *Syncom* motor are included in Table 10 for comparison. Motors P102 and P103 (submerged nozzles) produced abnormally large amounts of aluminum oxide/aluminum slag (1.4–1.5 lb) probably because of the low flame temperature of this propellant (4688°F). The vacuum specific impulse was quite low, 257 lb-s/lb at an expansion ratio of 50.

Motor P85 was fired with an external nozzle to see whether the slag could be eliminated and the vacuum specific impulse improved. The amount of resultant slag was reduced (0.53 lb) but not eliminated. The specific impulse, although higher than that for the motor with the submerged nozzle, was still low enough that the Saturethane propellant was dropped in favor of JPL 540 coarse.

G. Study of the Effects of Heat Sterilization and Vacuum Storage on the Ignition of Solid Propellant Rockets, *L. Strand, J. A. Mattice, and J. W. Behm*

1. Introduction

The utilization of solid propellant rockets in planetary space missions will require propulsion systems that are capable of performing properly after prior sterilization (if a landing is intended) and after long exposure to the vacuum of outer space. Consequently, a program was conducted to determine the effects of heat sterilization and vacuum storage on the ignition characteristics and performance of typical state-of-the-art solid propellant igniters and igniter materials. The ignition characteristics of a JPL propellant (Saturethane) specifically developed to survive heat sterilization cycling were also investigated. It is emphasized that this program was not an attempt to design an igniter for specific space application, but merely an attempt to demonstrate that existing materials could probably be used successfully to build such an igniter.

2. Heat Sterilization Program

The general approach was to subject igniters, igniter material samples, and Saturethane propellant samples to three and six cycles of heat sterilization. The results of the various measurements and tests conducted were then compared with those for unsterilized control samples. For purposes of this particular work, one heat-sterilization cycle is defined as turning a cold oven on with the thermostat control set for 275°F, holding the temperature at 275°F until 56 h from the oven-on time, and then turning the oven off and allowing it to cool to ambient temperature while remaining closed.

a. Test specimens. The materials and assemblies included as test specimens are listed below. Other materials used during these tests (i.e., O-rings and adhesive) were selected primarily because of their ready availability. Also, the results of earlier materials studies (Ref. 1) indicated they would be suitable:

(1) Holex 5700 squibs. Candidate heat-sterilizable squib.

(2) Igniter pellets. Three different pyrotechnic igniter pellet materials were selected for testing: (a) Aerojet-General Corporation's Alclo (Aerojet formulation AGC-001M, types AS8011A-5-195 and AS8011A-1-100), (b) Atlantic Research Corporation's "standard" type 2D boron/potassium nitrate (B/KNO$_3$), and (c) type 3D magnesium/Teflon (Mg/TFE) pellets. The nominal formulations for these pellets are given in Table 11.

(3) Igniter basket assemblies. Eleven igniter basket assemblies were built with each of the three pellet materials (Fig. 10). These assemblies consisted of an aluminum basket with a circular piece of aluminum foil bonded over the open end by Eccobond 55/9 adhesive to retain the pellets. Each of the Alclo igniters contained 25 of the type 195 pellets. The B/KNO$_3$ and Mg/TFE igniter assemblies each contained 100 pellets. The associated Viton-A O-rings (sizes 3–5 and ARP 568-028) were heat cycled along with the basket assemblies.

(4) Saturethane propellant arc-imaging-furnace ignition test samples. See SPS 37-33, Vol. IV, pp. 117–125 for a description of the samples.

b. Squib tests. Bridge and dielectric resistances for the Holex 5700 dual-bridgewire squibs were measured before and after sterilization. Bridge resistance (nominally 1.0 Ω) did not appear to change significantly, although a consistent slight increase in resistance was

Table 11. Nominal formulations of ignition pellets used in igniter sterilization tests

Pellet type	Proportion, %
Alclo (mix AGC-001M)	
Aluminum	31.1
Potassium chlorate	55.2
Lead	12.7
Sterotex	1.0
Boron/potassium nitrate	
Boron	23.7
Potassium nitrate	70.7
Binder	5.6
Magnesium/TFE	
Magnesium	~60
Teflon	~40

Table 12. Squib firing test results

Test	Sterilization cycles	Time from initial to peak pressure, ms	Peak pressure, psig
1	0	0.20	2225
2	0	0.25	2210
3	0	0.28	2305
4	0	0.70	2600
5	3	0.90	2055
6	3	1.10	2000
7	3	1.10	1815
8	6	0.60	1790
9	6	1.10	1855
10	6	1.20	1920

Fig. 10. Igniter basket assembly for heat sterilization tests

Table 12 shows the peak pressure and the time from initial pressure rise to peak pressure obtained during tests of 10 squibs that were fired in a test bomb. It seems apparent that sterilization *did* affect squib performance (longer burn times); however, the longer burn times would not be of concern for motor ignition, and the sterilized squibs *did* ignite sterilized pellets in subsequent igniter tests.

c. Igniter pellet tests. Before and after sterilization, pellet samples of each type were X-ray inspected. No apparent effects were noted in the radiographs. The thicknesses of the pellets were measured before and after heat cycling (Table 13). A 1-lb weight was placed on three pellets of each type during sterilization cycling. There were no gross dimensional changes; however, the Alclo showed a slight increase whereas the other two types showed a slight decrease in thickness. Pellet samples were weighed before and after sterilization. Total mass loss after six cycles of sterilization was about 0.1% for the Alclo and Mg/TFE pellets and about 1% for the B/KNO$_3$ pellets. The outer surface of the latter seemed powdery and readily adhered to the fingers when handled.

The minimum irradiation time in the arc-imaging furnace, as a function of the incident radiant flux density, was measured for the igniter pellets with zero, three, and six cycles of heat sterilization. Irradiation time was also measured for Saturethane propellant with zero and six cycles of heat sterilization as discussed in SPS 37-33, Vol. IV. The results for the three pellet types are plotted in Fig. 11a, b, and c. The uncertainty limits in the time measurements are illustrated in Fig. 11b and were: 10 ms for irradiation times less than 100 ms; 25 ms for
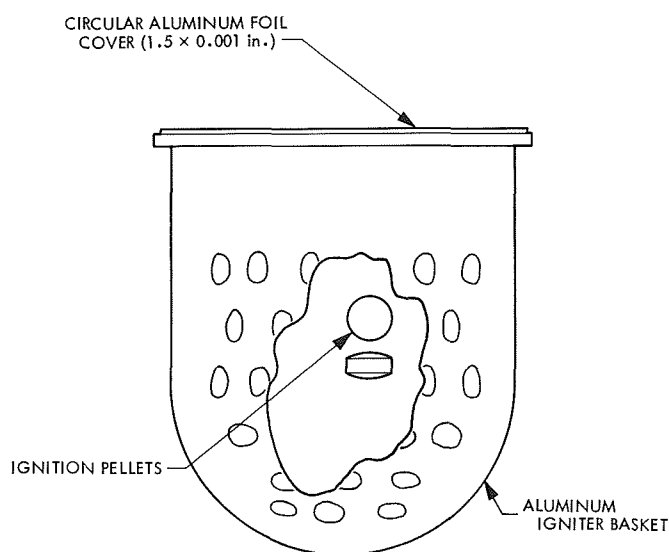
noted. Typical bridgewire resistances were 0.978–0.983 Ω (before and after sterilization, respectively) after three heat cycles, and 0.957–0.975 Ω after six heat cycles. The shorted pins-to-case dielectric resistance was quite variable for the 30 samples (0.04–250 GΩ) before sterilization, but was quite uniform (~200 GΩ) after sterilization. The dielectric resistance between the adjacent bridge circuits was fairly uniform (0.12 MΩ) before sterilization but increased and was more variable (0.003–3 GΩ) after sterilization. It may be possible that these changes were due to the thorough drying of the squib during sterilization.

(a) ALCLO PELLETS

(b) B/KNO$_3$ PELLETS

UNCERTAINTY LIMIT OF
TIME MEASUREMENT

UNCERTAINTY LIMIT

UNCERTAINTY LIMIT

(c) Mg/TFE PELLETS

(d) SATURETHANE PROPELLANTS

HEAT STERILIZATION CYCLES
○ ZERO
△ THREE
□ SIX

SOLID SYMBOLS: VACUUM STORED

TEST BOMB CONDITIONS

N$_2$ PURGE RATE $\approx$ 1 in./s

P = 20 psig

IRRADIATION TIME, ms

INCIDENT RADIATION FLUX DENSITY, cal/cm^2-s
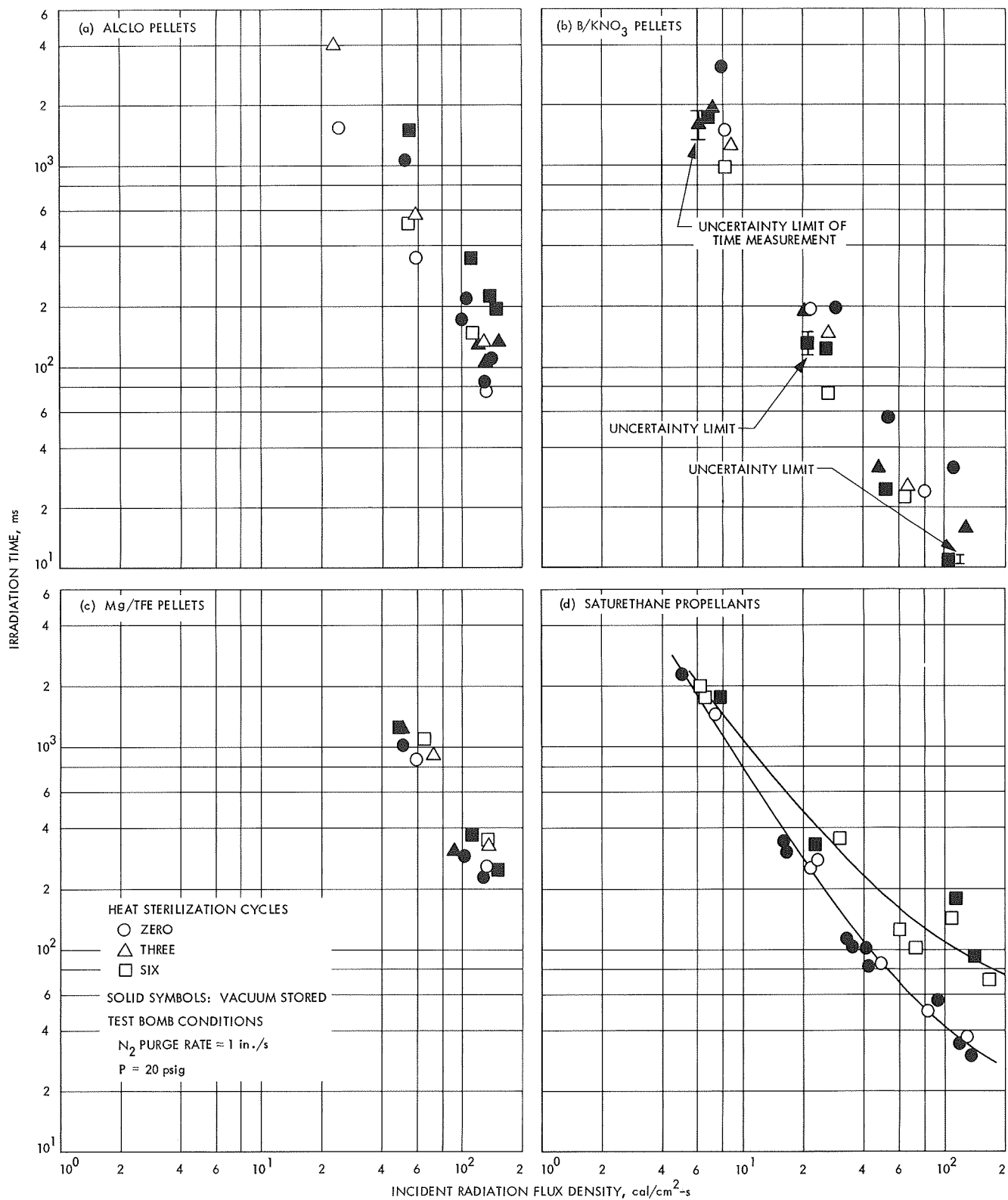
Fig. 11. Minimum irradiation time for ignition vs incident radiation flux density

Table 13. Pellet creep-test results

Pellet type	Number	Thickness, in.		
		0 cycles	3 cycles	6 cycles
Alclo	1	0.198	0.197	0.198
	2	0.199	0.199	0.201
	3	0.194	0.194	0.196
B/KNO₃	1	0.133	0.130	0.129
	2	0.134	0.131	0.131
	3	0.131	0.128	0.130
Mg/TFE	1	0.135	0.135	0.135
	2	0.136	1.133	0.133
	3	0.133	0.132	0.132

irradiation times from 100 to 1000 ms; and 250 ms for irradiation times greater than 1 s. The error in calorimeter measurements of heat flux density increased with increasing flux density as the measurement interval was shortened to reduce radiation losses and avoid damaging the calorimeter. A conservative estimate would be from 5 to 10% over the flux density interval. Wandering of the arc focal position during a test bomb series can introduce an additional error of at least comparable magnitude in the flux density value (Ref. 2).

The differences between the data for the various numbers of heating cycles in Fig. 11a, b, and c, are comparable to the estimated experimental errors. However, the following trends were exhibited: the minimum irradiation times for ignition increased with heat cycling for the Alclo and Mg/TFE pellets and decreased for the B/KNO₃ pellets. The ignitability data for the vacuum stored samples (solid symbols), which will be discussed later, exhibited the same trends with increasing prior heat sterilization cycles. Test results for the Saturethane propellant are shown in Fig. 11d. Heat sterilization had a definitely detrimental effect on the ease of ignition of this propellant.

d. Igniter test firings. After subjecting the igniter basket assemblies to three and six cycles of heat sterilization, two visual changes occurred. First, a darkening of the Eccobond adhesive occurred, but did not seem to adversely affect the bonded foil joint. Second, some of the B/KNO₃ pellets seemed to stick together after sterilization.

Test firings were conducted in a dummy 5- × 6-in. test motor that was cast with an inert propellant grain.

Figure 12 shows the test motor arrangement minus the nozzle and safety blowout diaphragm. For each igniter type, two tests were conducted for each of the sterilization conditions (zero, three, and six cycles of heat sterilization). Table 14 is a tabulation of the maximum chamber pressure value P_{max} and the time of maximum pressure t_{max} for each igniter test firing. Zero time is measured from the point of initial pressure rise. The pressure–time profiles for tests using Alclo, B/KNO₃, and Mg/TFE pellets are shown in Fig. 13 (a, b, and c, respectively). The B/KNO₃ igniters showed the least variation and the Alclo igniters showed the greatest. Heat sterilization delayed the buildup of pressure for the Alclo and Mg/TFE pellet igniters and hastened the buildup for the B/KNO₃ pellet igniters, in agreement with the previously discussed arc-imaging furnace data.

3. Vacuum Storage Program

a. Test system. The materials were stored for 180 days in a Bemco, Inc. vacuum tank system (Fig. 14), consisting of a 20-ft³ steel tank evacuated by an oil diffusion pump. The diffusion pump maintained a vacuum of better than 10^{-7} torr.

b. Stored materials. The stored material consisted of the following:

(1) Two JPL spin motors (SPS 37-55, Vol. III, pp. 173–177), including squibs and igniters. Each motor contained approximately 70 g of propellant. One motor had undergone six cycles of heat sterilization.

(2) Twelve igniter assemblies, consisting of the loaded baskets, initiating squibs (Holex 5700), and associated Viton-A O-rings. Four of the igniter baskets were loaded with Alclo pellets, four with B/KNO₃ pellets, and four with Mg/TFE pellets. One-half of the igniter assemblies of each type had undergone six cycles of heat sterilization.

(3) Three dozen squibs.

(4) The numbers and types of igniter pellets used were: 120 Alclo (type 100), 120 B/KNO₃ (type 2D), and 120 Mg/TFE (type 3D). For each type of pellet, ⅓ were unsterilized, ⅓ had undergone three cycles of heat sterilization, and ⅓ had undergone six cycles of heat sterilization.

(5) There were 120 Saturethane propellant arc-imaging-furnace ignition test samples, ½ were unsterilized, and ½ had undergone six cycles of heat sterilization.

Table 14. Igniter test: pressure—time characteristics

Test	Pellet type	Sterilization cycles	Motor throat diam, in.	Time from initial rise to peak pressure, s	Peak pressure, psig
Non-vacuum stored					
E-896	B/KNO$_3$	0	0.285	0.034	381
E-897		3		0.029	378
E-898		6		0.024	376
E-899	↓	6	↓	0.020	390
E-900		3		0.030	360
E-901	B/KNO$_3$	0	0.285	0.040	346
E-903	Alclo	0	0.481	0.041	386
E-904		3		0.043	327
E-905		6		0.066	354
E-906		6		0.080	353
E-907	↓	3	↓	0.094	344
E-908	Alclo	0	0.481	0.032	418
E-910	Mg/TFE	0	0.076	0.071	334
E-911		3		0.103	318
E-912		6		0.092	329
E-913		6		0.092	322
E-914	↓	3	↓	0.078	325
E-915	Mg/TFE	0	0.076	0.065	324
Vacuum stored					
E-1082	Alclo	0	0.481	0.048	350
E-1083		0		0.034	380
E-1084	↓	6	↓	0.094	330
E-1085	Alclo	6	0.481	0.037	345
E-1086	B/KNO$_3$	0	0.285	0.033	384
E-1087		0		0.037	367
E-1089	↓	6	↓	0.011	385
E-1090	B/KNO$_3$	6	0.285	0.012	377
E-1091	Mg/TFE	0	0.076	0.158	352
E-1092		0		0.064	341
E-1093	↓	6	↓	0.079	327
E-1094	Mg/TFE	6	0.076	0.096	340

①	SQUIB	⑤	HEAD END NUT	⑨	5- × 6-in. CHAMBER	
②	ADAPTER, SQUIB	⑥	IGNITER BASKET WITH PELLETS	⑩	NOZZLE PLATE	
③	O-RING	⑦	HEAD END	⑪	CHAMBER INSERT	
④	O-RING	⑧	CLAMP			
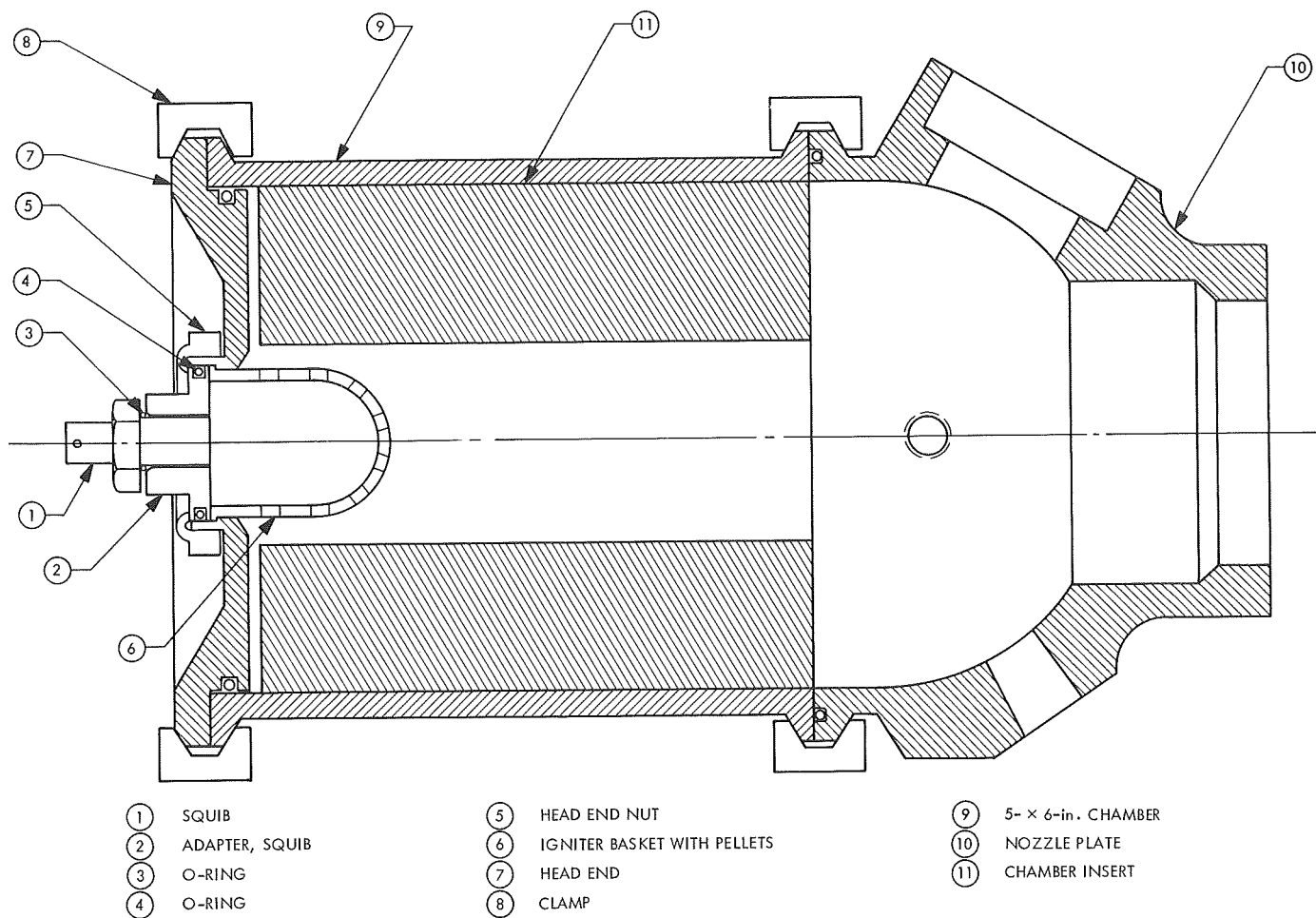
Fig. 12. Igniter test motor arrangement
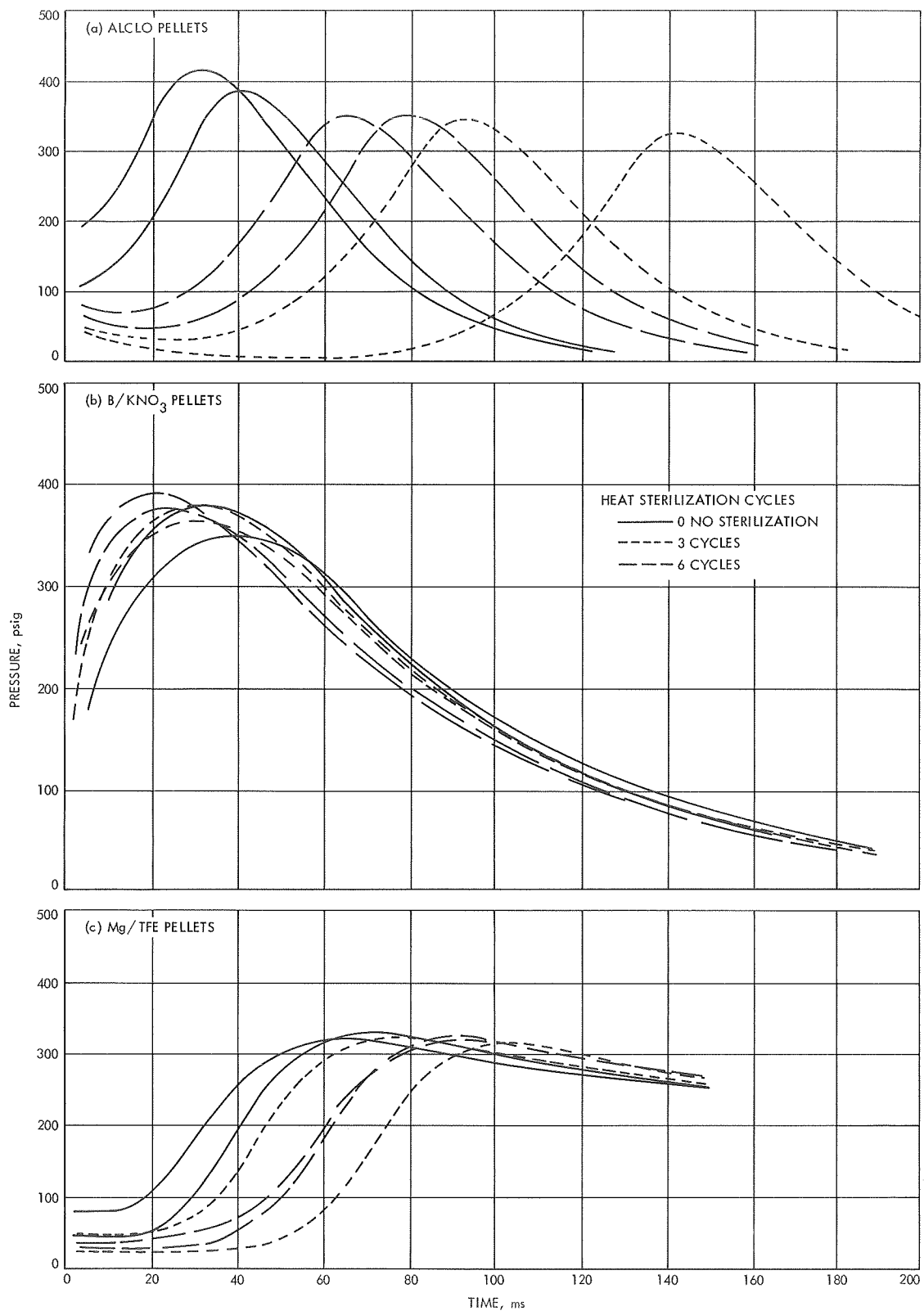
Fig. 13. Inert motor chamber pressure vs time
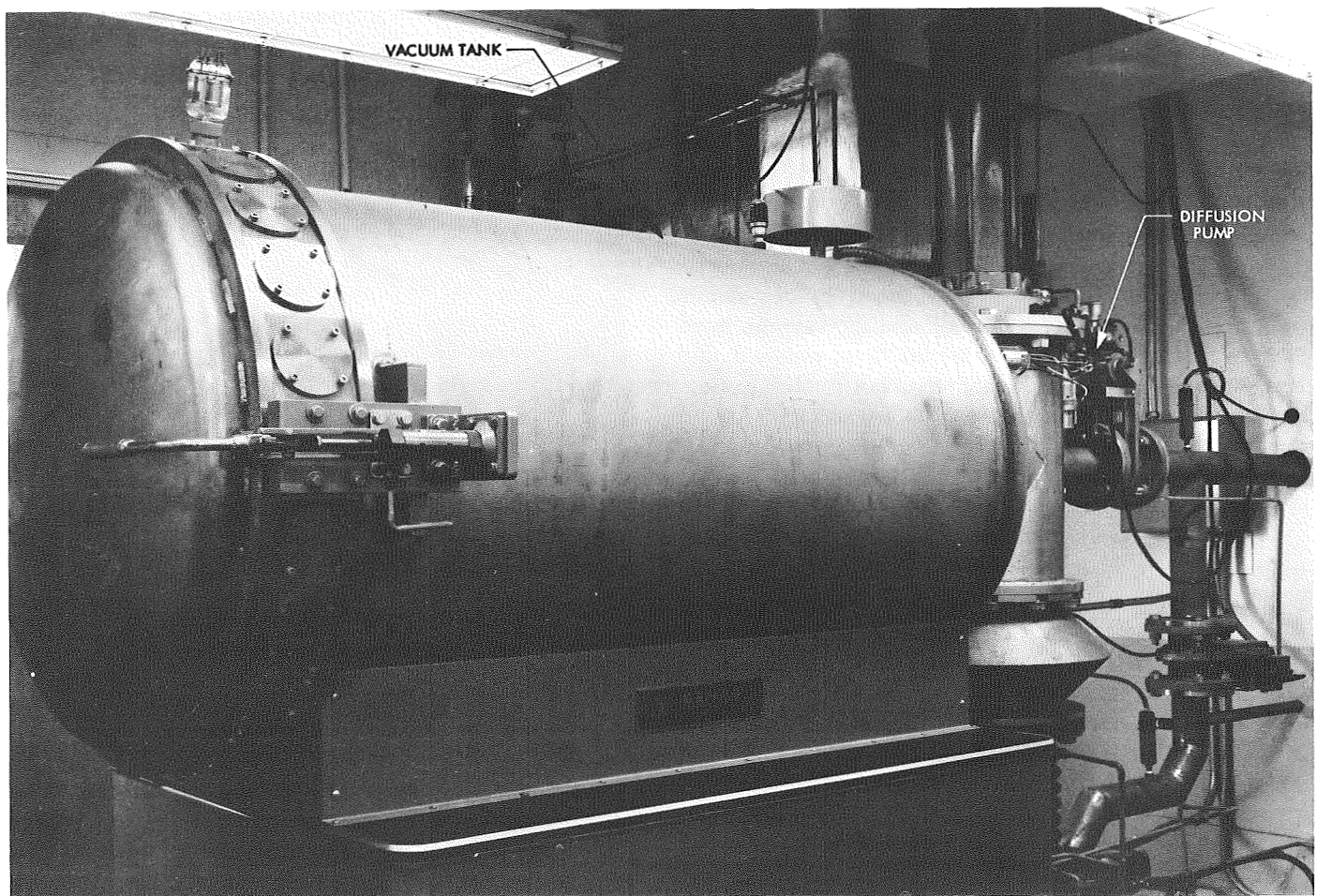
Fig. 14. High vacuum facility

The igniter pellets and propellant samples were stored in open glass bottles. Prior to being placed in the vacuum tank, each item was carefully weighed to an accuracy of four significant figures on a Mettler balance.

c. Vacuum storage test results. The silicon oil was drained from the diffusion pump following completion of the test. The oil was clear and indistinguishable from new oil. Samples of the drained and new oil were analyzed spectroscopically. The infrared absorption spectra were very similar, indicating no pronounced change. When the diffusion pump was dismantled for cleaning, the jet assembly was found to be partially coated with an oily, black residue (Fig. 15). Infrared spectral analysis of a sample revealed a spectrum similar to that of new silicon oil, but having more CH_3 groups. This indicated that some propellant hydrocarbon binder loss probably occurred during the vacuum exposure.

All of the stored items were placed in desiccators immediately after being removed from the vacuum tank. They were transported to another building, weighed, and then returned to the desiccators to await further testing. As expected, most of the items showed a slight loss in weight after 180 days of vacuum storage. The bulk of the loss was probably water vapor (Ref. 3).

The unsterilized B/KNO_3 igniter pellets had the largest total weight loss—0.014 g, 0.2% of the initial sample weight; the weight loss of the heat sterilized pellets (three and six cycles) dropped to 0.07%. The unsterilized Alclo pellets had no loss within the accuracy of the balance; both of the heat sterilized pellets (three and six cycles) had slight weight losses ~0.01%. The Mg/TFE pellets, both unsterilized and sterilized, showed no weight loss. The unsterilized propellant samples had a weight loss of 0.013 g, or 0.12%. The heat sterilized propellant samples were inconsistent, in that they showed a slight weight *increase* of 0.02%. The measurement was double-checked and the increase is believed to be real. The two spin motors, both unsterilized and sterilized, had weight losses of 0.02 and 0.03%, respectively.

d. Ignition test results. The minimum irradiation times for ignition, as a function of incident radiation flux density, were measured for the vacuum stored igniter pellets and Saturethane propellant, and the results (solid symbols in Fig. 11) are compared with the previously obtained data for nonvacuum stored samples of the same materials. The bulk of the tests were performed within a month after removal of the samples from the tank. The test results did not show any pronounced effect of the
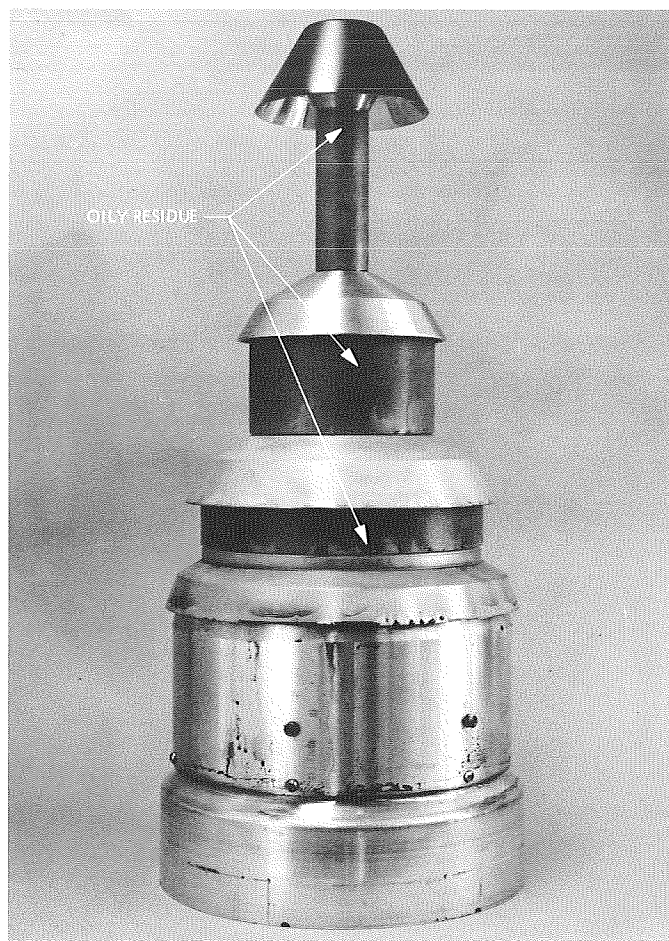
Fig. 15. Disassembled oil diffusion pump jet assembly—after test

vacuum storage on the ignitability characteristics of any of the igniter materials or the propellant.

The two motors were static fired approximately 1 wk after removal from the vacuum tank. The motors ignited and burned normally. The test motor pressure–time records were not readily distinguishable from those for previous firings of their nonvacuum stored counterparts.

Approximately 4 mo after removal from the vacuum tank, each igniter assembly was test fired in the dummy 5- × 6-in. test motor described earlier. The P_{max} and t_{max} values are tabulated in Table 14. The test motor pressure–time records were compared with the earlier test firings with nonvacuum stored igniter assemblies (Fig. 16). As with the nonvacuum stored tests, the pressure–time records for the Alclo and Mg/TFE igniters showed less reproducibility than those for the B/KNO_3 igniters. None of the comparisons showed any distinct effects of vacuum storage.
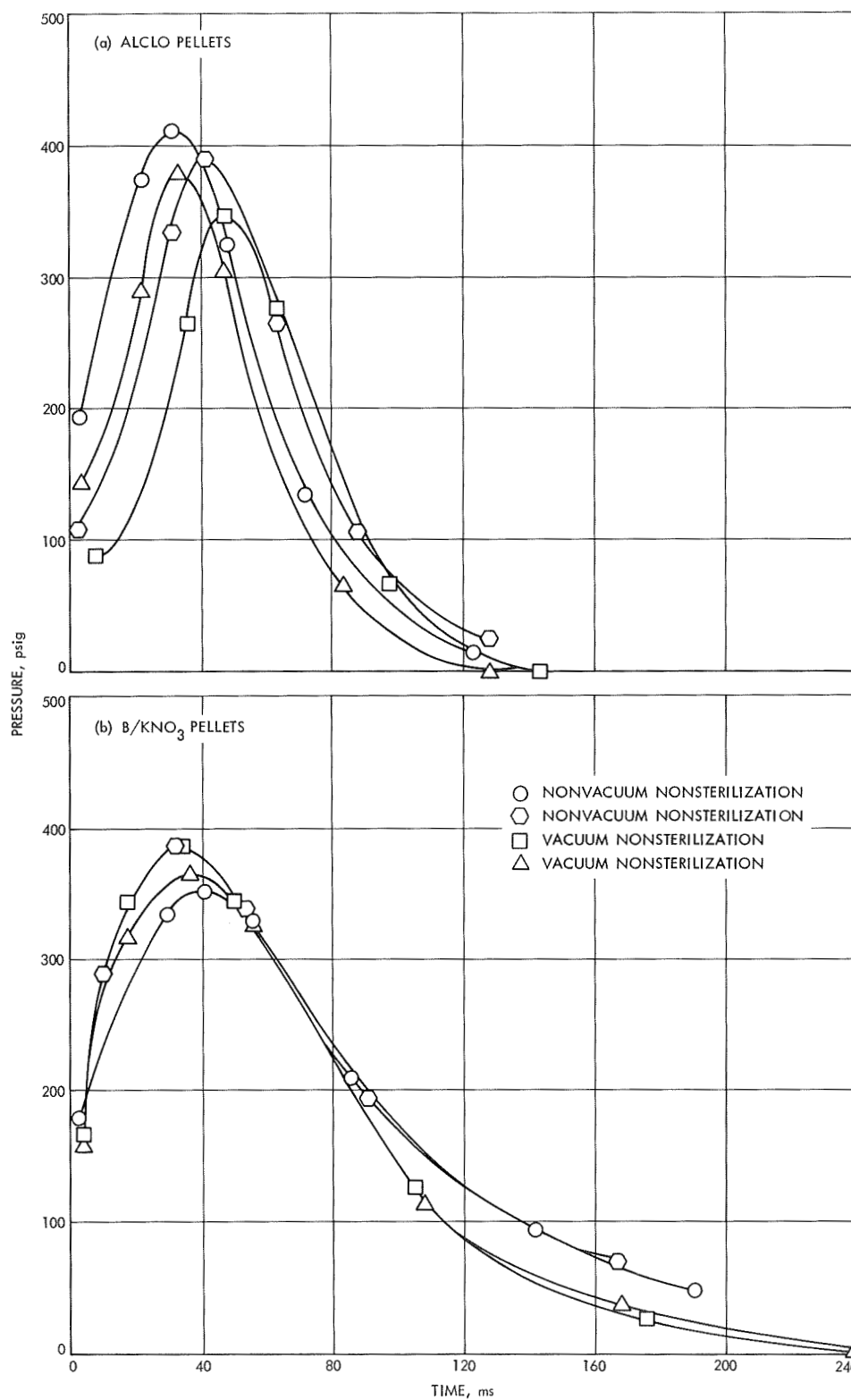
Fig. 16. Inert motor chamber pressure vs time for pellet igniter tests

4. Summary and Conclusions

a. Effects of heat sterilization cycling. Heat sterilization cycling reduced the burning rate and lengthened the burning time on the test squib (Holex 5700); however, the sterilized squibs did successfully ignite sterilized igniter basket assemblies. After six cycles of heat sterilization, total weight loss was about 0.1% for the Alclo and Mg/TFE pellets and about 1% for the B/KNO$_3$ pellets. In arc-imaging-furnace ignition tests, the trends were for the minimum irradiation times for ignition to increase with heat cycling for the Alclo and Mg/TFE pellets and to decrease for the B/KNO$_3$ pellets. The minimum irradiation times for ignition for the Saturethane propellant increased significantly with six cycles of heat sterilization. In a cursory series of igniter assembly test firings in an inert grain motor, heat sterilization delayed the buildup of pressure for the Alclo and Mg/TFE pellet igniters and hastened the buildup for the B/KNO$_3$ pellet igniters.

b. Effects of 6-mo vacuum storage. The sterilized and unsterilized Alclo and Mg/TFE pellets showed essentially no weight change. The unsterilized B/KNO$_3$ pellets had a total weight loss of 0.2%, and the sterilized pellets had a loss of 0.07%. The unsterilized propellant samples had a weight loss of 0.2%; the sterilized samples, no loss. Arc-imaging-furnace ignition tests did not show any pronounced effect of the vacuum storage on the ignitability characteristics of any of the igniter pellet materials or propellant tested. Igniter test firings in the inert motor showed no distinct effects of vacuum storage on the test pressure–time records.

c. Conclusions. Heat sterilization was found to have small, but measurable, effects on the ignition characteristics and performance of the solid propellant igniters, igniter materials, and on the ignition characteristics of the JPL Saturethane propellant tested. These effects would have to be taken into consideration in the future design and development of any motor required to undergo such heat sterilization, but would not prevent such a motor from being utilized. Similar tests on materials that had undergone vacuum storage for 6 mo did not reveal any distinct effects from the exposure, indicating that the effects of long-term exposure to vacuum on the solid propellant ignition transient should be small.

References

1. Kalfayan, S. H., and Campbell, B. A., *Effects of the Thermal Sterilization Procedure on Polymeric Products,* Technical Report 32-973. Jet Propulsion Laboratory, Pasadena, Calif., Nov. 15, 1966.

2. Beyer, R. B., McCulley, L., and Evans, M. J., "Measurement of Energy Flux Density Distribution in the Focus of an Arc Image Furnace," *Applied Optics,* Vol. 3, No. 1, pp. 131–135, 1964.

3. *Evaluation of Solid Propellants and Solid Propellant Systems for Space Applications,* NAS 8-1683. Battelle Memorial Institute, Columbus, Ohio, Aug. 31, 1963.

XIX. Polymer Research

PROPULSION DIVISION

A. A Generalization of the Boltzmann Superposition Principle, J. Moacanin, J. J. Aklonis,[1] and R. F. Landel

In previous work (SPS 37-58, Vol. III, pp. 199–201) a mathematical representation was developed for the stress-relaxation (or creep) behavior of an elastomer undergoing scission reactions. The method is based on the use of a parametric family of curves for the viscoelastic response of an elastomer in absence of chemical reactions. The parameter for this family of curves is the number of elastically effective chains per unit volume, ν_e. The latter is defined in terms of the equilibrium shear modulus, G_e, by

$$G_e = 3RT \, \nu_e$$

It was postulated that the response of an elastomer undergoing scission reactions can be mapped in the following fashion. Figure 1a shows the parametric family of curves as a function of time u, where each curve corresponds to a particular level of ν_e ($i > j > k > \ell$). Figure 1b represents a stress-relaxation experiment started at $t = \theta_i$ with an elastomer having $\nu_e = i$; hence, the response follows curve i as indicated in Fig. 1b. At θ_j an

[1]Department of Chemistry, University of Southern California, Los Angeles, California.

instantaneous ν_e change occurs, $i \to j$, and the response picks up the corresponding j segment from Fig. 1a. The same procedure is followed for further changes, i.e., $j \to k$ and $k \to \ell$. The time shift which is necessary to pick up the correct segment on the appropriate parametric curve was denoted $\bar{m}$; e.g., for the change $i \to j$, $\bar{m} = u' - u''$. Expressions for the case where ν_e changes occur continuously were derived applying the same principle (SPS 37-58, Vol. III). An important property of this mapping procedure is that at any particular time the response is determined entirely by the current ν_e value. It is only through $\bar{m}$ that the response depends on prior history. There is no other coupling between states.

For the case of stress relaxation (or creep), conditions for maximum coupling between viscoelastic relaxation and kinetics for chain scission were established (SPS 37-61, Vol. III, pp. 235–237). Coupling tends to be significant in the transition region. This article discusses a generalization of the above method from a single strain (or stress) application to include strains (or stresses) applied in an arbitrary manner. As before, considerations are limited to linear viscoelasticity and conditions where Boltzmann's superposition principle normally applies (Ref. 1). It is anticipated that a dynamic strain frequency could be selected so that coupling is maximized for a given relationship between the relaxation characteristic for the elastomer and the kinetic reaction rate constant.

Fig. 1. Schematic for mapping stress-relaxation response of polymer undergoing scission reactions

We start with the derivation of relationships for a case where changes in both the strains and in ν_e occur in discrete increments. In accordance with the Boltzmann principle, each strain increment may be treated as a new independent experiment which adds linearly to the total response of the system. Thus, consider that to an elastomer having $\nu_e = i$, strains $\Delta\gamma_p$ and $\Delta\gamma_q$ are applied at times θ_p and θ_q, respectively; for $t > \theta_q$, the total strain is $\gamma = \Delta\gamma_p + \Delta\gamma_q$. The stress for each contribution is characterized by a time-dependent modulus term such as $E_i(t - \theta_p)$. The total response is given by

$$\sigma(t) = E_i(t - \theta_p)\Delta\gamma_p + E_i(t - \theta_q)\Delta\gamma_q \qquad (1)$$

At t_j effect a change in ν_e: $i \to j$. Then, for $t > t_j$, the stress becomes

$$\sigma(t > t_j) = E_j(t - \theta_p + \overline{m}_p^j)\Delta\gamma_p + E_j(t - \theta_q + \overline{m}_q^j)\Delta\gamma_q \qquad (2)$$

Here each contribution is mapped onto the curve j following the procedure in Fig. 1 and then summed to give the total stress. The subscript for $\overline{m}$ identifies the appropriate strain increment whereas the superscript identifies the new ν_e value. For an additional change in ν_e, viz., $j \to k$ at time t_k, one writes

$$\sigma(t > t_k) = E_k(t - \theta_p + \overline{m}_p^j + \overline{m}_p^k)\Delta\gamma_p$$
$$+ E_k(t - \theta_q + \overline{m}_q^j + \overline{m}_q^k)\Delta\gamma_q \qquad (3)$$

It becomes apparent that for each term generated by a strain increment one has to keep a record of: (1) the strain application time, e.g., θ_p; and (2) the $\overline{m}$ shifts, one for each change in ν_e. We can now state the stress for m strain increments and n changes in ν_e:

$$\sigma(t > t_m) = \sum_{p=1}^{m} E_n \left\{ t - \theta_p + \sum_{j=1}^{n} \overline{m}_p^j \right\} \Delta\gamma_p \qquad (4)$$

Note that the summation for $\overline{m}$ gives the total shift between the curve n and the curve corresponding to the ν_e value at $t = \theta_p$. This sum may be defined as

$$\sum_{j=1}^{n} \overline{m}_p^j \equiv \overline{m} [t - \theta_p; \nu_e(\theta_p)] \qquad (5)$$

and is implicitly a function of the specific path taken to get from $\nu_e(\theta_p)$ to $\nu_e(t)$. With this definition Eq. (4) becomes

$$\sigma(t > t_m) = \sum_{p=1}^{m} E_n \left\{ t - \theta_p + \overline{m} [t - \theta; \nu_e(\theta)] \right\} \frac{\Delta\gamma_p}{\Delta\theta} \Delta\theta \qquad (6)$$

or going to the continuum, i.e., $\Delta\theta \to 0$:

$$\sigma(t) = \int_{\theta=0}^{t} E_{\nu_e}(t) \left\{ t - \theta + \overline{m} [t - \theta; \nu_e(\theta)] \right\} \dot{\gamma} d\theta \qquad (7)$$

In absence of chemical reaction, $\bar{m} = 0$, and $\nu_e = $ constant, and the integral reduces to

$$\sigma(t) = \int_{\theta=0}^{t} E_{\nu_e} \{t - \theta\} \dot{\gamma} d\theta \qquad (8)$$

which is the classical statement of Boltzmann's principle (Ref. 1).

Reference

1. Tobolsky, A. V., *Properties and Structure of Polymers*, Chapter 3. John Wiley & Sons, Inc., New York, 1960.

B. Evaluation of Spacecraft Magnetic Recording Tapes, *S. H. Kalfayan, R. H. Silver, and J. K. Hoffman[2]*

1. Introduction

Magnetic tape recorders exhibit certain types of failure. Those ascribable to head-to-tape interactions may cause phenomena such as stick-slip and complete seizure. The nature of the interactions can be complex and may be influenced by environmental factors, such as temperature, relative humidity, and the nature of the ambient gaseous atmosphere.

One property which plays a significant role in the stick-slip and seizure phenomena is tape-to-head friction. A quantitative estimation of this force for tapes under various environmental conditions and in dynamic contact with the magnetic head(s) would yield meaningful information about their behavior.

The coefficient of friction μ, or rather the product of μ and the "wrap" angle β, was determined, under various conditions, for three magnetic recording tapes of interest in the *Mariner* Mars 1971 Project.[3] The three tapes were: (1) 3M 20250, (2) 3M 990, and (3) CEC W-4. Both new and used (those that had been passed more than 800 times in an actual spacecraft tape recorder) tapes were evaluated. The tapes were tested at two speeds (0.133 and 0.333 in./s) and at two temperatures (25 and 55°C). All three tapes, new and used, were also evaluated at a relative humidity (RH) of 60 ±2%, at both 25 and 55°C, and at the speed of 0.133 in./s. In all cases, the ambient gas was high-purity argon.

This article covers the first phase of the present investigation of magnetic recording tapes used in spacecraft.

2. Experimental Methods

The test method used to determine the coefficient of friction μ was based on that established by the American Society for Testing and Materials (ASTM).[4] This method was modified to take into account the tape contact or "wrap" angle. The equation for flexible band friction may be expressed as follows (Ref. 1):

$$\log \frac{T_2}{T_1} = 0.434 \, \mu\beta \qquad (1)$$

where

$T_2 = $ force necessary to sustain motion

$T_1 = $ supported weight (110 g)

$\mu = $ coefficient of sliding friction

$\beta = $ angle of contact, or "wrap" angle, rad

a. Test apparatus and procedure. The test was performed in a variable speed, universal testing machine.[5] Each tape sample was passed 50 times over 5 magnetic heads placed in a semi-circular configuration (Fig. 2) to give a "wrap" angle of approximately 180 deg or π radians. The heads used in these series of experiments were made of brass and permalloy metal. The force was recorded during each pass. An MK 88129 temperature chamber,[6] housing the grips of the universal tester and the tape, was modified in order to make it more gastight. The chamber was capable of maintaining constant temperatures from −50 to 300°F.

For experiments performed in humid atmosphere, the argon was "bubbled" through a column of water before being introduced into the test chamber. A relative humidity of 60 ±2% was thus achieved without any further control. The RH of the chamber was monitored by an Alnor Model 7000U dewpoint meter.[7]

Tape specimens were 27 in. long. In the case of used tape samples, because of unavailability, shorter lengths were cut, but they were spliced to a section of new tape of the same type to bring them to the required length.

---

[2]Spacecraft Data Systems Section, Astrionics Division.

[3]The product $\mu\beta$ was used to avoid introducing an error in determining the value of β.

[4]*Coefficient of Friction of Plastic Films*, ASTM D 1894-63.

[5]Instron Table Model, Instron Manufacturing Co., Canton, Mass.

[6]Delta Design, Inc., La Mesa, Calif.

[7]Alnor Instrument Co., Chicago, Illinois.
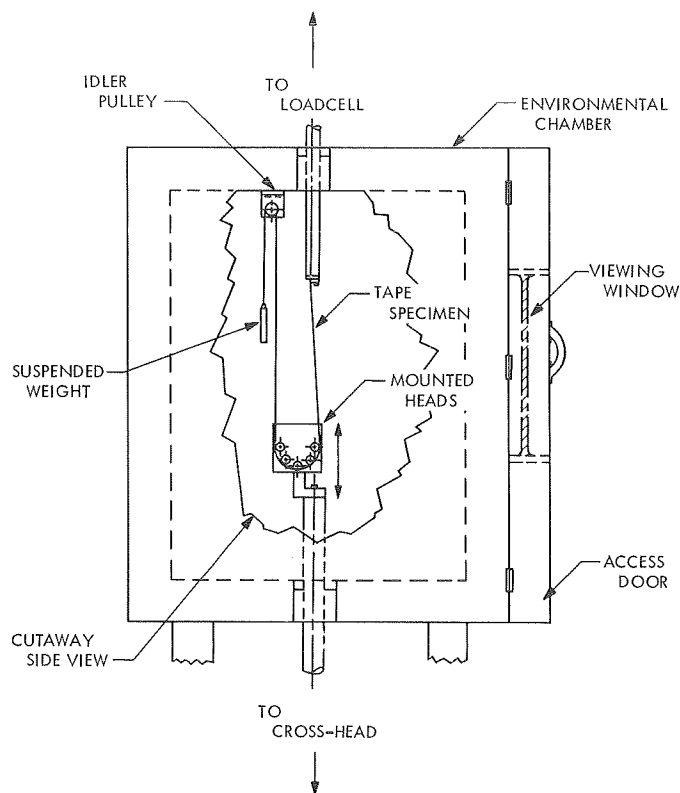
Fig. 2. Test assembly used to determine tape friction

The added tape was not involved in friction with the magnetic heads and, thus, the validity of the tests was not affected.

b. The gaseous atmosphere. Most of the experiments were performed in dry argon. To establish a flush period, the chamber was purged with this gas for 10, 20, and 40 min and after each period the effluent gas was analyzed by mass spectroscopy. A typical analysis was as follows:

After 10 min:	Ar	99.97 mol %
	H_2O	0.009
	N_2	0.009
	O_2	0.003
After 20 min:	Ar	99.99 mol %
	N_2	0.006
	H_2O, O_2	None
After 40 min:	Ar	100.00 mol %

Based on the results of such analyses, the chamber was flushed for a minimum of 20 min before each test.

3. Results and Discussion

Plots of $\mu\beta$ versus the number of passes over the five magnetic heads are shown in Figs. 3 to 6. A used 3M 990 tape, tested at 0.133 in./s in dry argon at 25°C, was the only case out of 36 in which the $\mu\beta$ value decreased during and after the 50 passes. Under all other conditions, the coefficient of friction of the three tapes increased as they passed over the magnetic heads. The increase ranged from 0.15 to 2.25 $\mu\beta$ units. The effects of the following factors on the coefficients of friction will be discussed: (a) temperature, (b) cross-head speed, (c) humidity, (d) state of tape (new versus used), and (e) static contact time or "wait" period of tape in contact with the heads.

a. Effect of temperature. Testing was done at 25 and 55°C. The effect of temperature on the behavior of tapes was influenced by such factors as the humidity and the state of tapes. For example, the new 3M 20250 tape experienced a decrease in μ with temperature increase, whereas the used 3M 20250 tape showed an increase in μ with temperature increase. Cross-head speeds and humidity did not affect the outcome in these cases. Similarly, the new 3M 990 tape showed a decrease or no change in μ with temperature increase, and the used tape indicated an increase in μ with temperature increase. In
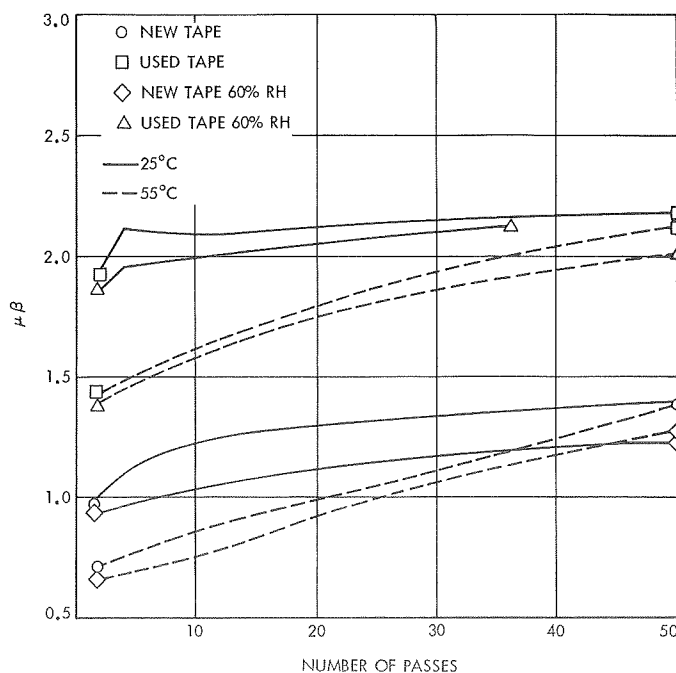
Fig. 3. Behavior of 3M 20250 tape tested at 0.133 in./s in argon
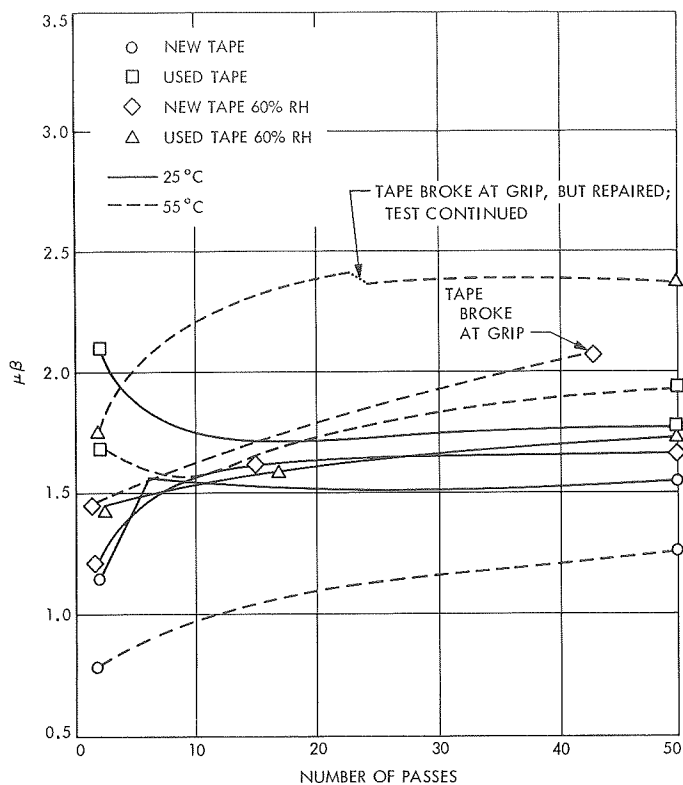
Fig. 4. Behavior of 3M 990 tape tested at 0.133 in./s in argon
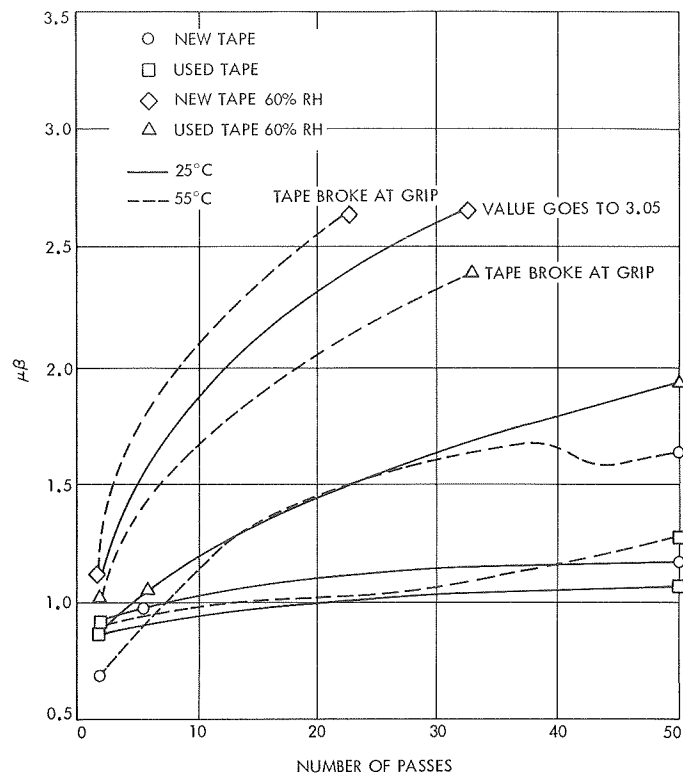
Fig. 5. Behavior of CEC W-4 tape tested at 0.133 in./s in argon
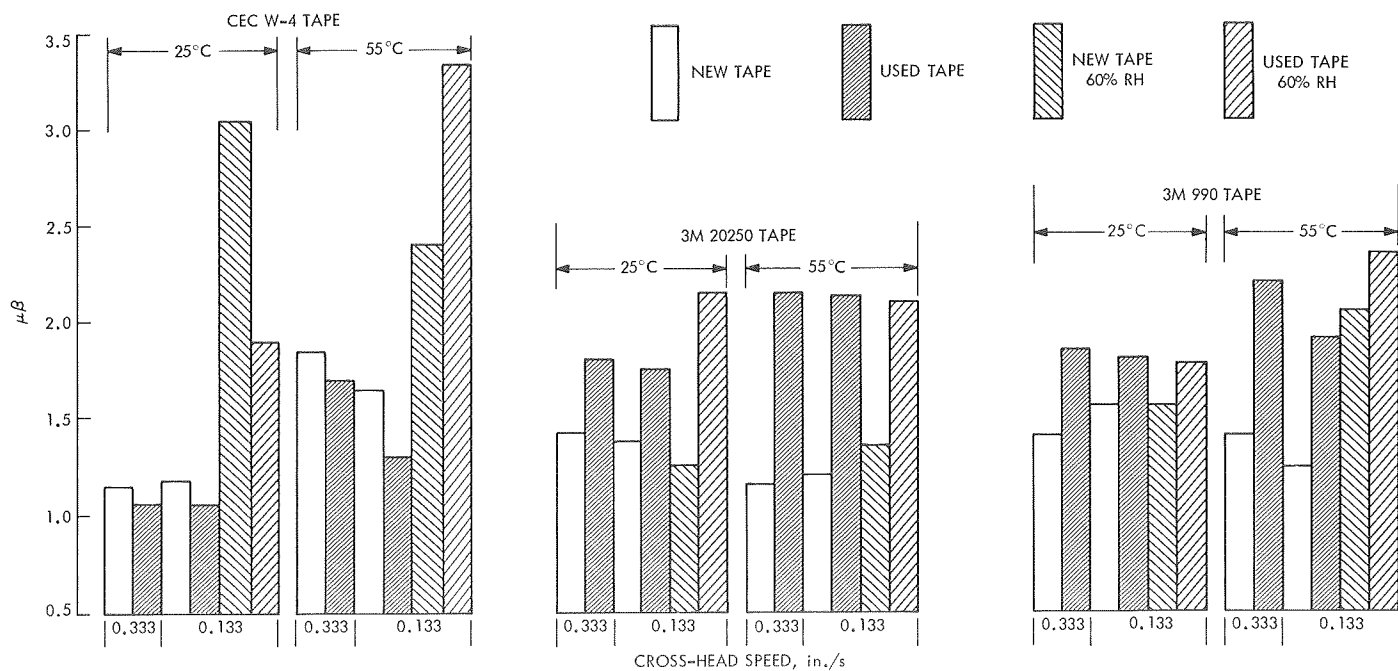
Fig. 6. $\mu\beta$ after 50 passes under various conditions

this case, however, humidity further increased the μ value (Figs. 3, 4, and 6). The μ values of CEC W-4 tape increased in all cases with temperature increase (Figs. 5 and 6).

Thus, with the exception of the new 3M 20250 and 3M 990 tapes, increase in temperature increased the coefficients of friction. The changes in the $\mu\beta$ values, $\Delta(\mu\beta)$, were highest for the CEC W-4 tape and lowest for the 3M 20250 tape, indicating the relatively high sensitivity of CEC W-4 to temperature.

b. Effect of cross-head speed. At constant temperature, higher $\mu\beta$ values were generally observed at the beginning and at the end of 50 passes when the cross-head speed was higher, i.e., 0.333 in./s. Notable exceptions to this trend were those of used 3M 20250 and new 3M 990 tapes tested at 25°C, and new 3M 20250 tape tested at 55°C. In these three cases, the coefficient of friction dropped with increase in cross-head speed. Curves obtained for the three tapes at the higher speed, i.e., 0.333 in./s, are not shown in the figures.

The new CEC W-4 tape had a peculiar performance at 25°C. Its μ was higher at the higher speed in the beginning of the experiment, but dropped below the μ value of the tape run at the lower speed at the end of the test.

Changes in μ with change in cross-head speed were negligible at 25°C. Exception to this was the used 3M 20250 tape as indicated above. Changes were more pronounced at 55°C, at which temperature μ increased with cross-head speed, new 3M 20250 tape being an exception here.

Thus, cross-head speed did not affect μ at 25°C, but did at 55°C. The 3M 20250 tape seemed to be the least sensitive to speed changes.

c. Effect of humidity (dry versus 60% RH). Experiments in humid argon were carried out at a cross-head speed of 0.133 in./s. The RH was 60 $\pm$2%.

Humidity had a marked effect on CEC W-4 tape. At both 25 and 55°C, μ increased considerably, so much so that the used specimen tested at 55°C broke at the grips

and the new specimens tested at 25 and 55°C had a tremendous increase in $\mu\beta$ value (Figs. 5 and 6).

The 3M 20250 specimens tested in humid argon showed little or no change in μ over the normal change occurring in dry argon. A glaring exception, however, was the used specimen tested at 25°C, which broke at the grips toward the end of the experiment (Fig. 3).

Humidity seemed to have a more adverse effect on the 3M 990 tape, notably at 55°C (Fig. 4). Both new and used tape specimens broke near the grips when tested at this temperature. At 25°C humidity did not play a significant role (Fig. 4).

Thus, relative humidity at the level used was of no benefit and was generally detrimental to the performance of the tapes with respect to head-to-tape interactions.

d. Effect of state of tape (used versus new). In the cases of the two 3M tapes (20250 and 990), the used specimens always had lower μ values at the conclusion of the test. At the start, however, μ values of used tapes were sometimes higher (Fig. 6).

e. Effect of static contact or "Wait." Most of the tapes were left motionless under tension in contact with the magnetic heads after undergoing the 50 passes. The duration of contact varied from 30 min to 16 h. The object was to ascertain whether the tapes were "sticking" to the heads when there was no motion. If so, a higher restarting force would be necessary after the "wait," compared to the force indicated before the "wait" period. It should be noted that during the wait periods, the flow of argon was stopped and so it must be assumed that the containing gas during these periods was contaminated with ambient air. The Instron chamber was flushed with argon before testing was restarted. The results of these tests are given in Table 1. The change in force ΔF, shown in the last column of the table, is the difference between the force experienced at the fiftieth pass and the force indicated by the first pass right after the inactive or wait period. Negative values indicate actual drops in the frictional forces after the wait period. Further tests on the effects of static contact are in progress, under controlled environmental conditions, to provide a clearer understanding of the effects of the static period on tape behavior.

The following observations summarize the data compiled in Table 1:

(1) The new 3M 20250 tape, when left motionless for 30–60 min and then tested in dry or humid argon, showed no or negligible ΔF, regardless of test temperature and RH. Only after long term contact with the heads, 960 min (16 h) at 55°C, did it show considerable increase in frictional forces, i.e., 1 lb.

(2) The used 3M 20250 tape showed negative ΔF under all test conditions. This indicates that the wait period of 30–60 min is not sufficient to induce meaningful stickiness or friction and, thus, testing after long term contact is in order.

(3) The findings for the 3M 20250 tape are also generally true for the 3M 990 tape. Only after an extended period of 195 min (3.25 h) did the new 3M 990 tape show any substantial increase in ΔF. One specimen of used tape showed a positive ΔF when tested at 55°C and 0.333 in./s after 30 min of inactivity.

(4) The CEC W-4 tape, stored and tested under dry conditions at 45°C after 960 min (16 h) of static contact, showed twice the force that the 3M 20250 tape showed after storage at 60% RH for a similar period at 55°C. Slight and medium amounts of sticking were shown by the used CEC W-4 tape after a short term storage of 30 min at 25 and 55°C, respectively. The effect of RH was inconclusive.

The data in Table 1 should be considered with caution, as full knowledge of the environmental conditions during the inactive periods was lacking.

4. Conclusions

The adaptation of ASTM D 1894-63 to the study of the frictional behavior of magnetic recording tapes with magnetic heads has proved useful in providing quantitative data not only with respect to the frictional forces, but also with respect to head-to-tape interactions under static conditions.

Table 1. Effect of "wait" period on sticking of tapes to magnetic heads

Tape	Tape condition	Test temperature, °F	Cross-head speed, in./s	Relative humidity, %	Inactive or "wait" period, min	Change in force, ΔF, lb
3M 20250	New	25	0.133	<1	30	0
3M 20250	New	25	0.133	60	30	0
3M 20250	New	55	0.133	<1	60	+0.03
3M 20250	New	55	0.133	<1	30	+0.10
3M 20250	New	55	0.133	60	960	+1.0
3M 20250	New	55	0.333	<1	30	+0.02
3M 20250	Used	25	0.133	<1	30	−0.34
3M 20250	Used	25	0.133	60	30	−0.10
3M 20250	Used	55	0.133	<1	60	−0.43
3M 20250	Used	55	0.333	<1	30	−0.30
3M 990	New	25	0.133	60	195	+0.30
3M 990	New	55	0.333	<1	30	−0.06
3M 990	Used	25	0.133	60	30	0
3M 990	Used	55	0.133	60	30	0
3M 990	Used	55	0.333	<1	30	+0.16
CEC W-4	New	25	0.133	60	30	+off scale
CEC W-4	New	45	0.133	<1	960	+1.93
CEC W-4	New	55	0.333	<1	30	0
CEC W-4	Used	25	0.133	60	30	+0.08
CEC W-4	Used	55	0.333	<1	30	+0.40

Measurements under various temperatures, humidity, cross-head speed, and gaseous environments are possible with the test setup used.

The results of the present tests show that the CEC W-4 tape is more susceptible to environmental changes than the 3M 20250 or 3M 990 tape. Among the three, the CEC W-4 tape also shows more stickiness to the magnetic heads after prolonged static contact, particularly at higher temperatures, such as 45°C. These observations indicate that the binder of CEC W-4 tape is less tem- perature resistant and more moisture sensitive than the binders of the two 3M tapes.

Compared with the 3M 990 tape, the 3M 20250 tape shows slightly less sensitivity to changes in temperature and humidity. In other respects they behave similarly.

Reference

1. Cox, C. N., and Plumtree, W. C., *Engineering Mechanics,* Second Edition, p. 117. D. Van Nostrand Co., Inc., New York, Feb. 1959.

XX. Research and Advanced Concepts

PROPULSION DIVISION

A. Reactor Simulator Runs With Thermionic Diode Kinetics Experiment, H. Gronroos

1. Introduction

This article describes the operation of the thermionic diode kinetics experiment with a nuclear reactor simulator in the loop. The response trajectories for two recently run cases are also shown; namely, the open loop response to an electric load change, and the events during a simulated reactor start-up run. Finally, the modifications presently being incorporated into the experimental assembly are briefly detailed.

A previous article (SPS 37-62, Vol. III, pp. 263–271) described the principles employed in developing the thermionic reactor simulator. The equations programmed on analog computers to obtain the desired dynamic characteristics were given. The article also briefly described the experimental assembly and gave references to other publications on the design and operation of the experiment. Therefore, these aspects will not be repeated here in any detail.

Three simulator versions reflecting increasing degrees of complexity (and simulation fidelity) have been developed. The reactor simulator runs discussed in this article were made with a version where only the diode structure and reactor are modeled in detail. The existing experimental liquid metal (eutectic NaK) heat rejection loop is regarded as representative for a prototypical plant.

The objectives of the latest series of runs were to investigate the open loop behavior of the chosen reference thermionic reactor. The large number of variables that can conceivably affect the dynamics of the system forces a selection. The investigations were restricted to a study of system responses to perturbations encountered under normal reactor operating conditions.

2. Reactor Simulator System

a. Experimental assembly. The reactor simulator for the thermionic diode kinetics experiment utilizes analog computers programmed so that the whole assembly with the computers in the loop exhibits the dynamic characteristics of a chosen reference plant. Thermocouple readings and measured diode currents and output voltages, together with the programmed equations, define the temperature states for the identified spatial regions in the model reactor diodes. This permits the generation of the internal feedback associated with the temperature coefficients of reactivity. The neutron density kinetics is

governed by this feedback and any applied control reactivity.

The practical implementation of the above scheme is illustrated schematically in Fig. 1. Shown is the NaK-cooled test bank with the available four experimental diodes in the enclosing vacuum chamber. The desired electrical interconnections between the diodes are selected with the coupling unit, and the total output is fed to a low voltage load. The relative locations of the emitter and thimble thermocouples, and the coolant inlet and outlet thermocouples, are indicated. The measured states are taken via buffer amplifiers to the data acquisition and control system and from there to the analog computer reactor simulator. The output signal is proportional to the neutron density and adjusted to a given power distribution in the model reference reactor. This signal sets the electron beam current I_{EB} for the electron beam
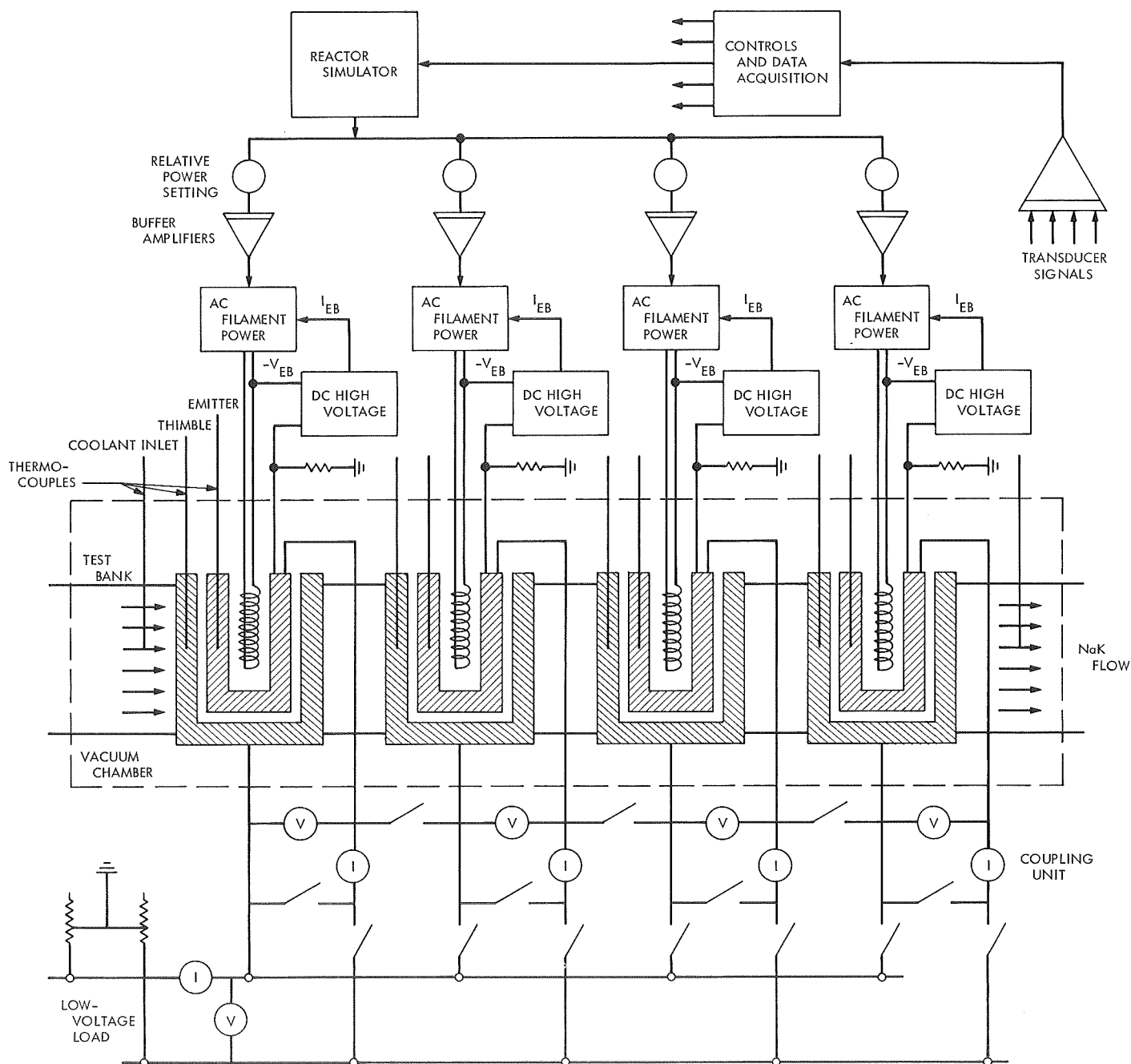
Fig. 1. Diode electrical output and power supply circuits

heater power supplies. The beam current is in turn controlled to the set value by the filament power supply. The high dc acceleration voltage V_{EB} is held constant. Since the total thermal power input to the diodes is the sum of the filament power and the electron beam power, the signal from the reactor simulator must be conditioned to maintain proportionality for the total power.

b. Analog computer application. The response behavior for the power supply-filament-emitter-thermocouple assembly is different than that of a prototypical reactor diode. This is accounted for by use of series compensation of the signal from the simulated neutron kinetics equations. To find the constants for the unity gain lead-lag compensator, a single reference reactor diode was analytically modeled using measured current–voltage data for the experimental diodes. This model was instrumented on an analog computer and the response to reactivity perturbations was determined. These response trajectories are then compared with trajectories (i.e., emitter thermocouple readings) seen in the experimental assembly, and the compensator is empirically adjusted until the trajectories are matched.

The above procedure gives a dynamic characteristic for the experimental power supply and emitter assembly that closely corresponds to the model reactor diode fuel and emitter regions. On the heat rejection side, i.e., the collector and regions external to it, the correspondence is only approximate because of differences in the designs between the experimental diodes and a prototypical reactor diode. The heat rejection loop also differs in this respect. The general dynamic responses are similar, however, and are characterized by a moderately slow response time for the collector and regions adjacent to it, and a large thermal lag in the heat rejection loop.

The required amount of analog computing equipment is obtained by link-up with the Analog Computing Facility via cables (CRS cables).[1] Only a small desk computer is used at the experimental site for simulation of the neutron kinetics equations and to provide the signals to the diode power supplies. The input to the desk computer consists of introduced reactivity perturbations and feedback reactivity obtained from the thermal balance equations generated in the Analog Computing Facility. Figure 2 shows the overall block diagram for the simulator in the Analog Computing Facility. Major state variables and feedback reactivity coefficients are indicated. The external inputs are the measured variables

---

[1] CRS = Central Recording Station.

for each diode and the output is the total feedback reactivity. The system was set up so that extensions or isolation of individual diodes can easily be made (i.e., the switches shown in Fig. 2). A master switch on the analog computer at the experimental site permits either running with this computer alone (for preparation purposes only) or closing the loop for the complete simulation system.

Table 1 identifies the variables shown on Fig. 2 and also lists other variables not directly used in the latest series of runs. The simulation equations were given in SPS 37-62, Vol. III. The maximum voltage for the CRS cables is ±10 V, while the analog computers are ±100-V machines.

c. Operational procedures. The initiation of a run begins with bringing the experimental assembly manually to the desired initial state. After a series of routine checks, the measured initial states are recorded. This information, together with the thermal input power, defines the initial values for the simulated states on the computers in the Analog Computing Facility. (An audio channel and a closed circuit TV facilitate the communication between this Facility and the experimental site.) Although the initial values for the simulated states are precisely defined through their respective governing equations, the given measured input states the integrators for $T_2/50$ (emitter temperature) and $T_4/20$ (collector temperature) are not normally exactly balanced, i.e., $dT_2(t=0)/dt=0$ and $dT_4(t=0)/dt=0$. This is because the heat loss from the emitter and collector regions in the experimental diodes is approximated by a term (scaled for analog computer programming)

$$\alpha\left[\left(\frac{T_2}{50}\right)-0.4\left(\frac{T_4}{20}\right)\right]$$

The nominal value for α is 0.42. However, depending on the chosen initial state, variations between 0.37 and 0.45 are observed at thermal balance. Therefore, the potentiometer for α is adjusted to bring simultaneously the integrators for both $T_2/50$ and $T_4/20$ to initial balance. After the above outlined procedures have been completed, the experiment is ready for a run.

3. Results

In the most recently completed series of runs, the open loop (i.e., no control system was incorporated) response to various system perturbations was studied for a selected

Fig. 2. Block diagram for simulator in Analog Computing Facility

$$\delta k_{fb} = \sum_{d=1}^{4} \left(\sum_{k=1}^{6} \alpha_{dk} \, \Delta T_{dk} \right)$$

Table 1. Measured and simulated variables in thermionic diode kinetics experiment

Variable	Device or signal source	CRS line scaling	Analog computer scaling	Variable range on analog computer
Inner fuel region temperature T_{11}, °C	Simulation		1/50	10–60
Outer fuel region temperature T_{12}, °C	W–Re thermocouple	1/500	1/50	10–50
Emitter temperature T_2, °C	Simulation		1/50	10–50
Collector temperature T_4, °C	Simulation		1/20	5–45
Insulator temperature T_5, °C	Simulation		1/20	5–45
Thimble temperature T_6, °C	Cr–Al thermocouple	1/100	1/20	5–35
Coolant temperature T_7, °C	Simulation		1/20	5–35
Diode coolant inlet temperature T_{7i}, °C	Simulation		1/20	5–35
Diode coolant outlet temperature T_{7o}, °C	Simulation		1/20	5–35
Test bank coolant inlet temperature T_{8i}, °C	Cr–Al thermocouple	1/100	1/20	5–35
Test bank coolant outlet temperature T_{8o}, °C	Cr–Al thermocouple	1/100	1/20	5–35
Cesium reservoir temperature T_{cs}, °C	Cr–Al thermocouple	1/100	1/10	2–40
Diode output voltage V_o, V	V-probe	2	20	0–50
Diode current I_o, A	Shunt	1/100	1/10	0–100
Load voltage V_L, V	V-probe	1	10	0–100
Load current I_L, A	Hall effect	1/100	1/10	0–100
Neutron density n, n/cm^{-3}	Simulation		1	0–100
Neutron density change Δn, n/cm^{-3}	Simulation	1	1	0–100
Steady-state reactivity δk, $\delta k/k$	Simulation	10^4	10^4	64.48
Feedback reactivity δk_{fb}, $\delta k/k$	Simulation	10^4	10^4	0–10
Control reactivity δk_c, $\delta k/k$	Simulation	10^4	10^4	0–10
Reactivity rate $\delta \dot{k}$, $\delta k/k \cdot s^{-1}$	Simulation	10^4	10^4	0–10
T_{11} feedback reactivity α_{11}, $\delta k/k \cdot °C^{-1}$	Potentiometer		$5 \cdot 10^5$	
T_{12} feedback reactivity α_{12}, $\delta k/k \cdot °C^{-1}$			$5 \cdot 10^5$	
T_2 feedback reactivity α_2, $\delta k/k \cdot °C^{-1}$			$5 \cdot 10^5$	
T_4 feedback reactivity α_4, $\delta k/k \cdot °C^{-1}$			$2 \cdot 10^5$	
T_5 feedback reactivity α_5, $\delta k/k \cdot °C^{-1}$			$2 \cdot 10^5$	
T_6 feedback reactivity α_6, $\delta k/k \cdot °C^{-1}$			$2 \cdot 10^5$	
T_7 feedback reactivity α_7, $\delta k/k \cdot °C^{-1}$			$2 \cdot 10^5$	
T_8 feedback reactivity α_8, $\delta k/k \cdot °C^{-1}$			$2 \cdot 10^5$	
Coolant flow rate ω, g/s	Electromagnetic flow meter		1/10	0–50
Electric load resistance R_L, Ω	Potentiometer		200	10^{-4}–10^{-2}

reference thermionic reactor power plant. As was mentioned above, only the reactor was modeled in detail, and the experimental heat rejection loop was regarded as representative for a prototypical plant. The variables in the runs may be summarized as follows:

Electrical coupling pattern
    Thermionic diodes in series
    Thermionic diodes in parallel

Temperature coefficients of reactivity

Response to system perturbation
    Reactivity
    Electric load
    Short circuit

    Open circuit
    Cesium reservoir temperature

Start-up and shut-down

Two examples are discussed below.

a. Effect of electric load change. Figure 3 illustrates the response to an electric load change for a case with the four diodes operating in series. This corresponds to a thermionic reactor with "flashlight" converter elements and no controller holding the reactor electrical output to a specified control law. The shown run is one of several where the temperature coefficient of reactivity for the thimble region α_6 (corresponding to the cladding-coolant-element support structure) was varied. For the case in
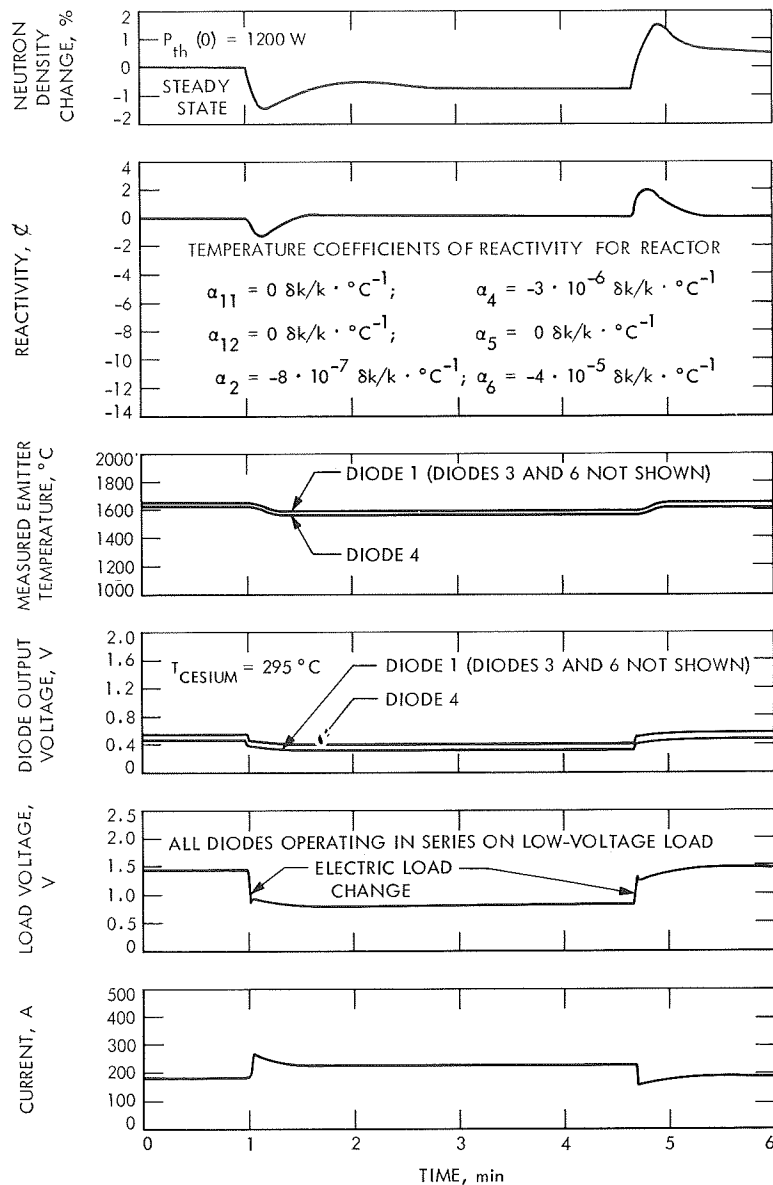
Fig. 3. Reactor simulator response to an electric load change

Fig. 3, α_6 is set at a high value. The other temperature coefficients are in the range of expected values. The initial thermal power input $P_{th}(0)$ to all diodes is 1200 W, i.e., a relatively low power point. The cesium reservoir temperatures are held constant at 295°C, which is near optimum for the given initial conditions.

As a result of the load change from 185 to 270 A, the fuel and emitter regions decrease in temperature but the collector and the regions external to it increase in temperature. This overrides the feedback from the emitter and a total negative reactivity initially affects the re-actor. This decreases the neutron density (proportional to the generated fission power). The resulting decreasing temperatures cause an increase in the feedback reactivity, which swings over to a small positive value before equi-librium is reached. The diode power delivered to the load decreased from 268 to 180 W, but the thermal power decreased only 1%. The conversion efficiency decreased considerably, and the shown run is a demon-stration of the inherently poor self-regulating character-istics of an open-loop thermionic reactor. The effect of changing α_6 to a small value decreases the negative re-activity peak and increases the positive peak, but the overall response is not materially altered from that shown on Fig. 3.

Note that the measured emitter temperatures and output voltages are not the same, although the input thermal power and the cesium reservoir temperatures are nominally the same. Experience indicates that the observed differences are mainly due to true performance differences between the diodes, with only a small part due to measurement error.

b. Reactor start-up. A variety of simulated reactor start-up runs have been made with the experimental diodes coupled in series or in parallel, and with various start-up strategies. Figure 4 shows a case where the reactor has first been brought to a low power level (450 W/diode) and with the converters in open circuit. The cesium reservoir temperatures have been set at the chosen value for the final operating point (295°C). The temperature coefficients of reactivity are the same as for the case described under *Paragraph a,* above.

The emitter temperature is first increased to about 1500°C by the introduction of reactivity. The diodes are next connected in series on a high impedance load and no appreciable current is drawn. Next, this load is further reduced to approximately half its value. (In the experimental assembly, these loads are introduced by the 10-Ω emitter-to-ground resistors in the high-voltage supplies, and when the mercury column in the low-voltage load reaches the bottom of the resistance loop.) The low-voltage load was then continuously reduced. At a low diode voltage point, the diodes ignite. This is accompanied by reduced emitter temperatures and momentarily increasing collector temperatures. If the emitter temperature and collector temperature had been raised another 100°C, the ignition phenomenon would not have been observed. Instead, a smoothly increasing current and decreasing voltage would have been seen.

The sequence shown in Fig. 4 is but one of several possible start-up methods. Normally, no particular anomalies are observed except for cases where the cesium reservoir temperature in one or all of the diodes is either too high or too low. Under such circumstances, a small transient oscillatory behavior may be seen. These cases have proven to be difficult to repeat systematically and will be the subject of further study.

4. Future Extensions

Presently, two additional thermionic diodes are being installed to bring the total to a full complement of six diodes. The new converters are of the same design as the previous four and were made by the same manufacturer, Thermo Electron Corporation.

To accommodate the additional diodes, a surplus vacuum-tube-type analog computer is being installed at the experimental site. This will bring the total of available amplifiers at this location to sixty-eight. The Analog Computing Facility will remain in use as discussed.

A special resistive load is being installed at the output of the power conditioner for the diode electrical power. The new load will permit continuous impedance variation from essentially open circuit to short circuit. The previous load was limited at the high-impedance end. When the power conditioner is not on-line, the existing low-voltage load will be in use.

The above-listed additions will bring the thermionic diode kinetics experiment to its planned full extension.

5. Conclusions

Two runs have been discussed that illustrate the behavior of a chosen reference thermionic reactor simulated on the thermionic diode kinetics experiment. In one of the two cases, the open-loop response to an electric load change is shown. This run illustrates the inherently poor self-regulating characteristics of an open-loop thermionic reactor system. To operate efficiently over a range of electric loads, a controller designed for a chosen control law must be included. Runs with a simulated controller in the loop are planned for the future.

The second case shows the events during a simulated reactor start-up run. The strategy was to first bring the emitter temperature to a relatively low value, and then to switch on a high-impedance load, which was gradually reduced. At low impedance, the diodes ignite and the attendant changes in the emitter and collector temperatures cause a change in the neutron density through the inherent reactivity feedback. The ignition does not cause any particular problems from a reactor operations point of view.

The above-described sample runs demonstrate the versatility of the thermionic diode kinetics experiment for simulation of the dynamics of a thermionic reactor power plant. The time spent to set up a series of runs is considerable. However, once this has been done a large number of cases can be investigated expediently.
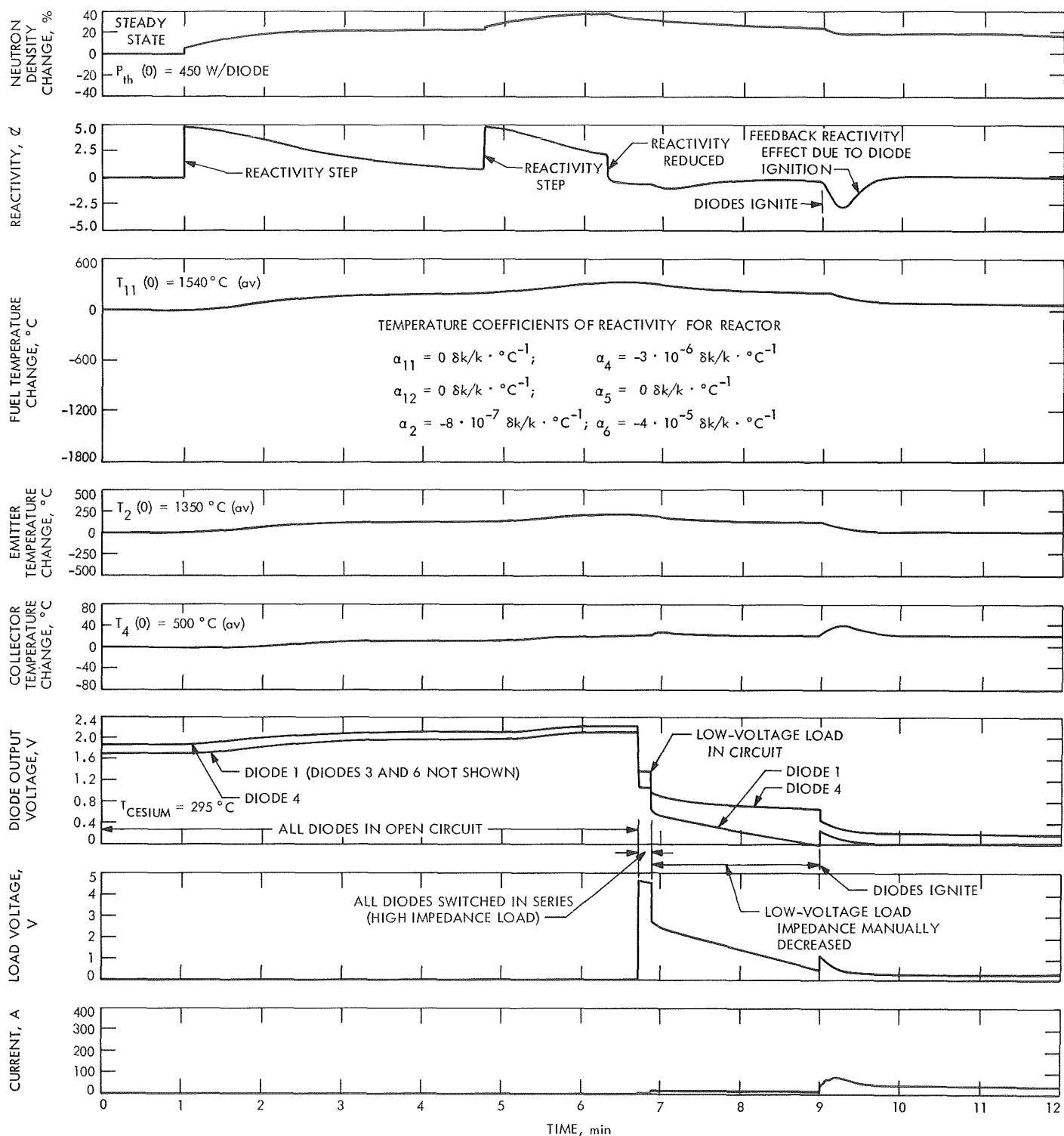
Fig. 4. Simulated thermionic reactor start-up run

B. Ion Thruster Control-Loop Sensitivity,
E. V. Pawlik

1. Introduction

Solar electric propulsion is currently of interest (Refs. 1 and 2) for a wide range of deep space missions and is, therefore, being investigated at JPL (Refs. 3 and 4). The JPL program utilizes a 20-cm-diameter ion thruster which employs a hollow cathode electron source. This cathode type, which provides long thruster lifetime and higher total efficiency, replaces an oxide cathode that was used earlier in the program. The control loops to control the output power and propellant utilization of the oxide cathode thruster were examined analytically (Ref. 5) to determine the required regulation on the fixed thruster parameters. The present study is directed toward determining, experimentally, the sensitivity of the hollow cathode thruster propellant controls to variations in these parameters.

2. Apparatus

A 20-cm-diameter thruster[1] was used in these tests. Figure 5 presents a schematic drawing of the thruster, power supplies, interconnections, and control loops. Mercury propellant is supplied to the thruster through two porous tungsten vaporizers. An ion beam reference is used to specify the ion beam current level. The propellant flowrate is controlled indirectly by the arc chamber performance. The vaporizer temperatures are varied to adjust the flowrates to provide the desired arc chamber performance. The propellant utilization is specified by an arc current reference signal which can be generated from the beam reference signal. The utilization is normally maintained near 90%. Arc voltage is controlled by the mercury flow through the hollow cathode.

A net accelerating voltage of 2000 V is used for the ion beam. An output power of 1000 to 2000 W is the normal range of operation. The present tests were conducted at the mid-range point, or 1500 W. The nominal thruster parameters used are presented in Table 2.

Laboratory power supplies with both current and voltage regulation are used for the operation of the thruster. Slight drifts in the settings are present (less than 2%). The gain of the cathode vaporizer controller permitted small steady-state errors (less than 1%) within the arc voltage–cathode vaporizer control loop.

---

[1]Pawlik, E. V., *Performance of a 20-cm-diameter Electron-Bombardment Hollow-Cathode Ion Thruster* (to be published).

Table 2. Nominal value of ion thruster parameters

Parameter	Current, A	Voltage, V
Accelerator	0.003	−1000
Beam	0.725	2000
Magnet-manifold	0.6	14
Cathode keeper	0.50	7
Arc	—	35

The cathode and main thruster vaporizers are calibrated by the mercury level change in precision bore glass tubes while the temperature is maintained constant. These calibration curves are used to determine mercury flow and propellant utilization during thruster operation.

3. Test Results

The thruster was operated with the control loops at a beam reference corresponding to 0.752 A. The beam voltage (net accelerating voltage) was maintained at 2000 V. After a several-hour warm-up period to allow the thruster to come to a thermal equilibrium with the vacuum tank environment, variations were introduced in each fixed parameter in turn. The effects of these changes were reflected in changes in vaporizer temperatures which, by use of the calibration curves, indicated the flowrates and propellant utilization variations. Strip chart recordings of the thruster parameters indicated when the system again reached a steady-state condition. At least a 10-min system settling time was necessary after each system change.

The effects of variations in the voltage applied to the accelerator grid are presented in Fig. 6. Two values of the arc reference are presented. Thruster operation was not extremely sensitive to variations in this parameter with voltage excursions of 500 V (±50%) presenting a maximum efficiency variation of about 1%.

Figure 7 presents the effect of magnet field strength variations for two values of arc current. Near the nominal magnet current value, the system was again not extremely sensitive to current variations. Current excursions greater than 10% were necessary to change the propellant utilization 1%.

Cathode keeper current variation effects on the propellant utilization are shown in Fig. 8. Large percentage excursions from the nominal 0.5-A operating point were necessary to vary the propellant utilization significantly.
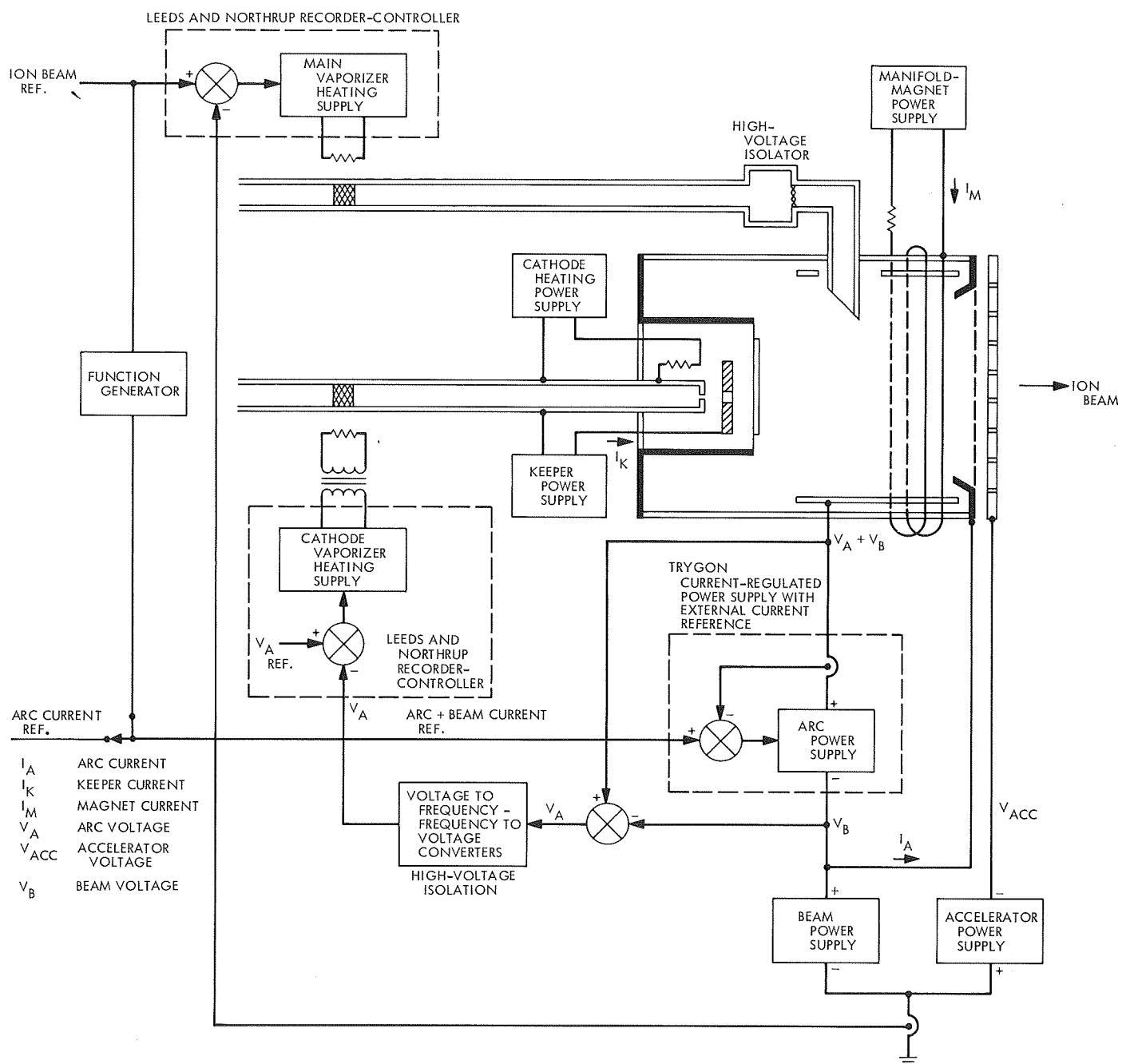
Fig. 5. Schematic of controls for a hollow-cathode ion thruster
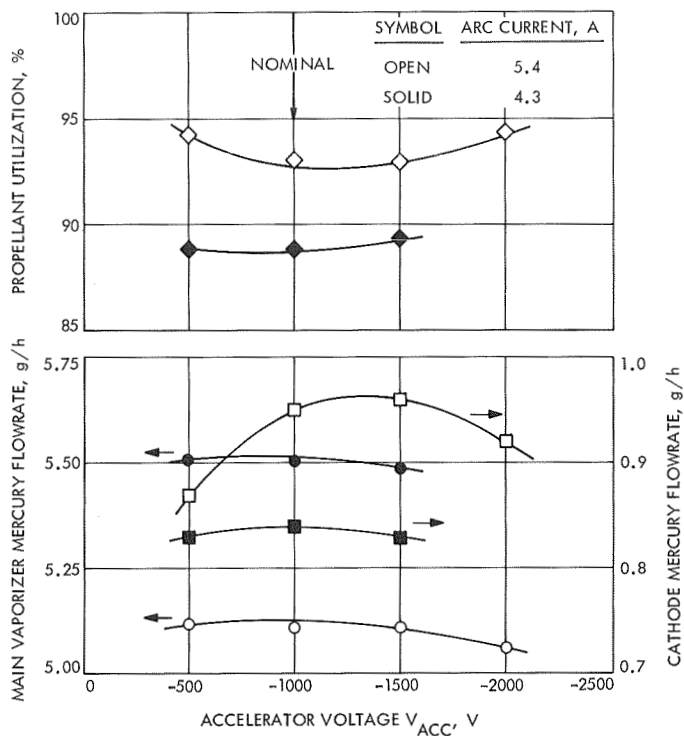
Fig. 6. Effects of accelerator voltage on propellant utilization
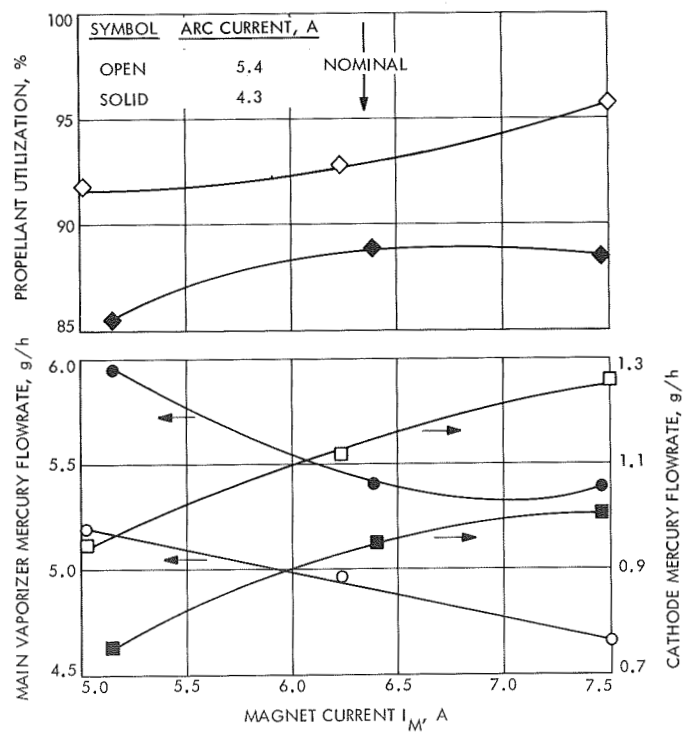
Fig. 7. Effects of magnet current on propellant utilization
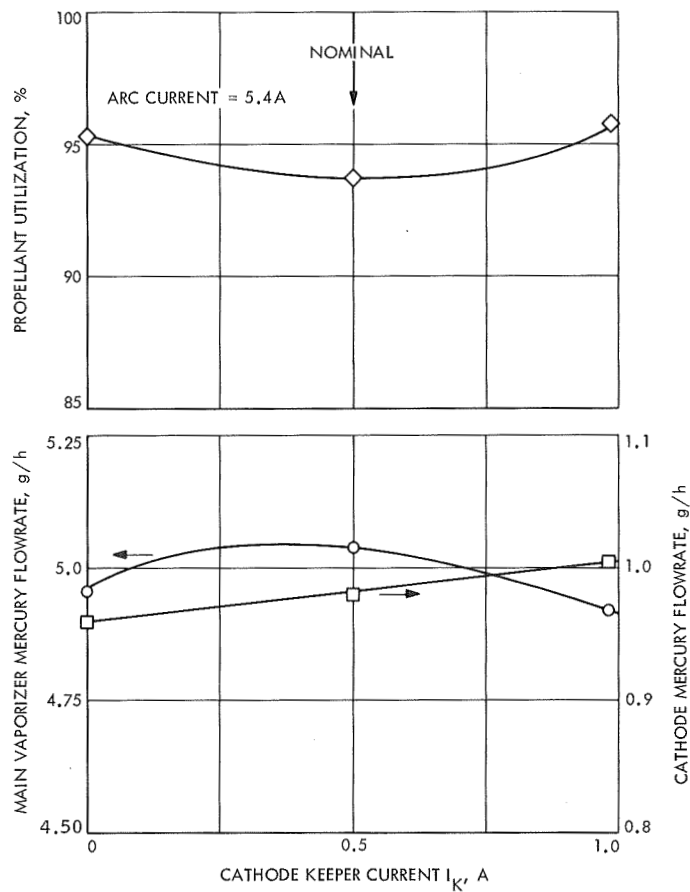
Fig. 8. Effects of cathode keeper current on propellant utilization

Changes in the cathode heating current from its nominal value of zero to its maximum value of 3.6 A (necessary to ignite the cathode) had no measureable effect on the control loops.

Results of variations in arc current and voltage are presented in Figs. 9 and 10. Propellant utilization was fairly sensitive to changes in either of these parameters. As in the case of the oxide cathode thruster, tight regulation of the arc current and voltage appears necessary to maintain close control of the propellant consumption.

4. Conclusions

The sensitivity of an ion thruster to variations in the fixed thruster parameters was investigated experimentally. If it is required that the thruster propellant utilization be maintained to within 1%, wide variations (on the order of 10%) of the accelerator voltage, magnet current, and cathode keeper current could be tolerated. Regulation requirements on these supplies is about one order of magnitude less than that required for the oxide cathode thruster. Close regulation is required for both the arc current and voltage (on the order of 1%).

References

1. *Study of a Solar Electric Multi-Mission Spacecraft*, Final Technical Report, JPL Contract 952394. TRW Systems Group, Redondo Beach, Calif., Jan. 1970.

2. *Solar Electric Propulsion Asteroid Belt Mission Study*, Final Technical Report, JPL Contract 952566. North American Rockwell Corporation, Space Division, Downey, Calif., 1970.

3. Masek, T. D., and Pawlik, E. V., "Thrust System Technology for Solar Electric Propulsion," AIAA Paper 68-541, presented at the 4th Propulsion Joint Specialist Conference, Cleveland, Ohio, Jun. 1968.

4. Macie, T. W., Pawlik, E. V., Ferrera, J. D., and Costogue, E. N., "Solar-Electric Propulsion System Evaluation," AIAA Paper 69-498, AIAA 5th Propulsion Joint Specialists Conference, U.S. Air Force Academy, Colorado, Jun. 1969.

5. Mueller, P. A., and Pawlik, E. V., "Control Analysis of an Ion Thruster with Programmed Thrust," AIAA Paper 69-239, presented at the 7th Electric Propulsion Conference, Williamsburg, Va., Mar. 1969.
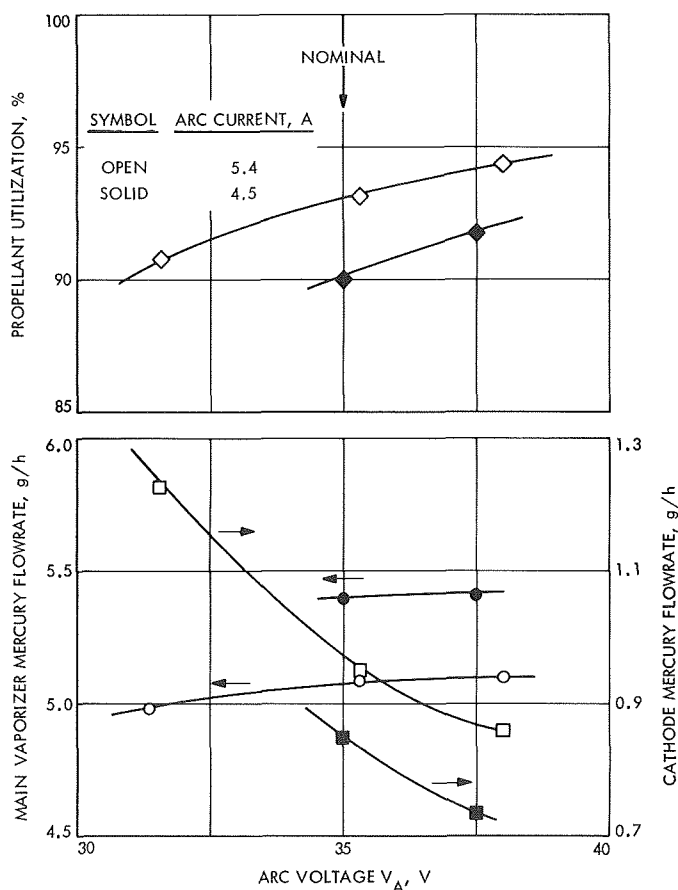
Fig. 10. Effects of arc voltage on propellant utilization

Fig. 9. Effects of arc current on propellant utilization

XXI. Liquid Propulsion

PROPULSION DIVISION

A. TOPS Trajectory Correction Engine,
A. Heidenreich

1. Introduction

The Liquid Propulsion Section is conducting advanced development of monopropellant trajectory correction thrusters in the 25-lbf thrust class in support of the Thermoelectric Outer Planet Spacecraft Program (TOPS) (Ref. 1). Typical missions now under consideration require up to nine trajectory changes spaced over a 10- to 12-yr flight. On previous *Ranger* and *Mariner* flights (Refs. 2, 3, 4), monopropellant anhydrous hydrazine was used with good results. However, the propulsion requirements of the longer duration, higher impulse, outer planet missions necessitated a reexamination of state-of-the-art propulsion capabilities.

A hydrazine-based, blowdown pressure-fed propulsion system was selected to meet the TOPS mission requirements. In an effort to achieve better overall system performance, a binary blend of anhydrous hydrazine and hydrazinium nitrate (75% N_2H_4, 24% $N_2H_5NO_3$, 1% miscellaneous, by weight) was chosen as the desired propellant for the advanced development effort.[1] This blend

---

[1]Draper, R., *Functional Requirement, TOPS Flight Equipment, Propulsion Subsystem,* Sept. 23, 1969 (JPL internal document).

offers a 6% increase in specific impulse, and a 9% increase in density, over anhydrous (neat) hydrazine. In addition, the freezing point of the blend is 4°F, compared with the 34°F for anhydrous hydrazine. Lower freezing point in propellant is a definite advantage in missions to the far reaches of the solar system, since thermal control becomes increasingly difficult at greater distances from the sun.

Since the state-of-the-art of catalytic monopropellant thrusters based on nitrate mixtures is not as well developed as that for anhydrous hydrazine motors, it was planned to first demonstrate that the trajectory correction propulsive requirements of the TOPS mission could be performed with a state-of-the-art engine using anhydrous hydrazine. After that, full attention will be given to developing motors based on the higher performance monopropellant blends.

Although there has been extensive development experience with hydrazine thrusters over the past several years, the applications have been either those which demanded one or two short duration (5 to 100 s) steady state burns (Refs. 2, 3, 4) or those which operated in a pulsed mode (Ref. 5). Therefore, there was a lack of empirical information about the effects of multiple cold starts, long duration (up to 800 s) steady state burns, and

low temperature incoming propellant. Accordingly, a number of firings was made with anhydrous hydrazine to determine these effects. This article will review the progress made to date in demonstrating the anhydrous hydrazine capability, and will also present the results of preliminary experimentation with a nitrate blend.

2. Apparatus and Test Procedure

The motor used for the neat (anhydrous) hydrazine tests was a bolt-up 23-lbf thrust engine available from a previous program. A cutaway schematic of this engine is shown in Fig. 1. The catalyst bed was layered: an upper bed 0.200 in. long packed with 25- and 30-mesh Shell-405[2] catalyst, and a lower bed 0.650 in. long packed with 14- to 18-mesh Shell-405. The upper bed was retained by a plate welded to a central spud on the injector body. This inhibits voids from forming in the upper bed. (Previous designs that had layered catalyst beds retained only by a screen suffered from short upper bed life as a result of the screen bowing outward and creating a void in which the catalyst granules could grind themselves into fines and pass through the screens).

Three high-response, 0.005-in.-diameter chromel–alumel thermocouples were installed in the upper bed. These were positioned 120 deg apart on a 1.000-in-diameter circle at distances of 0.050, 0.100, and 0.150 in. from the face of the showerhead injector.

The engine used for experimental testing with the nitrate blend was a bolt-up version of the *Mariner* Mars 1969 50-lbf thrust engine. A cutaway is shown in Fig. 2.

No thermocouples could readily be installed in the upper bed because of its inaccessibility but three thermocouples were placed in the center of the lower bed, located axially at the top, in the center, and at the bottom of the lower bed. The value (Table 1) of L^* (V_{cat}/A_t) could be reduced between tests by inserting various lengths of stainless steel spacers into the chamber and then positioning the bottom retention plate on top of the spacer.

All tests were run in Pit "J" at the JPL test facilities. The engines were mounted to fire vertically downward into ambient back pressure at the nozzle exit. The propellant was delivered from a nitrogen-pressurized facility tank. A coil of tubing was immersed in a tank filled with either warm water or water–brine solution to condition

---

[2]A product of Shell Development Company, Emeryville, California.

Table 1. Nomenclature

A_c area of cylindrical chamber, in.^{2}

A_t area of nozzle throat, in.^{2}

c^* characteristic velocity, ft/s

$$c^* = \frac{P_c A_t g_c}{\dot{w}}$$

G Bed-loading

     $G = \dot{w}/A_c$ lbm/in.^{2}-s

g gravitational constant, 32.174 lbm ft/lbf s^2

L catalyst bed length, in.

M average molecular weight

P chamber pressure, psia

R universal gas constant

     R = 18,528 in.-lbf/lbm mole °R

T gas temperature, °R

V_{cat} volume of empty chamber filled by catalyst, in.^{3}

$\dot{w}$ fuel flow rate, lbm/s

X amount of ammonia dissociated, %

ϵ volume fraction voids between particles

θ chamber residence time

     $\theta = \epsilon \, LMP/GRT$ s

the temperature of the incoming propellant. An automatic nitrogen gas purge system was incorporated into the test system. Upon shutdown, the purge line was automatically actuated, and any fuel remaining in the fuel line was purged through the engine. The flowing nitrogen blanketed the catalyst bed, and prevented high temperature oxidation of the catalyst from occurring. Instrumentation was recorded both on a CEC oscillograph recorder run at 25 in./s, and on a digital data recording system.

3. Test Results

a. Neat hydrazine testing. Results of the first series of tests, run with neat hydrazine, are summarized in Table 2. For the first five runs, the set nitrogen pressure on the fuel was decreased to simulate a blowdown pressurization system, and thus obtain off-design engine operating points. The inlet propellant temperature was initially conditioned by filling the tank containing the heat transfer coil with warm water. The temperature of the bath was allowed to cool by natural convection; thus the inlet propellant temperature for each run was decreased, simulating conditions on a mission to the outer planets. From Table 2 it can be seen that the combustion effi-
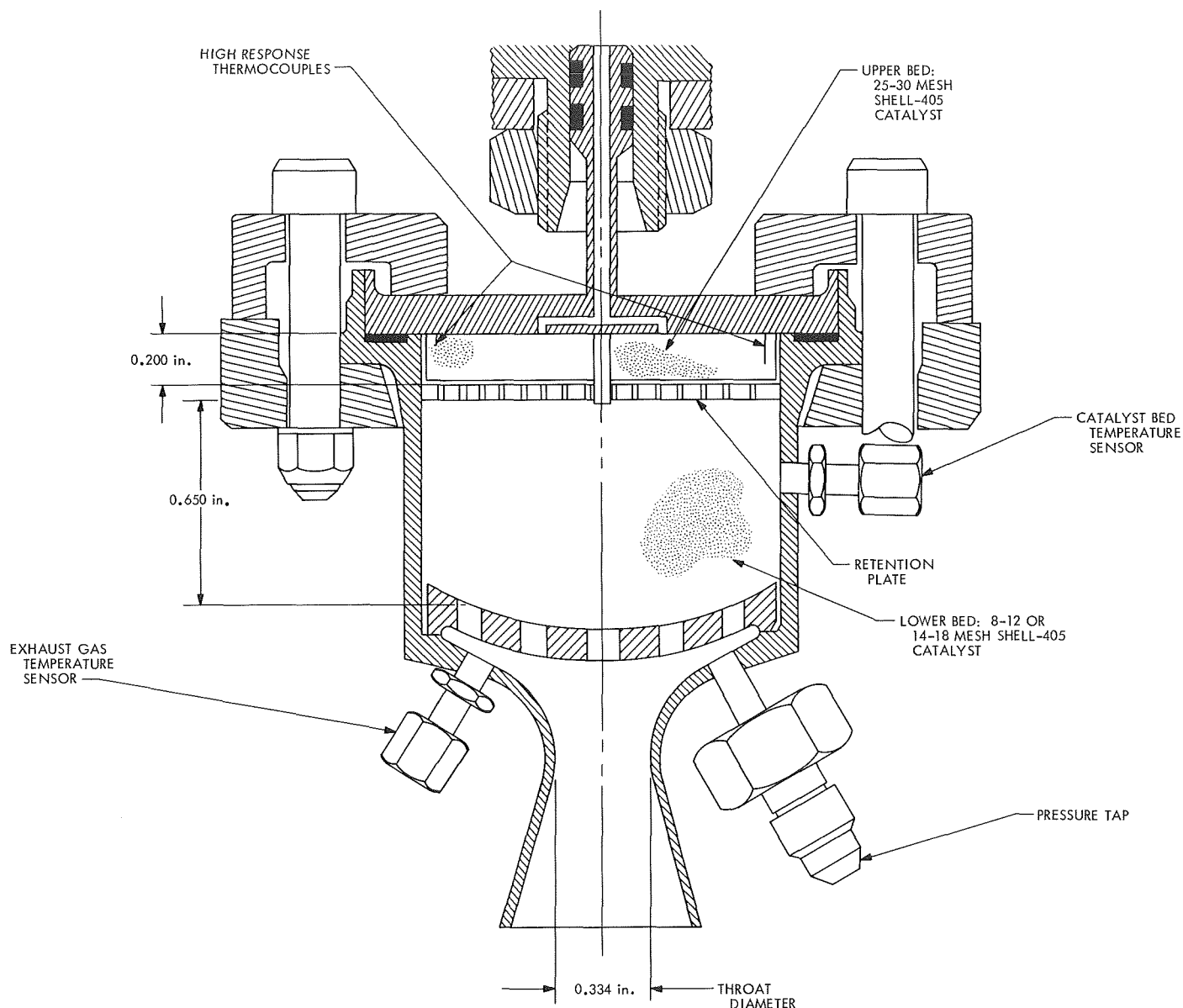
Fig. 1. Bolt-up 23-lbf hydrazine engine

ciency, as measured by the characteristic velocity c^*, deteriorated from the start to the end of a burn. By run 5, the performance was considerably worse than in run 1, and the engine was exhibiting definite evidence of what has been termed the "washout phenomenon." This is a change in engine operation from an essentially constant c^* mode to a mode of operation characterized by a decrease in chamber pressure and an increase in fuel flow rate, and therefore a decrease in c^* and specific impulse I_{sp}. This is illustrated in Fig. 3, where the change in the characteristic velocity as a function of run duration is plotted for run 5. Since the engine was operating

abnormally, the rest of the planned simulated-mission duty cycle was discontinued. Inlet propellant temperature had been determined elsewhere as a key variable influencing the onset of washout.[3] Also, the same workers found that if washout *were* occurring, a shutdown for a short period of time (1 to 4 s), followed by an immediate restart, could have the effect of rejuvenating the catalyst bed. So, for run 6, also shown in Fig. 3, the inlet propellant temperature was lowered to 55°F. In addition, it

---

[3]Private communication from K. Traynalis, Kidde Co., Belleville, N.J., Oct. 7, 1969.
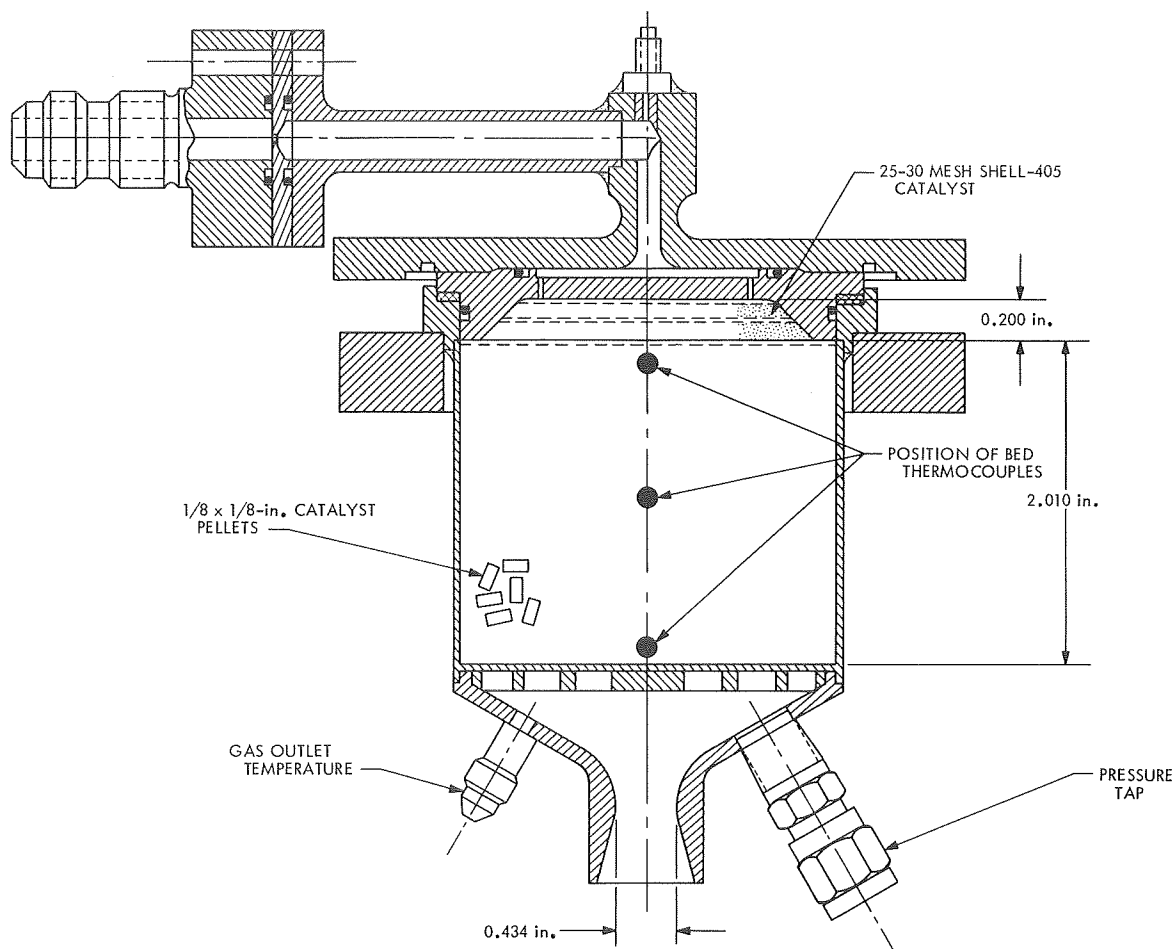
Fig. 2. Bolt-up *Mariner* Mars 1969 50-lbf hydrazine engine

was planned to try a brief shutdown with *no* purge and then an immediate restart in an attempt to confirm the rejuvenation effect in the event washout was encountered. Figure 3 shows the trace of characteristic velocity c^* vs time t for run 6. Upon startup, the c^* value for run 6 was 2400 ft/s compared with an expected value of 4250 ft/s. The c^* decayed to 1600 ft/s in 36 s. At this point, a 1-s shutdown and restart was tried. Upon restart, the c^* jumped to 4300 ft/s. After remaining stable for some 40 s, the c^* started falling. After 160 s (from the 1-s shutdown) it had reached a value of 2000 ft/s. Another 1-s shutdown was made, and again the c^* value jumped to over 4200 ft/s. The trailoff in c^* was slightly faster. In 134 s, the c^* was 2000 ft/s, and a normal shutdown with nitrogen purge was made. A seventh run was made with the inlet propellant temperature warmed to 92°F to obtain more information about the effects of temperature on engine washout. With this warmer inlet temperature, the chamber pressure decreased only very slowly, from 135 to 104 psia in 450 s.

The engine underwent seven cold starts for a total duration of 1536 s. It was then disassembled for inspection. The lower bed was still intact, but had lost 4% by weight of the catalyst. As far as could be determined without grinding off the upper bed retention plate, the upper bed was also intact. The lower bed was replaced and several more runs were made with cold incoming propellant (runs 8 through 10 on Table 2). These runs were made to determine the effects of total cumulative time on the catalyst, and also to ascertain whether reduced bed-loading would prevent washout. The bed-loading at the start of run 8 was 0.047 lbm/s-in.[2] compared with 0.07 lbm/s-in.[2] for run 1. The c^* value decreased steadily from 3750 to 2100 ft/s in 130 s. In run 9 the initial conditions were the same as in run 8. However, the c^* was only 2600 ft/s 10 s into the run. It took only 50 s for the performance to decay to a c^* of 2100 ft/s, compared with 130 s for run 8. Run 10 was made with the tank pressure lowered to 210 psig to reduce the bed loading even further. This did not happen, however,
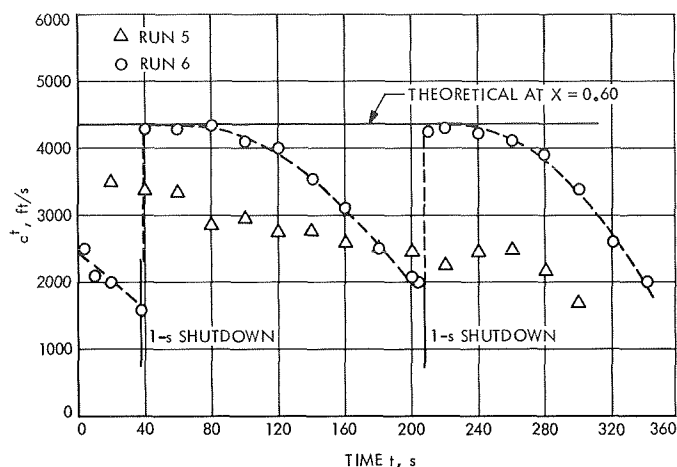
Fig. 3. Evidence of washout phenomenon: variation of characteristic velocity with time

because the c^* was unexpectedly low on startup, which resulted in a bed loading of 0.055 lbm/s-in.² By 50 s into the run the c^* had decreased to 2120 ft/s and a normal shutdown was made.

Upon examination, the upper bed had lost 7% by weight of the catalyst, while the lower bed had lost only 0.7% during runs 8, 9, and 10. The lower specific surface area of the larger catalyst in the lower bed (8 to 12 mesh instead of 14 to 18) is believed to be the principal cause of the washout, although runs 7 and 8

showed the phenomenon to be also quite sensitive to inlet propellant temperature.

Another series of tests was run to check the theory that the combination of bed length and specific area of the catalyst used in tests 1 through 10 was inadequate to sustain steady state engine operation. The lower bed catalyst was changed to 14 to 18 mesh, giving 67% more specific surface area compared with the 8 to 12 mesh. The inlet propellant temperature was held at about 50°F. Bed length remained the same as before. Table 3 shows the duty cycle used. The performance was high and did not change during any run. A total of eleven starts and 2017 s were accumulated, exceeding by 20% the longest TOPS mission burn time envisioned at present. During run 21, a small leak developed in a thermocouple insert in the injector and the testing was terminated. Examination showed the chamber to be in excellent condition. Less than 1% by weight of the catalyst was lost. Maximum chamber pressure roughness, measured in the converging section of the nozzle, was 13 psi, peak to peak, or ±6% of mean chamber pressure. By way of comparison, the life roughness for one flight engine in this same class (the *Titan* Transtage 25-lbf engine) is ±30 psi (Ref. 6), which corresponds to ±30% of mean chamber pressure.

b. Hydrazine–Hydrazine nitrate testing. The monopropellant blend of 76% hydrazine, 24% hydrazine nitrate (by weight) has a number of advantages, just

Table 2. Initial multiple-start long-duration tests with neat hydrazine

Test	Duration, s	Tank pressure, psig	Inlet propellant temperature, °F	c^*, (10 s after startup) ft/s	c^*, (just before shutdown) ft/s	Initial bed temperature, °F
1	152	325	83	4270	3690	55
2	46	315	79	3930	3780	77
3	95	310	71	4075	3550	77
4	73	305	69	3880	3660	72
5	307	300	63	3600	1812	81
6[a]	345	300	55	2550	1578	65
7[b]	518	300	92	4250	4270	66
8	130	240	57	3750	2100	60
9	50	240	57	2600	2100	80
10	50	210	57	2575	2120	130

[a]One-second shutdown and restart at $t = 38$ s and at $t = 204$ s.
[b]One-second shutdown and restart at $t = 456$ s.

Table 3. Additional tests for neat hydrazine with increased catalyst surface area

Run number	Time, s	Tank pressure, psig	Inlet propellant temperature, °F	c* at 10 s, ft/s	c* at shutdown, ft/s	Bed temperature before startup, °F
11	105	300	50	4068	4195	57
12	103	300	52	4175	4173	59
13	132	300	50	4204	4211	72
14	160	300	50	4208	4214	71
15	198	290	50	4178	4207	74
16	421	285	50	4164	4184	74
17	111	285	51	4188	4183	85
18	330	260	50	4167	4153	76
19	107	260	50	4066	4084	53
20	225	260	51	4063	4115	70
21	125	260	51	4057	4069	72

listed, that have made it the desired propellant for the TOPS mission. Some potential disadvantages are the substantial amounts of water vapor present in the decomposition products, a 400 to 600°F higher flame temperature, a lack of materials compatibility data, and the lack of operational experience. Of these, the most serious anticipated problem is the higher flame temperature. The Shell-405 spontaneous catalyst consists of an active metal impregnated on a high surface alumina carrier. However, the alumina undergoes a phase change from the γ–δ to the α phase (the most stable and compact form) at 2000 to 2200°F. This transition temperature is above the flame temperature of the neat hydrazine, but below that of the nitrate blend. The physical shrinkage and surface area reduction accompanying the phase change may cause wide variations in starting and operating characteristics when the nitrate blends are used.

Some preliminary firings were made with a bolt-up configuration of the *Mariner* Mars 1969 engine shown in Fig. 2. The objectives were to determine the effects of the nitrate propellant on the starting and steady state operation characteristics of the Shell-405 catalyst. Basic information such as number of starts obtainable and combustion efficiency in various catalyst bed configurations was desired. The bed configurations and lengths tested are shown in Table 4. Two important results of the testing were as follows:

(1) Five starts and a total of 240 s were obtained with an all Shell-405 configuration (configuration A of Table 4). Examination of the chamber revealed

that the upper bed retention screen was broken, and that part of the upper bed was dispersed into the lower bed. (The inability of thin screens to withstand repeated starts and firings of long duration is not unique to the nitrate propellant, but has been experienced with the neat hydrazine propellant as well. This problem will be eliminated in the future by going to a 0.125-in.-thick plate with screens spot-welded on both sides of the plate.) A sixth start would probably not have been successful.

(2) Only three starts, with a total of 300 s, were obtained with nonspontaneous H-7 catalyst in the lower bed (configuration E in Table 4). Examination of the chamber showed that the screen holding the upper bed was intact. Analysis of the Shell catalyst from the upper bed indicated that appreciable amounts of iron, nickel, and cobalt had been deposited onto the catalyst during firing.

Configurations B, C, and D in Table 4 comprised different catalyst bed mixes and different bed lengths. The engine used for these tests was too long for good performance because of the excess endothermic decomposition it engendered (Ref. 7). Therefore, performance is not reported in Table 4. The shorter catalyst bed configurations D and E did increase the outlet gas temperature however.

4. Discussion of Test Results

a. Neat hydrazine test. The first series of tests on the 23-lbf thrust engine using neat hydrazine exhibited evi-

Table 4. Various catalyst bed configurations tested with hydrazine/hydrazine nitrate

Configuration	Upper bed	Lower bed	L^*, in.	Number of starts	T out, °F	Comments
A	25–30 mesh Shell-405	1/8 × 1/8 in. Shell-405	64	5	1850	Total of 240 s
B	25–30/405	1/8 × 1/8 in. Shell-405	40	2	1770–1850	Leak in O-ring seal
C	25–30/405	1/8 × 1/8 in. HA-3	40	2	1710	Leak in O-ring seal; 342 psig pressure spike on start
D	25–30/405	1/8 × 1/8 in. HA-3	29	2	1850	Break in upper bed screen
E	14–18/405	3/16 in./H-7	29	3	1940–2240	Poisoning of catalyst suspected

dence of the washout phenomenon. For the initial condition of 0.069 lbm/in.^{2}-s bed loading, the predicted pressure drop across the lower bed was 43 psi. The recommended maximum pressure drop is 40 psi (Ref. 8), although values twice as high have been run for short durations. Since the TOPS application involves multiple starts for long durations, the pressure drop across the catalyst bed becomes a major concern. High pressure drop increases the rate of physical attrition of the catalyst bed, and therefore decreases bed life. The 8- to 12-mesh catalyst reduced the predicted pressure drop across the lower bed to 24 psi. However, the predicted required length of the catalyst bed increases as the specific surface area of the catalyst is reduced. The engine used for these tests (Fig.1) was originally designed for high response *transient* operation and had a total bed length of only 0.850 in. This is less than half the predicted required length (Ref. 8). Since the engine had shown no evidence of being unstable in previous tests with 14- to 18-mesh catalyst with a bed length shorter than the required value, the existing methods were unable to accurately predict what might happen. Specifically, the present tests have shown that the L^* parameter commonly used to correlate performance results is not sufficient in even conventional axial flow decomposition chambers, and probably rather meaningless in other types of injection-chamber geometry schemes. Some other parameter, including the effects of bed-loading, specific surface area, total catalyst volume, and residence time, might be more useful. More information concerning propellant and catalyst temperature effects on the mechanism of washout is needed.

There are other influence parameters that are known to affect the onset of washout. Among these are (1) water

content of the hydrazine, (2) total accumulated burn time, (3) number of cold starts, (4) inlet propellant temperature, and (5) injector and chamber design.

The next series of tests sought to reduce the number of variables known or suspected of influencing the onset of washout. The higher specific surface area 14 to 18 mesh catalyst was packed into the lower bed. Hydrazine with low water content (0.7%) was used. (MIL-P-26536 B specifies a maximum of 2.5% by weight soluble impurities.) Analysis of the hydrazine used for runs 11 through 21 showed the following: NH_3 0.3%; H_2O 0.7%; aniline 0.3%; N_2H_4 98.7%. The analysis for the first set of runs, 1 through 10, gave NH_3 0.4%; H_2O 1.9%; aniline 0.5%; N_2H_4 97.2%). The inlet propellant temperature was lowered to approximately 50°F to determine whether a serious problem existed at that temperature. The results are shown in Table 3 in the form of c^* data points 10 s into the run and again just before shutdown. As Table 3 shows, there was no decrease in performance even in the longest run of 421 s. The slight drop-off in c^* at the lower tank pressure (and therefore lower chamber pressure) is due to the increased endothermic ammonia dissociation, which is caused by the increased chamber residence time.

Thus, the two important results obtained from the testing are

(1) A washout phenomenon, that is, a large decrease in specific impulse in steady state operation can be encountered. This prenomenon is strongly dependent upon inlet propellant temperature and catalyst specific surface area; and is less dependent on prior catalyst history (total burn time, number of cold starts) and water content in the hydrazine.

(2) A nonoptimum 25 lbf thruster design has successfully completed a duty cycle which was 20% longer than the envisioned four-planet grand tour, with no degradation of performance under moderately severe conditions (50°F inlet propellant temperature).

b. Nitrate test. Multiple steady state firings for 30- to 60-s durations with an all Shell-405 catalyst bed configuration have been demonstrated. However, the severe thermal environment accelerates the deactivation and physical breakup of the catalyst so that it appears very doubtful that the 76% N_2H_4-24% $N_2H_4HNO_3$ could be used with the Shell-405 catalyst. Mixed catalyst beds, that is, a spontaneous upper bed of Shell-405, and a nonspontaneous lower bed of HA-3, or H-7 catalyst[4,5] are susceptible to catalyst poisoning, caused by the deposition of the metals from the nonspontaneous catalyst onto the Shell catalyst. Several alternative methods of using a nitrate blended monopropellant are recommended in *Subsection 5*.

5. Future Effort

More work is planned with neat hydrazine in coming months to investigate and characterize the effects of high vacuum on the catalyst bed integrity and on ignition behavior, and at the same time the effects on performance and washout of catalyst and propellant temperature. The induction time (time from liquid entrance into the chamber until noticeable pressure from gaseous decomposition products) has been found to be predictable, by using liquid residence time as determined from an analysis of liquid penetration into the pores (Ref. 9). This induction period is a strong inverse function of the liquid hydrazine inlet temperature. Pressure overshoots on ignition increase with increased induction time, but the magnitude of the overshoot is not as yet a predictable quantity. Other workers have shown that the catalyst bed temperature is also most important in determining ignition (Refs. 10, 11). Figure 4 shows the results of some tests both at sea level and in vacuo (Ref. 11). When the bed temperature is decreased to 40°F or lower, long ignition delays often occur. Thus, additional empirical work is needed in these areas to develop a

high degree of confidence in the engine design for missions to the outer planets.

The work planned with higher performing hydrazine blends will consist of (1) testing a thermal decomposition chamber with a pilot catalytic bed start chamber, (2) evaluating a "new" catalyst, (3) investigating a ternary blend of hydrazine, hydrazine nitrate, and water to give neat hydrazine performance with a lower freezing point, (4) analyzing new electric or electrolytic methods of initiating the thermal decomposition of hydrazine.

References

1. Pickering, W., "The Grand Tour," *American Scientist*, Vol. 58, No. 2, March–April 1970.

2. Lee, D. H., *Development of the Midcourse Trajectory-Correction Propulsion System for the Ranger Spacecraft*, Technical Report 32-335. Jet Propulsion Laboratory, Pasadena, Calif., March 1963.

3. *Mariner Mars 1964 Project Report: Mission and Spacecraft Development. Volume I. From Project Inception Through Midcourse Maneuver*, Technical Report 32-740. Jet Propulsion Laboratory, Pasadena, Calif., March 1, 1965.

4. *Mariner Venus 67 Final Project Report*, Technical Report 32-1203. Jet Propulsion Laboratory, Pasadena, Calif., June 15, 1968.

5. Morrisey, D. C., et al., "Development of the *Titan III* Transtage ACS Hydrazine Monopropellant Rocket Engine Modules," Paper 69-422, presented at the AIAA 5th Propulsion Joint Specialist Conference, U.S. Air Force Academy, Colo., June 9–13, 1969.

6. Steele, R., *Titan IIIC Hydrazine Attitude Control System Users' Manual*, MCR-69-543, page V-29. Martin Marietta Corp., Denver, Colo., November 1969.

7. Grant, A. F., *Basic Factors Involved in the Design and Operation of Catalytic Monopropellant–Hydrazine Reaction Chambers*. Report 20–77, Jet Propulsion Laboratory, Pasadena, Calif., Dec. 31, 1954.

8. Smith, W., *Development of Design and Scaling Criteria for Monopropellant Hydrazine Reactors Employing Shell-405 Spontaneous Catalyst*. Final Report under NAS 7-372, RRC-66-R-76 Volume II. Rocket Research Corp., Seattle, Wash., Jan. 18, 1967.

9. Kesten, A., *Study of Hydrazine Reactor Vacuum Start Characteristics*, First Annual Progress Report under NAS 7-696. United Aircraft Research Labs, East Hartford, Conn., December 1969.

10. Carlson, R. A., and others, *Space Environment Operation of Experimental Hydrazine Reactors*, Final Report 4715.3.68.27, Contract NAS 7-520. TRW Systems, Redondo Beach, Calif., July 1968.

11. Greer, H., *An Investigation of the First Pulse Characteristics of Monopropellant Hydrazine Reactors*, SAMSO-TR-69-244. Aerospace Corporation, Los Angeles, Calif., July 30, 1969.

---

[4]A JPL designed catalyst, 1/8 x 1/8-in. cylinders of alumina impregnated with nickel, iron, and cobalt.

[5]Similar to HA-3, but 1/4-in.-diameter spheres.
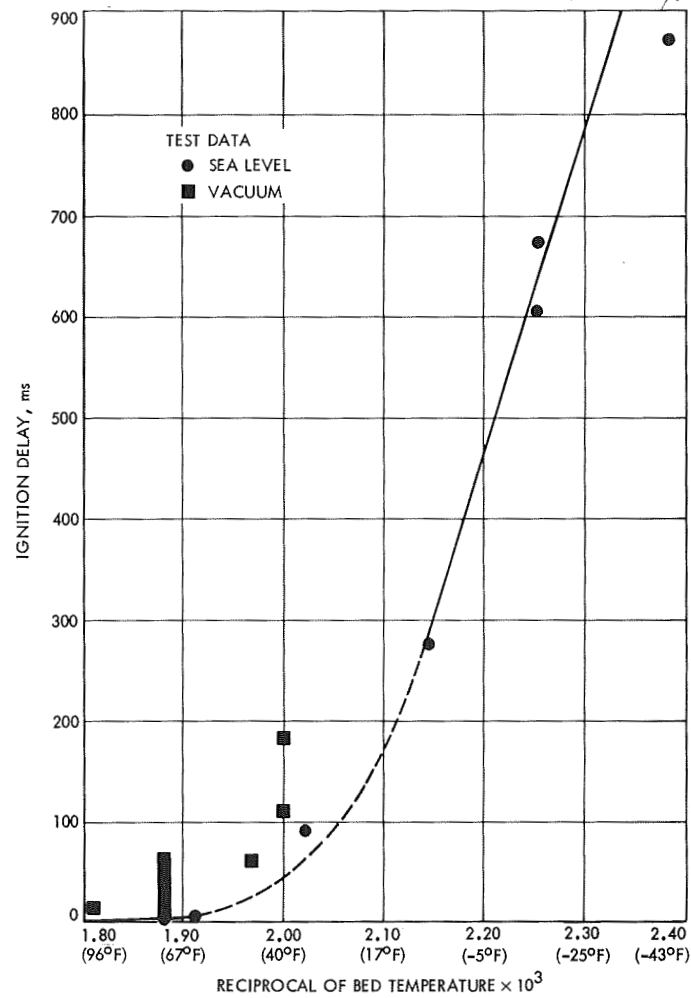
Fig. 4. Ignition delay vs catalyst bed temperature

XXII. Navigation and Mission Design
MISSION ANALYSIS DIVISION

A. Possible 1975 Jupiter–Pluto Gravity Assist Trajectories, W. Stavro

1. Introduction

A preliminary analysis was performed to determine if there are any possible Jupiter-to-Pluto trajectories for the 1975 opportunity. Both Flandro (Ref. 1) and Wallace (SPS 37-54, Vol. III, p. 35) mention that such trajectories are possible in 1975, 1976, 1977, 1978, and 1979. The 1977 opportunity was determined as the optimum launch year, and some trajectory data were given for that mission. No comment was made about the other opportunities.

2. Analysis

A patched conic computer program, SPARC,[1] was used to search for any possible Jupiter–Pluto trajectories. This is done by matching the Jupiter arrival energy C_3 with the required energy to continue to Pluto. Once the energy at Jupiter is equal to or greater than the required energy to continue to Pluto, the program will produce trajectory data for the two-planet trajectory. The program also produces the minimum energy (C_3) required at a specified arrival date at Jupiter to continue to Pluto regardless of whether that energy is available.

Figure 1 is a plot of launch date vs arrival date for the 1975 Jupiter opportunity showing contours of injection energy C_3 and arrival hyperbolic excess velocity V_∞. The *arrival* energy C_3 at Jupiter may be obtained from that figure by squaring the hyperbolic excess velocity, i.e., $C_3 = V_\infty^2$. Figure 2 shows the minimum C_3 value required at Jupiter to continue to Pluto vs arrival date at Jupiter.

In Fig. 1, an area is marked *ridge*. This is the limit that separates Type I trajectories, those with heliocentric transfer angles of less than 180 deg, from Type II trajectories, those with heliocentric transfer angles greater than 180 deg. Around 180 deg, the spacecraft must leave the ecliptic in order to fly by the target planet. To do so requires an extremely large injection energy. Thus the characteristics of trajectories launched in the ridge area are that they have large inclinations and extremely high injection energies.

The trajectories investigated by SPARC ranged in earth launch date from May 17, 1975 to July 31, 1975; and in Jupiter arrival date from July 10, 1976 to July 22, 1978. In its search for Jupiter–Pluto trajectories, SPARC found two kinds of possible trajectories:

(1) Those that were launched in the ridge area.

(2) Those that had Type II earth–Jupiter legs with very late Jupiter arrival dates.

---

[1]Derderian, M., *Space Research Conic Program, Phase III*, April 1968 (JPL internal document).

Fig. 1. 1975 Jupiter opportunity showing C_3 and V_∞ contours
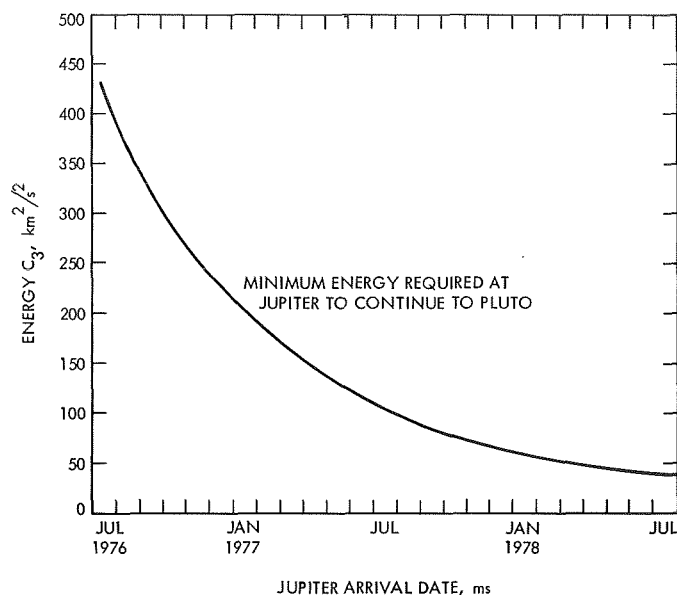
Fig. 2. Minimum C_3 required at Jupiter to continue
to Pluto

Type I earth–Jupiter legs with even later Jupiter arrival dates should also produce possible trajectories, but these combinations were outside the range of the SPARC search.

3. Ridge Trajectories

Because of high arrival energies, some of these trajectories could be continued to Pluto. Figure 3 shows a heliocentric ecliptic view of a typical, converged-ridge trajectory. Figure 4 shows a view of the same trajectory but looking *along* the ecliptic plane, and shows how the trajectory goes out of the ecliptic plane. This particular trajectory (marked with an X in Fig. 1) has an inclination of 31.7 deg, an injection energy of 412.5 km²/s² and a launch period of *one* day. Note that even though ridge trajectories are *possible*, they are unattractive for a mission because they require extremely high injection energies and have very short launch periods (1 day typically, 2 days maximum).

4. Type II Earth–Jupiter Leg Trajectories

Possible Jupiter–Pluto trajectories were found to exist for very late arrivals at Jupiter by using a Type II trajectory for the earth–Jupiter leg. A set is shown in Fig. 1 for a Jupiter arrival date of August 1, 1978. For a launch C_3 value of 153 km²/s², one can achieve a launch period of 15 days; and for a C_3 value of 120 km²/s², a launch period of 5 days.

EARTH LAUNCH: JUL 8, 1975
JUPITER ARRIVAL: JUN 12, 1978
PLUTO ARRIVAL: JUN 20, 1991
$C_3 = 412.5 \text{ km}^2/\text{s}^2$
LAUNCH PERIOD = 1 day
HELIOCENTRIC TRANSFER ANGLE = 180.2 deg
INCLINATION = 31.7 deg
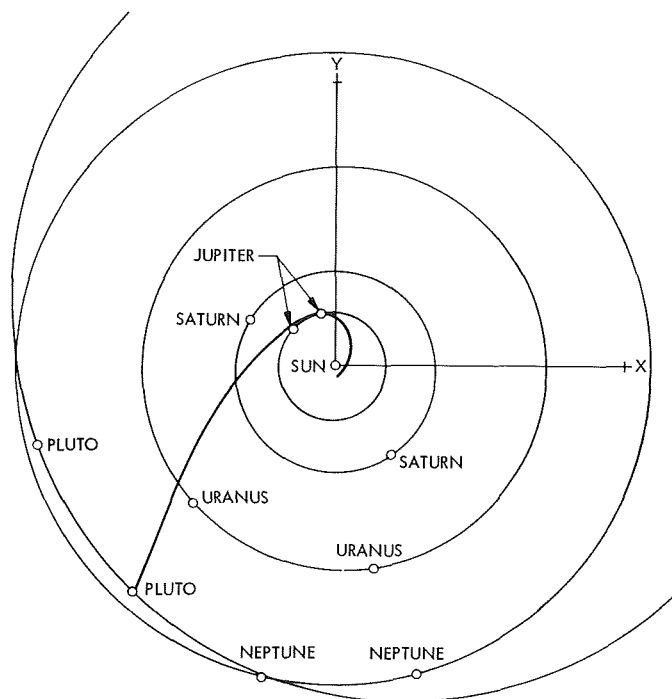
Fig. 3. Heliocentric ecliptic view of a possible 1975
Jupiter–Pluto ridge trajectory

Figure 5 shows a heliocentric ecliptic plot of the trajectory in this set with the minimum C_3 value. The heliocentric transfer angle is 220.6 deg for the earth–Jupiter leg. The flight time to Pluto is 30 years!

5. Conclusion

It is concluded from this analysis that a 1975 Jupiter–Pluto mission is not feasible. This can be determined by close inspection of Figs. 1 and 2. Looking at early arrivals at Jupiter (this is usually where attractive trajectories are found, e.g., the 1977 Jupiter–Pluto mission discussed in Ref. 1), we note the following: an arrival of August 9, 1976 at Jupiter has a C_3 value of approximately 145 km²/s² for a launch period of 8 days. The hyperbolic excess velocity (see Fig. 1) is approximately 16 km/s for this arrival date; i.e., the arrival energy is $16^2 = 256$ km²/s² in order to continue to Pluto and, therefore, a two-planet mission is not possible. By look-

ing at Figs. 1 and 2, we can inspect other arrival dates and conclude that no combination of low launch energy and early arrival date results in a possible Jupiter–Pluto trajectory.

Reference

1. Flandro, G. A., "Fast Reconnaissance Missions to the Outer Solar System Utilizing Energy Derived from the Gravitational Field of Jupiter," *Astronaut. Acta*, Vol. 12, No. 4, 1966.
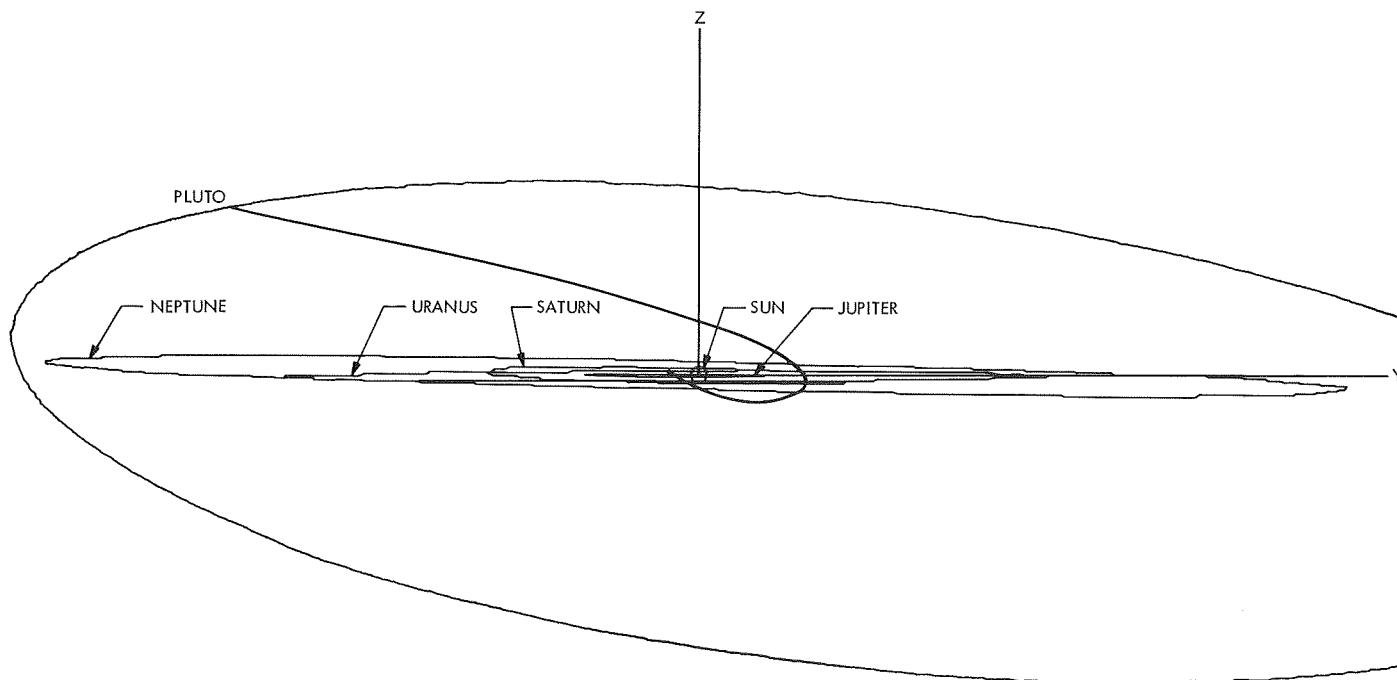
Fig. 4. View along the ecliptic of ridge trajectory

EARTH LAUNCH: JUN 14, 1975
JUPITER ARRIVAL: AUG 1, 1978
PLUTO ARRIVAL: JUN 17, 2005
$C_3 = 108.5 \text{ km}^2/\text{s}^2$
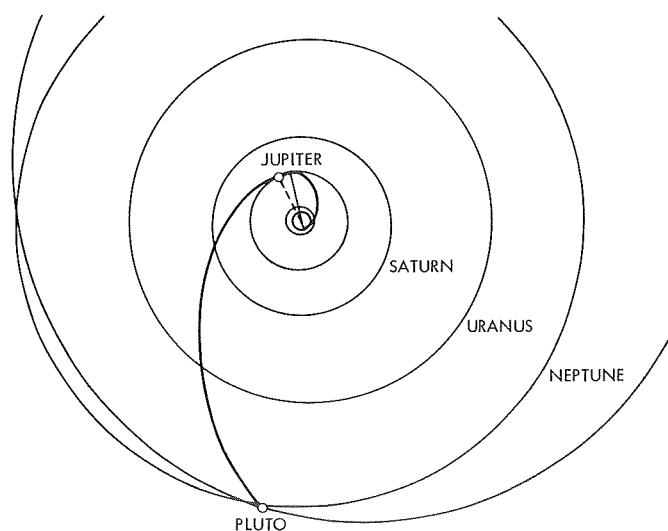
Fig. 5. Heliocentric ecliptic plot of a possible 1975 Jupiter–Pluto mission (Type II earth–Jupiter)

Subject Index

Subject Index (contd)

Subject Index (contd)

Subject Index (contd)